Tectonic Geomorphology

Douglas W. Burbank
Robert S. Anderson

Blackwell Science

TECTONIC GEOMORPHOLOGY

Douglas W. Burbank
Department of Geosciences
The Pennsylvania State University

Robert S. Anderson
Department of Earth Sciences
University of California, Santa Cruz

TECTONIC GEOMORPHOLOGY

TECTONIC GEOMORPHOLOGY

Douglas W. Burbank
Department of Geosciences
The Pennsylvania State University

Robert S. Anderson
Department of Earth Sciences
University of California, Santa Cruz

BLACKWELL PUBLISHING
350 Main Street, Malden, MA 02148-5020, USA
9600 Garsington Road, Oxford OX4 2DQ, UK
550 Swanston Street, Carlton, Victoria 3053, Australia

First published 2001 by Blackwell Science Ltd

7 2008

Library of Congress Cataloging-in-Publication Data

Burbank, Douglas West.
Tectonic geomorphology / by Douglas W. Burbank and Robert S. Anderson.
p. cm.
Includes bibliographical references (p.).
ISBN 978-0-632-04386-6
1. Geomorphology. 2. Geology, Structural. I. Anderson, Robert S., 1951-
II. Title.
GB401.5 .B86 2001
551.41–dc21 00-063021

A catalogue record for this title is available from the British Library.

Set by Software Services
Printed and bound in Singapore
by Fabulous Printers Pte Ltd

The publisher's policy is to use permanent paper from mills that operate a sustainable forestry policy, and which has been manufactured from pulp processed using acid-free and elementary chlorine-free practices. Furthermore, the publisher ensures that the text paper and cover board used have met acceptable environmental accreditation standards.

For further information on
Blackwell Publishing, visit our website:
www.blackwellpublishing.com

To Rachel and Suzanne, Helen and Jack, Flodie and Andy

CONTENTS

Preface viii

CHAPTER 1: Introduction to Tectonic Geomorphology 1

CHAPTER 2: Geomorphic Markers 13

CHAPTER 3: Establishing Timing in the Landscape:—Dating Methods 33

CHAPTER 4: Stress, Faults, and Folds 53

CHAPTER 5: Short-Term Deformation: Geodesy 85

CHAPTER 6: Paleoseismology 105

CHAPTER 7: Rates of Erosion and Uplift 131

CHAPTER 8: Holocene Deformation and Landscape Responses 159

CHAPTER 9: Deformation and Geomorphology at Intermediate Time Scales 175

CHAPTER 10: Tectonic Geomorphology at Late Cenozoic Time Scales 201

CHAPTER 11: Numerical Modeling of Landscape Evolution 231

References Cited 251

Index 267

PREFACE

No one can gaze at satellite images of the earth's surface without being struck by the crumpled zones of rocks that delineate regions of ongoing and past tectonic deformation. Landscapes in tectonically active areas result from a complex integration of the effects of vertical and horizontal motions of crustal rocks and erosion or deposition by surface processes. In a sense, many landscapes can be thought of as resulting from a competition among those processes acting to elevate the earth's surface and those that tend to lower it. The study of this competition and the interpretation of the geodynamic and geomorphic implications of such landscapes is the focus of tectonic geomorphology.

Tectonic geomorphology is a wonderfully integrative field that presents stimulating challenges to anyone trying to extract information from deforming landscapes. Consider, for example, a typical subject for a tectonic geomorphic study: a growing fold in the hangingwall of a thrust fault. The fault cuts the surface along much of its length, but diminishes in displacement towards its tip, where no surface break is present. How is the shape of the fold related to the mechanical properties of the faulted material? How much slip occurs in an individual earthquake on that thrust fault and what is the detailed pattern of deformation? Is a similar pattern of deformation repeated in successive earthquakes? What is the interval between earthquakes? Can the preserved structural form of the fold be explained as the sum of deformation during earthquakes alone, or is there significant interseismic deformation? How is the surface of the fold modified by erosion and deposition as it grows in length and height, and are there systematic changes along the fold that define a predictable evolutionary pattern of the landscape above such faults? Are the patterns and rates of erosion influenced more by tectonic or climatic forcing? What are the relative and absolute rates of rock uplift and erosion within the hangingwall and how is any imbalance reflected by the resulting landscape? In order to answer these questions, one has to draw on an understanding of paleoseismology, geodesy, structural geology, geomorphology, geochronology, paleoclimatology, stratigraphy, and rock mechanics, because each underpins some aspects of the interplay of tectonics and erosion. Key parts of the answer to each question are embedded in the landscape and are the subject of tectonic geomorphology.

Although efforts to interpret the processes that generate dynamic landscapes are not new, several key advances in the past few decades have provided a more robust foundation for rigorous analysis, and have opened up entirely new avenues of research.

- The development of new chronologic techniques permits us to inject time control into many facets of a landscape that were formerly unconstrained. The plethora of new dating approaches underpins most of the success in defining rates of processes.
- Process-oriented geomorphic studies have served to improve our understanding of the physical basis of surface processes. Insights into the key physical phenomena that control erosion and sediment transport have led to the development of both conceptual and quantitative models that can be applied in landscape analysis.
- Understanding of the record of past climate change has deepened immeasurably, such that the magnitude and rate of past climatic variability is now better calibrated than ever before. The impact of climate change on surface processes and landform development can now be better addressed in this detailed framework.
- New geodetic tools are providing an incomparable overview of rates of deformation of the earth's surface. Not only can changes in distances between specific points be documented with unprecedented accuracy, but the spatial pattern of deformation following an earthquake can now be documented across vast areas.
- Paleoseismology, the study of the record of past earthquakes, has matured into a diverse discipline and has provided a basis for documenting the behavior of faults, their impact on adjacent landscapes, and the societal hazards they pose.
- Instead of conducting regional tectonic analyses, many structural geologists have focused increasingly on the physical characterization of faulting and folding, on scaling relationships, and on the interactions among faults. Such studies show how fundamental building blocks like faults evolve through time and influence patterns of deformation.

- The widespread availability of digital topography and the development of new ways to obtain accurate topographic data through forest canopies, clouds, and oceans has facilitated a time-efficient quantification of topographic attributes that was previously unattainable.
- The accessibility to high-speed computing has underpinned the development of numerical models that exploit the results of many of the fields enumerated above. More importantly than providing a means to numerically re-create some observation, these models facilitate exploration of the potential interactions, sensitivities, and response times among changing processes.

The list could be much longer, but the point is clear: this is a time of unusual opportunity in tectonic geomorphology. The confluence of new approaches, tools, and databases is leading to rapid changes in our understanding of how the surface of the earth evolves in regions of active tectonism. These topics are the focus of the present book.

This book is organized somewhat differently than most other books on this topic. The initial chapters are devoted to fundamental building blocks and individual disciplines in tectonic geomorphic studies: geochronology, structural characteristics of faults and folds, the nature of geomorphic "markers" that can be used to keep track of deformation, geodesy, paleoseismology, and strategies for calculating rock uplift and erosion rates. Rather than following these chapters with discussions of tectonic geomorphology in specific geomorphic settings, such as fluvial or coastal environments, we have chosen to view the landscape within different time frames, ranging from $<10^4$ yr to more than 1 million years. The choice of each time window is not arbitrary, but instead reflects our understanding of how the tectonic and geomorphic information that can be extracted from a landscape varies as a function of time. In our view, these time scales reflect the relative dominance of surface or tectonic processes in shaping a landscape, the degree to which a landscape preserves the record of individual or small groups of events, and the time scale of interactions between climate, erosion, and tectonics. Contrasting types of tectonic geomorphic information are embedded in landscapes at these different time scales. The appropriate questions to ask and the proper techniques for extracting answers also differ as a function of time.

The reasoning behind this subdivision of our text may become more clear if one again considers the fold growing above a thrust fault. Individual earthquake ruptures occur at Holocene time scales. Essentially instantaneous, co-seismic deformation changes geomorphic gradients and forces adjustments within the geomorphic system. Just after the earthquake, the entire displacement field will be almost perfectly recorded by the deformed ground surface and consequently provides an excellent opportunity to delineate relationships among rock properties, displacement gradients, and seismic characteristics. Over the ensuing centuries, fault scarps will degrade, and geomorphic processes will modify the hillslopes and the channels of the landscape toward a new equilibrium with the altered geometry of the surface (until the next earthquake induces another cycle of adjustment). Throughout this interval, the average geomorphic surface is likely to mimic the aggregate strain accumulated over several seismic cycles. At time scales of 100,000 years or more, major swings in the climate will have occurred, dozens of earthquakes will have progressively deformed the fold, and geomorphic processes will have incised uplifted surfaces of the fold. The geomorphic surface is less likely to mimic the strain field, and climatic changes are likely to have created a distinctive imprint on the fold's surface. The steepest portions of a river crossing the fold may now occur over the fold crest, rather than on the forelimb of the fold. At these time scales, the geomorphic system associated with the fold will evolve as the structural relief increases and the fold propagates laterally. At intervals of a million years, it is likely that the blind thrust beneath the fold has linked up with other faults, or has died, or is now embedded in a series of growing structures. The topography and the regional pattern of accumulated strain may be largely decoupled, such that the highest topography may not match the structural crest of the fold. But the gradients of rivers, the presence of water gaps, and the spatial array of geomorphic elements, such as catchment geometries or slope distributions, will reflect the long-term evolution of the fold-and-thrust belt.

The final chapter of this book is devoted to numerical modeling of landscapes. These models have now evolved to be able to handle the complexity of the deformation fields, and the temporal and spatial complexity of the geomorphic processes that modify a landscape. They can be used to test old conceptual models of landscape evolution, to generate new strategies for field documentation of the relevant processes and their rates, and as educational tools to allow visualization of landscape evolution. We do not attempt to provide a complete guide or a cookbook for such modeling. Rather, this chapter represents an introduction to different types and scales of numerical models, and provides what could be termed "building blocks" for landscapes: the displacement fields associated with individual faults, and with orogen-scale deformation

fields at depth, and the "rules" commonly used for movement of regolith on hillslopes, the transport of sediment in channels, and bedrock incision of streams. We illustrate the linkage of tectonic and geomorphic process models with examples ranging from simple models of evolving fault scarps to more complex models of entire tectonically active landscapes.

The field of tectonic geomorphology has been advancing and expanding so rapidly that it has been difficult to keep this text abreast of the latest developments. Despite its obvious shortfalls, it is our hope that this text will serve as a useful springboard for those geologists wanting an introduction to tectonic geomorphology and as a helpful reference for those of us who are pursuing research in aspects of this broad, highly integrative, and rapidly evolving field. It is our hope that upper level undergraduates and students early in their graduate careers will find this to be a useful and accessible introduction to tectonic geomorphology.

Many people played a role in the production of this book. John Grotzinger invited one of us (DWB) to come to MIT as a Crosby Lecturer and to develop a course on tectonic geomorphology. The idea of this book sprang from those lectures and the realization that there appeared to be a need for such a text. Doug Hammond and Bob Douglas at USC and Dick Walcott at Victoria University provided logistical support during various stages of writing, while Bill Bull, Steve Wells, Ed Keller, and Paul Hoffman provided early suggestions regarding content and format. We greatly appreciate the wisdom and guidance of our own teachers and research advisors, who set us on a path that has allowed us to range widely through the disciplines of the earth sciences. These include Steve Porter, Tom Dunne, Noye Johnson, Bernard Hallet, Jim Smith, Peter Haff, and Gary Johnson. Our research collaborators, colleagues, and many former students provoked us with their ideas and engaged us in discussions that helped shape this book. In particular, we would like to thank Nic Brozović, Andrew Meigs, Julio Friedmann, Jaume Vergés, Richard Beck, Fritz Schlunegger, Ian Brewer, Mike Ellis, Jeff Marshall, Alex Densmore, Greg Hancock, Eric Small, Dan Orange, Kelin Whipple, Liz Safran, Eric Fielding, Jerôme Lavé, Niels Hovius, Rudy Slingerland, Hugh Sinclair, Marith Reheis, Peter Molnar, Euan Smith, Ann Blythe, Merri Lisa Formento-Trigilio, and Jamie Shulmeister. The extensive redrafting of figures would not have occurred without the dedicated efforts of Allan Tucker, Remberto Magbanua, and Karen Bezusko. The technical production of this book has benefited from the assistance of Doug Myers and the capable staff at Blackwell, particularly Jane Humphreys, Jill Connors, Nancy Duffy, and Irene Herlihy. Many ideas and concepts in this book were developed during research supported by the National Science Foundation (EAR 92-2056, 96-14765, 96-27865, 97-06269, 99-09647) and NASA (NAG W-3762, 5-2191, 5-7781). Finally, we would like to thank our families and particularly our spouses for their support of our efforts and their tolerance of our preoccupations.

D. W. B.
R. S. A.

CHAPTER 1

Introduction to Tectonic Geomorphology

The unrelenting competition between tectonic processes that tend to build topography and surface processes that tend to tear them down represents the core of tectonic geomorphology. Anyone interested in the earth's surface has wondered why it has the shape it does and what forces are responsible for that shape. For more than a century, this natural curiosity has inspired numerous conceptual models of landscape evolution under varied tectonic and climatic regimes. In the past, our ability to assign reliable ages to geomorphic and tectonic features was very limited. In the absence of a chronologic framework, it was nearly impossible to test competing concepts of landscape evolution. As a consequence, these unquantified models were often viewed skeptically and treated as speculative notions.

During the past few decades, the development of many new techniques for determining the ages of landscape features, for assessing the mechanisms and rates of geomorphic processes, and for defining rates of crustal movement, has helped revitalize the field of tectonic geomorphology. It is now possible to quantify at the scale of millimeters how rapidly a given site is moving with respect to another and how those rates of relative convergence or divergence are partitioned among various faults and folds. Similarly, we can now quantify how rapidly rivers and glaciers are incising into bedrock and the rates at which landslides are stripping mountain slopes. Clearly, the merger of such data sets can underpin a new understanding of the balance between the rates at which crustal material is added at a given site and the rates at which this material is eroded away. Defining this balance and interpreting the landscape that results from this competition represents a major component of modern tectonic geomorphology.

One of the remarkable attributes of tectonic geomorphology is the breadth of fields it encompasses. Few other fields easily blend topics as disparate as seismology, Quaternary climate change, geochronology, structure, geodesy, and geomorphology. In fact, such breadth makes this field particularly exciting, as new data and ideas emerge from fields as diverse as paleobotany and fault mechanics. This diversity also presents a formidable challenge, because successful studies commonly require blending of appropriate data from specialized fields that were traditionally considered to be unrelated. Certainly specialists in well-established disciplines like structural geology or stratigraphy often make important contributions to tectonic geomorphology. The fundamental leaps in our understanding, however, often emerge from an integration across several disciplines.

This book is intended primarily for readers who are familiar with basic geomorphological and structural concepts and terms. Although we define many terms and review basic concepts and models throughout the book, we assume that our audience understands many commonly used geomorphological and structural terms, such as base level or conjugate faults. For those readers without such a background, occasional reference to a basic geomorphological or structural text will probably be helpful.

It is beyond the scope of this book to cover the contributions of each of the subdisciplines of tectonic geomorphology. Instead, we focus on some of the key tools, approaches, and concepts that have served to advance tectonic geomorphologic studies during the past decade. There are several building blocks that underpin such studies. These include a knowledge of how the earth deforms both during earthquakes and between them, what sorts of features can be used to track deformation in the past, and what types of techniques are useful for dating features of interest.

Initially, we introduce geomorphic markers: landscape features, such as marine or fluvial terraces, that

can be used to track deformation. Prior to deformation, surfaces of these markers represent planar or linear features with a known geometry that can be predictably tracked across the landscape. Faulting or folding can subsequently deform such markers. Documentation of any departure from their unperturbed shape can serve to define the magnitude of deformation. Consequently, the recognition and measurement of such displaced or deformed markers is critical to many tectonic geomorphic studies. These are the raw data that cry out for interpretation.

In order to define rates of deformation, it is necessary to define both the timing and amount of deformation. There are dozens of techniques that have been used successfully to define the age of displaced features. In a chapter on dating, we present examples of some of the more commonly used techniques, and we try to convey a sense of the situations in which use of each technique would be appropriate. For each technique, we provide its conceptual underpinnings, discuss some of its limitations, and describe what data are actually collected in the field.

The oft-used term *tectonic processes* is a grab-bag expression that encompasses all types of deformation, including the motion of tectonic plates, slip on individual faults, ductile deformation, and isostatic processes. We concern ourselves here only with those processes that are most relevant to relatively localized deformation of the earth's surface. In this book, we have generally chosen to ignore deformation and surface processes related to volcanism. Many of the concepts that are developed here are descriptive of landscape responses to volcanic processes, but the time and spatial scales are commonly different between volcanic and non-volcanic settings.

Because many landscapes have been built by the accumulated movements of individual faults and folds, we describe some current concepts from seismology and structural geology concerning co-seismic displacement, the scaling of fault slip, and geometries of deformation in different tectonic settings (compressional, extensional, and strike-slip environments). Much has been learned about ongoing deformation of the earth's surface through geodetic studies: detailed surveys that delineate regional to local crustal displacements, often at time scales of a few years. During the past decade, the increasingly widespread application of new techniques, such as global positioning systems (GPS) and radar interferometry, has yielded spectacular new images of current crustal motions. In a chapter on geodesy, we describe these techniques and some of the insights gained from them. In many ways, it is in the context of this greatly improved understanding of modern deformation that we now can make the largest strides in interpreting past deformation and landscape evolution.

Naturally, discovering ways to measure the amount and rate of erosional losses from an area or to define changes in the height of the earth's surface in that same area through time lies at the heart of many tectonic geomorphic studies. Armed with new tools for dating and with digital topographic data bases, we can now address these topics more accurately than in the past. In a chapter on erosion and uplift, we describe several strategies for quantification of rates of erosion, surface uplift, and rock uplift, and illustrate how these can be synthesized to examine the balance between building and tearing down of topography.

In the latter half of this book, we step away from a focus on the key building blocks and instead introduce concepts and examples of landscape evolution and tectonic interpretations at different time scales. Moreover, rather than examining specific geomorphic environments or topics, such as the ways in which rivers and fluvial features can provide insights on tectonic processes, we focus on more integrated studies. The key issues can be encompassed by the questions, "What information from the earth's surface improves our understanding of the nature of the interactions between tectonics and geomorphological processes?" and "How do we interpret preserved geomorphic features in order to reveal rates and patterns of tectonic deformation in the past?" The more recent record is often best suited to answer the first question, whereas great value comes from studies that are able to answer the second question for intervals in the distant past.

There is a natural, time-dependent progression in the nature of tectonic geomorphic landscapes and the insights that can be gained from them. Perhaps surprisingly, part of this progression is dictated by past climate changes (Fig. 1.1). At Holocene time scales, we are confined to a postglacial era in which climatic conditions have varied relatively little. At time scales of 100,000 years or more, complete or multiple glacial–interglacial cycles have occurred. Large-scale changes in sea level, the size of glaciers, and the discharge of rivers at these time scales leave strong imprints on the landscape. It is often these climate cycles that generate the geomorphic markers, in the form of moraines or marine and fluvial terraces, that are so important in the field of tectonic geomorphology. At time scales of a million years or more, numerous climatic cycles create a more "time-averaged" landscape.

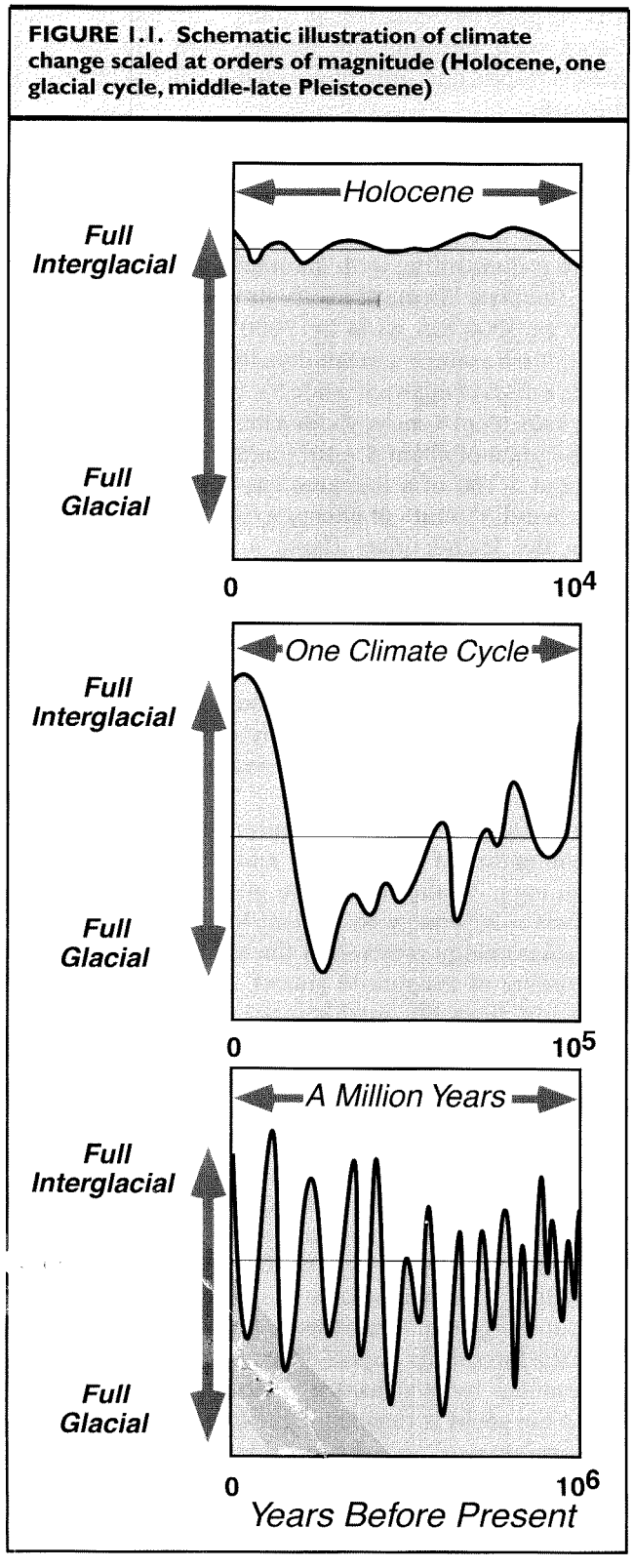

FIGURE 1.1. Schematic illustration of climate change scaled at orders of magnitude (Holocene, one glacial cycle, middle-late Pleistocene)

These different time scales also often create a natural segregation of the focus of tectonic geomorphic studies. At Holocene time scales, cause and effect can be examined rather directly. For example, if faulting causes the land surface to tilt in a given direction, the timing and rate of diversion of rivers in response to that tilt can be measured. Present rates of crustal deformation can be compared against the sediment load of rivers. Often geomorphic markers, such as river terraces, are almost untouched by erosion and can function as pristine recorders of Holocene deformation. The strength of Holocene studies is that the record is often most complete, the dating is most precise, rates of many competing processes can be directly measured, and their interactions can be examined. There are at least three potential disadvantages of Holocene studies. First, the rates of tectonic processes may be sufficiently slow or the occurrence of deformational events, such as earthquakes, may be sufficiently rare that the tectonic signal is obscure. Second, rates of geomorphic processes during Holocene (interglacial) times may not be very representative of long-term rates. Third, the time it takes for geomorphic systems to respond to a change imposed by tectonic forcing can be longer than the Holocene. Thus, the geomorphic system may be in a state of transition with respect to tectonic perturbations imposed upon it.

As described in subsequent chapters, the limited precision of most dating techniques means that, as one delves beyond the Holocene and farther into the past, it becomes progressively more challenging to associate specific events in time. Thus, it can be difficult to define direct responses to individual forcing events. On the other hand, major climate changes often have created robust geomorphic markers, such as river terraces, that persist as recognizable features and provide a lengthy time framework within which to document patterns of deformation. At short time scales, tectonic forcing is commonly unsteady, because it results from discrete events, such as earthquakes, that are widely separated in time. At time scales of more than 10^4 years, this unsteadiness is commonly smoothed out, and average rates of deformation can be defined. Because many geomorphic markers persist in the landscape at time scales of single glacial–interglacial cycles, this is an ideal interval within which to document past rates of tectonic forcing. At still longer time scales, erosion has typically removed most markers that are more than about 10^5 years old. Yet, it is at this time scale that large-scale landscape responses to sustained tectonic forcing can be clearly seen. Typically this requires treating

landscapes at a coarse spatial scale in order to examine the products of tectonic–geomorphic interactions, such as the topographic characteristics of a collisional mountain belt or the broad swath of deformation that occurs as a continent passes over a hot spot.

We conclude with a chapter on numerical modeling of tectonically active landscapes. In contrast to efforts aimed at directly measuring tectonic geomorphic processes, the interactions between deformation and surface processes can also be studied theoretically. If we could write numerical rules that represent phenomena such as the displacement of the crust due to faulting or the erosion and redistribution of mass due to surface processes, we could proceed to investigate interactions among these processes. Consider, for example, displacement on a normal fault that bounds the front of a mountain range. The topographic offset will change the gradient of any river crossing the fault, and a numerical rule for river incision could predict how that reach of the river would respond and how that response would be propagated upstream.

Rather complex models for landscape evolution in different tectonic environments have recently been formulated. It is not our intent to describe or compare these in detail. Instead, we describe several of the basic building blocks that could go into a numerical model, and illustrate some of the predictions of these models. In our view, the usefulness of numerical models is not in creating a reproduction of some actual landscape. Instead, it is providing a means to explore potential interactions within a landscape, so that we have a firmer basis for understanding how variables as diverse as crustal rigidity, susceptibility of bedrock to landslides, and the distribution of precipitation may interact with each other, perhaps in unexpected ways. Such models are meant to develop our insight into the complex interactions among the processes, and can serve to point toward measurements one might make in the field that would most efficiently constrain the process rates.

Energetics

Energy drives the interactions between tectonics and surface processes. In order to build topography, work must be done against gravity. The energy needed to accomplish this work comes ultimately from the conversion of a small fraction of the energy involved in the horizontal motions of the lithospheric plates that constitute the more rigid exterior of the planet. The energy driving plate tectonics comes from primordial heat associated with building the planet, from the decay of radioisotopes, and from phase changes in the interior of the earth.

It is perhaps surprising to cast the energy expenditure represented by plate motion in everyday terms. Consider, for example, a simple calculation of the kinetic energy of that part of the Indian plate lying south of where it is colliding with mainland Asia and building the Himalaya. We may specify its approximate dimensions as 3000 km wide by 7000 km long by 50 km thick. If we assume a mean density of 3000 kg/m^3, this yields a mass of approximately 3×10^{21} kg. Taking a mean plate velocity of 5 cm/yr yields a kinetic energy ($1/2\ m\ v^2$) for the plate of about 4×10^3 joules. This is equivalent to about 1/100 of a Snickers bar (10^6 joules)! On the other hand, the rate of energy expenditure required to move the Indian plate (force × distance/second) is equivalent to approximately 10^{13} joules/second or 10^7 Snickers bars/second! Over the past 50 million years, some tiny fraction (~1/100 of 1%) of that energy has been expended (or converted, really, to potential energy) in elevating the crust of the Himalaya and Tibet far above the geoid and thereby creating the world's largest topographic anomaly, averaging about 5 km above sea level.

The energy for driving surface processes derives from a combination of solar energy and gravitational potential energy. At the top of the atmosphere, the earth receives solar energy equivalent to about 1300 W m^{-2}. The solar energy received at the earth's surface is several orders of magnitude greater than the energy that leaks out from the earth's internal heat engine (~40 mW/m^2). All rocks that have been elevated above the geoid have a potential energy equivalent to the product of their mass, gravitational acceleration, and their height above the geoid ($PE = m\ g\ h$). The solar energy evaporates water and heats the air that carries the moisture with it as the air rises, expands, and cools. The water attains its maximum potential energy at the top of its atmospheric trajectory. When the vapor condenses and falls as precipitation, it converts some of its potential energy to kinetic energy that it delivers to the surface of the earth with the force of its impact. The potential energy that is represented by the mass of water at some elevation above the geoid is then available to be expended doing geomorphic work or to be lost through heat dissipation or frictional processes. Solar energy is also an important factor in chemical weathering processes, especially in any temperature-dependent reactions, as well as in

FIGURE 1.2. Classical models of tectonic forcing and landscape responses after the theories of Davis (top), Penck (middle), and Hack (bottom)

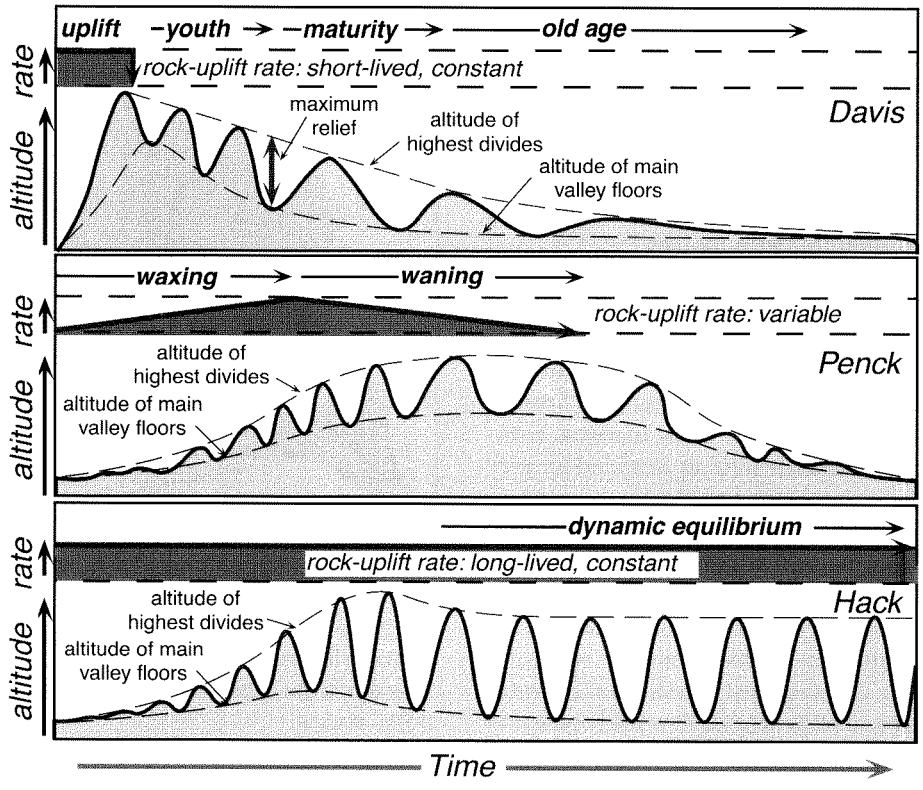

Note differences in the duration and rate of tectonic forcing (rock uplift) and the topographic response to different styles of rock uplift. Modified after Summerfield, 1991.

mechanical weathering processes, such as freeze–thaw cycles.

Active Tectonics and Models of Landscape Development

Sharp contrasts in the appearances of landscapes in a given climatic or tectonic regime inspired geologists in the past to devise schemes to explain those contrasts. One of the most prominent such geologists was William Morris Davis, who in the late 1800s and early 1900s developed the well-known geomorphic models showing a progression from "youth" to "maturity" to "old age." Living in the wake of the revolutionary ideas of Charles Darwin, it was perhaps natural to conceive of landscapes as evolving from one stage to the next. In Davis's models, tectonic forcing is an impulsive event that occurs at the beginning of the "geomorphic cycle." All of the building of topography occurs at the start of the cycle (Fig. 1.2). Subsequently, geomorphic processes attack and degrade the topography, with the end result predicted to be a peneplain. This view of landscape evolution prevailed through much of the 1900s and is still widely cited by introductory geology textbooks.

A new theory of landscape development that opposed Davis's models was promoted by Walther Penck in the 1950s. Rather than having all of the tectonic deformation at the beginning of a cycle, Penck suggested a more wave-like pattern of tectonic forcing through time. In this scheme, the magnitude of deformation gradually increases toward a climax and then slowly wanes away.

Instead of calling on an impulsive building of topography followed by long intervals of erosion, Penck's model invoked steadily increasing rates of deformation that would accelerate rock uplift and gradually build the topography toward a maximum state of topographic relief. Geomorphic processes were conceived as attacking the uplifting region throughout the period of mountain building, so that the resulting landscape could be interpreted as a product of this competition between deformation and erosion. As the rate of mountain building waned, erosion was proposed to overtake deformation rates, thereby causing a gradual reduction in the residual topography (see Fig. 1.2).

A third approach to landscape development was proposed by John Hack who suggested that, when rates of deformation and rates of erosion are sustained for long intervals, landscapes will come into a sort of balance or dynamic equilibrium. Given the finite strength of rocks, Hack realized that topography could not increase without limit, even if rates of tectonic forcing persisted for very long periods. At some point, as topography grew and grew, the relief on hillslopes would create forces exceeding the rock strength, and they would collapse. With continued uplift of the bedrock, additional slope failures would limit the height that the topography could attain. Eventually, the topography would enter into a rough steady state or a dynamic equilibrium. Consequently, in this model, rates of mountain building and rates of erosion would come into a long-term balance (see Fig. 1.2). Unlike the models of Davis or Penck, there is no need for rates of deformation to become negligible, or even to wane at all. Similarly, after attaining a maximum sustained topography, there is no need for the landscape to "evolve"; instead it simply fluctuates around an equilibrium topography until such time as the rates of tectonic forcing change.

One might wonder whether any of these theories are applicable to real landscapes. One way to consider this problem is to compare the time scales of deformation and of geomorphic responses. For example, an earthquake is a very impulsive event that "instantaneously" creates topographic change, say in the form of a fault scarp. If the time between earthquakes is long relative to the time it takes geomorphic processes to cause significant topographic evolution, the scarp will be degraded before the next earthquake. This could be thought of as a small-scale version of a Davisian scheme for landscape evolution. On the other hand, if the recurrence interval between earthquakes is short, then the scarp will be continuously refreshed and will not degrade in a predictable fashion toward a low-relief surface. In fact, some balance might be expected to develop between the renewal of the scarp by faulting and erosion of it during interseismic periods. Thus, even though the total displacement grows through time, the scarp itself might attain a "steady-state" shape.

FIGURE 1.3. Geomorphic elements of a drainage basin

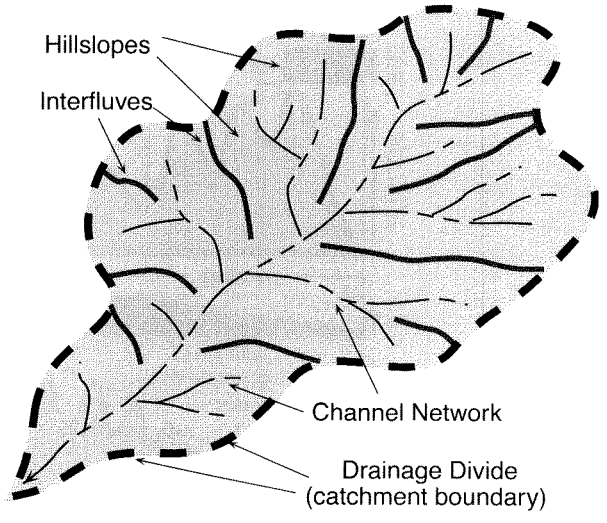

It is also useful to consider the response times or inertia of different elements in a geomorphic system. Consider, for example, a drainage basin in a mountain belt (Fig. 1.3). The basin consists of river channels, hillslopes, the crests of interfluves, and the drainage divide that defines the shape of the catchment. Some of these elements will respond more rapidly to changes imposed on them than will others. Suppose that, near its outlet from the mountains, this basin is bounded by a normal fault. How will the various basin elements respond to displacement on that fault? The channel that crosses the fault will "see" the displacement first. The local base level will have fallen abruptly, causing the river gradient to steepen locally and erosion of the channel to intensify. At this point, all other positions in the catchment will have been undisturbed by the faulting event, so the faulting elicits no initial geomorphic response. Subsequently, a wave of erosion of the channel bed can be expected to propagate up the fluvial system. As this channel erosion passes the base of an adjacent hillslope, it causes the hillslope gradient to increase and initiates a change in the rate of hillslope processes. These hillslope processes could eventually affect the interfluves and finally the shape of

the entire catchment. Large geomorphic elements, such as the catchment shape, are unlikely to be affected by individual seismic events. Thus, there is a clear hierarchy of response times (rivers respond sooner than hillslopes, etc.), and there is a hierarchy of topographic inertia (catchment shape is resistant to change, whereas river gradients are susceptible to small perturbations).

Consideration of the scaling of elements in a given geomorphic system; of response times or inertia of those elements with respect to imposed changes; and of the rates, magnitude, and duration of different styles of tectonic forcing suggests a way in which the apparently incompatible landscape evolution concepts of Davis, Penck, and Hack can be reconciled. In fact, recent numerical models of tectonically perturbed landscapes have explicitly addressed this problem. Using a surface-process model that links channel incision, sediment transport, and hillslope erosion, Kooi and Beaumont (1996) developed a model that predicts a lag between the onset of deformation and the response of the geomorphic system to that deformation (Fig. 1.4). The overall response of the geomorphic system and the magnitude of the lag depends strongly on the nature of the tectonic forcing. If the forcing is impulsive (à la Davis), then the topography is rapidly created and simply degrades through time. If the deformation increases to a maximum through time and then wanes (à la Penck), topography gradually builds in the face of progressively increasing rates of erosion. The maximum topographic expression occurs slightly after the rate of deformation begins to wane, because the rock uplift still outpaces the rate of erosion. Finally, in the latter half of the cycle, the topography wanes under gradually diminishing rates of erosion. If the tectonic forcing is continuously sustained, then the Kooi and Beaumont model predicts that, after an initial interval of building of topography, rates of rock uplift and erosion will become balanced (à la Hack), and the topography will attain a persistent dynamic equilibrium. A change in the rate of tectonic forcing would push the system toward a new equilibrium, whereas cessation of deformation would return the system to an almost Davisian state in which the topography is systematically degraded.

These predictions are simply the output of a numerical model that represents a great simplification of both tectonic and geomorphic processes. In fact, the physics of many of these processes are still poorly understood. Nonetheless, it is satisfying to think that the thoughtful, yet apparently contradictory, landscape-development models put forth during the past 100 years are indeed reconcilable

FIGURE 1.4. Schematic output of a process-response model in which the duration and magnitude of rock uplift (the vertical tectonic flux) is compared with the erosional sediment flux from the uplifted mountains

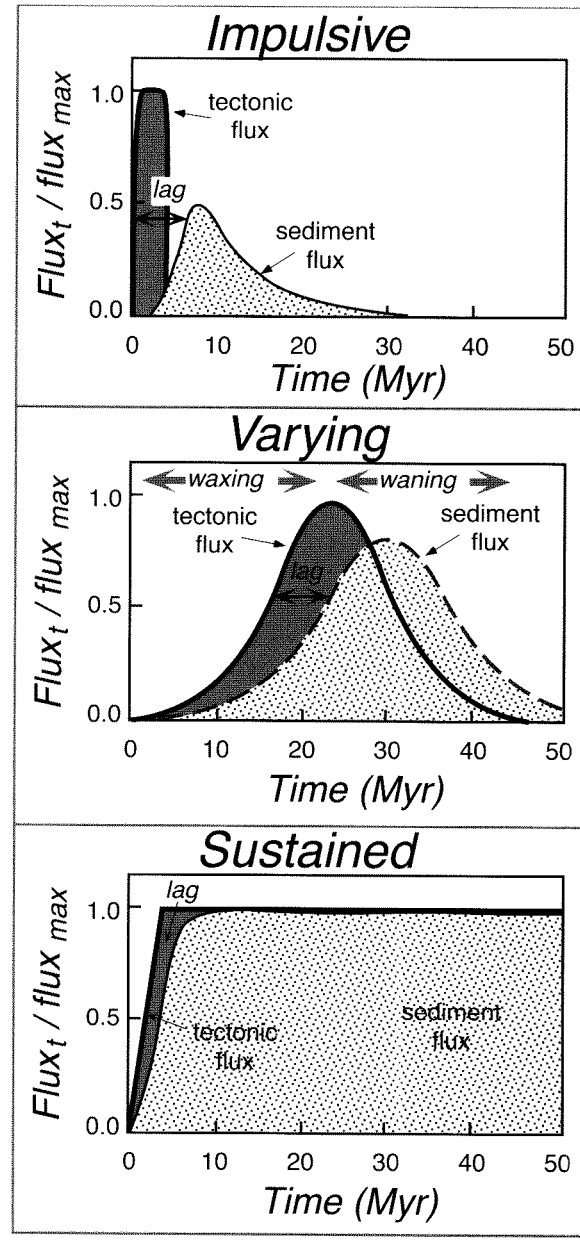

The three scenarios (impulsive, varying, sustained) are analogous to the models of Davis, Penck, and Hack. Note that the time lag between tectonic forcing and sediment response is variable. Modified after Kooi and Beaumont, 1996.

and that simple numerical models can help enhance our understanding of tectonically active landscapes.

Some Modern Controversies

At present, there are many lively controversies in tectonic geomorphology. Some of these provide an interesting backdrop for reading subsequent chapters of this book. For example, the history of Cenozoic cooling of rocks within many mountain ranges has been interpreted to suggest that the ranges experienced accelerated rates of uplift during late Cenozoic times. With increased recognition that this apparent increase was approximately coeval with the onset of the "Ice Ages," it was commonly believed that mountain uplift led to cooling and helped to precipitate the Ice Ages. In 1990, Molnar and England (1990) challenged this entrenched idea and suggested nearly the opposite: as climate changed to more glacial conditions in late Cenozoic times, enhanced rates of erosion within mountain belts caused increased rates of valley incision, which in turn incited isostatic uplift of the residual peaks. Although this can produce ranges with higher summits, it does not implicate tectonic uplift as the cause of climate change.

So, how do we tell whether the climate caused uplift of the summits or whether surface uplift of the ranges caused changes in climate? Potential resolutions to this quandary require many ingredients, including the nature and magnitude of changes in mean elevation of mountains, in rates of erosion, in climate, and in elevations of summits and valley bottoms. Moreover, we would like to know when and how rapidly changes took place. If you think carefully about any one of these ingredients, you quickly realize the reason why tectonic geomorphologic studies are often interdisciplinary in nature. Consider, for example, the concept of mean elevation of a range. Using digital topographic data, it is easy to determine modern mean elevations. But how do you determine mean elevations in the past? As described in subsequent chapters, approaches to calculating former altitudes range from paleobotanical to isotopic studies. Or, consider the effects of changes in climate. During Ice Age times, was there more precipitation or less? Did the expansion of glaciers lead to enhanced rates of erosion? There is intense interest in, and considerable argument about whether glaciers are effective agents of erosion in comparison to rivers. The controversy has spawned a flood of recent research into the physical and chemical processes involved in erosion of bedrock by both fluvial and glacial processes.

Can enhanced erosion drive uplift of mountain summits? Yes, but only if there is an increase in topographic relief associated with the erosion. In essence, there has to be less erosion of the summits than there is of the valley bottoms. Think about an ice cube floating in a drink (Fig. 1.5). Its upper surface is at a mean elevation equivalent to about 1/10th of its total thickness (equivalent to $[1-\rho_{ice}/\rho_{water}]$). If you were to cut canyons into the upper surface of the cube, the mean elevation of the cube's surface would decrease and the base of the cube would bob upward in the water in order to maintain the isostatic balance (maintaining 1/10th of the total mass above the water surface). If you could cut the canyons without "eroding" other parts of the upper surface of the cube, these remnants would actually rise higher than their original height in response to the lowering of the mean elevation.

Although melting of an ice cube demonstrates that peak uplift can occur due to enhanced erosion, has this commonly occurred in the past, is it related to a more "erosive" climate, and what are the magnitudes of the uplift of peaks involved? The common view has been that increased rates of erosion tend to increase topographic relief and, therefore, would promote the uplift of summits. On the other hand, theoretical studies of river profiles suggest that increased erosive power causes river gradients to decrease. If this is true, then in order to generate an increase in topographic relief in the landscape, hillslopes would have to be concurrently lengthened and steepened. Tectonic geomorphic studies that document the temporal evolution of both the valley bottoms and the adjacent hillslopes are needed to resolve these issues.

Another modern controversy in tectonic geomorphology revolves around earthquake prediction. Over the past two decades, a substantial research effort has focused on answering such questions as, "Which fault is most likely to rupture in the next large earthquake?", "When is that event likely to occur?", and "How large an earthquake can we expect to occur?" Many scientists would maintain that the best way to make such predictions is to understand the past history of faulting. Such topics fall into the realm of paleoseismology, a field that focuses on the reconstruction of past earthquakes in terms of their distribution in space and time, displacements along a fault, surface expressions of faulting, and interactions among faults. If paleoseismological studies were to indicate that successive ruptures of a particular fault occurred at regularly spaced intervals in time, it would then be possible to define a "recurrence interval."

FIGURE 1.5. Isostatic uplift of mountain summits due to enhanced erosion as exemplified by an ice cube

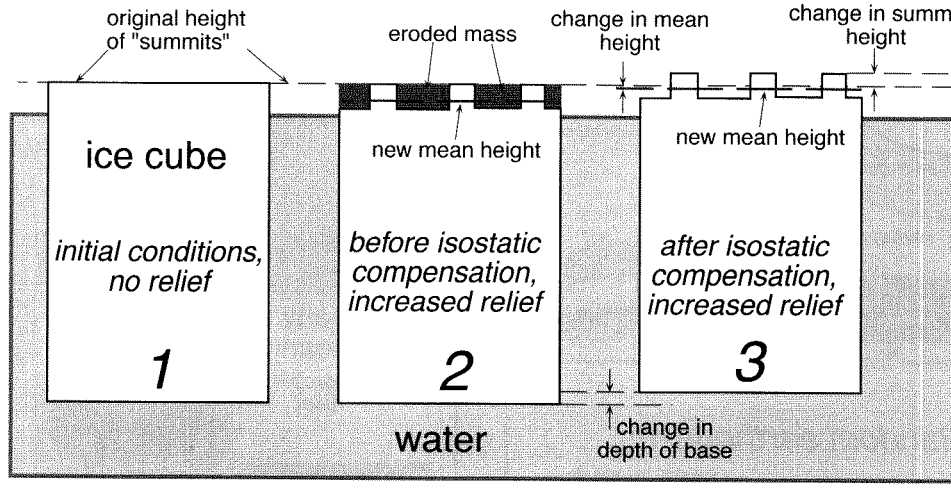

The ice and water are analogous to crust and mantle, respectively. Erosion of the top of the ice cube decreases its mass and its mean height. More rapid erosion of valley bottoms than of summits leads to increased relief and uplift of summits, at the same time that the mean elevation decreases. Note that stage 2 will never occur unless some force restrains the ice cube from rebounding due to melting at the surface.

If we also know when the last rupture occurred, we could predict when the next earthquake was likely to happen. But, do faults display regularity in their rupture histories? The known paleoseismological record commonly extends back through only a few earthquakes, making it difficult to define a statistically significant recurrence interval.

One popular model among paleoseismologists suggests that many faults can be said to experience "characteristic earthquakes," implying that each successive rupture mimics the displacement of the previous event. If true, this implies that, along any particular section of a fault, the amount of displacement that results from a single earthquake will be duplicated in subsequent ruptures (Fig. 1.6). Imagine the predictive power that would result if faults were shown to generate both characteristic earthquakes and predictable recurrence intervals! City planners and paleoseismologists would all be delighted. For most faults, however, this seductively attractive concept has yet to be demonstrated. Consequently, much current debate revolves around whether or not certain faults display characteristic earthquakes and predictable recurrence intervals. Or, could some faults display a very irregular behavior in both the time between ruptures and displacement variations in successive events? Far from being resolved, this debate lies at the core of paleoseismology, and has spawned much recent work both in the field and in numerical models of the faulting process.

The rates of convergence between tectonic plates, as well as measured rates of local deformation, indicate that in many active mountain ranges, rocks are moving upward with respect to sea level at rates of several millimeters per year. Recall that a rate of 1 mm/yr is equivalent to 1 km in a million years. Thus, in the absence of erosion, vertical rock-uplift rates of several mm/yr would build very high mountains in only a few million years. Clearly, mountains do not grow indefinitely; only a few peaks poke more than 8 km above sea level. But what controls their ultimate height? Is there a limit to the energy available to lift the mass of rock and increase its potential energy? Does rock strength set the height limits, or do changing rates of erosion determine the topography of ranges? Such questions lie at the core of another current controversy in tectonic geomorphology: can the concept of dynamic equilibrium be applied in active orogens at the mountain range scale? *Dynamic equilibrium* implies that, on average over time, the

FIGURE 1.6. Schematic illustration of characteristic earthquake displacement versus unpredictable, random displacement

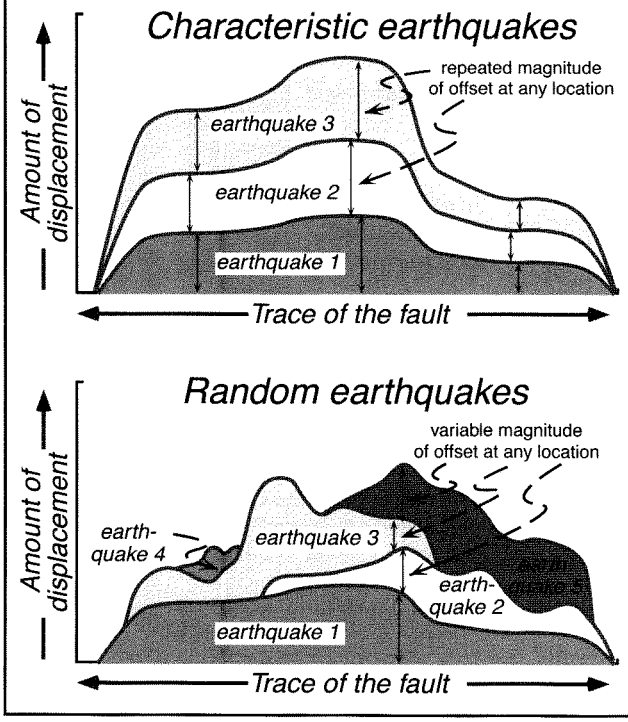

FIGURE 1.7. Steady-state versus non-steady state topography

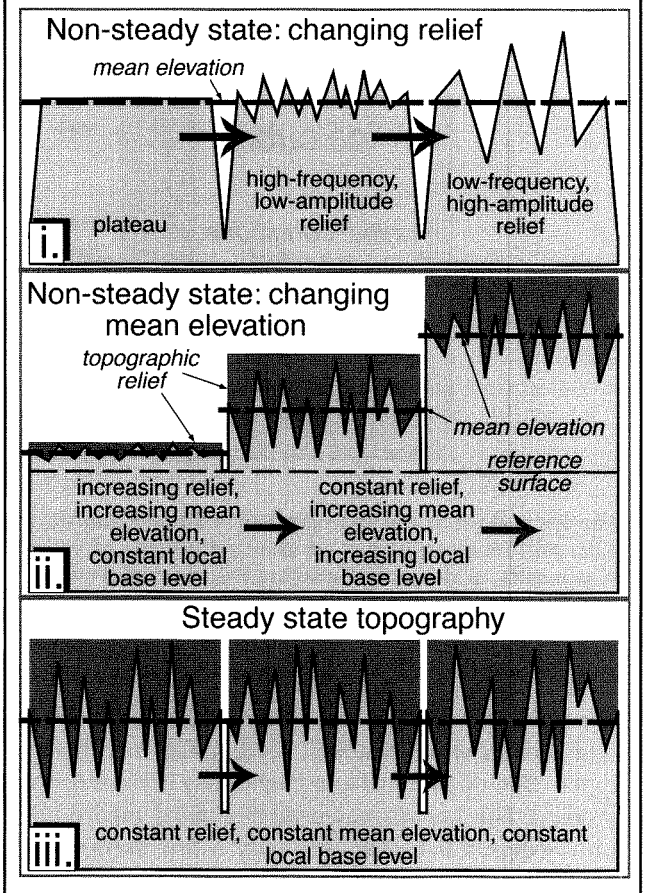

Non-steady-state topography can have constant mean elevation but changing topographic relief (top), or constant relief but changing mean elevation (middle). In steady-state conditions (bottom), relief, mean elevation, and base level remain constant, although the elevation of an individual point can vary through time.

landscape maintains a steady-state form, whereby the height of the summits, the steepness of the valley walls, and the topographic relief fluctuate around long-term mean values. If the mean height of the mountains stays the same through time, this implies that rates of rock uplift (vertical movement of rocks with respect to sea level or the geoid) are balanced by rates of erosion. How is this accomplished? Are surface processes capable of eroding at several mm/yr? Which processes are responsible (river erosion, landsliding, glacial erosion, conversion of rock to soil) and do these processes operate in different ways in different mountain belts? Or, is the traditional idea correct that rapid rates of rock uplift are commonly compensated not by geomorphic agents at all, but by events of tectonic erosion (extensional faulting) that efficiently lower the regional height of the landscape?

In order to answer such questions, we have to be able to document rates of modern and past erosion, to quantify rates of rock uplift and changes in the mean elevation and topographic relief of mountain ranges (Fig. 1.7), and to document the role of extension within orogens. Also, because climate undergoes large glacial–interglacial fluctuations at 100,000-year intervals, rates of erosion that are responsive to climate (most erosional processes are) will also vary strongly through time. Consequently, when thinking about the problem of dynamic equilibrium and steady-state topography, it is most useful to consider time spans that exceed a full glacial–interglacial cycle, so that average rates can be determined. These constraints present some great challenges to researchers in tectonic geomorphology. It is inadequate to document only modern rates (which are difficult enough to measure

accurately!). Rates from intervals throughout a climate cycle or rates that integrate an entire cycle are needed. This requires clever ways to measure quantities of material removed or added from a landscape. Moreover, researchers must somehow inject a reliable "clock" into the rock record, because rate calculations can be no more precise than the time interval across which they are measured. These are difficult measurements to make. An alternative approach would be to determine the operational "rules" by which various surface processes erode the landscape, and to incorporate them into a theoretical model of landscape evolution. For example, how does the rate of bedrock erosion at the base of a glacier relate to the speed at which the glacier is sliding, its thickness, the steepness of its bed, freezing and thawing at the ice–rock interface, and the resistance of the bedrock beneath it? Only if we can both define these rate relationships and determine how glaciers have extended and retreated in the past, will we be able to model the mean rates of erosion within this portion of the landscape.

Looking Ahead

Resolutions to these controversies are beyond the scope of this book, but they provide a framework for thinking about many of the topics discussed in the subsequent chapters. These controversies illustrate some of the breadth of modern tectonic geomorphological studies. Any serious consideration of potential solutions to these controversies quickly reveals the interdisciplinary nature of the research required to address them. Although certainly not unique in its demands for interdisciplinary work, tectonic geomorphology attains much of its current vibrancy from the cross-pollination that is occurring between specialists of many disciplines who are coming together to address major unresolved issues. It is our intent that the following chapters provide some insight into the tools, approaches, and interpretational techniques that are currently used in tectonic geomorphologic studies. We hope to convey the striking innovation and creativity of past researchers, upon whose shoulders future advances will be made.

CHAPTER 2

Geomorphic Markers

In order to measure the amount of deformation that has occurred due to tectonic processes, it is typically necessary to have an identifiable feature that has been displaced. Unique rock types or structures that formerly extended across a fault in an unbroken pattern provide a datum or "piercing point" from which the magnitude of subsequent displacements can be determined. In order to calculate the displacement reliably, the pre-deformational geometry of a presently offset feature has to be reconstructed accurately. The better that geometry is known, the more reliably the offset can be calculated.

In tectonic geomorphology, we are often concerned with offset geomorphic *markers*, by which we mean identifiable geomorphic features or surfaces that provide a reference frame against which to gauge differential or absolute deformation. The best geomorphic markers are readily recognizable landforms, surfaces, or linear trends that display these three characteristics: 1) a known initial, undeformed geometry; 2) a known age; and 3) high preservation potential with respect to the time scale of the tectonic process being studied. Oftentimes, only some of these characteristics may have been determined for a displaced marker. Because of the usefulness of geomorphic markers, considerable effort and care are warranted in defining their geometry and age. In this chapter, we examine the pristine shape of many useful markers, such as river or coastal terraces, and discuss the conditions under which they are likely to form.

The geometry of a pristine geomorphic feature is a crucial attribute of a marker, because it is the deformation of the surface of such a feature that records the tectonic signal. Modifications of an original undisturbed feature by subsequent erosion or deposition, however, may make it difficult to define the original geometry of a presently offset geomorphic surface. In such cases, the probable geometry of the feature can sometimes be predicted through comparison with undeformed modern analogues. For example, river terraces are frequently used as geomorphic markers to document fault offsets or folds (Molnar et al., 1994; Rockwell et al., 1984). Unfortunately, the preservation of river terraces becomes increasingly fragmentary as they get older and more extensively dissected. In such a situation, the geometries of young, nearly undissected terraces along the same or analogous reaches of the river provide models for the smooth downstream changes in the longitudinal profiles of rivers. Such profiles can then be used to predict the geometry of older terraces prior to deformation.

It is important to establish the age of geomorphic markers in order to calculate rates of deformation. Most markers form in response to either climatic or tectonic controls. Some markers form due to autocyclic processes, such as the avulsion of river channels that occurs due to aggradation on floodplains. If the relationship of a suite of markers to known and dated climatic variations can be established, the markers themselves can be indirectly dated through correlation to the climatic record. For example, climate change often affects the water discharge in a river and its sediment load. Consider the situation in which, due to a climatically induced increase in discharge, a river begins to incise its bed. After sufficient incision, the river may be flanked by fluvial terraces (geomorphic markers) which now represent a geomorphic response to the climate change. If we know the age of the climate change that caused the change in discharge and sediment load, then the age of the terrace itself can be estimated from the climatic record. With these terraces as time markers in the landscape, it becomes possible to measure both the amount and rate of deformation since they were created. Therefore, it is very useful to understand aspects of the climatic record that are most likely to be relevant to creation of geomorphic markers. In the absence of climatic calibration, or for markers whose origin may not reasonably be attributed to

climatic cycles, direct dating of a marker is required. A variety of dating approaches is discussed in Chapter 3.

Ephemeral features, such as small levees or even tire tracks, that could wash away in the next storm can provide markers that are adequate to calibrate co-seismic offsets of a recent earthquake (McGill, 1994). Long-lived geomorphic features, however, are required to document deformation over many thousands of years. But, erosion is continually modifying the geometry of such markers and ongoing tectonic and climatic changes are overprinting the landscape with new features. Consequently, a tectonic geomorphologist benefits from a knowledge of a marker's potential for long-term preservation in the landscape and from an ability to recognize useful fragments of older markers within the complexly intertwined geomorphic elements of most natural landscapes.

The sensitivity (amplitude of the response) and response time of geomorphic systems to changes in the variables that control them vary markedly. The discharge of rivers, for example, will respond almost instantaneously to changes in precipitation, whereas glaciers often take several years to translate increases in snowfall into an advance of the snout of the glacier. In general, the response time of a geomorphic system to changes in the climatic forcing of the system increases dramatically with the scale of the system, and inversely with respect to the efficiency of the processes involved. When the variables that control a geomorphic system change, highly sensitive components of an integrated system, such as the cross-sectional area of a river or the elevation of its bed, can usually achieve a new equilibrium rapidly. In contrast, larger systems, such as an entire drainage basin, can take thousands of years or more to come into equilibrium with any new controls on the system.

Planar Geomorphic Markers

To be useful as a reference frame against which to measure displacement, the initial, pre-deformation geometry of a geomorphic feature must be defined. Because erosion and/or deposition continually modify old geomorphic markers, a map of a presently exposed marker often reveals only fragments of formerly continuous surfaces or features. The task of anyone wishing to use such markers to calibrate deformation is to create a reliable reconstruction of the undeformed geometry of the marker. Often modern analogues of either recently created or currently forming features provide the best model to use in reconstructing the shape of older, presently fragmented features. Therefore, we will describe coastal, lacustrine, fluvial, and terrestrial markers that have been commonly used to define tectonic deformation.

Marine Terraces, Beaches, and Shorelines

Along coastal regions of many parts of the world, bench-like features, or *marine terraces*, have been created by the interaction of the ocean with the adjacent landmass. Marine terraces fall into two classes: constructional terraces associated with coral reefs, and destructional or erosional terraces. Terraces ultimately result from the wide variation in sea level with time, this variation being driven by a combination of the histories of the local movement of the landmass with respect to the geoid and the global variations in sea level. The global or *eustatic* sea level changes within the Pleistocene are caused primarily by changes in the volumes of the continental ice sheets. The associated swings in sea level are huge: 120–150 m. Only 18 kyr ago, sea level was 150 m below its present level (Fairbanks, 1989). As both physical and biological processes are strongly focused at the intersection of air, land, and sea, it is not surprising that the variations in the location of this interface through time have left a pronounced and, therefore, useful geomorphic record.

The constant attack on the shoreline by waves creates erosional marine terraces. As waves crash against a coast, fluid turbulence and hydraulic pressure are capable of loosening and plucking fragments of bedrock, and sediment entrained in the water can impact forcefully against the cliffs. In places, this can form a *wave-cut notch* at the base of a sea cliff. As plucking and abrasion continue, the notch deepens, the base of the cliff retreats, and the shore platform widens. In response to undercutting, the slope of the sea cliff is effectively steepened and can be expected to collapse when stable slope angles are exceeded. If the material that is loosened at the cliff face is not removed, it simply mantles the bedrock and prevents subsequent erosion. More commonly, however, a seaward-sloping shoreline platform or *abrasion ramp* permits wave energy to transport the eroded debris into deeper water offshore. This ramp typically slopes at about 1° and extends sufficiently seaward to allow sediment that is transported along its surface to be dumped into deeper water, dissolved, or transported away in suspension following further comminution. Because wave energy is needed to transport sediment on the abrasion ramp, these ramps do not extend below typical wave base (~10 m in most coastal areas). Given the 1° slope of the ramp, this sets a maximum width of about 500 m for most abrasion ramps. Wider ramps can result from a

FIGURE 2.1. Abrasion platform, sea cliff, wave-cut notch, and shoreline angle

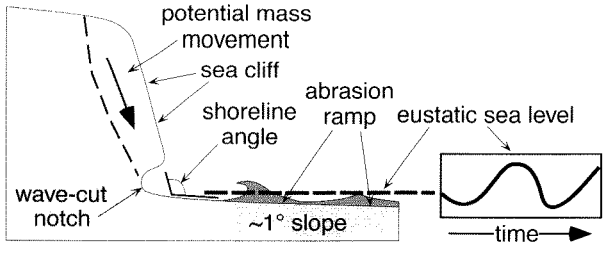

The vertical position of the abrasion ramp varies through time as a function of sea-level variations.

deeper wave base, gentler seaward slopes, or multiple occupations of approximately the same or slightly higher relative sea-level positions.

A newly created erosional marine terrace typically consists of two distinct surfaces: an abrasion ramp dipping seaward at ~1° and a sea cliff dipping seaward at the stable angle of repose, given the strength and cohesion of the bedrock which it comprises (Fig. 2.1). The junction of these bedrock surfaces is called the *shoreline angle* (also called the *inner edge* of the platform) and it is here that a wave-cut notch may be preserved. Because this wave-cut notch and/or the junction between the abrasion ramp and the sea cliff occurs at the shoreline, it represents a marker that closely approximates local sea level at the time of its formation. Formally, this feature records the intersection of sea level, averaged over many tidal cycles (which closely approximates the geoid), and the landmass. Hence, it becomes a paleo-horizontal indicator that permits both tilting parallel to the coast and spatial variations in vertical motions of the crust to be assessed. When reconstructing the former inner edge of an uplifted abrasion platform, it is important to try to pinpoint the position of the shoreline angle. Commonly, however, the shoreline angle will have been obscured by downslope motion of eroded material from topographically higher slopes. In these circumstances, sometimes the surface of the abrasion platform well away from the paleo-sea cliff and that of the sea cliff itself can be projected to an intersection that approximates the former shoreline elevation. In contrast, the depth below sea level of the outer edge of the abrasion ramp can vary by 10 m or more. Moreover, the position of the preserved outer edge of the platform depends on how much it has retreated due to erosion and smoothing since it became emergent. Consequently, the position of this outer edge provides a much less reliable marker with which to measure deformation, even though it may be more readily preserved and observed in the landscape.

Constructional marine terraces can form when marine conditions are favorable for the growth of corals and coralline algae. Typically, these conditions occur where water temperatures in winter remain above about 18°C, where clear water permits penetration of sunlight to support photosynthesis, and where the salinity is normal. Under conditions conducive for growth, coral reefs can be rapidly built upward toward the sea surface (at rates exceeding 10 cm/yr) and outward toward available space. When sea level is stable for sufficiently long periods, corals will build platforms that are closely tied to sea level, and therefore provide useful geomorphic markers. During a relative rise in sea level, there is a predictable upward and outward coral growth (Fig. 2.2A and B). If the rise is particularly rapid, the rate of vertical growth of the crest may lag behind the relative sea level rise. Only when the sea level stabilizes will the reef crest attain its maximum height near the sea surface. During a subsequent fall in relative sea level, wave-cut notches may cut into the forereef during brief stillstands (Fig. 2.2C). If sea level stabilizes at a new local level, corals will build a reefal bench.

Because different coral species are adapted to different marine conditions, there is a marked zonation of species within a reef. For example, wave-resistant corals will be found in the nutrient-rich waters on the leading edge of a reef, whereas less robust forms occupy the backreef (Chappell, 1974a). Knowledge of this zonation (Fig. 2.2A) and an ability to recognize various coral species, some of which are more faithful recorders of sea level, permits reconstruction of the geometry of presently emerged reefs and their relationship to former sea levels at the time of their growth. For constructional terraces comprising coral reefs, the reef crest and buttress represent the leading edge of the reef and yield the best approximation of sea level. Because this edge is most subject to erosion if the reef is uplifted above sea level, knowledge of the depth below the sea surface at which various coral species are found must often be combined with a recognition of the preserved species zonation within a reef (Fig. 2.2A) to estimate the position of the former reef crest.

Along many tectonically rising coasts, there are flights of marine terraces that provide direct evidence for multiple decreases in relative sea level. But when do these terraces form, and how are they related to sea level

FIGURE 2.2. Coral reef stratigraphy and sea-level change

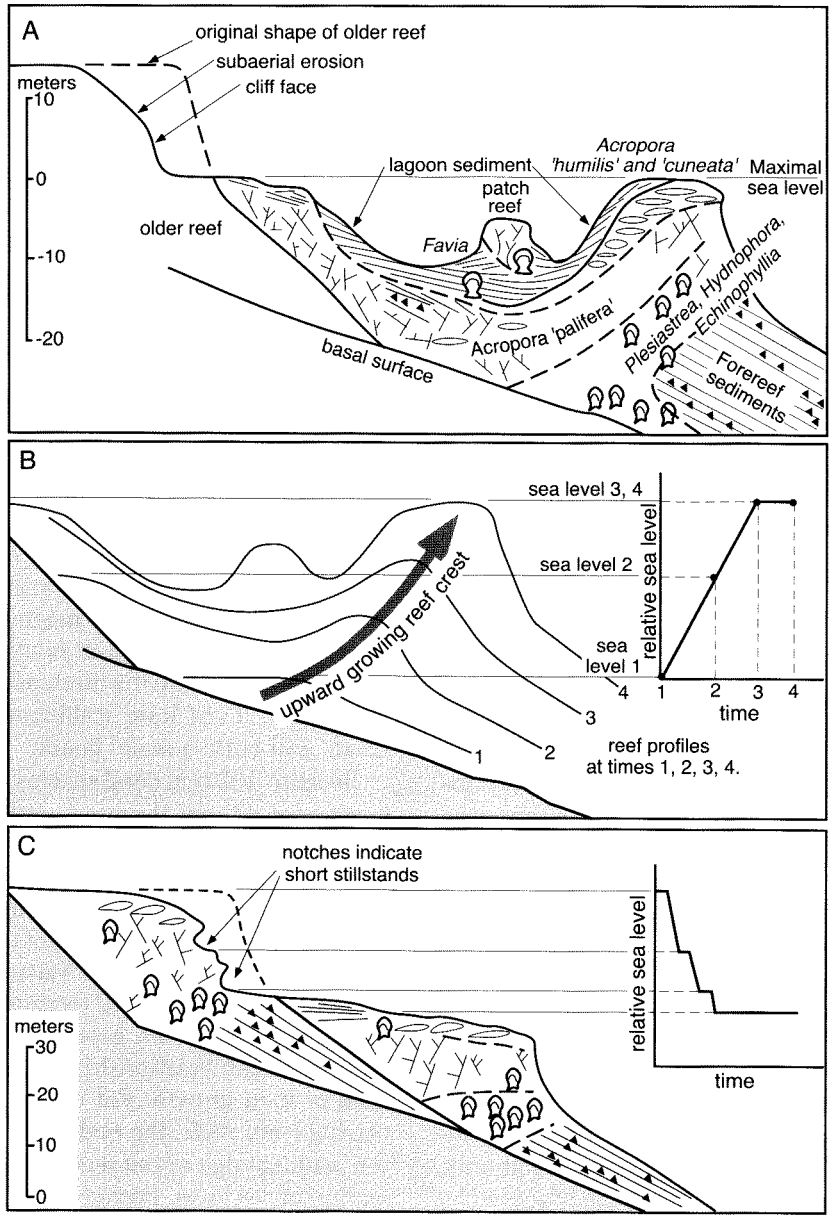

A. Idealized model of facies zonation and geometry of a coral reef that grew in response to rising sea level. Note that the coral species *Acropora humilis* and *cuneata* occupy the reef crest and most closely approximate sea level. These can be eroded, however, and often species that reside slightly below the mean surface are better indicators of former sea levels. B. Idealized cross section of the reef in A showing how the topography of the reef is related to changing relative sea level. During the intervals of rapid sea level rise (from SL1 to SL3: inset), the crest of the reef grows upward, but remains below the sea surface. As sea level stabilizes, the reef reaches sea level and grows seaward. C. Wave-cut notches are a response to falling sea level. A new reefal platform can be built once sea level stabilizes. Modified after Chappell (1974a).

Box 2.1. Isotopic Changes in the Ocean Due to Glaciation

The history of climatic change in Quaternary times is primarily a function of the growth and decay of ice sheets. The key record of changing volumes of glaciers through time comes from the isotopic record of the oceans. During glaciations, water evaporated from the ocean is stored in ice sheets. The ratio of two common isotopes of oxygen. ^{16}O and ^{18}O, is different in ice sheets than in the ocean due to a fractionation process. When water evaporates (primarily near the equator), the lighter isotope (^{16}O) is preferentially evaporated, causing the ocean to become enriched in ^{18}O. During condensation and precipitation, ^{18}O is preferentially removed in the water vapor, so that during its poleward transport, the remaining vapor becomes increasingly enriched in ^{16}O. Precipitation at high latitudes is therefore strongly depleted in ^{18}O compared to "standard mean ocean water" (SMOW). This causes the ice sheets to be isotopically "light" compared to SMOW (lower $^{18}O/^{16}O$ ratio). Conversely, the oceans become isotopically heavier (higher $^{18}O/^{16}O$ ratio) due to the storage of "extra" ^{16}O in the ice sheets. The more ice stored on land, the isotopically heavier the ocean becomes.

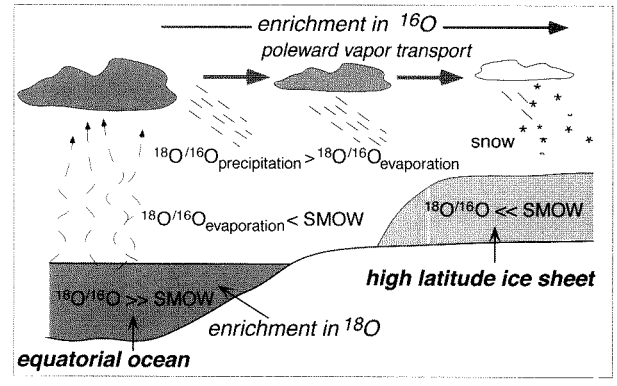

Foraminifera that grow in equilibrium with the sea water record its isotopic composition. Consequently, the stratigraphic record of isotopic changes displayed by foraminifera during the Quaternary can be interpreted as a record of changing ice volumes.

changes? In order for a coastal terrace to be generated, sea level must remain at approximately the same relative position with respect to the land so that corals can build outward to form a reefal terrace or so that wave attack is focussed along the same abrasion platform through time. Due to rapid rates of lateral erosion and of coral growth, it often takes only a few thousand years to create a broad terrace (Anderson et al., 1999). Consequently, we expect terraces to form during intervals when rates of vertical movement of the land and rates of sea level change are nearly equivalent. If we knew well the history of sea level and could correlate between individual terraces and former sea level positions, we would have a basis for calculating vertical deformation rates.

Fortunately, within the past few decades, the history of Quaternary sea level has been reconstructed with increasing accuracy (Bloom et al., 1974; Chappell, 1974a; Chappell et al., 1996). During maximum glacial conditions, the volume of water stored in ice sheets on land caused average sea level to be lowered by more than 100 m. On the other hand, during the peak of the previous interglaciation at about 125 ka, there was apparently less ice on earth than there is today, and mean sea level was approximately 6 m higher than it is today. The most detailed reconstructions of the growth and decay of ice sheets have been derived from variations in the oxygen isotopic composition of sea water (Box 2.1). The removal of water from the ocean via evaporation and the sequestering of this isotopically lighter (lower $^{18}O/^{16}O$ ratio) water in ice sheets caused the oceans to become isotopically heavier (higher $^{18}O/^{16}O$ ratio) during glaciations. Thus, the pattern of isotopic fluctuations derived from deep-sea cores provides a proxy record for both climate and sea-level variations (Fig. 2.3).

There is not, however, a one-to-one correspondence between isotopic and sea-level changes. This is the case for several reasons: the world's oceans are not simple bathtubs, meaning that an equal volume of water does not translate into an increment in sea level because, as sea level rises, the surface area of the ocean also increases. In addition, withdrawal of water from the ocean and sequestration on land re-arranges the water load on the earth's crust and drives isostatic rearrangements of deep crustal and mantle materials, which differ from place to place. Therefore, the best estimates for past sea-level variations require calibration, and have been largely derived from studies of radiometrically dated coral terraces on tectonically rising coasts. The key calibration studies have been conducted on the striking successions of coral terraces preserved on the Huon Peninsula of New Guinea (Bloom et al., 1974; Chappell, 1974a; Chappell et al., 1996), a coastline responding to

FIGURE 2.3. Isotopic composition of the oceans during the Pleistocene viewed at three different time scales

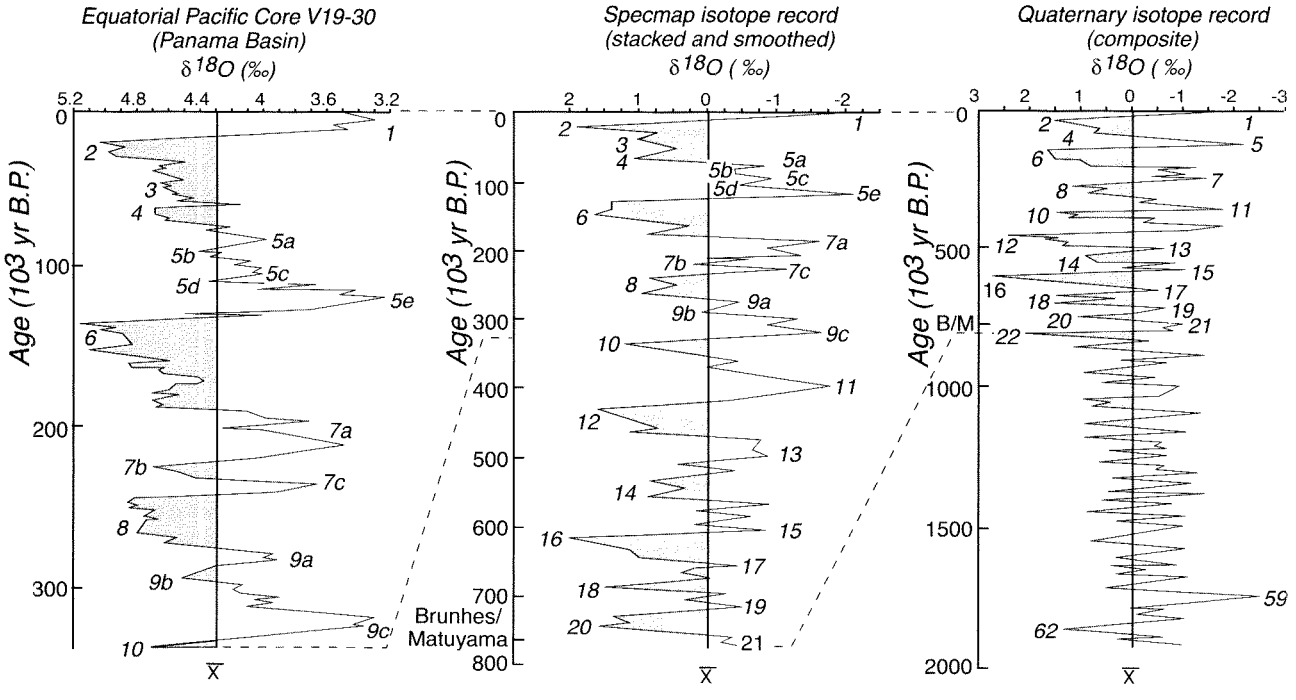

Heavier oxygen isotopic compositions (increasing to the left) correlate with greater ice-sheet volumes and lower mean sea level. Interglacial intervals correspond with high sea level stands. Note that there is a prominent, 100-kyr periodicity during the past 800 kyr. Prior to that, periodicities are dominated by a 40-kyr cycle. 20-kyr cycles are superimposed on both 100- and 40-kyr cycles. Labels next to the peaks and troughs refer to isotopic stages. Stage 5e, for example, represents the last interglacial maximum. A. 0–350 ka. B. 0–800 ka. C. 0-2 Ma. Modified after Porter (1989).

rapid collision of an island arc terrain against the edge of the Australian Plate. These terraces get older with increasing elevation, and they record the *relative* sea-level change through time. This relative change results from the sum of the *real* changes in sea level and the *apparent* changes in sea level (Fig. 2.4):

$$relative = real + apparent$$

Real sea-level changes are due to absolute vertical changes of the ocean surface (due primarily to changing volumes of water in the ocean as a result of glaciation; also called *eustatic*) and can be global in extent. Apparent sea level changes result from and represent the inverse of the actual vertical displacement of the land, that is, tectonic uplift or subsidence. For example, if you are standing at present sea level, and you see an ancient abrasion platform high above you, either the sea level has fallen from that elevated height to its present position (real sea level fall) or the terrace has been tectonically raised above the position at which it formed (causing apparent sea level fall). Such deformation is clearly local or at most regional in extent. If tectonic rates are assumed to be steady during the time interval encompassed by a flight of terraces, then the apparent sea-level change will be linear. In any case, apparent sea level represents the difference between the relative and the real sea-level change:

$$apparent = relative - real$$

So, how does one use these relationships to calculate real sea-level changes in the past? Consider a flight of emergent marine terraces for which the age of each terrace

FIGURE 2.4. Relationship between relative, real, and apparent sea levels

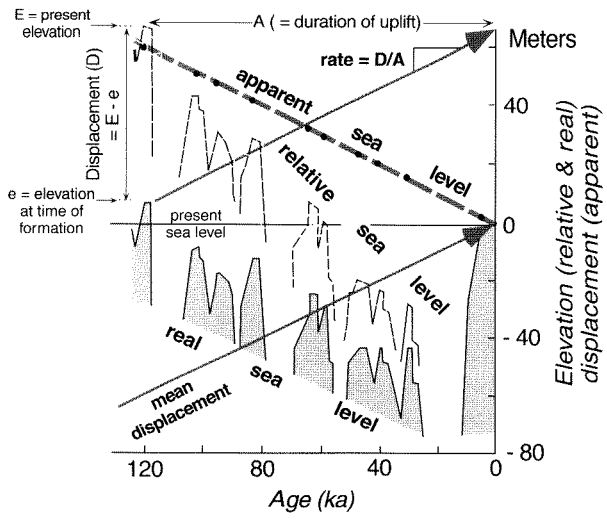

Apparent sea level is defined as the inverse of the vertical tectonic displacement (*D*). Displacement is determined as the difference between the present elevation of a terrace (*E*) and the original elevation of the terrace (*e*); thus $D = E - e$. The rate of tectonic displacement is assumed constant here and is equal to the displacement divided by the age (Rate = $D/-A$). Relative sea level is represented by the altitudinal position of preserved terraces with respect to present sea level (dashed line). Real sea level represents actual changes in the height of the ocean surface. Because the apparent and real sea levels add to yield the relative sea level, if two of these quantities are known, the third can be derived. Modified from Lajoie (1986).

FIGURE 2.5. Variations in real sea level based primarily on dated terraces on the Huon Peninsula, New Guinea

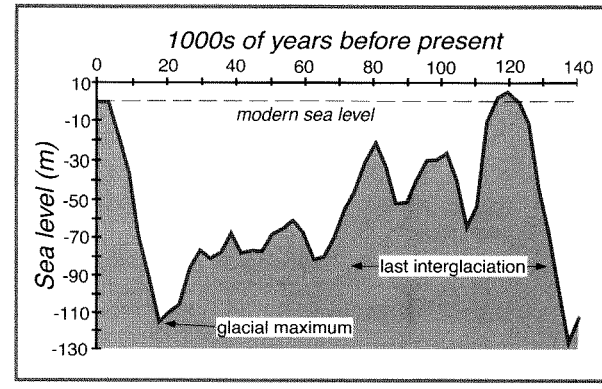

Modified from Chappell et al. (1996).

and its elevation above modern sea level are known. This suite of terraces represents the relative sea-level change through time. To determine the apparent sea level change, the tectonic uplift rate has to be determined. If data from other areas have revealed the position of sea level at some time in the past with respect to the present sea level, and if a terrace of that age is present within the terrace succession, then the difference between the present elevation of the terrace and the elevation of the sea level at the time the terrace formed defines the amount of tectonic uplift. For example, if a 125-ka terrace is presently 131 m above sea level (this is its relative sea-level position), it can be assumed to have formed during the last interglacial maximum sea level of +6 m. The tectonic uplift is consequently 125 m (131 m–6 m), and the average uplift rate is 1 m/kyr (125 m/125 kyr). The rate of apparent sea-level change is, therefore, –1 m/kyr. Either the graphical or the arithmetic subtraction of the magnitude of the apparent sea level from the elevation of the correlative, dated terrace yields the real sea-level change through time (Fig. 2.4):

$$real = relative - apparent$$

The curve of "real" sea-level change that has been derived from studies of coral terraces is quite well known for the past 135 ka, especially for the high stands (Fig. 2.5), but is less confidently defined before that time. In part the uncertainty arises from imprecision in dates of older terraces and in part from the paucity of reliable sea-level calibration points that are older than 135 kyr. It is questionable whether tectonic uplift rates defined for more recent intervals can be confidently extrapolated into the past, so that apparent sea-level changes are difficult to define at longer time scales. As a consequence, the sea-level curve prior to 135 ka is often closely modelled on the variations shown by the oxygen isotopic record. Comparison of the sea-level curve for the past 135 ka (Fig. 2.5) with the oxygen isotopic curve (see Fig. 2.3) shows that they are clearly similar, but the magnitude of successive peaks varies considerably. Hence, our knowledge of sea levels prior to 135 ka should be regarded as only approximate. Although the reliability of the sea-level record decreases as older and older successions of

FIGURE 2.6. Beach ridges

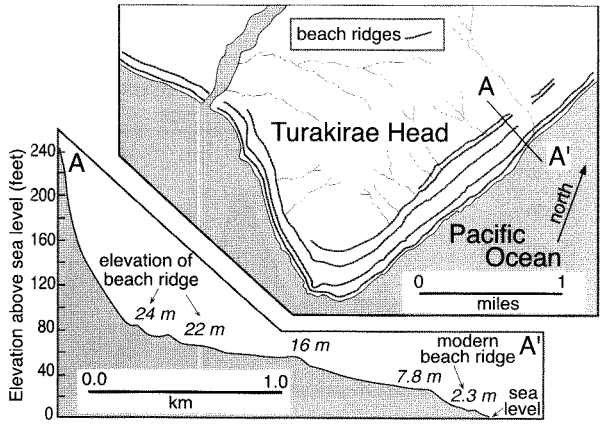

Top. Map of beach ridges at Turakirae Head, southern tip of the North Island of New Zealand. The Wairarapa fault is situated a few km to the east of the beach and has caused co-seismic uplift of the ridges. Bottom. Cross section of topography of beach ridges showing modern storm beach and successive co-seismically uplifted ridges. Modified after Stevens (1974).

terraces are considered, along many tectonically active coastlines, flights of marine terraces provide a very powerful tool for calibrating absolute and differential uplift and tilting all along the coast.

Eustatic sea level has not varied much during the past several thousand years. As a consequence, well-developed abrasion platforms and coral terraces exist along many coastlines. In addition, several features with a much more limited preservation potential can provide useful markers for delineating Holocene deformation. Along stony beaches during major storms, gravelly beach ridges and berms are formed a few meters above the typical high tide line (Stevens, 1974). Because the crests of these features are parallel to the sea surface, they provide a horizontal reference surface (Fig. 2.6). If the height of the present storm ridge above sea level is known, then uplifted and deformed older ridges can be used to define deformation (e.g., Marshall and Anderson, 1995).

Although not geomorphological in nature, zonations of marine plants or animals can sometimes provide useful biological markers for defining deformation. For example, those creatures that are attached to rocks and grow just below the high tide line can be used to define the local sea surface just as easily as can abrasion platforms. If this coastal community were uplifted co-seismically, the upper elevational limit of these organisms would record the vertical displacement at that spot on the coast (Plafker and Ward, 1992). Although such a record can be quite precise, it is clearly more transient than most geomorphic markers: attached organisms exposed continuously to the air soon die and eventually fall off the rocks to which they were attached, implying that the record of such instantaneous uplift events must be obtained within a few months to years of the event (Carver et al., 1994).

Lacustrine Shorelines

Like marine terraces, lacustrine shoreline features are almost perfectly horizontal at the time of their formation. As waves impinge on the shore, they create *wave-cut benches* or *lacustrine strand lines.* The width of these benches depends on the erosional resistance of the bedrock at the shoreline, the length of time during which the lake level remained constant, and the strength of wave attack, which is a function of fetch, storm winds, and local shoreline geometry. Along the margins of Pleistocene Lake Bonneville in Utah, for instance, benches as much as 100 m wide have been formed. In G. K. Gilbert's (1890) pioneering study on Lake Bonneville, he identified many of these shorelines and used them as markers to document crustal rebound that followed the shrinkage of the lake (Fig. 2.7A).

Lake levels in closed tectonic depressions fluctuate significantly in response to the water balance in the catchment. Unfortunately, unlike major changes in eustatic sea level, which are essentially synchronous on a global basis, lake–level changes (Fig. 2.8A) can vary between adjacent basins (Benson et al., 1990). Compilations of lake-level records from the southwestern United States (Smith and Street-Perrott, 1983) show that, even in a limited geographic region, the timing of high stands can be quite variable (Fig. 2.8B). This results at least in part from the complex routing of water through the landscape, such that one basin may begin to fill only after an adjacent basin overflows (Adams et al., 1999). Once the water in a lacustrine basin fills to the height of an outlet, the water level cannot get significantly higher, even if the discharge into the lake continues to increase. Conversely, bedrock thresholds which control the level of a lake outlet and its maximum height may erode and can cause the lake level to drop, irrespective of climatic variations. These regional and local factors dictate that the age of a displaced shoreline must be determined within the particular basin being examined, rather than inferred

FIGURE 2.7. Lacustrine shorelines formed by Pleistocene Lake Bonneville

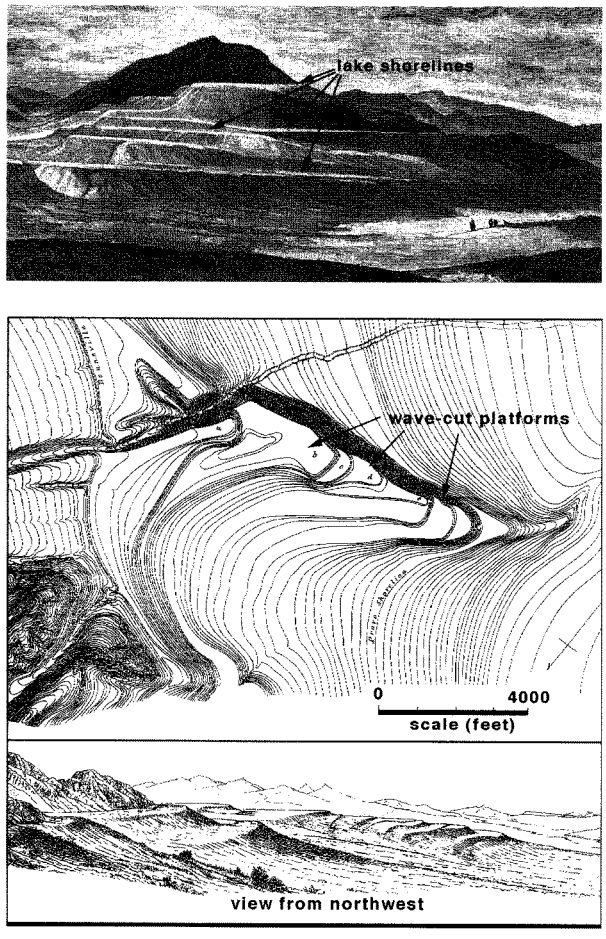

Wave-cut platforms are incised into headlands, the flanks of islands, and across spits. A: perspective view of shorelines; B: topographic map of wave-cut platforms incised into an elongate spit; C: perspective view of the strandlines on the spit. Modified after Gilbert (1890).

FIGURE 2.8. Lake-level changes

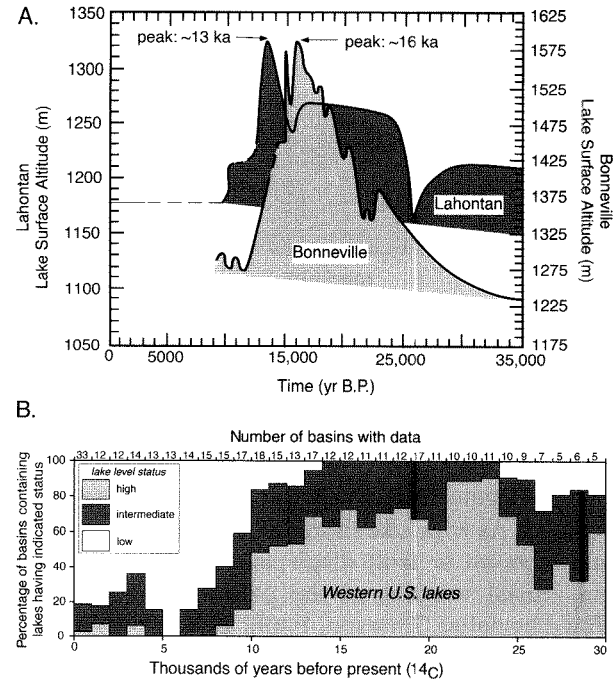

A. Lake-level history for Lake Bonneville and Lake Lahontan. Despite the proximity of these two large lakes in the Great Basin, they have significantly different histories due both to contrasts in discharge and to changing topographic thresholds within each basin. Modified after Benson et al. (1990). B. Late Quaternary lake-level records in southwestern United States. These data indicate that the majority of lakes fluctuate synchronously at the time scale of a few thousand years, but that lake-level variations in any individual lake may differ markedly from the mean. Modified from Smith and Street-Perrott (1983).

through correlation with dated shorelines elsewhere, or with global climate records.

Deltas

Both marine and lacustrine deltas provide clear geomorphic evidence for former water levels. Deltas have an advantage over terraces or wave-cut benches in that they are often larger geomorphic features that are therefore more likely to be preserved. The disadvantage of deltas is that they only form where rivers enter bodies of water, and thus they often offer less extensive spatial coverage than do shoreline features: they provide control on changes in elevation at a point, rather than along a line. Gilbert (1890) described the internal bedding geometries of lacustrine deltas long ago and showed that the contact of the topset and foreset beds closely approximates the level of the body of water into which the delta is prograding (Fig. 2.9). If a lake existed during only one particular interval, mapping of the foreset-topset contact for many deltas formed along its margin would define a

FIGURE 2.9. Internal bedding geometries in a simple delta

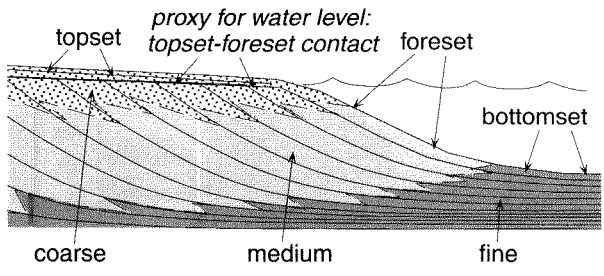

The contact between the foreset and topset beds closely approximates the lake level or sea level at the time of delta growth.

paleo- horizontal surface that may have been subsequently displaced. As with lake shorelines, the magnitude of isostatic rebound or fault displacements can be deduced from crustal warping of the paleo-horizontal surface defined by deltas (Thorson, 1989). If, however, multiple high lake levels occurred within the basin, then not only must the height of a topset-foreset contact be determined, but the age of the delta must be ascertained as well to permit reliable correlation of deltas formed in the same interval.

River Terraces

All of the previously discussed markers provide a horizontal reference frame for assessing deformation. Even if the geomorphic evidence for a displaced shoreline feature is discontinuously preserved across the area of interest, the former geometry of the pristine feature is known to be horizontal, such that vertical displacements can be confidently calculated. If the timing of the surface cannot be determined, one can still often have confidence in the relative displacements of points, and hence determine vertical displacement field (but not the displacement *rate*). When geomorphic features that were not originally horizontal are used as markers, considerable care must be taken to ascertain the gradient and geometry of the feature prior to offset. For example, if a change in gradient is used to define tectonic warping, one needs to be confident that these gradient changes are not natural ones resulting from some non-tectonic cause, such as variable resistance of bedrock to erosion or the normal downstream gradient of a river.

Stream power refers to the rate of expenditure of potential energy per unit length of stream (Box 2.2) and is proportional to the slope of the water surface and to the river discharge. As stream power increases, the energy supply at the channel bed also increases, such that more energy is available to overcome friction, erode the bed, or transport sediments. *Unit stream power* or *specific stream power* represents the stream power per unit area of the bed and is related to bed shear stress and mean velocity. It can be easily imagined that changes in stream power will affect the behavior of a river, such as whether it is aggrading or degrading (Whipple and Tucker, 1999). Other variables, however, such as the sediment load, the caliber of the sediment, and the roughness of the bed also influence the aggradational or degradational state of the river. Increases in load, caliber, or roughness increase the resistance of the river bed to erosion. A river that is neither aggrading or degrading can be considered to be in equilibrium (Bull, 1991) and to be at the *threshold of critical power* (Fig. 2.10). At this threshold, the stream power is just sufficient to transport the sediment load that is being supplied from upstream, and the height of the bed remains constant. In general, if other factors are held steady, increases in river slope or in discharge or decreases in bed roughness, sediment load, or sediment caliber will cause the river to cross the threshold of critical power and begin to erode its bed. In contrast, changes in the opposite sense will push the river into an aggradational mode. The concept of a threshold of critical power is useful in the interpretation of the genesis of river terraces, because it indicates the potential linkages among different variables and suggests how changes in climate or tectonics could cause the river to switch from aggradation to degradation, or vice versa.

River terraces are common examples of preserved, sloping geomorphic features. Two classes of river terraces are typically defined: *aggradational* (or constructional or fill) and *degradational* (or erosional or cut or *strath*). The former result from aggradation of river-transported alluvium along a river's course, followed by downcutting, which leaves the former aggradational surface abandoned as a terrace. This can be regarded as a consequence of crossing the threshold of critical power, such that the river moves from an aggradational or equilibrium mode to a degradational mode (Fig. 2.11). As the water discharge of a river increases downstream, its surface slope generally decreases. Thus, at the regional scale, the longitudinal profile of the terrace should typically be represented by a smoothly decreasing, concave gradient

Box 2.2. Stream Power

Consider a packet of water that flows along a river. As it loses altitude along its course, it loses potential energy. This energy loss (Δ potential energy) occurs over some increment of time (Δt), during which the altitude of the packet of water is lowered by some amount (Δh) along some length of stream bed (Δx). Power is the rate of doing work or energy expenditure. Therefore, stream power is defined as the rate of change of potential energy (p.e.). *Stream power/unit length* defines the amount of energy which is available to do work over a given length of stream bed during a given interval. Thus,

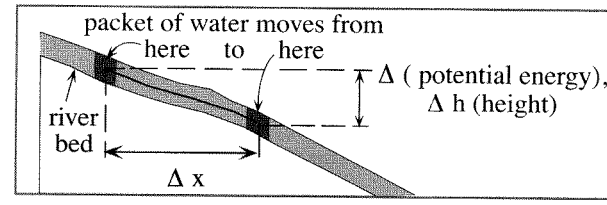

stream power / unit length =

Ω = Δ potential energy / (Δt · Δx).

Recall that Δ p.e. = m · g · Δh,

and that (m / Δt) = ρ_w · Q,

where ρ_w = density of water, Q = discharge.

So, Δ p.e. / (Δt · Δx) = (m · g · Δh) / (Δt · Δx) =

(m / Δt) · g · (Δh · Δx) =

ρ_w · Q · g · s =

k · Q · s,

where s = slope (Δh / Δx),

and k = a constant = ρ_w · g.

Specific stream power is defined as the power available per unit area of the bed:

specific stream power = Ω / width =

(ρ_w · g · Q · s) / w.

But Q = w · d · Δx / Δt, so Ω / w =

(ρ_w · g · w · d · Δx / Δt · s) / w =

ρ_w · g · d · s · Δx / Δt =

$\tau \cdot \overline{v}$,

where τ = bed shear stress; $\overline{v}$ = mean velocity

Variations in stream power define the changes in the amount of energy available to do work on the bed of a stream. Overcoming frictional forces, transport of sediment, and erosion of the bed are all dependent on stream power. Therefore, increases in discharge or in slope will have a strong effect on the energy expended at the river's bed.

in the downstream direction. Tectonic perturbations to such a gradient often are straightforward to determine.

Degradational terraces can form in several ways, some of which provide more predictable downstream profiles than others. For example, if a river is incising into alluvium and reaches an equilibrium during which incision ceases and the river bevels sideways into the valley fill, or even aggrades a bit, paired terraces (correlative terraces preserved on both sides of the river) with considerable downstream continuity can be formed. If a river is degrading through alluvium, and is also switching its course back and forth within a valley during degradation, it can create terraces that are unpaired (no correlative terrace on the opposite side of the river). The downstream geometry of such terraces may be hard to reconstruct (Merritts et al., 1994), because there are unpredictable successions of terraces at any location and an age-equivalency would need to be demonstrated prior to confident correlation among terrace remnants. Such terraces can provide useful markers for deformation that is contained within an individual terrace remnant, but they are much less practical for examining broader patterns of tectonic deformation.

A river incising into bedrock can create a bedrock terrace or *strath terrace*. Such bedrock incision typically occurs within or immediately adjacent to mountains, where there often are variations in bedrock resistance to erosion along the river's course. Across less resistant bedrock, stream power might tend to be lower due to some combination of river widening and gradient decrease. Even in an equilibrium condition without tectonism, the river gradient in a bedrock river will be more variable than in an alluvial river. Thus, as with unpaired degradational terraces, strath terraces provide useful local geomorphic markers, but are not as useful in the documentation of regional deformation patterns. This is all the more true due to the limited downstream extent of such strath surfaces, many of which are only 100 m or so in extent.

In order to use deformed terraces to calculate tectonic rates, the age of the terrace must be known. Although this is often a difficult task, we know that many paired

FIGURE 2.10. Schematic representation of the threshold of critical power as a balance between eroding and resisting forces

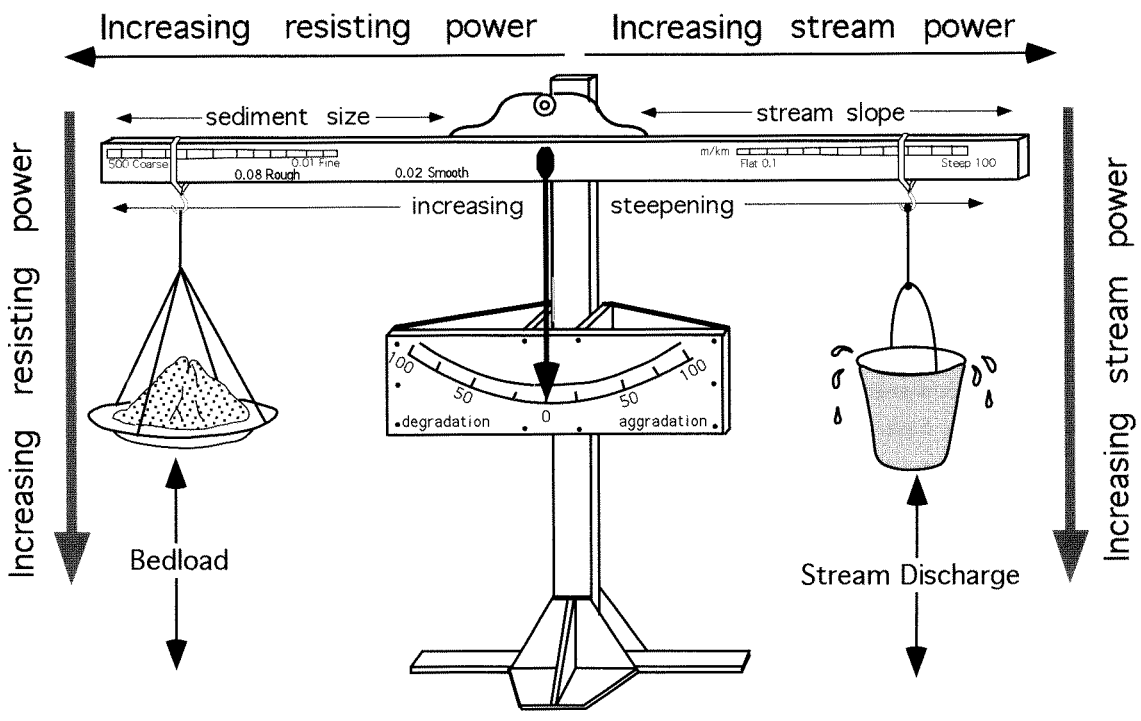

An increase in stream slope or discharge or a decrease in sediment load, sediment caliber, or bed roughness will move the system toward erosion of its bed. Modified after Bull (1991) and Chorley et al. (1984).

aggradational terraces form in response to climatic cycles. In many areas of alpine glaciation, for example, fluvial terraces can be demonstrated to correlate with moraines associated with glacial advances or stillstands (Penck and Brückner, 1909). Changes in sediment and water fluxes during these climatic intervals can lead to river aggradation that is followed by incision. The ages of such climatically controlled surfaces are often similar across a region that has experienced similar climatic conditions. Thus, correlation of undated surfaces with ones dated at another locality or with known climatic changes has often been used to estimate the age of the unknown surface (Avouac and Peltzer, 1993).

Unfortunately, little is known about what controls the formation of bedrock straths. They have been suggested to result from episodic tectonic uplift, in which periods of quiescence lead to strath cutting, and from climatic changes in which increased water fluxes cause lateral planation, or, alternatively, in which increased water discharge causes enhanced incision, leaving the former bed of the river as an abandoned strath. They may form irrespective of direct climate or tectonic controls. For example, if a landslide upstream provides an abundance of sediment to a river, this extra load may mantle the river bed. A river can't incise into underlying bedrock if it is covered with debris, so perhaps it expends some of its energy eroding laterally into bedrock valley walls, thereby creating a strath. Most important, at present one can neither generalize about what controls strath formation nor assume downstream continuity at the time of formation (Merritts et al., 1994). Therefore, individual strath surfaces often have to be dated to define rates of tectonic processes. Even so, typically they will only be useful in providing rates of river incision at localized spots on the river profile.

Even where the physical downstream continuity of a terrace is clear, it is not always safe to assume that the upper surface represents an essentially isochronous horizon.

FIGURE 2.11. Schematic configurations of river terraces

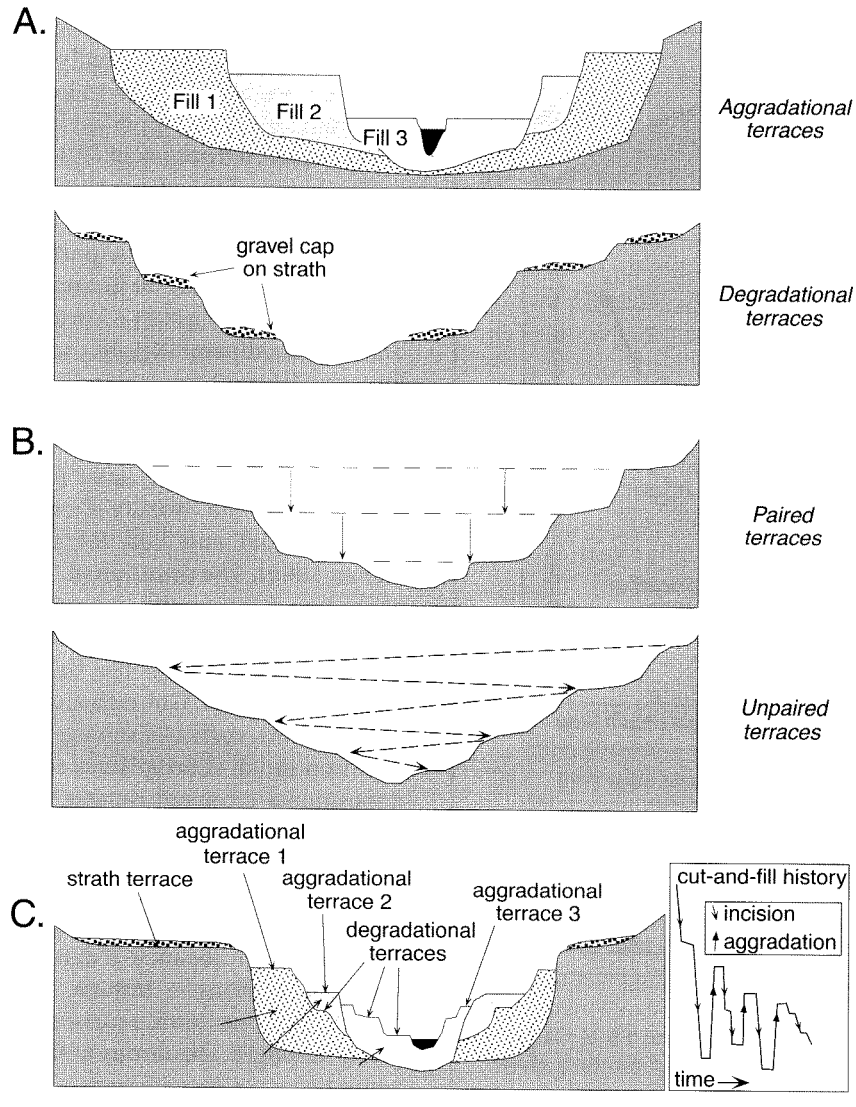

A. Cross-sectional sketches of aggradational and degradational fluvial terraces. B. Paired and unpaired river terraces. C. Cross-section showing complex sequence of aggradational and degradational surfaces. Multiple cut-and-fill events are outlined in the right-hand box.

The potentially complex nature of terrace formation is strikingly illustrated by a terrace that crosses the San Andreas fault in southern California near Cajon Pass (Weldon, 1986). When the terrace surface is compared with the modern stream gradient, the terrace appears to have been warped upwards more than 30 m (Fig. 2.12A), although it is not physically disrupted across the fault. Careful dating of the aggradational fill underlying the terrace, however, was facilitated by the discovery of organic debris within the sediments. These ages indicate that both the initiation of aggradation and the initiation of incision are remarkably diachronous (Fig. 2.12B) along

Figure 2.12. Terrace formation

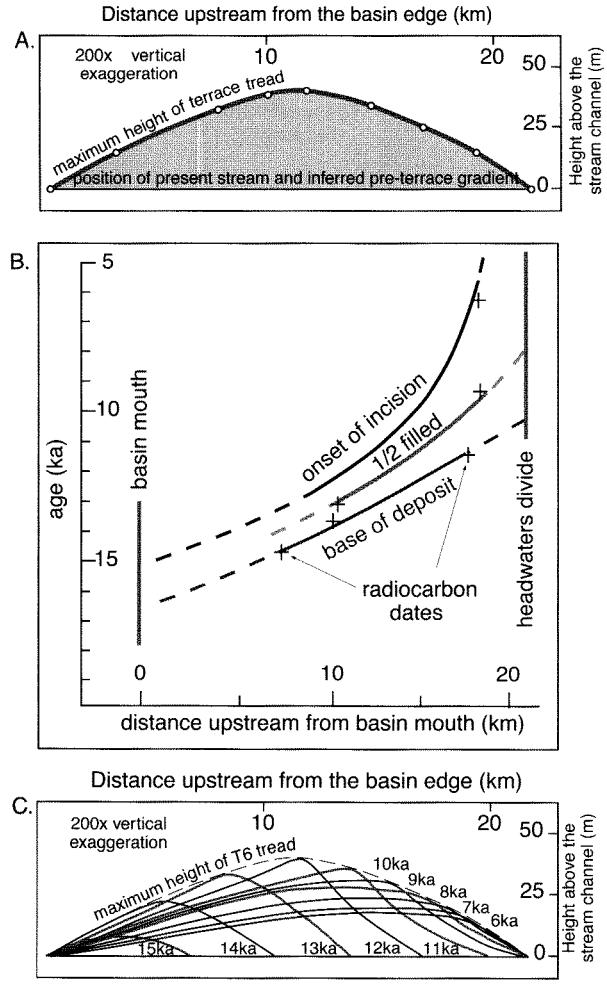

A. Height of the top surface of terrace T6 at Cajon Creek, California, compared with the modern river. The gradient of the modern river is removed, in order to emphasize the apparent upward bowing of the surface. The highest part of the terrace occurs where it crosses the San Andreas fault, but there is no apparent offset here. B. Variations in the timing of initiation of aggradation and incision along Cajon Creek, both of which are highly diachronous. Radiocarbon dates (crosses) on the fill are used to calibrate the aggradation–degradation cycle. Incision is assumed to begin shortly after the maximum thickness of fill is attained. C. Interpretation of the evolving topographic profile of the terrace due to migration of the locus of deposition and erosion. Modified after Weldon (1986).

the terrace surface. Compared to the upstream reaches, deposition commenced ~4 kyr earlier in the downstream reaches, and incision of the aggraded surface began there ~7 kyr earlier. Thus, while upstream parts of the terrace were just beginning to aggrade, the dissection of the downstream areas had already begun! Even though the entire terrace is less than ~15 kyr old, the age and time of abandonment of the upper surface of the terrace varies by ~7 kyr across a distance of ~10 km (Weldon, 1986).

The cause of this diachronous response is unknown. Alluvial terraces form within coupled, complex systems that include erosion, transport, and deposition of sediments. Such systems do not respond instantaneously or uniformly to changes in controlling parameters, such as discharge, sediment supply, rock uplift rate, or base-level lowering (Humphrey and Heller, 1995). Instead, changes in aggradation or degradation propagate up- and downstream through both alluvial and bedrock systems at rates which may be related to the diffusivity of each system and to the velocity of kinematic waves that move along alluvial and bedrock reaches (Humphrey and Heller, 1995). The duration of these waves of deposition or erosion often greatly exceeds the duration of the perturbation that initiated the wave. Many drainage basins have equilibrium response times that are considerably greater than 10^5 yr. Given that many changes imposed on river systems, such as discharge variations due to climate, occur on much shorter times scales, it seems likely that depositional/erosional systems will be constantly integrating the responses to successive variations in controlling parameters. Thus, equilibrium may be rarely attained in fluvial systems. The diachrony displayed by the Cajon terrace (Weldon, 1986) may typify many fluvial terraces. In the common absence of data to delineate chronologic differences along a terrace, however, most workers assume the upper terrace surface is essentially isochronous along its length. Diachrony at the scale of a few thousand years becomes less important when older terraces are considered, but for postglacial and Holocene terraces, such variability would significantly distort rates that were calculated assuming an isochronous terrace surface.

Alluvial Fans

In many respects, the surfaces of alluvial fans are similar to fluvial terraces. Slopes generally decrease down-fan and any longitudinal section displays a slightly concave upward profile. Deposition on most fans is considerably more episodic than in rivers, and in addition to channelized fluvial processes, various types of mass flows

and unchannelized flows tend to dominate deposition. Although most fans are characterized by steady, down-fan decreases in gradient, some fans appear to be segmented (Bull, 1964), such that in cross section, they comprise a suite of fairly straight slopes that abruptly change where the linear slopes intersect. Such segmentation can result from shifting of the boundary between deposition and erosion up or down the fan. For example, if deposition is focussed on the fan apex (also termed the fanhead), alluvium will accumulate and steepen this area with respect to the rest of the fan. If the fanhead is subsequently entrenched, remnants of the abandoned steeper surface will remain, but the apex of deposition will shift down-fan. As aggradation on this gentler, down-fan surface proceeds, the upper surface of aggradation may eventually intersect and begin to overlap the steeper, up-fan surface, such that an abrupt slope change occurs at the intersection. In this situation, the upper and lower parts of the fan surface will have different ages. In such circumstances, before using fans as geomorphic markers, the age of each surface should be separately determined. Even in the absence of fan segmentation, most fans are composed of a mosaic of surfaces of different ages, ranging from the modern channels to dissected remnants of long-abandoned surfaces. Weathering of clasts on the surface of a fan often permits the relative ages of different segments of a fan to be defined. Following isolation from deposition, weathering processes, such as fracturing, rind and varnish development, reddening of the underside of clasts, and granular disintegration, begin to modify the appearance and character of the fan surface (McFadden et al., 1982; Ritter et al., 1993). Often, in arid regions, readily visible contrasts in surface color permit classification of the relative ages of different fan surfaces (Bull, 1991). In more humid fans, more time-consuming quantification of changes in the depositional surface may be required to divide the fan into surfaces of differing ages. In order to use a fan surface as a reference against which to measure deformation, only similarly aged portions of the fan should be used to define a reference plane.

Many arid alluvial fans are dominated by deposition from debris flows (Whipple and Dunne, 1992). The surface topography of debris-flow deposits (up to several meters) and the roughening of the fan surface that results from them can determine the scale at which the local surface of the fan can be considered to have a predictable geometry and therefore to be useful as a geomorphic marker. Even surfaces with considerable roughness, however, can often be used successfully as markers, because, despite its irregularities, the average surface gradient can be defined (Avouac et al., 1993), and offsets of this gradient by faulting can be readily recognized (Fig. 2.13).

FIGURE 2.13. Faulted fan surfaces of the Tien Shan

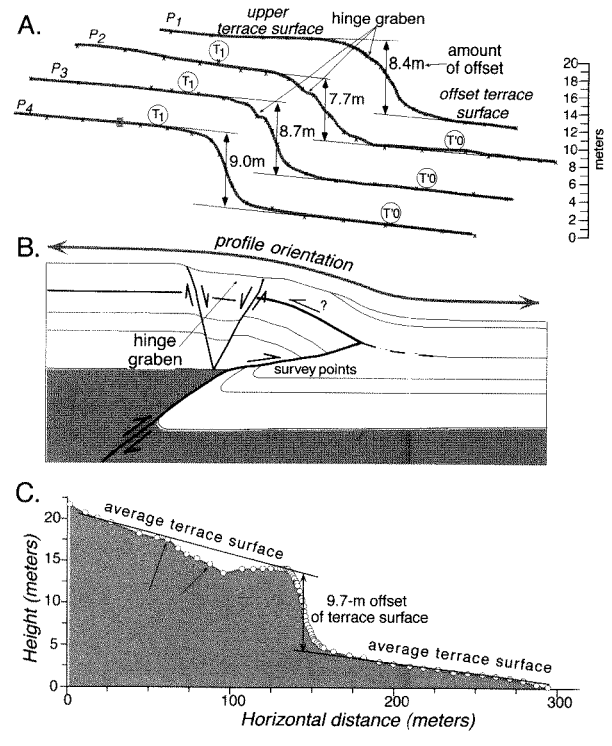

A. Surveyed offsets of the surface of alluvial fans where cut by a thrust fault. Fresh faults scarps have been degraded. B. Interpretation of the schematic structure beneath the faulted terraces. Note that even small irregularities in the surface, such as the "hinge graben," can sometimes be interpreted in terms of the underlying structure. C. On surfaces displaying several meters of local relief, displacements of the "average" down-fan gradient can be derived from surveyed profiles. Modified after Avouac et al. (1993).

Lava Flows, Debris Flows, and Landslides

Despite the meter-scale roughness of the upper surface of most lava flows, the surfaces of elongate flows can provide excellent geomorphic markers. Topographic gradients along the flow surface can be measured directly and numerous surface features can be recognized for cross-fault correlation, the highly resistant flows have a high preservation potential, and the flow itself is often directly datable with radiometric methods.

The surface topography of mass movement deposits, such as debris flows, mudflows, and landslides, often depends in part on their water content and viscosity at the time of deposition (Whipple and Dunne, 1992). The higher the water content, the smoother the upper surface of the deposit and the greater the downstream travel distance are likely to be. These mass movement deposits have the advantage of having formed as the result of an instantaneous event, thereby avoiding the problem of diachrony in the surface seen, for example, in the fluvial terrace case. Moreover, it is not uncommon that they overrun or contain within their deposits organic debris that can be radiocarbon dated. As a consequence, a date from anywhere within them can often pinpoint the age of the deposit closely. In contrast, a ^{14}C date within the strata of an aggradational terrace simply provides a lower limit on the time of abandonment of the depositional surface. Multiple dates are often needed on such surfaces in order to judge the rate of aggradation and the timing of abandonment (Weldon, 1986) (see Fig. 2.12).

Erosional Surfaces

It has long been recognized that, during long intervals of tectonic quiescence, topography can be bevelled off by erosional processes and a low-relief landscape can be produced. Isolated erosional remnants (monadnocks or inselbergs) may be surrounded by *pediments*: erosional surfaces of low relief carved into bedrock. Across broader geographic regions, *peneplains* characterized by slightly undulating and generally featureless topography can result from long-continued erosion and deposition in the absence of active deformation. When such erosional surfaces formed in the distant geologic past, they were often eventually buried by subsequent deposition, such that a regionally extensive unconformity is preserved. When such low-relief surfaces (pediments, peneplains, regional unconformities) are uplifted tectonically, they can form prominent markers in the landscape. Typically these erosional surfaces are identified by the low-relief of the uplifted surfaces, an accordance between summit heights, and/or the smoothly varying topography of broadly folded or faulted terrains. Often this low relief stands in contrast to a nearby tectonically active front characterized by high relief. For example, the Wind River Range of Wyoming rises about 2 km above the adjacent basins and has steep-walled, glaciated canyons cutting its flanks. In many of the high-altitude parts of the range, however, there are rolling, low-relief surfaces. The elevation and tilt of many of these remnant surfaces can be extrapolated laterally to join other, similar remnants and to define a regionally extensive high-altitude surface of low relief (Small and Anderson, 1998). Such surfaces can not have formed at high altitude, but instead represent uplift of a surface that was created near the regional base level in the distant past. Similarly, in the Tien Shan of Central Asia, a regionally extensive erosion surface was bevelled across Paleozoic rocks and buried by Cenozoic sedimentary rocks (Chediya, 1986; Sadybakasov, 1990). This surface has been recently exhumed due to rock uplift. The striking contrast in erodability of the rocks above and below the unconformity has caused the Cenozoic sediment to be rapidly eroded, revealing the unconformity surface (Fig. 2.14), which provides an excellent marker for recording folding and faulting of ranges that rise as much as 2 km above the surrounding terrain (Burbank et al., 1999). Not only do erosion surfaces like those in the Wind River Range or the Tien Shan serve to define rock uplift, but the unconformity surface itself forms a reference for calibrating the amount of erosion that has occurred beneath it (Small and Anderson, 1998).

FIGURE 2.14. Exhumed unconformity surface in the Kyrgyz Tien Shan

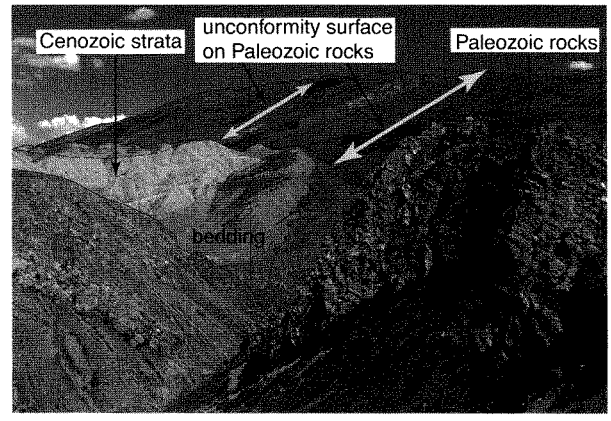

The erosion surface was cut across folded Paleozoic bedrock and was later buried by 3 to 5 km of Cenozoic strata. Late Cenozoic uplift above local base level has caused the Cenozoic strata to be stripped off the unconformity. Today the surface is folded and rises about 1.5 km above the adjacent basins. Deformation of this regionally extensive marker surface readily defines the magnitude of differential rock uplift.

Linear Geomorphic Markers

Whereas the previously described geomorphic markers represent areally extensive surfaces, it is also possible to use linear geomorphic and man-made features to determine deformation. Although displaced planar features are more suitable for defining regional tilting, linear features can provide ideal piercing points from which an offset can often be unambiguously measured. Unlike many two-dimensional surfaces, such as marine or fluvial terraces, many linear geomorphic features can be formed by individual events, some of which may have occurred instantaneously, from a geological perspective: for example, the levees that form on the margins of a debris flow. Such features often have no direct relation to climatic variations, so that ages need to be determined for each event in order to determine rates of deformation.

Rivers and Ridge Crests

The courses of rivers and ridge crests that are displaced across strike-slip faults can clearly record lateral offsets (Fig. 2.15A). It is important to ascertain, however, that the deflection of a stream is due directly to differential displacement of its course by faulting and is not the result of the intersection between a regionally sloping surface and a fault scarp. If streams are offset in directions that oppose the regional slope, the cause of the offset is more likely to be tectonic than when the deflection occurs in the direction of the regional slope. Due to strike-slip motions, streams can be "beheaded," by which it is meant that an abandoned stream channel abruptly terminates as it crosses a fault (Fig. 2.15B). The difficulty in assessing offsets of rivers and ridge crests lies in making reliable correlations from one side of a fault to the other. Commonly multiple ridges and streams cut across faults, so that specific correlations can be ambiguous.

Because rivers are capable of incising and modifying any displaced profile, vertical movements often are underestimated by the apparent displacement of the river channel at the location of the fault. If the upstream part of a stream bed is elevated by faulting with respect to its downstream continuation, the stream will tend to incise through the scarp. Remnants of the former valley floor may be preserved as small terraces on either side of the channel, and their height above the downstream, but offset continuation of the channel can be used to assess the amount of vertical displacement (Beanland and Clark, 1994).

FIGURE 2.15. Beheaded Streams

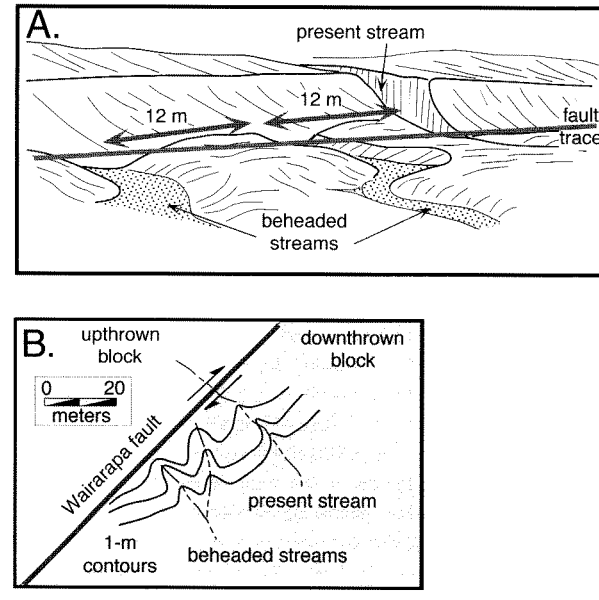

A. Sketch of beheaded streams along the Wairarapa strike-slip fault, North Island, New Zealand. Spacing between stream indicates two previous earthquakes with about 12 m of displacement in each event.
B. Map with 1-m contour of offset and beheaded stream channels along the Wairarapa fault. Modified after Grapes and Wellman (1993).

Glacial Moraines

The elongate ridges of ice-transported debris that form glacial moraines provide linear geomorphic markers that have an obvious direct climatic cause. Lateral displacements can often be readily measured from the offset in map view of the linear trend of the moraine crest, whereas vertical offsets can be assessed by comparing the topographic trend along the length of the moraine crest on either side of a fault.

If advances attributed to surging glaciers are excluded, then most major glacial advances are responses to major climatic changes. Thus, one might expect to be able to correlate the record of successive glacial advances with the record of Quaternary climatic fluctuations (see Box 2.1). For the most recent advances, this is often true, although the timing of the maximum extent of alpine glaciers in any particular mountain range often differs by thousands of years from the time of maximum ice sheet extent

Box 2.3. The Problem of Moraine Survival

Ever since the first synthesis of the record of alpine glaciation (Penck and Brückner, 1909), it has been common to recognize three or four major moraines in glaciated valleys. At the same time, the global climate record indicates that there have been at least 10 major glaciations in the past 1 Myr and many more in the previous 1 Myr. Why is there such a mismatch between the number of glaciations and the preserved morainal record of those glaciations? One answer comes from a statistical analysis of the probability of moraine preservation (Gibbons et al., 1984). Let's assume that there has been a succession of fifteen glaciations and that, with respect to other glaciations, the relative magnitude of each glaciation and its associated advance is randomly distributed. What would happen if the most recent glacial advance were also the largest? It would wipe out most or all of the geomorphic record of all previous advances. If, on the other hand, the glaciations happened to fall sequentially from the most extensive at the beginning to the least extensive at the end, then every single glaciation would be represented. The question of how many moraines will survive can be posed statistically as follows: the probability (P) that n moraines will survive, if there were N glaciations is

$$P(n/N) = 1/N \sum_{N=n-1}^{N-1} P\left((n-1)/N\right)$$

For example, the probability of two moraines surviving, if there were four glaciations, is

$$P(2/4) = 1/4[P(1/1) + P(1/2) + P(1/3)]$$

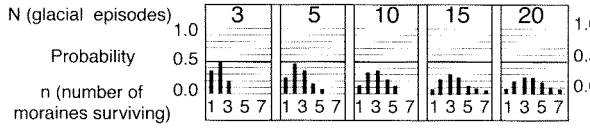

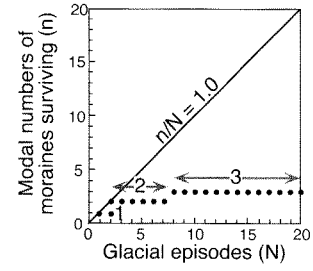

Because P (1/N) = 1/N, P (2/4) = 1/4 (1 + 1/2 + 1/3) = .458. The probabilities for differing numbers of preserved moraines can be quite readily computed. Perhaps surprisingly, they indicate that, for eight to twenty glaciations with randomly distributed magnitudes, the most likely number of moraines to survive is three!

Overall, it is clear that a succession of glacial moraines will typically provide only a fragmentary record of climate change. Similarly, to the extent that aggradational terraces are correlated with the magnitude of glacial advances (as is often supposed), it is likely that the preserved aggradational terraces have buried older, smaller terraces beneath them.

Source: Gibbons, A.B., Megeath, J.D., and Pierce, K.L., 1984, Probability of moraine survival in a succession of glacial advances: Geology, v. 12, p. 327–330. *Fig. 3 and 4, p. 328.*

(Gillespie and Molnar, 1995). Therefore, while an absolute date on a moraine is always preferred, an approximate age can be assigned to undated moraines and tectonic rates (with appropriate uncertainties) can be calculated based on observed offsets.

When moraines other than those associated with the most recent advances are considered, the one-to-one correlation with the climatic record typically breaks down due to incomplete moraine preservation (Box 2.3). In such circumstances, a local glacial chronology associated with specific preserved moraines needs to be established in order to have reliable control on long-term rates of deformation. It is commonly assumed that within any area experiencing a regionally consistent climate, most of the glaciers would be expected to advance and retreat approximately synchronously, but there are few well-dated tests of this contention (Gillespie and Molnar, 1995). In the absence of dates, it is therefore not uncommon to try to correlate with the global climatic record, but such correlations should be made with considerable skepticism.

Other Linear Features

Numerous other linear features, both naturally occurring and man-made, can be used as markers for gauging displacement. Fairly viscous debris flows can create raised levees of coarse debris along their channel margins (Beanland and Clark, 1994). Fence lines, railroad tracks, curbs, sidewalks, lines painted on streets, and even tracks created by cars, motorcycles, or bikes can provide linear markers that are readily measured and are useful

for documenting either co-seismic offsets of recent earthquakes (e.g., the scarp of the 1992 Landers earthquake in California displaced alluvial fans that sported hundreds of motorcycle paths) or slower rates of creep. These man-made markers are not geomorphic features in a strict sense, but when trying to generate a catalogue of displacements along a recently ruptured fault zone, any displaced linear feature with a known pre-faulting geometry should be evaluated.

Commonly Encountered Problems with Markers

The most typical difficulty in extracting the maximum information from a displaced geomorphic surface is the absence of a well-documented age for the surface. Considerable effort often is warranted to try to uncover datable material that can constrain the age of the feature. A knowledge of the array of available dating tools, experience with the appropriate field procedures for collecting suitable material for a specific dating method, and a both thorough and innovative approach to the problem of defining geomorphic ages is a boon to anyone attempting to obtain reliable age constraints and hence deformation rates.

Correlation of partially preserved geomorphic features presents another challenge. As older and older markers are examined, their preservation typically becomes increasingly fragmentary. Unless there are distinctive characteristics that permit discrimination among features of differing ages, the correct correlation among the remnants may be difficult to achieve. A traditional field technique for terrace remnants, for example, has been to survey the height of terraces along local reaches and to correlate the terraces from one site to another based on their relative height above the river. This can be misleading, because it assumes a consistency in the longitudinal profile of the terrace through time. A better technique is to employ continuous, geodetic surveying along terrace surfaces (Merritts et al., 1994) and to document the connection from one reach to the next whenever possible (Fig. 2.16). Even with such data, reconstruction of the long profiles of multiple terraces can be ambiguous. It is important also to distinguish between strath and aggradational terraces, because, when aggradational terraces primarily result from a downstream rise in local base level, their gradients are likely to be gentler than those of most upstream strath terraces. Recognition of different terrace types, continuous geodetic surveying, dating of terraces, and analysis of how and why the terrace sequence developed all assist in creating a reliable reconstruction.

Other problems can arise when a regional chronology of geomorphic markers has been developed and is subsequently applied to the deformational analysis of local sites. Suites of aggradational terraces or of glacial moraines are often dated by assembling ages from individual outcrops spread over a broad area. This is a reasonable, and often the only practical approach. Nonetheless, it is important to be aware of the possible presence of terraces or moraines that are unrelated to the regional sequence. Surging glaciers, for example, often advance largely independently of climatic controls. Yet, they create moraines that are typically indistinguishable from those of non-surging glaciers. Ages assigned to those moraines based on correlation to a climatic record would be erroneous. Similarly, a very large landslide in a catchment may overwhelm the transport capacity of a river. This would cause the river bed to aggrade, and an aggradational terrace could be left behind that is unrelated to terraces in nearby drainages which reflect instead the regional climatic controls.

Summary

Geomorphic markers abound within many landscapes. Common geomorphic markers include wave-cut benches (marine and lacustrine), fluvial surfaces (terraces and fans), and linear features, such as moraines. Clever reading of the landscape and innovative adaptations of the general principles and approaches discussed here provide a basis for utilizing geomorphic markers in almost any geomorphic setting. One must attempt to understand the pristine, undeformed shape of the marker (formally, the initial conditions of the problem), because this forms the basis for all interpretations of deformation. Dating of geomorphic features takes persistence, familiarity with available techniques, innovation, and some luck. The search for datable material is often tedious, but as one geologist said, "If you haven't found datable material, it's because you haven't looked carefully enough!" All calculations of deformation rates depend on assigning ages to displaced features. Therefore, those long searches can often pay off by yielding new insights into how rapidly deformation has occurred in the past. In the next chapter, we examine several approaches to dating of geomorphic, stratigraphic, and structural features that record deformation. Just as geomorphic markers, such as moraines, terraces, and alluvial fans, have some

FIGURE 2.16. Correlation of remnants of river terraces based on an example from the Mattole River, northern California

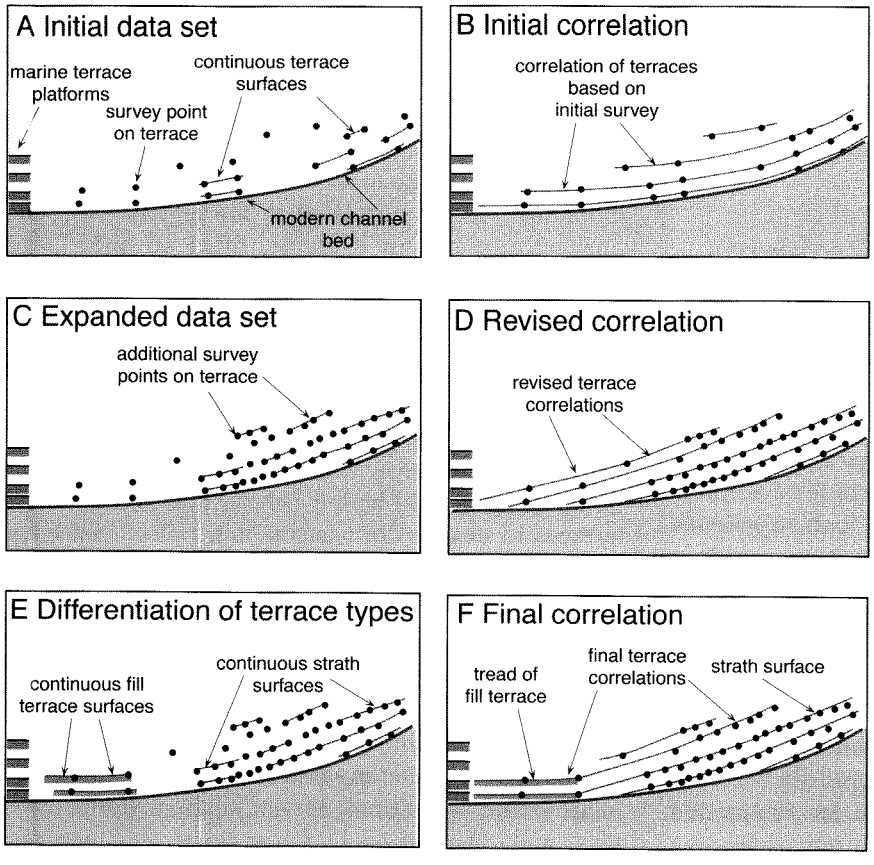

A. Traditional technique of surveying the altitude of terraces in local reaches provides isolated points that must be correlated. B. If it is assumed that the past and present river gradients were parallel, correlations are then based on the height of a terrace above the modern river bed. C. More spatially continuous surveying of the upstream extent of terraces can define their gradients more reliably than can be done solely with correlated spot heights. D. When compared with the modern gradient, the reconstructed terraces are clearly not parallel to the modern profile. E. When the surfaces of aggradational terraces are distinguished from those of strath terraces, contrasts in gradients between the two terrace types become apparent. F. Terrace reconstruction based on survey, dating, and geomorphic field evidence shows strath terraces with steep gradients merging into the present river profile. Aggradational terraces with gentle gradients result from deposition forced by rising sea level (rising base level). Modified after Merritts et al. (1994).

predictable geometries, different kinds of faults and folds display contrasting styles of surface deformation, as discussed in an ensuing chapter. When fault-zone displacements are combined with rates derived from dated and deformed geomorphic markers, a three-dimensional reconstruction of fault-zone evolution, rupture history, landscape perturbations, and geomorphic responses can be attained.

CHAPTER 3

Establishing Timing in the Landscape:— Dating Methods

The science of tectonic geomorphology relies strongly on placing time controls on the landscape. In order to determine the rate at which a fault moves or a surface deforms, we must establish the age of offset features. The precision needed depends on the questions being asked, and on the recurrence time scales of the events themselves. Until the advent of radioactive dating methods, the principal means of establishing timing in the landscape was through the use of relative dating methods. The distinction between relative and absolute dating methods is that relative methods yield relational information only (surface *X* is older than surface *Y*, which is in turn older than surface *Z*), whereas absolute dating allows us to place a number on the age (terrace *X* was created 3565 years before the present). The latter is absolute in the sense that it does not require attention to any other surface, but one must be aware of the potential errors inherent in each of the absolute dating methods. When calibrated against some absolute ages, several relative dating techniques lend themselves to some degree of quantification, making them "semi-quantitative" methods. In Tables 3.1 and 3.2 we list several of the frequently applied methods, the age ranges for which they can be used, and a primary reference to the literature where they are better discussed. This chapter does not present an exhaustive review of the available techniques, but rather illustrates a few of the techniques, focusing on the newer and more quantitative methods. For a rather comprehensive review of dating techniques, see Noller et al.'s (2000) *Quaternary Geochronology.*

Relative Dating Methods

Clink versus Thump, and its Quantification: The Clast Seismic Velocity Method

For years, geomorphologists have determined the relative age of a surface by walking up to the surface to be dated and hammering on the boulders protruding from it. The resulting sound, which is a sharp bell-like clink if the boulder is fresh, and a dull and boring thump if the boulder is old and decrepit, is then used to assign a relative age. Many boulders are pounded and a statistical sense is developed about the age of this surface relative to some other. About fifteen years ago, this method was modified to allow quantification (Crook, 1986). The clast seismic velocity method is based on the principle that a rock exposed at the earth's surface will develop microcracks through a variety of weathering processes, and that the number of microcracks controls the propagation speed of seismic waves (compressional waves, or sound) through the rock. Although it is difficult to measure microcrack density, it is quite easy to measure the seismic velocity by using a micro-seismic timer, as illustrated in Figure 3.1A. For each of several spacings between the accelerometer and the hammer, many measurements of travel time are made. The travel time is recorded, and is converted to velocity by dividing through by the separation distance between hammer and sensor. The clast seismic velocity of a particular boulder is then calculated, and the next boulder is selected. Many boulders on each surface to be dated (e.g., moraine, alluvial fan,

TABLE 3.1. Relative Dating Methods

Method	Age Range	Materials Needed	References
Clast seismic velocity	1–100 ka	Boulders	Crook, 1986; Gillespie, 1982
Obsidian hydration	1–500 ka	Obsidian lavas	Pierce et al, 1976
Soils	10–500 ka	Soils	Harden, 1982
Mineral weathering	10 ka–1 Ma	Boulders	Colman and Dethier, 1986
Landform modification	10 ka–1 Ma	—	Davis, 1899; Cotton, 1926

FIGURE 3.1. Clast seismic velocity measurements

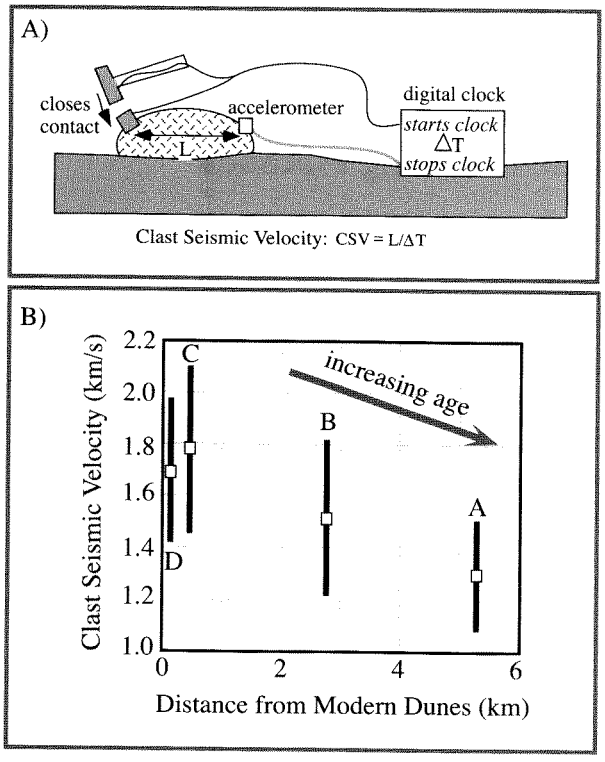

A. Cartoon of clast seismic velocity (CSV) method. B. Results of application of CSV method to the dating of debris flow benches in Panamint Valley, California. Inferred age increases as the CSV declines, reflecting growth of microcrack population within the boulders sampled. Modified after Anderson and Anderson (1990).

debris flow terrace) are measured (Fig. 3.1B). Where the conditions are appropriate, the resulting age progressions have made sense (Crook and Gillespie, 1986) such that surfaces expected to be older than others have clast seismic velocities that are slower, indicating higher microcrack densities. The applicability of the technique is limited to sites where one may assume that the production rate of microcracks is uniform among the boulders to be sampled. This forces us to focus on sites with uniform lithologies, or at least ones where many boulders of the same rock type are available, as the rate of production of microcracks, from any of many possible production mechanisms, is likely to be strongly dependent upon rock type. As with many of the other relative dating methods, however, the assignment of absolute ages from such data is difficult, given that we have no theoretical basis for predicting the rate of decline of clast seismic velocity through time. We do not know how long it will take for the clast seismic velocity to decline by 50%. This forces us to calibrate the technique locally against surfaces of known age, or to consider the resulting differences in clast seismic velocity in only a semi-quantitative sense (Gillespie, 1982).

Weathering Rinds

Rocks exposed to temperature and wetness conditions at the surface of the earth weather by a variety of mechanisms. In general, this weathering proceeds inward from the surface of the rock, where moisture is most accessible and where temperature changes most rapidly and with greatest magnitude on both daily and storm-cycles. This can result in the production of a weathering rind: an identifiable layer that has experienced more weathering than the material beneath it. Crack open most clasts from an old surface, and you will see that a thin layer near the surface of the rock is discolored, revealing that the minerals near the surface have been altered in some way. The thickness of this layer is thought to be a proxy for the time the rock has spent in near-surface conditions. Like the clast seismic velocity technique, this technique is fraught with problems associated with variability of the rind thickness among the surface clasts, the lithologic dependence of the rate of

FIGURE 3.2. Weathering rinds

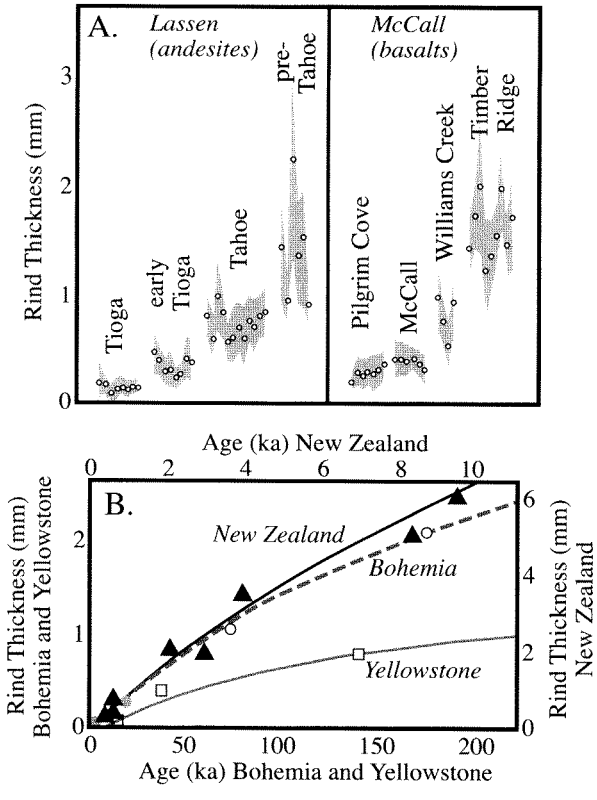

A. Weathering rind thicknesses are used to distinguish glacial deposits in Mt. Lassen, and McCall, Idaho. Absolute age control is lacking on these moraines; bottom axis is arbitrary. B. Growth histories of rinds in Bohemia and Yellowstone (left and bottom axes) and New Zealand (right and top axes). Note decline in growth rate with time. Modified after Colman and Pierce (1992).

rind growth, and inheritance of a weathering rind from previous exposure. Nonetheless, one may control for many of these problems at selected sites. Moreover, the method is inexpensive, low-tech, and readily applied to a variety of deposits. It has been argued that the growth of the weathering rind ought to proceed as the square root of time (Colman, 1986). Presumably, this reflects the fact that the mineralogical changes required to create a visible rind are mostly chemical and require diffusion of species into and out of the rock. Because diffusive processes always result in thicknesses that vary as the square root of the diffusivity multiplied by the time since the process was initiated [$L \sim \text{sqrt}(\kappa t)$], one might expect a square root relation of rind thickness to age. Rarely has sufficient data been arrayed to test this model, as absolute ages on a variety of surfaces are required for the test. Figure 3.2B shows one such test.

In a recent review of chronologies derived for alpine glaciations in the western United States, Colman and Pierce (1992) note that this decline in the rate of rind growth through time (no matter what the exact nature of the nonlinearity) allows one to place limits on the relative ages of deposits based on the ratios of the rind thicknesses. In other words, the ratio of the ages (old/young) should always be greater than the ratio of the rind thicknesses (thick/thin).

The primary problems with the technique are the need for calibration of the effects of local climate, the dependence of weathering rates on the lithology of the clasts, and the possibility of inheritance of rinds from prior exposure. This latter complexity is especially important if the clasts are highly resistant to abrasion within the transport system that delivers the clasts to the site to be dated. For instance, quartzite clasts weathering out of Jurassic conglomerates in central Utah appear on the surface with both weathering rinds and percussion marks from transport during the Jurassic (and perhaps even earlier episodes of transport). Most studies have therefore focused on weathering rinds developed in easily weathered, more abradable clasts such as andesites and basalts (Colman and Pierce, 1992) (Fig. 3.2).

Obsidian Hydration Rinds

A technique used to great effect in archeology is based on the growth of a hydration rind as a glassy surface weathers. Obsidian is a natural glass, generally having a high silica content. The glass hydrates once a surface is exposed to the air. The thickness of the weathered rind is measured in thin section normal to the exposed surface, and is identified by an abrupt roll-off in the refractive index of the glass. The rind is on the order of several microns thick. Because the rate of hydration rind growth is dependent at least slightly on the composition of the obsidian, and surely on the temperature to which the surface has been subjected, the technique requires calibration against surfaces of known age to yield quantitative dates.

Working in a field area containing dated lava flows, Pierce et al. (1976) demonstrated the usefulness of the technique in dating both glaciated volcanic bedrock and glacial moraines that incorporated clasts that had been

FIGURE 3.3. Hydration rind thickness as a function of age

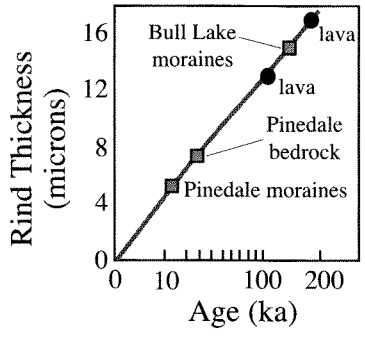

Semilog plot shows logarithmic falloff in growth rate with time. Calibration line from rinds in cracks on surfaces of independently dated rhyolite lava flows, and from subglacially produced cracks in last glacial maximum (Pinedale) bedrock. Circles indicate data from cracks on surfaces of boulders in undated glacial moraines. Modified after Pierce et al. (1976).

glacially abraded. The glaciation is presumed to have generated new cracks in the rocks, which then hydrated (Fig. 3.3). Again, this technique suffers from the likelihood that the rind growth rate is dependent on both rock type and climate. Given that climate varied significantly over the late Pleistocene, during which most of the surfaces with which we are concerned have evolved, this is a significant drawback.

Soil Development

It is common to be faced with the need to date a depositional surface in which a soil has developed. Several techniques have evolved, most of them quite qualitative, to attempt to place ages or relative ages on these surfaces based on the degree of soil development. Soil color is often the easiest indicator of soil age, although as in the identification of minerals, there are many ways to go wrong using such a simple criterion. More robust indicators include the accumulation of carbonate, clays, and iron within the subsurface. In formal pedogenic studies that attempt to quantify the soil development through time on a series of geomorphic surfaces of similar parent material (a soil chronosequence), many indicators are documented. One integrated measure that synthesizes diverse indicators of pedogenic maturity, including soil clay content, soil color, and soil structure, is called the Harden index (Harden, 1982). While it is not our purpose here to review all such techniques (see, for instance, Birkeland (1990) for such a review), we will illustrate a couple of methods that have been used to obtain ages.

Carbonate Coatings and Other Pedogenic Indicators

In arid regions, soils accumulate calcium carbonate in the near-surface. Rainwater delivers some calcium directly and dissolves calcium-bearing minerals (mostly carbonates) from both the parent material and from airborne dust that has accumulated on the soil surface. This can be re-precipitated at depth as the water is wicked back up to the surface during evaporation or uptake by plants, leaving the remaining water supersaturated with respect to calcite. Precipitation is also favored if the CO_2 content decreases or if the temperature increases in the soil, lowering the solubility of calcite. The total mass of carbonate in the soil, and that part of it that occurs as coatings on the bases of soil clasts, have both been used in documenting relative ages of surfaces. Recent work in Idaho (Vincent et al., 1994) has shown that the rate of growth of carbonate coatings has varied by at least a factor of two and perhaps three over the last few tens of thousands of years (Fig. 3.4). The mean rate over the last 20 kyr has been about 65 microns per kyr. Those clasts

FIGURE 3.4. Carbonate coatings as a function of deposit age, from soils in the Lost River Valley, Idaho

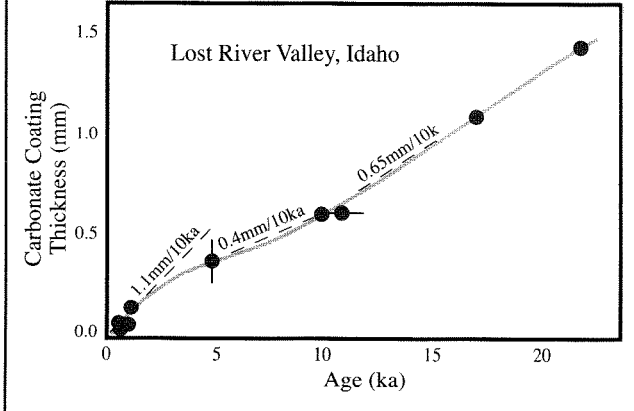

Although rates vary by a factor of more than two, the long-term average rate of about 0.6mm/10kyr appears to hold for this setting. Modified after Vincent et al. (1994).

from surfaces well over 100 ka commonly have coatings on the order of 10 mm thick. We note that, whereas in this particular region of Idaho one might be able to determine the age of a surface by documenting the thickness of these coatings, the technique requires a local calibration, which in turn necessitates having some surfaces of known absolute age. Uncertainties therefore creep in, not only from the variability of the coating thicknesses themselves, but from the errors in the dating methods used to obtain the absolute ages of the surfaces used in the calibration.

Lichenometry

A technique that has long enjoyed use in geomorphic studies is lichenometry, in which the diameter of a specific type of lichen is used as a proxy for the time a rock has been exposed at the surface (e.g., Innes, 1984; Innes, 1985; Locke et al., 1979; Porter, 1981a). The lichen most commonly employed is *rhizocarpon* (one or another subgenus), which is crudely circular in shape and whose diameter is thought to increase linearly with time. Until recently, the practice was to record the largest lichen found from the surfaces of often hundreds of boulders on the surface to be dated, or to take the mean of the five largest lichens. Again, local calibration is necessary, as climate dictates the rate of lichen growth. Typically, the calibration of the growth-rate curve comes from surfaces that have been exposed for a known period of time, most commonly from human-made structures. One clever approach uses lichens on tombstones, which of course have the age stamped on them! Lichenometry has been used effectively to date moraines in glacial settings (Denton and Karlen, 1973; Porter, 1981a) (Fig. 3.5) and major rockfalls in rugged landscapes (Porter and Orombelli, 1981).

This technique has seen a resurgence recently through the work of Bull (Bull, 1996; Bull and Brandon, 1998; Bull et al., 1994). He argues that the lichenometric method is much more robust if one records the maximum diameters of lichens on many hundreds to thousands of rocks on the feature to be dated (he does this using a digital micrometer linked to a mini-computer in his back-pack). A major problem with the previous practice was that one relied heavily upon the regularity of the statistics in the population of lichen diameters, i.e., that after sampling *n* random boulders one would record the same maximum diameter, even though *n* is relatively small. Bull's (1996) revision of the technique retains all the population statistics and builds up a dense histogram (probability density) of the lichen diameters. Bull has applied his technique in several settings, recording thousands of measurements, and developing quite impressive statistics. He calibrates his growth-rate curve using surfaces that are independently dated, often on the basis of tree-ring counts. From the resulting distributions of maximum lichen diameters, he argues convincingly that one can resolve discrete events in the record that are separated by a few decades or even less. Most interestingly, and most pertinent to our topic, Bull argues that he can resolve discrete pulses of rockfall material associated with seismic activity, at sites in both California (Bull, 1996) and New Zealand (Bull and Brandon, 1998). At the rockfall sites in California, the composite probability density plots of lichen diameters (Fig. 3.6) revealed several peaks, which when calibrated using the tree-ring dated sites correspond to historical Sierra Nevada and San Andreas earthquakes within a few years. Importantly, the breadths of the distributions allow assignment of error estimates, which in this case are ± 3–10 years, a remarkably small error for ages on the order of hundreds of years, given that the clock is a biological one.

FIGURE 3.5. Lichen diameter as a function of age

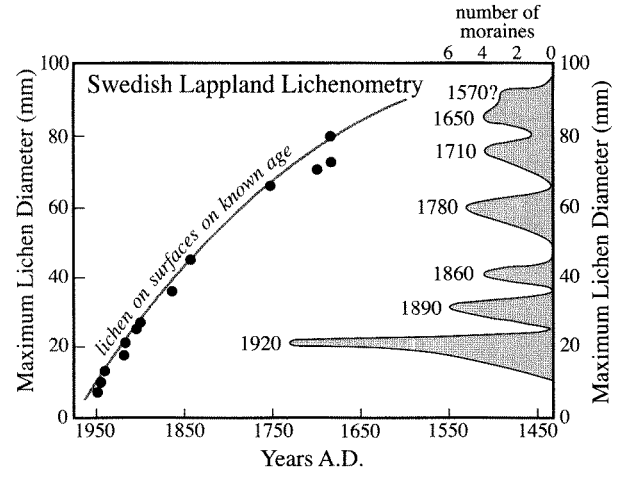

Lichen growth curve calibrated using surfaces of known age in the Swedish Lapland. Note non-linear growth, with the most rapid growth for youngest surfaces. On right is a histogram of the number of moraines (top axis) with a given maximum lichen diameter, and hence of a given age inferred from the calibration curve. Modified after Denton and Karlen, 1973.

FIGURE 3.6. Histograms (probability density functions) of rhizocarpon lichen diameters on boulders on talus in the Sierra Nevada, California

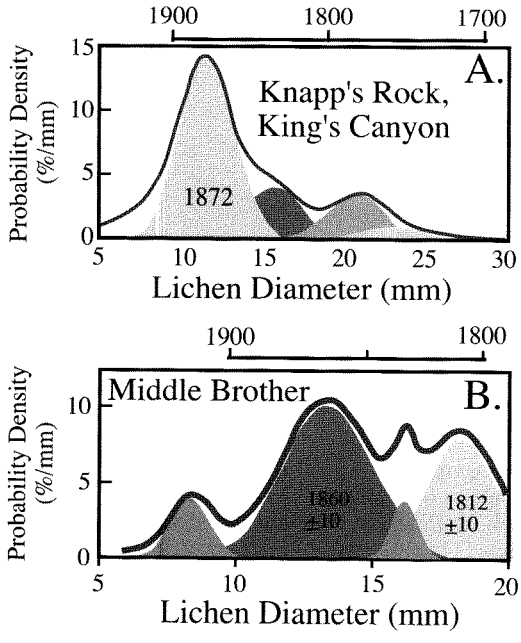

Peaks record times of generation of new talus blocks, corresponding to major historical earthquakes in California. Modified after Bull (1996).

As in all techniques, there are limitations and uncertainties. Here one must obviously have a climate in which a well-behaved lichen thrives, and must be able to obtain independent ages on surfaces for use in calibrating the growth-rate curve. There will always be some lag between deposition of a rock on a surface and its colonization by lichen. In addition, lichens apparently grow rapidly at first (the great-growth phase), before entering their linear growth phase. Some studies (Porter, 1981a) have suggested that lichen growth rates may be higher on fine-grained volcanic substrates than on coarser-grained intrusive rocks, whereas other studies conclude that lithology, smoothness of the substrate, local mean annual temperature, precipitation, and length of the growing season apparently do not exert a strong influence on the growth rate. Protection from the sun and wind does promote more rapid growth, so that Bull (1996), for instance, measured only exposed lichens. Whereas further testing of the population techniques for lichenometry is warranted, this approach holds remarkable promise for developing rather detailed chronologies on geomorphic surfaces of less than 500 years old. This is an age range of great interest to paleoseismology, but one in which absolute age control is often difficult to achieve.

Absolute Dating Methods

Most absolute dating methods rely on some process that occurs at a regular rate—in essence, a clock. In some instances, these clocks leave a physical record that may be biological, as typified by tree rings, or geological, as represented by annual lake beds or varves. The remaining techniques rely on either atomic clocks or cosmic clocks or both. Here we review the fundamental concepts of the atomic clocks we will use.

Some (parent) atoms spontaneously decay through fission to other (daughter) atoms plus associated nuclear fragments plus energy. These events are called radioactive decays. Whereas any particular parent atom may decay at any random instant, the probability of such decay depends on the parent-daughter pair. The lower the probability of decay at any instant, the longer it will take for a population of parent atoms to decay to half its size, and vice versa. This is the notion of the half-life. Mathematically, the process is captured in the differential equation

$$dN/dt = -\lambda N \qquad (3.1)$$

This is a commonly used example of a first-order linear differential equation found in the front of many introductory differential equation textbooks. Here N is the number of parent atoms, dN/dt is the rate of change of this population, and the decay constant λ expresses the probability of decay of any parent atom at any instant. The solution to this equation is an exponential function:

$$N = N_0 e^{-\lambda t} \qquad (3.2)$$

where N_0 is the abundance of the parent atom at time 0. You can easily see that the time it takes for the decay of the population from N_0 to N_0/e (recalling that $e = 2.718\ldots$, this is roughly $N_0/3$) is $1/\lambda$. The half-life, found by solving for the time at which $N = N_0/2$, is $t_{1/2} = [-\ln(1/2) / \lambda]$, or $0.693/\lambda$. In Table 3.2 we list a few of the commonly used radioactive isotopes, their decay constants, and their associated half-lives. We will see that in some cases it is either more instructive or easier to measure the

TABLE 3.2. Absolute Dating Methods

Method	Useful Range	Materials Needed	References: Classic and recent
Radioisotopic			
14C	35 ka	wood, shell	Libby, 1955; Stuiver, 1970
U/Th	10–350 ka	carbonate (corals, speleothems)	Ku, 1976
Thermoluminescence (TL)	30–300 ka	quartz silt	Berger, 1988
Optically stimulated luminescence	0–300 ka	quartz silt	Aitken, 1998
Cosmogenic			
In situ ^{10}Be, ^{2}6Al	3–4 Ma	quartz	Lal, 1988, Nishiizumi, 1991
He, Ne	Unlimited	olivene, quartz	Cerling and Craig, 1994
^{36}Cl	0–4 Ma		Phillips et al., 1986
Chemical			
Tephrochronology	0–several Ma	volcanic ash	Westgate and Gorton, 1981; Sarna-Wojicki et al., 1991
Amino acid recemization	0–300 ka; range temperature dependent	carbonate shell	Bada et al., 1970; Bada, 1972; Wehmiller et al., 1988
Paleomagnetic			
Identification of reversals	>700 ka	fine sediments, volcanic flows	Cox et al., 1964; 1964
Secular variations	0–700 ka	fine sediments	Creer, 1962; 1967; Lund, 1996
Biological			
Dendrochronology	10 ka, depending upon existence of a local master chronology	wood	Fritts, 1976; Jacoby et al., 1988; Yamaguchi and Hoblitt, 1995

accumulation of the daughter isotopes, or the ratio of the parent to the daughter, rather than the parent.

Tree Rings

An entire science of dendrochronology has evolved around the dating of surfaces using tree rings and the exploration of climatic change using the tree-ring width as a surrogate for climatic stresses. In climates with a distinct growing season, trees put on new wood in discrete layers that may be counted to reveal the age of the tree. Growth is rapid in the wet season and the summer, then slows in the winter, resulting in relatively low-density wood with large cells in the growth season, separated by layers of denser, finer wood. Whereas the easiest application is obviously to date a surface with the trees still growing (by cutting down the tree or by coring the tree with a boring device), the technique has been augmented greatly by extending the time series derived from living trees through the addition of time series from dead trees. As the thickness or width of the annual growth ring is dictated by the climatic conditions of water availability and temperature, tree-ring width time series can be viewed as a proxy for a climatic time series. That this climate time series reflects at least a regional, if not a global, phenomenon means that trees far separated should record the same temporal pattern of ring widths. We note that one must take care to account for both the species of the tree, and the long-term trend (decrease) in the rate of ring growth through time as any tree matures (Fig. 3.7). A ring-matching technique is therefore based on a master tree-ring time series that is compiled from a set of trees whose ring-width series overlap. For example, Yamaguchi (1995) demonstrated the time of burial of trees on Mt. St. Helens by debris from prehistoric volcanic eruptions by matching the ring-width time series from trees embedded in or buried by lahars with that of the master tree-ring chronology. This entailed choosing a date for the volcanic event (= the age of the outermost ring), calculating the correlation coefficient between the sample tree-ring width series and that of the master tree-ring series, choosing another sample age, recalculating the correlation, and so on. The resulting plot of correlation versus outermost ring age reveals a strong spike in a particular year, which is interpreted to be

FIGURE 3.7. Tree-ring widths as a function of time for three Douglas fir trees in the Pacific NW of the United States

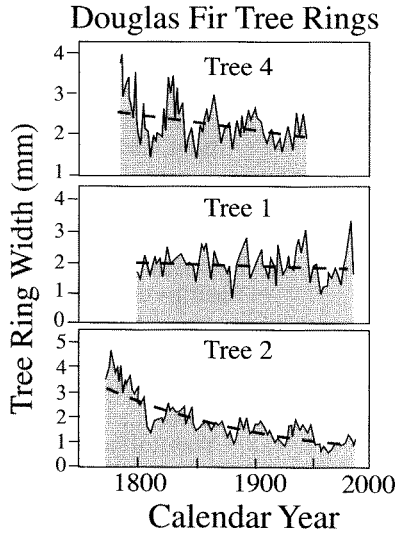

The tree-ring width shows decline in growth rate with age, best seen in Tree 2 (dashed line). Superposed on this are the modulations in growth rate associated with variations of local climate. Modified after Yamaguchi (1995).

FIGURE 3.8. Correlation of tree-width time series with the master tree-ring time series as a function of chosen start year

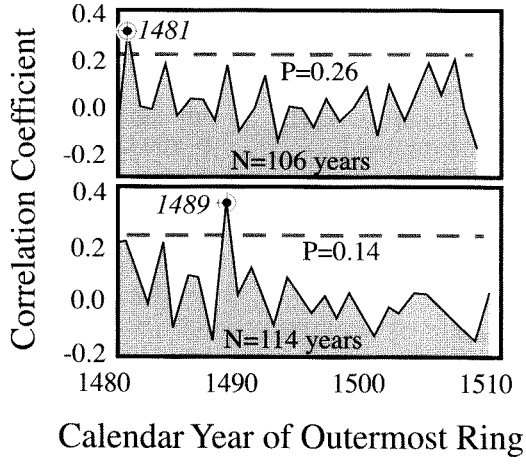

Top series shows strongest correlation for a start date (outermost ring) of calendar year 1481, while bottom series is strongest for start date of calendar year 1489. Correlation coefficients for all other start years have probabilities of random occurrence that exceed the labeled probability, *P*. Modified after Yamaguchi (1995).

the correct match (Fig. 3.8). The technique relies strongly on a trustworthy master tree-ring time series, and works best for dating large trees with longer ring width time series to test against the master chronology.

Tree ring studies have also provided the basis for calibration of the radiocarbon method (see following section). The carbon from a particular tree ring of known age (from counting backward from the bark) can be ^{14}C dated using recently developed techniques that permit dating of very small samples. This calibration holds out to about 10,000 years, the longest compiled tree-ring record.

Detailed studies of tree rings have allowed geoscientists to place very precise dates on important short-lived prehistoric geological events, including rockslides, volcanic flows, and even earthquakes. We will revisit this technique in our discussion of prehistoric Cascadia earthquakes.

Radiocarbon Dating

The most commonly used technique to date geomorphic features and surfaces that are less than about 30 to 40 ka employs carbon 14, known also as radiocarbon because it radioactively decays. ^{14}C and ^{13}C are formed in the atmosphere by cosmic radiation interactions with atmospheric N, resulting in a mixture of atmospheric carbon that is roughly 98.9% ^{12}C, 1.1% ^{13}C, and $1.17*10^{-10}$% ^{14}C, most of it in the form of CO_2. As the atmosphere is well mixed on short time scales, this relative abundance is uniform around the globe. It is from this pool that the carbon in CO_2 is fixed through photosynthesis in plants. Plants should therefore be made of organic carbon that mimics the isotopic ratio in the atmosphere during growth, although it is offset from that ratio due to fractionation during photosynthesis. Once a plant or animal cell dies, it no longer incorporates new carbon into its organic material. Radioactive decay takes over, and begins to modify the ratio of the carbon isotopes in the cells. So it is upon death that the clock starts. We will see that the ^{14}C dating technique is intertwined with at least two other methods, U/Th and tree-ring dating, demonstrating how interdependent some of these techniques have become.

There are two principal means of measuring the ratio of ^{14}C to ^{12}C in a sample. Conventional dating is done by

FIGURE 3.9. Decay of ^{14}C concentration with time follows classic exponential curve

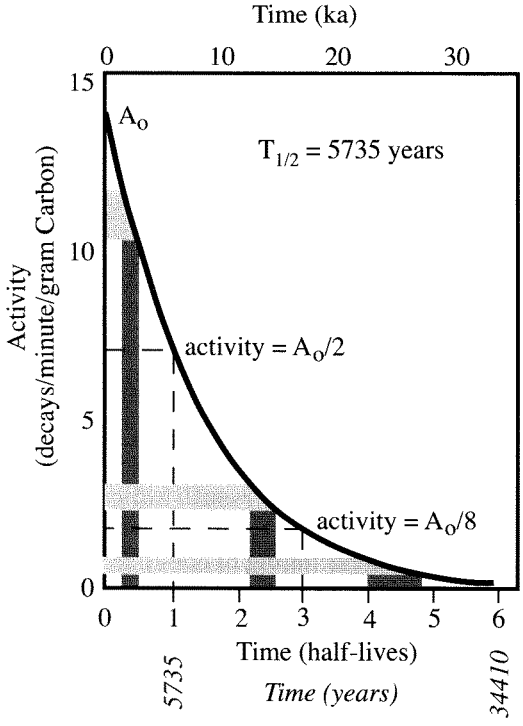

Shaded bars show transformation of uncertainty in activities to uncertainties in age. Uncertainties become very large for low activities. Ages greater than about 7 half-lives cannot be distinguished from infinite ages. Modified after Olsson (1968).

counting the decays of ^{14}C to its daughter ^{14}N through emission of an electron: a beta (β) particle. The rate of decay, as represented by the beta particles, is often measured in decays per minute per gram of carbon and requires samples on the order of a few grams of carbon in size. For old samples, it is necessary to count decays for long periods of time to record enough decays for statistical reliability. Even so, one can see easily from the graph in Figure 3.9 that, because our ability to measure the activity is limited and inevitably has finite error bars associated with it, the meaning of these errors grows for older and older samples until we cannot distinguish between a sample of, say, 40 ka and one of infinite age. This is because, with a half-life of 5735 years, there is a little less than 1% of the original ^{14}C left in a sample if it is older than about 7 half-lives ($(1/2)^7$), or about 40 ka. For example, a gram of modern carbon experiences about 15 decays/minute. If this sample were 40 ka, it would have spanned about 7 half-lives and would generate about $15/2^7$ decays/minute or only about 7 decays/hour. Although such low rates of decay can be counted, incoming cosmic radiation can also trigger the detectors and consequently causes large uncertainties in the detector counts attributable to decay of ^{14}C. (This is why ^{14}C labs are often either deep underground or lead-shielded or both.) Although measuring the decay rate remains the dominant (and far cheaper) technique, it has been augmented tremendously within the last decade or so by the development of accelerator mass spectrometric (AMS) techniques. In AMS dating, the carbon is measured according to its isotopic weight, not according to its radioactivity, or rate of decay. This means that one counts all the carbon atoms in a sample, not just those that decay, so that the sample size can be dramatically reduced to a milligram. When AMS dating was first introduced, it was hoped that AMS would also allow extension of the age range of the technique to many more half-lives. In practice the technique is still not capable of extending beyond about 50 ka. There are both commercial and academic labs that will run samples using one or the other method.

Although ^{14}C dating revolutionized archaeology and allowed scientists to establish the absolute timing from organic remains for the first time in the 1950s, there are pitfalls that one must acknowledge. In order to estimate the age of an object using ^{14}C, one must know 1) the starting ratio of $^{14}C/^{12}C$, 2) the decay rate, and 3) the final ratio. We know the decay rate well, characterized by a half-life of 5735 years, and can measure the present ratio well using AMS or can estimate it based on measured rates of decay. However, because ^{14}C is created in the atmosphere by cosmic radiation, any variations in the production rate of ^{14}C result in a different starting ratio in the organic material. Variations in production rate result from several sources, chiefly variations in the cosmic ray flux, which are associated with fluctuations of the earth's and the sun's magnetic fields. As our measurements of these have lasted for only a few decades, we must rely on calibration. Happily, as mentioned previously, tree rings provide an organic record that can be pieced together back several thousand years—and in the case of bristlecone pines, 10 ka. It is from this record that we know the ^{14}C production-rate record, which is itself of interest to those studying the magnetic fields of the sun and earth. With a ^{14}C ratio in hand, from which

FIGURE 3.10. Correspondence between radiocarbon and calendar years from 1500 to present (jagged black band)

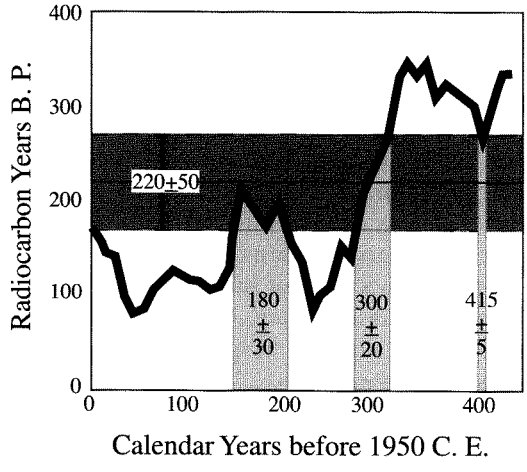

Shaded bar shows how interpretation of a radiocarbon age of 220+50 years can be ambiguous: it could mean the sample came from any of the three light-shaded regions on the calendar year axis. Modified after Porter (1981b).

a radiocarbon age is calculated using the half-life, one may turn to published computer codes (e.g., Stuiver and Reimer, 1993) that allow translation to calendric years (generating a "calibrated radiocarbon age"). The problems are largest at young ages, where the conversion between radiocarbon ages and calendric ages is actually ambiguous (Fig. 3.10): a given sample could be either x or y years old, owing to a large fluctuation in the ^{14}C production rate within the last couple of millennia. This tree-ring calibration method is valid to about 10 ka, beyond which another calibration method is needed. Here we turn to the precise dating of calcium carbonate deposits (in particular, corals) by both AMS with ^{14}C and U/Th dating.

Uranium/Thorium Dating

The uranium decay series represents a very trustworthy set of clocks. The series consists of a set of several isotopes that are generated from their parents at varying rates, and that decay to their own daughters at yet other rates (Fig. 3.11). The ultimate parents of the chains are ^{238}U, ^{235}U, and ^{232}Th. Decays take place at a statistically steady rate that is independent of temperature, of the magnetic fields of the earth and of the sun, and of all other environmental factors that are the bane of many geological and biological clocks. Fortunately, the decay constants for some of these pairs include those that correspond to half-lives that are very useful in neotectonic and climatic investigations.

Because the U/Th series is a more robust clock than is ^{14}C, it has recently been used as a means of calibrating the ^{14}C clock beyond the end of the tree-ring record (Fig. 3.12). In a clever sampling scheme, Bard and others (Bard et al., 1990) used the calcium carbonate from submerged corals off Barbados as a means of obtaining sample pairs from the same material. The corals contained both ^{14}C as some small fraction of the carbon, and U substituting for Ca in the carbonate lattice. Accelerator mass spectrometric (AMS) measurements of the ^{14}C and accurate measurements of the U/Th revealed a consistent offset between the two clocks for samples older than the Holocene. This important result indicates that ages calculated using ^{14}C are as much as a few thousand years too young for samples dating to about 25 ka.

The substitution of U for Ca in carbonate lattices makes shells and carbonate coatings in soils prime targets for U/Th dating. Unfortunately, not all carbonate materials retain the parents and the daughters in their lattice through time, that is, they are not "closed systems." In particular, most shells (for instance, typical clams) leak uranium, making them essentially worthless as clocks. Luckily, most unrecrystallized corals work well, both the colonial and solitary types. In Barbados, Fairbanks (1989) reconstructed past sea levels using *Acropora palmata*, a coral that grows within a couple meters of sea level. The west coast of North America sports numerous marine terraces whose ages are needed in order to determine deformation rates of the coastline. Because most of the coastline is at higher latitudes than those at which colonial corals grow, the target has been instead the solitary coral *Balanophyllia elegans*. These are difficult to find, as they are centimeter scale, and look like wagon wheel spaghettis. Nonetheless, they have been used by numerous workers (see review in Muhs, 1992) to identify which marine terrace was formed during which sea level highstand. U/Th has also been used to date the carbonate coatings on pebbles in soils, whose thickness has already been discussed as a surrogate for soil age. The method entails scraping off all but the innermost coating, adjacent to the clast upon which it is growing, in order to analyze this innermost rind. While this works in some desert settings (e.g., Ku et al., 1979),

FIGURE 3.11. Uranium and Thorium decay chains

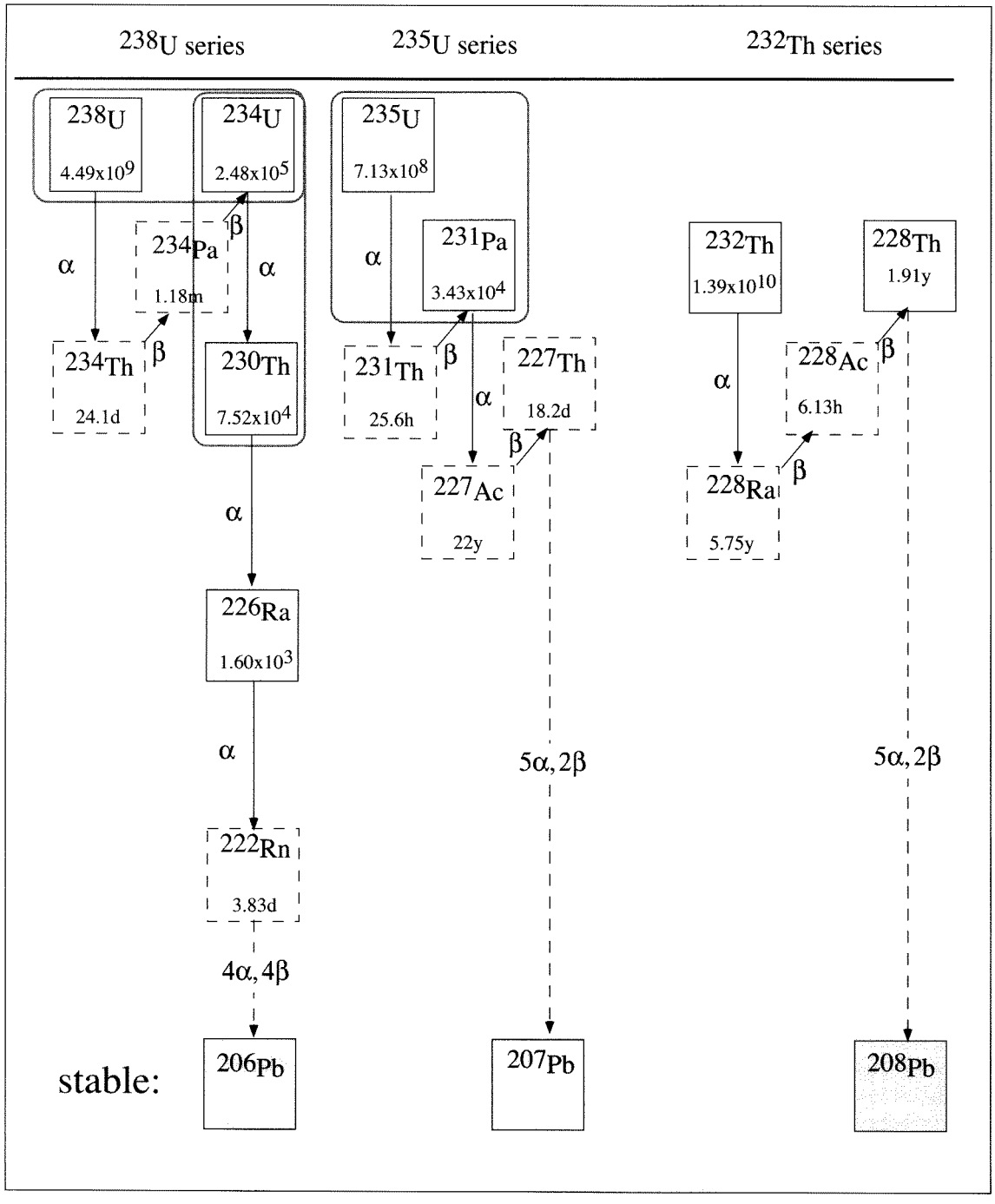

Radioactive parents ^{238}U, ^{235}U and ^{232}Th decay through α and β decay steps to stable daughter isotopes of Pb. Half-lives shown in boxes are in years except where noted.

FIGURE 3.12. Paired U/Th and radiocarbon ages of corals

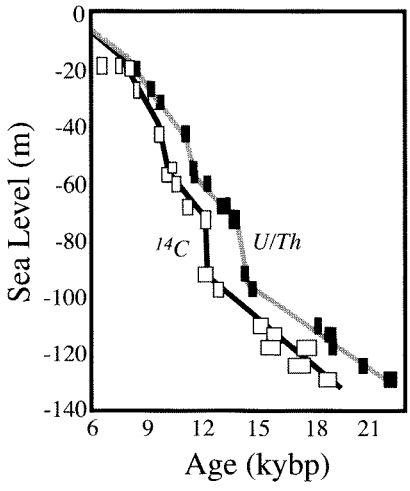

The sampled corals from Barbados grew during rise of sea level from its last glacial maximum of roughly −150 m to within 10 m of modern levels. Dates obtained using both radiocarbon and U/Th series methods are shown. Two strong spikes in sea level rise rates (glacial meltwater pulses) correspond only if the radiocarbon ages are systematically shifted to older ages. The U/Th clock is more trustworthy given its independence from fluctuations in the rate of cosmic ray bombardment. Modified after Bard et al. (1990).

it fails in many, owing either to leakage of one or another product from the carbonate, or to severe impurity of the coatings. This makes it a tool of low priority, to be used only if no other can be identified. Thankfully, one can determine if significant leakage has occurred, and hence whether the age obtained is worthy of interpretation (see, for example, Muhs et al., 1994, for discussion of these tests).

Whereas both societal concerns and geological efforts to understand well the most recent tectonic events often require that we focus on the past thousand years, this interval is difficult to date accurately using ^{14}C (Fig. 3.10). Although the measurement precision in the best labs may be as little as 10 to 20 years, the calendric uncertainty is often many decades due to the fluctuations of atmospheric ^{14}C during the past 1000 yr (see Atwater et al., 1991; Sieh et al., 1989, for examples of high-precision ^{14}C dating). High-precision U-Th dating of corals that grew during this same interval, however, can have calendric uncertainties of <10 yr, and thus can provide a detailed time resolution that was previously unattainable with most other techniques (Edwards et al., 1988; Edwards et al., 1993).

Amino Acid Racemization

All fossils contain at least trace amounts of organic matter than can be retained for long periods of time. The proteins that constitute this organic material in both skeletal and shell material are themselves composed of large numbers of amino acids. After death, the amino acids in these proteins alter through a set of chemical and physical processes. The degree to which this alteration has taken place can be used as a clock. Although transformations represent a very complex set of processes, there are some that appear to be reliable enough to provide both a relative and absolute dating method (Kaufman et al., 1992). Many types of organic materials have been used, including bivalves, gastropods, foraminifera, coral, and the shells of birds. In addition, the gas chromatographic methods used for measurement are relatively inexpensive, making the analysis of large numbers of samples possible. Only about 2 mg of sample is needed.

Living organisms utilize amino acids only in a left-handed (or *L*, for levo-) configuration of their isomers. Upon the death of an organism, these restrictive biological processes are terminated, which frees the amino acids to racemize (flip) into their right-handed (*D*, for dextro-) isomeric state. The ratio of *D*/*L* configurations is therefore a clock. The reaction behaves as a first-order reversible chemical reaction, with an equilibrium established when the backward reaction (*D*-*L*) balances the forward (*L*-*D*). As in all other chemical reactions, the rate constants are temperature dependent, reflecting the Arrhenius relation. Like the radioactive and cosmogenic dating methods that entail both production and decay, this restricts use of the clock to the period of time over which the measurable ratio (here the *D*/*L* ratio) is changing significantly. The time to equilibrium varies from one amino acid to another, and depends strongly upon the thermal history to which a sample has been subjected subsequent to death. For instance, isoleucine attains its equilibrium value of about 1.3 in 100 to 300 ka in equatorial sites, while in the Arctic it may take 10 Ma (Miller and Brigham-Grette, 1989) (Fig. 3.13). The thermal dependence is both a problem to be dealt with in the absolute dating of a sample, and a paleoclimatic tool in itself if the date is already known through other dating or correlation methods (inset in Fig. 3.13). Because the

FIGURE 3.13. Theoretical curve of amino acid racemization through time

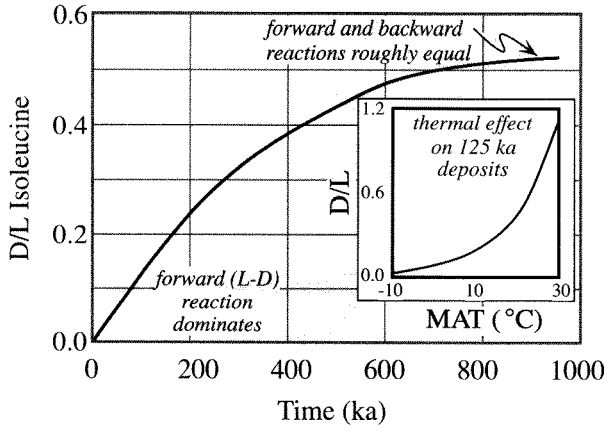

For early times, L-D transitions dominate, while back-reactions D-L become roughly equal at later times. Inset shows effects of higher mean annual temperatures (MAT) on reaction rates, and hence of D/L ratio expected at a given age (125 ka). Modified after Kaufman and Miller (1992) and Hearty and Miller (1987).

rate constant is apparently influenced by the type of animal (the taxonomic effect), researchers typically focus on a few common genera.

Typical application of racemization to absolute dating involves sampling a site of known age (say independently dated using ^{14}C), and a nearby site that is presumed to be late Pleistocene. The same fossil genera are collected from each site. The *D/L* ratio of the Holocene sample yields an empirical rate constant that is both geographically and taxonomically specific. The interpretation of the late Pleistocene *D/L* ratio takes into account the fact that the average temperatures since the late Pleistocene are likely lower than the average since the Holocene sample was deposited, meaning that the use of the Holocene rate constant will yield an underestimate of the late Pleistocene sample age.

Luminescence Dating

The applicability of many of the dating techniques discussed thus far is often limited by the availability of suitable material for dating, such as carbonaceous debris, shells, or corals. In most terrestrial settings, shells or corals are absent, and even where carbonaceous material is preserved, the age of the deposit of interest may exceed the practical range of ^{14}C. Luminescence dating has the potential to be both broadly applicable to terrestrial deposits and to extend well beyond the age limitations of radiocarbon dating.

The basis of luminescence is the trapping and release of energy by electrons within crystals (Aitken, 1985; Wintle, 1993; Duller 1996). When energy is added to electrons through radiation, they tend to move from a lower energy level (the valence band) to a higher energy level (the conduction band). Some of these energized electrons can be trapped metastably by crystal defects between these two energy levels. Trapped electrons can be made to drop back to their valence band upon the addition of a small amount of energy, at which time they release photons of light equivalent to the change in their energy state. This released light is termed *luminescence*. The radiation that initially causes the energy state of electrons to increase within a crystal comes largely from the decay of nearby radioisotopes within a sedimentary deposit. That this rate of decay should be approximately constant is the basis of the luminescence clock. The electrons can be reset (zeroed) to their low energy state by exposure to either intense heat or sunlight. When luminescence is caused by the addition of heat in the laboratory, it is termed *thermoluminescence* (TL), whereas when it results from the addition of light, it is termed *optically stimulated luminescence* (OSL).

In TL dating, luminescence is measured as the sample is incrementally heated (Fig. 3.14A). In OSL, the sample is exposed to light of a certain wavelength and the emitted luminescence is measured as a function of time (Fig. 3.14B). OSL has some important advantages over TL that are making it a generally preferable dating technique (Aitken, 1998). In particular, TL measures luminescence signals that are sensitive to light, heat, and any other types of energetic stimulation, whereas OSL measures only signals that are sensitive to light. In addition, TL destroys the signal of interest during measurement and, therefore, cannot be repeated, whereas OSL can be applied in short bursts that modify the total luminescence only slightly, such that multiple measurements can be made.

The number of electrons residing in "traps" in a crystal, and the intensity of luminescence released in the laboratory due to exposure to heat or light, are a function of the total dose of radiation received by the sample over time. If one can quantify that past radiation exposure, termed the

FIGURE 3.14. Thermal and optically stimulated luminescence

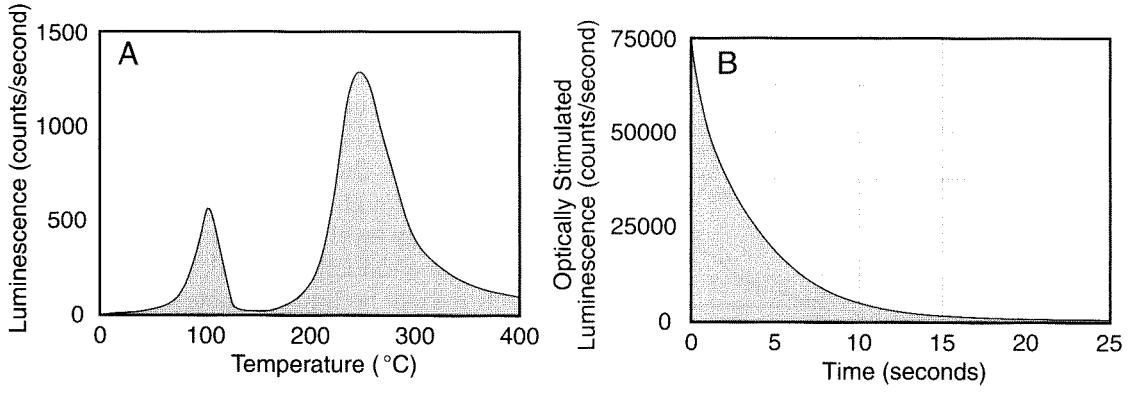

A. Example of a thermoluminescence "glow curve" that results from the progressive heating at a rate of a few degrees/second. In this quartz sample, most of the traps are emptied by 400°C. The peak at 100°C results from optical stimulation for 25 seconds at 420–560 nm shown in (B) and is not seen in the natural sample. B. Luminescence signal recorded at ~340 nm due to optical stimulation of the same sample as in (A) using a light source with wavelengths ranging from 420–560 nm. Modified after Duller (1996).

"paleodose," and the rate at which the sample was irradiated, then an age for the sample can be calculated:

$$age = paleodose\ P\ (Gy) / \ dose\ rate\ (Gy/ky)$$

where Gy (grays) is the SI unit for radiation.

The dose rate is typically measured either *in situ*, by leaving a radiation detector for an extended time (1 year, for example) in the sediment from which the sample was collected, or by laboratory measurements of the sample itself. Ideally, samples should be collected from the center of homogeneous beds that are at least 60 cm thick, because a 30-cm radius defines the approximate volume that will produce most of the radiation received by a sample. Collecting from such thick, homogeneous beds is especially important when the dose rate is to be determined in the laboratory.

The paleodose can be calculated in one of several ways (Duller, 1996). The additive dose method relies on measuring the luminescence resulting from different levels of irradiation in the laboratory. A curve drawn through these points and through the point defined by the sample's natural luminescence is extrapolated to zero to estimate the paleodose (Fig. 3.15A). In the regenerative method, several subsamples are measured for their natural luminescence and the remainder are zeroed through exposure to light, then exposed to known doses of radiation and remeasured for their luminescence. The curve developed from these measurements can be matched against the observed luminescence to estimate the paleodose (Fig. 3.15B). In the partial bleach method, some subsamples are subjected to the additive dose method, whereas others are exposed to a short burst of light (partial bleaching) in order to remove a proportion of their light-sensitive luminescence prior to measurement. The paleodose is defined by where these two extrapolated curves cross (Fig. 3.15C).

When luminescence dating is applied to sediments, a key assumption is that the traps were emptied or "zeroed" prior to deposition, such that each grain began its life within the deposit with no record of previous radiation. For optically stimulated luminescence, prolonged exposure to sunlight is sufficient to empty the traps, whereas for TL, sunlight will partially, but not completely remove the thermally stimulated luminescence. In either case, one must assess the sedimentological setting in the field, asking whether it is likely that there was sufficient exposure to sunlight during transport to empty the traps. Loess and aeolian sands, both of which blow around on the surface, are good bets to have been zeroed. Lacustrine silts and clays, which are transported as suspended sediments and should receive sunlight in the upper parts of the water column, also seem to yield reliable dates. On the other hand, sediment that traveled as bedload or

FIGURE 3.15. Paleodose determination in luminescence dating using three methods (see text)

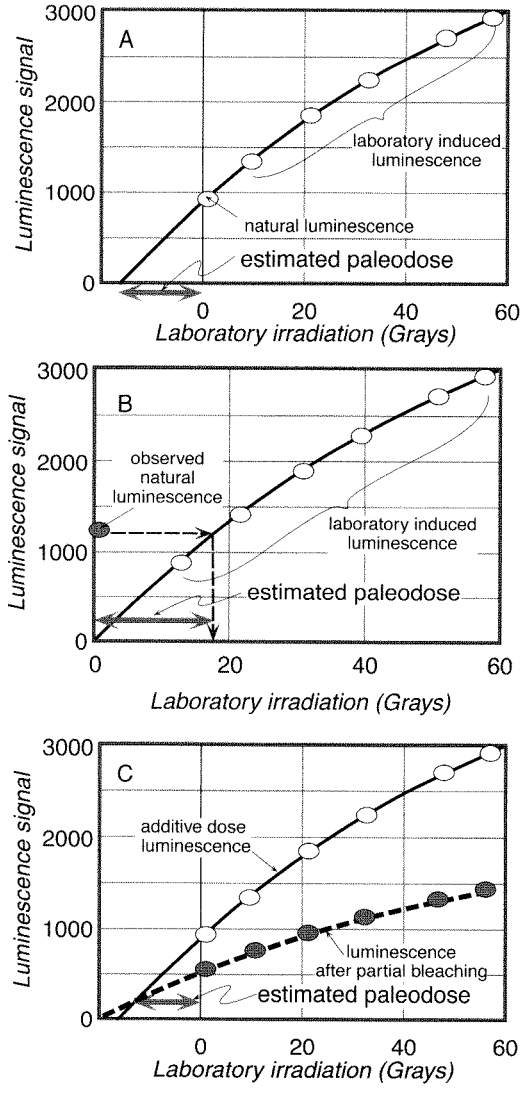

A. Additive dose method. B. Regenerative method. C. Partial bleach method. Modified after Duller (1996).

was transported in mass flows would be generally poor candidates for luminescence dating. The range over which luminescence dating can be successfully applied theoretically extends from less than 1 ky to more than 1 My. Using OSL and very sensitive detectors, aeolian sediments only a few hundred years old have been dated (Wolfe et al., 1995). Unfortunately, for dating older strata, during prolonged exposure to radiation, the trapping sites may eventually become saturated; their luminescence signal will cease to increase linearly despite additional radiation. Sediments derived from highly radiogenic rocks, like granites, will experience higher dose rates and reach saturation long before sediments derived from rocks like carbonates that emit low-levels of radiation. Practically speaking, high dose rates may limit luminescence dating in granite source areas to less than 60 to 200 kyr. Nonetheless, this technique has the potential to fill a critical gap beyond the range of radiocarbon dating. Moreover, because target minerals of quartz and feldspar are abundant minerals in many strata, these techniques can be applied to aeolian and lacustrine beds where few other means of dating may be possible. Some studies have tried to use luminescence dating in alluvial fans and colluvial wedges associated with faults. In such settings, zeroing of the sediment by sunlight prior to deposition cannot safely be assumed. Use of an additional dating technique, such as radiocarbon, would have to be employed on at least some pairs of samples to validate the luminescence dates.

Cosmogenic Radionuclide Dating

Within the last two decades, the nuclear physics community has introduced the geologic community to a new technology that allows dating of bare bedrock surfaces and of alluvial deposits that have been continuously exposed to cosmic radiation since formation. These techniques are fast-evolving. For the first decade much of the work was performed in geomorphic situations in which both the geomorphic and nuclear physics communities could benefit. Using surfaces previously dated using other methods, the production rate resulting from cosmic ray bombardment of rock was calibrated, showing a strong dependence on both altitude and latitude. Since then, surfaces of unknown age have been dated in a wide variety of settings. As the materials being dated are commonly available rocks, and the time scale over which the technique may be applied covers the entire Quaternary, this new technique is often the only method available. Here we briefly review the theory of the use of cosmogenic radionuclides (CRNs) in a variety of geomorphic settings. This treatment is by no means exhaustive, but is intended to serve as an introduction to this new and exciting field. More detailed reviews may be found in Lal (1991), Morris (1991), Bierman (1994), and Cerling and Craig (1994). We will see that the major problems facing the community lie in the interpretation of the CRN concentrations, that considerable care

needs to be exercised in sampling appropriately, and that much effort must be put into developing a relevant geomorphic model of the site. Although much work has been accomplished in this new field, the techniques continue to evolve.

Background

We summarize here and in the cosmogenic primer (Box 3.1) the concepts that underpin the essential uses of cosmogenic radionuclides in geomorphological studies. Cosmic rays isotropically bombard the solar system, meaning they come in essentially uniformly from all angles. Being charged, they are steered by the magnetic field of the earth, generating a stronger beam of particles at high geomagnetic latitudes, and reducing the downward flux at lower latitudes. These particles interact with atoms in the atmosphere, creating such familiar species as ^{14}C. Such interactions reduce the number of energetic particles that penetrate to lower altitudes in the atmosphere; the production rate of radionuclides declines with a 1/e length scale of roughly 1.5 km within the lower atmosphere. Due to this atmospheric attenuation, production rates of cosmogenic nuclides at altitudes of 3 km will be e^2, or about seven times higher than at sea level. These nuclides generated in the atmosphere have been dubbed "garden variety" radionuclides. Cosmic rays that survive to impact the surface of the earth are capable of producing CRNs in near-surface materials: "in situ" cosmogenic radionuclides. The production rate is highest at the surface, and decays with depth with a 1/e scale of roughly 60 to 70 cm, the difference in length scales reflecting the relative density of rock and air. Minerals comprising atoms that are susceptible to the nuclear reactions that generate CRNs must be present in these near-surface materials to be useful. For instance, and quite fortunately, the very common mineral quartz (SiO_2) is a target mineral for both ^{10}Be and ^{26}Al, ^{10}Be being produced from ^{18}O, and ^{26}Al being produced from ^{32}Si. See the table in the cosmogenic box (Box 3.1) for a compilation of the most commonly used species, their half-lives, and the sea-level, high latitude production rates.

Note that the production rates are only a few atoms per gram of target mineral per year (see Box 3.1), rates that result in such low concentrations that conventional mass spectrometry and counting of decays are unreasonable methods for measuring concentrations. Analyses of the concentrations of those CRNs produced in situ requires first separation of the target mineral from the rock, ridding the sample of garden variety CRNs by a leach step, and subsequent chemical separation of the CRN. The minuscule sample is then analyzed in an accelerator mass spectrometer (AMS), several of which have been converted from use in physics and defense industries for application in this field.

In Situ CRNs

In situ CRNs have been used in two distinct settings: bare bedrock surfaces, where one is interested in either or both of the exposure age of the surface and the erosion rate of it, and depositional surfaces. Each setting poses its own dilemmas, requiring differing sampling strategies. But there is often no other game in town.

Bedrock Surfaces. Consider a bare bedrock surface exposed to the full cosmic ray flux (no blocking by nearby outcrops or valley walls). The concentration in a parcel of rock is dictated by the differential equation describing both production and decay of CRNs in the parcel:

$$dN/dt = P - \lambda N \tag{3.3}$$

where N is the number of CRNs per unit volume of rock, t is time, P is the production rate, and λ is again the decay constant (related to the half-life by $t_{1/2} = \log(1/2)/\lambda$). Much of the complexity in the interpretation of the measured CRN concentrations resides in the history of the production rate, P, to which the parcel has been subjected. Let us address a few simple examples. Consider a bare bedrock surface exposed at $t = 0$ by a landslide. This treatment will equally well apply to a sample obtained from within the headscarp, or from a boulder on the surface of the landslide which we can safely assume to have been at great depth prior to the slide we would like to date. Assume that the rock involved is much older than the half-life of the CRN we wish to employ, assuring that all CRNs produced in a prior exposure at the surface have decayed. In other words, all "inheritance" is negligible. CRNs will begin to accumulate within the rock, most rapidly at the surface, more slowly at depth. At early times, the concentration, N, is so low everywhere within the rock that the rate of growth is essentially linear at the local production rate P, i.e., $N = Pt$. Since P falls off exponentially with depth (see box), an exponential concentration profile develops: $N = P_0 te^{-z/z^*}$, where P_0 is the production rate at the surface and z^* represents the depth in the rock at which the production rate is P_0/e. If a sample is collected from this surface ($z = 0$), and we know the local production rate

Box 3.1. An in situ cosmogenic radionuclide primer

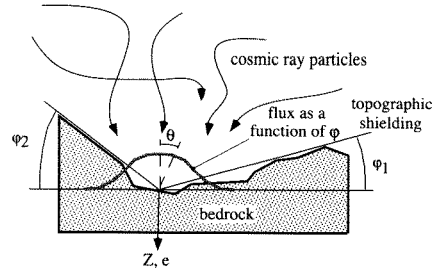

Cosmic ray particles are isotropically distributed as they enter the earth's atmosphere. The atmosphere attenuates this production such that the particle flux is lower from higher angles, θ, with respect to the zenith (gray cosine curve). On a flat surface they would produce cosmogenic radionuclides at a rate P_o. Any intervening rock also blocks production (called topographic shielding), reducing the effective surface production rate below P_o. Measurement of this effect is done in the field by measuring φ in 4–8 directions. The sample site, at $Z = 0$, may be eroding at a long-term rate of r.

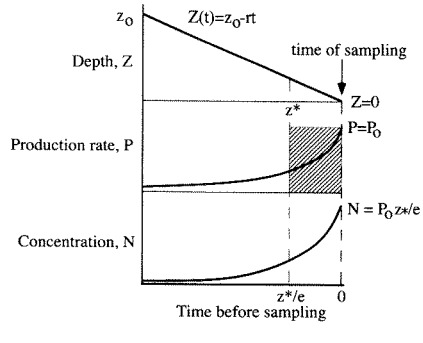

The case of steady erosion. As the depth of the sample decreases due to erosion of overlying rock, the production rate increases exponentially. The concentration therefore increases exponentially. The concentration upon sampling the parcel when it reaches the surface is equivalent to the integral of the production rate history. Given that z* is a material property, dependent largely upon the density of the overburden, the sample concentration is higher for slower erosion rates, and for higher surface production rates. Note that the sample concentration is equivalent to that the parcel of rock would have obtained had it sat on the surface for a time equal to that it takes the rock to be exhumed by a length z* (shaded box).

References: Lal, 1988, 1991; Nishiizumi et al., 1994; Bierman, 1994; Nishiizumi et al., 1996

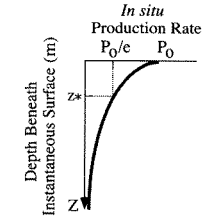

Production rate, P, decays exponentially with depth below the instantaneous surface, z, where the surface production rate, P_o, is scaled by altitude and geomagnetic latitude. The rate of decay beneath the surface is scaled by the constant, z*, which is roughly 50–60 cm for most lithologies.

In general, the rate of change of concentration (N) equals the rate of production less the rate of decay (λN):

$$\frac{\partial N}{\partial t} = P(t) - \lambda N$$

The rate of production with depth is

$$P = P_o e^{-z/z^*}$$

The depth can vary with time, z(t), due to either erosion or deposition.

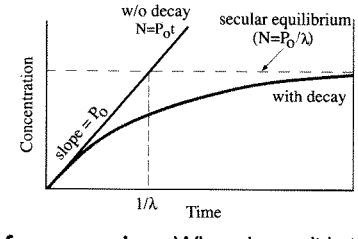

The case for no erosion. When the nuclide is stable, the concentration simply increases linearly with time at a rate P_o. When the nuclide is radiogenic, the concentration approaches a steady value, or secular equilibrium, at which point the rate of decay equals the rate of production. The achievement of secular equilibrium takes several characteristic decay times ($1/\lambda$).

	^{14}C	^{10}Be	^{26}Al	^{36}Cl
P_o	21.0	5.81	34.9	4 - 9
λ	1.2×10^{-4}	4.62×10^{-7}	9.9×10^{-7}	4.81×10^{-7}
$1/\lambda$	8276	2.16×10^{6}	1.01×10^{6}	2.1×10^{6}
$t_{1/2}$	5735	1.5×10^{6}	0.7×10^{6}	0.3×10^{6}

Commonly used cosmogenic radionuclides, their in situ production rates (P_o) in atoms/gram of quartz/year at sea level in mid to high latitudes, their decay time scales (λ, $1/\lambda$) and their half-lives (in years).

at the surface, then measurement of N allows solution for the exposure time, t. However, as the concentration builds up, the second term in equation 3.3, representing decay, begins to play a larger role. This results in a decline in the rate of increase in concentration, until ultimately there is a balance between new production and decay. This "secular equilibrium," represented by $dN/dt = 0$, limits the concentration to a maximum of $N = P/\lambda$ (see Box 3.1). Note that in these circumstances, when the sample has reached secular equilibrium, no information about the exposure time can be extracted from a measurement of N. Happily for the geomorphic community interested in dating surfaces in Quaternary Period (roughly 1.8 million years long), this secular equilibrium takes several half-lives to be achieved. Since ^{10}Be and ^{26}Al have half-lives on the order of 1 million years (see table in Box 3.1), they remain useful throughout the Quaternary. Dating of glacially polished surfaces (e.g., Nishiizumi et al., 1989) in the Sierras is one example of dating surfaces of negligible erosion. Exposure dating of fluvial strath terraces along the Indus River, on which the fluvial polish is still intact and where the fluted and potholed nature of the fluvially carved bed has clearly not degenerated since abandonment of the strath, is another example of this circumstance (Burbank et al., 1996).

More commonly, the rock surface being sampled is eroding at some rate that we would like to determine. This erosion can take place on a grain-by-grain basis, or through spalling of parcels of various finite depths representing joint spacing, for instance, or fire spall depths (e.g., Bierman and Gillespie, 1991). If the erosion is continuous and steady, the production rate in equation 3.3 can be rewritten

$$P = P_0 \exp(-rt/z^*) \tag{3.4}$$

where r is the erosion rate of the surface, and t is time, $t = 0$ being the time of sampling and t into the past being positive. For the moment ignoring decay, and solving equation 3.3 with this steady production-rate history yields:

$$N = P_0(z^*/r) \tag{3.5}$$

which can be solved for the erosion rate. Here the term (z^*/r) represents the time it takes the sample to travel through the boundary layer where the production rate is significant. The faster the parcel is exhumed, the lower the resulting concentration. Including decay alters the equation to

$$N = P_0 z^*/(r + (z^*/\lambda)) \tag{3.6}$$

If, on the other hand, the erosion occurs in steps (due to fire spalls, for instance (Bierman and Gillespie, 1991) or to joint block removal (Small, 1997)), then the calculation of a long-term erosion rate from employment of Equation 3.6, and the CRN measurement of a surface sample, will vary depending on the time since the last spall event. The error in the estimate will depend on the thickness of the spall. In situations like those involving spalls, the averaging of several sample sites ought to provide a more robust sense of the mean rate at which the surface is being lowered (Small, 1997).

If one would still like to extract an exposure age from this site, and not just an erosion rate, Lal (1991) has shown that the use of two cosmogenic radionuclides with differing half-lives allows some additional constraint on the exposure age in certain scenarios. Working in the ^{36}Cl system, supplemented by ^{10}Be analyses, Phillips et al. (1997) has demonstrated the usefulness of this technique in constraining the age of large boulders whose surfaces have been slightly eroded since emplacement on the surface to be dated.

Depositional Surfaces. Depositional surfaces, such as fluvial and marine terraces, present their own problems, even if the surfaces can be safely assumed not to be eroding. The principal problem lies in the possibility that the clasts being used to assess the concentration of CRNs have likely experienced prior exposure ("inheritance") elsewhere within the geomorphic system prior to being deposited on the surface to be dated. Consider first a fluvial terrace. The inheritance derives from a combination of exhumation through the cosmogenic nuclide-production boundary layer as the hillslope surface is lowered; transport within the hillslope system; transport within the fluvial system, which will entail occasional burial in fluvial bars; and final deposition on the terrace to be dated. Tactics must be employed in the sampling of the terrace materials that allow separation of the inheritance signal. In several fluvial systems studied to date, the inheritance can represent a significant (several tens of percent) portion of the total CRN concentration measured in clasts sampled from the terrace surface (e.g., Anderson et al., 1996; Repka et al., 1997) (Fig. 3.16). Because the inheritance differs markedly from one surface to another, one must employ some means of constraining this inheritance on a site-by-site basis.

FIGURE 3.16. Use of cosmogenic radionuclide concentration profile to deduce both inheritance and age of the surface

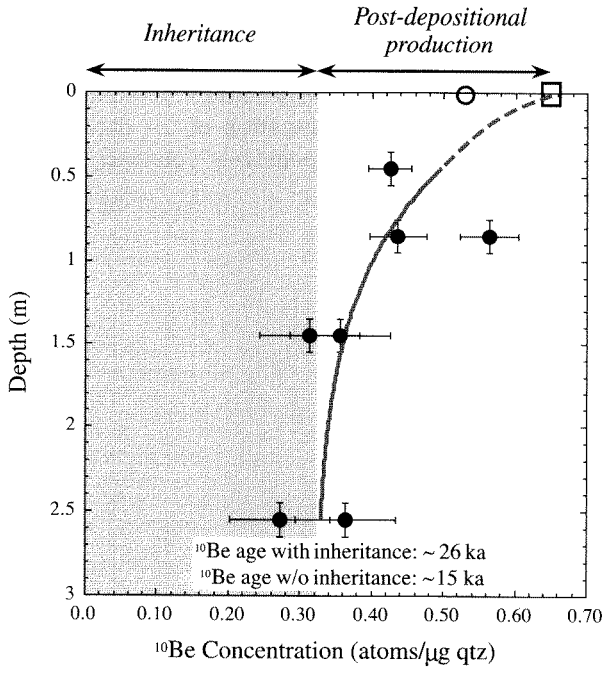

Dated surface is the Stockton bar of Lake Bonneville, associated with the latest highstand of the lake, at roughly 14.5 ka. Grayed box represents the concentration due to inheritance of cosmogenic radionuclides by the quartzite clasts prior to deposition in the bar. Best-fit line is exponential shifted to account for inheritance. Age deduced from this method is 15 ka. If inheritance were not accounted for, and a single surface sample were used to deduce age, the estimated age would have been ~26 ka, too old by roughly 11 ka.

One apparently effective strategy is to collect samples at varying depths in the terrace profile. Each sample should consist either of sand or of a contribution of an equal amount of rock from numerous clasts buried at the same level, for example, 10 grams from each of 30 clasts. Assuming that the terrace aggraded quickly so that each sampled layer was rapidly buried to near its present depth, then the age of each sample represents a combination of the time since deposition and the inheritance at the time of deposition. When samples are drawn from deep enough in the terrace, say greater than ~2m, their concentrations should reflect almost exclusively the inherited nuclides, because CRN production rates are negligible at this depth.

These kinds of surfaces have also been dated using garden variety CRNs produced in the atmosphere and subsequently rained out in precipitation (see review in Morris, 1991). In particular, ^{10}Be is found to be useful in that its chemistry is such that it is held tightly by clays in soils (Pavich et al., 1984). The soil therefore acts as a reservoir within which the ^{10}Be slowly builds up with age of the surface. If surfaces are well chosen to limit the role of soil erosion (i.e., are nearly flat), then the total ^{10}Be inventory on grain surfaces within the soil column can be used to constrain the age of the surface.

Using Cosmogenic Nuclide Dates

The numbers one extracts from such studies are, at best, only as good as the knowledge of the production rates over the age of the surface at that site. These production-rate histories are difficult to know. Typical calibrations rest on independent dates from surfaces, such as glacially polished bedrock associated with moraines that can be dated with ^{14}C (e.g., Nishiizumi et al., 1989). Two cautions are warranted: 1) these independent ages can be and are being reassessed with new techniques at new sites that may better constrain the true age of the glacially polished surface (e.g., Clark et al., 1995), and 2) production rates estimated from these sites, that are therefore relevant to this altitude and latitude, are averaged production rates over the age of the sample. Use of these production rates for dating other surfaces must be done carefully, as the magnetic field intensity has been shown to vary significantly over the last 140 ka (e.g., Meynadier et al., 1992). This record of field intensity variations will no doubt be extended by future research. The production-rate history at a sampling site should be calculated from a knowledge of the average production rate deduced from a sample of known age, the magnetic field history, and the relationship between field intensity and production rate (e.g., Clark et al., 1995).

In addition, the quality of the interpretation of the CRN concentration extracted from a sample, for either the exposure age or the erosion history at the site, is dependent on the degree to which the geomorphic processes active at that site over the history of the surface can be captured in a quantitative model. Not only must the inheritance of a particular sample be assessed, but the post-depositional processes that might alter the production-rate history of the sample should be dealt with. On boulders presently at the surface, one must worry about whether the boulder has always been at the surface, as well as the likelihood of erosion of the boulder once it was emplaced on the surface. At present,

there is much interest in this new set of techniques. This set of problems provides an excellent opportunity for the marriage of new chronologic tools with new modeling tools, to which we turn later in the book.

Conclusions

In this chapter, we have sampled the array of dating methods available to provide the time scales for tectonic geomorphic studies. The choice of method must be dictated by the availability of the proper materials, the details of the geomorphic setting, and, of course, the cost. While relative dating methods are "quick and dirty," they should not immediately be shunned. They do produce immediate results, while other techniques might take months to a year for processing of samples. In using any method, it is incumbent upon the researcher to document carefully both the geomorphic and depositional setting. Interpretation of the dates, sometimes painstakingly and expensively obtained, relies on this field information.

CHAPTER 4

Stress, Faults, and Folds

When rocks are subjected to stresses that exceed their strength, they rupture, fold, or flow. Different varieties of faults (strike-slip, normal, thrust) characterize contrasting tectonic settings and stress regimes in the upper crust. When faults break the earth's surface either in a single earthquake or during many seismic events, they often create geomorphic features that can be associated with a particular type of fault. Sometimes earthquakes occur on faults that do not reach the earth's surface, and therefore, there are no ground ruptures directly associated with the fault trace. Nonetheless, the earth's surface will deform by folding in response to these earthquakes along buried faults. The geometry of deformation and the evolving shape of a fold can reveal useful information about the nature of the subsurface faulting and the way in which the rocks adjacent to the fault respond to fault motions.

In order to take full advantage of the information to be gleaned from geomorphological surfaces, it is important to understand the typical ways in which rocks deform due to both seismic and aseismic movements. A primary goal of this chapter is to examine the nature of faulting and folding and to discuss concepts related to scales of faulting and similarities between successive earthquakes on the same fault, the displacements of the ground surface that are expected for different types of faults, and the geomorphic imprint of faults of different types.

Stress, Strain, and Faults

Stress

All rocks in the crust are subjected to forces due to gravitational acceleration; the mass of rocks, water, and air around them; and plate tectonic motions. We typically identify two kinds of forces: *body forces* and *surface forces.* Body forces act equally on every element throughout a volume. The magnitude of a body force is proportional to the mass of the element on which it is acting, or its volume times its density. An example of a body force would be the weight of an object, which is the mass of the object times the acceleration due to gravity. Surface forces are forces that act across or along surfaces, and include forces such as friction or pressure. Strictly speaking, these are termed *tractions,* which are defined as the force per unit area acting on a surface.

A stress or traction acting on a plane with any orientation can be resolved into two components: a normal stress (σ_n) acting perpendicular to the surface and a shear stress (σ_s) acting parallel to the surface. The units of stress in the mks (meters-kilograms-seconds) system are pascals. One pascal (Pa) represents the stress produced by one newton acting across or along a surface of one square meter ($(kg \cdot m \cdot sec^{-2}) \cdot m^{-2}$). Pressure can also be expressed in bars, whereby one bar equals 10^6dynes/cm^2. Because one pascal represents a rather small force acting over a large area, pressures are often expressed in megapascals (MPa = 10^6 pascals) which is also equal to 10 bars. A column of rock 1 km high would typically exert a pressure at its base of 25–30 MPa. The shear strength of many crustal rocks ranges from 10–100 MPa.

Each of the tractions acting on a rock surface and resulting from tectonic, lithostatic, buoyancy, or hydrostatic forces can be represented as a vector which can be summed with all other imposed tractions to define the total magnitude and orientation of the imposed stress on any specified plane. The total stress can be subdivided into three orthogonal components, which are typically labelled σ_1, σ_2, and σ_3, for the maximum, intermediate, and minimum principal stresses, respectively. For simplicity in discussing types and

FIGURE 4.1. Schematic figure of fault orientations with respect to principal stress orientations

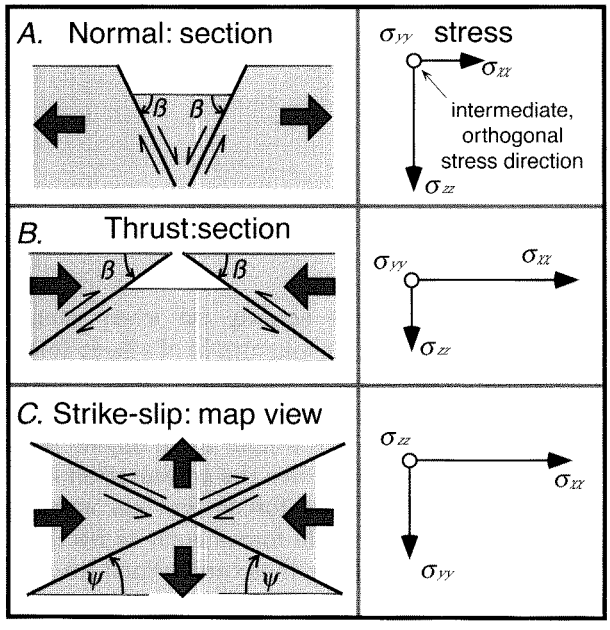

A. Normal faults. $\beta = 45° + \theta/2$. B. Thrust faults. $\beta = 45° - \theta/2$. C. Strike-slip faults. Modified after Turcotte and Schubert (1982).

orientations of faults and associated structures, we will refer to three orthogonal stress vectors, in which one (σ_{zz}) is vertical and the other two vectors (σ_{xx}, σ_{yy}) are contained in a horizontal plane (Fig. 4.1). The vertical stress results from the rock overburden at some depth z, such that $\sigma_{zz} = \rho g z$, where ρ is the mean density of the overlying rock and g is gravitation acceleration. This is termed the *lithostatic stress*. When the orthogonal horizontal stresses are equal to the vertical lithostatic stress, such that $\sigma_1 = \sigma_2 = \sigma_3$, this is termed a *lithostatic state of stress*. To the extent that stresses differ from this lithostatic condition, they are termed *deviatoric stresses*. In most of the situations involving faulting, the deviatoric stress ($\Delta\sigma$) results from a tectonic contribution.

Strain and Faults

The presence of deviatoric stresses can cause a rock to undergo *strain*: any deformation that involves a change in size (dilation) and/or a change in shape (distortion). Strain in rocks can be observed and quantified, whereas the deviatoric stresses that caused the strain commonly can only be inferred. Various components of strain, such as the amount of rotation or the magnitude and orientation of extension, shortening, or stretch, can be defined through direct observations.

Not all strain in rocks is permanent. Below a certain stress threshold, termed the *elastic limit*, strain is recoverable. Thus, during the initial build-up of differential stresses, a rock will deform elastically, and, if the differential stress is eliminated during this stage, the rock will return to its original unstressed shape. Once a rock's elastic limit or *yield strength* is exceeded, it will either deform plastically or rupture; either case causes a permanent change in shape. When a rock deforms by rupture, discrete surfaces, or *faults*, are formed along which rocks are offset by movements parallel to the fault surfaces.

Consider the stresses that are responsible for normal faults. The vertical component of stress is the lithostatic pressure, $\sigma_{zz} = \rho\ g\ z$, and there is an applied deviatoric stress $\Delta\sigma_{xx}$ that is tensile and exceeds the yield strength of the rock (Fig. 4.1A). Therefore, $\Delta\sigma_{xx} < 0$, the horizontal stress is less than the vertical stress, $\sigma_{xx} = \rho\ g\ z + \Delta\sigma_{xx}$, and $\sigma_{xx} < \sigma_{zz}$. If we assume that there is no strain (deformation) in the y direction, then the deviatoric stress in the y direction either is zero or is also tensile, but is some proportion (p) of the deviatoric stress in the x direction. Therefore, $\Delta\sigma_{yy} = p\ \Delta\sigma_{xx}$, where p is less than 1. The total stress in the y direction, $\sigma_{yy} = \rho\ g\ z + p\ \Delta\sigma_{xx}$, is less than σ_{zz}, but greater than σ_{xx}. Thus, for normal faulting, $\sigma_{zz} > \sigma_{yy} > \sigma_{xx}$. In theory, a fault plane should make an angle with the principal compressive stress of $45° - \theta/2$, where θ is equal to the angle of internal friction for the faulted material. Thus, a normal fault formed in a relatively strong rock like granite should be inclined at about 30° to σ_{zz}, and the fault trend should be oriented perpendicular to σ_{xx} (Fig. 4.1A). Two different fault planes, each dipping in opposite directions at 60° from the horizontal, satisfy these conditions and thus represent *conjugate* fault planes. Given these stresses and this fault orientation, the *hanging wall* (the fault block that is located above the fault plane) moves down across the *footwall* which is beneath the fault plane.

For thrust faults, there is a compressional deviatoric stress in the x direction, typically resulting from tectonic forces. Thus, $\Delta\sigma_{xx} > 0$, and $\sigma_{xx} > \sigma_{zz}$. Once again, the deviatoric stress in the y direction can be considered intermediate, so that $\sigma_{xx} > \sigma_{yy} > \sigma_{zz}$. For a horizontally

oriented maximum compressive stress, conjugate fault planes should be inclined at 45° – θ/2 from the horizontal and also at 45° – θ/2 from σ_{xx} (Fig. 4.1B). For thrusts, the hanging wall moves upward with respect to the underlying footwall.

Strike-slip faults are characterized by deviatoric stresses of opposite sign in the *x* and *y* directions. For example, if σ_{yy} is tensile, then $\Delta\sigma_{yy} < 0$. Consequently, σ_{xx} must be compressive, such that $\Delta\sigma_{xx} > 0$. Therefore, for strike-slip faults, either $\sigma_{yy} > \sigma_{zz} > \sigma_{xx}$, or $\sigma_{xx} > \sigma_{zz} > \sigma_{yy}$. For any stress regime in which the lithostatic stress is the intermediate stress, two conjugate vertically dipping fault planes oriented at 45° – θ/2 to the maximum compressive stress will accommodate strike-slip motion (Fig. 4.1C).

Clearly, faulting occurs in response to imposed stresses. But why should we care about the orientation and magnitude of local stresses? Perhaps the most important reason is that there are large gaps in our understanding of faulting within the truly heterogeneous rocks of the crust. Much of our current knowledge of the mechanics of faulting derives from laboratory studies, which commonly involve homogeneous rocks of hand-specimen size. In the real world, we need to know how stress is distributed along a fault. How do real rocks actually deform when their yield strength is exceeded, and how are the resulting structures oriented with respect to prevailing stresses? How does the stress across a fault surface change as a result a faulting event? What is the role played by fluids? Until these questions are answered, our ability to quantify and predict deformation in earthquakes will be impeded.

FIGURE 4.2. Dipmeter measurements of changes in lengths of two perpendicular axes in a section of a vertical borehole

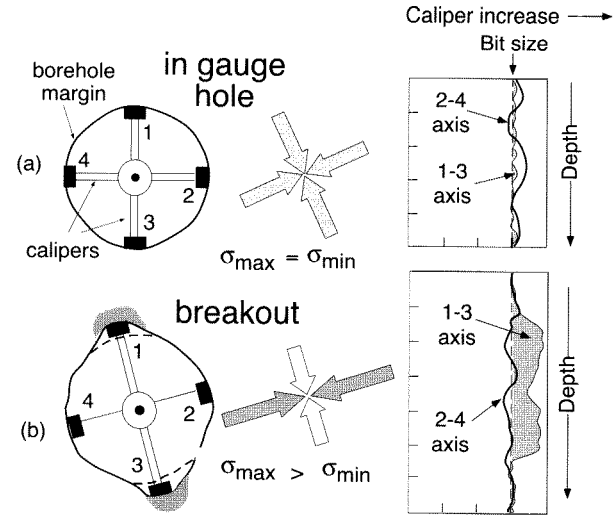

When there is no elongation due to differential stress, the two axes are nearly equal (top) such that there is little variation from the diameter of the drill bit. If a borehole breakout has occurred, then the hole is elongated in one direction, and there is a distinct difference in the lengths of the axes. The axes oriented in the direction of the least compressive stress, or perpendicular to the maximum compressive stress, will be longer. Modified after Plumb and Hickman (1985).

Present-Day Stress Directions

Given the fact that differential stresses drive deformation, determination of the local stress field is of great value. Although a regional stress regime due to relative motion between plates may be well defined, the orientation of the modern stress field in any specific locality may vary considerably from the predicted regional orientation. Because progressive fault motion can rotate structures out of their original orientation with respect to the local stress field, the present-day orientation of fold axes and fault traces may not be a reliable guide to the modern stress field. Direct measurements of stress are rarely achieved. Proxy indicators for the orientation of *in situ* stresses, however, can be made in several ways. After a well is drilled, its sides may deform in response to horizontal stresses imposed on the surrounding rocks. Stress is concentrated around the borehole and can create small, secondary fractures. As a result of minor slip along these fractures, the circular cross section of a drill hole can be deformed into an elliptical shape, in which the major axis of the ellipse (the direction of elongation) is interpreted to represent the orientation of the least compressive principal horizontal stress (Plumb and Hickman, 1985). These elongations are also called *borehole breakouts* (Fig. 4.2). Measurements of the vertical pattern of elongation in a drill hole can, therefore, reveal the distribution of horizontal stresses with depth. *Hydrofracturing* is a second technique that utilizes drill holes, but it employs pressurized water to generate fractures which subsequently propagate in the walls of the well (Hickman et al., 1985). The cracks are interpreted to form perpendicular to the minimum horizontal principal stress, and their

orientation can be determined with a borehole camera following depressurization. Hydrofracturing has the additional advantage that the water pressure that causes fracturing or reopening and propagation of existing fractures is known and is expected to be equivalent to the magnitude of the minimum horizontal stress. With additional knowledge of the ambient pore pressure in the rocks, the maximum compressive stress can also be estimated.

The Earthquake Cycle

The "Classical" Model

Since at least the turn of the century, geologists have attempted to understand the deformation that precedes, coincides with, and follows an earthquake. The time and deformation that encompasses an earthquake and all of the interval between successive earthquakes is termed the *earthquake cycle*. As originally described, the earthquake cycle had two parts: an interseismic interval and a coseismic one (Reid, 1910). Imagine two nearby pieces of the crust that are moving in opposite directions with respect to a fault that separates them. At some depth below the surface, the fault slips continuously and aseismically in a zone of ductile deformation, but in the brittle crust during the interseismic interval, the fault is "locked" such that no slip occurs along it (Fig. 4.3). At some distance from the fault, the rocks are moving at the same rate as the crustal blocks. The amount of displacement decreases to zero at the fault, such that an originally straight marker that was oriented perpendicular to the fault would be bent into a sigmoidal shape. The 2-*d* shear strain, which could be envisioned as the amount of bending of the formerly straight marker, is greatest near the fault (Fig. 4.3). This bending can be considered as "elastic strain" in that it is recoverable, rather than permanent. When the frictional strength of the fault is exceeded by the imposed stress, the fault ruptures during an earthquake. Coseismic displacement is greatest along and adjacent to the fault. In the context of the earthquake cycle model, slip is just enough to balance the slip deficit and restore the marker to a linear trend, perpendicular to the fault, but now offset by the amount of relative motion of the two crustal blocks during the entire earthquake cycle. In this model, all of the elastic strain is recovered in each seismic event, so that there is no permanent strain within the blocks that slip past each other on opposite sides of the fault (Fig. 4.3), although the rupture causes an abrupt discontinuity along the fault itself.

FIGURE 4.3. Model of the earthquake cycle for a strike-slip fault

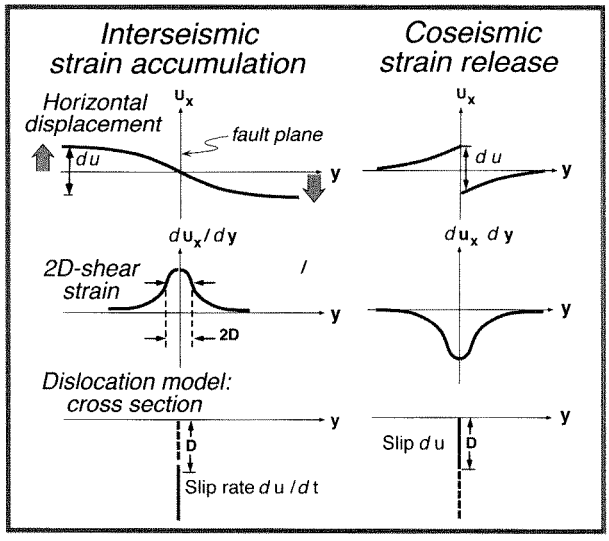

The far-field strain (large arrows; top panel) of one block with respect to the other remains constant through time, as does aseismic slip (du/dt; bottom panel) in the ductile zone below the locking depth (D). Interseismic displacement is greatest farthest from the fault, but most of the shear strain (du_x/dy; middle panel) occurs within two locking depths (2D) of the fault. During coseismic displacement, the greatest displacement (du) occurs along and near the fault and compensates for the "slip deficit" developed during the interseismic interval. The coseismic shear strain is equal and opposite to the interseismic shear strain. Modified after Thatcher (1986b).

Data on pre- and coseismic deformation prior to and following the 1946 M8 earthquake in the Nankai trough of southwestern Japan provide support for aspects of this model (Fig. 4.4). Measured interseismic strain replicates the shape, but is opposite in vertical direction to the coseismic strain caused by that large subduction-zone earthquake. This behavior is clearly consistent with Reid's model. There is, however, considerable topography across the deformed zone which suggests that coseismic subsidence does not fully compensate all of the interseismic uplift: some permanent strain is represented by this topography.

FIGURE 4.4. Comparison of leveling data recording interseismic, coseismic, and postseismic deformation in the Nankaido region, Japan

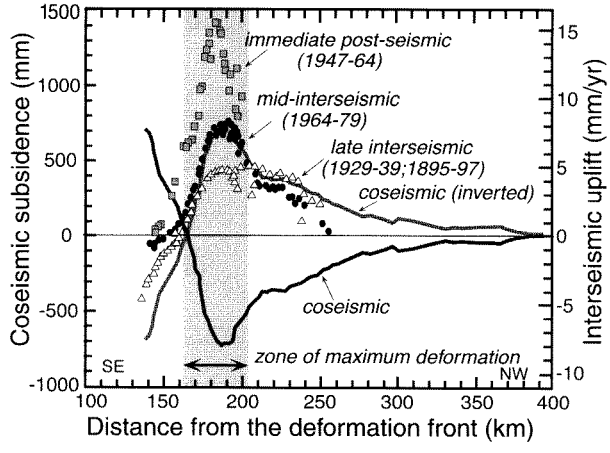

Three intervals of interseismic or postseismic deformation are represented: immediate postseismic (1947–64); mid-interseismic (1964–79); and late interseismic (1895–97, 1929–39). These are compared with the inverted coseismic deformation profile. Note the spatial coincidence of the peak zone of deformation for each data set. The regional pattern of interseismic deformation closely mimics the inversion of the coseismic deformation. Modified after Hyndman and Wang (1995).

Alternative Earthquake Models

As a result of observations related to numerous earthquakes, Reid's simple model of the earthquake cycle has been significantly modified. First, the deformation observed along faults, such as folds and fault offsets, indicates that not all of the pre-faulting strain is recovered. In other words, as seen in the example from Japan (Fig. 4.4), there is often some permanent, unrecoverable strain. Second, the interseismic interval may sometimes be further subdivided into a post-seismic interval and an interseismic one. The post-seismic interval immediately follows an earthquake and is one during which strain accumulates more rapidly than in the subsequent interseismic interval (Stein and Ekstrom, 1992). In some recent earthquakes, the amount of post-seismic deformation and energy release has been shown to be equal to that of the coseismic event (Heki et al., 1997). Newly recognized "slow" earthquakes (Beroza and Jordan, 1990; Kanamori et al., 1993) in which deformation occurs over periods of hours to years can release vast amounts of energy and cause large-scale deformation without generating the catastrophic energy releases of normal earthquakes. Third, new variations on Reid's periodic earthquake cycle have been postulated. In Reid's periodic model, the frictional strength of the fault, the stress drop, and the slip associated with each earthquake is constant from event to event, such that both the time of each earthquake and its magnitude are predictable (Fig. 4.5A). In a *time-predictable model,* earthquakes always occur when a critical stress threshold is attained (Fig. 4.5B). The amount of stress drop and the magnitude of slip, however, varies from one earthquake to the next. Assuming there is a constant accumulation rate of interseismic strain and assuming that the amount of slip in the previous earthquake is known, this model permits a prediction of the time until the next earthquake, because the stress needed to attain the failure stress is known. The displacement of that forthcoming earthquake, however, is unknown. Alternatively, a *slip-predictable model* suggests that slip during an earthquake always terminates when the stress has dropped to a critical level

FIGURE 4.5. Models for earthquake recurrence

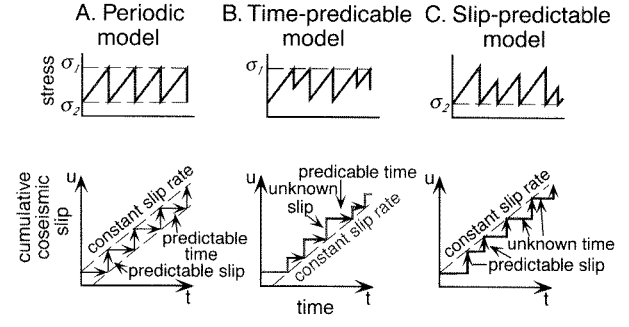

A. Periodic earthquake model in which stress levels at the time of rupture and after it are known. These yield a predictable time and slip for each earthquake.
B. Time-predictable model based on a consistent stress level at which failure occurs. Stress drop and slip magnitude are unpredictable, but given previous slip, time until the next earthquake (with unknown slip) is predictable. C. Slip-predictable model based on a consistent stress level at the end of an earthquake. Given time since the last rupture, magnitude of slip is predictable. Modified after Shimaki and Nakata (1980).

(Fig. 4.5C). The stress level and strain accumulation at the time of rupture, however, varies between earthquakes, as does the time between successive ruptures. Thus, given a constant interseismic strain-accumulation rate, knowledge of the time since the previous earthquake permits prediction of the amount of slip that would occur at any given time. But, it doesn't reveal when the next earthquake will occur, because no critical stress threshold is common to successive earthquakes.

Asperities, Barriers, and Characteristic Earthquakes

What Controls Ruptures?

In an effort to understand why and when earthquakes occur, many scientists have searched for patterns of ruptures which, if fully understood, could form a basis for predicting subsequent seismic events. It is clear that earthquakes occur when the strength of a fault is exceeded. But, what controls the strength of a fault and does the strength change between earthquakes? In southern California, all of the recent large earthquakes ($M \geq 5$) have occurred on faults that were "loaded," that is, the stress was increased on them by a nearby earthquake in the previous 18 months (Harris et al., 1995). Moreover, it seems probable that there are localized segments or patches of some fault planes that control the strength of some faults, whereas other parts are at times relatively stress free (Fig. 4.6). These "sticky" patches of faults have been termed *asperities*. These may be analogous to irregularities that jut out from a planar surface and which, if two planar surfaces were juxtaposed, would be the points where frictional forces would have to be overcome in order to permit sliding between the surfaces. Thus, asperities represent irregularities that can concentrate stresses along a fault, and their strength with respect to shear stresses exerted on them may control when faulting occurs. If the strength of asperities persists from one earthquake to the next, it might be expected that the recurrence pattern would follow a time-predictable model (Fig. 4.5B).

Alternatively, earthquakes may be thought of as causing ruptures along a heterogeneous fault plane in which some strong patches fail to break. These unruptured regions are termed *barriers* (Fig. 4.6). Aftershocks following the main earthquake will be concentrated around these barriers (Aki, 1984). If the fault plane is considered to be uniformly stressed prior to rupture, the presence of barriers after faulting represents a "stress roughening" because the stress is less uniformly distributed after the earthquake. If the same strong barriers control successive earthquakes, such a fault might display recurrence patterns based on slip-predictable behavior (Fig. 4.5C).

FIGURE 4.6. Model of asperities and barriers along a fault plane

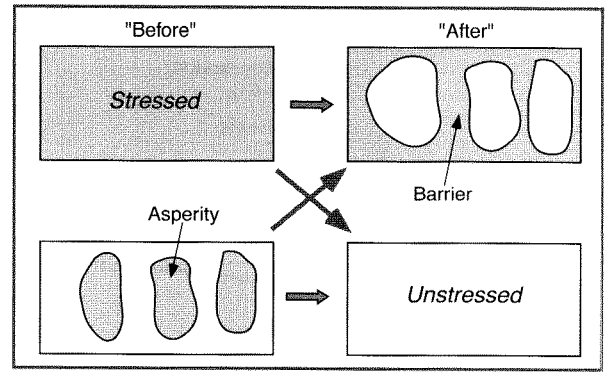

Barriers (unruptured regions) can remain after faulting and may stop the propagating rupture. Asperities may exist before rupture and determine the strength of the fault. Modified after Aki (1984).

Characteristic Earthquakes and Fault Models

It has been proposed that some faults are typified by *characteristic earthquakes*, in which a fault or a segment of a fault ruptures repeatedly and displays approximately the same amount and distribution of slip during each successive event (Schwartz and Coppersmith, 1984). If a fault did indeed display characteristic earthquakes, knowledge of a single faulting event would provide a remarkable understanding of both previous and future rupture patterns, because the strain build-up and release, stress drops during faulting, variations in displacements along the fault, and the length of the rupture would be approximately duplicated in successive earthquakes. Thus, tremendous predictive power may reside in faults that rupture via characteristic earthquakes. If ruptures along a fault were controlled by stable asperities and barriers (i.e., consistent failure stress and terminating stress), that persisted from one earthquake to the next, this could provide a mechanism for generating similar "characteristic" slip along the fault in multiple events.

In order to test whether or not a fault is typified by characteristic earthquakes, either a suite of well-documented

historical earthquakes, or information from paleoseismic studies has to be used to reconstruct the temporal distribution of events and the spatial pattern of slip in any particular event in the past. The patterns of displacements of past ruptures need to be compared with respect to the length and position of the rupture and the distribution of displacement along the fault. Given a regional strain field, such as that controlled by relative plate motions, several different scenarios can be envisioned to accommodate the regional strain, only some of which would involve characteristic earthquakes (Schwartz and Coppersmith, 1984). In one scenario (Fig. 4.7A), displacements and rupture lengths are randomly distributed in such a fashion that, over time, all regional strain is accommodated, and there is an essentially uniform slip rate along the length of the fault. In this *variable-slip* scenario, the displacement experienced at any given point, the size of the earthquake, and the position of the rupture segment each vary unpredictably between successive events. Consequently, there are no faults exhibiting characteristic earthquakes in this scenario. A second scenario (Fig.4.7B) suggests that, at any given point, the displacement is consistent from one earthquake to the next, although displacement can vary along strike. Over time in this *uniform-slip* model, there is again a consistent slip rate all along the fault. In addition, the large earthquakes have a repetitive pattern in terms of rupture length and displacement variations along the rupture, and moderate sized earthquakes occur more frequently. In the *characteristic earthquake* model (Fig. 4.7C), there is also a consistent displacement at a point from one event to the next. Over time, however, the slip rate varies along the fault because the displacement varies along the length of the fault. Each large earthquake represents a repetition of the rupture location, length, and displacement pattern of the previous large earthquake, and there are infrequent moderate-sized earthquakes that only accommodate a fraction of the residual slip variation along the fault.

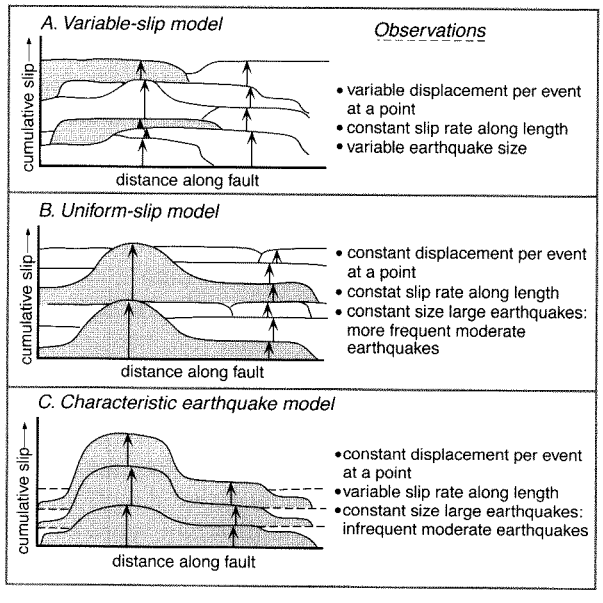

FIGURE 4.7. Models for slip accumulation (vertical axis) along a regional suite of faults

Models for variable slip (A), uniform slip (B), and characteristic earthquakes (C). Modified after Schwartz and Coppersmith (1984).

In viewing these models, it is easy to envision how variation in slip along normal or reverse faults that are associated with characteristic earthquakes would progressively build an irregular topography. If the site of greatest structural displacement along a fault were to be essentially fixed in the landscape through time, mountain peaks and basin depocenters would occur in predictable positions above the zone of maximum uplift or subsidence. Both structure contours and the landscape topography might be expected to be closely related to these repetitive cycles of displacement.

How could one test whether a fault displays characteristic earthquakes? In the vicinity of the "Parkfield asperity" on the San Andreas, for example, five moderate thrust-fault earthquakes (M~6) with rather similar rupture patterns have occurred during the past century (Bakun and McEvilly, 1984). These are suggestive of characteristic earthquake displacement patterns. Usually, however, the historical record is both too brief and incomplete to permit reconstruction of the displacement patterns during several ruptures of an entire fault or a segment of it. Consequently, we often have to interpret the geological record of deformation and faulting to assess past rupture patterns. At least two different approaches can be used for such an assessment. In one, the variability of displacement along a fault is compiled for several past earthquakes using measured displacements of strata, structures, and geomorphic features. We describe this approach in a subsequent chapter on paleoseismicity. In the second approach, the deformation observed to have resulted from a single, recent earthquake is compared with nearby deformed geologic markers, such as the surface of a fold

FIGURE 4.8. Loma Prieta shoreline displacement compared with the warped marine terraces

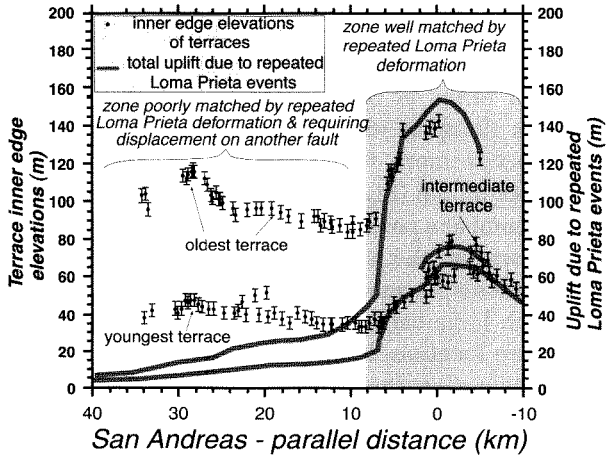

The variations in displacement and terrace altitudes are projected orthogonally on to the trend of the nearby San Andreas fault. Coseismic displacements in the southern half of the transect mimic the height variations of the warped marine terraces. This suggests that warping of these terraces could result from multiple earthquakes with Loma Prieta-like displacements. Modified after Anderson and Menking (1994).

or deformed marine or fluvial terraces, which represent the cumulative deformation of multiple earthquakes. If the spatial pattern of deformation shown by the long-lived structure could be created through repeated application of the deformation due to the individual faulting event (Stein et al., 1988), then it is reasonable to suggest that the fault may have a characteristic behavior. An example (Fig. 4.8) of such a comparison can be made using a) the strain resulting from the 1989 M6.9 Loma Prieta earthquake south of San Francisco, and b) deformed marine terraces (Anderson and Menking, 1994). The Loma Prieta earthquake caused deformation extending from the San Andreas fault to the California coast, where shoreline displacement has been well documented by detailed surveying. A comparison of the shoreline coseismic displacement with the shape of the warped marine terraces clearly indicates that the terrace deformation could result from repeated Loma Prieta-like events. The match between the terraces and the coseismic strain is very good for the southern part of the terraces, but is unconvincing farther north (Fig. 4.8). To explain that northern pattern of deformation, repetitive faulting on another fault has been invoked (Anderson and Menking, 1994). While the excellent match of the warped terraces with the pattern of coseismic deformation does not prove that the Loma Prieta rupture was an oft-repeated, characteristic rupture, it certainly suggests that this is a reasonable interpretation.

Displacement Variations Along a Fault, Fault Growth, and Fault Segmentation

Fault Length and Displacement Variations

The concept of characteristic earthquakes contrasts with studies suggesting that, as a fault accumulates a greater total displacement, it lengthens, such that with each earthquake, the rupture is extended a bit more. But, does displacement vary systematically along a single rupture, or is it unpredictable? In order to collect a data set on fault growth and displacement, it is useful to study faults that developed in a homogeneous material and are sufficiently young to ensure that the faults have not been significantly modified by erosion. These conditions are met by the Bishop Tuff, an extensive ashflow that is about 800 ka (Bailey et al., 1976). Studies of faults offsetting this tuff in central California display similar displacement patterns for normal fault lengths spanning about two orders of magnitudes (20 m to 2000 m; Fig. 4.9A) (Dawers et al., 1993). In particular, there is a bow-shaped displacement variation, such that there is no displacement at the fault tips, the amount of displacement rapidly increases over the first third of the fault, and then it rises more gradually to a maximum near the midpoint of the fault. On all of these particular faults, the maximum displacement (D) is about 1–2% of the fault length (L). This displacement pattern is similar to theoretical predictions, laboratory experiments, and other field studies (Pollard and Segall, 1987; Schlische et al., 1996). A compilation of displacement data (Fig. 4.9B) from a variety of settings and different types of faults (Scholz, 1990), clearly suggests that there exist predictable scaling relationships between the length of the fault and the displacement along it, but that these relationships vary for different settings and perhaps different types of faults. For the Moine thrust and modern thrust earthquakes (Fig. 4.9B), there appears to

FIGURE 4.9. Length scaling relationships

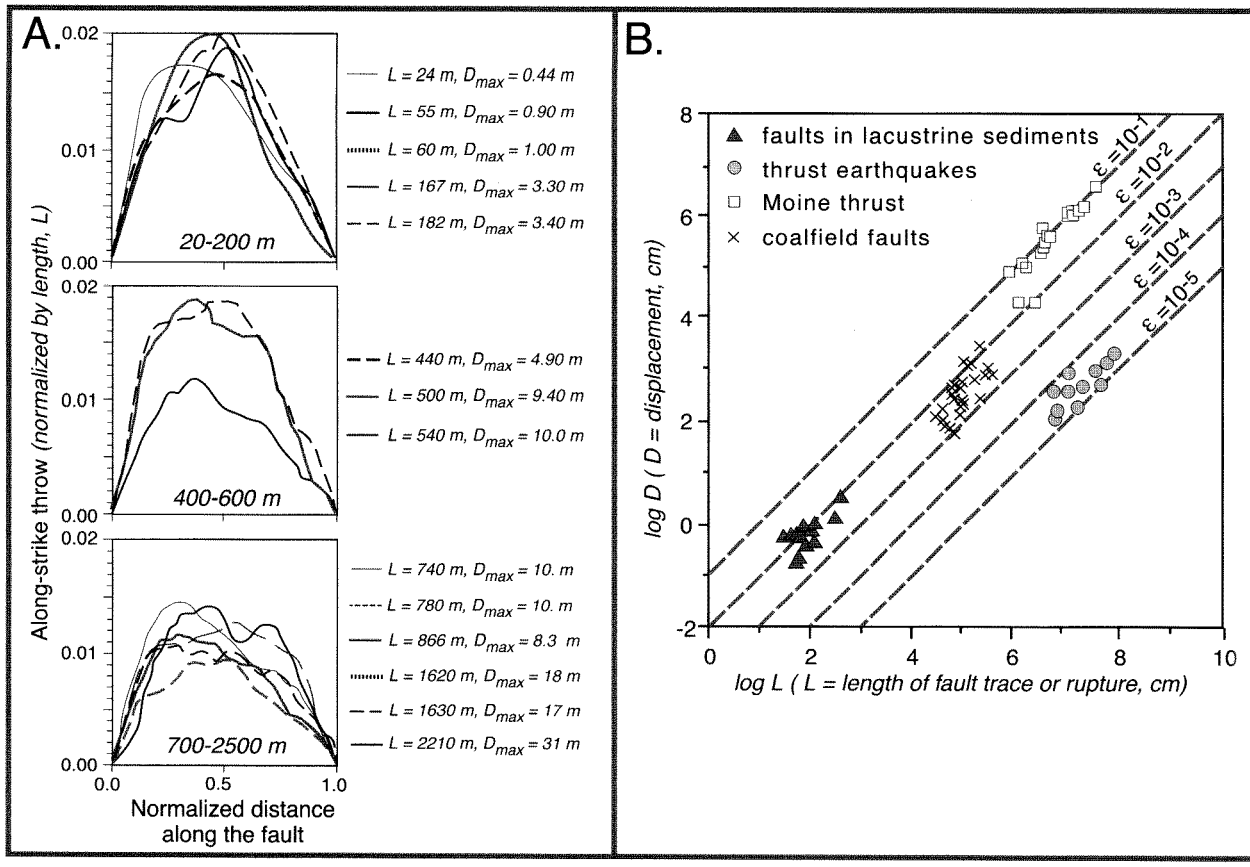

A. Displacement versus distance along fault traces on normal faults cutting the Bishop Tuff, California. Note the characteristic bow-shaped displacement variation for faults spanning two orders of magnitude in length. For all faults, the maximum displacement is between 1 and 2% of the fault length. Modified from Dawers et al. (1993).
B. Systematic fault scaling relationships are apparent when maximum displacements versus fault lengths are plotted. No universal scaling rule describes these data because they represent several different tectonic settings, fault types, and rock types. Within each subset, however, displacement versus length variations could be readily quantified. The dashed lines are lines of equal strain (D/L). Modified from Scholz (1990).

be a linear relationship, such that $D \alpha \varepsilon \bullet L$, where ε is the strain, which varies over four orders of magnitude from about 10^{-1} to 10^{-5}. In contrast, the coalfield faults (Watterson, 1986) suggest (Fig. 4.9B) that displacement is proportional to fault length squared, $D \alpha \varepsilon \bullet L^2$. At present, clearly there is no single model that universally explains displacement/length scaling, but the available data suggest that, in a particular setting with fairly homogeneous rock properties, predictable D/L relationships of the general form $D \alpha \varepsilon \bullet L^n$ can be defined.

If it is assumed that the measured displacements are the result of repeated seismic ruptures, then these data clearly argue that faults indeed lengthen as they accumulate displacement. Thus, over long time intervals and many seismic events, these data suggest that no fault can be consistently typified by characteristic earthquakes: the fault has to lengthen over time. On the other hand, once a rupture plane is fairly large (several km in length), the incremental change in length due to several successive earthquakes may be insignificant compared to its total length. Thus, at the time scale of several events, the

FIGURE 4.10. Two models for fault growth

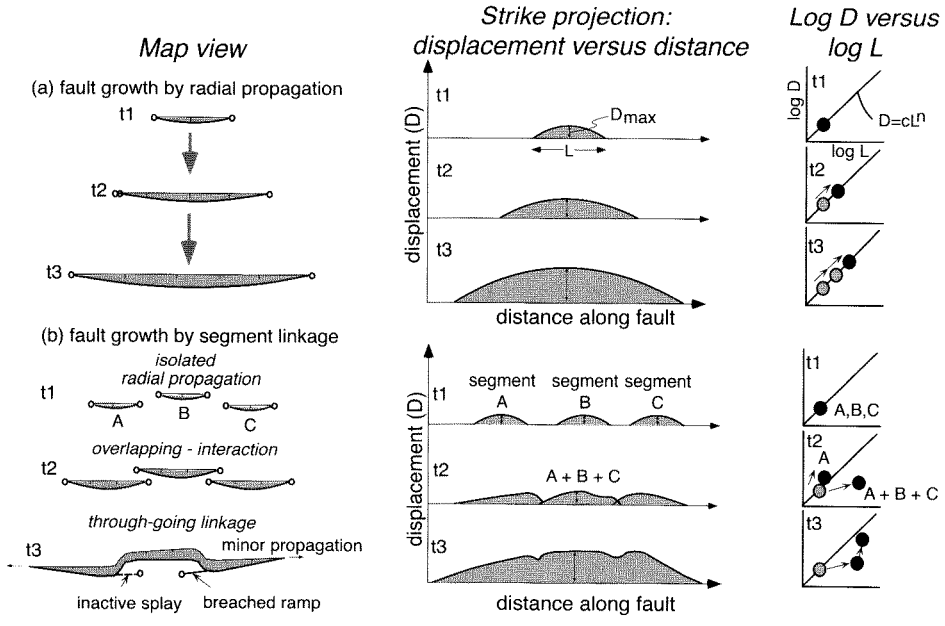

During fault growth by radial propagation, an individual fault simply lengthens and accumulates more displacement through time. Plots of displacement versus fault length (right column) show a steady increase in displacement as the fault grows. Map view on the left shows a different scheme for fault growth, whereby small individual faults gradually link up to create one large, through-going fault. Whereas the accumulation of displacement follows a predictable path for the individual segments, when they link up, displacement becomes considerably less than that predicted for a fault of this length (see right-hand column). Through time, the slip deficiencies near the points of segment linkage are reduced. Ultimately, the only indication that the large fault resulted from linkage of smaller ones may be the presence of the perturbations to the smooth, bow-shaped displacement near the former zones of overlap and linkage. Modified after Cartwright et al. (1995).

concept of characteristic earthquakes may be applicable in such cases and may be usefully applied for predictive and modeling purposes.

Fault Segment Linkage

What happens when individual faults extend toward each other during the course of multiple faulting events? Are large faults the result of linkage between several smaller fault segments, or do they represent simple lateral propagation of a single fault? How can we distinguish in the modern record between different modes of fault growth? If faults don't link up, how is regional deformation accommodated among multiple faults?

Simple models (Cartwright et al., 1995) suggest two ways in which elongate faults may develop (Fig. 4.10). During fault growth by radial propagation, an individual fault simply lengthens through time and accumulates more displacement, following the idealized bow-shaped displacement gradient. Displacement increases steadily as the fault grows. Alternatively, fault segments which link up may show similar modes of growth for smaller, individual faults. But, at the moment their tips link up, the total length of the fault suddenly increases, whereas the total displacement does not substantially change. This causes a departure from any previously established displacement-length relationship (Fig. 4.10). Over time, the composite fault may smooth out the slip deficit near the former segment boundaries, such that only small departures from the expected displacement may mark these boundaries. Eventually, the displacement-length geometry for a fault resulting from segment linkage may be indistinguishable from that of a similarly long fault that grew from a

single rupture. Only in situations in which syntectonic sediments record how fault displacements varied through time (Anders and Schlische, 1994) might it be possible to distinguish these different modes of fault growth.

Another way to visualize linkage among faults is to imagine a competition among different fault segments in which the "big guy wins." Consider a homogeneous medium subjected to tensile stresses which cause numerous small defects or extensional faults that are randomly distributed across the surface. With continuing extension, these "defects" lengthen, and as they grow laterally, some of them happen to encounter other lengthening faults. These segments then link up, creating a longer fault that accommodates increasingly more displacement. This linkage also creates a "shadow zone" where previously formed faults become inactive, because the larger fault is taking up all the strain in that sector of the deforming plate. Eventually, larger fault segments link together to form a through-going, master fault, and virtually all the other faults die. Both numerical models and limited field examples support this competition model (Gupta et al., 1998).

Displacement Compensation Among Multiple Faults

Consider two parallel faults for which the ends of the faults are not linked, but they do overlap. Often, as the displacement decreases on one fault, the offset on an overlapping fault strand increases, such that the net slip across the overlapping region decreases only slightly (Willemse et al., 1996). Along the 1983 Borah Peak (M = 7.0) rupture (Crone and Machette, 1984), for example, the overall displacement shows a bow-shaped gradient (dashed line, Fig. 4.11), and there are several overlapping zones of compensating offsets between individual fault segments, such as in the vicinity of Cedar Creek or between Arentson Gulch and West Splay Junction (Fig. 4.11, bottom panel). This compensating behavior can be more clearly seen along a 7-km-long, linear zone of interrelated, overlapping normal faults that cut the Bishop Tuff (Fig. 4.12A). This fault zone comprises four major, overlapping fault scarps and numerous subsidiary faults with lesser throw (Dawers and Anders, 1995). When the displacement on individual faults is summed along the length of the entire fault zone (Fig. 4.12B), a broadly bow-shaped displacement gradient emerges. This suggests that the whole array of faults is deforming as if it were a single fault and that overall displacement is being smoothly partitioned among multiple structures. In some places, however, a clear decrease from a smoothly changing displacement curve (for example, between major faults b and c, Fig. 4.12) coincides with a segment boundary. Thus, there is an apparent "slip deficit" near this zone of overlap. In contrast, there is no net slip deficit in the overlap zone between faults a and b (Fig. 4.12B), because numerous smaller faults and tilting between faults fully compensate for decreasing displacement near the tips of the major faults. One can imagine that with increasing displacement, these faults may amalgamate into a single irregular, but continuous fault trace. At present, the displacement gradient by itself (Fig. 4.12B) would probably be interpreted to indicate that only two faults were linking up (due to the slip deficit between b and c), because the summed displacements give little indication of the existence of faults a and b as separate ruptures. Thus, it is obvious how difficult it can be to use simple along-strike displacement variations as a basis to choose between lateral propagation and segment linkage as a means of fault growth.

Segmentation of Range-Front Faults

Some large mountain ranges, such as the Sierra Nevada of California or the Wasatch Range of Utah, are bounded by a range-front fault system that is hundreds of kilometers long. The range-bounding fault never ruptures along its entire length in a single seismic event. Instead, smaller segments break in individual earthquakes, and multiple seismic events are required to displace the entire range front. Along some of these long range fronts, it appears that there is a recognizable *segmentation* of the bounding fault zone into smaller rupture lengths that have definable terminations (Fig. 4.13). Along the Wasatch Fault system, four different types of segment boundaries (Machette et al., 1992a) are recognized (Fig. 4.14). The most commonly observed boundary occurs where bedrock spurs or salients extend into the adjacent basin and major range-front faults terminate against them. Some of these spurs are bounded by Quaternary faults that are active, but have less displacement than the range-front faults. Other segment boundaries are delineated by an *en echelon* step in the range-bounding faults. Still others occur where the range-front faults are intersected by a cross-fault which trends at a high-angle to the range front. Finally, some segment boundaries are simply defined by the absence of a rupture between two active range-front faults (Machette et al., 1992a). Several of the segment

FIGURE 4.11. Map of the 1983 Borah Peak rupture

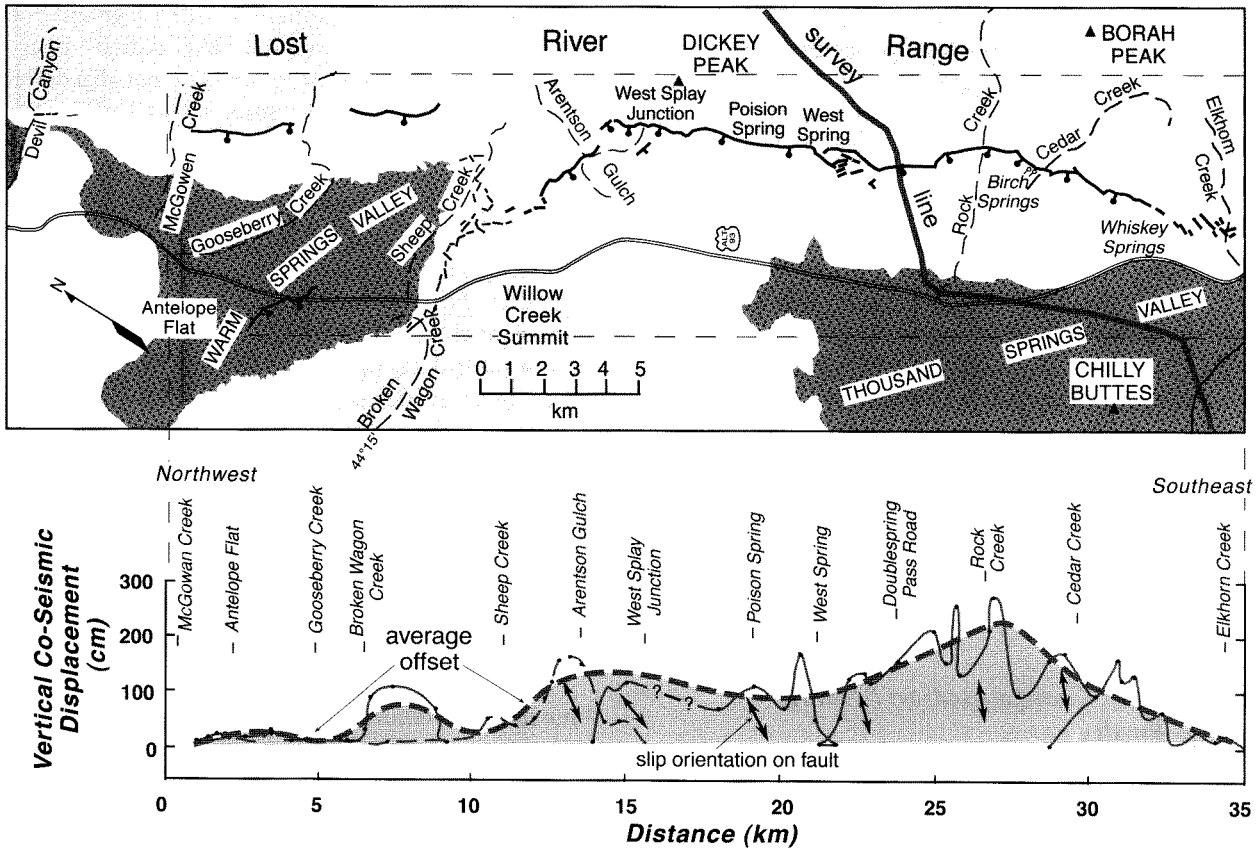

Top map shows discontinuous rupture trace and several zones of complex faulting, such as near Arentson Gulch, West Spring, and Elkhorn Creek. Displacement along strike (bottom) shows greatest vertical offset near Rock Creek (where the highest peak is also found in the footwall), overlapping offsets where decreasing displacement on one fault is compensated for by increasing displacement on another fault (Arentson Gulch to West Splay Junction), and a broadly bow-shaped displacement pattern (dashed line) along this succession of fault traces that is similar to the pattern seen on individual normal faults (Fig. 4.9A). Double arrows depict orientation of striae on the fault plane and indicate oblique dip-slip on this fault. The location of the levelling line survey (Fig. 4.23) runs approximately perpendicular to the rupture trace. Modified after Crone and Machette (1984).

boundaries display a combination of spurs, cross-faults, and *en echelon* offsets. If the positions of the terminations persist through time and if entire segments typically rupture in a single seismic event, each segment might be typified by characteristic earthquakes (Schwartz and Coppersmith, 1984). At present, however, neither the persistence of the terminations nor the tendency for an entire segment to rupture "characteristically" is well established. Moreover, along several mountain fronts where the surface traces of reverse faults suggest the presence of segment boundaries, historical earthquakes have simultaneously ruptured across several of these apparent segments (Rubin, 1996).

Geomorphic Expression of Faults

Faults in which the hanging wall moves only vertically, that is, directly up or down the fault plane, are termed *dip-slip* faults, whereas pure horizontal motion results

FIGURE 4.12. Map of a zone of related normal faults

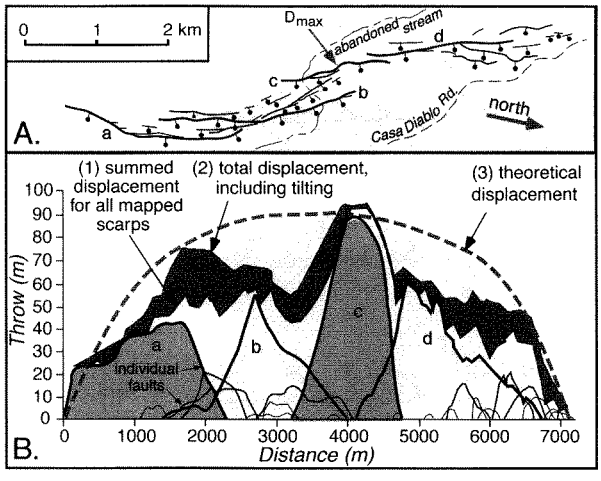

A. The fault zone consists of four overlapping major faults (labelled a, b, c, and d) and >20 lesser faults. These faults cut the 0.78 Ma Bishop Tuff in east-central California. All of the faults are displaced down to the east, and some tilting of the original surface also occurs between the faults. B. Displacement versus distance along the fault zone. Thin lines show the displacement attributed to individual faults. The dark, overall displacement envelope is bounded on its base by the summed throw of the mapped faults and on its top by this summed throw and that displacement attributable to tilting between faults. Note the bow-shaped displacement along the total fault zone. A slip deficit occurs between faults b and c, but none is apparent between faults a and b or c and d. Modified after Dawers and Anders (1995).

FIGURE 4.13. Segmentation of the Wasatch fault zone

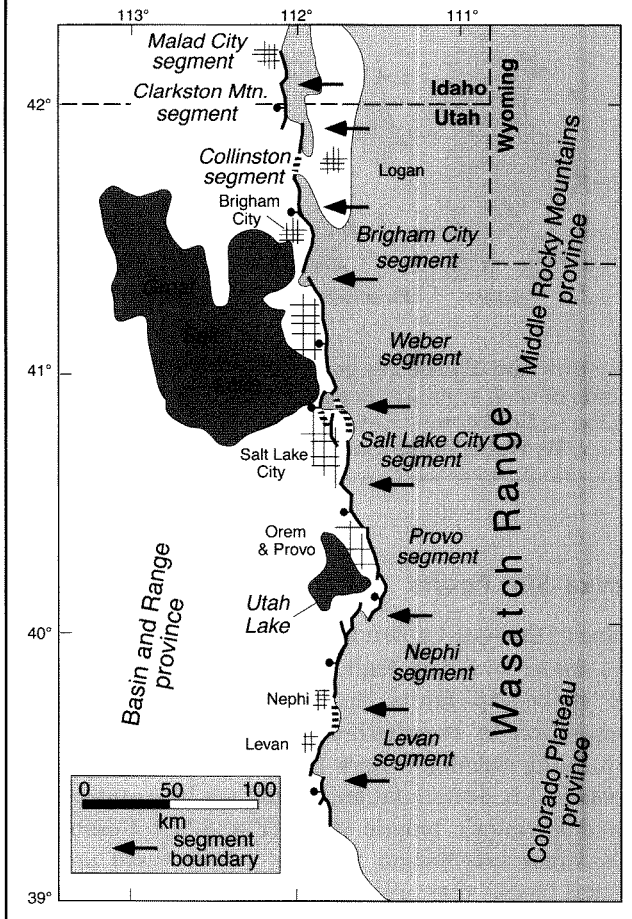

At least eight segments have been identified along the 400-km-long system of normal faults that delineate the Wasatch front. Modified after Machette et al. (1992b).

in *strike-slip* faults. Few faults, however, are purely dip-slip or strike-slip. Most have some component of both horizontal and vertical motions. Nonetheless, it is useful to describe the structures and geomorphic features that are expected for the primarily dip-slip and strike-slip end-members, because their contribution to a given natural fault setting can then be more readily recognized. Experimental results using homogeneous materials with known physical characteristics often depict an idealized array of structures that is associated with a particular stress field. Such structures are described in the following paragraphs. Natural heterogeneities in rocks, however, dictate that they will not deform uniformly, so that few natural situations exactly duplicate model predictions.

We typically envision a fault as an irregular, but singular surface dipping into the crust. In fact, at the scales of less than 10 km, most faults consist of a tabular volume of typically unconnected or anastomosing smaller faults (Scholz, 1998). These component faults will span a broad spectrum of sizes, ranging from a few meters to several kilometers. The complexity of surface deformation, therefore, is not solely attributable to the heterogeneous materials of the crust, but also to the fact that, during an earthquake, hundreds of small rupture surfaces actually accommodate the total displacement. Not surprisingly, the resulting deformation pattern is complex, too!

FIGURE 4.14. Types of segment boundaries observed along the Wasatch Fault

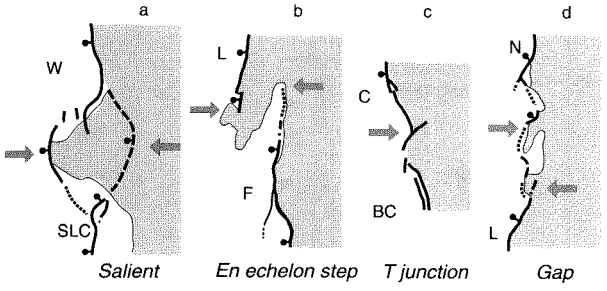

Arrows identify the key geometries that define the ends of each segment. Segment names: BC: Brigham City; C: Colliston; L: Levan; N: Nephi; SLC: Salt Lake City; W: Weber. Modified from Machette et al. (1992a).

Strike-Slip Faults

Some of the best-known faults in the world, such as the San Andreas, Altyn Tagh, and North Anatolian faults, are strike-slip faults that have caused widespread destruction in twentieth-century earthquakes. Strike-slip faults develop where the maximum compressive stress (σ_1) is horizontal and there is a horizontally oriented deviatoric tensile stress (Fig. 4.1C). Commonly, this stress orientation prevails where there are two crustal blocks that are moving essentially horizontally and approximately parallel to the boundary between them, but in opposite directions. Thus, a shear couple is created across this boundary zone.

As observed in laboratory experiments and field studies, there is a predictable geometry of structures that may form in shallow crustal rocks and alluvium in response to this stress field (Fig. 4.15). A *principal displacement zone* commonly forms parallel to the shear couple. This is the orientation you would expect a strike-slip fault to have, if the crustal blocks on either side had a high rigidity with respect to a weak boundary fault zone between them. Normal faults should form perpendicular to the direction of maximum elongation and maximum tensile stress. *Reidel* shears (R) form at an angle of $\theta/2$ (~15-20°) with the principal displacement zone, where θ is equal to the angle of internal friction for the faulted material. These will have the same sense of strike-slip motion as the principal displacement zone, and these shears typically form a suite of *en echelon*

FIGURE 4.15. Orientation of structural features formed in response to strike-slip shear couple

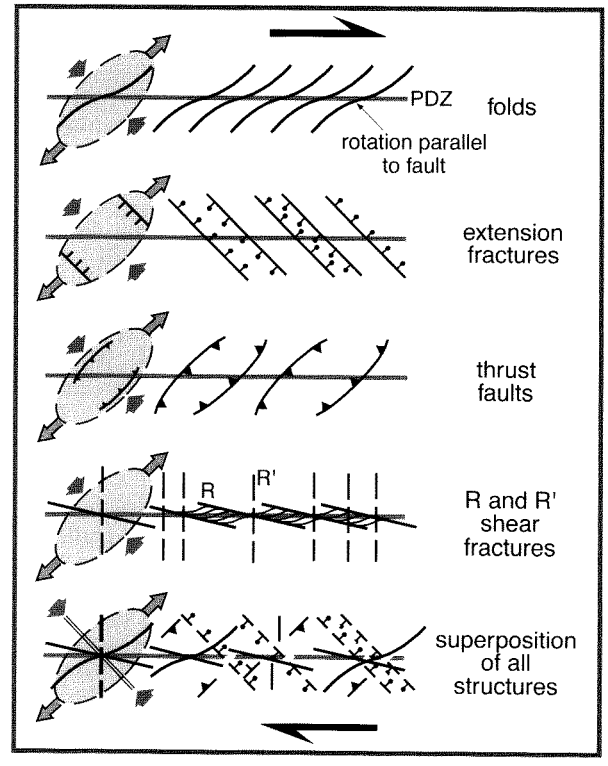

Folds, normal and thrust faults, Reidel shears and conjugate shears form at predictable angles with respect to the principal displacement zone (PDZ). Modified after Sylvester (1988).

fractures (Fig. 4.15). As shearing continues, the propagating tips of the Reidel shears tend to curve to become parallel with the normal faults and to display normal-fault displacements with little strike-slip motion in the tip zone. Conjugate Reidel shears (R') can form at $90° - \theta/2$ (60–75°) to the principal displacement zone. These conjugates have the opposite sense of strike-slip motion as the main fault. Finally, folds and thrust faults should form with their axes or traces, respectively, approximately perpendicular to the main compressive stress. The fold axes will initially be oriented at about 45° to the main displacement zone, but, as fault motion continues, they can be rotated into more complete parallelism with the main fault due to shearing adjacent to the principal displacement zone. In nature, some of these structures may represent responses to different

FIGURE 4.16. Regional-scale structures along a strike-slip fault

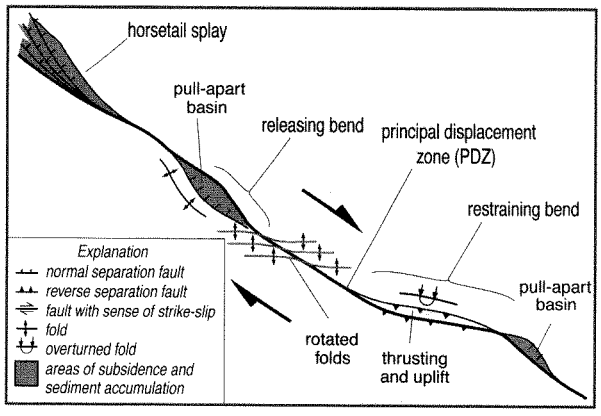

Features include restraining bends associated with thrusts and mountain building, releasing bends associated with basin development and rapid subsidence, and horsetail splays of either normal or reverse faults where deformation is spread over a broader zone. Modified after Christie-Blick and Biddle (1985).

FIGURE 4.17. Development of pull-apart basins at step-overs

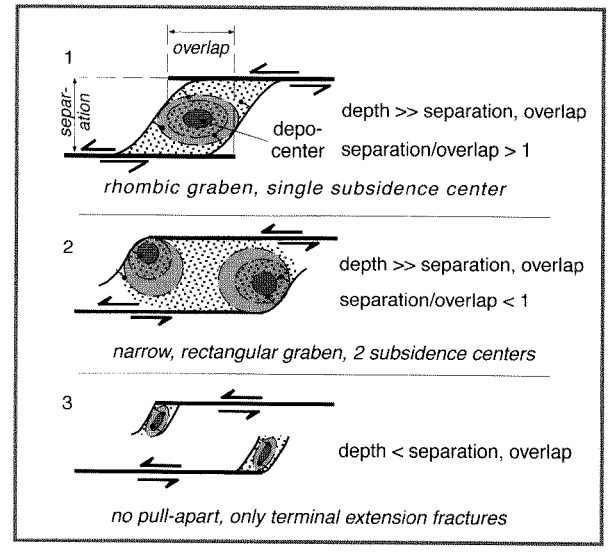

Modelling suggests that the geometry of the basin is dependent on ratios among the magnitude of overlap of the ends of the strike-slip faults, the separation distance between the faults, and the depth to basement. Modified after Deng et al. (1986).

generations of motion, and all of them can be superimposed, making for a very complicated array of structures within abroad shear zone (Sylvester, 1988). Although the development of structures along a newly formed strike-slip fault does not follow an invariant pattern, there is often a predictable succession of structures, which initially involves discrete folds and tension gashes and eventually results in a through-going, anastomosing shear zone (principal displacement zone) along which pull-apart basins and compressional uplifts are juxtaposed (Anderson and Rymer, 1983).

Whereas all of these structures can be associated with a relatively straight segment of a strike-slip fault zone, many strike-slip faults have traces that bend such that slip between the adjacent blocks will create important compressive or tensile stresses in the curved fault segments. For example, in a restraining bend (Fig. 4.16), the fault trace curves into the path of the blocks on either side of the fault. This generates contractional structures that lead to development of thrust faults, folds, and ultimately mountains (Biddle and Christie-Blick, 1985). In the vicinity of a releasing bend, the fault curves away from the path of the blocks on either side such that extensional structures, such as normal faults and basins, form between them (Fig. 4.16). Alternatively, strike-slip faults may display major lateral step-overs, in which one fault trace ends and a second with the same sense of displacement commences. A combination of the sense of motion on the strike-slip fault and the geometry of the step-over determines whether this intervening zone will be one of compression or extension. With a compressional step-over, a zone of uplift forms between the fault tips, and thrust faults may form to accommodate shortening across the uplift. With an extensional step-over, normal faults form to accommodate subsidence within a *pull-apart* basin (Fig. 4.17). The geometry of a pull-apart basin and the locus of the zone of maximum subsidence is predicted to be a function of the separation between the overlapping fault strands, the amount of overlap, and the depth to the basement (Deng et al., 1986). When the separation between faults is greater than the overlap and the depth to basement is much greater than either separation or overlap, then a single depocenter tends to develop. In contrast, two depocenters will tend to develop adjacent

FIGURE 4.18. Overview of strike-slip geomorphology

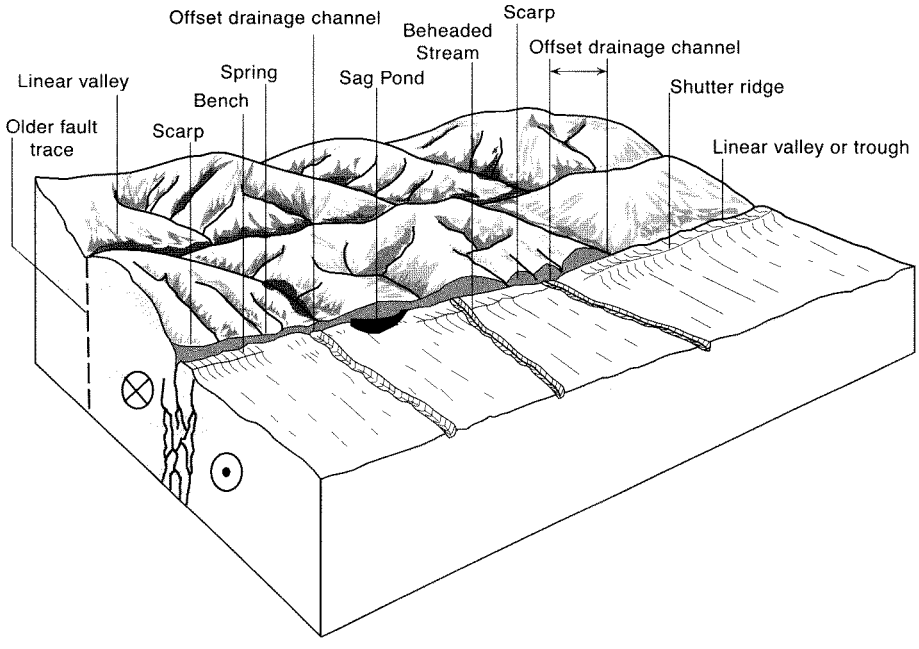

A linear trough along fault, sag ponds, shutter ridges, offset ridges and drainages, springs, scarps, and beheaded streams are typical geomorphic features indicative of strike-slip faulting. The older, abandoned fault trace displays analogous, but more erosionally degraded features. Modified after Wesson et al. (1975).

to the bounding normal faults when the separation is significantly less than the overlap.

The geomorphological expression of strike-slip faults can be viewed at the scale of individual seismic events or as a result of long-term strain accumulation. Because individual faulting events vary so widely in terms of the magnitude of offset, length of rupture, and material that they deform, it is not possible to specify a single set of geomorphic features which characterize them. At the scale of a few meters or less, it is typical to find *en echelon* faults rupturing the surface, small collapsed basins at releasing step-overs, and small, thrusted uplifts at restraining step-overs. It is also typical to find apparent vertical displacements along the fault trace. Some of these result from simple horizontal translation of higher topography into an area of lower topography on the opposite side of the fault or vice versa. Many scarps, however, result from some component of vertical displacement along the fault that is a consequence of the fact that the fault is not a simple vertical plane or that the movement is not wholly strike-slip. Along a steeply dipping, but undulating fault plane, one can visualize small-scale releasing and restraining bends which cause subsidence or uplift of one side of the fault with respect to the other. If such a configuration were to persist over long intervals, large basins and mountains would develop that would be restricted to one side of the fault. It is common along fresh ruptures of strike-slip faults, however, to find that the uplifted scarps do not persistently face in the same direction, but rather that the upthrown side varies along the fault trace.

Over long time intervals, strike-slip faulting typically leads to some well-known geomorphologic features (Fig. 4.18). A linear trough commonly forms along the principal displacement zone, because structural blocks are slipping past each other along this zone and because the fractured materials are more readily eroded along the fault zone. Recent numerical modelling suggests that simple deflection of streams across strike-slip faults can create linear valleys along the fault trace in the absence of any special "softening" due to brecciation (Braun and Sambridge, 1997). Irrespective of

how the troughs are generated, within them, *sag ponds* may form in low-lying regions. Scarps can be preserved on either side of the fault. Linear features like streams and ridges become offset along the fault and can yield a clear sense of slip directions. Some care must be used, however, when inferring displacement directions from offset streams. Offsets determined from streams that are displaced in an uphill direction with respect to the local hillslope gradients are more reliable than downslope displacements which could result from stream capture. When a ridge that has been translated along the fault blocks a drainage, it is termed a *shutter ridge*. On the downslope side of strike-slip faults, *beheaded stream valleys* may be preserved (Fig. 4.18). These are abandoned valleys that have been rafted laterally beyond the course of the stream that formerly flowed through them (Keller et al., 1982). On both the upstream and downstream sides of a fault, river terraces may be systematically offset. Commonly, streams crossing a strike-slip fault will exit from a mountainous terrain into a gentler one. Upstream, their valleys will have been more confined, whereas downstream of the fault, they may build alluvial fans in the less-confined topography. Offsets of both the margins and the crest of a fan may be used to determine fault displacements (Fig. 4.19). Horsts, grabens, small-scale pull-apart basins, and various thrusts and folds can also have clear geomorphologic expression and can often be understood in the context of the imposed shear couple and stress field.

FIGURE 4.19. Sketch map of geomorphic features along the southern San Andreas fault in the arid setting of the Salton Trough

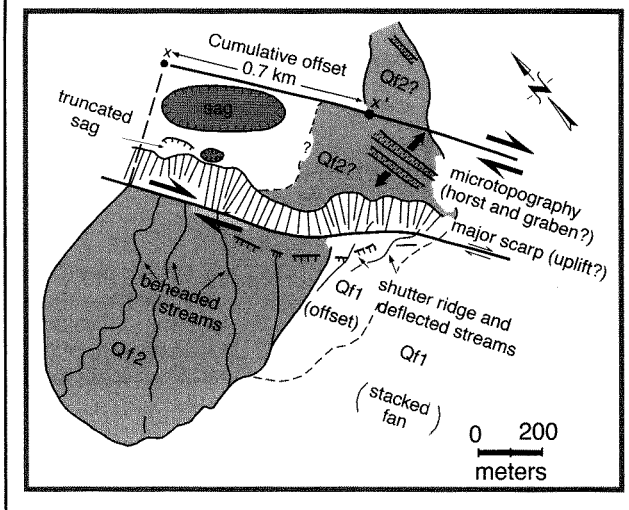

Note the large offset fan, the beheaded streams, shutter ridges, and various extensional features. Modified after Keller et al. (1982).

Normal Faults

Normal faults form in settings where the maximum compressive stress (σ_1) is vertical and there is a deviatoric tensile stress in a horizontal orientation (Fig. 4.1A). Typically normal faults cut the surface at high angles (~50–60°). In cross section, coseismic displacements on normal faults are commonly asymmetric with respect to a horizontal datum, such that subsidence of the hangingwall is typically several times greater than uplift of the footwall. Although down-dropped keystone blocks (grabens) and uplifted horsts (blocks bounded by normal faults on both flanks) were once thought to typify regions of normal faulting, unpaired normal faults creating half-grabens or *fault-angle depressions* occur more frequently (Fig. 4.20). The down-dropped hangingwall of a normal fault commonly generates a basin in which sediments accumulate, whereas the footwall experiences uplift and, in terrestrial settings, becomes a site of erosion. Thus, many normal faults bound asymmetric ranges with one steep, fault-bounded flank and a gently sloping, largely unfaulted opposite flank (Fig. 4.20). Secondary *synthetic* (dipping in the same direction with similar sense of throw) or *antithetic* (dipping in the opposite direction with an opposite sense of throw) faults may develop within the hangingwall block.

Rather than amalgamating into a single fault zone, displacement during extension can also be transferred between adjacent faults by a variety of structures (Gawthorpe and Hurst, 1993), including 1) *transfer faults* which are oblique to the traces of the main faults, but which link them together; 2) *relay ramps* which may or may not be faulted and which bridge between two faults facing the same direction; 3) *antithetic interference zones* which are tilted (±faulted) ramps developed between normal faults facing each other and dipping in opposite directions; and 4) *antithetic interbasinal ridges* that develop where normal faults change polarity and step into the footwall (Fig. 4.21). Each of these structures provides a mechanism whereby the total regional displacement can vary smoothly, despite the fact that individual faults die out, that displacement is variable along each fault, and that both fault lengths and amount of overlap change through time. Any relatively broad

FIGURE 4.20. Schematic of cross section of normal faults in an extensional regime

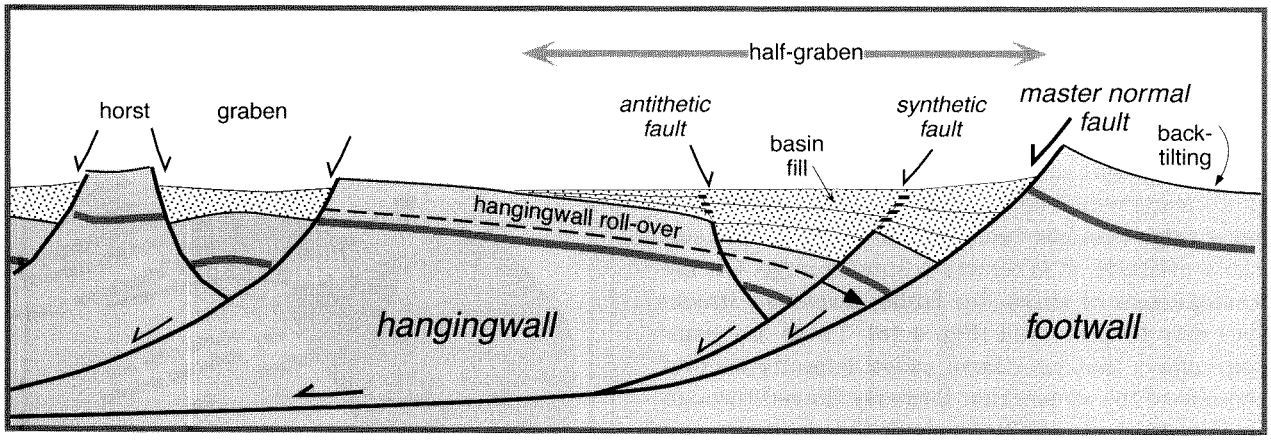

The master fault delineates footwall and hangingwall blocks. A broad half-graben is cut by synthetic and antithetic faults. Note the curvature of the hangingwall toward the master fault (hangingwall roll-over).

FIGURE 4.21. Interbasin transfer zones

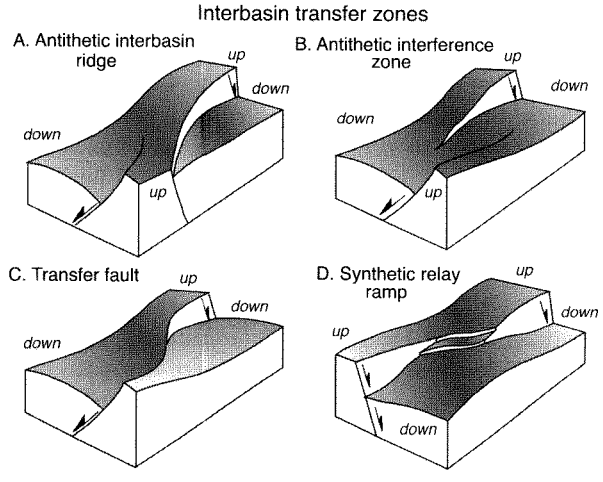

Simplified geometries of structures that assist the transfer of deformation between two regional-scale, overlapping or non-overlapping normal faults. Modified after Gawthorpe and Hurst (1993).

region that is undergoing extension will display some of these displacement-accommodation features. For example, during much of Cenozoic time, active extension has been occurring across eastern Africa. As a consequence, an elaborate network of mature normal faults has developed. Within many segments of the East African rift, *en echelon* normal faults joined by relay ramps and complex transfer zones (Fig. 4.22) exemplify the spatially varied distribution of faults and strain that accommodates crustal extension.

Deformation caused by two recent earthquakes helps us visualize aspects of the actual vertical displacements and spatial variations in coseismic strain on active normal faults. The 1983 Borah Peak earthquake illustrates the typical asymmetry of footwall uplift and hangingwall subsidence: the footwall rose about 30 cm, whereas the hangingwall dropped about 130 cm (Fig. 4.23). Following an earthquake such as this, interseismic strain (Stein et al., 1988) and isostatic uplift due to erosion of the footwall block often increase the total bedrock uplift within the footwall. Despite this footwall uplift, the load of sediments that accumulates in and depresses the hangingwall basin guarantees that considerable asymmetry in net displacement usually persists. At Borah Peak, Thousand Springs valley represents a half-graben that has accumulated the sediments eroded from the rising footwall (Fig. 4.23).

In three dimensions, the pattern of uplift and subsidence resulting from multiple surface ruptures during a single earthquake can be complex. As a result of the 1959 Hebgen Lake (M = 7.3) earthquake, maximum

FIGURE 4.22. Schematic fault geometry in the East African Rift system

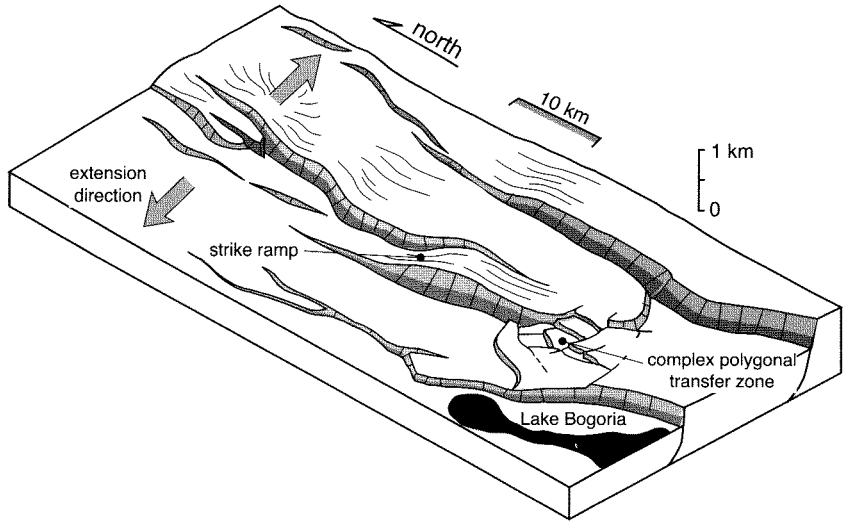

Relay ramps, transfer faults, and smaller scale synthetic faults facilitate transfer for displacement between the major faults. Note that for any cross section perpendicular to the traces of the major faults, the net displacement across the region is nearly equal despite large along-strike differences in displacement on individual faults. Modified after Morley (1989).

subsidence (~7 m) occurred along the middle segment of the Hebgen Lake fault and decreased systematically toward either tip and away from the fault (Fig. 4.24). But, the nearby Red Canyon fault has a highly curved trace, so that in places, contours of subsidence strike at high angles toward one margin of the fault and imply that this margin acted as a transverse structure or hinge along the side of a scooped-shaped zone of subsidence that strikes at right angles to the elongate zone of subsidence along the Hebgen Lake fault (Fig. 4.24). In contrast to the observed displacement on the Hebgen Lake fault and to fault models of decreasing displacement toward the fault tips, displacement on the Red Canyon fault is highly asymmetric and suggests that the western termination of that fault acts as a "free boundary" where it abuts the Hebgen Lake fault (Fig. 4.24).

Thrust Faults

Thrusts faults develop where the maximum compressive stress (σ_1) is horizontal and there is a vertically oriented deviatoric tensile stress (Fig. 4.1B). In theory, thrusts should cut a horizontal land surface at about 30° angles, but in fact, thrusts and reverse faults can cut the surface at any angle and may occasionally be overturned at the surface. In comparison to normal and strike-slip faults, fewer ground ruptures resulting from thrust faults have been studied in detail, so that statistics and geometries of displacement-length relationships are poorly known. Due to the low-angle intersection of thrust faults with the earth's surface, the traces of thrusts are often affected by topography and can be highly sinuous, rendering it more difficult to measure offsets if the direction of fault motion is not well defined. Geodetic measurements of coseismic deformation (Stein et al., 1988) indicate that, during thrusting, hangingwall uplift is typically considerably greater than footwall subsidence (Fig. 4.25). This is the mirror image of the coseismic deformation associated with many normal faults (Fig. 4.23). The area affected by the coseismic deformation depends on the magnitude of displacement, on the geometry of faulting, and on the rigidity of the crust that is being deformed. In the 1952 Kern County earthquake in southern California, deformation extended for about 40 km on either side of the rupture (Fig. 4.25). Although the total vertical offset in this earthquake (~100 cm) was considerably less than in the Borah Peak rupture (~150 cm: Fig. 4.23), the width of the deformed zone was twice as wide, due in large part to the higher crustal rigidity in the vicinity of the Kern County earthquake.

FIGURE 4.23. Normal faulting in the Lost River Range, Idaho

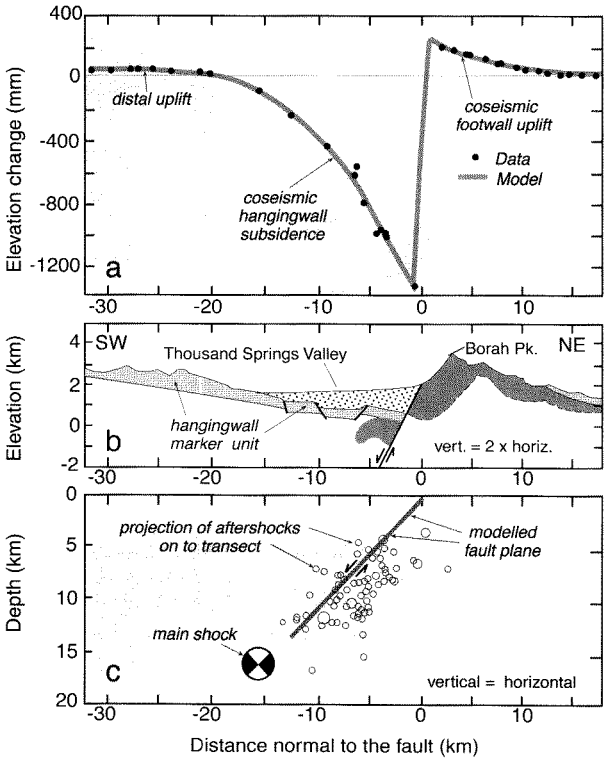

A. Coseismic displacement resulting from the 1983 Borah Peak earthquake. Note the asymmetry of displacement across the fault, such that the hangingwall is downdropped four to five times more than the footwall is uplifted. Note also that the faulting caused deformation of a zone at least 35 km wide. For location of levelling line, see Figure 4.11. B. Schematic geologic cross section through the footwall uplift (Borah Peak) and adjacent hangingwall basin (Thousand Springs valley), which is a half-graben. C. Main 1983 shock and aftershocks define the rupture plane which dips about 45° to the SW. Modified after Stein et al. (1988).

FIGURE 4.24. Ground displacement (in feet) resulting from the 1959 Hebgen Lake (M = 7.3) earthquake in West Yellowstone

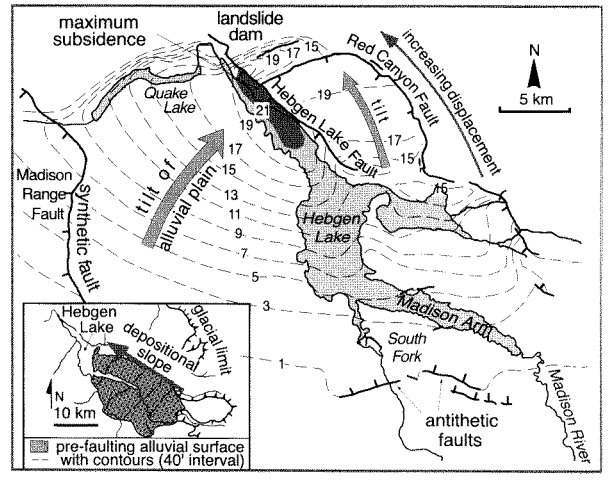

Maximum offsets of about 7 m (>21') occurred adjacent to the Hebgen Lake fault. Note the complex three-dimensional geometry of displacement and the small antithetic faults in the SE. Minor offsets are associated with the Madison Range fault, whereas additional large offsets occurred along the Red Canyon fault. The Madison River was dammed by landslides triggered by this earthquake. Given the sensitivity of rivers to small changes in gradient, it is likely that the fault-induced tilting would cause rivers to migrate toward the zone of maximum subsidence. Modified after Alexander et al. (1994).

Convergent plate margins are capable of producing very large magnitude earthquakes. The interface between overriding and underthrusting plates commonly represents an irregular, earthquake-prone, regionally extensive surface. The 1964 Alaskan (M = 8.3) earthquake along the Aleutian subduction zone south of Anchorage was the largest earthquake to affect North America this century (Wyss and Brune, 1967). Thrusting along the subduction interface caused deformation that affected a zone over 350 km wide and about 800 km long (Fig. 4.26). The hangingwall experienced spectacular uplift (maximum of 8-10 m) across a 200-km-wide zone on the north side of the Aleutian trench, whereas still farther north, the hangingwall subsided up to 2.5 m within a 150-km-wide zone (Fig. 4.26). It may at first seem surprising that the hangingwall, which is sitting above the thrust fault, would experience subsidence, as well as coseismic uplift. Two factors contribute to this pattern. First, thrusting of the hangingwall causes a redistribution of regional loads on the crust. Given an elastic crust with some specific wavelength of flexure, such a thrust load should produce a sinusoidal flexure that is dampened with increasing distance from the load (Turcotte and Schubert, 1982). Second, during the interseismic phase, part of the subduction interface is locked. As a consequence, part of the overlying crust

FIGURE 4.25. Coseismic and geologic displacements associated with thrust faulting

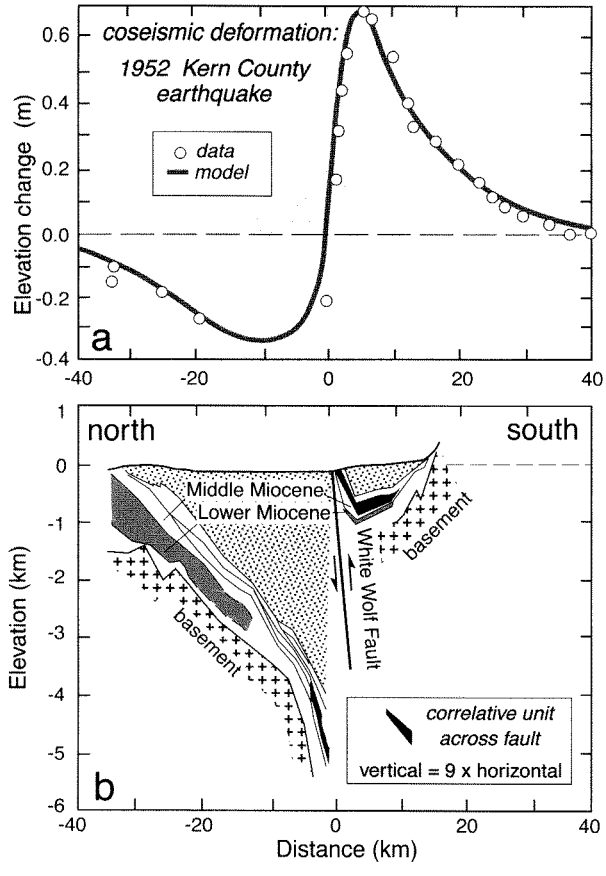

A. Coseismic displacement due to thrust faulting during the 1952 Kern County, California (M = 7.3) earthquake. Note the asymmetry of hangingwall uplift and footwall subsidence. B. Geologic cross section of the footwall basin and hangingwall block of the White Wolf fault which ruptured during the Kern County earthquake. Miocene marker beds are offset about 5 km. Note that the Miocene units do not thicken appreciably as they approach the fault. This indicates that the fault did not become active until Pliocene time. Modified after Stein et al. (1988).

FIGURE 4.26. Displacement due to the 1964 Alaska (M = 8.3) earthquake in the Aleutian subduction zone

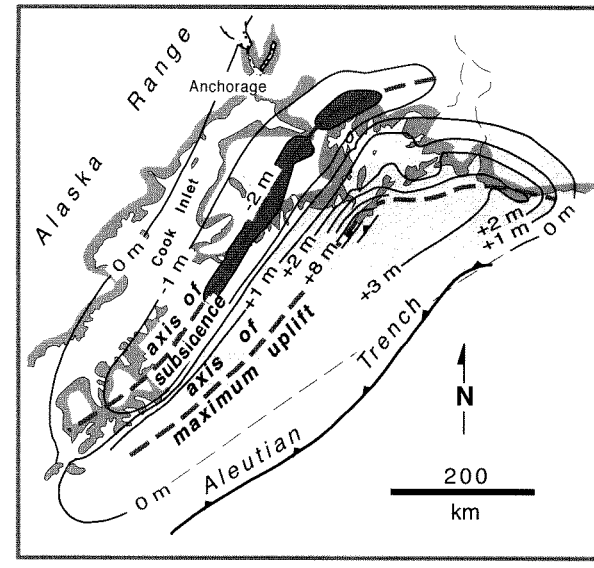

Over 2.4 x 10^5 km^2 were deformed by this earthquake. Strong uplift (up to 10 m) occurred in an elongate zone in the proximal hangingwall, and lesser subsidence (up to 2.5 m) occurred in more distal parts of the hangingwall. Most of the deformation is determined from displaced shorelines. Footwall deformation (outboard of the trench) due to the earthquake remains unknown. Modified after Plafker (1972) and LaJoie (1986).

bulges upward or downward as crustal plates on either side of the locked zone move inexorably toward each other. Much of this elastic strain is recovered by coseismic uplift or subsidence during the subsequent earthquake. In most earthquakes, the more distal, damped flexure is undetected, but in a large earthquake (as in Alaska) where an extensive shoreline can serve as a marker of uplift, the variable flexure leaves a clear signature.

Despite the initial coseismic asymmetry during thrusting which results in accentuated hangingwall uplift compared to the footwall (Fig. 4.25A), erosion of this uplifted hangingwall, deposition in the depressed footwall, and isostatic adjustments to these changing loads and to the coseismic load lead to a geologic structure in which subsidence of the footwall basin is commonly comparable to the bedrock uplift of the hangingwall (Fig. 4.25B). Thus, the preserved geologic structure can be conceptualized as resulting from both coseismic and interseismic deformation (Fig. 4.27). The relative importance of the coseismic versus the interseismic deformation in creating the preserved geologic structure depends on the size of the structure with respect to the strength of the crust and on the efficiency

FIGURE 4.27. Conceptual model of strains in thrust-faulting regimes that produce observed geologic structures

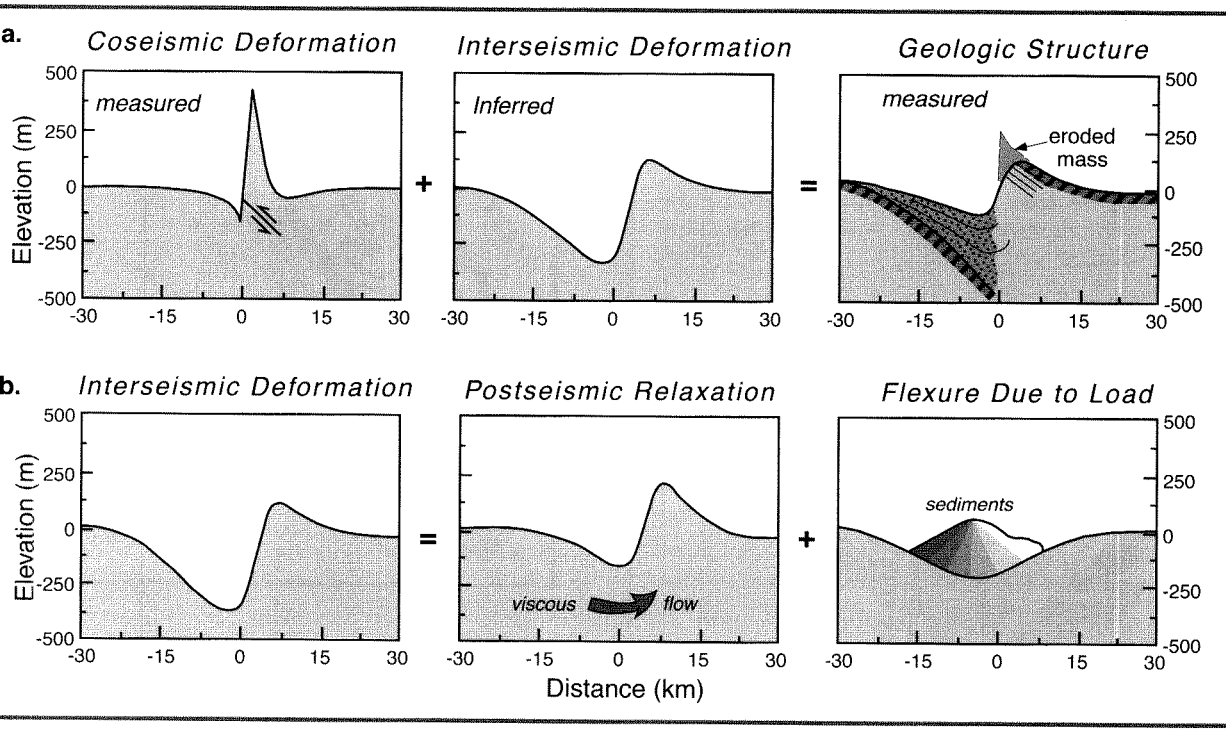

A. The mismatch between the observed coseismic deformation and the geologic structure (which integrates over many earthquake cycles) defines the pattern of interseismic deformation. B. The interseismic strain is suggested to result from viscous flow in the mantle and isostatic responses to sediment loading and erosion. Note carefully the horizontal offsets in the deflections from one panel to the next because these indicate how the distribution of deformation varies for each of the contributing variables. Modified after Stein et al. (1988).

of surface processes at eroding and redistributing the load. If the load is small compared to the crustal rigidity, there will be less isostatic response to the load, and additional footwall subsidence due to sediment loading of the flexural depression will be limited. Conversely, if erosional processes are highly efficient, they will tear down the uplifted hangingwall and cause enhanced sediment loading (and subsidence) on the footwall.

Commonly, the amount of displacement on a thrust fault dies out toward the thrust tip. As a consequence of this decrease in displacement, the hangingwall is typically folded adjacent to the thrust tip. The coseismic displacement during the Kern County earthquake (Fig. 4.25A) displays this folding, and if this pattern of deformation persisted through many successive earthquakes it would generate a hangingwall anticline. Similarly, folding of the hangingwall and extensive surface rupture occurred during the 1980 El Asnam (M = 7.3) earthquake in Algeria (Philip and Meghraoui, 1983). Across the crest of the hangingwall anticline, grabens due to bending-moment faulting (see description in next section) opened in several sites. The obliquity of the shortening vector with respect to the trace of the thrust can be judged by the orientation of these crestal grabens. Where the trend of the normal faults bounding the grabens and the trend of the thrust trace are parallel, shortening occurred approximately perpendicular to the trace of the thrust (Fig. 4.28). On the other hand, where the grabens trend obliquely to the anticlinal crest and to the thrust trace, shortening is inferred to have been oblique to the thrust trace (Fig. 4.29). This obliquity of the shortening vector is also consistent with the orientation of the conjugate shears that develop along the thrust front. In each case,

FIGURE 4.28. El Asnam thrust front and axial crestal grabens in the hanging wall

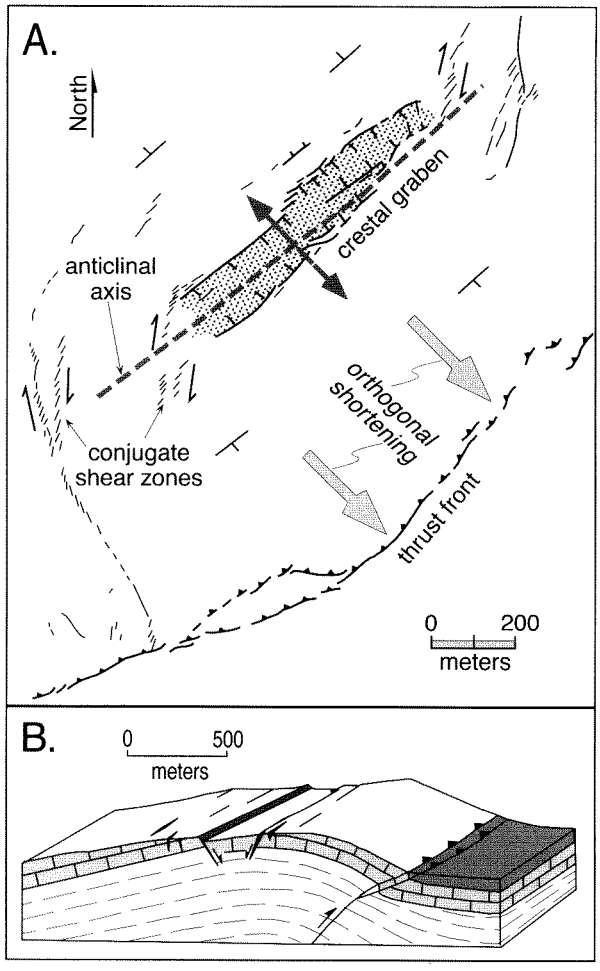

A. Map of surface ruptures resulting from the 1980 El Asnam earthquake. Parallelism of the crestal graben (bending-moment faulting in the hangingwall) and the frontal thrust and the orientation of the shear zones suggest that shortening was perpendicular to the thrust trace. Note that the orientation of the conjugate shear zones is consistent with the local bending-moment, or tensile stresses across the crest of the anticline, rather than with the regional stresses responsible for the thrusting. B. Schematic block diagram showing crestal graben orientation in zone of perpendicular shortening. Modified after Philip and Meghraoui (1983).

FIGURE 4.29. El Asnam thrust front and oblique grabens

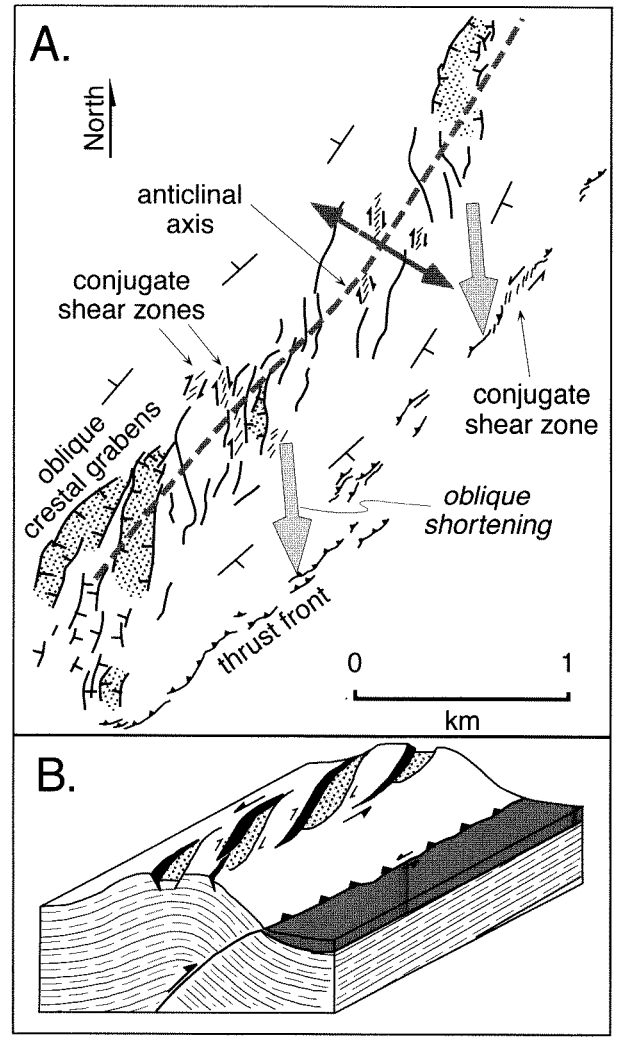

A. Map of surface ruptures in the 1980 El Asnam earthquake, defining *en echelon* crestal grabens and shear zones with respect to the thrust trace. Note the differing orientations of the conjugate shear zones in the map area. In the crestal region, anticlinal flexure creates bending-moment tensile stresses, whereas shearing due to oblique shortening controls orientation of tensile stresses along the thrust front. B. Schematic block diagram depicting oblique graben where shortening is oblique to the thrust trace. Modified after Philip and Meghraoui (1983).

FIGURE 4.30. Schematic view of principal styles of deformation and their inferred relation to the stress patterns for shallow structures in the El Asnam earthquake

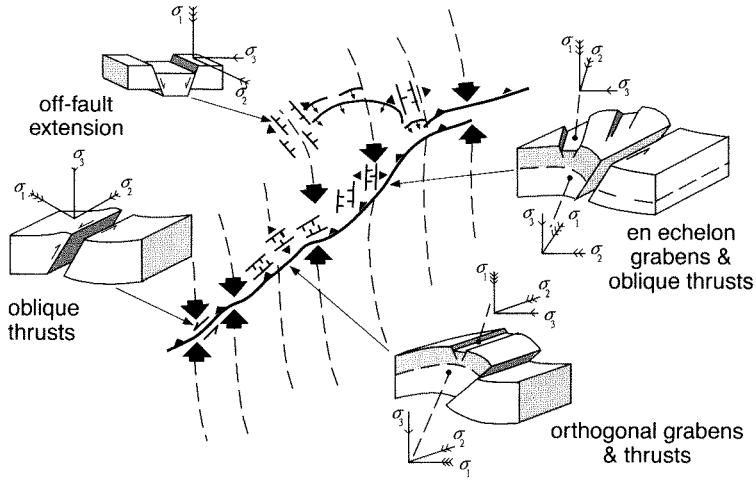

Dashed lines represent the approximate orientation of the regional maximum compressive stress. Local stress variations due to flexing of hangingwall anticlines result in bending-moment crestal grabens. Modified after Philip and Meghraoui (1983).

the locally observed strain can be seen to result from the orientation of the local stress field (in the case of the grabens or conjugate shear zones) or regional stress field (in the case of the thrusts) with respect to the orientation of the fault surfaces (Fig. 4.30).

Flexural-Slip and Bending-Moment Faults

In reality, fault geometries are often far more varied than might be expected with simple models related to regional stress fields (Fig. 4.1). In part, this is due to the inhomogeneities in rocks. They have variable strengths, may be bedded, and may have had a diverse deformational history prior to the current deformation. The orientation of weaknesses within rocks that are subjected to stresses can exert a strong control on how they deform. Anyone who has observed books tilted on a shelf can recognize that tilting of rigid entities (like rock strata) requires slip between the rigid blocks. Thus faulting along bedding planes is common whenever relatively rigid strata are tilted. Similarly, folding of a deck of cards results in relative slip between each of the cards. When strata are folded, if the initial length of each bed is preserved, then *flexural-slip faults* develop along bedding planes to accommodate the differential motion between adjacent beds.

When strata are folded, local stresses are created because the convex side of a folded bed is lengthened, whereas its concave side is shortened. The folding can be considered analogous to bending an elastic plate around a fold axis, such that equal and opposite moments are applied at the ends of the plate. The faults that result from the tensile stresses along the convex regions of the folded plate or from compressive stresses in the concave regions are called *"bending-moment"* faults (Fig. 4.31). Thus, normal faults are expected to form across the convex regions in order to accommodate length changes along these surfaces, whereas thrust faults will form in the concave regions. Anticlinal grabens, such as those seen at El Asnam (Figs. 28 and 29), and out-of-syncline thrusts are examples of bending-moment faulting.

Complex combinations of normal, thrust, bending-moment, and flexural-slip faults are exhibited by ruptures during the El Asnam earthquake (Fig. 4.32) in areas where there was a strong coupling between bedding orientations and fault geometries (Philip and Meghraoui, 1983). Folding of strata caused flexural-slip faulting which is expressed at the surface as a

FIGURE 4.31. Bending-moment faults resulting from flexure of an elastic plate

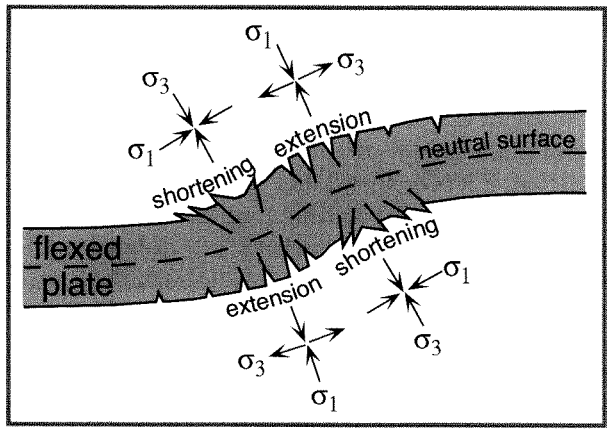

Folding causes stretching along the outer, convex surface of the warped layer, while shortening is induced along the inner, concave surface.

FIGURE 4.32. Complex fault geometries in the El Asnam earthquake

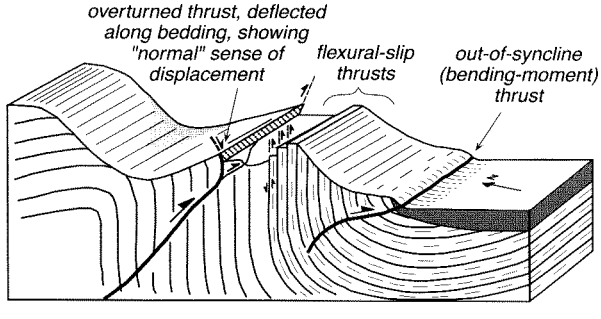

Multiple rupture patterns result from thrust faulting in folded strata. Coseismic slip along bedding planes creates flexural-slip faults and overturning of the thrust plane in places. Footwall folding leads to out-of-syncline thrusting. Modified after Philip and Meghraoui (1983).

succession of high-angle reverse faults. Bending-moment stresses caused out-of-syncline thrusts to develop due to compression along the concave surface of folds. As the main thrust plane ramped toward the surface, it encountered steeply tilted strata and was diverted along weak bedding planes. In places as the fault followed bedding, it passed through a vertical orientation and became overturned. This caused the displaced ground surface along the fault plane to appear analogous to a normal fault, rather than a thrust fault (Fig. 4.31). The diversity of structures associated with the El Asnam earthquake and the contrasts in their orientations clearly emphasize the importance of examining the full spatial array of rupture geometries and investigating the role of underlying bedding during faulting before using coseismic rupture patterns to specify the stress field at the time of the earthquake.

Folds

Relationships of Folds to Faults

Many faults do not rupture the earth's surface. Typically faults nucleate within the brittle crust at depths of several kilometers, and as they accumulate displacement, they commonly propagate toward the surface. Until they actually break the earth's surface, however, they are termed *blind faults*. In basins with a thick sedimentary fill, it is not uncommon for even large earthquakes to fail to rupture the surface. Instead, the highly localized strain that occurs along a fault plane at depth is accommodated by folding within the strata overlying the fault tip. This folding typically is not random, but rather is intimately linked to the underlying fault geometry. Consequently, whenever a fold's geometry and its evolution through time can be documented, much can be learned about the geometry of faulting in the subsurface. This is a particularly important fact in some urban areas, such as Los Angeles and Seattle, where the seismic risk is high, but where many of the faults capable of causing destructive earthquakes are buried beneath Quaternary sediments. Learning to interpret the folds at the surface and to link them to coseismic displacements represents a significant, but worthwhile challenge for tectonic geomorphologists.

The geometry of the faults themselves is commonly influenced by the mechanical properties of the rocks through which they rupture. As might be expected, thrust faults in the subsurface exploit zones of mechanical weakness, and, within sedimentary rocks, they often follow bedding planes. At irregular intervals, they ramp upward from an underlying bedding-plane decollement to an overlying one. In contrast to sedimentary rocks, igneous or metamorphic rocks commonly display more isotropic mechanical properties. Folding of formerly

planar strata in metamorphic rocks distorts mechanically weak layers. As weak and strong layers become more spatially disorganized, they have no consistent orientation with respect to the regional stress directions, and overall the rock becomes more isotropic. Both planar and curving ruptures occur within isotropic bedrock. Kink-like changes in fault angle may occur where rock bodies with contrasting mechanical properties are juxtaposed.

The trajectory of a thrust *fault* within sedimentary rocks is often visualized as following a staircase-like pattern with long *flats* connected by shorter *ramps* along which the thrust steps upward through the stratigraphy. Thrusting of a hangingwall along a fault comprising ramps and flats causes uplift of the hangingwall above the ramps, whereas rocks are commonly translated laterally without uplift above the flats. The geometric consequence of this pattern is that folds will be created above each ramp. Folds also occur above faults that cut through more mechanically isotropic rocks. Deformation above the tip lines of faults and changes in the angle of the fault cause differential uplift at the surface and create folds.

In many cases, deposition occurs synchronously with folding. Newly deposited strata that are associated with the fold are termed *growth strata*, and they often provide the best means of deciphering the history of fold growth. The reason that growth strata are particularly useful is that we know their initial geometry quite reliably: their beds are essentially horizontal at the time of deposition. Consequently, even when we do not know the pre-folding geometry of the bedrock that cores the fold, growth strata provide robust markers that track deformation. When aggradation is more rapid than the rate of uplift of the highest part of the fold, growth strata will cover the entire fold and will faithfully record the dips, limb lengths, and geometry of its upper surface (Burbank and Vergés, 1994: Suppe et al., 1992; Vergés et al., 1996). Under these conditions, there may be no topographic expression of the fold at the earth's surface, but the subsurface record will clearly show changes in the fold shape through time. If the rate of aggradation is less than the crestal uplift rate, then the fold will become emergent, and its uneroded topographic shape will more clearly reflect the geometric controls exerted by displacement along an underlying ramp (Burbank et al., 1996).

Models of Folding

From among the many types of folds that have been described, only a few of the popular models are described here. When rocks in the hangingwall of a thrust fault are carried up and across a buried flat-ramp-flat transition, they are forced to deform into a f*ault-bend fold* (Suppe, 1983) due to the non-planar shape of the thrust surface. Both in front of and behind the ramp, apparently unfolded strata may be present in the hangingwall. But over the ramp itself, a fold will grow. For a given length and angle of footwall ramp and for a thickness of the hangingwall, the geometry of folding can be predicted, if it is assumed that bed length and thickness do not change during folding (Fig. 4.33A). In the fault-bend fold model, *axial surfaces* are defined by kink bends in the deforming hangingwall strata. Between any two adjacent axial surfaces, beds remain parallel that were parallel to each other prior to folding, and these parallel beds define a *dip domain*. Although fault-bend folding due to thrusting is emphasized here, folds obeying similar geometric "rules" have also been modelled for ramps along normal faults.

In a *fault-propagation fold,* a blind thrust creates a new ramp by progressively propagating upward toward the surface (Suppe and Medwedeff, 1990). The thrust never needs to reach the surface, but through time, it accumulates more and more displacement. Folding occurs because there is a gradient in the amount of displacement along the ramp (Fig. 4.33B); at the tip of the thrust, there is no displacement, whereas maximum displacement occurs at the base of the ramp. In both the fault-bend and fault-propagation fold models (Suppe, 1983; Suppe and Medwedeff, 1990), the dip of the forelimb is established during the first increment of folding, and it retains this dip throughout subsequent growth. Note that for both models, the geometry of the growth strata changes with each increment of folding (Suppe et al., 1992) and can become very complex (Fig. 4.33). If smaller scale ramps and flats were incorporated into the overall ramp in either model, more axial surfaces and dip domains would be introduced and would create an increasingly complicated folding geometry.

Commonly, it appears that length and thickness of beds do not remain constant during folding. If the requirement for constant bed length is relaxed and only bed area is preserved, then *displacement-gradient folds* (Wickham, 1995) can be defined (Fig. 4.33C). As in fault-propagation folds, the amount of displacement varies systematically along the ramp. Because bed lengths change, however, the forelimb is allowed to rotate. Even if the thrust tip does not propagate, such folds can continue to amplify by accumulating more displacement along the ramp behind the thrust tip. In the absence of

FIGURE 4.33. Models for folds associated with thrust faults

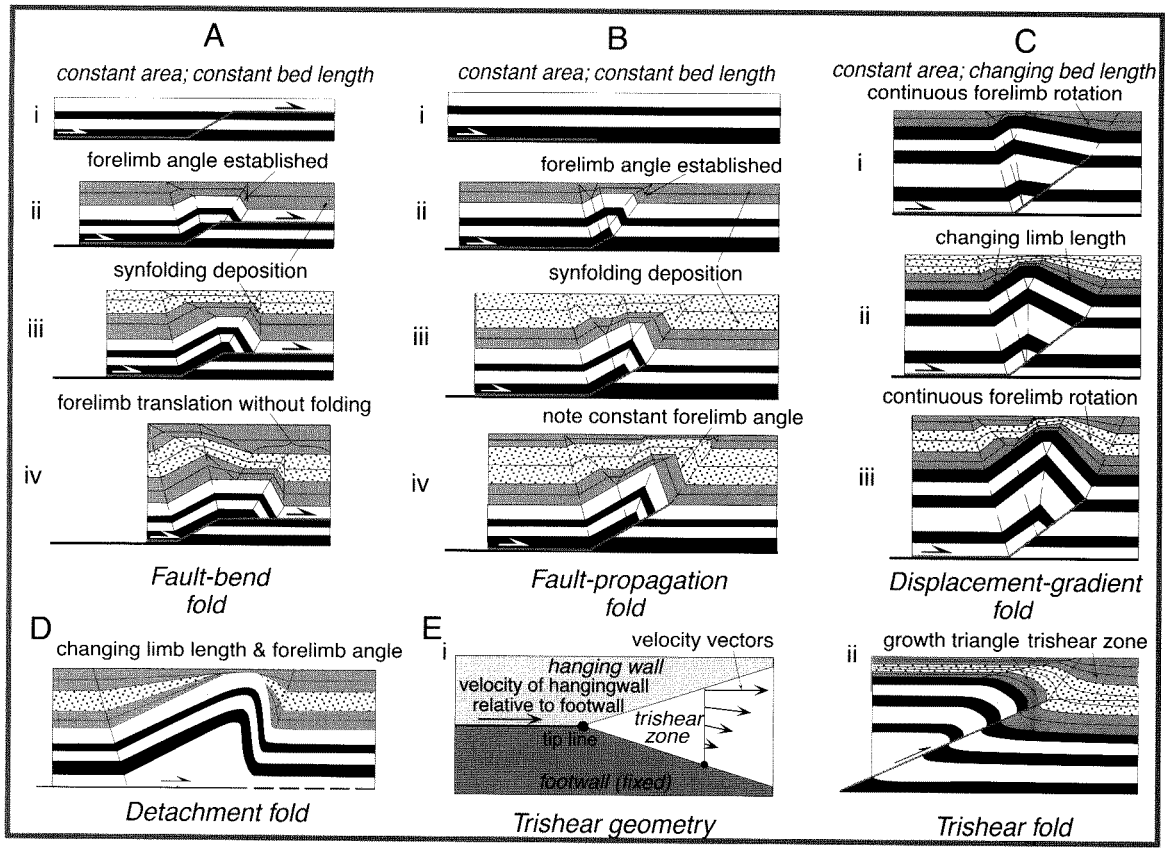

Each fold is shown in a situation where uplift of the anticlinal crest is slower than the rate of sediment accumulation in the unfolded regions off the flanks of the folds. This creates growth strata that record the development of the fold. Note that the final shape of the deformed bedrock can be very similar among these different models, but that the geometry of the growth strata differs markedly among them. Reliable reconstruction of the fold growth is commonly dependent on analyzing the growth strata. A. Fault-bend fold. B. Fault-propagation fold. C. Displacement-gradient fold. D. Detachment fold. E. Trishear fold. (i.) Geometry of the deforming region of a trishear fold showing rotation of slip vectors and change in magnitude from the top of the trishear zone to its base. (ii.) Model of trishear fold and growth strata above a thrust. Modified after Wickham (1995) and Allmendinger (1998).

growth strata, the final geometries of fault-propagation and of displacement-gradient folds may be nearly indistinguishable. Growth strata, however, can reveal whether the forelimb rotated or was fixed and will display distinctive differences both over the crest of the fold and in its forelimb (compare Fig. 4.33B and C).

A *detachment fold* forms by buckling above a fault that is subparallel or parallel to original layering (Fig. 4.33D). No ramp is needed to create such folds: they grow simply because displacement dies out toward a fault tip. At some stage, the fault may propagate upward through the overlying detachment fold, and the resulting final shape may be geometrically similar to a fault-propagation fold. Detachment folds are commonly associated with readily deformed strata, such as evaporites or shales, because such strata provide weak horizons along which the detachment can propagate, and these weak strata flow readily into the cores of growing folds. Limb rotation during folding is commonly observed in detachment folds, whereas dip domains and linear axial surfaces are often difficult to define due to the more continuous curvature of the beds on the flanks

of the fold (Hardy and Poblet, 1994; Poblet et al., 1998; Vergés et al., 1996).

A *trishear* fold (Fig. 4.33E) develops when a single fault at some depth expands outward to form a triangular zone of distributed shear (Allmendinger, 1998; Erslev, 1991; Hardy and Ford, 1997). This triangular zone is symmetrical with respect to the dip of the fault. Within this trishear zone, slip varies systematically in both orientation and magnitude. At its top, slip vectors match the slip of the hangingwall and are parallel and equal to that of the master fault. At the base of the trishear zone, the slip decreases to zero. In between these two boundaries of the trishear zone, the slip vectors systematically decrease in magnitude and rotate away from the hangingwall slip direction toward parallelism with the lower (no-slip) boundary of the trishear zone. The shearing which results from differential slip causes both bed thickness and forelimb dips to change as the fold grows. The ratio between the rate at which the tip line of the fault propagates and the amount of slip on the fault itself controls the geometry of the forelimb. Low values of propagation-to-slip cause the forelimb to thicken and create tight folding in the trishear zone. Conversely, high values of propagation-to-slip cause less thickening and more open folding (Allmendinger, 1998).

As originally described, both fault-bend and fault-propagation folding were characterized by axial surfaces which create kink bends in the hangingwall and which abruptly divide the hangingwall into contrasting dip domains. In the real world, it is quite common to observe these dip domains or "panels" of folded strata all displaying similar dips. The transition from one dip domain to the next, however, is often not abrupt (a kink bend), but occurs gradually through a change in curvature. In recognition of this curvature, fault-bend and propagation fold models have been modified to incorporate the possibility of rounded hinges (Suppe et al., 1997), rather than relying exclusively on kink bands. Bedding dips in the forelimbs of trishear folds tend to change continuously, rather than abruptly. Therefore, kink bands and dip domains do not commonly occur in such folds. These differences in the geometry of growth strata help to discriminate among different fold models.

Lateral Fold Growth of Folds as Three-Dimensional Features

Because faults grow by extending sideways, as well as forward, fault growth in the subsurface will cause the lateral growth of folds at the surface (Fig. 4.34). Consider the case of a single blind thrust fault. Folding at the surface will wane above either end of the buried rupture. The consequence of this is to generate folds with doubly plunging terminations. Variations in displacement along the underlying thrust should also be reflected by the amplitude of folding at the surface. Thus, the structural crest of the fold should vary in height, and the fold axis should plunge toward zones where there is less displacement on the underlying fault. As illustrated previously (Fig. 4.10), individual faults may simply lengthen, or they may link together with adjacent faults. In the latter case, if the linked structures are blind thrust faults, variations in displacement along them will create multiple plunging folds at the surface with structural saddles marking the zones of linkage.

Why should one care about the shape of a growing fold or various folding models? Folds are a fundamental component of many orogenic settings. Folding is ubiquitous above blind thrusts, as well as almost any thrust fault that ruptures the surface. When trying to reconstruct the strain that has occurred in a given region, there has been a tendency in the past to focus almost exclusively on the displacement along faults. Although more subtle offsets may occur in folds, the deformation represented by them can constitute an important fraction of the total strain. Much of the

FIGURE 4.34. Lateral propagation of blind thrust faults and surface folds

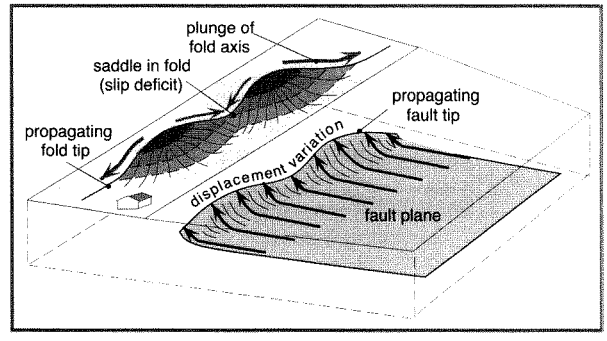

Displacement variations in the subsurface fault is directly related to the magnitude of rock uplift at the surface. The noses of plunging fold occur above fault tips, and structural saddles mark zones of fault linkage or slip deficits.

landscape that is preserved today in active fold-and-thrust belts results from the initiation and amplification of growing folds (Fig. 4.35). The shape of those folds determines the pristine geometry of the land surface. In such cases, the dip of the forelimb and backlimb determines the surface slope and the position of the drainage divide. The shape of the fold can, therefore, strongly influence both the nature and efficiency of surface processes which erode and redistribute mass. If we want to understand the modern landscape as a product of the long-lived interactions of surface processes with deforming structures, we need to know how those structures evolved through time.

Geomorphology provides one key to this understanding. In cross section, most folds have a steeper forelimb than backlimb (Fig. 4.33). Even when the uplifted surfaces have been dissected by erosion, contrasts in the dip of the limbs of the folds are commonly discernible in the modern topography and indicate the "facing direction" or orientation of the underlying blind thrust. For example, stream lengths are often asymmetrical across a fold. Shorter, steeper streams occur on the forelimb, causing the drainage divide to be displaced toward the forelimb. Information about how folds have grown laterally can also be revealed by stream patterns. As a plunging fold begins to grow laterally, rivers that flow across the axis of the fold must either incise into the uplifted area or be deflected out of their present courses and around the nose of fold. Initially, rivers usually tend to maintain their course across a fold. To do so, they need sufficient stream power to erode enough of the newly uplifted material so that they can maintain a downstream gradient across the fold axis (Burbank et al., 1996). Through the process of erosion, they create *water gaps* across the fold axis (Fig. 4.35). If at some time, the rate of lowering of the stream bed by erosion is insufficient to keep pace with the rate of structural uplift of the fold, then the stream will be "defeated," a *wind gap* will develop along the abandoned river course, and the river will flow subparallel to the limb of the fold until it finds a low point where it can traverse the fold (Fig. 4.35). The pattern of rivers adjacent to folds and the presence of wind and water gaps can be interpreted to indicate the direction of propagation of a fold (Jackson et al., 1996). If the time of abandonment of the wind gaps is known, or the age of the uplifted surfaces along the fold's flanks, then the rate of propagation can also be defined (Medwedeff, 1992).

FIGURE 4.35. Wheeler Ridge, a plunging fold in California

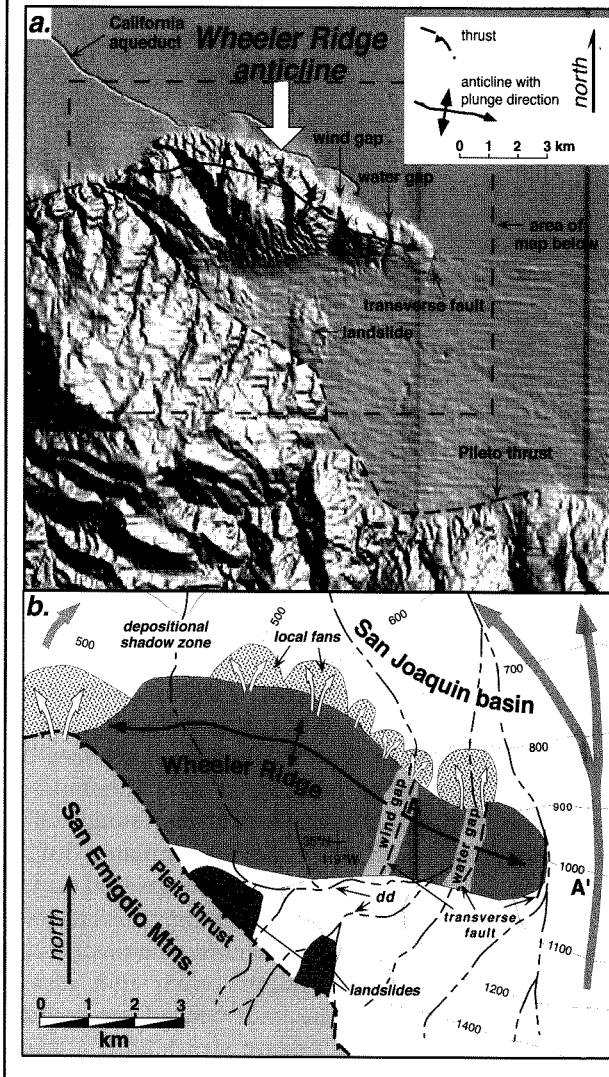

Top: Shaded 30-m DEM of Wheeler Ridge fold and Plieto thrust fault system in the southern San Joaquin Valley, California. Wheeler Ridge anticline plunges and propagates to the east. Dissection is more intense on the more steeply dipping forelimb of this asymmetric anticline. Bottom: Map of geomorphology around Wheeler Ridge. Stream patterns indicate deflection of streams toward the east by the growing fold. Antecedent streams persist in water gaps, but these appear localized by transverse faults. dd: deflected drainage. Modified after Burbank et al. (1996).

It is becoming apparent in many areas that blind thrusts pose major seismic hazards for urban areas. Most of the recent destructive earthquakes in the Los Angeles basin, for example, occurred along blind thrusts. Even when enlightened city planners have prohibited building adjacent to known faults, the failure to recognize the potential for strong vertical accelerations due to faulting along buried structures has led to inadequate building standards and huge loss of property and lives during recent earthquakes. To the extent that the geometry of folds can be used to infer the shape of underlying faults and to the extent that unravelling the history of folding provides insight into rates of deformation, analysis of folds can provide fundamental constraints on tectonic rates, patterns of past and probable future deformation, and seismic hazards.

Summary

A diverse array of faults and folds has formed at the earth's surface in response to variations in stress fields, inhomogeneities in rocks, contrasts in crustal strength, and interactions among multiple structures. It seems clear that the build-up of stresses across and along rupture surfaces causes earthquakes. Unfortunately, direct measurements of stress are difficult to make, and understanding of changes in the distribution of stresses before, during, and after faulting is still incomplete. Nonetheless, earthquakes can be usefully thought of as part of a cycle in which strain that accumulated during interseismic intervals is fully or partly recovered during rupture events. Contrasting models for controls on stress release propose that 1) faulting occurs whenever a certain stress threshold is attained, such that strong patches, or asperities, on the fault control the rupture pattern; or 2) earthquakes release stress until a minimum threshold stress is achieved, in which case barriers, or patches of the fault plane that remain unruptured, may control the pattern of faulting. It is not clear whether either model adequately describes the behavior of many faults.

It has been proposed that some faults are typified by characteristic earthquakes, which is to say that they display a similar rupture length, magnitude of displacement, and distribution of offset along the rupture in successive earthquakes. Rupture patterns along such faults could be controlled by long-lived asperities. If characteristic earthquakes exist, knowledge of their displacement history provides strong predictive capabilities. Given the societal importance of earthquake prediction, we need to improve our understanding of recurrence intervals, fault strength, characteristic behavior of faults, and controls on fault displacement and timing. Through field observations, patterns of displacements along faults and styles of fault growth are becoming better known.

In a given structural and lithologic setting, there is often a predictable relationship between the maximum amount of displacement on a fault and its length. This ratio, however, varies by several orders of magnitude between different settings. Along a single fault, displacements typically describe an arcuate pattern with large displacement gradients near the fault tips and small gradients along the mid-section of the fault. As faults accumulate more displacement, they also lengthen. If faults extend toward each other, they sometimes appear to link into a single amalgamated fault. Even prior to this, the cumulative displacement along a fault zone may display an arcuate pattern, suggesting that, although it comprises numerous individual faults, the entire zone is deforming similarly to a single fault. Despite evidence for fault lengthening and linking between adjacent faults, some range fronts are characterized by segmented faults that appear to have existed far longer than would be required for them to amalgamate into a single fault. If boundaries between fault segments do persist through time, this implies that these faults accumulate displacement without lengthening: a behavior that is incompatible with models for systematic lateral extension of fault tips.

Our ability to refine and choose among the contrasting models for controls on earthquake cycles, accumulation of displacement, characteristic earthquakes, and fault-zone segmentation depends on developing more complete data for both past offsets and present rupture patterns. Part of these data will come from studies of the tectonic geomorphology of fault zones. Predictable patterns of fault rupture and geomorphic expressions of faulting are associated with strike-slip, normal, and thrust faults and can be interpreted in terms of imposed stresses. Nature, however, is complicated, and in nearly every "compressional" or "extensional" setting, an overlapping array of growing folds and active normal, thrust, and strike-slip faults will be found. It is the job of the field geologist to sort out the relationships of these structures to local stress fields and to define how these stresses interact with inhomogeneities in the underlying rocks to produce the observed deformation.

Geomorphological studies can successfully document deformation following faulting when surface features have been offset. But what about folding of the surface during faulting or far-field deformation? These are often undetectable in geomorphologic studies. Similarly, the build-up of strain prior to faulting and the proportion of recovery of interseismic strain during faulting usually can not be resolved through examination solely of coseismic displacements. Instead, precise surveying techniques are required to define both near-field and far-field deformation prior to, during, and after earthquakes. Such geodetic measurements are the subject of the following chapter.

CHAPTER 5

Short-Term Deformation: Geodesy

Due to plate motions and gravity, the surface of the earth is in constant movement at a regional scale. Deformation of the earth's surface as a consequence of faulting and folding results from differential motion of adjacent parts of the crust. If contrasting velocity vectors can be resolved for neighboring regions, then the amount of deformation that must be accommodated by the intervening region can be determined. Consequently, delineation of the regional pattern of crustal motion and the recognition of differences from one area to the next serve to pinpoint where and how much tectonic deformation should be occurring. A few decades ago, for example, transform plate boundaries were conceived of as narrow, elongate zones of focused deformation bounded by rigid plates. With this as a model, a major strike-slip fault like the San Andreas fault was defined as the boundary between the North American and Pacific plates. Today, geodetic measurements clearly indicate that this boundary is instead a diffuse zone of deformation more than 500 km wide (Minster and Jordan, 1987; Molnar and Gipson, 1994; Ward, 1990) and that the San Andreas fault is only one among many faults that accommodate the relative motion between these plates.

Whereas regional patterns of relative and absolute crustal velocity indicate where strain should occur and may suggest the likely orientation of local stress fields, local measurements of deformation due to folding and faulting serve to characterize the style and magnitude of the displacements which accommodate differential crustal velocities. Such information reveals how the land surface deforms due to individual seismic events, it provides data on the variability of displacement along the length of any surveyed structure, and it illustrates how the earth's surface deforms between major earthquakes (interseismic deformation) or in the absence of significant seismicity (aseismic creep). Careful measurements of local deformation, therefore, provide insights into specific crustal responses, such as the wavelength, amplitude, and orientation of folding, to imposed stresses.

Geodesy, as used in geological studies, is the measurement of the exact position of geographic points. Typically, repeated surveys are made of the same locations, for example, before and after an earthquake, or of specific sites in the interior of two contiguous plates. In order to obtain the most reliable geodetic history of deformation, records with many measurements are preferable. The duration of such surveys is limited by the interval over which appropriate instrumentation has been available and the date when initial baseline measurements were made. By comparing the geodetically determined positions of various sites through time, both the magnitude of spatial changes and the rate at which they are occurring can be calculated. The spatial scales (Fig. 5.1A) across which geodetic measurements are collected vary from a few meters, for example, during calibrations of motion across a specific segment of an individual fault, to thousands of kilometers, such as when the relative motions of lithospheric plates are calculated (Dixon, 1991; Minster et al., 1990). Clearly, different geodetic tools are appropriate for obtaining these highly varied scales of measurements (Fig. 5.1A). The choice of tool and approach depends on both the scale of the problem and the precision and accuracy required. Based on global positioning systems (GPS) and very long baseline interferometry (VLBI), plate velocities can be calculated to plus or minus 1–2 mm/yr. This level of precision is unwarranted and is perhaps misleading when describing offsets of geomorphic features that have been

FIGURE 5.1. Spatial and temporal scales of geological processes and of various geodetic techniques

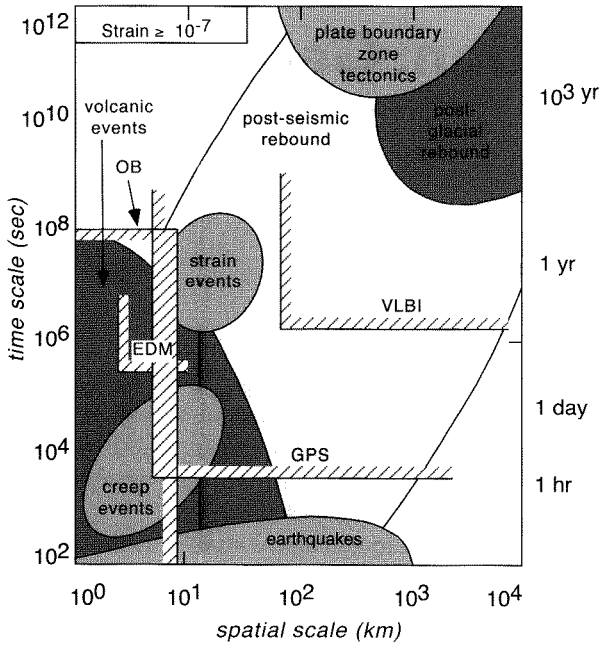

Shaded ellipses depict typical ranges for classes of processes. Hachured boundaries indicate the present range of various techniques for making geodetic measurements. Minimum strain at all spacial scales is greater than 10^{-7}. EDM: electronic distance meter; GPS: global positioning system; OB: observation; VLBI: very long baseline interferometry. Modified after Minster et al. (1990).

displaced due to faulting. Because geomorphic surfaces typically have natural irregularities at scales of greater than or equal to 1–2 centimeters, measuring and reporting offsets with a resolution of 1–2 mm suggests a precision that simply does not exist.

In this chapter, various geodetic approaches are described, and examples of their applications are used to illustrate the types of positional information that can be obtained with these methods. *Near-field* techniques are those used to examine deformation on the scale of meters to a few tens of kilometers, whereas *far-field* techniques examine regional to global deformation fields. Simpler, traditional techniques of surveying are often appropriate for near-field observations and are described here first. Many far-field measurements require more complex, recently developed approaches and are described in the second half of the chapter. Several techniques, such as those using the global positioning system, are used in both near- and far-field applications.

Near-Field Techniques

Styles of Deformation

The geometry of displacement that occurs along a fault zone is strongly dependent on the strength of the crustal material both within the fault zone and on either side of it. Consider the situation in which the fault zone is very weak and is surrounded by strong rocks. Here, it is likely that nearly all of the displacement would be localized on the fault zone itself and that the adjacent regions would be relatively undeformed (Fig. 5.2). Alternatively, if the fault zone is relatively strong, then strain will tend to be distributed across the terrain bounding the fault, and there may be no strong change in the displacement gradient as the fault is crossed. Simple models of patterns of displacement (Fig. 5.3) clearly illustrate the influence of rock strength or rigidity. For example, when rocks bounding a fault have equivalent rigidities, a symmetrical pattern of strain occurs across the fault. As the rigidity of one side becomes increasingly high with respect to the other, less and less strain will occur within the more rigid block, and more will be focused along the fault zone and within the weaker block (Fig. 5.3). Thus, the asymmetry of displacement across a fault can be used to judge the relative rigidities of the blocks on either side, whereas the relative proportion of the total displacement which is accommodated along the fault itself reflects its strength with respect to adjacent blocks. Faults that are continuously creeping will lead to lesser amounts of stored elastic energy in the adjacent blocks, whereas large earthquakes will be more likely to occur along faults which are "locked" and are relatively strong.

Alignment Arrays

Horizontal motions along strike-slip faults can sometimes be measured with alignment arrays. These can consist of simple lines of nails that are hammered into the ground along a linear trend, typically less than 100 m long, that is oriented perpendicular to the trace of the fault. Because the initial orientation of the nails is well

FIGURE 5.2. Conceptual models for deformation associated with strike-slip faulting

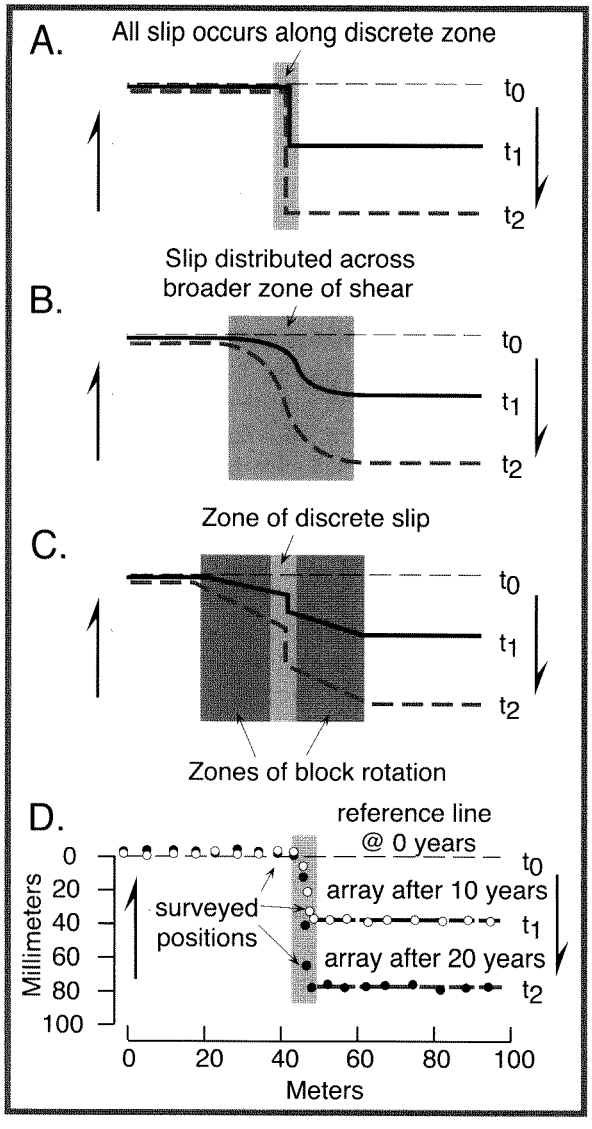

Displacement at three intervals, beginning with t_0 is illustrated. A. Fault zone is very weak and is creeping so that all motion occurs directly along fault. B. Fault zone is relatively strong and strain is distributed across broad zone on either side of the fault. C. Some creep occurs on the fault, and rigid block rotations occur on either side of the fault, taking up the additional motion. D. Schematic results from an alignment array along a creeping fault that is displaced about 80 mm in twenty years. Modified after Sylvester (1986).

FIGURE 5.3. Velocity as a function of distance from a fault in which two fault blocks and the fault zone all have different rigidities

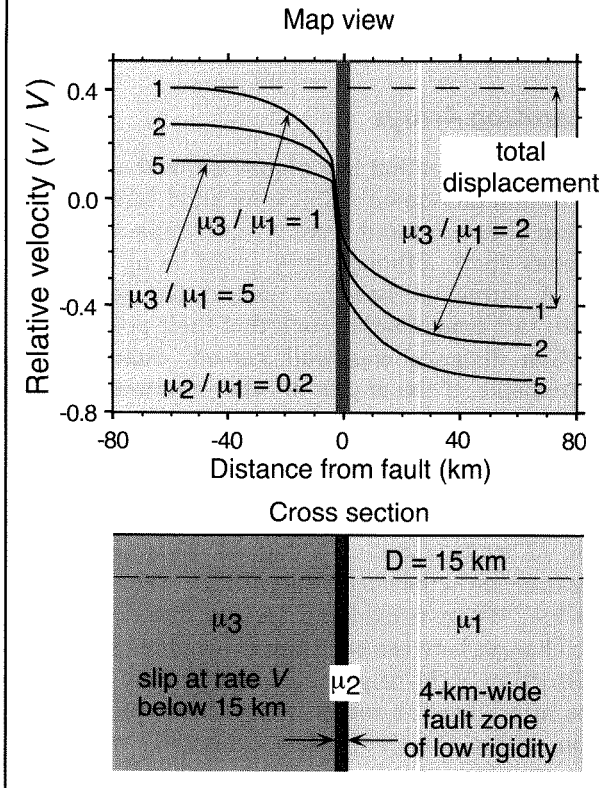

V is the rate of relative motion between the two blocks, and v/V is the fraction of the total motion that is exhibited by any point. The rigidity of the fault (μ_2) is one-fifth that of the right-hand block (μ_1). The rigidity of the left-hand block (μ_3) is equal to, twice as great, and five times as great as the right-hand block for lines labeled 1, 2, and 5, respectively. Note that in all cases, most of the displacement occurs along the weak fault zone. Note how the relative rigidity of the blocks affects the shape of the displacement within each block. For the highest rigidity (line 5, left-hand block), there is very little deformation within the rigid block. Modified after Lisowski et al. (1991).

known, any subsequent displacement along the linear trend can be readily detected. Alignment arrays can reveal whether aseismic segments of a fault are creeping or whether they are locked. If they are creeping, alignment arrays can indicate whether there is a discrete offset along the trace of the fault, and can document the breadth of the region within which significant shear is

occurring (Fig. 5.2D). Sometimes man-made structures provide linear features that are serendipitously arranged across a fault. The offsets of fence lines, foundations, curbs, pipelines, railroad tracks, painted lines on highways, and even tire tracks can provide useful indicators of both seismic and aseismic displacement.

Trilateration Arrays

Traditional trilateration techniques utilized an array of triangulation monuments that were sited across a fault or region of interest and were typically spaced several kilometers apart, although they could be up to 50 km apart. A surveyed baseline would be determined between two benchmarks, such that their position and separation distance was well known. Subsequently, measurements of the angles to other monuments from both benchmarks served to define the positions of these other points. These triangulation angles were measured with theodolites, which typically permit angular measurements with an accuracy of less than or equal to 1 second of arc (<1/3600 of a degree). This uncertainty results in errors in the length calculations of about 3–6 cm in 10 km. When considered in two dimensions, the length changes between each pair of benchmarks defines the distortion of the original geometry of the array and can be interpreted to result from differential tectonic motion within the array. Most commonly today, distances within a fairly complex regional array are measured with some sort of laser-ranging electronic distance meter (EDM) which has a precision of about 1 ppm. The laser beam is refracted as a function of the temperature of the air through which it passes. Consequently, measured distances also depend on air temperature, which of course varies throughout the course of a survey. The resultant uncertainties dictate that, when several trilateration points are surveyed from any single site at any given time, the ratios of one distance to another are more accurate than the distances themselves.

Most trilateration surveys are used to investigate horizontal, rather than vertical, fault movements. Survey results can be used to assess both regional patterns of differential motion, as well as the magnitude and nature of slow, aseismic displacements on individual faults. As with alignment arrays, abrupt changes in displacements across an aseismic fault suggest that the fault is creeping (Fig. 5.2), whereas if there is a smooth, undisrupted trend in the amount of displacement as a fault is approached or crossed, the data suggest that considerable elastic energy is being stored in the volume of rock adjacent to the fault. In the context of large regional strains, identification of zones across which strain is most rapidly occurring, and the differentiation between creeping and non-creeping faults using trilateration surveys can play an important role in defining those faults with the potential for destructive earthquakes.

When there is a sufficiently dense array of surveyed benchmarks, distinctive contrasts in the style and magnitude of displacements at the regional scale can be delineated. With strike-slip faults, it is usually instructive to examine changes in the velocity field along transects oriented perpendicular to major faults and to the orientation of the regional strain field. Often, due to the limited number of surveyed benchmarks, however, there are only a few data points along any single transect. In this situation, the data are most readily interpretable when the velocity data from many sites are projected on to a single plane perpendicular to the strain field. EDM surveys along the San Andreas fault in California (Figs. 5.4 and 5.5) clearly depict the contrast between locked and creeping segments of the San Andreas and adjacent faults (Lisowski et al., 1991). Throughout this zone, the relative velocity of the North American versus the Pacific plate is about 50 mm/yr. A trilateration array east of Monterey Bay depicts sharp offsets in the velocity field across the San Andreas and Calaveras faults, whereas there is little differential movement for 20–30 km on either side of these faults (Fig. 5.4A and B). Of the nearly 40 mm/yr of offset parallel to the San Andreas fault that is recorded in this region, more than 75 percent of the offset is accommodated by creep along and immediately adjacent to the San Andreas and Calaveras faults. In contrast, in the central Transverse Ranges of southern California (Fig. 5.5), <25 mm/yr of the differential crustal motion parallel to the San Andreas is recorded along a 90-km-wide swath centered on the San Andreas fault. Moreover, there is no evidence for creep (in terms of rapid spatial changes in the displacement gradient) as the San Andreas is crossed. Given the absence of other major strike-slip faults in this transect and the considerable strain that is occurring across the fault, these data from the Transverse Ranges suggest that there is a potential for a major earthquake along this locked segment of the fault in the future. A weak fault zone is apparent in the Monterey array (Fig. 5.4), where most of the North American-Pacific plate motion is accommodated in a narrow swath that is 10–15 km wide. In fact, in that swath, 90 percent of the strain

FIGURE 5.4. Monterey trilateration array

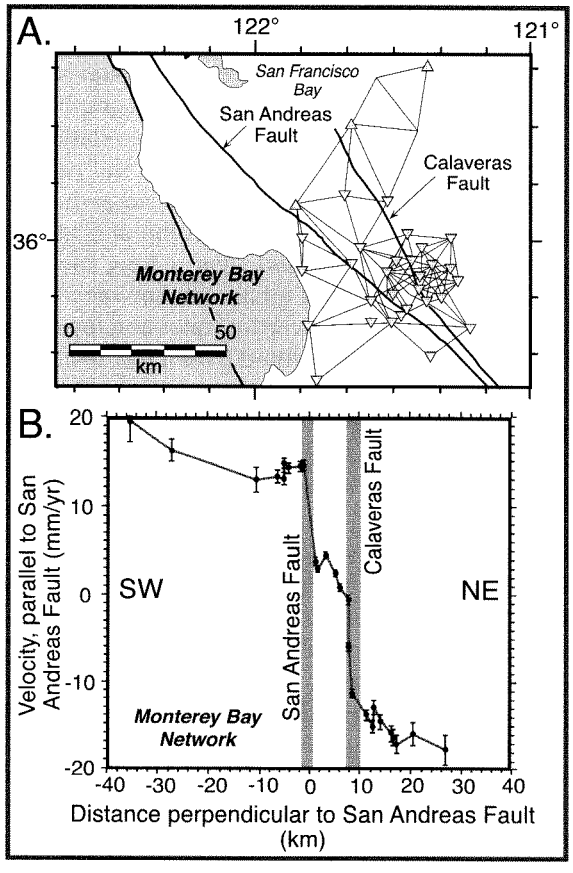

A. Monterey geodetic network showing triangulation stations in the vicinity of the San Andreas and Calaveras faults. B. Results of trilateration surveys between 1973 and 1989 across the San Andreas fault zone near Monterey Bay. Data (projected on to a traverse oriented perpendicular to the trend of the San Andreas) define the component of movement parallel to it. Long-term slip rates across the San Andreas region are about 35 mm/yr in this area. About 15 mm/yr of North America-Pacific relative plate motion is accommodated on other faults beyond the surveyed area. The San Andreas and the Calaveras faults are clearly marked by abrupt changes in relative velocity. These discontinuities show that most of the relative motion across this 80-km-wide zone is accommodated by slip on these two faults. Little deformation occurs in the bounding blocks. Over a span of sixteen years, the total motion across the profile averages about 35 mm/yr, indicating that most of the expected plate motion is accounted for by the measured velocities. Modified after Lisowski et al. (1991).

FIGURE 5.5. Transverse Ranges trilateration array

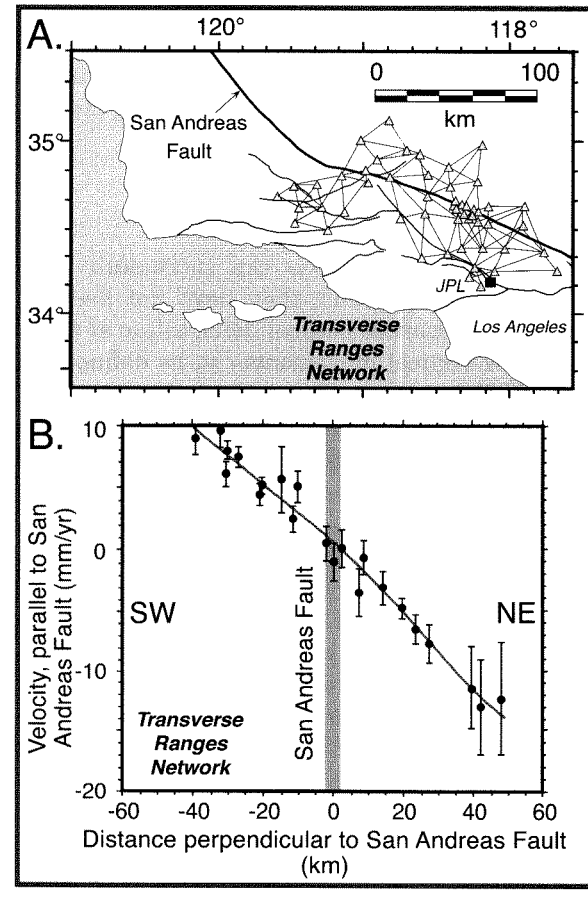

A. Triangulation network in the vicinity of the Transverse Ranges of southern California. B. The Transverse Range data (1973–1989) shows no differential displacement across the San Andreas fault, which can be interpreted as being locked in this region. Instead, strain is occurring across the entire surveyed zone. There is a suggestion of flattening at the ends of profiles that could be interpreted as representing the expected sigmoidal shape of a deformation profile across a locked fault (see Figure 5.2). Note that less than 25 mm/yr of relative plate motion is accommodated by displacements along the profile. This indicates that considerable strain due to Pacific–North American relative plate motion occurs well beyond the San Andreas fault zone. Modified after Lisowski et al. (1991).

occurs on two highly localized fault zones (San Andreas and Calaveras faults). In contrast, the broad regional strain pattern in the Transverse Ranges (Fig. 5.5) emphasizes the potential for stored elastic energy within this array, whereas the fact that less than 50 percent of the relative plate motion occurs within the array itself indicates that considerable plate motion must occur along faults and folds beyond the surveyed area.

Precise Leveling

Although trilateration arrays can successfully depict horizontal velocity fields, they have not been used extensively to examine vertical deformation at regional scales. Slow vertical movements can be defined using precise leveling surveys. The conceptual basis is similar to that for a trilateration survey. Established benchmarks and newly defined sites are re-surveyed over the course of several years to decades in order to define the magnitude and rate of deformation in the intervening period. Because the absolute height of a benchmark is often poorly known with respect to the global reference frame, relative heights are used to calculate rates of vertical change in most leveling surveys. Naturally, the largest deformation signal will usually be recorded with the longest measurement interval. Thus, precise surveys of railway lines across the Alps in the first half of the century provide a baseline against which more recent deformation can be calculated. On the other hand, the precision and accuracy of measurement techniques typically improve over time. Thus, there is a tradeoff between the range of time spanned by a survey and the evolution of our instrumentation. Greater uncertainties commonly result from reliance on less accurate, older surveys. But, because the total signal is larger for longer intervals of measurement, these older surveys can sometimes provide excellent deformation histories, despite the imprecision of individual measurements.

As with any survey, the precision and accuracy of the measurements need to be evaluated. Slope-dependent errors can be assessed by plotting the tilt (the spatial derivative of the height changes) versus surface slope (the spatial derivative of the topography) (Jackson et al., 1992). Because leveling lines typically comprise an extensive succession of surveyed sites, errors associated with each measurement accumulate and propagate through the entire survey (Fig. 5.6). With long survey lines, it is not uncommon for the accumulated uncertainty due to the imprecision of measurements to be considerably larger than the measured differential uplift. In such cases, it is sometimes possible to consider smaller subsets of the data by dividing the survey into segments. Within these segments, the uncertainty is smaller with respect to the signal, and differential uplift or subsidence can be more reliably determined.

It is often instructive to compare the spatial variation in vertical uplift rate with the mean topography along the transect in order to examine possible relationships between them (Fig. 5.6). For example, if the pattern of vertical uplift mimics the topography, it suggests that the present landscape could result from the persistence of the present deformation field over a long interval of time. On the other hand, a mismatch between the spatial variation in short-term vertical rates and topography may indicate that rates defined over a few decades are not representative of the long-term pattern of deformation. Because the interval between large earthquakes is often long, most surveys span part of the interseismic period and do not include coseismic deformation. During the interseismic interval, elastic and sometimes permanent strain slowly accumulates. This strain is commonly measured through repeated surveys, whereas deformation during an earthquake may rapidly release the elastic energy and produce deformation in the opposite sense. For example, during the Prince William Sound earthquake in Alaska in 1964, the eastern part of the Kenai Peninsula underwent about 2 m of coseismic subsidence. Recent geodetic surveys 30 years after the earthquake (Cohen et al., 1995) indicate that nearly 1 m of uplift has occurred since 1964. This uplift has been interpreted as a response to interseismic strain accumulation, but it may in fact represent permanent strain resulting from migrating deformation along the subduction-zone interface.

A mismatch between the topography and the uplift pattern along a leveling line may indicate that surface processes successfully re-shape and modify any pristine topography. Under these circumstances, a differential vertical deformation field could be well recorded by an underlying geologic structure, such as a fold, but the fold itself may be uplifting strata that are readily eroded as soon as they are raised above base level. This appears to be the case in the Himalayan foreland of Nepal (Jackson and Bilham, 1994b), where active folding is displayed by shallow structures and by the surveyed uplift rates associated with the Main Siwalik thrust (MST: Fig. 5.6A), but the deformation is not reflected in the topography (Lavé and Avouac, 2000). This is not very surprising here, because the fluvial strata of the Himalayan foreland often appear to be eroded nearly as rapidly as

FIGURE 5.6. Comparison of large-scale structure and topography with uplift velocities

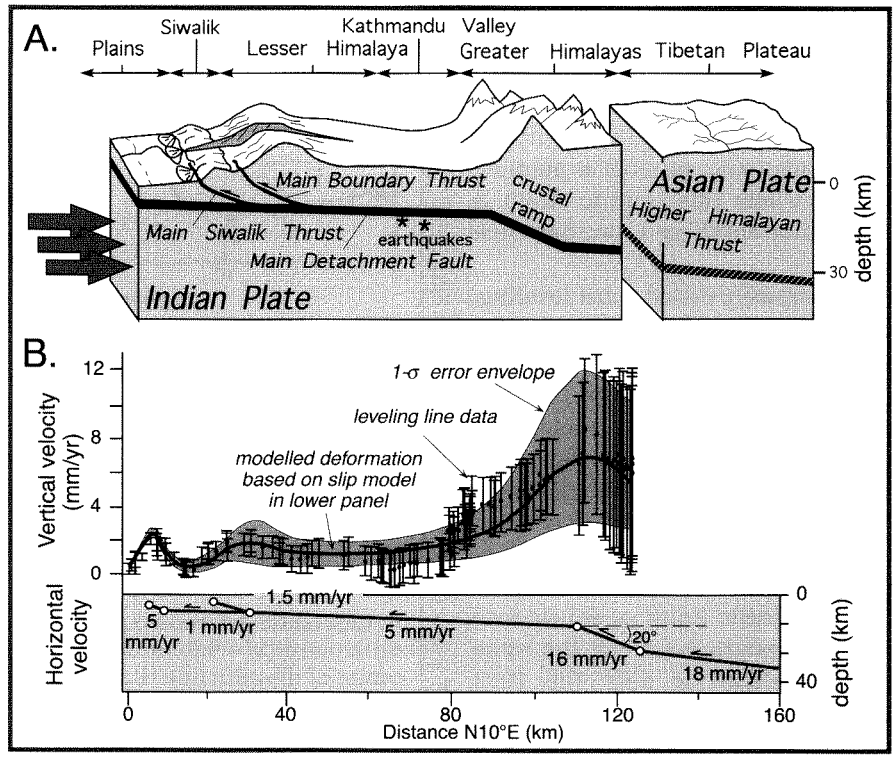

A. Schematic structure and topography of the Nepalese Himalaya. B. Relative uplift rates along a 250-km-long spirit-leveling line oriented perpendicular to the Himalayan Range in central Nepal. The profile is fixed at its southern end, and errors become cumulatively larger to the north. The southernmost peak of uplift (~2 mm/yr) is interpreted as a response to a growing anticline within the foreland. No distinct topographic signature is associated with this deformation, probably due to ready erosion of the uplifted strata. The leveling line through the Lesser Himalaya shows uplift spatially associated with the Main Boundary Thrust and subsidence in the intermontane Kathmandu region. Uplift within the Greater Himalaya occurs at the highest rates (~6 mm/yr) and is associated with high topography. Finite-element modelling of deformation of elastic crust (bottom panel) suggests that strain above and south of a crustal ramp separating the Indian and Asian plates could generate the observed pattern of uplift. Modified after Jackson and Bilham (1994a).

they are uplifted (Burbank and Beck, 1991). On the other hand, the highest rates of uplift along this transect coincide with the high topography of the Greater Himalaya. In these bedrock ranges, rates of erosion and of bedrock uplift may be in a rough equilibrium (Burbank et al., 1996), so that the average surface topography is changing very little despite the rapid bedrock uplift.

The pattern of vertical deformation can provide a data set against which models for ongoing deformation can be tested. The Himalayan survey, for example, traverses both known structures, such as the Main Boundary and Main Central thrusts, and inferred ones, such as the crustal ramp beneath the Greater Himalaya (Fig. 5.6A). The survey reveals broad regions of more rapid uplift that are 20–50 km wide (Fig. 5.6B) and that appear to be related to deformation on these underlying structures. The overall pattern of surveyed deformation can be imitated using models that treat the crust as an elastic medium which will deform in response to differential slip along faults. The orientation of a fault, its slip rate, and the thickness of its hangingwall

determine the deformation attributed to it in the model. One such model (Jackson and Bilham, 1994b) for the Himalayan transect suggests that the uplift pattern of the Greater Himalaya results from a large decrease in slip rate between the crustal ramp and the main detachment farther south (Fig. 5.6B). More limited slip on faults in and adjacent to the foreland could cause the observed deformation there. Although the results of such models are not unique, they provide a possible explanation for why and where interseismic strain is occurring and can help guide thinking about deformation within orogenic belts.

Leveling-line surveys, formerly called spirit leveling, of coseismic deformation across structures underlain by thrust faults serves to examine the vertical deformation attributable to individual seismic events. Changes in displacement along serial traverses can be compared with theoretical models that suggest how offsets should vary along the length of a fault from zero at fault tips to a maximum near the center. If one were interested in whether a particular earthquake represented a characteristic quake for this fault, it would be informative to compare the pattern of coseismic uplift or subsidence along a traverse with the topography along the same traverse. According to leveling-line data, the 1983 Coalinga earthquake (M = 6.5) in central California (King and Stein, 1983; Thatcher, 1986) caused a maximum of about 40 cm of uplift and 20 cm of subsidence along a 25-km-long profile (Fig. 5.7). This survey traversed the crest of a hangingwall anticline which developed above a blind thrust fault. Nearer to the nose of this plunging fold, the Los Gatos river traverses the same fold in a water gap and has incised through a 2550-^{14}C-year-old fluvial terrace. Whereas the terrace is about 1–3 m above the current bed of the river both above and below the water gap through the anticline, in the center of the anticline, it is about 10 m above the river (Fig. 5.8). Comparisons of the vertical coseismic deformation with the topography of the deformed terrace (Figs. 5.7 and 5.8) suggest that they have rather similar shapes. This similarity could be interpreted as evidence that this fault is typified by characteristic earthquakes (Fig. 4.7), which create comparable displacements in each seismic event. This similarity between displacement observed from a single earthquake and the shape of the folded river terrace also suggests that numerous repetitions of earthquakes similar to the 1983 quake could create the observed pattern of terrace deformation. In fact, knowing the height and age of the terrace (2550 ^{14}C years) and amount of coseismic uplift in 1983, one can calculate that about 25 similar earthquakes with a recurrence interval of about 100 years would be required to create the observed folding of the terrace.

FIGURE 5.7. Comparison of leveling-line data and deformed river terraces along a growing fold

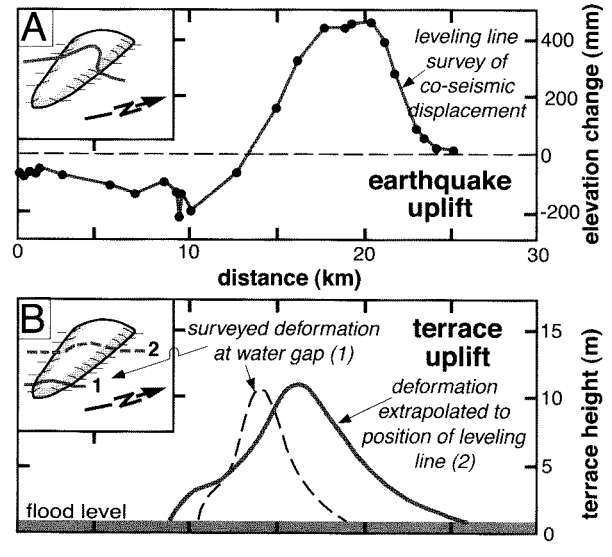

A. Coseismic deformation from the 1983 Coalinga earthquake (M = 6.5) from leveling-line data along the center of the anticline (line, inset). B. Deformed terrace profile surveyed near the nose of the same anticline (line 1, inset). For comparison with the coseismic deformation (A), the profile is scaled to the width of the fold in the vicinity of the leveling line (line 2, inset). Similar deformation patterns are displayed by both data sets, suggesting that the long-term pattern of terrace deformation could result from the accumulation of deformation similar to that caused by the 1983 Coalinga earthquake. Modified after King and Stein (1983).

Tide Gauges

Sea level provides a reference surface against which height changes may be assessed. It might be imagined that sea level would change synchronously and in equal amounts all over the earth's surface and, therefore, that sea level would provide a global reference frame. The variable isostatic response of the crust to

FIGURE 5.8. Folding along the Los Gatos River as shown by upward warping of both surveyed terraces and river bed

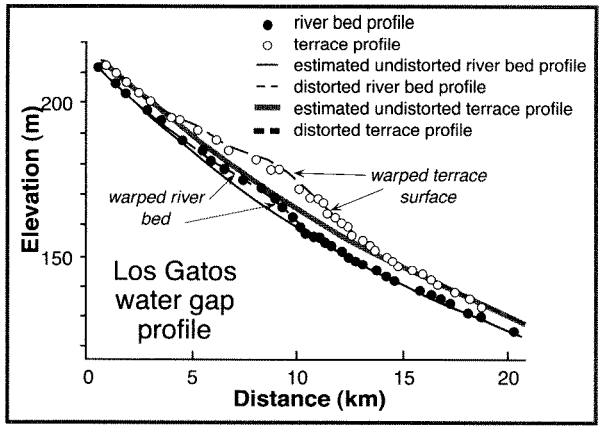

The magnitude of warping (shown in Fig. 5.7B) is calculated by subtracting the estimated undisturbed terrace profile from the observed profile. Modified after King and Stein (1983).

FIGURE 5.9. Oceanographic correction from the southwest coast of Japan

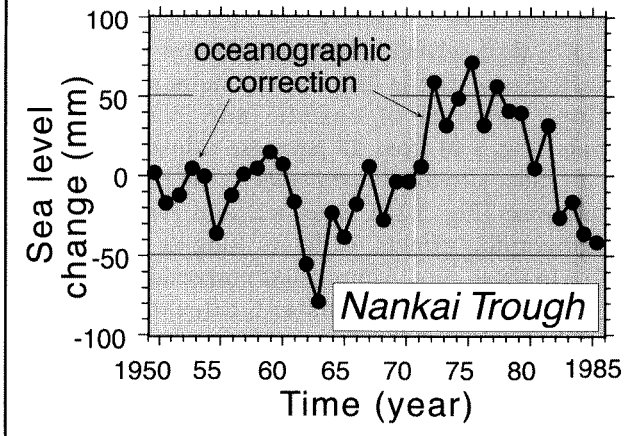

Note that the total variability (~150 mm) and the year-to-year variability are large and unsteady compared to the rate of tectonic deformation. Modified after Savage and Thatcher (1992).

loading, however, and the variable configuration of the load on the earth represented by the oceans dictates that a change in ocean volume will cause different isostatic compensation (and different subsidence or uplift) at sites around the world. This poorly known isostatic response, therefore, makes it difficult to predict the site-specific effects of a global eustatic change. Nonetheless, the use of local sea level as a reference surface can be exploited to assess vertical deformation. Because there are numerous localities worldwide where tide gauges have been routinely used to record mean sea-level heights, a large data base exists from which vertical changes can be extracted. Where tide-gauge records have been obtained along an irregular, embayed coastline, a three-dimensional reconstruction of the regional uplift pattern can be determined. In order to use tide-gauge data to define vertical changes of the shoreline, two corrections are typically applied. First, changes attributed to eustatic sea level are removed. At the time scale of years to decades, the volume of the oceans is affected by growth and decay of glaciers and by thermal expansion or contraction of the water column. At present, melting glaciers and warming temperatures appear to be increasing ocean volume at a rate which causes mean sea level to rise at about 2 mm/yr (Douglas, 1991). Second, local oceanographic effects resulting from changes in salinity, ocean temperature, atmospheric pressure, and ocean currents are removed. There is a remarkable interannual sea-level variability due to these factors (Fig. 5.9), and they often cause local sea-level changes that are far greater than those attributable to tectonic effects. The oceanographic correction is usually determined through principal component analysis of a regional set of tide gauges (Savage and Thatcher, 1992). The objective of this analysis is to identify those components, termed *common mode signals*, of the observed sea-level variation that, after the eustatic effect is removed, are shared among all of the stations. Following scaling for each site, the oceanographic correction is removed from the locally measured tidal record. The resultant data are then interpreted to represent changes in relative sea level due to vertical rock movement.

The use of tide-gauge data to reconstruct a regional pattern of vertical deformation is well illustrated by a study from the southwestern coast of Japan, where an excellent record spanning 1950–1985 has been analyzed (Savage and Thatcher, 1992). In 1944 and 1946, two large (M_s 8) earthquakes occurred offshore along the Nankai Trough subduction zone. Due to the

nearly continuous tidal record since those earthquakes, it is possible to use this record to address questions relating to the nature of crustal deformation between seismic events. For example, does interseismic strain accumulate at a steady rate, or is there an interval of rapid, post-seismic deformation immediately after an earthquake that is followed by more steady deformation? Removal of eustatic and oceanographic signals (Fig. 5.9) from 27 Japanese tide-gauge records reveals clear site-to-site contrasts in the rate of vertical deformation (Fig. 5.10). Even without removal of the oceanographic effects, different long-term trends are visible in these data. Appropriate corrections, however, suggest that nearly constant rates of uplift or subsidence have been sustained at many sites during the past 30 years, but that the period prior to 1955 was characterized by more rapid rates of deformation (Fig. 5.10). These data suggest that there is indeed an interval of more rapid post-seismic deformation that may last for several years following a major earthquake. Moreover, they suggest that interseismic deformation in subduction-zone settings may be characterized by steady rates of deformation. A map view of the tide-gauge data (Fig. 5.11A) provides a coherent overview of the regional deformation. The maximum rates of uplift occur 100–200 km from the trench. The trend of this zone of high rates is nearly parallel to the trench. Farther from the trench, rates diminish and even define a zone of subsidence west of Osaka (Fig. 5.11A).

This pattern of uplift and subsidence can be interpreted in several ways. One could assume that, following the post-seismic interval, elastic strain has been accumulating above a presently locked fault plane represented by the shallow part (<30 km) of the subduction zone interface. If this were the case, then elastic half-space models suggest that, above the trailing edge of the locked thrust, the overlying hangingwall should buckle upwards, whereas the leading edge of the hangingwall should be flexed downward toward the trench. If this elastic strain were released during a subsequent subduction-zone earthquake, strong subsidence in the southeastern coastal region and uplift west of Osaka would be predicted from these tide-gauge data. If the interseismic deformation is compared with the coseismic displacement resulting from the 1946 Nankaido Ms 8.2 earthquake (Fig. 5.11B), there is a striking spatial correspondence between the zones that have been uplifted most extensively during the interseismic interval and those that experienced the greatest

FIGURE 5.10. Relative sea-level change and coastal deformation from three sites in Japan adjacent to the Nankai Trough

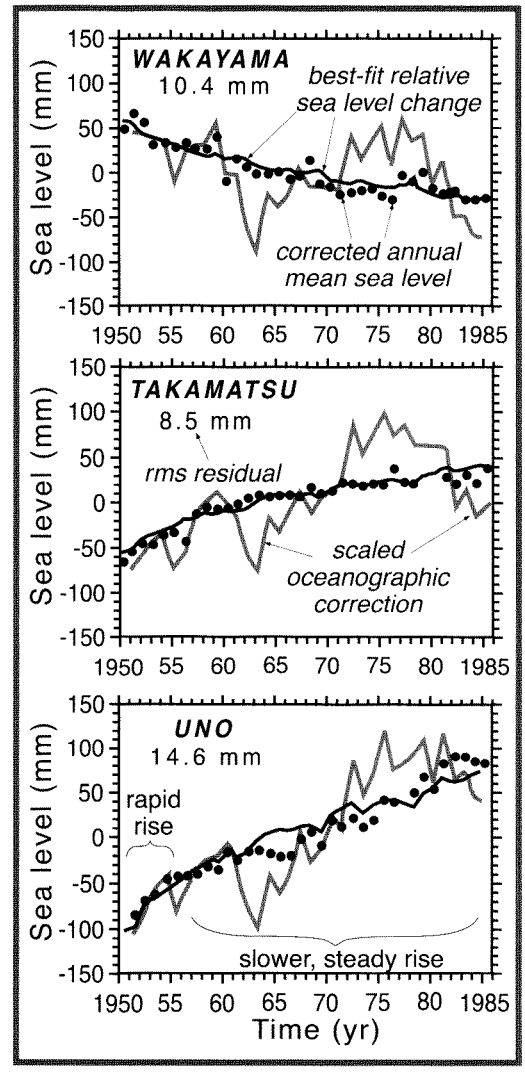

Subtraction of the oceanographic correction (which is scaled for each site) from the original measurements yields the corrected annual mean sea level. The line fitted to the corrected data defines the long-term tectonic deformation. The rms (root mean squared) residual quantifies the deviation of the annual data points from the long-term fitted line. All sites show a steady trend in sea-level change from 1955–1985. Note that at Takamatsu and Uno, there is clear evidence for an interval of rapid subsidence (seen as a rise in sea level) prior to about 1955. Modified after Savage and Thatcher (1992).

FIGURE 5.11. Interseismic and coseismic deformation of southwest Japan

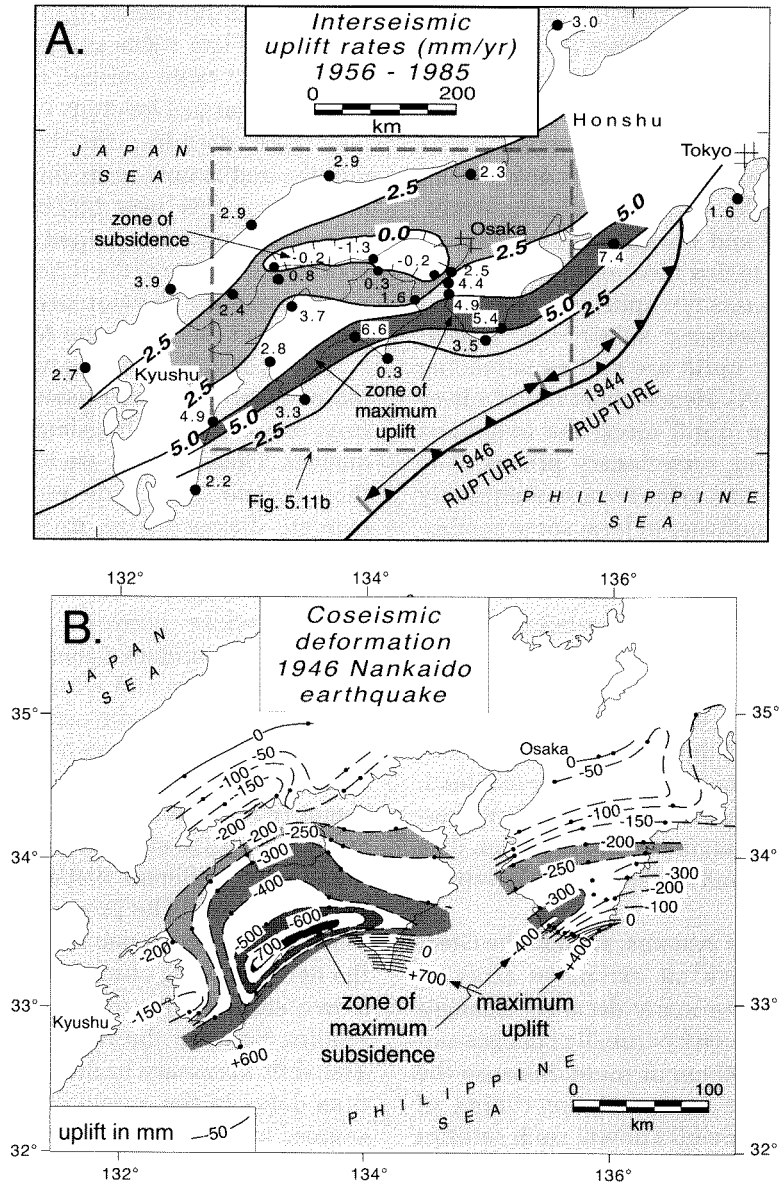

A. Interseismic deformation of southwest Japan as determined from tide-gauge data. Rupture lengths of two magnitude 8 earthquakes (1944, 1946) are shown along the Nankai Trench. Highly irregular coastline provides excellent spatial distribution of data. Note elongate zone of maximum uplift along the southeastern coast and zone of subsidence to the northwest. Modified after Savage and Thatcher (1992). B. Coseismic deformation resulting from the 1946 Nankaido earthquake (M = 8.2). Note maximum uplift along southeastern coast parallel to the Nankai trench. Strong subsidence occurred just northwest of the zone of maximum uplift. When coseismic and interseismic deformation (Fig. 5.11A) are compared, zones of maximum coseismic subsidence coincide with zones of maximum interseismic uplift and appear compatible with an elastic rebound model. The southeasternmost sites in both data sets, however, show uplift both during (7b) and after (7a) the earthquake and are not directly compatible with such a model. Modified after Fitch and Scholz (1971).

coseismic subsidence. These data lend support to the concept that the pattern of interseismic strain accumulation is mirrored by the coseismic deformation. An alternative explanation suggests that the deformation defined with the tide-gauge data represents a response to a down-dip migration of slip along the subduction zone following the major earthquakes. If this were the case, then the observed deformation is more analogous to a migrating ripple of deformation (Pollitz et al., 1998) and would represent little storage of elastic strain. Comparison of the inter- and coseismic displacement maps lends some support to this idea, as well. Although the axis of maximum interseismic uplift coincides with the axis of maximum coseismic subsidence, coastal zones of strong coseismic uplift are still experiencing interseismic uplift (Fig. 5.11). Hence, there is no "mirror image" of subsidence and uplift along the outermost coastal areas. Finally, along accretionary prisms, it is observed that both strata and marine terraces commonly dip toward the arc. This indicates at least some component of nonrecoverable deformation occurs within the overriding plate.

Despite the uncertainties in the interpretation of these tide-gauge data, the Japanese coastal data clearly demonstrate their usefulness in delineating vertical deformation patterns. On highly digitate coasts with numerous embayments and islands, a regional three-dimensional pattern of emergence and submergence can be readily obtained. Because tide-gauge records are available from many harbors with a long-history of use, these provide a rich data base for studies of temporal and spatial changes in vertical motions in coastal regions.

Some large navigable lake systems, such as the Great Lakes (Walcott, 1975), have an extensive array of water-level records that span many decades. Changes in water level are largely driven by climatic changes and may have magnitudes of 100 cm or more. Because the configuration of the water load and the timing of changes in its total mass are well known, such settings provide excellent settings in which to investigate the isostatic response of the crust to loads that are emplaced instantaneously in a geological sense.

Far-Field Techniques

Very Long Baseline Interferometry (VLBI)

In order to define relative motion between lithospheric plates, near-field measurement techniques are both inadequate, inappropriate, and time consuming. To measure between plate interiors that are assumed to be relatively stable, a technique is required that permits precise distances to be measured over distances of hundreds to thousands of kilometers. VLBI was developed in the late 1960s as a technique to study compact extragalactic radio sources, and has evolved to become a geophysical tool for study of real-time tectonics. In the last three decades, the technology has developed rapidly, and is now in its third generation. The discoveries using this new technique have at times been surprising and have helped change the way we think about the integrity of the lithospheric plates. For a recent summary of the development of VLBI techniques and applications, see Ryan and Ma (1998).

The VLBI system utilizes two or more widely separated radio telescopes simultaneously observing radiation from very distant (extragalactic) radio sources, typically quasars. These sources are broad band in the sense that they radiate in a wide range of frequencies. Their extreme distance from earth (billions of light years) makes them very small, fixed points in the sky, which therefore form good reference points from which to measure distances between sites on the earth. The complicated, random signal from the quasar is recorded at very high rates and with very accurate clocks at the two ends of each baseline on the surface of the earth. The tapes of these recordings are then sent to a central processing site, each containing the identical incoming signal (with added noise associated with atmospheric and ionospheric effects), but differently shifted due to the slightly different distance from the quasar to the radio telescope. The processing involves correlation of these recordings in pairs, one pair for each baseline in the network being observed. The signal from one site is slowly shifted while the other is held fixed until the correlation between the two signals reaches a maximum. The shift necessary to maximize the correlation is the time delay in the arrival of the signal from the radiosource, which is directly proportional to the baseline distance. As the rotation of the earth continuously changes the delay times, signals are typically measured over an entire 24-hour period, during which time about 12 quasars are imaged. The resulting measurements can have a precision of as high as 1 mm in the horizontal and 3 mm in the vertical.

The most recent system (Mark III) is dual frequency (2.3 and 8.4 GHz) in order to subtract out the delay associated with the earth's ionosphere. It uses a very stable hydrogen maser system for determination of all frequencies and timing signals (Rogers et al., 1983). In

addition, the delay associated with the propagation of the radiation through the troposphere is calibrated against meteorological measurements at each telescope. The Mark-III system deployed by the NASA-funded Crustal Dynamics Project consists of a combination of fixed radio-telescopes and mobile stations, the latter being either mobile units that connect to fixed antennae, or entire stations with antennae (Coates et al., 1985). Today, there are approximately 40 VLBI antennas around the world where measurements are systematically recorded. Horizontal velocity estimates with an uncertainty of about 1 mm/yr are available for about 60 sites, while uncertainties in the vertical dimension are approximately two to three times greater.

Applications

Starting in July 1980, the NASA Crustal Dynamics Project and the International Radio Interferometric Surveying (IRIS) project have run many full dual-frequency-band observing sessions in which many pairs of radio telescopes were simultaneously occupied (Ryan and Ma, 1998). A small sampling of the results to date includes repeat measurements of the distance between North America and Europe (Herring et al., 1986), more detailed studies of the tectonics of western North America (Ward, 1990), and an even greater focus on the Transverse Ranges of southern California (Molnar and Gipson, 1994).

Even early results from the VLBI program resulted in a strong constraint of the NA-Europe relative plate velocity of 19 ± 10 mm/yr (Herring et al., 1986), which compared well with the long-term averaged rates of 15-17±3 mm/yr obtained from geological constraints over time scales of millions of years.

Much research effort in this far-field geodesy community has been focused on attempting to uncover the source of the San Andreas fault discrepancy: the difference between the geologically determined slip rate on the San Andreas fault (roughly 33 mm/yr) and the relative plate motion between the North American and Pacific plates (52 mm/yr). After a decade of operation, the high density of fixed radio telescopes in the coastal western United States and the availability of mobile VLBI units allowed testing of rigid plate models based solely on space geodetic data from sites in the interiors of the Pacific and North American plates. More interestingly, 16 sites nearer the plate boundary showed that significant right lateral shear occurred within North America across a distance of several hundred km east of the San Andreas fault (Ward, 1990), implying small right lateral speeds on a diffuse set of structures extending into Nevada. In addition, the VLBI data suggested significant (8±1 mm/yr) compression normal to the trend of the San Andreas fault within the Transverse Ranges north of Los Angeles.

Further work on this region using VLBI has documented relative motions between crustal blocks that strongly imply clockwise block rotations within the Transverse Ranges, with rotation rates matching rates determined from paleomagnetic studies (Luyendyk, 1991) that are average rates over 10 to 15 Myr (Molnar and Gipson, 1994). These are interpreted to require that the faults bounding the crustal blocks be weak, and that the source of relative motions lie at depth within the lower crust or upper mantle (Molnar and Gipson, 1994).

As the time over which such measurements have been made grows, as the technology advances (faster tape speeds, better clock resolution, etc.), and as our models of atmospheric effects become better constrained, the errors on these rate estimates ought to continue to diminish. This will allow even smaller time-scale variations to be detected, to rise above the noise, making the technique yet more relevant as a real-time plate tectonics tool.

Global Positioning System (GPS)

Two recent developments have revolutionized geodetic approaches for the accurate determination of positions at the scale of hundreds of meters to hundreds of kilometers. First, more than 24 satellites have been launched which continuously transmit coded radio messages that specify the time of transmission and the satellite's position as a function of time. This constellation of satellites is referred to as the global positioning system (GPS). Second, highly sensitive receivers measure the transit time and phase of the radio signal in order to determine the distance to the transmitting satellite. Simultaneous solution of the distance from the receiver to several (usually >4) satellites permits the location of the receiver to be specified with high precision. Given the orbital geometry and spacing of the GPS satellites, acquisition of positional data from four or more satellites is now usually feasible almost anywhere in the world. Thus, based on radio transmissions from satellites more than 20,000 kms above the earth's surface, this remarkable technology permits calculation of one's horizontal location to within less than 1 cm! At this time, the accuracy of GPS measurements in the horizontal dimension is several times greater than the vertical accuracy.

Two strategies are commonly employed for collecting geodetic data using GPS in order to define regional strain fields at scales of 10 to several hundred kilometers. In areas of high seismic activity or risk, especially close to major population centers, an array of permanent GPS receivers that continuously record positional data is sometimes installed. These permanent arrays have the drawback that each individual receiver (they are not inexpensive!) has to be wholly dedicated to a single measurement site. On the other hand, permanent arrays offer more precise positioning and can resolve questions that require high precision and a dense time-series of measurements. Since the mid-1990s, numerous permanent GPS arrays have been installed, including dense networks in southern California (SCIGN), the San Francisco Bay area (BARD), Taiwan, and Japan, and hundreds of permanent GPS stations now dot the world.

More commonly, an array of GPS sites that are placed at carefully chosen localities across the region of study are periodically re-surveyed. With this strategy, numerous sites can be visited with a small number of receivers, and the same receivers can be used by different research groups for various projects. For rapid acquisition of geodetic data across a broad region, the campaigns with mobile receivers are highly effective. Survey sites are usually marked by a monument fixed in an immobile substrate, such as bedrock, so that the GPS receiver can be positioned over precisely the same point on subsequent surveys. In order to achieve a high level of accuracy (a few mm), GPS observations are typically collected for eight hours to several days at each site. GPS surveys or "campaigns" are currently being conducted in many of the actively deforming parts of the earth's surface. The high precision and accuracy that can be attained with GPS permits researchers to define deformation rates more accurately and over much shorter time intervals than has previously been possible.

Four factors contribute to the calculated GPS position. First, there is motion driven by large-scale plate tectonic movements. This encompasses the relative velocity between interacting plates. Second, there is deformation at a more local scale due to individual seismic events and aseismic deformation. Third, seasonal changes in groundwater levels can cause the earth's surface to inflate or deflate. Fourth, there is the measurement error that results from variations in atmospheric conditions, transmission and reception of the GPS data, and positioning of the GPS receiver. Obviously, considerable efforts are typically expended to reduce the measurement error to a minimum. Extraction of a plate-motion signal or a seismic signal from the data is then possible, if the strain related to one or the other is known. In fact, one check on calculated seismic displacements is to subtract independently measured or modelled ground offsets due to seismic phenomenon from the total displacement to see whether the expected rates of plate motion represent the remaining measured motion in the data set. Alternatively, by subtracting the expected plate motion, the resultant seismic displacements can be compared with measured offsets (Larsen and Reilinger, 1992).

GPS measurements in southern California have helped to further refine the way geologists perceive deformation along this plate boundary (Fig. 5.12). In comparison to the earlier VLBI data for the southwest US, a much denser array of GPS measurements is available, and this provides a more detailed view of the pattern of deformation. For example, the spatial partitioning of broadly distributed deformation across the Pacific–North American plate margin can be better quantified with the GPS data. It is useful to compare the locally determined GPS directions and velocities with those that would be expected based on the Pacific–North American rotational pole (dashed line, Fig. 5.12). If all of the relative plate motion occurred along the San Andreas, all of the vectors east of the fault would have nearly the same magnitude, they would be parallel to the small circle of rotation, and there would be no relative motion west of the fault. GPS-determined velocities east of the San Andreas are indeed largely parallel to the small circle, but their magnitudes vary considerably and decrease toward the west, indicating shearing across this zone of diminished velocities. Whereas the San Andreas fault itself is parallel to the small circle along much of its trace, its trace clearly deviates from the expected rotation direction (and the small circle) in the area of the Big Bend in southern California (Fig. 5.12). Here, major departures from the expected rotation directions are also displayed by GPS-determined velocities. They veer southward on the west side of the Big Bend and define considerable north-south compression across the Los Angeles and Ventura basins. In fact, the mountains and basins that make up the Los Angeles region have largely been created by thrust faulting and transpression in response to this shortening. Most of the destructive earthquakes that have occurred in the Los Angeles basin in the past 20 years have resulted from offsets on thrust faults, rather than strike-slip faults. Several of these earthquakes did not rupture the surface (blind thrusts), but nonetheless, their effects were devastating

FIGURE 5.12. Rates of horizontal crustal strain in southern California, based on GPS and VLBI data

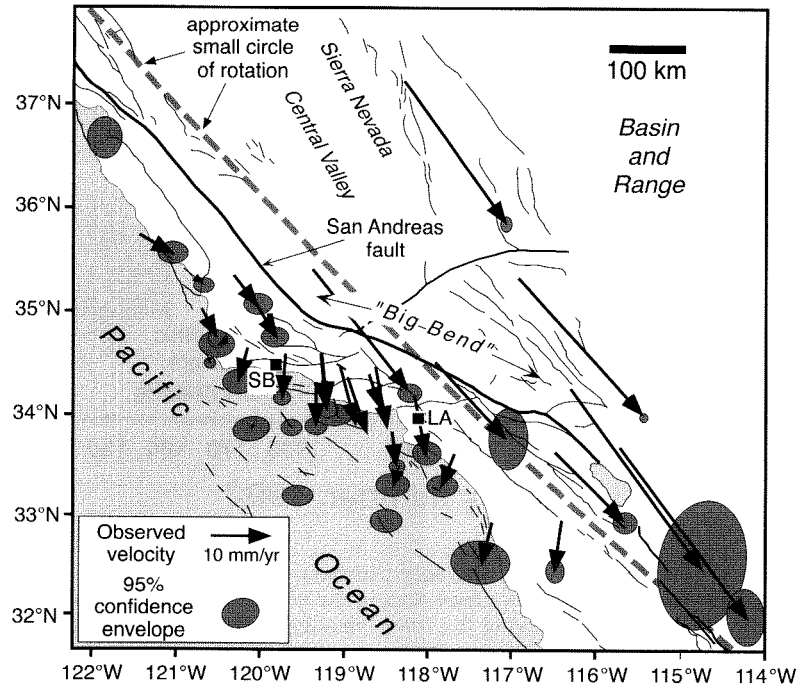

Rates are shown relative to a fixed point on the Pacific plate. A small-circle derived from the rotational pole for the North American and Pacific plates is shown by the dashed line. Note that most of the displacement vectors east of the San Andreas fault are parallel to the fault and to the North American–Pacific small-circle of rotation. West of the fault between Santa Barbara (SB) and Los Angeles (LA), considerable displacement occurs 30–90° away from the trend of the San Andreas and is accommodated by folds and thrust faults. This variability in directions also highlights the differential rotation of crustal blocks in this region. Note that the relative rates gradually decrease both east and west of the San Andreas. This provides strong evidence that the plate boundary, rather than being simply concentrated along the San Andreas fault, is represented by a diffuse zone of deformation several hundred kilometers wide. Modified after Feigl et al. (1993).

to the region because strong vertical accelerations along thrusts occurred beneath densely populated areas.

At present, the array of permanent GPS sites is being "densified" in southern California, as well as in many other actively deforming regions around the world. The geodetic perspective that is emerging from these arrays provides the clearest view to date of the way in which strain is partitioned across deforming zones. In some areas, it appears that the deformation patterns defined through GPS observations at the decadal scale are very consistent with the plate tectonic rates determined at time scales of millions of years. Numerical models for plate motions, rotation of crustal blocks, accumulation and release of elastic strains, and geometries of folds and faults will be tested and refined with these new geodetic data sets. As a consequence of these geodetic data, our understanding of crustal responses to loads and tectonic forcing will greatly improve.

The precision of GPS measurements is in part a function of the duration of data collection. For any given occupation of a single GPS site, a longer interval of data collection will yield more precise positioning information. Good quality data collected for 24 hours can have an uncertainty of greater than 4–5 mm. If data are collected for several days, the uncertainty can be reduced considerably more by smoothing the noise inherent in daily measurements. Continuously operating, permanent GPS receivers can reduce the uncertainties still

FIGURE 5.13. Continuous GPS data collected prior to and after the June, 1992 magnitude 7.3 Landers earthquake in southern California

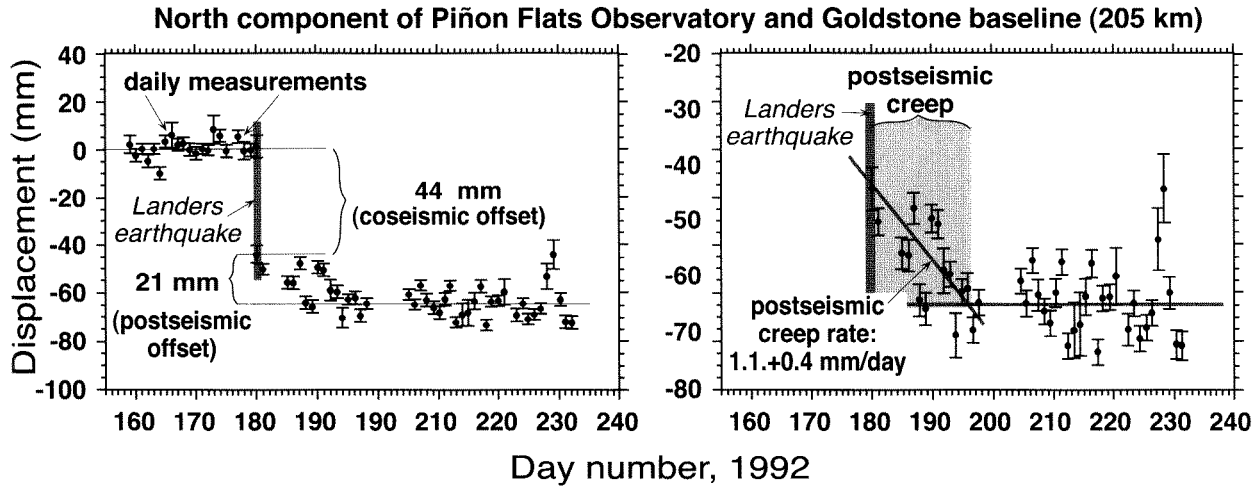

Despite the typical day-to-day variability of 5–15 mm, very precise positions are defined using multiple days of readings. An abrupt coseismic offset of 44 mm occurred during the earthquake. A remarkable aspect of this record is the post-seismic slip of 22 mm that occurred during the few weeks following the quake (right panel). This has never before been documented. Given the background noise in the observations, it is only with continuous GPS readings that this trend (1.1 mm/day) is observable. Modified after Bock et al. (1993).

further and can provide a temporal resolution that is impossible to achieve with occasional re-occupation of GPS sites. When examining regional strain patterns, campaign-style data collection is suitable, but if a permanent array is operating within an active seismic region, there is the possibility of observing detailed, far-field effects of individual seismic events that will not be discerned when data are collected on an annual basis.

A permanent GPS array was operating in southern California when the M_w 7.3 Landers earthquake struck in June, 1992 (Bock et al., 1993). The daily GPS positions (Fig. 5.13) collected for several weeks prior to the quake define an unambiguous mean position (±1 mm) for a baseline between two sites on opposite sides of both the San Andreas fault and the faults that ruptured during the Landers earthquake. These sites are situated more than 100 kilometers apart. During the earthquake itself, 44 mm of instantaneous displacement was recorded by the two sites, as illustrated in Figure 5.13. In the 15 days following the quake, the data show rapid post-seismic creep (about 1 mm/day); such creep has never before been documented in sites far from the rupture. Because both of the stations were located more than 80 km from the fault rupture, these data record far-field effects that are much smaller than the displacements on the fault itself which displayed horizontal offsets of as much as 8 m.

Radar Interferometry

A new geodetic technique for measuring ground displacements over larger areas has been developed based on radar interferometry. Using *synthetic aperture radar* (SAR) carried aboard satellites at 785 km altitude, radar pulses are transmitted along west-pointing ray paths at an angle of 23° from the vertical. Based on the return signal, the distance from the satellite to the ground is calculated, and a phase shift due to the ground reflection is recorded. These measurements are made for each pixel (picture element with dimensions of 4 by 20 m). If the same area of the earth's surface is contained within two different SAR images, if the position of the satellites is well known, and if the ground moisture is approximately the same for both images, then the differences in path lengths between the two images are attributable to some combination of 1) the ground

topography as seen stereoscopically from the satellite in slightly different orbital positions and 2) changes in the position of the ground in the time between acquisition of the two images (Massonnet et al., 1993). If two images are used to construct the topography of a region, then a third image can be used to determine ground deformation with respect to that topography along the "look" direction of the radar. Alternatively, if a detailed digitized topography already exists for the area, then the differences between two images can define the ground deformation. The resultant depiction of ground displacements is termed a *SAR interferogram.* The wavelength of the radar emitted by the satellite is 56 mm, and, using interferometry, it is relatively easy to define displacements of 28 mm (half a wave length) or more. Under favorable conditions, even displacements of less than 10 mm with uncertainties of less than 5 mm can be delineated (Massonnet et al., 1994). In order to reduce noise, the values from dozens of pixels can be averaged together to create a displacement value for an area of approximately 90 m by 110 m. Radar interferograms for use in tectonic studies are probably best suited for arid settings where seasonal changes in vegetation and moisture are minimal.

The greatest research attribute of radar interferometry lies not in its resolution (which is considerably less than that achieved through extensive GPS measurements), but rather in the tremendous spatial coverage it provides. One 60 km by 60 km SAR image comprises more than 300,000 pixels measuring 100 by 100 m! The distance changes recorded by these many thousands of pixels can be displayed as a contour map of deflections in which each successive "fringe" represents an additional 28 mm of displacement. In addition to seismic displacements, volcanic inflation or subsidence (Massonnet et al., 1994), large landslides (Fruneau et al., 1996), and the details of glacial flow (Dowdeswell et al., 1999; Mohr et al., 1998) can be observed and depicted through radar interferometry. Unlike most other geodetic techniques, radar interferometry can be done remotely, and it provides regionally extensive, high-resolution maps of interference patterns resulting from surface displacements. Although radar interferometry will have restricted applicability in highly vegetated regions, it can be extremely useful for quantitative analysis of deformation in remote, relatively arid areas.

An interferogram of the ground displacement associated with the Landers earthquake (Fig. 5.14) shows concentric, but asymmetric fringes that extend at least 75 km in an east-west direction (Massonnet et al., 1993). Note that the pattern appears to consist of several groups of distorted, concentric fringes. One explanation for the abrupt changes in displacement along the trace of the Landers rupture is that faulting occurred along a segmented fault. In fact, the rupture appears to have linked together individual fault segments that were not previously known to be connected. Eight separate ruptures of varying sizes have been hypothesized along different segments of the fault. The complex suite of interferometry fringes, particularly along the eastern side of the fault, can be roughly interpreted to depict the effects and sphere of influence of these individual ruptures. The analysis also shows that earthquake appears to have triggered slip on other faults as much as 100 km from the primary rupture. It is possible not only to look at the direct effects of an earthquake shortly after the event, but also to examine continuing ground deformation in the subsequent months and years. Continuing interferometric studies of the Landers region following the June, 1992 earthquake have recorded deformation of up to 10 cm due to a magnitude 5 aftershock on a nearby fault and have shown that less than 28 mm of post-seismic and interseismic slip has occurred in other areas (Massonnet et al., 1994).

Summary

Technological advances in measurement techniques during the past decade are ushering in a new era of high-precision geodesy. This geodesy is providing a much clearer view of partitioning of deformation at annual to decadal time scales. Now it is possible to detect small differences in the velocity vectors between nearby crustal blocks and even within individual blocks. These measurements help to pinpoint those zones where these differential movements must be accommodated. Through GPS and VLBI observations, the regional-scale driving forces represented by lithospheric plates moving with respect to each other are becoming better defined. Whereas continuously recording GPS networks now can provide almost real-time records of seismic deformation, radar interferometry is providing an unprecedented, detailed view of coseismic and interseismic deformation at a regional scale. These data sets are generating new perceptions of both the near- and far-field surface effects of earthquakes, and they are guiding the development of new models that more faithfully mimic actual deformation. Within the next decade, GPS campaigns will have been conducted within many of the actively deforming

FIGURE 5.14. Radar interferogram of the Landers earthquake

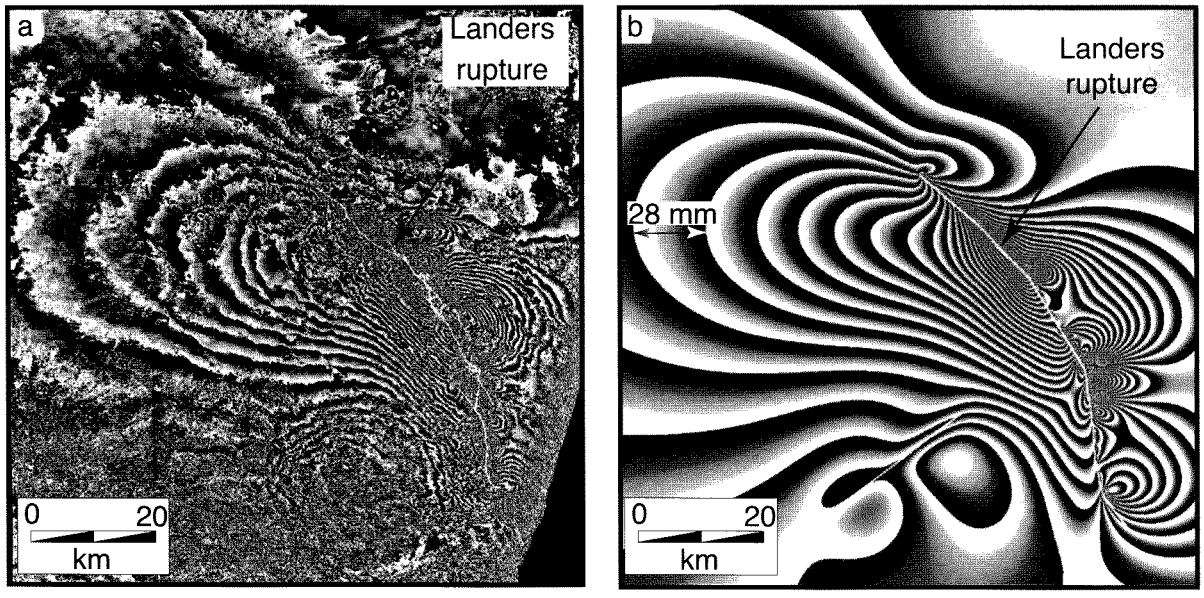

A. SAR interferogram of ground displacement associated with the Landers M_w 7.3 earthquake of June, 1992. Each fringe represents 28 mm of displacement and at least 20 fringes are visible near the fault (equal to 560 mm of displacement). Coherence is lost as the ground rupture is approached, probably because the displacement gradient is greater than 28 mm/pixel. Note the broad, asymmetric deformation in an east-west direction covering >75 km and the abrupt termination of major deformation near the ends of the fault. The detailed deformation patterns seen here can be used to constrain models of surface displacement due to the Landers rupture. B. Modeled interferogram pattern based on eight fault segments rupturing along vertical planes in an elastic half-space. The excellent match between the observed and modeled results indicates that a simple half-space model can quite successfully mimic the observed deformation pattern. Modified after Massonnet et al. (1993).

areas of the world, and we should have a far better understanding of the regional deformation field of the earth. Numerous permanent GPS networks will be installed by then, particularly in the vicinity of urban centers confronted with a significant seismic hazard. Interferometry studies of lightly vegetated, seismically active regions will probably become commonplace, as will monitoring of volcanoes and other environmental hazards whose movements through time are indicators of the threat posed by them.

There is still a place for traditional geodetic studies. Many important geodetic problems in tectonic geomorphology can be addressed without recourse to expensive, high-precision instrumentation. Alignment arrays, trilateration surveys, leveling lines, and tide gauges all offer useful information on short-term deformation. Sometimes, better vertical resolution can be obtained through these approaches than through GPS measurements. Often the instigation for a more elaborate study will originate from simple observations of the deformation associated with faults and folds. Moreover, the data base for these older measurements extends farther back in time, and thus provides a longer temporal basis for calculating deformation rates.

The expanded geodetic knowledge that is rapidly emerging prompts a new array of important unanswered questions. We can now determine plate motions, rotations of crustal blocks, near- and far-field fault displacements, and folding rates with a greater precision and across a broader area than ever before. Armed with the knowledge of present-day rates of deformation, we'd like to know the persistence of these rates in the past. Were the same faults and folds that are accommodating differential motion today also primarily responsible for accumulating

strain in the past? Were the displacement patterns and lengths of ruptures due to major earthquakes repeated consistently in the past, or were different patterns associated with each earthquake? Given a steady plate-tectonic forcing, what causes the formation and abandonment of faults? As the poles of plate rotation changed position in the past, how were the new stress orientations accommodated at plate margins? As discussed in the next chapter, some of the answers to these questions can be revealed through paleoseismological studies that seek to reconstruct deformational patterns associated with past earthquakes.

CHAPTER 6

Paleoseismology

Geologic maps of either Quaternary deposits or older bedrock often indicate the presence of faults in a given area. Through examination of displaced land features or of lithologic contacts in outcrops, we can tell that these faults have been active at some time in the past. But, how active have they been? Have they ruptured in large earthquakes that broke long sections of the fault, or are they associated with smaller displacements? Have the faults moved aseismically or in discrete events that generated earthquakes? When did the last rupture and the ones previous to that occur? Is there regularity to the timing of events? Is there a spatial pattern to the rupture that is repeated from event to event? Can the fault be divided into independent segments that rupture in characteristic events? Does an earthquake on one fault increase or decrease the likelihood of rupture on other nearby faults, and how are those changes dependent on the orientation of the fault? Can we estimate the likelihood that a fault will produce an earthquake of a given magnitude within a specified period of time? What has the past slip rate on a fault been and how does that compare with geodetically determined rates? What can be done to estimate rupture histories when a fault is not exposed?

Answers to questions such as these constitute the focus of paleoseismological studies. Such investigations typically use stratigraphic, structural, geomorphic, and biologic evidence to reconstruct the sequence of displacements on a fault. When combined with dating of displaced features or of other indicators of faulting, the timing of past ruptures can also be determined. When multiple offsets can be dated on a single fault, it becomes possible to determine recurrence intervals and longer term rates of displacement, and to define the variation in the displacement that occurred during each of several earthquakes along the same fault.

Why do we want to know this? If we are interested in understanding how the brittle upper crust responds to imposed stresses, we need to know how and when it ruptures during earthquakes. In order to develop a basis for predicting the location and magnitude of future earthquakes, we need many details of past earthquakes. If we want to determine whether or not a fault exhibits "characteristic" or repeatable behavior, we have to know its rupture history and the variability of displacement along it in the past. We recognize that, in areas of active deformation, the interplay between tectonic movements and surface processes controls the geomorphology of these deforming landscapes. In order to quantify such interactions, we need to know both the magnitude and three-dimensional geometry of faulting or folding events, as well as the timing of these events.

A remarkably diverse array of approaches, ranging from determining the growth record of trees that grew along a fault trace to interpreting the stratigraphy of beds that have been affected by faulting and are now exposed in an artificial trench across a fault, has been employed in paleoseismological studies. The calculation of recurrence intervals and of rates of displacement depends both on the correct interpretation of the geologic record of past offsets and on reliable dating of the timing of those offsets. Approaches to dating and some of the pitfalls and applications of various dating techniques were described in Chapter 3. Generally, these are not discussed in more detail here. Instead, in this chapter we focus on some of the many techniques that have been successfully used to reconstruct the record of seismicity along faults that have been active during the Holocene.

Seismic Moment and Moment Magnitudes

Any time an earthquake occurs, it releases seismic energy, E_s. The energy released is proportional to the area of the rupture plane, A, the average displacement along it, d, and the stress drop, $\Delta\sigma$, across the fault during the earthquake:

$$E_s = 1/2 \cdot \Delta\sigma \cdot d \cdot A \qquad (6.1)$$

The stress drop actually refers to the mean stress, σ_{mean}, acting across the fault during the earthquake and is calculated as the average of the stresses before and after the earthquake:

$$\sigma_{mean} = (\sigma_{start} - \sigma_{finish})/2 \qquad (6.2)$$

If it is assumed (as is often done) that the fault is stress free at the end of rupture ($\sigma_{finish} = 0$), then the mean stress is equal to one-half of the stress drop, $\Delta\sigma$.

Although it is now both possible and very useful to compare earthquakes on the basis of the energy released during them, traditionally the size of an earthquake has been assessed on the basis of its magnitude. The first quantitative measure of size was the local magnitude (M_L) scale which was based on Richter's (1935) observation that, with increasing distance from seismic sources in southern California, the maximum amplitude of ground motion decayed along a predictable curve. When the data for distance versus the logarithm of the amplitude of ground shaking were compared for several earthquakes, they followed parallel curves of decay with increasing distance. By measuring the amplitude of shaking, A, in a given earthquake and comparing it with the amplitude, A_o, of a "reference event," it was possible to define a local magnitude (M_L):

$$M_L = \log A - \log A_o \qquad (6.3)$$

For a reference earthquake with $M_L = 0$, the amplitude of shaking at a distance, Δ, of 100 km from the source was 1 mm. A calibration of these curves using the reference event led to the following expression for local magnitude:

$$M_L = \log A - 2.48 + 2.76 \log \Delta \qquad (6.4)$$

The original Richter magnitude scale was developed based on measurements of southern Californian earthquakes during the 1930s using a certain type of seismometer (Wood-Anderson torsion instruments), and the equation above is only strictly applicable to these seismometers in this setting. Today, however, local magnitudes are calculated in many areas using a variety of seismometers. The coefficients in Equation 6.4 have been modified to yield consistent estimates of the local magnitude, despite these differences in instrumentation and regional contrasts in the transmission of seismic waves due to geological variability.

Several other magnitude estimates are commonly used. Surface-wave magnitudes, M_s, are typically calculated for events at distances exceeding 600 km by measuring amplitudes of surface waves with a period of approximately 20 seconds. Body-wave magnitudes, m_b, are based on the amplitude of direct compressional, P, waves measured from short-period seismograms, typically with periods of about 1 second. Empirical relationships have been established between these earthquake magnitudes and seismic energy, E_s, released:

$$\log E_s = 11.8 + 1.5\, M_s \qquad (6.5)$$

$$\text{and } \log E_s = 5.8 + 2.4\, m_b \qquad (6.6)$$

A different measure of the energy released in an earthquake is the seismic moment (M_o, measured in dyne-cm) which is equivalent to the product of the rupture area, a, average displacement, d, and the rigidity, μ or shear modulus of elasticity of the crustal material involved in the rupture:

$$M_o = \mu \cdot d \cdot a \qquad (6.7)$$

where μ is commonly taken as 3×10^{11} dyne/cm^2 for the crust and 7×10^{11} dyne/cm^2 for the upper mantle. Thus, instead of measuring the amplitude of a deflection on a seismograph, observations of the rupture length, the probable total area of rupture, and the mean displacement are combined with estimates of rigidity to yield the seismic moment. Moreover, the magnitudes of many earthquakes today are reported as "moment magnitudes," M_w, and are based on the seismic energy released during an earthquake, that is, the seismic moment, M_o:

$$M_w = (\log M_o / 1.5) - 10.73 \qquad (6.8)$$

In theory, the seismic moment is a single, definable quantity that reliably characterizes the seismic energy

release. As a consequence, moment magnitudes should theoretically provide a direct means for comparing different earthquakes. In reality, today seismic moments are calculated both from the actual characteristics of the rupture and from empirically derived functions that relate body or surface waveforms to seismic energy and moment.

It is impossible to reconstruct quantitatively the amplitude of shaking in pre-historic earthquakes. Consequently, it is difficult to estimate directly the magnitudes of ancient earthquakes based on paleoseismologic studies. What can be measured, however, are rupture lengths, mean displacements, and approximate rupture areas. These observations provide a means of determining the absolute size of past earthquakes for which there are no instrumental records. Such a quantification through paleoseismological studies represents a powerful basis for comparing ancient and modern earthquakes. Modern studies have defined relationships between the seismic moment and the amount of ground displacement and shaking. Building on these relationships, paleoseismological determinations of rupture lengths, fault geometry, and coseismic fault displacement provide key constraints on the assessment of modern seismic hazards along faults.

Direct Observations of Paleoseismic Displacements

Two types of data can be brought to bear on the reconstruction of the history of past earthquakes. Direct observations of displaced or cross-cutting features provide unambiguous information about displacements. Such information can be stratigraphic, structural, or geomorphic in nature, and includes features such as faulted beds, offset stream channels, and raised beaches. Indirect indicators of earthquakes require a conceptual linkage between the observable data and the earthquake that caused it. In some instances the evidence reflects the coseismic offset itself, while in others it reflects other parts of the seismic cycle. For example, stratigraphic evidence of tsunamis or the chronology of rockfall deposits require an interpretation of their genesis in order to tie them into specific faulting events. We discuss the types of information that can be generated with direct observations first, and later examine several kinds of indirect paleoseismological observations.

Trenching

In order to provide a detailed record of past displacements and their timing, excavated trenches across faults often provide key insights. Overall, the basic practical objectives in trenches are 1) to identify and date layers within a stratigraphic succession that either have been disrupted by faulting or overlie fault traces without disruption, and 2) to document the amount of displacement in past faulting events. Sites for trenches have to be carefully chosen in order to maximize the useful information that they may generate. To the extent possible, trench sites should contain abundant datable material, and they should provide stratigraphic or structural markers that can be used to measure offsets. Typically, it is impossible to know what is likely to be found in the subsurface as a trench is excavated, so good judgment and good luck combine to create a data-rich excavation. Because radiocarbon dating is still the most frequently applied dating technique in trench analyses, it is not uncommon for trenches to be located in swampy areas where fault displacements have dammed up local streams or have ponded the groundwater table. In such circumstances, organic matter that can be dated using radiocarbon methods is more likely to be preserved within the young strata associated with the fault. Similarly, thinly bedded deposits are more likely to reveal discrete, measurable offsets than will massive deposits, such as debris flows, that are rather homogeneous in all directions. Thus, the likelihood of having a rich stratigraphic record can be enhanced by choosing sites of low-energy deposition and/or sites where it is expected that there will be linear stratigraphic markers preserved with which to measure offsets. For example, if relict lake shorelines or small-scale channels are oriented approximately perpendicular to a fault, they can offer particularly good stratigraphic markers or piercing points across a fault.

In trenches, the analysis of the stratigraphic record of earthquakes is typically a time-consuming process. Thus, the choice of sites for trenches is not a trivial exercise: you want the maximum information for the time invested. Trade-offs have to be made between competing objectives: obtaining more detailed information in a single segment of a fault, comparing rupture histories in different areas, obtaining maximum information on the magnitude of offsets, and developing the most extensive chronology of past events. Two different strategies are typically used for orienting trenches with respect to faults. In most situations, a single trench is excavated perpendicular to the trend of the fault. The stratigraphy and structures

FIGURE 6.1. Trenches on a strike-slip fault

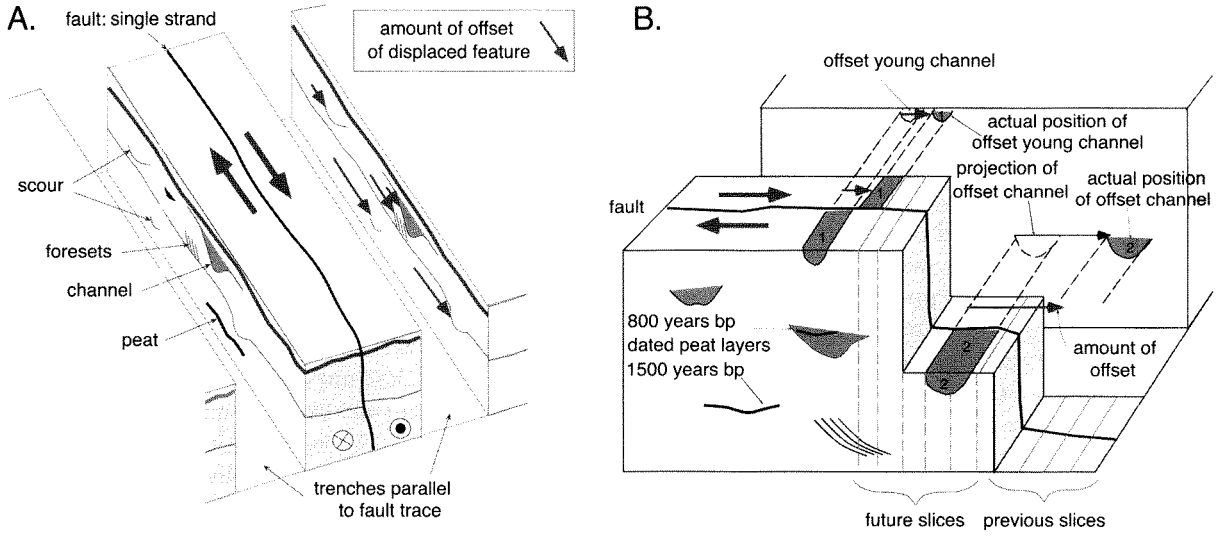

A. Orientation of trenches with respect to a strike-slip fault, when two trenches are employed to determine the history of previous ruptures. On the walls closest to the fault trace, the stratigraphy is carefully surveyed and material, such as peats, for dating is collected. Hypothetical amounts of offsets of stratigraphic markers are depicted by the arrows on the trench wall. Note the general downward increase in displacement. Despite their difference in stratigraphic height, the top two offset markers, a channel and a scour, have identical offsets because they were both displaced in the most recent earthquake. B. "Salami slicing" across the fault trace between two surveyed trenches. Offsets of linear features like channels are clearly revealed, and displacements of the margins of these features are measured in order to determine the amount of offset in individual earthquakes. Similar magnitudes of offset are expected for all of the features that were created between each successive pair of earthquakes. When the stratigraphy in the trench walls has been well dated, both the age and the displacement of past earthquakes can be quantified.

revealed in the walls of the trench are meticulously surveyed and mapped, material for dating of various stratigraphic horizons is collected, and a fault displacement history is interpreted based on these data. Alternatively, two trenches parallel to the fault trace are sometimes employed along strike-slip faults (Fig. 6.1A). The stratigraphy on the faces nearest the fault trace is mapped, surveyed, and dated in each fault. Special attention is paid to linear features, such as channels, planar crossbeds, shoreline features, or unusual bedding configurations, that trend approximately perpendicular to the fault. After mapping the two trench walls parallel to the length of the fault, the intervening strata that are cut by the fault are "salami sliced" perpendicular to the fault trace (Fig. 6.1), which is to say that they are incrementally cut back along vertical planes. Each stratigraphic feature that could act as a piercing point is traced to the fault and the magnitude of offset vis-a-vis the correlative feature on the opposite side of the fault is measured. Along a fault trace where multiple earthquakes are recorded and where the sense of offset has not changed between successive ruptures, the amount of the measured offset should increase with increasing stratigraphic age, that is, with depth in the trench. This increase, however, should not be steady; rather, it should be stepwise, such that between two stratigraphic horizons that correlate with different faulting events, all of the displaced features should display similar offsets (Fig. 6.2A). Each cluster of comparably offset features will be bounded by abrupt changes to smaller offsets above and larger offsets below, marking the accumulation of displacement in successive earthquakes. Ideally, the horizons that correlate with the abrupt changes will be well dated and hence will reveal directly the timing of previous earthquakes (Sieh, 1978).

FIGURE 6.2. Examples of stratigraphic and structural relationships that relate to past deformational events

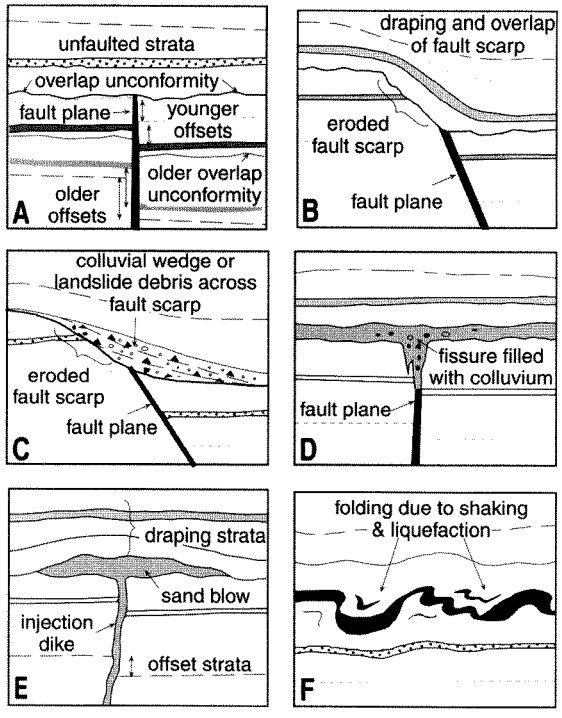

A. Strata offset across a fault are beveled by an unconformity and overlain by undisturbed strata. The unconformity developed after the last earthquake. The amount of displacement increases downward. The two different amounts of offset of strata and the presence of an older offset unconformity provide evidence for a previous earthquake. B. If the topography across a faulted surface is incompletely beveled off, succeeding strata will drape across the eroded fault scarp. They will be unbroken, but may appear deformed due to the topography on which they were deposited. Often they will show thickening above the downthrown fault block. C. Similar to B, but with a colluvial wedge derived from erosion of the upthrown block. D. Fissures that open along a fault plane are typically filled with colluvial material shortly after faulting. E. Injection dikes in the subsurface and sand blows or sand volcanoes on the surface provide evidence for past earthquakes. The age of the youngest strata cut by the dikes or underlying the sand blow provides a maximum age on the faulting. F. Liquefaction due to shaking can cause folding of weakly consolidated sediments near or at the surface. The age of the deformed beds provides a lower limit on the time of the earthquake that deformed them. Modified after Allen (1986).

The "salami slicing" approach can reveal detailed data on both the timing and magnitude of offsets in previous earthquakes along strike-slip faults. Even when the coseismic displacements are more than several meters in each rupture, a long trench can record multiple offsets. In fact, cumulative offsets of the oldest markers can be equal to the length of the trench. Many dip-slip faults that are of interest to paleoseismologists have displacements of 2 to 4 meters in individual earthquakes. In order to find the record of multiple ruptures in the past, trenches on dip-slip faults have to be deep, rather than long. A trench 10 meters deep might record only two ruptures, if the displacements were 4 meters in each event. The instability of trench walls (which must be shored up and braced) often imposes a practical limit on how deeply trenches can be dug, and therefore limits the number of previous rupture events that can be examined. As a result, the paleoseismic records in trenches of large thrust or normal faults are commonly limited to one or two events (Rubin et al., 1998).

Offset strata above dip-slip faults can present difficulties that are not present with strike-slip faults. Stratigraphy that is displaced by strike-slip faults is translated horizontally into new positions where the strata on both sides of the fault are often preserved. Thus, more sediments can accumulate above the displaced strata and piercing points recorded by the older strata will be preserved. On the other hand, when dip-slip faulting occurs, the strata on one side of a fault are upthrown with respect to the opposite side. In theory, it is the offset of the strata on opposite sides of the fault that will record the magnitude of displacement. Unfortunately for paleoseismologists, strata on the upthrown block are often subjected to subaerial erosion. Consequently, the specific stratal layers that could define the offset precisely can be eroded away (Machette et al., 1992), such that reconstruction of past displacements becomes considerably more difficult.

In order to reconstruct the history of offset that is recorded by strata within a trench, stratigraphic and structural relationships revealed in the walls have to be interpreted. As with traditional structural geologic studies, cross-cutting relationships can provide unambiguous evidence of past deformation (Fig. 6.2). For example, if older strata are cut by a fault, but overlying younger strata are continuous across the trace of the fault, an earthquake is interpreted to have occurred between deposition of the youngest strata that are cut by the fault and the oldest strata that are not displaced by it. If these strata can be dated, they provide bracketing ages on the faulting event.

One goal of paleoseismic studies is to determine the amount of coseismic displacement from the apparent offset of strata exposed in a trench wall. To do this, the direction of slip along the fault must be known. Consequently, indicators of the slip direction, such as striae, slickensides on the fault plane, fold axes of deformed strata, or the displacement of piercing points, should be sought. Progressively larger structural offsets of stratigraphic horizons farther beneath the unconformity or the identification of older offset unconformities can indicate both the timing and magnitude of earlier earthquakes (Fig. 6.2A). Topographic scarps formed during faulting events are rapidly "attacked" by erosional forces. If the scarp forms in an area where active deposition is occurring all around it, the scarp is likely to be draped with younger strata soon after the rupture (Fig. 6.2B). If the scarp forms in a predominantly erosional environment, its upthrown side will be steadily eroded and will often provide colluvial debris that accumulates along the degrading scarp as a *colluvial wedge* on the locally downthrown block (Fig. 6.2C). During strike-slip earthquakes, there may be relatively little differential vertical motion, but movement along the irregularly shaped fault plane will cause fissures to open in places (Fig. 6.2D). These fissures are open to the surface and typically fill quite rapidly with colluvial, alluvial, or aeolian debris. In repeated ruptures, fissures may re-open with each rupture (Sieh et al., 1989). Consequently, a single fissure with multiple filling events may record several different earthquakes (Fig. 6.3). Seismic shaking can cause liquefaction of sediments having a high water content (Fig. 6.2F). Liquefied sand represents a slurry of sand and water which may be "erupted" on the surface to form sand blows or sand volcanoes (Fig. 6.2E).

FIGURE 6.3. Fissure filling showing evidence for three earthquakes

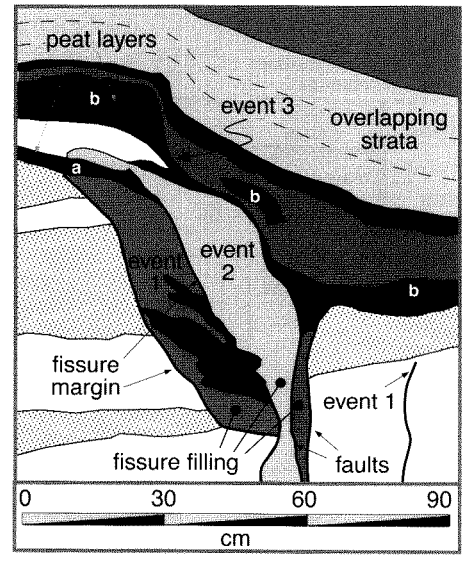

Event 1 caused a fissure to open. The fissure-filling post-dates the event, contains some datable peat, and is overlain by peat "a." Event 2 re-opens the fissure and cuts peat "a." Event 2 is overlain by peat "b," which is cut along a small fault along the fissure trend during Event 3. Despite its complexity, this is a good example of the detail that can be extracted from a good exposure and provides some insight into how overlapping, cross-cutting, and fracture-filling relationships can be exploited. Modified after Sieh et al. (1989).

The interpretation of the stratigraphy and structures found in trenching sites is often not straightforward. In some fortunate circumstances, clear cross-cutting relationships and abundant material for dating are present (Fig. 6.4). At such sites, ruptures of older strata and draping or erosion across the upper termination of fault strands provide direct evidence for faulting. Even in these conditions, it is important to remember that faults don't always propagate to the surface and that new ruptures can form in successive earthquakes. Thus, a newly formed fault splay may branch out from the main rupture and terminate at some random level in the subsurface in an isolated outcrop or trench. In this case, the undisturbed layers overlying the fault termination will pre-date the faulting event, which is the opposite of the case when undisturbed layers depositionally overlie a fault termination. Consequently, in examining fault terminations, it is important to seek evidence for surface erosion across the fault trace, for bed thickness changes above the fault termination that indicate the filling of small-scale topography related to the fault, for discrete groupings of the amounts of stratal offsets found in older layers cut by the fault (indicating that deposition was synchronous with faulting and that previous earthquakes had occurred on the fault), and for significant displacement on the fault just below the undisturbed layers, rather than a progressive dying out of displacement along the fault. If it can be shown that the same stratigraphic level in several places overlies fault traces, it is likely that this represents a fault that did propagate to the surface.

FIGURE 6.4. Record of normal faulting along the Wasatch fault bounding the Wasatch Range near American Fork Canyon, Utah

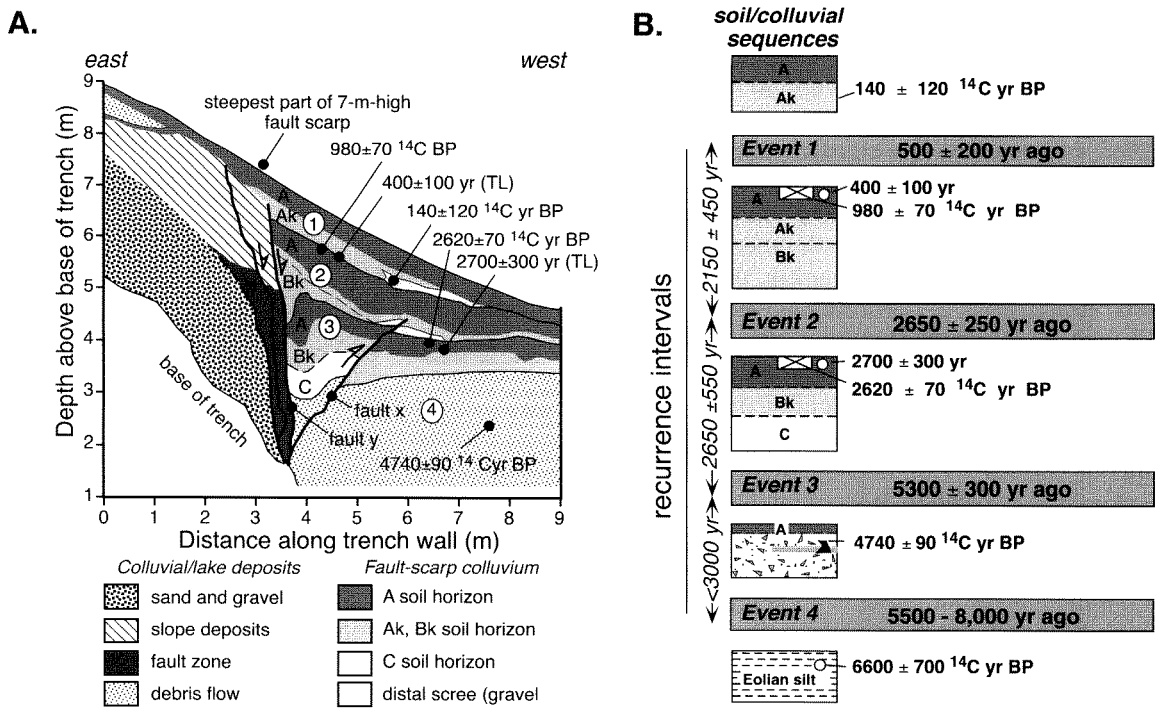

A. Evidence for three faulting events is revealed in this trench. The excavation is > 9 m deep, and yet, because markers typically show 1–3 m of offset per earthquake, only three rupture events are recorded here. A repetitive soil zonation (A – Ak ± Bk) delineates the top of each of three colluvial wedges (labeled 1 through 3). The magnitude of offset for each wedge can be estimated by restoring the top surface of the wedge back to the ground surface such that the "A" soil horizon is continuous onto the upthrown block. Radiocarbon and thermoluminescence dates are used to constrain the timing of faulting events. Cross-cutting relationships with faults and soils define rupture events. Fault "x" cuts soil sequence 3 and is overlain by sequence 2. Fault "y" cuts soil sequence 2 and 3, but is overlain by sequence 1. Note that with the exception of the lowest and topmost stratigraphic units on the downthrown side, none of the downthrown strata are represented on the upthrown block. B. Interpretation of the rupture history based on the trench stratigraphy. Evidence for the oldest faulting event is based on a nearby trench. Note that on the trenched segment of the Wasatch fault, the ruptures appear to be evenly spaced in time, but the magnitude of rupture varies, with the latest offset (~1 m) being about half as large as the offsets during the previous two events. Modified after Machette et al. (1992).

The stratigraphy of soils can provide useful controls on the interpretation of trench stratigraphy. For example, colluvial wedges (Figs. 6.2C and 6.4) are often associated with dip-slip faults. Each colluvial wedge is commonly interpreted to result from a single rupture of the bounding fault (Machette et al., 1992; Schwartz and Coppersmith, 1984). Steepening of slopes, localized uplift, or overthrusting of the land surface along a rupture plane destabilizes weakly consolidated surface strata. Quaternary sediments that have been uplifted to a higher topographic position along these steepened slopes quickly erode and produce colluvial wedges which accumulate along the toe of the exposed scarp. If the faulted strata are well consolidated, they may maintain steep faces for many centuries. Nonetheless, it is commonly assumed that raveling of a steepened slope occurs rather quickly (about 100 years in many sediments), such that not long after faulting, the surface of a

colluvial wedge is at or below the angle of repose for unconsolidated debris (~30°) and the deposition rate is low enough for pedogenic processes to begin to develop soil zonations (A, B, K horizons). Recognition of such soil horizons in trench walls pinpoints the upper surface of colluvial wedges formed during earlier earthquakes and delineates some of the vertical extent of the wedges (Fig. 6.4A). Particularly in colluvium that is poorly stratified and contains few stratigraphic horizons with which to judge offsets, even subtle soil horizons provide markers for delineating displacements. In addition, the degree of soil development can be related to the interval between earthquakes, that is, the time from first stabilization of the colluvial wedge to its burial by the next youngest wedge (Fig. 6.4B).

Many fault zones actually have more than one fault strand at the surface. In order to account for all of the displacement along a fault zone, it is necessary to identify all of the strands or surface traces, and a paleoseismic record for each should be developed. It is not uncommon for strike-slip faults to splay into several branches as they approach the surface. Sometimes these splays all occur within a fairly compact zone for which a single trench or small set of trenches will reveal the entire displacement record (Fig. 6.5A). However, when strands are separated by tens or hundreds of meters, each has to be examined separately. In compact zones with multiple splays (Fig. 6.5B), it is often very informative to locate a distinctive marker bed and map its displacement across each of the strands (Lindvall et al., 1989).

Dating of fault-disrupted strata in trenches forms the basis for determining the timing of individual ruptures, which in turn is the basis for assessment of recurrence intervals. It is always wise to generate as many reliable dates as possible for a given stratigraphy, particularly if it will underpin key interpretations of the seismic record. Radiocarbon dating of buried organics is still the most commonly used dating technique in trenches. Given analytical uncertainties in laboratory analyses, the possibility of contamination with young carbon, and the background variations in atmospheric carbon in the past (see Chapter 3), each radiocarbon date should be carefully interpreted. Combining different dating techniques, such as radiocarbon with thermoluminescence, can provide a check on the consistency of dates. In a trench along the normal fault along the Wasatch front (Fig. 6.4), for example, some radiocarbon dates vary by 400 to 700 years from their calendar ages. These temporal offsets can be assigned from the calibration curve for radiocarbon ages (Stuiver and Reimer, 1993), but it is also reassuring to have another estimate of the age of the strata from a different dating approach. In the Wasatch trench, thermoluminescence dates (Fig. 6.4A) reinforce the interpretation of the radiocarbon dates.

FIGURE 6.5. Trenching a strike-slip fault with multiple splays

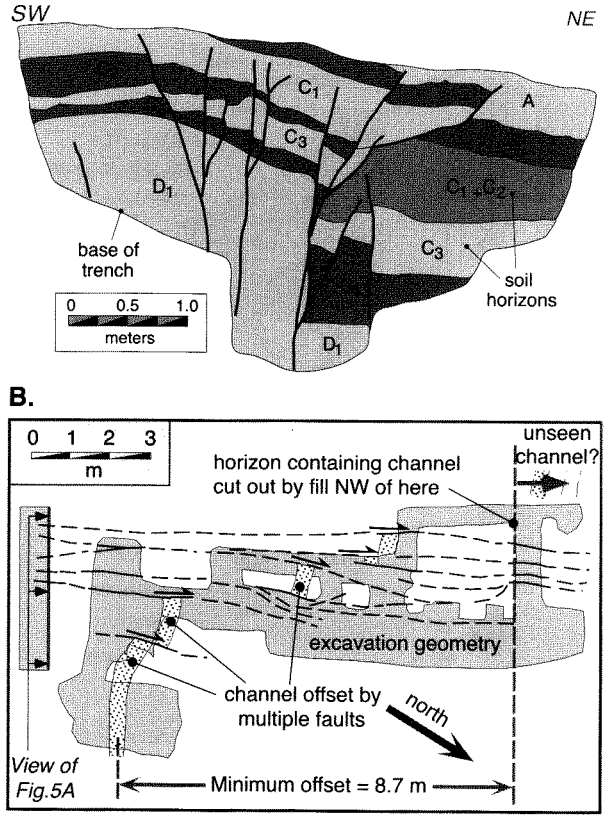

A. Sketch of a trench wall oriented approximately perpendicular to a suite of splays along a strike-slip fault. This outward branching geometry or "flower" structure displays 10 different splays across a zone ~3 m wide. Not all splays have been active in each earthquake. Note, for example, two faults on the right cut the upper B_t soil horizon, whereas the other splays do not. For orientation of the trench, see Fig. 6.5b. Modified after Lindvall et al. (1989). B. Displacement of a marker horizon (a fluvial channel) across multiple splays of a strike-slip fault. Map shows a network of shallow trenches that reveals the offset of the marker channel. Across any strand, the offset is typically 1–3 m, but the cumulative offset is > 8 m. Modified after Lindvall et al. (1989).

In most trenches, the strata that contain datable material do not consistently coincide with the strata that record rupture events. In such cases, dates on strata above and below the "event horizon" are used to bracket its age. In order to reduce the uncertainty in timing as much as possible, datable material should be sought as close as possible to the rupture horizon, and the highest laboratory precision available should be used to reduce the analytical uncertainty on the individual ages (Atwater et al., 1991; Sieh et al, 1989). Concerted efforts to provide the best possible time control are warranted, because reliable calculations of recurrence intervals are highly dependent on the quality of the ages assigned to rupture events.

Recent studies along the San Andreas fault clearly illustrate the importance and utility of high-precision dating. Because the San Andreas fault runs near or through several of the major population centers in California and because it has generated "great earthquakes" (magnitude 8) in the past, there is great interest in knowing 1) how often earthquakes occur along it; 2) the length, displacements, and spatial patterns of past ruptures; and 3) the recurrence interval between major earthquakes. During the past 30 years, much effort has gone into paleoseismological studies along many parts of this major plate-bounding fault. Some of the earliest insights on recurrence intervals of San Andreas faulting came from trenches dug at Pallett Creek about 55 km from Los Angeles (Sieh, 1978). Several subsequent studies have attempted to improve on the dating of the faulting events at this site, where 11 major earthquakes are recorded. A comparison of the faulting chronologies published in 1984 (Sieh, 1984) and in 1989 (Sieh et al., 1989) is illuminating (Fig. 6.6). Based on the 1984 data (Sieh, 1984), the recurrence intervals between major earthquakes fall into two groups: prior to about 1100 A.D., the recurrence interval was about 100 years, whereas from 1100 A.D. to the present, the interval lengthens to 160–200 years. Within each grouping, the resolution of the radiocarbon dates suggests that the earthquakes may have been approximately evenly spaced in time. When radiocarbon dates with higher precision are used to date the earthquakes (black bars, Fig. 6.6), a rather different rupture history emerges (Sieh et al., 1989). Rather than being evenly spaced in time, the earthquakes appear to cluster. Two or three earthquakes appear to have occurred during spans of 100–200 years, whereas each cluster is separated from the succeeding cluster by an earthquake-free interval of 150–300 years. The uneven temporal spacing of San Andreas earthquakes presents a challenge to seismologists trying to understand rupture physics and recurrence intervals. Moreover, the clustering of events suggests that seismic risks along this segment of the San Andreas are very different than previously thought. Based on the 1984 data, it was thought the earthquakes were regularly spaced in time and had a recurrence interval of about 140 years. Given that the last large rupture in this area was in 1857, this scenario would suggest that the next big rupture could be imminent. In contrast, the 1989 data suggests that, because clustered earthquakes commonly occur within a few decades of each other and because no major rupture has occurred in the past 140 years, we

FIGURE 6.6. Recurrence intervals as determined by radiocarbon dating for major earthquakes along the San Andreas fault at Pallett Creek, California

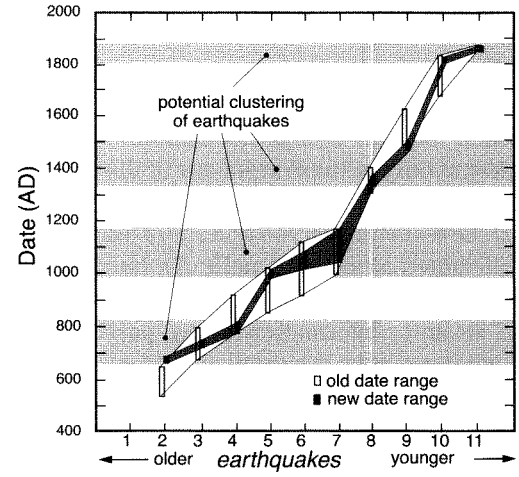

The dates published in 1984 (open boxes indicate the time range of each date) suggest two groupings of earthquakes. In each group, the earthquakes are evenly spaced in time, but prior to ~1100 A.D., they had a recurrence interval of ~100 years, whereas from 1200 A.D. to present, the recurrence interval was 150–200 years. Higher precision dates published in 1989 indicate a distinct clustering of earthquakes (shaded bands) into groups of two or three ruptures each that were separated from each other by a few decades, whereas the clusters themselves are separated from each other by 100–300 years. The higher precision dates define a step-like event-versus-time curve (dark shading), as opposed to the smoothly changing curve (no shading) comprising the less precise dates. Modified after Sieh et al. (1989).

are presently in one of the quiescent periods between clusters and that this quiet period could last for another 100 years!

Displaced Geomorphologic Features

Although detailed stratigraphic records in trenches can provide constraints on multiple earthquakes in the past, each trench requires a large investment of time and is most relevant only to those segments of the fault directly adjacent to it. Offset geomorphic features, on the other hand, can be readily observed and surveyed, and they are often distributed along the length of a fault. Thus, such features provide a means to document the spatial variations in seismic deformation along past ruptures. In alluvial environments, typical displaced geomorphic features include stream channels, terrace risers, channel walls, debris flows and their raised levees, small alluvial fans, ridges, and gullies. In coastal environments, displaced features could include beach ridges, coral platforms, delta plains, and wave-cut notches.

Terrestrial Settings

Although it is often possible to obtain a rough estimate of the amount of displacement of a displaced feature with a tape measure, it is almost always preferable to create detailed topographic maps of displaced features and the area surrounding them because these permit a more rigorous geometric reconstruction (Fig. 6.7A). Typically, such maps are constructed using a theodolite with a built-in electronic distance measuring device (an EDM or "total station"). In many field situations, displaced features no longer directly intersect the fault plane because slope processes have either eroded or buried part of them. In such cases, the trend of a feature, as represented by planar surfaces, such as terrace risers, or by linear features, such as debris-flow levees or the intersection between a terrace tread and riser, has to be projected onto the fault plane (Fig. 6.7A). To the extent possible, a structure contour map of the fault plane should also be constructed, especially with dipping faults. In order to measure a horizontal offset, once the fault plane is specified, the distance is measured between the projections of linear features on to the fault plane after any vertical component of offset is subtracted. Clearly, the vertical displacement must also be measured, and this can be done using a similar methodology, but is based on projections of subhorizontal features, like terrace treads or channel bottoms, on to the fault plane. With a detailed topographic map, often the uncertainties in such a projection can be estimated and incorporated into the displacement estimate (Fig. 6.7A).

In order to obtain reliable estimates of past offsets, care must be taken either to choose features that have been little modified since they were displaced, or to reconstruct accurately their post-seismic evolution. For example, when the channel walls along a stream are offset along a strike-slip fault, one side of the displaced channel in the downstream direction will have been moved more directly into the path of the stream and is likely to be strongly modified by erosion, whereas the other side of the displaced channel will be sheltered from erosion (Fig. 6.7B). These protected features provide the most reliable estimates of displacements.

In theory, every large earthquake on a fault could be represented by a suite of displaced features. In order for this to be true, some new geomorphic markers would have to form in the interseismic interval between faulting events, and older markers that were displaced previously would have to be preserved until the time of measurement. Such conditions are not uncommon, because each seismic displacement commonly forces some aspects of the geomorphic system to adjust, thereby producing new markers. In natural landscapes, therefore, one might expect to find numerous markers that had been displaced in the most recent earthquake, a lesser number displaced during the penultimate rupture, and so forth. Such landscapes could be described as *palimpsest* landscapes in which the imprint of older features is only partially overprinted or obscured by younger features. In addition, the size of the offset may not be large enough relative to the scale of the geomorphic feature to have altered it significantly, or to have caused its abandonment. This ratio of scales is therefore important in determining if a particular landscape will record individual coseismic offsets, or if instead it will record only the long-term average slip on the fault, smearing out the effects of individual events.

Clearly, the record of offset features represents an interaction between the processes that create geomorphic markers and the tectonic events that displace them. The variability of climate suggests that some intervals will be more conducive than others to the formation of clear geomorphic markers. For example, during times of fluvial incision, many steep-sided geomorphic features, such as channel walls, terrace risers, and gullies, are etched into the land surface and gently dipping features like terrace treads are left behind, whereas during aggradational phases, broad alluviated surfaces provide fewer

FIGURE 6.7. Use of offset terraces and channels to define fault displacements

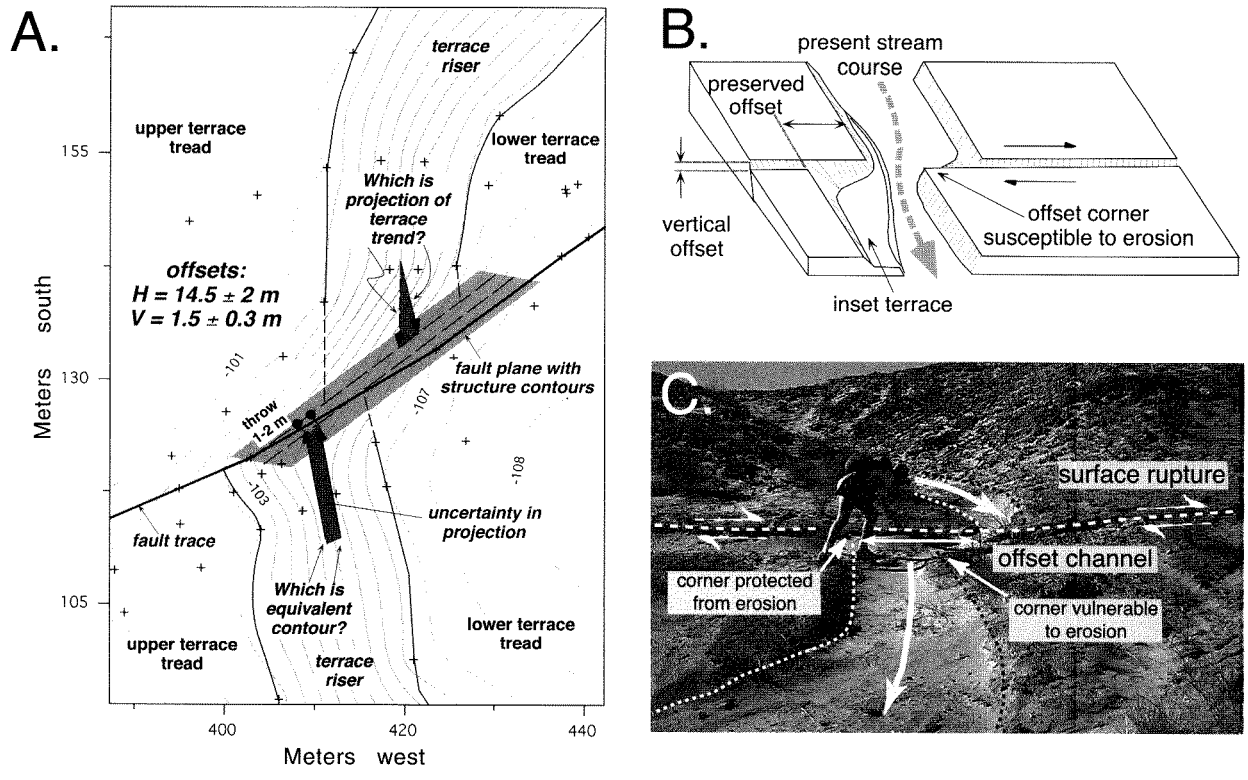

A. Gridded and contoured topographic map of late Holocene terrace riser offset by Awatere Fault at Grey River, Awatere Valley, New Zealand. Map derived from total-station measurements. Dashed lines subparallel to the fault are two structure contours on the fault plane which is dipping to the SSE (contour interval 1.5 m). Top structure contour on the fault plane is at the same elevation as mid-riser contour on the south side of fault that is used to project the position of the terrace riser on to the fault plane. Lower structure contour on fault is 1.5 m lower down (mean throw on both the lower and upper terrace surfaces). Shaded uncertainty region on S side fault is uncertainty in projection of riser contour to eroded fault surface on upthrown (SE) side of fault. Shaded uncertainty belt on north side of fault represents uncertainty in knowledge of which contour on N side of fault originally corresponds to the south-side riser contour prior to displacement. This is the same as the uncertainty in throw for the lower terrace surface (± 0.3 m). Modified after Little et al. (1998). B. Sketch of the geometry of the displaced channel wall and terrace and the optimal position in which to measure offset along the fault. The offset "corner" to the right of the stream is likely to be modified by erosion as the stream impinges on it. Therefore, it is far better to measure the displacement based on the protected channel wall on the opposite side of the channel. Modified after McGill and Sieh (1991). C. Ephemeral channel offset by dextral slip during the Superstition Hills earthquake. Note that the downstream channel margin on the right is vulnerable to erosion, such that the magnitude of offset could be underestimated.

distinctive features that could serve as geomorphic markers. Moreover, aggradation can cause burial of offset features, and thus obscure the record of older earthquakes. As a consequence of these climatically controlled contrasts, earthquakes that occurred after intervals of incision are likely to be more clearly represented in the geomorphic record than are those that occurred during times of aggradation. Paleoseismologists exploit these contrasting regimes of incision and deposition. The offset geomorphic features of incisional areas allow ready identification of faults, whereas places where faults cut areas of active deposition are ones where the fault trace may be obscure, but the past record of earthquakes can be discerned through trenching.

FIGURE 6.8. Displacement of geomorphic markers with respect to distance along a strike-slip fault

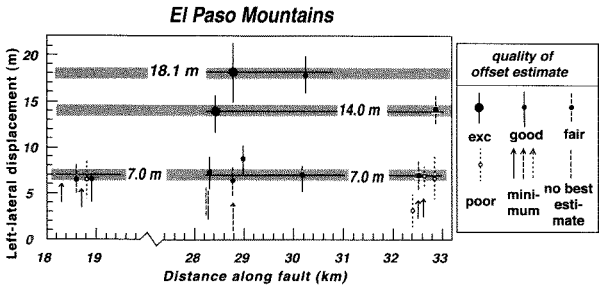

Plot of displaced markers along the Garlock fault: a sinistral strike-slip fault bounding the northern margin of the Mojave Desert, California. Note that there appear to be three groups of displaced markers: —7m, 14 m, and 18 m—and that there appear to be fairly consistent offsets all along this segment of the fault. Modified after McGill and Sieh (1991).

FIGURE 6.9. Histogram of displacements in the vicinity of Pilot Knob valley along the Garlock fault

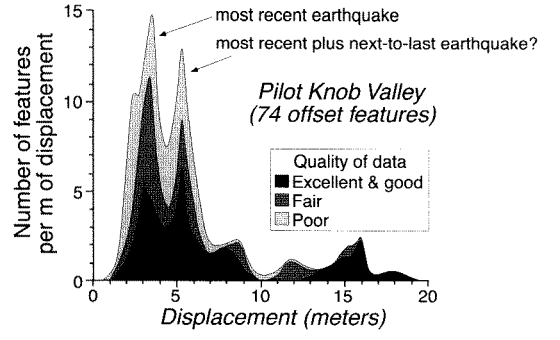

Each displacement is represented as a Gaussian probability density function with a mean equal to the measured offset and a standard deviation equal to one half of the uncertainty in the offset. The Gaussian functions are summed to create the histogram. The peak for the smallest displacement (~3 m) is interpreted to represent offsets in the last earthquake. Peaks at ~5.5 m and ~8 m have been interpreted to represent cumulative offsets after two and three earthquakes, respectively. Modified after McGill and Sieh (1991).

How is a catalogue of displaced features along a fault transformed into a useful estimate of paleoseismicity? First, the magnitudes of displacements are plotted as a function of distance along the fault (Fig. 6.8). Such a plot will clearly show whether there are consistent patterns of offset along the fault, whether the displacements fall into discrete groups, and whether there is evidence for decreases in displacement toward the terminus of the rupture. Given the bow-shaped displacement variations that appear to typify many faults, it might be expected that diminishing amounts of displacement would help to define the ends of past ruptures. More commonly, however, mapped fault terminations, jogs in the fault trace, or step-overs are used to define segment boundaries.

Second, histograms of the magnitude of displacement and the reliability of each measurement are constructed for all of the displaced features along a fault. If a segment of a fault were typified by repetitive ruptures of similar magnitudes, then histograms of displacements along that segment would tend to display groupings of offsets that were multiples of each other. For example, repetitive offsets of comparable amounts occur along individual segments of the Garlock Fault (Fig. 6.9) in southern California (McGill and Sieh, 1991). When displacements are compared among neighboring segments of the fault, however, there are distinct contrasts in the average displacements on each segment (McGill and Sieh, 1991). Whereas such data might be interpreted to indicate that each segment of the fault displays "characteristic" earthquakes (Schwartz and Coppersmith, 1984), a more conservative approach would simply define a mean coseismic offset for each segment. Obviously, if the displacement histograms display more than one peak and are interpreted to record more than one earthquake, there should be some geomorphic evidence indicating that those features showing greater displacements relate to older earthquakes in comparison to features along the same fault segment with smaller displacements.

Third, given the length of each ruptured fault segment and the mean displacement along it, a seismic moment can be estimated, if the depth of the fault and a crustal rigidity are assumed or known (Equation 6.3). Often, the local depth of the seismogenic layer is relatively well known, and because most large earthquakes will rupture through the entire seismogenic layer, reasonable estimates of the seismic moment can be made. Various rupture scenarios can be evaluated along a segmented fault, ranging from rupture of its entire length

to rupture of the shortest segment (McGill and Sieh, 1991). In each case, the mean displacements for the relevant fault segment are fed into the calculation, and the moments for each segment are summed to yield a total seismic moment and moment magnitude for the rupture scenario. Such an approach clearly provides a very useful data set for assessing seismic hazards along such a fault.

Whereas the data from trenches often allow determination of when past ruptures occurred and sometimes permit the magnitude of offset to be determined, geomorphic studies of offset features clearly define displacements, but often say little about timing or recurrence intervals. There are at least two ways to address the issue of timing. The most obvious approach is via direct dating of the offset features. With several such ages, it is often possible to define the interval during which past earthquakes occurred and to place constraints on the recurrence interval between them. Alternatively, if mean slip rates across a fault are known, the magnitude of measured displacements can be divided by the long-term slip rate to obtain an estimate of the recurrence interval. The mean slip rate could be derived either from geodetic measurements at the decadal scale or from longer-term rates based on displaced and dated Quaternary features, such as strandlines or terraces.

One potentially controversial aspect of using multiple offset features to characterize fault displacements in several different earthquakes is the fact that the age of most, if not all, of the features is usually unknown. At some sites, it may be possible to show that there are two or more sets of features that are displaced by distinctly different amounts and that can, therefore, confidently be interpreted to represent two or more earthquakes. More commonly, individual displacements all along the fault are amalgamated and compared with little knowledge of their relative age. If they seem to fall into clusters, especially ones with displacements that are multiples of each other (Fig. 6.9), there is a natural tendency to interpret each cluster as representing a past earthquake. Although this seems reasonable, data from the recent Landers earthquake (June, 1992, $M_w = 7.3$) in southern California suggest that there are pitfalls with this approach. Although the total Landers rupture was approximately 85 km in length, the map pattern clearly indicates that the rupture comprises an elongate zone of several known faults that were linked together either by previously unrecognized or by newly formed faults. Mapping of offsets along one of the previously known faults (central Emerson fault: Fig. 6.10A) showed there were

FIGURE 6.10. Measured displacements along a 5-km segment of the South Emerson fault resulting from the 1992 Landers earthquake

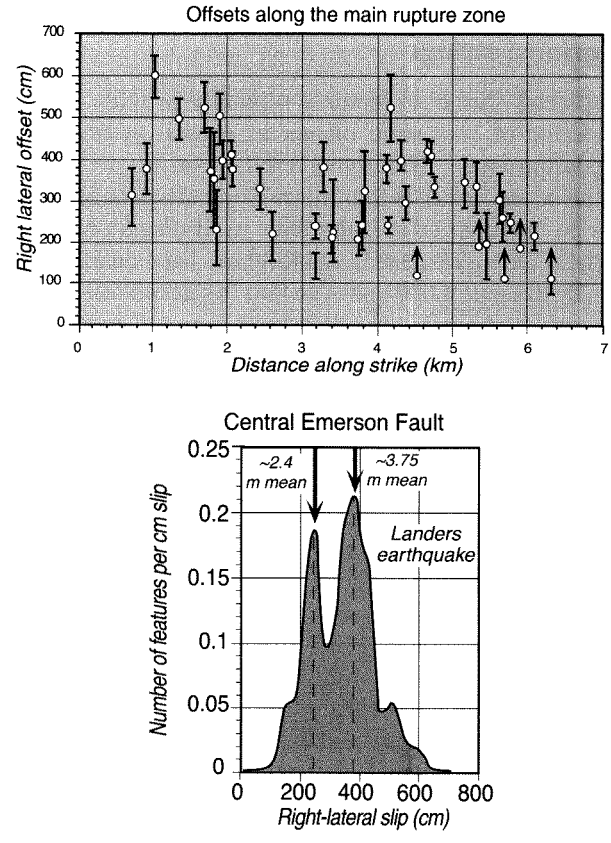

A. These data were collected shortly after the rupture and include ephemeral linear features, such as tire tracks, that were offset by the earthquake.
B. Histogram of displacements (represented as Gaussian probability density functions) along the South Emerson fault. Note the bimodal nature of the histogram which would typically be interpreted to have resulted from two earthquakes, rather than one. Modified after McGill (1994).

abrupt changes in the amount of offset along its 5-km-long trace (McGill, 1994). Numerous ephemeral features, such as offset tire tracks, indicate that the displacements all occurred during the 1992 earthquake. When the displacements were synthesized in a histogram, however, they showed two discrete peaks (Fig. 6.10B) at about 2 and 4 m. In a paleoseismic study, such peaks would probably be interpreted as being due to two different earthquakes, rather than resulting from variations along a short rupture

during a single event. Although the integral difference between these offsets is probably an uncommon case, clearly, some caution is warranted when interpreting histograms of offset features.

Marine Settings

Displaced shoreline features typically provide the best evidence of coseismic offsets in coastal settings. One appealing aspect of studying coastal features, in addition to the ocean vistas, is that information about deformation can be obtained even if the fault itself doesn't break the surface. On a global basis, sea level has been nearly steady during the past 6,000 years, so that displaced features can be evaluated against the reference frame of modern sea level. The nature of appropriate displaced features varies from one site to another and depends on the geomorphology of the Holocene beach.

Along uplifting coasts bounded by coral reefs, coseismic uplift causes a relative sea-level fall and exposes the seaward faces of fringing and barrier reefs to wave attack. The shape of the resulting platform depends on the geometry of the reef at the time of emergence, its orientation with respect to waves, and the time between successive uplift events. For example, as sea level rose and stabilized in the early and mid-Holocene in Papua New Guinea (Ota et al., 1993), transgressive fringing and barrier reefs first grew upward and then outward, so that by the mid-Holocene, the reef crest was up to 500 m wide, but was bounded by relatively steep forereef slopes (Fig. 6.11). Following coseismic uplift events, waves attacking the dipping forereef area typically carved a notch just above sea level in the transgressive limestone. Broader surf benches (as much as 100 m wide) were formed 10–40 cm above the high-tide level, especially across the broader parts of the transgressive reef crest (Fig. 6.11). Shallow pools with living corals developed along the surface of these benches, while encrusting corals may also have colonized the much narrower wave-cut notches or the subtidal spur-and-groove topography (Ota et al., 1993).

The amount of uplift during successive seismic events can be easily derived from surveyed heights of the benches and notches with respect to analogous features forming at the modern high-tide line. Whereas the presence of corals which colonized these features should provide a ready means to date them, such dating is not always straightforward, because both the substrate and the encrusting organisms are corals. Commonly, suites of dates from the benches and notches contain ages related both to the

Figure 6.11. Surf benches and wave-cut notches resulting from coseismic uplift in Papua, New Guinea

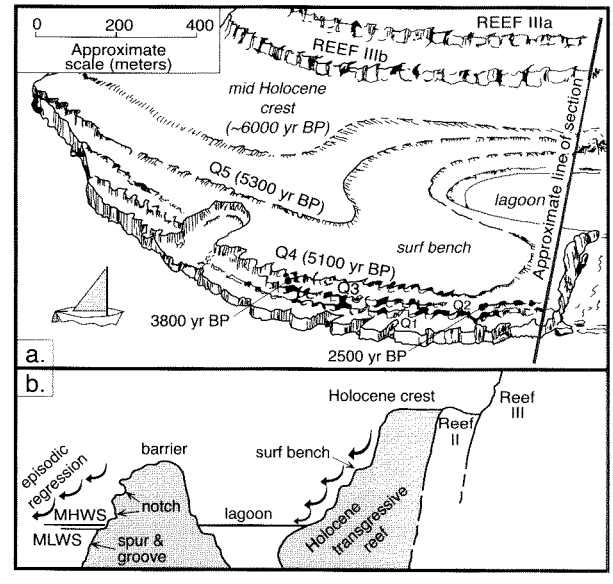

A. The mid-Holocene reef crest (~6000 BP) was broad because the fringing reef and barrier reef had merged. Unusually wide surf benches developed following the first two or three seismic events at 5300, 5100, and 3800 yr BP. Notches and narrow benches characterize the last two earthquakes and the steeper part of the reef faces. B. On the steep, seaward face of both the fringing and barrier reef, wave-cut notches mark each regressive episode related to faulting. For location of section, see A. MHWS: mean high-water spring tide level; MLWS: mean low-water spring tide level. Modified after Ota et al. (1993).

Holocene transgression, as well as to the seismically triggered regression events. With sufficient dating, these two groups can usually be distinguished: ages related to the transgression become younger with higher elevation, whereas ages related to coseismic uplift since the maximum transgression become younger with lower elevation (Fig. 6.12A). By combining dating, mapping, and correlation along tropical coastlines, it is possible to develop reliable reconstructions of the number, timing, and displacements of past seismic events, as well as to depict patterns of differential tilting and uplift.

The timing and magnitude of Holocene coseismic coastal deformation can sometimes be utilized in a predictive sense. Consider, for example, the circumstance in which the age and offset in successive events

FIGURE 6.12. Chronologies of coseismic regression and uplift in coastal areas

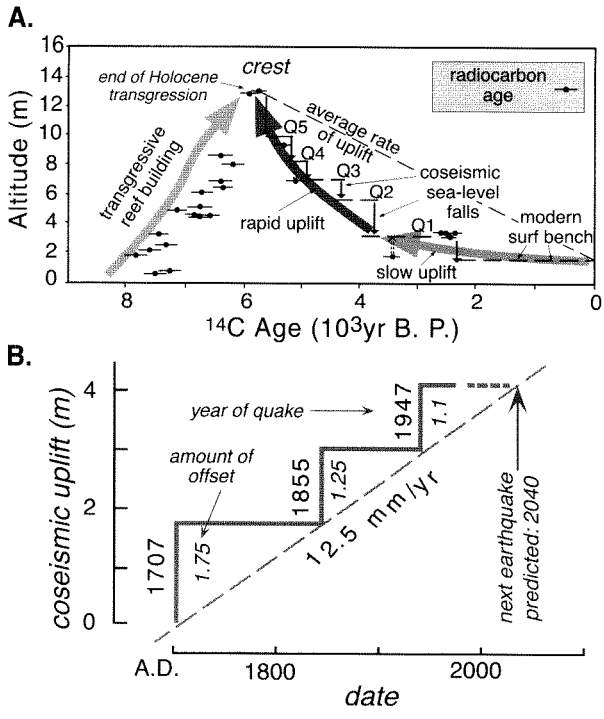

A. Radiocarbon ages on transgressive reef and coseismic regressions, Papua New Guinea. Between 8 ka and 6 ka, the reef built upward 12 meters as sea level rose. By 6 ka, sea level had stabilized and a wide reef crest developed. Surveyed and dated benches and notches indicate five earthquakes have occurred since 6 ka. Their spacing is irregular in time: four occurred between 6 ka and 3 ka, while only one has occurred since then. Presumably similar coseismic regressions created benches prior to 6 ka, but these would have been submerged during the ongoing transgression. Modified after Ota et al. (1993). B. Time-predictable coseismic uplift from southwest Japan. The offset and timing of previous earthquakes define a steady uplift rate, such that the timing of each successive earthquake is predicted by the amount of offset in the previous earthquake. This rupture sequence suggests the next earthquake should occur around 2040. Modified after Lajoie (1986).

sum together in such a way as to define a constant long-term uplift rate (Fig. 6.12B). If the previous earthquakes define a time-predictable sequence (see Fig. 4.5), then it should be possible to predict when the next earthquake will occur. Alternatively, if previous offsets define a displacement-predictable uplift, then the coseismic displacement of an earthquake at any time in the future can be predicted. For example, a coastal record of coseismic uplift for three earthquakes in southwest Japan since 1707 (Fig. 6.12B) appears to define a time-predictable pattern of uplift at an average rate of 12.5 mm/yr (Lajoie, 1986). The magnitude of displacement in the most recent event (1.1 m in 1947) divided by the mean uplift rate indicates the next earthquake should occur about 90 years after the previous one, or around 2040.

In some reefal settings, detailed reconstructions of both coseismic and interseismic deformation are possible. (Recall that except for permanent deformation, the coseismic movements should be equal and opposite to the interseismic displacement.) Hemispheric heads of corals that are coseismically uplifted die back to the new high-tide line, and wave attack may slightly erode the sides of the subaerially exposed dome (Zachariasen, 1998). Meanwhile, new corals grow upward and outward along the new waterline and create a fringing platform around the coral head (Fig. 6.13). During slow submergence in the interseismic interval, these corals continue to grow upward, such that the upper part of the "fringing reef" is separated from the dead coral of the previously emergent part of the head by a small unconformity. When a new earthquake occurs, the "fringing reef" will become emergent and will die, and a new fringing platform will develop. Imagine the detailed paleoseismic record that can be extracted from such a site! All you need is an underwater chainsaw to slice open a coral head in order to document the amount of coseismic emergence and interseismic subsidence in each previous earthquake cycle. Because many corals show annual growth rings, it is possible to pinpoint when these events occurred. Moreover, with new high-precision ^{230}Th dating techniques (Edwards et al., 1988), it is possible to date corals with far greater accuracy than is possible with radiocarbon dating. New insights into the seismic cycle of earthquakes during the past several thousand years in large subduction zone settings promise to emerge from such studies.

Unfortunately, coralline reefs and the paleoseismic records derived from them are available only in tropical regions. Elsewhere we typically have to rely on erosional, rather than constructional, features. In some mid- and high-latitude sites, marine platforms are rapidly carved into readily eroded coastal rocks. Successive Holocene earthquakes can uplift these platforms and provide a record of coseismic deformation that is analogous to that derived from the notches and surf benches in the

Figure 6.13. Schematic representation of the growth of a hemispheric coral head during several seismic cycles

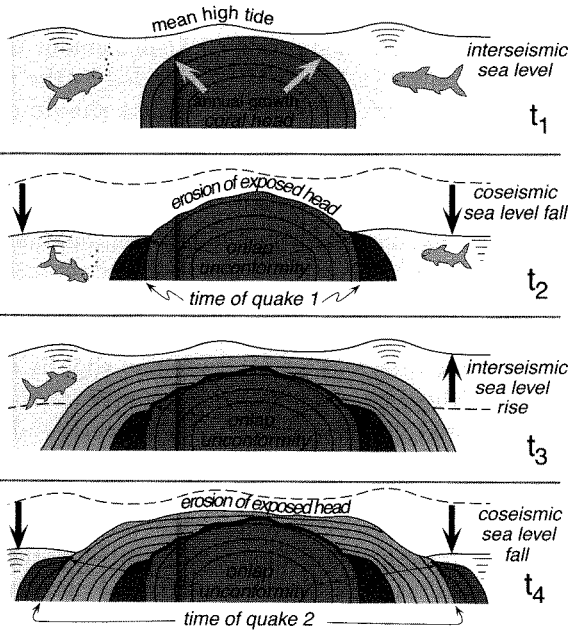

Subsidence during the interseismic interval allows the reef to grow upward (t_1). Following coseismic uplift, a fringing platform develops and the exposed coral head is partially eroded (t_2). Interseismic subsidence allows the coral to grow upward again and mantle the unconformity surface (t_3). A new fringing platform develops following coseismic uplift (t_4).

Figure 6.14. Schematic cross section of raised beach ridges at Turakirae Head, New Zealand

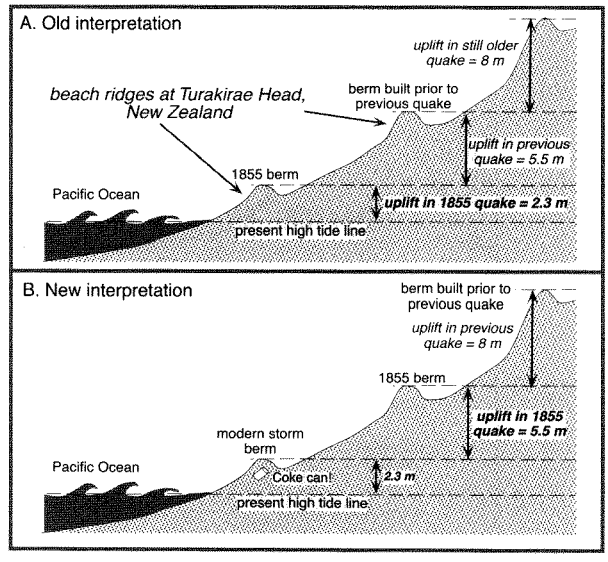

In the earlier interpretation of these ridges (A), the beach ridge 2.3 m above the modern high-tide line was interpreted to represent the vertical coseismic uplift of the 1855 earthquake. At present (B), this ridge is recognized as the active storm ridge (+2.3 meters), whereas the second ridge was raised ~6 m in the 1855 Wairarapa earthquake. Other, more inland ridges resulted from additional earthquakes since about 6000 years ago when the Quaternary sea level rise ended.

reefs (Grapes and Wellman, 1988). In some less-erosive settings, constructional beach ridges provide useful markers (see Fig. 2.6). For example, at Turakirae Head in New Zealand, beach ridges are built through the accumulation of clasts, shells, and organic debris during large storms. The modern storm beach ridge is about 2.3 m above the average high-tide level. Nearly 6 meters above the modern ridge is a storm beach ridge that was uplifted in the 1855 earthquake along the nearby Wairarapa Fault (Fig. 6.14). Still higher above the modern shoreline are three additional beach ridges that are interpreted to represent older coseismic offsets of 8, 6, and 2 m and that probably extend back to about 6000 B.P., when Holocene global sea level stabilized.

Note, however, that one must exercise caution in deducing actual uplifts from such storm berms, as the initial height of the storm berm above the mean tide at the time of the storm depends on the magnitude of the waves; this must be known or deduced if we are to use such markers in calculating the amount of local coseismic uplift. Such berms are often the only geomorphic markers in the Holocene.

An interesting lesson can be learned from the Turakirae succession in this regard (Grapes and Wellman, 1988; Grapes and Wellman, 1993). Until recently, it was thought that the beach ridge at 2.3 m above the modern shoreline was uplifted during the 1855 earthquake (Fig. 6.14A). The underlying idea was that this ridge formed at the pre-1855 high-tide line, and presumably a new ridge was forming at the present-day high-tide line. The discovery of late twentieth-century human litter in the lowest beach ridge indicates, however, that it formed during major storms long after the 1855 earthquake (Fig. 6.14B).

Re-examination of the pre-1855 historical record confirms that there was indeed a beach ridge present 2–3 m above high-tide line prior to the earthquake and that this ridge was displaced nearly 6 m during the earthquake. The amount of coseismic uplift (2.3 m) calculated under the earlier interpretation is only half of the actual uplift (~6 m), as represented by the difference in altitude of the second ridge and the lowest (Fig. 6.14). This example clearly illustrates the importance of understanding the positions and geometries of potential geomorphological markers in modern conditions before using them to assess past earthquakes.

Indirect Observations of Faulting

Stratigraphic Evidence

In recent years, interpretation of the Holocene stratigraphic record has been used to constrain the timing of past earthquakes in several areas where faults do not break the surface or are not otherwise available for study. Consider the great subduction-zone earthquakes. The largest earthquakes in the world this century, the 1960 Chile event and the 1964 Alaska event, have occurred in subduction zones along the interface between an overriding and an underthrusting lithospheric plate. Given the human population density in many coastal areas, and the fact that roughly half of the world's population lives along tectonically active plate margins, such earthquakes pose a major hazard. Most of these ruptures occur both at significant depths (often not breaking the surface) and beneath the surface of the ocean. Hence, they are largely inaccessible. Given these facts, how can a record of past subduction-zone earthquakes be generated?

One strategy that has been successfully pursued is to examine the terrestrial stratigraphic record on the overthrusting plate. Simple models for the seismic cycle in such a setting suggest that elastic strain accumulation during the interseismic period should cause upward flexing of much of the accretionary prism and adjacent coastal areas (Fig. 6.15), and that this strain would be released during the subsequent earthquake (see Fig. 4.4). Thus, abrupt coseismic submergence should occur in many coastal areas. Even though these coastal areas are well removed from the actual site of faulting, it might be expected that there would be a record of these submergence events. Indeed, this sort of record has been recently discovered along the Cascadia subduction zone of Washington and Oregon and is being used to address

FIGURE 6.15. Interseismic strain at subduction zones

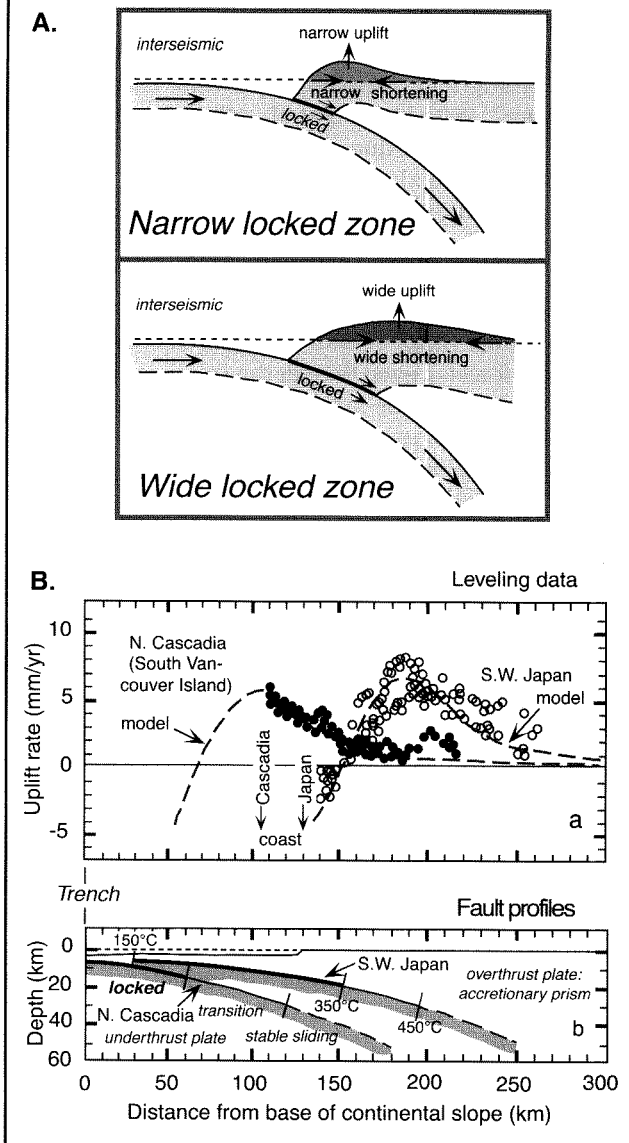

A. Schematic model for interseismic strain related to subduction zones. The width of the upwardly flexed region depends on the length of the locked part of the fault. Modified after Hyndman and Wang (1995).
B. Data from the Cascade and southwestern Japanese (Nankai margin) subduction zones showing geodetically determined interseismic deformation (top) and its spatial relationship to the locked section of the interplate boundary (bottom). Modified after Hyndman and Wang (1995).

what had been a major unsolved question: Is there a major seismic hazard associated with this subduction zone? In the mid-1980s, Thatcher (1986) wrote: "No great earthquake has been recorded off the Washington coast and the hypothesis that subduction occurs seismically will not be proven until one does." Today, as a result of stratigraphic studies by Atwater and co-workers (Atwater, 1992: Atwater et al., 1991), we now know that this zone has produced very large subduction-zone earthquakes as recently as 300 years ago.

In estuaries along the coastal areas of Washington and Oregon, several superposed, buried lowland soils crop out at low tide (Fig. 6.16). The estuaries are typically within 0.2–1.0 km of the coastline. The uppermost soil contains rooted snags of dead, but still-standing spruce trees (ghost forests), even though the soil is presently 1 m below the modern tide-marsh surface. Above the soil, there is a layer of fine-grained sand which can be traced inland along the banks of a coastal river. Above the sand is mud in which the roots of pioneer species from the saltwater tideflats are preserved. The sand layer thins and becomes finer grained inland. Soils of the buried spruce swamps can be traced seaward into buried saltwater marsh soils, some of which contain rooted stems and leaves of a tufted grass. Tufts project up out of the soil and are encased in a sandy layer that is analogous to that found above the spruce swamp soil. Preservation of the tufted grasses indicates that they were buried in less time than that needed for subaerial decomposition (<2 years). Similarly, study of tree rings from the snags suggests that they died suddenly, rather than being gradually submerged and killed. Given the elevation of modern coastal spruce forests above sea level, the presence of the tideflat species above the soil that bears the rooted trees dictates that these forests were submerged by at least 0.5 m. Detailed investigation of ostracod assemblages, which are zoned vertically within the tidal marsh, corroborate this estimate of vertical displacement (Hemphill-Haley, 1995). The overlying sand layer, which becomes finer grained and thinner inland and which entombs grasses in growth position, is interpreted to result from a tsunami that swept across the coastal region. (Note that along rivers, the normal trend is for downstream fining (Paola et al., 1992), whereas tsunami deposits become coarser toward the coast.) The two underlying buried soils are similarly associated with roots, stems, overlying sands, and tideflat muds. All of these observations are consistent with repeated subduction-zone earthquakes that caused instantaneous coastal submergence.

FIGURE 6.16. Stratigraphy and chronology of deformation along the Washington coast due to Cascadian subduction-zone earthquakes

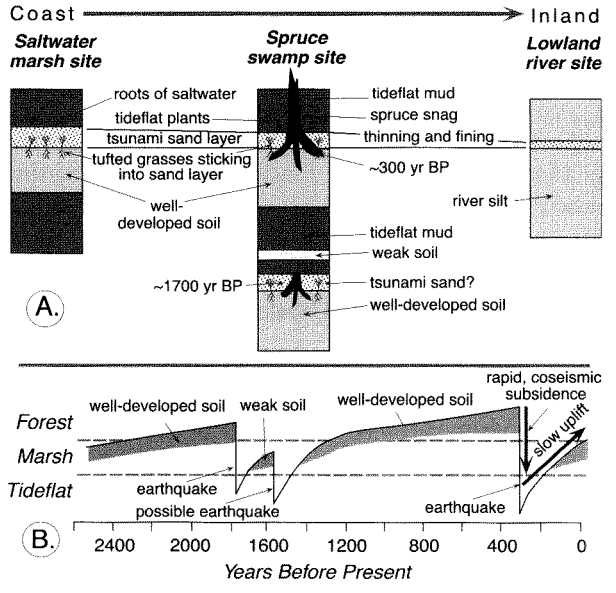

A. Schematic stratigraphy of buried soils and associated plants in saltwater tideflats, spruce swamps, and riverine settings. Abrupt drowning of trees and burial of grasses in growth position result from coseismic submergence and an accompanying tsunami. Buried soils can also indicate coseismic submergence, but also could result from slow, nonseismic subsidence. B. Schematic chronology of development of buried soils and drowned forests in response to subduction-zone earthquakes along the Washington coast. Modified after Atwater (1992).

As a result of these stratigraphic studies which documented the presence of large Cascadian earthquakes, the key remaining questions changed from whether they occurred in the past, to when did they occur and did the entire length of the subduction zone rupture (a single night of horror) or were there several individual earthquakes (a decade of terror)? High-precision radiocarbon dates (Atwater et al., 1991) and studies of the tree rings of the spruce snags suggested that the most recent earthquake occurred about 300 years ago, probably in the winter according to the tree rings and local oral histories. But the resolution of the dating was insufficient to tell whether the earthquakes recorded in southern

Oregon and Washington represented one or several closely spaced events. A possible solution to this problem comes from across the Pacific. Historical records of tsunamis in Japan indicate that a large tsunami with no known local source inundated the east coast in January, 1700 (Satake et al., 1996). The timing of the tsunami and the pattern of coastal inundation in Japan suggest the Cascadian subduction zone as a likely source. In addition, numerical models have been developed to describe how tsunami waves dissipate as a function of original size and distance while traversing the Pacific. By comparing the model results for different lengths of Cascadian ruptures with different sizes of waves and run-up on the Japanese coast, it appears quite possible that nearly the entire locked portion of the Cascadian subduction zone ruptured 300 years ago. A similar rupture today could produce a magnitude 9 earthquake!

Paleoseismic studies of Holocene stratigraphy in coastal areas are often fruitful, because sea level both provides a reference frame and strongly affects depositional environments (Ota et al., 1995), such that events of emergence and submergence are obvious. Paleoseismic studies utilizing terrestrial stratigraphy can also be successful, but frequently the interpretations are more ambiguous. The clearest records come from settings where a stratigraphic signal can be discerned that is uniquely attributable to seismic deformation, rather than to variability in climate or sediment supply. For example, the 1980 (M 7.3) El Asnam earthquake in Algeria caused hangingwall uplift and temporarily dammed the Cheliff River (Meghraoui et al., 1988; Philip and Meghraoui, 1983) where it traversed the folded hangingwall through a water gap (Fig. 6.17A). Eventually, the river will erode through the dam represented by the upthrown fault block, and at that time, the lake will drain. Until that time, lacustrine sediments are deposited in the earthquake-dammed lake. This stratigraphic response to a thrusting event provides a conceptual model for interpreting the stratigraphy in trenches located on the footwall at some distance from the main rupture. Seismic shaking may induce local faulting and cause sand blows or other features indicative of faulting which can be exposed in trenches. Most importantly, however, lacustrine deposits will mantle the flooded topography and form identifiable seismo-stratigraphic markers. With such a model in mind, it is fairly straightforward to interpret the Holocene stratigraphic record (Fig. 6.17B). At El Asnam, a trench reveals flood deposits alternating with paleosols (Meghraoui et al., 1988). For six of the lacustrine layers, there are some associated indicators of faulting or seismic shaking. Therefore, six stratigraphically defined earthquakes are identified as occurring between 6000 yr B.P. and 1900 yr B.P., after which tilting apparently shifted the position of the earthquake-dammed lake away from the trench site.

Tree Rings

As discussed earlier in the chapter, determination of the length of surface ruptures in past earthquakes is a necessary ingredient in assessment of the seismic moment that a fault can produce, and hence represents a key objective in many paleoseismological studies. The geomorphic evidence for ground ruptures is ephemeral in many settings. If the scarps were formed in weakly consolidated sediments, if surface fissures have been filled with colluvium, or if abundant vegetation surrounds the surface trace, then the evidence of a surface rupture may be removed within a few decades of an earthquake. Clearly, trenching and radiocarbon dating of offset layers is one approach to determining the length of surface rupture. But this is a time-consuming and sometimes expensive undertaking, and will likely require several trenches in order to document where the rupture terminates.

A rather different technique has been applied in some areas where faults pass through forested landscapes. During the sudden displacements that occur in an earthquake, the roots of trees growing along the fault line are often disturbed and can be sheared off. During large earthquakes with sufficient ground shaking, some trees can literally have their crowns shaken off. Clearly, both of these events (breaking off the roots or lopping off the top) traumatize a tree. The branching pattern of such trees can indicate that they lost their crowns at some time in the past: the main trunk abruptly ends and forks into lesser trunks, so that it looks like a tuning fork. In response to such a disturbance, the rate at which a tree grows can plummet (Jacoby et al., 1988; Sheppard and White, 1995; Van Arsdale et al., 1998). One could imagine, therefore, that by simply examining the temporal pattern of annual ring widths produced by trees growing adjacent (±20 m) to a major fault, one might be able to discern past earthquakes as represented by times of decreased ring widths.

Unfortunately, analyzing ring widths is somewhat complicated (see Chapter 3), because ring widths are also a sensitive function of climatic conditions. In fact, most studies of tree rings have been undertaken in an

FIGURE 6.17. Geomorphologic setting and trench stratigraphy related to the El Asnam earthquake near the Cheliff River

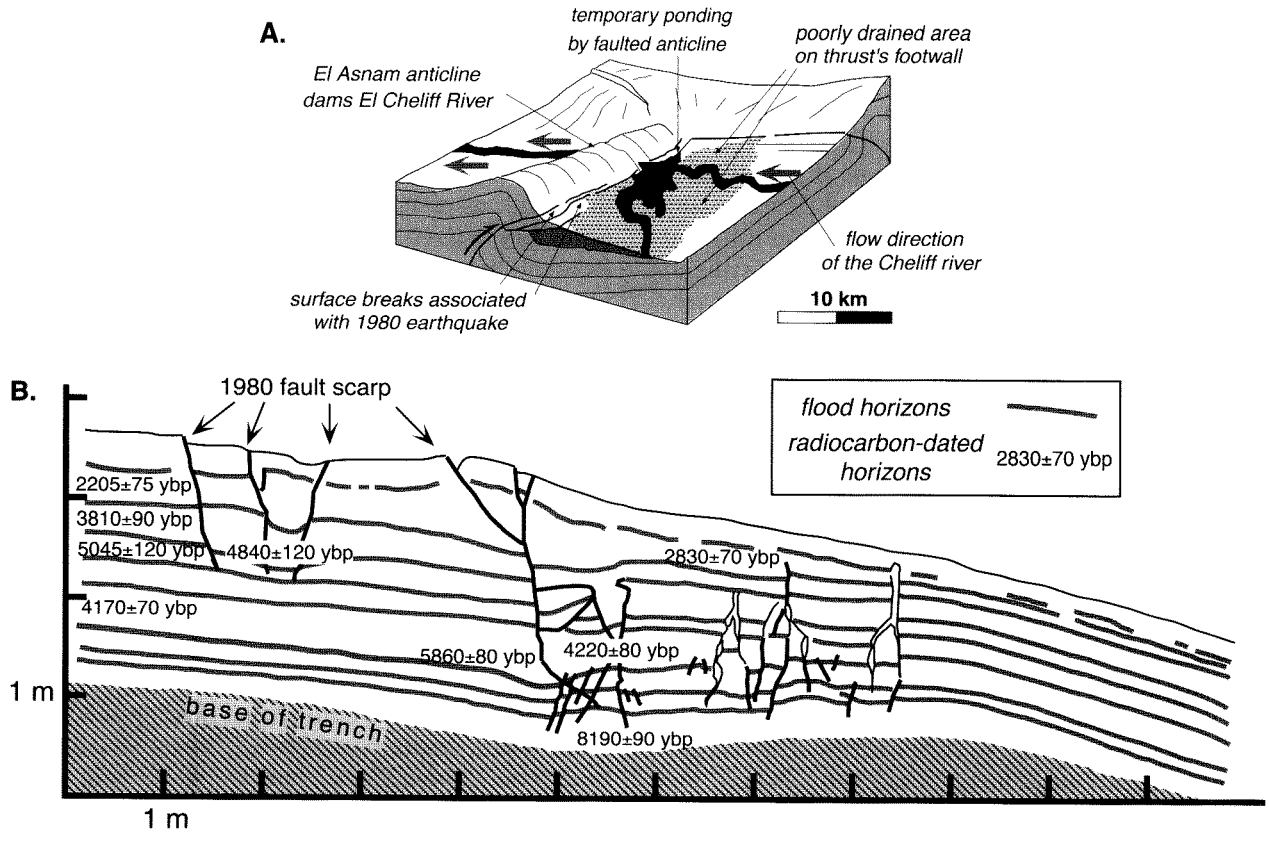

A. Oblique view of the damming of the Cheliff River by the upthrown hangingwall during the 1980 El Asnam earthquake. The river flows through a water gap, where uplift due to thrusting temporarily dammed the river. B. Stratigraphy of a trench in the footwall of the El Asnam rupture. The often faulted, but formerly continuous lacustrine beds are interpreted to result from previous Holocene earthquakes. The presence of faults cutting the layers and sand blows is used to distinguish those layers that are clearly associated with major thrust faulting events from those that might be due to natural flooding. Note that although the master fault is a thrust fault, it occurs at some distance from this site, and all the faults here are small normal faults developed in the footwall of the thrust. Modified after Meghraoui et al. (1988).

effort to reconstruct past climate. Many factors affect ring widths, including moisture availability, air temperature, and seasonal variability. In general, when trees are stressed, they produce narrow rings (little growth). So, how does one separate narrow rings produced by earthquakes from those formed in response to climate variations? The solution requires a two-step procedure. First, a master tree-ring chronology has to be developed for an area (Fig. 6.18). This would represent the average ring-width variation for trees not located on the fault, and would be interpreted as the climatically induced signal. Second, the ring-width chronologies from trees growing along the fault are compared with the master chronology. Parts of the record that display distinct mismatches and, in particular, prolonged intervals of reduced ring width with an

FIGURE 6.18. Tree ring-width chronologies from along the San Andreas fault near Wrightwood in southern California

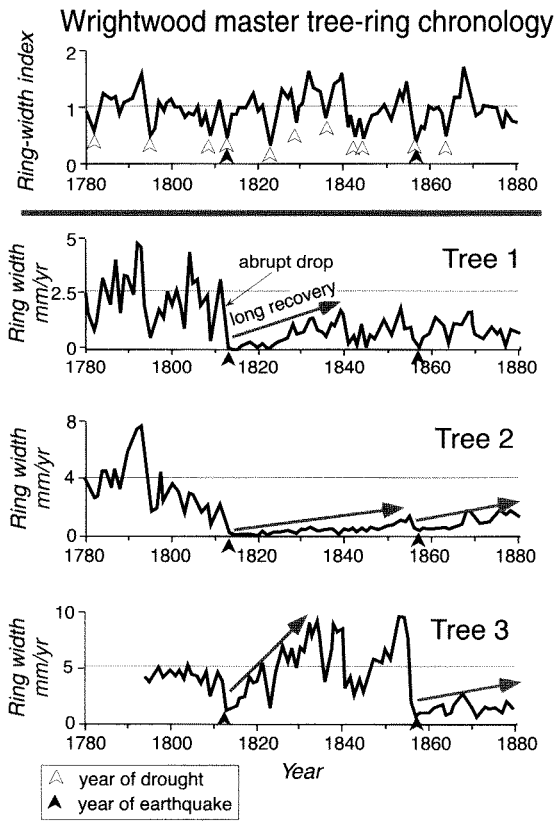

The master tree-ring chronology portrays the climatically induced variations in ring widths as determined from a regional synthesis of many trees unaffected by faulting. A low index corresponds with narrow rings (low growth) and correlates with years of drought (marked by open arrowheads). Ring-width chronologies for trees 1 to 3 display an abrupt decline in ring width (to lower than any previously formed ring) in 1812–1813. Although this also corresponds to a year of drought, the accentuated decrease in ring width and the long period of recovery after 1813 indicate that an earthquake, rather than climate, caused the tree to be highly stressed. These data provide the first clear evidence that the earthquake of 1812 (known primarily from coastal records) actually occurred along the San Andreas fault. The better known San Andreas earthquake of 1857 (Ft. Tejon earthquake) is also well represented in trees 2 and 3. Modified after Jacoby et al. (1988).

abrupt beginning, can be interpreted to have resulted from past earthquakes (Fig. 6.18). Whereas climatic conditions change on a year-to-year basis and ring widths responding to climate show similar year-to-year variability, recovery from coseismic shearing of the root system can take many decades.

Ring-width studies along the San Andreas fault provide clear evidence for an earthquake in 1812–1813 and a less well-expressed earthquake in 1857 (Fig. 6.18). Interestingly, both of these years coincide with drought years in the master chronology. In the regional master chronology, the ring widths bounce back to average within a few years. In contrast, all of the trees damaged by earthquakes show a slow recovery over several decades; some never recover fully to the previous rates of growth. Such studies are particularly useful because they serve to clarify the paleoseismic record. In 1812, California was sparsely populated, and, due to seismic damage in some coastal communities, it was thought that the earthquake occurred on some fault near the coast. The tree-ring data show that it occurred instead along the San Andreas fault, and when combined with trench data from distant sites, these data help define the extent of ground rupture and permit an estimate of the magnitude of these nineteenth-century earthquakes (Jacoby et al., 1988).

Rockfalls

Earthquakes near rugged mountains trigger rockfalls. Clouds of dust due to tumbling rocks enveloped hillslopes in southern California even during the larger aftershocks (typically ~M_L 4–5) of the 1994 Northridge earthquake (Harp and Jibson, 1996). The effects of seismic shaking are not confined to areas directly adjacent to a rupture; large earthquakes can trigger rockfalls greater than 300 km from the epicenter (Bull et al., 1994). John Muir reported seeing rockfalls in the Sierra Nevada associated with the 1872 Owens valley earthquake which occurred over 100 km away. Consider for a moment a talus cone or other accumulation of fallen blocks. There are likely to be additions of individual blocks or groups of blocks that have been loosened by weathering and that have tumbled as a result of avalanches, freeze-thaw cycles, or other biological or meteorological events that loosen and dislodge blocks. These additions to the talus are considered to be randomly distributed with respect to time. Against this background of intermittent, randomly spaced additions of blocks,

FIGURE 6.19. Histogram of maximum lichen diameters collected from >5,000 rockfall blocks distributed across 20,000 km^2 on the South Island, New Zealand

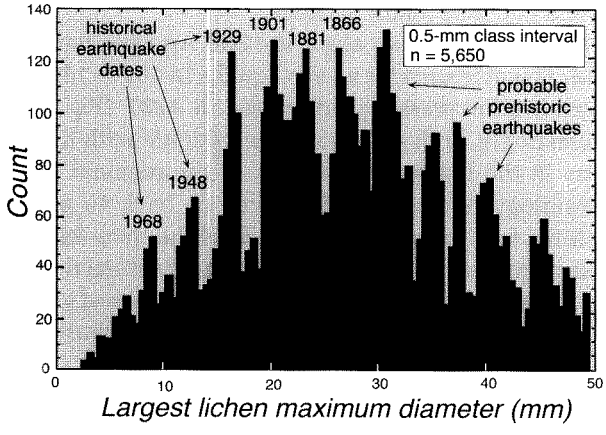

Note the clustering of maximum diameters that rise above the background level. This indicates that discrete events caused episodic input of rockfall blocks. The presence of these peaks separated by < 3–4 mm indicates that growth rates can not vary significantly between or within the study sites. The ages of historical South Island earthquakes are shown with the appropriate peak in the histogram. Modified after Bull et al. (1994).

rockfalls triggered by earthquakes will add a pulsed signal in which many tumbling blocks are added instantaneously to the talus deposits. Presumably, if we could date the time of addition of each block exposed on the surface of a talus cone, we would discern a "spiky" record of seismically triggered rockfalls poking through a background of talus growth unrelated to earthquakes (Fig. 6.19). This, of course, assumes that earthquakes, as opposed to very large storms, avalanches, or spontaneous rockfalls, are responsible for episodic addition of large numbers of blocks. Avoidance of rockfall deposits fed by avalanche chutes and selection of sites situated beneath short, steep slopes of weakly consolidated bouldery material, such as young glacial moraines, can enhance the likelihood that earthquakes will have caused most of the major additions of new blocks (Bull and Brandon, 1998).

But how do we date the time of addition of individual blocks? One recently developed method relies on the concept that lichens colonize freshly exposed, stable rock surfaces and that, after an initial period of more rapid growth, lichens grow at a steady and predictable rate (Bull et al., 1994; Locke et al., 1979) (see Chapter 3). A lichen growth curve can be developed based on maximum lichen sizes of a particular species found on rock surfaces of a known age, including dated geomorphic features and cultural ones, such as walls, buildings, or gravestones. Careful choice of the rockfall site combined with knowledge of historical earthquakes can help establish growth rates, if not previously known. For example, on rather stable slopes, only intense shaking due to rupture on a nearby fault is likely to dislodge boulders. Often rockfall deposits in such sites may only include blocks that were added during earthquakes on that fault. Peaks in histograms of lichen sizes corresponding to those events will provide calibration points for a growth curve that can be used to date other sites.

Recent studies in the South Island of New Zealand have demonstrated the utility of lichenometric dating of rockfall deposits (Bull and Brandon, 1998; Bull et al., 1994). For each rockfall deposit studied and on each block that meets a certain size criterion, the largest lichen diameter was measured, such that hundreds of measurements were assembled at a site. The data collection was aided greatly by the use of a digital caliper, which was automatically downloaded to a small computer database. When several thousand lichen measurements from a large region are synthesized into a histogram (Fig. 6.19), a very irregular and spiky distribution of lichen diameters is apparent. If lichen growth rates were highly variable from place to place or if rockfall events were randomly distributed through time and space, then the histogram should not exhibit discrete peaks in lichen diameter. In fact, given the density of these data, it is clearly possible to differentiate peaks separated by only 2–3 mm. When converted to ages, these size increments represent age differences of approximately 30 to 40 years. In the New Zealand study, six of the peaks can be assigned to specific historical earthquakes; it is probable that five other earthquakes predating 1866 are also represented (Bull and Brandon, 1998).

In addition to dating past earthquakes, Bull et al. (1994) have utilized their lichenometric data to estimate the amount of shaking that occurred at a site. All other variables being equal, the number of rockfall blocks resulting from a given earthquake might be expected to be a function of the size of the earthquake and the proximity of the site to the epicenter. Larger earthquakes produce more shaking at any site, and the greater the

Box 6.1. Ground Acceleration During Earthquakes

Although the vertical acceleration in past earthquakes is of great interest to construction engineers and urban planners, measurements of vertical accelerations in pre-historic earthquakes have been rare. Neither the stratigraphic nor the geomorphic record commonly yield data that reveal peak vertical accelerations, because these data sets record net ground displacement, rather than the rate of slip, or its derivative, the acceleration. Two geomorphic approaches using boulders can sometimes provide useful limits on vertical acceleration. If seismic accelerations exceed gravitational acceleration, unattached objects will be thrown in the air. In the 1989 oblique-slip Loma Prieta earthquake in California, there were numerous reports of massive objects (cars, stoves, fireplaces) that were thrown into the air, indicating that at least locally the ground accelerations exceeded 1 g. Boulders that are lying on the surface can actually be moved some distance laterally if the accelerations are oblique and approach or exceed 1 g in the vertical direction. During the 1992 (M_s = 7.4) Suusamyr earthquake in Kyrgyzstan, boulders weighing up to 1.5 tons were displaced 2 m horizontally and were overturned on a nearly horizontal surface (Ghose et al., 1996). The overturning suggests that the boulder partially rolled into its new position, but first it had to move upward out of the depression (~30 cm deep) in which it had been situated.

A second approach to estimating vertical and horizontal acceleration in past earthquakes uses "perched" boulders to place limits on the amount of shaking in the past. In arid regions, jointed bedrock can weather to produce fields of perched boulders. Initially, the bedrock weathers along the joint surfaces. Erosional removal of the disaggregated debris creates core stones that rest and sometimes balance on underlying bedrock. When such boulders have a long vertical dimension, they appear to be precariously perched, and should be highly susceptible to shaking (Brune, 1996). In fact, recent studies show that if such boulders are less than 0.3 m high, they tend to be blown over by strong desert winds (Shi et al., 1996). Boulders larger than this appear to require seismic accelerations to topple them. Field tests and modeling of the forces required to topple the boulders indicate that accelerations of greater than 0.2 g would knock over the more precarious boulders, whereas accelerations of 0.3–0.4 g would be required for the "semi-precarious" boulders. Such numbers provide very useful paleoseismological limits on the magnitude of past shaking. If these boulders are still standing, then they haven't been subjected to sufficiently strong ground motions to knock them down since the time they became precariously perched. A key to the analysis thus becomes the determination of the time when the boulders became susceptible to shaking and toppling. Presumably a precarious state was achieved when the boulder was significantly undercut to create a "pedestal" at its base. Radiocarbon dating of the desert varnish around boulder pedestals has provided time control in several areas of the southwest United States. Surprisingly, these data suggest that the amount of ground shaking during the past 10–30 ky in the areas of perched boulders has been much less than that predicted by the Working Group on California Earthquake Probabilities (1995) which has tried to assemble all of the relevant seismic, geodetic, and paleoseismologic data into quantitative models of earthquake hazards. Not all areas have perched boulders, but where they are present (or where they have been toppled over), they represent a useful paleoseismic tool.

BOX 6.1. Vertical accelerations

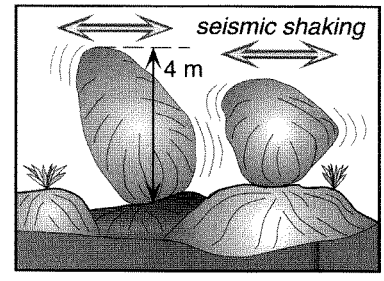

Sketch of perched boulders in Granite Pass, California. Drawing based on photo by Brune (1996).

distance from the epicenter the lower the shaking at a site. Based on the dates of historical earthquakes and the lichen diameters associated with those events, it is possible to decompose the lichen data for a given site into a suite of Gaussian curves, each of which is centered on the appropriate diameter for a specific earthquake and is assigned a height such that the suite of curves will sum together to yield the overall distribution of measured lichen sizes (Fig. 6.20). The relative height of the individual Gaussian curves is used to infer the amount of shaking at the site during each earthquake. By analyzing the local lichen records from many areas, it is possible to determine a seismic shaking index for each site for each earthquake. Moreover, for pre-historic

FIGURE 6.20. Histogram of lichen sizes at a local site showing decomposition into three Gaussian curves, each associated with a separate earthquake

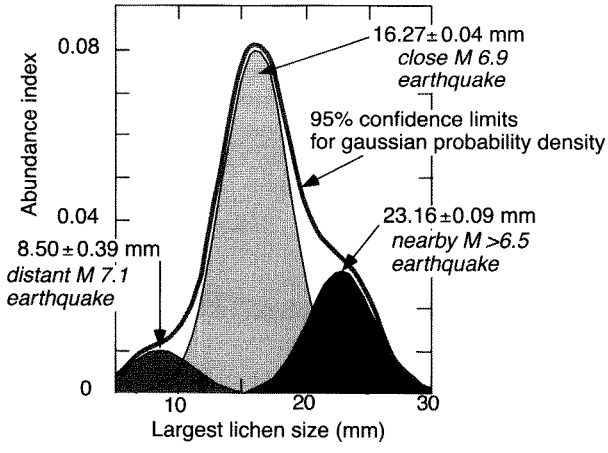

The curves sum to yield the approximate original distribution of sizes. The amount of locally felt seismic shaking determines the height of each Gaussian curve and is a function of the distance to the epicenter and the size of the earthquake. Modified after Bull et al. (1994).

FIGURE 6.21. Seismic-shaking index map for the effects of two 1929 earthquakes, South Island, New Zealand

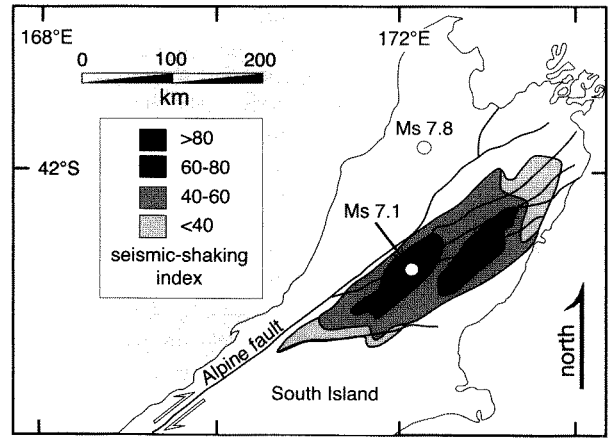

Shaking indices for the 16-mm diameter lichen peak from 53 sites have been contoured. The epicenter and magnitude of the earthquakes are shown. The M_s 7.1 earthquake (depth ~15 km) caused strong shaking in an area concentric to the epicenter, whereas the larger M_s 7.8 earthquake affected a broader region. Note that no data are available to the northwest of the shaded areas. Modified after Bull et al. (1994).

or poorly known earthquakes, these shaking indices can be contoured for individual earthquakes (Fig. 6.21) in order to define the subregion where the epicenter was located (Bull and Brandon, 1998).

This is a remarkable result with significant social applications. When environmental assessments are made for construction of buildings intended for "high-risk" usage (nuclear power plants or chemical manufacturers), the question is often posed, "Are there any faults within a certain distance that have been active during Holocene times?" When faults do not break the surface, this can be a particularly difficult question to answer. If lichenometric dating of rockfalls resulting from seismic shaking can quantify pre-historic events and even specify previous epicentral areas, it will provide invaluable insights for paleoseismic studies.

Remaining Problems

Several types of paleoseismic studies have been described here. They are generally suitable for assessing past activity along faults that break the surface or for defining deformation that occurred where a good spatial reference frame is available. When successful, such studies reveal when earthquakes occurred in the past, the magnitude of offset, and the extent of rupture associated with each earthquake. Numerous paleoseismological problems remain to be solved, however, and some will require innovative approaches that are presently untested.

One major unresolved problem is to define the seismic record of faults in terrestrial settings that do not rupture the surface. Recently, it has been discovered that a suite of buried thrust faults underlie the Los Angeles basin. The 1994 M_w 6.7 Northridge earthquake on one such fault caused more than $30 billion worth of damage in Los Angeles. Vertical accelerations exceeded 1 g above the reverse fault responsible for the earthquake, and yet the fault rupture did not extend to the surface. At the crest of a broad warp above the footwall ramp, only about 40 cm of vertical displacement occurred (Souter and Hager, 1997). So, with no surface rupture and a broadly distributed warping of the surface, how does one investigate the history of past

earthquakes on this fault and assess the threat for the future? Some long-term rates of displacement can be interpreted from the subsurface shapes of folds and displacements of beds across the buried fault, as known from borehole or seismic data (Hummon et al., 1994), but such data reveal nothing concerning the more pressing problem of when the last ten earthquakes occurred or how much displacement occurred in each.

We have seen that trenching along strike-slip faults can yield a history of multiple earthquakes, even if each earthquake causes displacements of several meters (Fig. 6.6). What practical means can be used to develop similar histories for dip-slip faults with large offsets during each earthquake? Deeper trenches can help, but such trenches are often dangerous places to work. Can aspects of the stratigraphic record be tied unambiguously to recurrent fault movements, as has been attempted at El Asnam in Algeria?

Determining precise timing for deformational events is a primary concern and an almost never-ending problem for paleoseismologists (and for many geomorphologists!). In this chapter, applications of high-precision radiocarbon dating, ^{230}Th dating, lichen diameters, and annual growth rings in corals and trees have been discussed. There is a perennial search for ways to improve existing techniques and for new ways to date the record of deformation. The limitations, assumptions, applicable age range, accuracy, and precision should be evaluated prior to applying any technique to a particular dating problem. As researchers confront the chronologic problems and possibilities of trenches and outcrops, new ways to use existing techniques, as well as new techniques themselves should be forthcoming. Similarly, more ways to assess vertical and horizontal accelerations and the distribution of seismic shaking in prehistoric earthquakes need to be developed.

Despite the many challenges and problems confronting paleoseismologists, tremendous progress has been made in the past two decades in understanding the past history of faulting on many of the major faults near population centers. We now know much more about the timing, displacement, and rupture length of many prehistoric earthquakes. As more faults that rupture the surface are studied and as new techniques are developed for investigating buried faults, the knowledge will continue to expand, providing constraints for engineers and city planners and for the broader geological community just trying to understand how the earth works.

CHAPTER 7

Rates of Erosion and Uplift

We recognize that the landscape in actively deforming areas results from interactions among the processes of uplift, subsidence, and surface processes that can lead to local erosion and deposition. It is useful, therefore, to try to calibrate the rates and relative contributions of each process at a particular time or over some span of time. The goals of this chapter are to describe approaches that can be employed to define geomorphic and tectonic rates at several spatial and temporal scales. In particular, the focus is on:

- Determining rates of erosion;
- Calculating mass balances and material fluxes;
- Determining rates of uplift; and
- Reconstructing the past geometry of tectonically active landscapes.

Studies that define rates of erosion and uplift lie at the heart of tectonic geomorphology and represent some of the most interdisciplinary research that occurs today. Successful studies typically include geochronology, structure, stratigraphy, geomorphology, and numerical modeling. Those that address the cause of changes in rates also encompass paleoclimatology, tectonics, and geochemistry. Much current debate revolves around whether climate or tectonics is responsible for changes in erosion rates or in the shape of the landscape (Masek et al., 1994; Molnar and England, 1990; Whipple et al., 1999). Potential feedbacks between climate and tectonics have been hypothesized, but remain poorly documented. For example, did surface uplift of mountain ranges globally accelerate in late Cenozoic times and drive climate change, or did climate change cause accelerated erosion that drove isostatic uplift? Has glacial erosion sufficiently changed the shape of valleys (the cross-sectional difference between a V-shaped and a U-shaped valley) that peaks have risen isostatically in response to the eroded mass? Are the aprons of Quaternary conglomerates that bound many mountain ranges indicators of tectonic or climatic events? Did uplift of the Tibetan Plateau cause strengthening of the monsoon, changes in rates of chemical weathering, and changes in atmospheric CO_2, thus precipitating major Northern Hemispheric glaciation (Edmond, 1992; Raymo and Ruddiman, 1992)? This chapter does not answer these questions. Rather, it encompasses a rich variety of approaches that help to define the key attributes which will permit a choice among the competing alternatives.

Rates of Erosion and Denudation

Definitions

The changing vertical position of a point on the land surface (Fig. 7.1) at any time is a function of a) the rate at which bedrock is being carried upward by tectonic processes (known as the "bedrock uplift rate"); b) the rate at which material in the subsurface is compacting; and c) the rate of denudation or deposition at the surface (England and Molnar, 1990):

$$\textit{Surface uplift} = \textit{bedrock uplift} + \textit{deposition} - \textit{compaction} - \textit{erosion}$$

Bedrock uplift and deposition contribute to raising the land surface, whereas erosion, compaction, and bedrock subsidence (in which case the sign on "bedrock uplift" is negative) serve to lower it. Because compaction and deposition both occur primarily in sedimentary basins

FIGURE 7.1. Schematic of factors controlling position of the land surface: bedrock uplift, denudation, compaction, and deposition. Note that denudation can be erosional or tectonic.

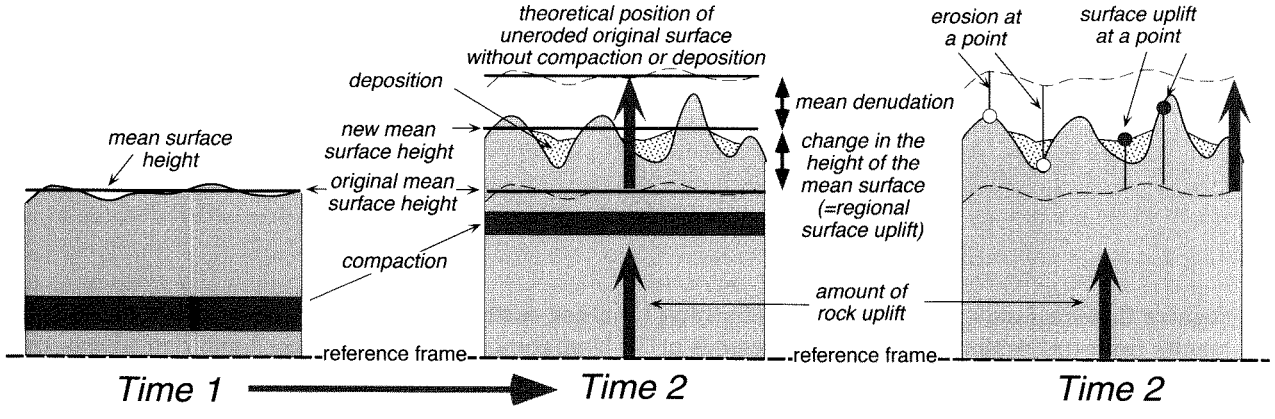

near local base level, they are generally ignored in this chapter in favor of denudation and bedrock uplift, which are the main determinants of topography in tectonically active or mountainous landscapes.

Denudation results from the removal of material from a point or region on the earth's surface and can occur in response to two very different processes. *Geomorphic erosion* (referred to subsequently simply as erosion) results from mechanical and chemical weathering of rock and removal of loosened or dissolved material by geomorphic agents. Although erosional removal of debris is often incremental, processes like deep-seated, bedrock-involved landsliding can be instantaneous and volumetrically significant. *Tectonic denudation* typically occurs through processes of extension and normal faulting, and it can result in the rapid removal of large volumes of nearly solid rock. A common reference frame for calculating rates of denudation is the geometry of the past land surface. *Surface uplift* or *lowering* generally refers to changes in the elevation of a surface, whereas *bedrock uplift* refers to changes in the vertical position of rocks with respect to a fixed reference frame, such as the geoid.

In most situations, removal of mass from a region will be isostatically compensated by crustal rebound. Given typical crustal and mantle densities, erosion of an average of 100 m of rock across a broad surface will cause the crust to rebound isostatically about 85 m and will yield only 15 m of lowering of mean surface elevation. Similarly, crustal thickening will lead to surface uplift, but, due to the isostatic sinking of the thickened crust, the magnitude of surface uplift will be only about one-sixth of the amount of crustal thickening. Thus, direct measures of the change in elevation of the land surface, which are themselves very difficult to obtain, can only be used to estimate erosion or bedrock uplift rates when other controls, such as changes in mean surface elevation, time scales and lags of isostatic response, volumes of eroded material, and variations in crustal density, are known.

When calculating rates of denudation or surface uplift, it is important to distinguish between local versus regional rates. A local rate may typify a single drainage basin or any point for which a rate can be defined (Fig. 7.1), whereas a regional rate should represent an integrated rate for a large area, commonly greater than 1000 km^2. It is these regional rates that are geophysically important, because the crust responds isostatically to regional loading and unloading, but is sufficiently rigid to be insensitive to local changes. Locally determined rates can be strongly influenced by the focused action of a geomorphic agent, like a landslide or a rapidly incising river, and such rates are likely to vary in time and space much more rapidly than will rates determined for larger areas. In addition, any given point in the landscape, such as a mountain summit, could be going up or down with respect to the geoid at the same time that the average elevation of the landscape is changing in the opposite direction. For example, erosion that deepens and widens river

FIGURE 7.2. Denudation rates as a function of topographic relief and mean elevation

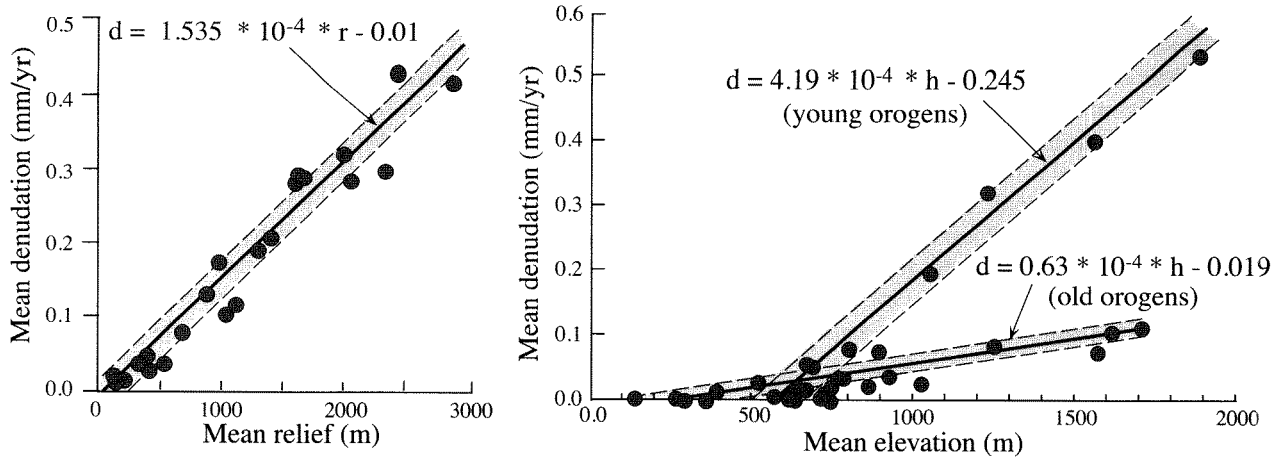

Left: Topographic relief versus erosion rate shows a clear correlation in mid-latitude, temperate mountains. Modified after Ahnert (1970). Right: Mean elevation versus denudation rate. Note the difference between young (Cenozoic) and old (Mesozoic and older) orogens. Modified after Pinet and Souriou (1988).

valleys but doesn't erode the peaks will reduce the mass of an area and drive isostatic uplift (see Figure 1.5). As a consequence, the altitudes of the peaks could increase at the same time that the mean height of the region is decreasing (Burbank, 1992; England and Molnar, 1990; Small and Anderson, 1998; Small and Anderson, 1995).

Conceptual Framework

Both *mechanical* and *chemical weathering* interact to erode the land surface. For example, chemical weathering can convert micas and feldspars to clays or can dissolve minerals. Such processes weaken rocks and increase their susceptibility to mechanical disaggregation. At the same time, mechanical breakdown of rocks continually exposes unweathered material and provides fresh surfaces for efficient chemical attack. In temperate to alpine and arctic terrains, a key mechanical weathering process is frost cracking. The geomorphic effectiveness of frost cracking is strongly dependent on the time a parcel of rock spends within a certain subzero thermal window, and on the presence of water (Hallet et al., 1991; Walder and Hallet, 1985). Frost cracking can dominate disaggregation processes and facilitate efficient chemical weathering, even in cool climatic regimes. In most tectonically active regions, mechanical weathering appears to dominate locally measured erosion rates, and rates of dissolution are often uncalibrated.

Rates of erosion are commonly defined in terms of lowering of the *bedrock* surface, and are often argued to be a function of the *local topographic relief* (altitudinal difference within an area that is typically smaller than the entire catchment). Due to the greater potential energy of elevated areas with respect to the local base levels represented by valley bottoms and due to the generally steeper slopes that prevail in regions of high relief, it is reasonable to imagine that high relief promotes high erosion rates. Measured and estimated sediment fluxes out of drainage basins having contrasting relief, but all within a similar temperate climatic regime, have been statistically related to relief (Ahnert, 1970) (Fig. 7.2). Similarly, rates of erosion can also be correlated to mean basin elevation (Pinet and Souriau, 1988), and there is a generally strong statistical correlation between mean relief and mean elevation (Summerfield and Hulton, 1994). Few studies have been completed, however, that describe how the distribution of relief, topography (hypsometry), slope angles, or active surface processes within an area affects rates of erosion.

When considering the basin- to range-scale evolution of the land surface, long-term, average rates of erosion, deposition, and uplift are more important than are short-term rates. Nonetheless, given the techniques available, most measured sediment fluxes out of basins sample only short intervals of time. Given the well-known glacial-interglacial climatic variations of Quaternary times, it is expected that sediment fluxes out of basins occur in irregularly spaced pulses. The timing of major episodes of erosional or sediment discharge may also vary between nearby basins. Thus, while sediment discharges in glaciated temperate regions often appear synchronous with glaciation, they may reach a peak in early post-glacial times in more arid areas (Bull, 1991) or may be a function of the stability of hillsides influenced by climatically modulated vegetation (Leeder et al., 1998).

Several approaches can be used to estimate erosion rates (Fig. 7.3). With appropriate age control, an average denudation rate can be readily computed with three types of data: the volume of eroded material, the area from which that material was derived, and the duration of erosion. The volume of material eroded from a catchment can be estimated using direct measurements of erosion within the catchment itself, gauging the sediment flux out of the catchment, or by assessing the volume of sediment stored in a basin to which that catchment is tributary. These sediment volumes have to be converted to rock volumes with appropriate corrections for density differences. Whereas direct measures of erosion rates in the catchment are informative, rates at individual points must be integrated across the entire catchment. Commonly, basin-wide estimates with large and unknown uncertainties result from extrapolation of a few point measurements. If, over the span of several years, for example, the total, time-averaged sediment flux, including the dissolved load, out of a catchment could be measured, this would provide a good estimate of average, short-term denudation rates. Similarly, if the volume and age of sediment stored in a basin are known, if it can be shown that significant volumes of sediment did not bypass the basin en route to another basin, and if the tributary catchments throughout deposition can be reliably reconstructed, then a long-term mean erosion rate for the tributary catchments can be determined. Measurement of both fluxes and volumes are useful, because they commonly encompass different temporal intervals.

FIGURE 7.3. Approaches to estimating denudation rates

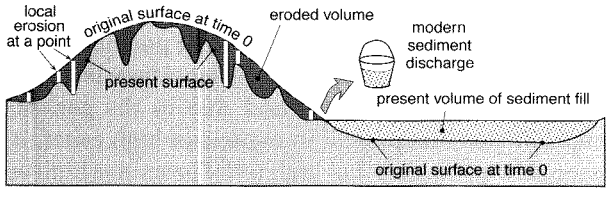

If the original surface topography can be reconstructed, then the missing volume of material can be determined by subtracting the present-day topography from the pre-erosion topography. If the age of that initial surface is known, then a mean erosion rate can be calculated. Similarly, if the volume of sediment in a basin and the age of the beginning of its filling are known, and if the size of the area contributing sediment to the basin can be estimated, a mean erosion rate can be approximated. Alternatively, the modern rate of sediment discharge and the contributing area can be used to compute a mean erosion rate.

Sedimentary Fluxes in Rivers

The sediment load of a river can be partitioned into the bedload, suspended load, and dissolved load, If the average contribution of each component over time is known, then mean denudation rates can be calculated. Whereas the highest bedload and suspended load fluxes typically occur during high water discharge, the highest solute concentrations typically occur during low flows and can have a strong seasonal dependence. For rivers that are "underloaded" with respect to their transport capacity, sediment discharges may peak early in a storm cycle as material in the bed is mobilized, and then, despite continuing high water discharge levels, diminish as all available sediment has been exported. Input of sediment from adjacent hillsides can vary in predictable ways in different climatic regimes. For example, most landslides occur under saturated conditions. In many areas, this requires sustained rainfall prior to the triggering storms. In some locales, such as Taiwan, the intensity of typhoon precipitation is often sufficient to trigger landslides without significant prior storms. Clearly, because of such variations, it is necessary to average over a sufficiently long time to be able to characterize the sediment flux at different river stages and at different times of the year. Reliable measurement of the contributions from the dissolved, suspended,

and bed load is only rarely achieved. When estimating suspended loads, both the vertical and horizontal sediment concentration profiles, as well as the spatial distribution of water velocities, have to be either calculated or measured. Bedload sampling almost always consists of isolated measurements at a point in a channel. These measurements then have to be extrapolated to the entire stream bed and over the seasonal or flood cycle. Although the flux of bedload material is generally greatest during flood stage, bedload sampling during flooding is often difficult, if not impossible. All of these complexities contribute to the fact that the true bedload flux is poorly known in most rivers.

Despite these difficulties, fluvial sediment fluxes, primarily suspended load only, have been estimated for many rivers near their entry into the ocean (Milliman and Meade, 1983; Milliman and Syvitski, 1992). When the major rivers of the world are considered, those draining the Himalaya and the Tibetan Plateau contribute a disproportionate amount of the sediment discharge to the world's oceans (Table 7.1). There, the combination of exceptional topographic relief, ongoing bedrock uplift, and monsoonal precipitation along the margins of the uplift lead to rapid denudation. Based on the suspended fluxes alone, a mean rate of erosion of 0.3 mm/yr over a region of about 2.6×10^6 km^2 can be calculated from these data. Moreover, approximately 20–40 percent of the Indus and Gangetic drainage basins are represented by foreland basins which have been net sediment sinks during Cenozoic times. If this were still true over the period of measurement, then the mean erosion rate in the hinterland (the tectonically active mountains themselves) would increase to about 0.4–0.5 mm/yr. When compared with mean erosion rates of approximately 0.04 and 0.07 mm/yr for the Mississippi and Amazon Rivers (Table 7.1), respectively, the magnitude of modern Himalayan erosion can be appreciated.

Erosion rates generally decrease with increasing catchment size (Milliman and Meade, 1983; Milliman and Syvitski, 1992) (Fig. 7.4). Even in small catchments, the maximum rates of erosion based on fluvial sediment loads at the river mouth rarely exceed 3 mm/yr (Milliman and Syvitski, 1992). Such rates are less than the rapid vertical rock uplift rates that prevail in some very active compressional tectonic regimes (Hallet et al., 1996). If such a mismatch persisted, then the mean erosion rate would not balance the bedrock uplift rate, and the mean topography in such areas would continuously grow. Studies in glaciated basins

FIGURE 7.4. Comparisons of erosion rates calculated for glaciated basins (right) and for both fluvial and glacial basins (left)

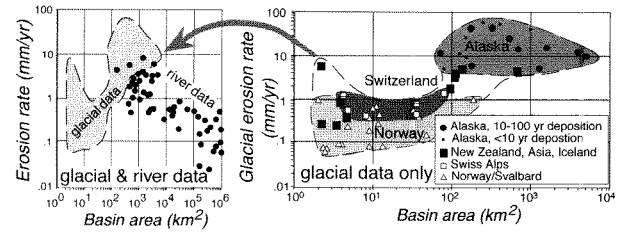

Fluvial erosion rates generally decrease with larger basin size and glacial rates can be much higher than the fluvial rates, which are restricted here to suspended sediment load at the mouth of the river. Note that the glacial data show much higher rates for large glaciers in Alaska than for the smaller glaciers in the Alps and Norway. Modified after Hallet et al. (1996).

of sediment fluxes over the past 10 to 100 years reveal mean, basin-averaged denudation rates that range as high as 50 mm/yr (Fig. 7.4). Although it is probable that some of the higher rates in the glaciated basins result from remobilization of sediment stored within a catchment (Church and Slaymaker, 1989), the rapidity of erosion in the moist, alpine settings of Alaska and New Zealand suggests that glacial erosion may be a very effective erosional agent. These glacial erosion rates are sufficiently high to balance almost any tectonically generated rock uplift rate. We note again, however, that the rates so calculated are mean rates. If the glaciers are etching deeply their rocky beds while the alpine ridges between them are not eroding rapidly, then local relief can indeed continue to increase while mean erosion and uplift rates are balanced.

Rather than trying to measure sediment fluxes in a river at high stage, a better estimate of total solid sediment discharge can sometimes be obtained from natural or man-made reservoirs, or from closed depositional basins. These are typically efficient traps of fluvially transported sediment, and they store sediment transported throughout the year. If the shape of the valley prior to damming or the geometry and age of any other stratigraphic horizon in the fill is known, if the density of the sediment and the volume of the fill can be calculated, mean rates of sediment delivery and of erosion in the catchment are readily derived. Unfortunately, few of the world's major rivers debouch into reservoirs.

TABLE 7.1. Catchment Area, Sediment Load, Sediment Yield, Erosion Rates, and Runoff for World's Rivers with Catchments >250,000 km² (after Milliman and Syvitski, 1992)

River	Area ($\times 10^6$ km²)	Load ($\times 10^6$ t/yr)	Yield (t/km² • yr)	Erosion Rate (mm/yr)	Runoff (mm/yr)
		A. High Mountain (>3000 m)			
Magdalena (Col)	0.24	220	920	0.341	990
Irrawaddy (Burma)	0.43	260	620	0.230	995
Brahmaputra (Bangl)	0.61	540	890	0.330	
Colorado (USA)	0.63	120	190	0.070	32
Indus (Pak)	0.97	250	260	0.096	245
Ganges (Bangl)	0.98	520	530	0.196	
Orinoco (Ven)	0.99	150	150	0.056	1100
Yangtze (China)	1.9	480	250	0.093	460
Parana (Arg)	2.6	79	30	0.011	165
Mississippi (USA)	3.3	400	120	0.044	150
Amazon (Braz)	6.1	1200	190	0.070	100
		B. Mountain (1000-3000 m): South Asia/Oceania			
Krishna (India)	0.25	64	260	0.096	140
Godavari (India)	0.31	170	550	0.204	270
Pearl (China)	0.44	69	160	0.059	690
Huanghe (China)	0.77	1100	1400	0.519	77
Mekong (Viet)	0.79	160	200	0.074	590
		C. Mountain (1000-3000 m): N/S America, Africa, Alpine Europe, etc.			
Fraser (Can)	0.22	20	91	0.034	510
Columbia (USA)	0.67	15	22	0.008	375
Limpopo (Mozam)	0.41	33	80	0.030	13
Rio Grande (USA)	0.67	20	>30	>0.011	
Danube (Rom)	0.81	67	83	0.031	250
Yukon (USA)	0.84	60	71	0.026	230
Orange (SA)	0.89	89	100	0.037	100
Tigris-Euphrates (Iraq)	1.05	>53(?)	>52(?)	>0.019	45
Murray (Austr)	1.06	30	29	0.011	21
Zambesi (Mozam)	1.4	48	35	0.013	390
MacKenzie (Can)	1.8	42	23	0.009	170
Amur (USSR)	1.8	52	28	0.010	180
Nile (Egypt)	3.0	120	40	0.015	30
Zaire (Zaire)	3.8	43	11	0.004	340
		D. Upland (500-1000 m)			
Vistula (Pol)	0.20	2.5	13	0.005	165
Uruguay (Urg)	0.24	11(?)	45(?)	0.017(?)	
Pechora (USSR)	0.25	6.1	25	0.009	415
Hai (China)	0.26	14	55	0.020	
Indagirka (USSR)	0.36	14	39	0.014	150
Volta (Ghana)	0.40	19	48	0.018	91
Don (Ukr)	0.42	0.77	18	0.007	
Sao Francisco (Braz)	0.63	6	10	0.004	
Niger (Nig)	1.2	40	33	0.012	116
Volga (Rus/Ukr)	1.4	19	15	0.006	400
Ob (USSR)	2.5	16	6	0.002	130
Lena (Rus)	2.5	12	5	0.002	205
Yenisei (Rus)	2.6	13	5	0.002	220
		E. Lowland (100-500 m)			
Yana (USSR)	0.22	3	14	0.005	130
Senegal (Sen)	0.27	1.9	8	0.003	48
Sevemay Dvina (USSR)	0.35	4.5	13	0.005	330
Dnieper (USSR)	0.38	2.1	5.2	0.002	86
Kolyma (USSR)	0.64	6	9	0.003	140
Sao Francisco (Braz)	0.64	6	9	0.003	150
St. Lawrence (Can)	1.1	4	4	0.001	435

Some, like the Columbia River in Washington, are interrupted by numerous low dams. During times of high discharge, however, sediment is flushed out of the reservoirs behind each dam. Of the five large rivers draining the Himalaya and Tibet, only the Indus River enters a major reservoir (the Tarbela Reservoir). Although the Tarbela Reservoir was estimated to have a usable lifetime of about 70 years, since the mid-1970s, the toe of the delta has already prograded over 80 km and now lies close to the dam. The mismatch between the estimated and the likely usable lifetime of the reservoir demonstrates how poorly the sediment fluxes along this river were known prior to construction, despite the importance of such data to the viability of the project. The rate of sediment infill into Tarbela reservoir requires an average erosion rate of 0.4 mm/yr over the upstream catchment: a rate four times higher than that over the entire Indus drainage (Table 7.1). Put another way, the sediment flux into the reservoir also reveals that 20% of the Indus catchment area (this mountainous region) accounts for 80% of the eroded material that is measured near its mouth (Milliman and Syvitski, 1992).

Sometimes human intervention provides an opportunity to measure erosion rates quite reliably. For example, along the southern flank of the San Gabriel Mountains of California, many river valleys debouch on to densely populated areas of the Los Angeles basin. Because much of the historical damage from floods has been caused by large debris flows, Los Angeles County engineers have built debris basins at the mouth of each of the canyons. These basins are efficient sediment traps and have been reasonably effective in preventing widespread damage by debris flows to the expensive homes built on the alluvial fans below the mouths of the canyons. When the debris basins approach capacity during flooding, the deposits are excavated and removed by trucks. The amount of debris removed provides an effective measure of the denudation in the catchment (Scott and Williams, 1978) and is recorded in county registers in units of truckloads!

Rates of Erosion Based on Structural and Stratigraphic Controls

If the volume of rock eroded during a deformational episode and its duration can be delineated, long-term erosion rates can be defined. In order to do this, several conditions must be met. Both the pre- and the post-deformational geometry of the displaced mass must be known, such that the volume of eroded material can be calculated. The ages of key overlapping and cross-cutting relationships between structures and strata must be known, so that the initiation and termination of deformation and erosion can be determined.

Whereas such volumetric calculations are simple in concept, they can be reliably applied only in unusually well-documented situations, and even then may require a set of often untested assumptions. One potentially straightforward geometry to consider is the erosion of the hangingwall of a thrust sheet. The Salt Range thrust in the Himalayan foreland fold-and-thrust belt of Pakistan provides a clear example for application of this methodology (Burbank and Beck, 1991). The hangingwall of the Salt Range thrust comprises Eocambrian evaporites of variable thickness, a Paleozoic-to-Eocene carbonate and clastic succession about 1 km thick, and a 2.5–3 km thickness of Miocene and younger fluvial strata of the Himalayan foreland basin: the Siwalik molasse (Fig. 7.5). Prior to deformation, the fluvial strata formed a predictable wedge-shaped package of strata that gradually tapered toward the south. The known starting thickness and geometry of these strata are keys to determining how much erosion has subsequently occurred. During thrusting, the hangingwall was raised up a 1-km-high footwall ramp and was translated about 20 km to the south (Baker et al., 1988). Stratigraphic evidence indicates that translation took place in two stages: between 6.3 and 5.8 Ma, approximately 5 km of shortening occurred, and the remainder occurred between 1.5 Ma and present. During the first stage of thrusting, erosion of the fluvial strata from the leading edge of the hangingwall was great enough to expose Permian rocks at the thrust tip. This requires about 3 km of erosion during 0.5 Myr: a rate of approximately 6 mm/yr or 6 km/Myr! Since about 1.5 Ma, a second episode of thrusting translated the hangingwall an additional 15 km to the south. At the present time, with the exception of a few infolded inliers, the Miocene and younger strata have been completely stripped off the hangingwall, and a resistant carapace of carbonate strata defines the existing land surface across an area of about 1500 km^2 that spans the Salt Range. Thus, approximately 2.5–3 km of strata have been eroded in the past 1.5 Myr, yielding a mean erosion rate of 1.5–2 mm/yr across a large area.

Whereas this technique tells one nothing about the geomorphic processes by which the erosion was accomplished, it unambiguously defines some rapid, long-term rates. Although it is estimated that horizontal shortening

FIGURE 7.5. Calculations of erosion rates based on combined structural and stratigraphic data in the Salt Range, northern Pakistan

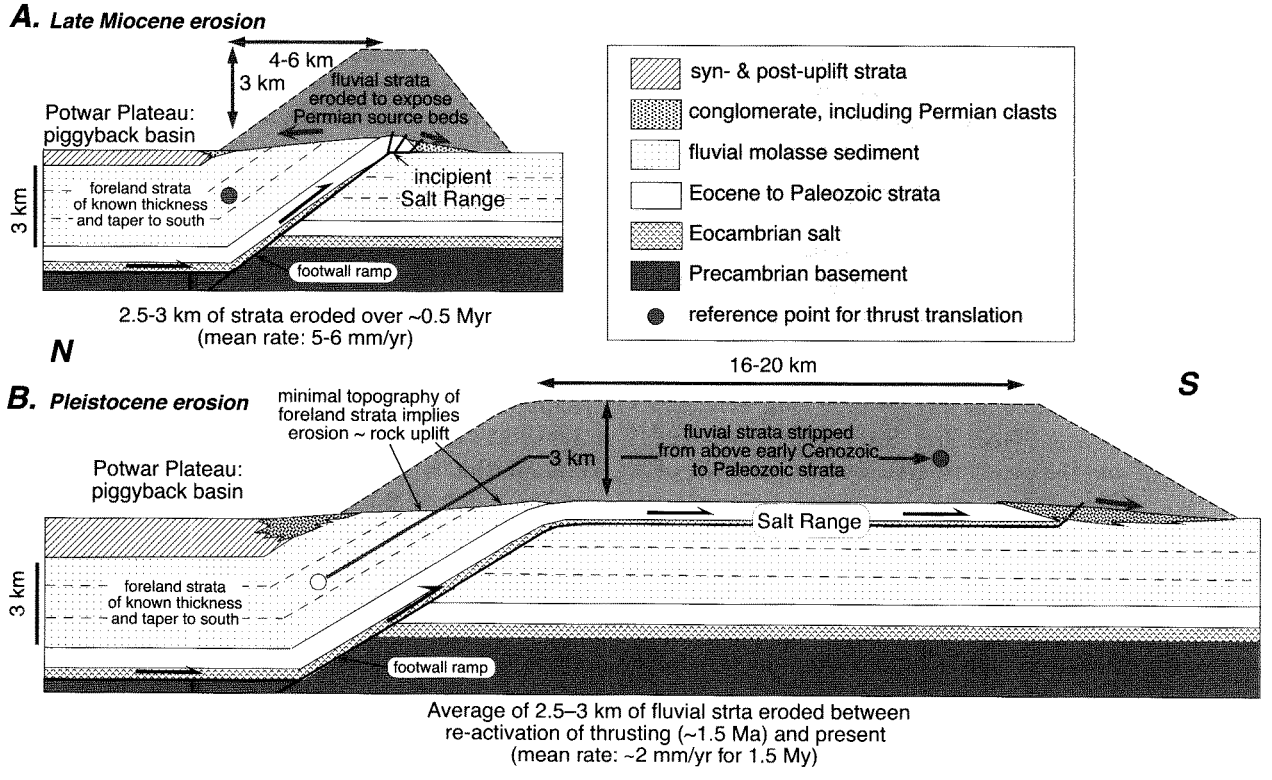

The geometry of deformation, its timing, and the pre- and post-deformational surface must be established. A. First stage (Miocene) of thrusting leads to exposure of rocks near the base of the hangingwall, so all of the fluvial strata must have been stripped off prior to exposure of these source rocks. B. Second stage of thrusting is synchronous with the stripping of all of the fluvial strata across the entire uplifted hangingwall. Given that the fluvial strata on the north side were much more recently uplifted in comparison to those to the south, the fact that they are completely beveled indicates that the calculated erosion rates significantly underestimate the actual erosion rates of these strata. Modified after Burbank et al. (1991).

of about 1 cm/yr is still occurring on this thrust, virtually all of the Miocene strata have been stripped off the hangingwall directly above the footwall ramp. This has important implications for the rapidity of erosion, because, as the foreland-basin strata (2–3 km thick) are carried up the footwall ramp, one might expect them to form considerable topographic relief. Instead there is almost no relief above the ramp. This suggests that the rate of rock uplift and erosion of Miocene strata are nearly equal here (Fig. 7.5). Given a 30° ramp and 1 cm/yr of shortening, the rate of vertical uplift of the hangingwall and the local rate of erosional stripping of the Miocene rocks should both be about 5 mm/yr.

One typically encounters many difficulties when attempting this type of analysis. In order to reconstruct the eroded mass, its pre-deformational geometry must be assumed or reconstructed. In regions where there are predictable variations in stratal thicknesses, such as in many foreland basins or passive margins, this can be done with some confidence. Given dated strata that either are cut by or overlie the fault that accommodated the displacement, the duration of deformation can be defined. Oftentimes, however, one does not know how closely the dates limit the deformation; frequently either the beginning or end of deformation, but more rarely both, can be defined. In many terrestrial sequences,

moreover, it is very difficult to determine accurately the relevant stratigraphic ages. In these sorts of studies, magnetic polarity stratigraphy has provided a powerful tool for creating precise ages for Cenozoic terrestrial strata and in calculating rates of deformational and erosional processes (Burbank and Raynolds, 1984; Burbank and Raynolds, 1988; Raynolds and Johnson, 1985).

Topographically Constrained Erosion Rates

If the geometry and age of a former land surface can be reconstructed, a straightforward differencing with the modern land surface yields a mean erosion rate (Fig 7.3). For example, individual growing folds experience dissection as they are elevated above local base level. Typically, dissection is focused along river valleys and concavities, such that segments of the pre-deformational land surface may be preserved in a folded, but undissected state. If the geometry of the undissected surface of the fold can be reconstructed, the modern dissected topography can be subtracted from it in order to define both local and average rates of erosion. The availability of digital elevation models can make such calculations quite straightforward. Minimum volumes of eroded material can be objectively calculated simply by filling each dissected part of the landscape to the height of the lowest topographic boundary surrounding it (Brozovic et al., 1995) and then subtracting the present topography (Fig. 7.6). Alternatively, a reconstructed surface that represents the hypothesized topography in the absence of erosion can be created, and the modern topography (which has experienced erosion) can be subtracted from that surface to estimate spatially variable amounts of erosion.

On a considerably larger scale, former planation or low-relief surfaces have been identified in several mountain ranges. These may be defined by concordant summits, some of which are nearly flat-topped, or by largely undissected, but isolated surfaces (Fig. 7.7). If the former continuity of such surfaces can be demonstrated and the age of the surface can be ascertained, an extensive datum can be defined. Subtraction of the modern topography from this datum can define the volume and mean rate of erosion since the surface began to be incised. Given a knowledge of the eroded mass of rock, the isostatically driven response to its removal can be calculated, and it is therefore possible to determine to what extent the undissected peaks and surfaces would be raised in response to an overall lowering of the mean elevation due to erosion.

The reconstruction of formerly contiguous, low-relief surfaces can provide a powerful tool for assessing erosion.

FIGURE 7.6. Calculation of masses of eroded material using a digital elevation model

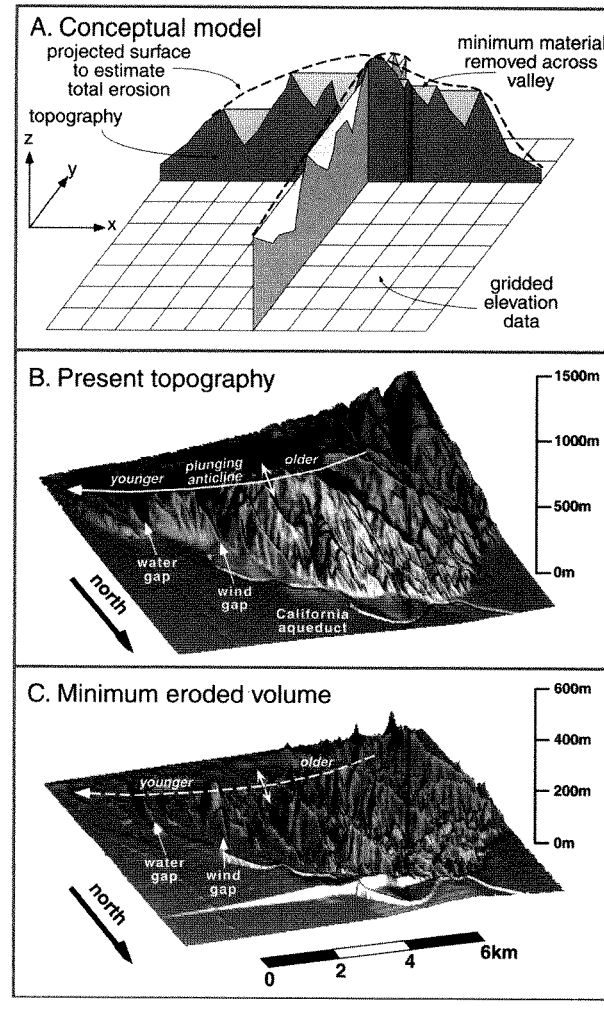

A. Strategy for calculating minimum eroded volume with orthogonal traverses of a digital elevation model. Subtraction of the present topography from the filled topography yields a volume of eroded material. The actual total mass loss may be better approximated by connecting the high points (dashed line), but this is a more subjective interpretation. Perspective view of the folded and dissected Wheeler Ridge anticline in southern California. Note that the fold plunges to the east where it emerges from the plain and that it is much more dissected in its western region. C. Perspective view of the minimum volume of material eroded from the Wheeler Ridge anticline. The material removed from the wind and water gaps is clearly displayed, but obviously most erosion has occurred in the western part of the fold. Modified after Brozovic et al. (1995).

FIGURE 7.7. Topographic cross sections of dissected plateaus in the NW Himalaya

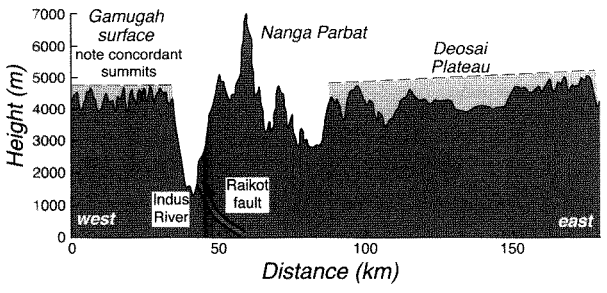

Nanga Parbat is one of the fourteen peaks in the world that rise over 8 km high. It is currently experiencing rapid rates (~5 mm/yr) of rock uplift (Zeitler, 1985). The Gamugah and Deosai regions typify two different expressions of plateaus. The Gamugah has many accordant summit heights, and despite its high average elevation, the degree of dissection is minor. The Deosai has parts of a surface that is low-relief and largely undissected. Its outer margins have been dissected and peaks there have experienced some uplift due to erosional unloading.

For example, extensive remnants of low-relief surfaces are preserved near the summits of numerous peaks in the Wind River Range, Wyoming. Cosmogenic nuclide exposure-age dates on these upland surfaces (Small et al., 1999) show that the bare bedrock is eroding at a rate of about 10 m/Myr : a rate that is likely to be more than ten times (and probably up to one hundred times) slower than the erosion rates of the glaciated valley bottoms. After creating a reference surface that connects all of these erosional remnants and then subtracting the modern topography from this surface, the average amount of erosion, as well as local erosion estimates at each point, can be made (Small and Anderson, 1998). One unknown in the Wind River Range is when the major canyon cutting commenced; without this constraint, mean rates of erosion can not be determined. The timing of the initiation of incision can be estimated, however, either by extrapolating the modern rates of erosion sufficiently far back through time to account for the observed mass that has been lost to erosion, by assuming an erosion rate for the valley incision, or by assuming that the incision commenced in concert with well-known climate changes, such as the initiation of major Northern Hemisphere glaciation at about 2.5 Ma. If the latter approach is taken, a consistent story emerges in which much of the modern valley-ridge relief of the range can be generated within the glacial epoch.

Erosion Rates Based on Isotopic Interpretations

The isotopic signature contained in river water samples or transported sediments is a function of the variation in isotopic ratios and erosion rates across a source area and changes in composition during transport. If there are contrasts in the isotopic composition of eroding rocks across a source area, these variations can be reflected in the isotopic ratios of the water and eroding sediment as they leave the source area. A spatially uniform flux of water or sediment across an eroding region would yield an integrated isotopic signal in which the magnitude of the contribution from an area would potentially be proportional to its aerial extent. To the extent that rates of erosion are variable across a source area, the downstream composition will integrate the isotopic ratios and erosion rates of each isotopic province within the catchment.

Isotopes may be used as tracers of distinctive source areas and may define relative rates of erosion. Consider, for example, a mountain range in which a zone containing the high peaks near the drainage divide has isotopic ratios that are much different from those in the surrounding terrain. Near the headwaters of the rivers and adjacent to the high peaks, one would expect that isotopic ratios in water or sediment samples would reflect the local rock chemistry. Now imagine measuring water or sediment in the stream at a point many kilometers downstream from the drainage divide, where the zone containing the high peaks constitutes only a small fraction of the upstream catchment. If the water or sediment chemistry in this area is still dominated by contributions from the high peaks, it would indicate that they are the sites of the most rapid denudation.

Such a scenario is observed in some parts of the Nepalese Himalaya. Detrital clay minerals display isotopic ratios of Sr and Nd that are unique to the High Himalaya. This High Himalayan "signature" dominates the detrital clay geochemistry throughout the Lesser Himalaya and even into the Himalayan foreland (Galy et al., 1996). Even when the Lesser Himalaya constitute more than about 60 percent of the source area, their isotopic contribution is less than 30 percent of the total. Although such isotopic ratios do not reveal the absolute flux of sediments or rate of erosion from an area, they can be employed to infer which areas are experiencing

FIGURE 7.8. Determining relative and absolute erosion rates using isotopic ratios in detrital or dissolved loads

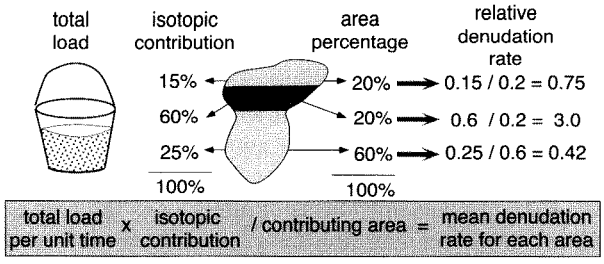

The relative erosion rate of each contributing area is equivalent to isotopic contribution from that area divided by its proportion of the total area. The erosion rate is then obtained by multiplying the total sediment flux by the proportion of the isotopic load attributable to a given source area and then dividing by the size of that source area.

the highest rates of erosion, and they can be used to define relative rates of erosion. Even this is important if our goal is to determine what controls the rates of erosion in a mountainous region, and to test the idea, for instance, that erosion rates are controlled by local relief (e.g., Ahnert, 1970).

Even if you know only the isotopic contributions and the area of each isotopically distinct source area, you can estimate the relative denudation rates between different source areas (Fig. 7.8). If you also know the total sediment load in either the trunk stream or from one of the source areas, then you can also calculate absolute erosion rates for each contributing area (Fig. 7.8).

Hence, a simple mass balance based on isotopic and source-area ratios provides a powerful tool for estimating modern erosion rates and their basin-to-basin variation. It is important to keep in mind, however, that any calculated erosion rate is relevant only for the phenomenon being measured. For example, if isotopic compositions of bedload are measured, then one can calculate the rate of mechanical erosion that produces the observed bedload. If one considers a carbonate terrane versus a granitic one, it is easy to imagine that the relative contributions of these rocks to the dissolved load and the detrital load will vary greatly between these areas, irrespective of the relative erosion rate. In the northwest Himalaya, for example, calcite accounts for less than 1 percent of the outcrop area, but, because it dissolves much more readily than do the prevalent aluminosilicates, it dominates the Sr isotopic composition of the surface waters in some areas (Blum et al., 1998).

Whenever an attempt is made to infer long-term conditions from short-term measurements of isotopic ratios, one must ask whether present conditions are representative of the long-term average. Certainly, one year's sediment flux should not be considered to typify even decadal rates. Commonly, the impact of unusual or catastrophic events on isotopic distributions is unknown. For example, in several places in the Nepal Himalaya, massive rockfalls and landslides have originated from the slopes of high peaks within the Higher Himalaya (Fort, 1987). The run-out of some of these landslides carried them more than 30 km into the Lesser Himalaya (Yamanaka and Iwata, 1982). Today, the Lesser Himalayan rivers have incised into the landslide debris, leaving behind steep risers sweeping up to the former upper surface of the deposit. As these rivers continue to cut into the bases of these landslide deposits, debris collapses into the river and is washed away. Such landslide deposits distort the isotopic signal in at least two ways. First, because they are banked against the adjacent slopes, they create a barrier or buffer that inhibits entry into the river of locally derived bedrock material with its Lesser Himalayan isotopic signature. Second, the poorly consolidated landslide debris with its isotopic signature of the Higher Himalaya is actively being input into the river due to erosion of the steep risers. In this circumstance, even in the Lesser Himalaya, the isotopic composition of the river might be expected to be dominated by the Higher Himalayan contributions, until much of the landslide debris was eroded away. For a large landslide, this erosion might take 10–30 Kyr, such that any modern study during this interval might document a dominant isotopic contribution of the Higher Himalayan rocks due to the ongoing erosion of this large landslide. Therefore, any inferences based on these isotopic studies about the relative contributions of the Lesser versus Higher Himalaya over the long term could be strongly biased and probably misleading.

Regolith Production Rates

In soil-mantled landscapes and in the absence of surface processes that remove unweathered bedrock, the rate of bedrock lowering or erosion is primarily a function of the rate at which bedrock is converted into transportable material (regolith) by chemical and mechanical processes. In the past, these rates have typically been

FIGURE 7.9. Bedrock erosion and regolith production rates using cosmogenic radionuclides

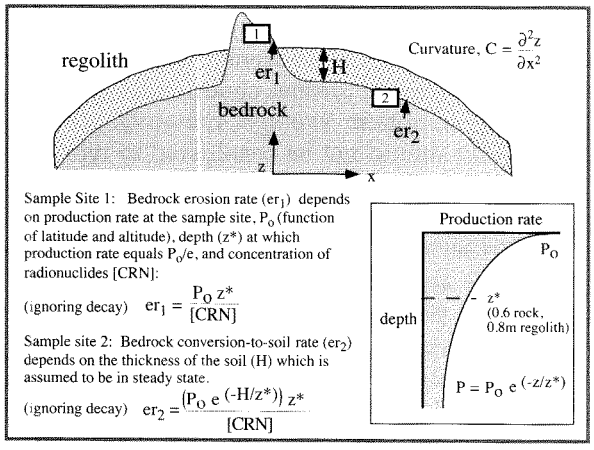

Concentrations of *in situ* produced cosmogenic radionuclides in samples from sites such as 1 yield bare bedrock long-term erosion rate estimates (er1), while those at sites such as 2 yield bedrock-regolith conversion rates beneath a regolith cover assumed to be steady at a thickness, H. If the entire system is in steady state, these rates should agree. The curvature of the hillcrest, C, can be used in combination with the regolith production rate, er2, to yield an estimate of the landscape diffusivity, k (=erosion rate/C), which relates regolith flux to local slope. Inset shows how the cosmogenic radionuclide production rate varies with depth.

poorly known and difficult to measure. Nonetheless, if the average regolith-production rate across a landscape can be determined and if the landscape is in an approximate steady state, then long-term rates of bedrock lowering can be estimated. With the advent of cosmogenic radionuclide techniques, rates of conversion of bedrock to soil can now be assessed more reliably (see primer on cosmogenic nuclides in Chapter 3).

On a bare bedrock knob that is steadily eroding, the concentration of cosmogenic nuclides [CRN] is dependent primarily on the rate of bedrock lowering (E) (Fig. 7.9):

$$[CRN] = \frac{P_0 z^*}{E} \qquad (7.1)$$

where P_0 equals production rate at the surface and z^* equals the rock depth (commonly ~60 cm) at which the production rate drops to 1/e of P_0, and we have ignored any decay of the isotopes. Results from the employment of this technique have been summarized by Bierman (1994). Subsequent work in alpine areas, for example, Small et al. (1999), have shown that rates of the order of 5–15 microns per year (5–15 m/Myr) are very common on exposed bedrock surfaces.

In regolith-mantled landscapes, regolith shields the bedrock from bombardment by cosmic rays, such that nuclide production rates are lower at the bedrock interface. If the landscape is in a steady state, so that the thickness of regolith (H) on a site is constant through time, then the concentrations of nuclides at the regolith-bedrock interface can similarly be used to define the rock-to-regolith conversion rate (Fig. 7.9):

$$[CRN] = \frac{(P_0 e^{-H/z^*}) z^*}{E} \qquad (7.2)$$

This technique has been fruitfully employed on the high surfaces of the Wind River Range (Small et al., 1999), where the rates are found to be consistent within a factor of several tens of percent with those obtained on bare bedrock tors nearby—all on the order of 10 microns/yr.

At steady state, the thickness of regolith will also vary as a function of slope ($\delta z/\delta x$), with thinner soils on steeper slopes. In certain landscapes, the thickness variability is a predictable function of the downslope flux of regolith, which can itself be related to the curvature ($C = \delta^2_z/\delta x^2$) of the slope through the landscape diffusivity constant (κ). The rates so obtained will be average rates over the time it takes to convert about 0.6 m of rock to regolith under steady state conditions. Heimsath (1997) has used this relationship to attempt to define the dependence of regolith production on regolith thickness.

Bedrock Incision Rates

Rivers, along with glaciers, are the most important geomorphic agents for "setting" the local base level. Incision by rivers determines adjacent hillslope gradients, and the success of a river in removing debris supplied from adjacent slopes influences its ability to incise underlying bedrock. If more material comes off the slopes than the river can transport, it will not incise the underlying bedrock or lower the local base level, and adjacent slope angles will tend to decrease. Thus, a suite of self-regulating feedbacks tends to develop in which the long-term rate of base-level lowering by river erosion, the stream power of the river, and the rate of sediment supply from adjacent slopes are in rough equilibrium.

FIGURE 7.10. Schematic approach to calculating incision rates using dated strath terraces

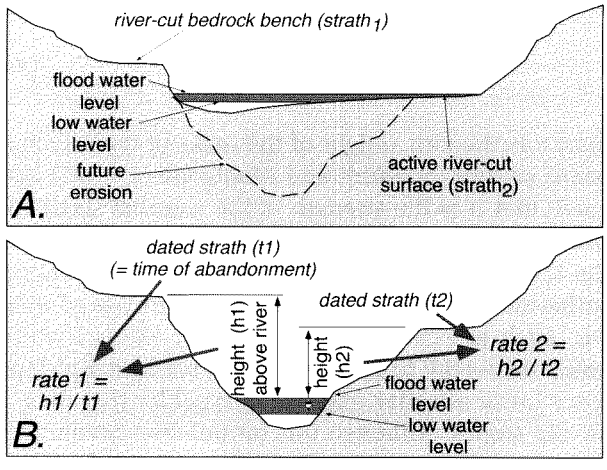

A. After abandonment of strath$_1$, the river bevels a lower bench in the bedrock. This will become strath$_2$ after more incision occurs. B. Rates of river incision can be calculated using the age of the strath surface and the height of the strath above the river.

Bedrock incision rates can be calculated directly whenever the geometry and age of a former land surface can be reconstructed. Because of their predictable longitudinal and cross-sectional geometries, river terraces often provide reliable datums for such calculations. One has simply to measure the elevation difference from the terrace tread to the present river level. Due to their unconsolidated nature, alluvial river terraces are highly susceptible to erosion. Consequently, the history of cut and fill represented by alluvial terraces reveals repeated crossings of the threshold of critical power (Bull, 1991), but tells little about long-term rates of regional denudation or bedrock incision. In contrast, fluvial terraces etched into bedrock (strath terraces) record previous positions of an actively incising river (Fig. 7.10). Using the height of the strath above the modern stream, if it is assumed that the strath resulted from erosion at or near the low point of the river channel, and if the elapsed time since the abandonment of the strath by the incising river is known, then long-term rates of bedrock incision can be calculated (Fig. 7.10).

Determining the age of an abandoned strath is commonly a challenge to the field geologist. Oftentimes, a veneer of fluvial gravel mantles the strath surface, and occasionally preserved organic matter within the gravels can be radiocarbon dated (Lavé, 1997; Merritts et al., 1994; Weldon, 1986). For straths lacking a gravel cover, calculation of the duration of exposure of the strath surface to cosmic radiation can provide an estimate of the time since abandonment of the strath by a downcutting river. In such cases, it must be assumed or demonstrated that the strath has remained uncovered by alluvial material, landslide debris, or persistent snow cover since abandonment, and that the strath surface itself has not significantly degraded. If the strath displays well-preserved original bedforms, such as potholes, flutes, and polished surfaces, that were created by abrasion in a river channel, then it can be argued that little degradation has occurred.

Recent studies along the Indus River in northern Pakistan have used cosmogenic exposure ages of well-preserved straths to define fluvial incision rates of metamorphic and igneous rocks (Fig. 7.11 A, B). In this arid area, some of these straths are extremely well preserved despite their positions more than 100 to 200 m above the modern river. Along a 100-km-long reach of the Indus River, incision rates vary from about 1 mm/yr to greater than 8 mm/yr (Burbank et al., 1996). If such rates were sustained, they would lead to as much as 8 kms of incision every million years. As this is a region where some of the most rapid bedrock uplift rates in the world are inferred to prevail (Zeitler, 1985), it appears that downcutting of the Indus River is in remarkably good balance with the rates of bedrock uplift (Fig. 7.11 C). This is perhaps not an unexpected result. If rock uplift and denudation were not in balance and if rates of more than 5 mm/yr rock uplift were sustained for very long, rivers that failed to incise rapidly enough to keep pace with the uplift would instead develop highly unusual profiles. A mismatch of as little as 20 percent would creat 1 km of relief along the river's course in less than 1 Myr!

Rates of Denudation by Landslides

It has long been recognized that, in actively deforming areas, landsliding often provides an important mechanism for delivering material from hillslopes into valley bottoms occupied by rivers or glaciers. However, because landslides are sporadic events, calculating their time-averaged contribution to erosion can be difficult. Several different approaches could be used to assess erosion by landslides. We know that landslides result from interactions between rock strength (cohesion (c) and the angle of internal friction (ϕ)), hillslope gradients (β), relief, pore pressure, and seismic accelerations. In a

FIGURE 7.11. Bedrock incision along the Indus River, Pakistan

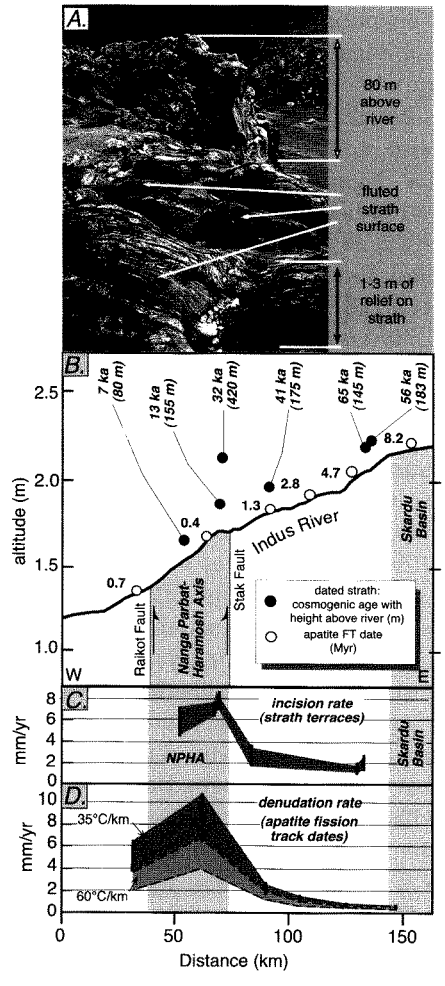

A. Photograph of strath surface about 80 m above the Indus River. Note the polish fluted surface which has several meters of relief on the river-carved features. B. Strath terraces are shown with their cosmogenic nuclide exposure ages and their heights above the modern river level. At river level, apatite fission-track ages are shown. Note that the fission-track ages get progressively older toward the Skardu basin in the east. C. Incision rates versus distance along the Indus. Rates calculated from cosmogenic ages. Note that the highest rates are associated with the steepest river gradient. D. Rates of denudation based on apatite fission-track data. Two calculations are made, each with a different geothermal gradient (35°C/km and 60°C/km). Note that the zone of maximum long-term denudation coincides with the zone of most rapid river incision. Modified after Burbank et al. (1996).

two-dimensional, steady-state, slope-stability model (Culmann, 1875) and in the absence of pore pressure or seismic shaking, the maximum hillslope height (H_c) can be expressed as:

$$H_c = \frac{4c}{\gamma} \frac{\sin\beta\cos\phi}{[1-\cos(\beta-\phi)]} \tag{7.3}$$

where γ is the unit weight of the rocks of the hillslope. Recent studies (Schmidt and Montgomery, 1995) have shown that it is the strength of the weakest strata in a hillslope that determine its failure characteristics, rather than the mean rock strength measured in a laboratory. Furthermore, the orientation of beds or planes of weakness, such as schistosity or foliation, exerts a strong control on overall hillslope strength, because dip slopes have a lower effective angle of internal friction than do anti-dip slopes. Although this formulation predicts the maximum hillslope height in a landscape, and suggests that, in an equilibrium condition, there should be predictable limits to local topographic relief, it doesn't predict a rate of denudation by landsliding, because there is no time dependence in the formulation. Instead it suggests that, under threshold conditions, peaks will be lowered by landsliding at the same rate that the valley bottoms are lowered, such that this relief is maintained. If the rate of valley lowering or river incision is known, then in this equilibrium landscape, the time-integrated contribution of landsliding can also be predicted. The rates themselves would be dictated by the rates of valley incision, and the hillslopes basically come along for the ride.

Another approach to quantifying denudation by landsliding is to develop a relationship between landslide size and frequency. This has the advantage of recording a direct time dependence. On the western slopes of the Southern Alps of New Zealand, repeat aerial photographs spanning 60 years have been used to define the distribution and aerial extent of more than 7000 landslides within an area of about 5000 km^2 (Hovius et al., 1996). These landslides range in size from approximately 100 m^2 to approximately 1 km^2 and define a power-law, magnitude-frequency distribution over two orders of landslide size (Fig. 7.12). Stated in cumulative form, the number of slides of magnitude equal or greater than area A_c,$[n_c(A \geq A_c)]$, is

$$n_c(A \geq A_c) = \kappa(A_c/A_r)^{-\beta} A_r \tag{7.4}$$

where A_r is a reference area, κ is the intercept of the regression when $A_r = 0$, and β is the dimensionless scaling

FIGURE 7.12. Landslide frequency-magnitude distributions from the Southern Alps of New Zealand

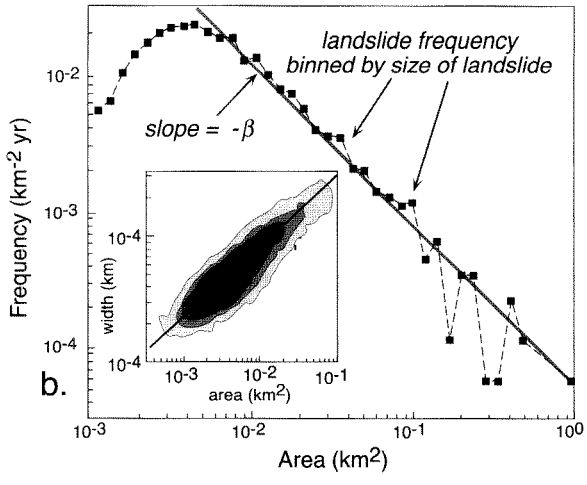

Analysis is based on a 50-year record of aerial photos documenting about 7500 slides. These have been converted into denudation rates based on field calibrations of area-volume relationships. Modified after Hovius et al. (1997).

exponent equivalent to the best-fit linear regression through the linear region of the log-log plot (Fig. 7.12) of the cumulative distribution. When β is greater than 1.5, small events are predicted to dominate the total area covered by landslides, whereas if β is less than 1.5, large events are more important. In the Southern Alps, β equals 1.17, indicating the statistical importance of events with larger areas.

In order to determine the volume of erosion attributable to landsliding, the aerial extent of a landslide measured on a photograph has to be converted to a rock volume. Although not well quantified in the Southern Alps, studies in Japan (Ohmori, 1992) suggest a linear relationship between the length (L) of the displaced mass and its depth (d), such that $d = \varepsilon L$, where ε is a constant less than 1. In the case of New Zealand, ε is estimated to be 0.05 (Hovius et al., 1996). Integrating over the distribution of landslide sizes, the total volume eroded by landslides is then modelled as:

$$V = \frac{2\beta\varepsilon\kappa L_1^{3-2\beta}}{(3-2\beta)} \qquad (7.5)$$

where L_1 is the maximum length of a landslide in a particular setting and is limited by the available relief. In the Southern Alps, L_1 is estimated at about 1 km, and the erosion rate calculated from the above equation averages 9 mm/yr over the entire study area and ranges from 5 to 12 mm/yr within individual catchments. Although these are extraordinarily high erosion rates, they appear to be consistent with the rates of long-term denudation estimated from fission-track ages in the Southern Alps (Tippett and Kamp, 1993; Tippett and Kamp, 1995). When β is less than 1.5, as it is in the Southern Alps, the largest landslides dominate the denudation rate, even though they are less important aerially than smaller slides (Hovius et al., 1996). Because these volumetric estimates are clearly very sensitive to the value assigned to ε, a field-based effort to quantify ε is desirable. Interestingly, the rates of calculated denudation by landsliding, the rates of rock uplift estimated from fission-track ages, and the amount of annual precipitation all co-vary in the Southern Alps, such that areas of high rainfall, high landslide denudation, and high rock uplift spatially coincide. Despite these high rates of hillslope denudation, the rivers in the Southern Alps are "underloaded," such that they export nearly all of the landslide debris delivered to them, and they incise their beds at rates essentially equivalent to the rock uplift rate. Thus, a steady-state landscape can be envisioned here, where balanced rates of river incision and landslide denudation maintain hillslope length and relief through time.

Denudation Rates Derived from Cosmogenic Radionuclide Techniques at the Basin Scale

Imagine the power of a technique whereby dating a handful of sand in a modern river could reveal the average rate of erosion of the entire upstream catchment! Under some geological circumstances, assessing the cosmogenic radionuclide concentrations in detrital mineral grains can indeed indicate the mean erosion rate across a catchment (Brown et al., 1995; Granger et al., 1996). The rate of accumulation of cosmogenic nuclides in rocks at the earth's surface is a function of rate at which the rock surface is being lowered by erosion (Fig. 7.13). If there were no erosion, then the nuclide abundance would increase to a maximum where the rate of production was balanced by the rate of radioactive decay of the nuclide (i.e., "secular equilibrium"). In the face of erosion, a parcel of rock in the subsurface is gradually brought toward the surface, is exposed to increasing amounts of cosmic-ray bombardment as it approaches the surface, and attains a cosmogenic

FIGURE 7.13. Cosmogenic radionuclide concentrations as a function of erosion rate

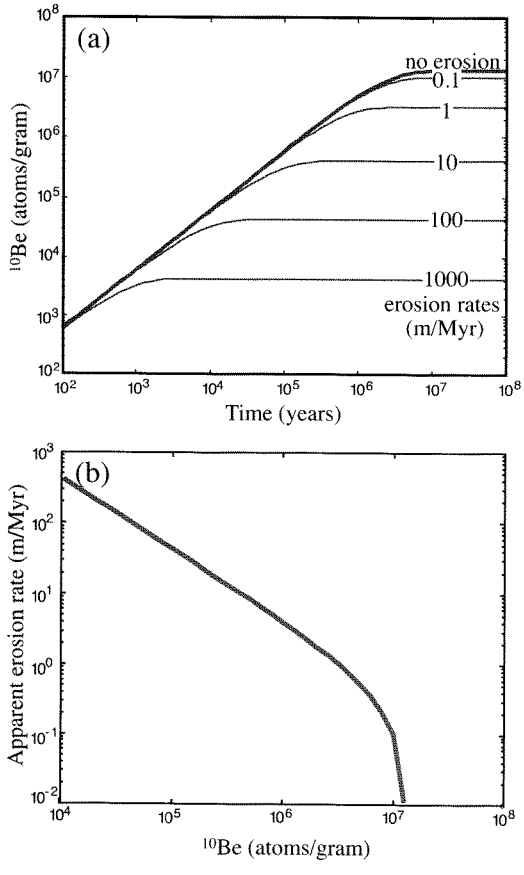

A. Theoretical ^{10}Be accumulation in rock at the surface as a function of time and erosion rate. Rates of erosion vary from 0 to 1000 m/Myr. With more rapid erosion, the time to reach steady state is shorter and the steady-state concentration is lower. Concentrations are calculated for production rates at sea level and would scale with the production rate at higher elevations. B. Apparent erosion rates as a function of steady-state ^{10}Be concentrations. At rates less than 1 m/Myr, radioactive decay accounts for most of the nuclide loss and steady-state concentrations do not indicate mean erosion rates. Modified after Brown et al. (1995).

nuclide abundance that is a function of the rate at which the surface is being eroded (Fig. 7.9). If quartz grains from throughout the catchment contribute to the sediment load in proportion to the local erosion rate, then assessment of the concentration of cosmogenic radionuclides in a sample consisting of many detrital quartz grains can reveal the basin-wide mean erosion rate. A recent study in Puerto Rico of a well-monitored approximately 3 km^2 catchment defined an average denudation rate of about 40 m/My, based on the ^{10}Be concentrations of discharge-weighted average size classes of river sediments (Brown et al., 1995). Unlike short-term measurements of sediment fluxes during recent decades, the cosmogenic nuclide signal integrates thousands of years of denudation and therefore has the potential to yield erosion rates that are largely free of anthropogenic perturbations.

Although attractive in concept, there are clear restrictions on the applicability of this technique. Because cosmogenic nuclide production rates vary strongly with altitude (~3 times higher for every 1700 m increase in altitude), only catchments with limited relief (less than a few hundred meters) are suitable for this technique. The distribution of quartz needs to be nearly uniform throughout the catchment, such that all sites have an equal opportunity to be represented in the detrital quartz load. Thus, a catchment that is situated entirely within a single pluton would be ideal, whereas one encompassing many different lithologies would generally be unsuitable. Sediment sizes in a river vary in part as a function of the erosion process at their source. For example, grain-by-grain erosion on a ridge crest will yield generally smaller grain sizes than will landslides that involve bedrock. Nuclide concentrations in sediments vary as a function of the erosion process that generates the sediments. Because the deeper parts of a bedrock landslide will have had almost no exposure to cosmic rays, the coarse detritus generated by the landslide will have a low nuclide concentration in comparison to fine sands slowly eroded from a ridge crest. Consequently, in order to determine a mean erosion rate, the nuclide concentrations in each size fraction need to be assessed, along with a quantification of the relative contribution of each size fraction to the total detrital sediment load. Despite these many caveats, however, when geological conditions permit, measuring nuclide concentrations in sediments in order to determine mean erosion rates has great appeal because it can integrate an erosional signal from an entire catchment.

Long-term Erosion Rates Based on Radiometric Ages

Rocks in the crust cool for one of two reasons: either a thermal pulse related to a magmatic, hydrothermal, or metamorphic episode wanes, or the rocks are being

TABLE 7.2. Radiometric dating systems and closure temperatures for some minerals

Mineral and dating system	Closure temperature
hornblende (K-Ar)	525±25°C
muscovite (K-Ar)	325±25°C
biotite (K-Ar)	300±25°C
k-feldspar (K-Ar)	200±25°C
sphene (fission-track)	275±55°C
zircon (fission-track)	300±55°C
apatite (fission-track)	120±20°C
muscovite (Rb-Sr)	500±25°C
biotite (Rb-Sr)	275±25°C
monazite (U-Pb)	525±25°C

FIGURE 7.14. Cartoon of contrasting cooling histories derived from ^{39}Ar-^{40}Ar dates on hornblende, muscovite, and potassium feldspar on two different rock samples

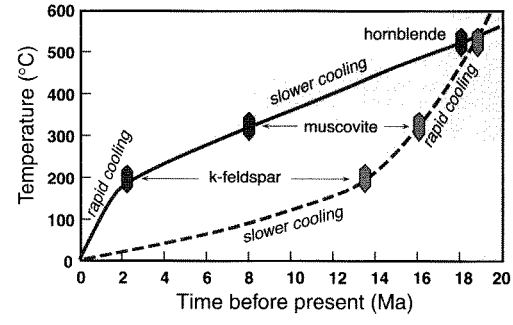

One sample (solid line) displays rapid cooling at ~100°C/My since ~2 Ma, whereas the other (dashed line) shows cooling at a mean rate of ~15°C/My for the past 13 My. Even with significant uncertainties in the geotherm, these data would suggest rapid denudation for the first sample (>2 mm/yr).

moved closer to the earth's surface due to either tectonism or erosion. In response to persistent erosion, deeply buried rocks move upward along the local geotherm toward the surface. During this cooling, various minerals within the rocks will pass through the closure temperatures for different radiometric dating systems (Table 7.2).

For example, in the ^{39}Ar-^{40}Ar dating system, hornblende, muscovite, and potassium feldspar pass through their closure temperatures at about 525, 325, and 200°C, respectively. If hornblende, muscovite, and k-feldspar were then separated from a single rock specimen, the ^{39}Ar-^{40}Ar ages derived from them would yield a cooling history for that rock (Fig. 7.14). Contrasts in the rate of cooling through time can be interpreted from the radiometric data, such that during intervals of rapid cooling, cooling rates of 100°C/My might prevail, whereas rates of 1–20°C/My might persist during intervals of slower cooling. When cooling rates accelerate toward the present day, they are often interpreted to result from enhanced rates of denudation. If there is no local geological evidence for recent normal faulting which could have accelerated cooling, enhanced erosion by surface processes is typically invoked to explain the rapid cooling.

The perennial problem encountered when trying to convert cooling rates to erosion rates is that the local geothermal gradient is almost never reliably defined. Most commonly, a "typical" continental geotherm of 20–30°C/km is assumed and cooling rates are converted to erosion rates on this basis. First, the depth (z) from which the rock came to the surface is calculated:

$$z = c/(dT/dz) \qquad (7.6)$$

where c = the closure temperature for the dated mineral, and dT/dz = the geothermal gradient. Then the mean erosion rate (E) is estimated as:

$$E = z / a \qquad (7.7)$$

where a = the time of cooling through the closure temperature. Thus, combining equations 7.6 and 7.7, a rock that cooled below 200°C about 2 Ma would be interpreted to have been at 6–10 km depth at that time, assuming a geothermal gradient of 20–30°C/km, and to have been brought to the surface, via erosion, at a rate of 3–5 km/Myr (3–5 mm/yr). Even if the geothermal gradient were known at the start of accelerated denudation, that gradient would not persist during rapid erosion. The "rise" of rocks toward the surface would advect heat upwards, such that the local geotherm would be steepened. Theoretical models of warping of isotherms during rapid erosion and cooling (Craw et al., 1994; Mancktelow and Grasemann, 1997; Stüwe et al., 1994) suggest that gradients as high as 60–100°C/km might be achieved with erosion rates greater than 5 mm/yr. The unknown nature of the local geotherm during cooling suggests that large uncertainties should be placed on most erosion rates that are deduced from radiometric cooling histories. Even with 50 percent uncertainties, however, statistically significant changes in erosion rates can often be interpreted

FIGURE 7.15. Calculated cooling age pattern of three geochronometers exhumed at the earth's surface for a two-dimensional, V-shaped topography with 4 km relief and 10 km wavelength

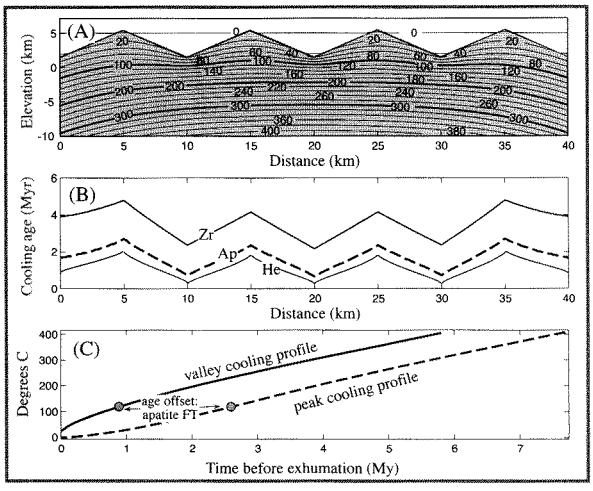

Lapse rate on the surface is set to 6.5°C/km. The erosion rate is spatially uniform at 2 mm/yr, implying the landscape has achieved a steady-state form, and the calculation is carried out over several million years. The chronometers are zircon (assumed annealing temperature of 220°C), apatite (assumed annealing temperature 110°C), and He-U-Th system (assumed closure temperature of 60°C). A. Thermal structure. Most reliable predictions occur between 10 and 30 km on the horizontal scale. Note the warping of isotherms near the surface and the contrasts in gradients beneath the peaks and the valleys. B. The expected spatial pattern of the cooling ages for the three chronometers; C. The temperature paths taken by rocks being exhumed in the central valley (solid) and a central peak (dashed) of the topography. As expected from the distance between the deep, flatter isotherms and the surface, the cooling age variation inferred from zircon fission-track dating should tightly mimic the topography. As the closure or annealing temperature lowers, the influence of the topography on the thermal structure increases, both lowering the amplitude of the cooling age contrast from peak to valley, and imparting a nonlinearity to it. This influence will be larger in the higher erosion cases.

from radiometric data derived from multiple mineral systems. Moreover, these radiometric ages typically provide the best and often the only means to define average erosion rates at million-year time scales.

Rather than simply assuming a geothermal gradient, coarse quantification of the local geotherm can be attempted. Sometimes nearby boreholes penetrate deeply enough to provide a calibration of the coolest part of the geogherm. At a depth of greater than or equal to 15 km in the crust, isotherms are generally parallel to each other and are unaffected by surface topography. Variations in the depth of a given isotherm can be caused by local heat production and by advection of rock. At shallower depths of the order of a few times the local relief, the position of an isotherm is a function of the surface topography and of the rate of vertical and lateral advection of the surrounding rock. Beneath high summits, for example, a given isotherm will be at a higher altitude than beneath a valley (Fig. 7.15), and the near-surface geothermal gradient will be less steep beneath the summit than beneath the valley bottom (Stüwe et al., 1994). If samples for radiometric dating could be collected from near-vertical rock walls several kilometers high, the differences in the times and temperatures of cooling of different minerals across that vertical span would define a rough geothermal gradient during the cooling (Zeitler, 1985). Without knowledge of how past topography perturbed the isotherms, however, this would only be an approximate solution. Moreover, although "vertical sections" for radiometric dating are often described, with very few exceptions, these sections are actually spread out across considerable horizontal distances (e.g., on a transect from a river bottom to a ridge crest), such that the samples from the valleys will have experienced a steeper geothermal gradient than will those samples collected from the peaks.

Consider an example of an alpine landscape with 4 km of local relief and a wavelength of 10 km between summits. If the topography is in steady state, such that erosion and rock uplift are everywhere in balance, a steady-state thermal structure can be modeled as function of the erosion rate (Fig. 7.15). In this particular example, the erosion rate is 2 mm/yr. The predicted age variations at the surface for several geochronometers with different annealing or closure temperatures are striking! The ages vary by a factor of 2 to 4, with the lowest temperature geochronometer being most affected (Fig. 7.15). Cooling rates for Helium dates (~75° closure temperature) would be estimated to vary from over 150°/Myr in the valley bottoms to less than 40°C/Myr at the summits. If an "average" geothermal gradient were chosen, say 30°/km, as a basis for calculating erosion rates, the estimated rates would vary from about 5 mm/yr in the valley bottoms to about 1 mm/yr at the summits.

Whereas these rates clearly bracket the actual erosion rate (2 mm/yr), any individual age and associated rate is likely to be misleading.

Given such uncertainties, why bother with this geochronologic approach? The strongest argument is that cooling histories provide a useful long-term perspective that is related to denudation. It is difficult to get such a perspective without a means of measuring time over millions of years. Second, the example given here is perhaps not typical. If mean erosion rates or the topography relief were lower, the perturbation of the isotherms and apparent rate variations would be less. Finally, even with the valley-to-summit age differences, the data define the limits of past cooling rates and provide useful brackets on acceptable long-term erosion rates.

To improve estimates of the past geotherm, it may be necessary to determine radiometric ages for samples collected along multiple topographic traverses, to determine spatial variations in radiometric heat production in the bedrock, to interpret the dated samples in the context of the actual topography, and to solve iteratively a three-dimensional heat-flow equation in the context of a topography evolving in the face of spatially variable erosion.

Some radiometric techniques permit an estimate of both the past geothermal gradient and the amount of denudation that has occurred. In fission-track dating, spontaneous decay of uranium creates a damage zone or "track" in a crystal which is about 15 μm long and which will gradually anneal and disappear if the temperature is sufficiently high for long enough. For fission tracks in apatite, annealing occurs at temperatures above about 110–120°C. Below that temperature, tracks are retained, so that counting of the number of fission tracks, coupled with documentation of the uranium content of the crystal can be used to define the time at which the apatite crystal cooled below the annealing temperature. Annealing doesn't magically stop at temperatures lower than 110°C; it simply occurs sufficiently slowly that tracks are retained over geologic time. The rate of annealing is kinetically controlled and is a strong function of temperature. Below 60°C there is no appreciable annealing, and tracks remain close to the length they had upon being cooled to that temperature. Think of the "partial annealing zone" as that region of rock in the subsurface lying between 60° and 110°. Within this thermal zone, tracks gradually shorten with more rapid shortening occurring at higher temperatures (Fig. 7.16). A distribution of track lengths evolves that reflects the balance among the ongoing creation of new 15 μm tracks and the shortening of older tracks by annealing. At the base (high temperature end) of the partial annealing zone, the rocks would yield a zero age, because no tracks would be retained, whereas at the top of the zone (low temperature end), rocks would record a time that is somewhat shorter (due to annealing of tracks) than that taken for the sample to move from the base to the top of the partial annealing zone. Below this temperature, outside the partial annealing zone, the gradient of ages would simply reflect the rate of denudation (Fig. 7.16).

Wherever you are standing today, somewhere beneath your feet (and probably within a few km of the surface), fission tracks are being annealed within the partial annealing zone. Imagine what would happen if those rocks were suddenly cooled, say due to an interval of rapid erosion. As soon as they were cooled below 60°C, the distribution of track lengths at that time would be "frozen" into the crystals. Any tracks formed since that time would retain their original track lengths. By examining a suite of samples that spanned the former partial annealing zone, you could reconstruct that zone. Its base should be delineated by a clear break in the slope of the age-versus-elevation curve. Based on the vertical extent of the exhumed zone of partial annealing, you could estimate the former geothermal gradient and approximate amount of denudation that had occurred (Fig. 7.16). If during this same denudation event there had been no change in average surface elevation, then the bedrock uplift and the denudation would be equal and would be documented by the vertical displacement of the former partial annealing zone.

Tectonic Denudation

Tectonic denudation occurs when faulting thins the crust and brings formerly buried rocks closer to the land surface. Such thinning can abruptly redistribute large loads from an elevated region on the surface to a topographically lower area, and it promotes an isostatic response that can locally cause bedrock uplift.

It has been suggested that many compressional tectonic regimes, such as those found at convergent plate margins, can be modelled as critically tapered wedges of a Coulomb material (Davis et al., 1983) that is everywhere at the point of failure. Like a wedge of snow driven before a plow, the taper of the wedge is defined as the angle between its upper and lower surfaces and is a function of the frictional coupling at its base, the dip of the basal detachment surface, and the material properties of the wedge itself. Under conditions of constant shortening and consistent

FIGURE 7.16. Use of a partial annealing zone in apatite fission-track dating to estimate both denudation and surface uplift

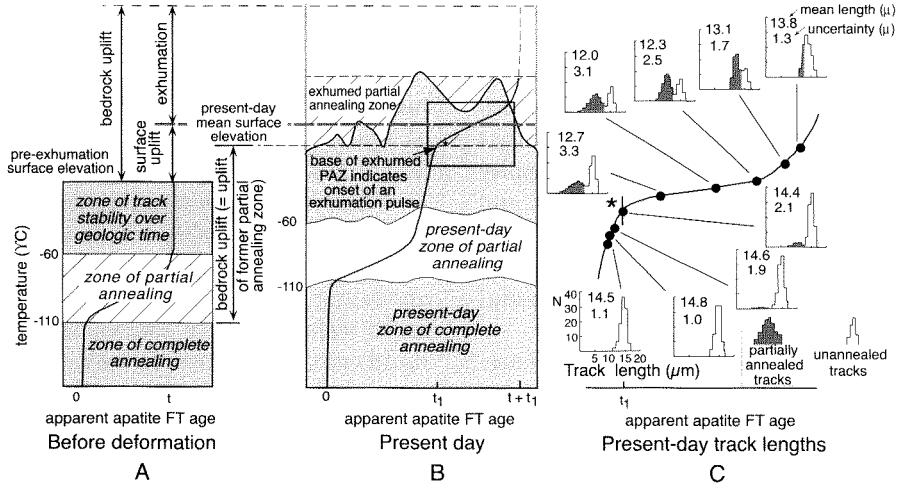

A. At some time (t) in the past, these rocks were subjected to a thermal episode which reset all the ages to zero. At a later time, low-relief topography covers the study area and fission tracks are annealing within the partial annealing zone (PAZ). Samples from the base of the PAZ or below it record an apparent age of zero. Ages gradually increase to the top of the PAZ, above which all ages record the time of the last cooling below 110°C. B. Present-day geometry. At time t_1, an interval of rapid denudation and rock uplift began. This promoted rapid cooling of the rocks in the PAZ and "locked in" the distribution of track lengths. The former PAZ is now represented as an exhumed PAZ, while a new PAZ forms at depth below the surface. In this example, the elevation of the surface prior to "uplift" can be geologically constrained, so that the change in the mean surface elevation can also be documented. Note that the surface uplift represents the rock uplift minus the denudation. C. Track-length distributions in the exhumed PAZ plotted against age and height. The asterisk marks the lowest sample within the former PAZ and coincides with t_1. Dark histograms record track-length shortening in the former PAZ, whereas the open histograms record track lengths since rapid cooling began. Note that age, mean track length, and standard deviation of track lengths change systematically as a function of former position within the PAZ. Modified after Fitzgerald et al. (1995).

material properties and geometries, the wedge will adjust internally to the addition of new material at its toe (or anywhere else) in order to maintain its taper. If any of the controlling conditions or properties change, the wedge should adjust to a new equilibrium taper.

Geologically, this model implies that an orogenic wedge should undergo constant deformation throughout its mass to accommodate the irregular addition of new material to the wedge, losses of material through erosion, and redistribution of mass through deposition or faulting. Geological materials, however, are not truly Coulomb-like in their behavior. Rather than deforming everywhere, they break and deform along discrete planes (faults). Thus, raising of the surface of the wedge in order to counteract erosion typically occurs through thrust faulting or underplating. When conditions change such that the taper of the wedge becomes too great (supercritical), it can adjust itself by three different mechanisms: propagation of the toe (the leading edge) of the wedge, erosion of the elevated surface, or normal faulting. Normal faulting causes a rapid thinning of the wedge and can promote nearly isothermal uplift and decompression in the underlying rocks.

Large-scale normal faulting under regimes of contraction has been identified in many orogens, including the Betics (Johnson et al., 1997; Gelindo-Zaldivar et al., 1999), the Alps (Platt, 1986), and the Himalaya (Burchfiel et al., 1992). Based on the preserved stratigraphy of the hangingwall and footwall, it is sometimes possible to figure out how much material was removed by normal faulting. Usually it is difficult to establish the rate and amount of displacement, so that tectonic denudation rates are not well constrained. When pressure-temperature-time studies of the rocks beneath

the normal fault show rapid depressurization, however, the magnitude, timing, and rate of denudation can be estimated more precisely.

The Miocene history of the Himalayan orogen is one in which tectonic denudation via normal faulting plays a major role. To the north of the High Himalayan summits, a major detachment fault has been recognized as extending for hundreds of kilometers along the strike of the orogen (Burchfiel et al., 1992; Burg and Chen, 1984). This large-scale normal fault, known as the South Tibetan Detachment fault, juxtaposes unmetamorphosed sedimentary rocks with mylonitized crystalline rocks. In places, the fault appears to have accommodated more than 30 km of extension (Hodges et al., 1998). Interestingly, extensional faulting appears to have been synchronous with motion on the Main Central Thrust: the major Miocene-aged thrust found along most of the orogen. Thus, as thrust faulting was causing crustal thickening, normal faulting was extending and thinning the hangingwall of the thrust fault! It is tempting to suggest that the rate of normal faulting, plus erosion, was just enough to balance the rate of crustal shortening, so that the orogen maintained a steady-state topography. In any case, the evidence is unambiguous that thrusting and normal faulting were coeval.

There has been a tendency in the past to ascribe rapid decompression and rapid cooling events to tectonic denudation, that is, normal faulting. Pressure changes on the order of 1 kilobar/My (~3 km/My) were commonly thought only to be possible via normal faulting. Indeed, this may be the correct interpretation. However, recent measurements of surface erosion rates by landsliding (Hovius et al., 1996), glacial erosion (Hallet et al., 1996), and river incision (Burbank et al., 1996) suggest that geomorphic erosion rates of up to 10 mm/yr can be sustained over long intervals in rapidly deforming mountains. Thus, it is no longer clear that rapid unloading associated with some ultra-high-pressure rocks is exclusively caused by normal faulting. In fact, documented erosion rates are fast enough to accommodate nearly all of the documented rates of unloading.

Rates of Uplift

A distinction has already been drawn between rock uplift, surface uplift at a point, and uplift of the mean surface. Each of these is typically referred to some agreed upon reference frame, such as the geoid or mean sea level. Relative uplift can also be useful to define, particularly at a local scale. By relative uplift, we refer to differential displacement of some point or points relative to others. For example, when an anticline grows, there is a relative uplift of rocks in the core of the fold with respect to its flanks. Often, the scale of the fold is such that there is no geophysical response to it. Even if the whole area is subsiding and the mean surface is lowering, it is still useful to document the relative uplift within the fold, as it carries implications for the local tectonics and erosion. Within a local reference frame, it serves to pinpoint the shape of the deformation pattern. Deformed fluvial terraces, provide examples of relative uplift or subsidence on a local scale.

Marine Terraces

One of the classic means for documenting uplift of rocks comes from studies of marine terraces. As depicted in Figure 2.4, a terrace of known age and elevation above present sea level can be used to compute a rate of bedrock uplift. Correlation of multiple terraces in a single transect can define changes in rates through time, whereas regional studies of dated terraces can yield two- and three-dimensional bedrock uplift patterns (Chappell, 1974). Where terraces are well preserved, dating of these terraces to define their appropriate correlation to the eustatic record often provides the biggest challenge (Anderson and Menking, 1994). Where dissection has been extensive, however, simple identification of former terraces within the landscape can be very difficult. On the South Island of New Zealand where rock uplift and dissection have occurred at rapid rates over the past few million years, Bull (1986) used the presence of rounded "beach" pebbles on bevelled spurs as a basis for defining remnants of former abrasion platforms more than 1000 m above present sea level.

Stratigraphic Constraints

As soon as the terrestrial realm is entered, the sea-level reference frame is removed from direct observation. This presents a formidable challenge when trying to interpret rock or surface uplift. Common sense and geologic observation, however, tell us that both depositional environments and the characteristics of river systems tend to vary in systematic, predictable ways as one heads upstream from the coast. Except where there are mountains adjacent to the coast, depositional systems near the continental margins have low gradients. The presence in the stratigraphic record of extensive floodplains, swamps, meandering rivers, estuaries, or

fine-grained and far-travelled sediments generally indicates a low-gradient depositional system. Particularly if "low gradient" terrestrial deposits can be correlated with nearby marine strata of the same age, it is reasonable to infer that the terrestrial system was developed close to sea level. If these strata are now incorporated into a mountain range, the rock uplift of individual points and the change in mean surface elevation can be estimated by comparing the mean present topography with the extent of the former low-lying depositional area.

More commonly, the "low elevation" strata are not preserved within the mountains, but along their flanks. If it could be shown that strata on opposite sides of the range correlate with each other and contain sedimentologic evidence that former rivers flowed *across* the present range, connecting these stratigraphic remnants, this would be strong evidence for surface uplift (Fig. 7.17). Even if it can be shown that a river system on one side of a range had a distant source area on the far side of the range, this will demonstrate growth of the range since deposition. Calculation of the amount of surface or tectonic uplift will depend on how reliably the paleoelevation of the ancient depositional system can be constrained. Correlations of the Neogene stratigraphic record in Alaska have been used to argue that, only a few million years ago, low-altitude rivers flowed across the present site of Mt. McKinley (Denali), the highest peak in North America (Fitzgerald et al., 1995). Although far from the present coast, these strata provide a reference frame for assessing surface uplift.

FIGURE 7.17. Use of stratigraphic evidence to interpret surface and bedrock uplift

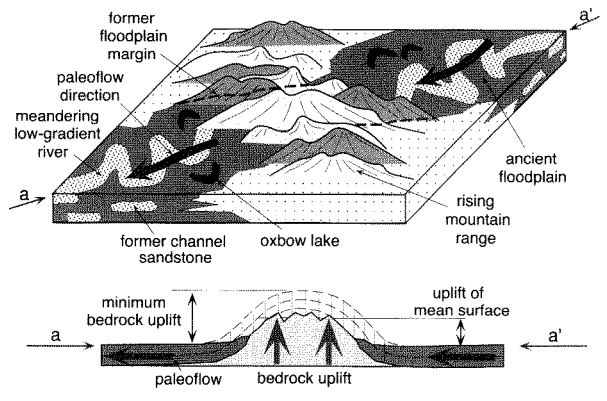

Top: Stratigraphic evidence for a low-gradient paleoriver system, including meanders, oxbow lakes, and broad floodplain. Paleoflow direction of the river is across the site of the present mountain range. Correlation of stratal units and paleocurrent and provenance data indicate that stratal remnants on opposite sides of the mountain range were once contiguous and part of a single, meandering river system. Bottom: Cross-sectional view of the deformed range. Low-gradient river deposits project into the air above the uplifted rock massif. The amount of surface uplift can be assessed by comparing the mean height of the former depositional surface with the mean height of the present mountain range. The minimum bedrock uplift can be calculated by projecting appropriate stratal thicknesses across the summits of the mountains where they have been eroded.

River Profiles

Although often far removed from coastal areas, reconstructed river profiles can be used to document bedrock uplift through time, if certain assumptions are met. It must be assumed that the longitudinal gradients of the modern and ancient valley bottoms were approximately the same, and any differences in former and present base levels must be small compared to the magnitude of rock uplift. Both aggradational and strath terraces can be used to reconstruct former river profiles.

In the Himalaya of central Nepal, the Kali Gandaki River flows southward across the axis of the range. Correlated terraces along its upper reaches show strong divergence (Fig. 7.18) in the downstream direction (Iwata, 1987). Although there is no absolute reference frame to define bedrock uplift with respect to the geoid, these profiles define dramatic differential uplift in the hangingwall above the Main Central Thrust. The northward tilting of the terraces clearly indicates there has been more rock uplift to the south than to the north, and the tilting suggests that the dip of the footwall ramp beneath the thrust decreases toward the north.

Usually as rivers incise farther into their valley bottoms, terraces along their sides are gradually eroded away by hillslope processes. Thus reconstruction of older river profiles can be nearly impossible in many mountainous regions. Sometimes, however, fortuitous circumstances provide a different means of preserving former valley bottoms. In the Sierra Nevada of California, for example, lava flowed down some alpine valleys during Miocene times and overran the former river bed. Because these lavas were more resistant to erosion than were the surrounding rocks, they have been better preserved and actually stand above the modern valley bottoms, where they provide fine examples of inverted topography. These lavas help define the former profile of

FIGURE 7.18. Kali Gandaki River terraces in central Nepal

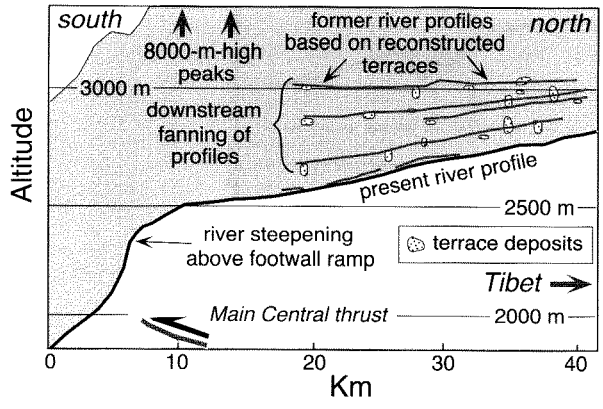

These terraces lie within the hangingwall of a major south-vergent Himalayan thrust fault: the Main Central Thrust. The divergence of the terraces in a downstream direction and their northward tilting indicate differential bedrock uplift above the thrust fault (more uplift to the south) and place some limits on the geometry of the footwall ramp. Modified after Iwata et al. (1987).

a major river flowing west from the Sierra crest. When combined with the modern river gradient in the same valley and the age of the flows, the difference between the profiles constrains the amount and rate of differential bedrock uplift since the lava flow engulfed the valley (Huber, 1981); in essence, these are huge tilt-meters. Although these flows seem like robust markers, they are preserved much closer to the edge of the range than to its crest. Hence, their tilt only places loose constraints on the total tilt and differential uplift of the range.

Tectonic and Surface Uplift Rates

Recall that the mean surface is the same as the mean elevation, but that individual points on the surface may increase in elevation at the same time as the mean elevation or surface height is decreasing. Increases in the mean elevation of a region can only occur in response to tectonic processes of crustal thickening, flexural support due to bending of rigid lithosphere, or changes in the density distribution of the crust and underlying mantle. When assessing changes in mean surface elevation, generally we would like to know how much the mean elevation has changed and what role isostatic uplift played in raising parts of the surface. *Tectonic uplift* can be defined as that portion of the total uplift of the mean surface that is not attributable to an isostatic response to unloading. In order to resolve these different components of uplift, we need to know the geometry of the surface at the start of deformation, the present geometry, the volume of material eroded off the original surface, and any changes in the reference frame, such as in sea level, that are used to assess displacement. If we want to define rates, then ages for the beginning and end of deformation are also needed.

Initially we can note that the total bedrock uplift for a point (Abbott et al., 1997) (Fig. 7.19A) is defined as

$$U_i = (Z_i - Z_{oi}) + E_i + SL_i \qquad (7.8)$$

where at any point i: U_i = total bedrock uplift, Z_i = present topographic elevation, Z_{oi} = original topographic elevation, E_i = thickness of eroded material, and SL_i = change in sea level between the beginning of uplift and the present (a sea-level rise is assumed to be positive).

The total bedrock uplift can be expressed as the sum of a tectonic and isostatic component:

$$U_i = U_{ti} + U_{ei} \qquad (7.9)$$

where at point i: U_{ti} = tectonic component of uplift and U_{ei} = isostatic component of uplift. Combining the above equations and adding in the time of deformation (t), the tectonic uplift rate at a point is:

$$U_{ti}/t = [(Z_i - Z_{oi}) + E_i - (U_{ei} + SL_i)]/t \qquad (7.10)$$

The average of the tectonic uplift rates computed for a series of points across a range then defines a mean rate for the whole range. Note that the data have to be collected across a broad enough area to encompass the region that will respond isostatically to the removal of material by erosion. Thus the rigidity of the crust and its effective elastic thickness, which together set its flexural wavelength, serve to define the approximate minimum dimensions of a study area. The isostatic response to localized erosion will be compensated and smoothed across this entire area.

Unfortunately, although the approach described is conceptually straightforward, there aren't many ranges in the world where it is practical to apply this methodology. The availability of digital topography makes it easy to calculate the present mean surface elevation, but defining a reliable paleoelevation for an ancient surface is often impossible. The optimal strategy for making calculations of tectonic uplift rates (Fig. 7.19) appears

FIGURE 7.19. Topographic variables that need to be defined in order to calculate the tectonic component of uplift

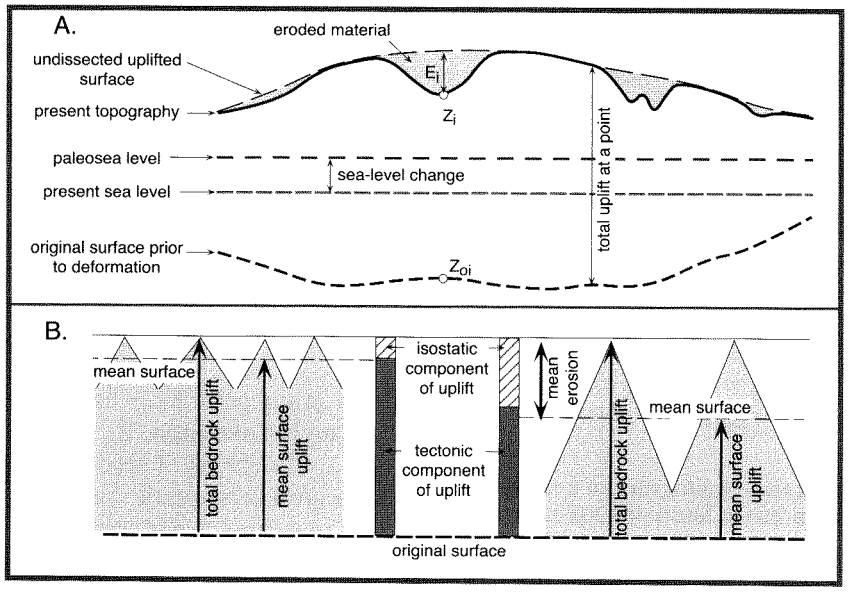

A. Critical estimates of paleodepth can sometimes be obtained using faunal assemblages. Similar estimates of paleoaltitudes are usually far less reliable. Z_i = present elevation, Z_{oi} = initial elevation; E_i = thickness of eroded layer. Modified after Abbott et al. (1997). B. Effects of erosion on isostatic uplift. Given an identical amount of bedrock uplift, the relative amount of erosion determines the proportion of the total rock uplift that is due to an isostatic response. In each case, the isostatic contribution is ~5/6 of the mean erosion.

to require that we study ranges that have experienced large changes in mean elevation, where good dates are available for former surfaces, where enough of an original surface is preserved to permit calculation of the amount removed by erosion, where the amount of sea level change (*SL*) is small compared to the change in mean elevation, and where there is some means to define paleoelevation (Z_{oi}).

One such study has been recently completed in the Finisterre Range of Papua New Guinea (Abbott et al., 1997), where the focus was an only slightly denuded surface of carbonates that had been recently uplifted from considerable depths in the ocean. Foraminiferal assemblages were used to estimate the depositional depth of these carbonates and to determine the time of deposition. These estimates constrain both the paleoaltitude and the duration of deformation (*t*). Although the former depositional surface has been uplifted from water depths of as much as 3 km up to altitudes of more than 2 km, much of the original surface is still preserved. By smoothly interpolating among these preserved surface remnants, an envelope was defined that represents the pre-eroded, but uplifted surface. Subtracting the modern topography from this envelope provides an estimate of the amount of eroded material (*E*), and an isostatic response to this unloading can be calculated. In the Finisterre Range, Abbott et al. (1997) showed that the uncertainties resulting from erosional isostatic compensation and paleo-sea level estimates are small (<10%) compared to a tectonic uplift rate that averages 1–2 mm/yr over the past 2–3 Myr. In the Finisterre Range, the small contribution of erosional isostasy to uplift is not surprising, because the raised surface is still only slightly dissected. In contrast, in settings where erosion has removed all but a few remnants of a former surface, isostasy may drive much of the observed rock uplift at isolated points in the landscape (Fig. 7.19B).

Sometimes it can be possible to use large-scale patterns of deposition to discriminate between tectonic loading and erosionally driven isostatic rock uplift. Both of these can drive local surface uplift of peaks, but in the former case, it results from crustal thickening, whereas in the latter case, it results from erosional

FIGURE 7.20. Schematic contrasts in subsidence and depositional patterns in foreland basins adjacent to mountains undergoing either tectonic loading or erosional unloading

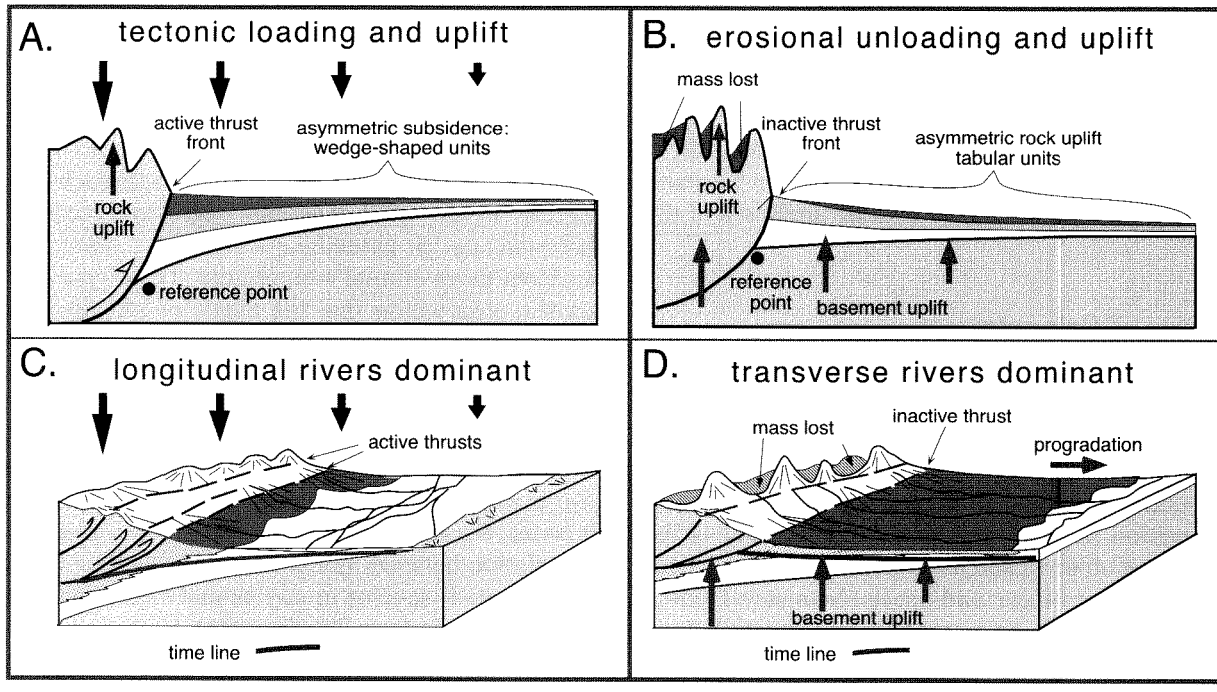

Both scenarios can cause uplift of individual summits, but during erosional unloading, the mean surface elevation decreases. A. Tectonic loading is typified by asymmetric subsidence in the foreland basin. B. Erosional unloading results in rock uplift in the proximal foreland. C. During tectonic loading, transverse rivers are short and join a longitudinal river in a proximal to medial part of the foreland basin. Coarse grained deposits are restricted to near the mountain front. D. During erosional unloading, transverse rivers flow across much of the foreland, longitudinal rivers are in a distal position, and coarse facies may prograde far across the basin. Modified after Burbank (1992).

thinning of the crust. Collisional mountain belts typically abut basins that receive sediments derived from the adjacent mountains. Two aspects of the basin fill and river systems can distinguish between tectonic loading and erosional unloading (Burbank, 1992). During crustal thickening associated with tectonic loading, maximum basin subsidence occurs near the mountain front. This depression is commonly occupied by a longitudinal river flowing parallel to the mountain front in a medial to proximal part of the basin (Fig. 7.20). Transverse rivers debouching from the mountains join this trunk stream a short distance from the mountain front and turn to flow parallel to the mountains. Coarse-grained sediment tends to be trapped in the proximal setting by the rapid subsidence (Heller et al., 1988). In the subsurface, a prism of sediments that thickens toward the mountains provides evidence of the persistent tectonic loading in the hinterland (Flemings and Jordan, 1989).

If the regime switches to one in which erosion prevails over tectonic thickening, such that the crust actually thins, then the reduced mass of the mountains will drive isostatic uplift within the proximal foreland as well, reflecting the finite flexural rigidity of the crust (Fig. 7.20). Erosion will occur in the proximal foreland, and coarse-grained sediments may prograde as tabular, thin sheets across the medial and distal foreland (Heller et al., 1988). Transverse rivers can flow across nearly the entire foreland basin before merging with a longitudinal trunk stream which may itself be pushed toward the far edge of the basin by the proximal rock uplift (Burbank, 1992).

Such a pattern appears to be consistent with the geometry of modern rivers in the Himalayan foreland

(Burbank, 1992). Whereas during Miocene times, coarse strata remained near the mountain front and axial rivers dominated the medial foreland basin, during Quaternary times, tabular sheets of strata prevail in the medial and distal foreland, and transverse drainages over 200 km in length stretch across the foreland. These changes suggest that the relative balance between crustal thickening and thinning has changed during the past few million years. If this is true, then any uplift of summits observed today would represent an isostatic response to a reduction in the overall thickness of the crust.

Estimates of Paleoaltitude

Determining the paleoaltitude of a surface or rock sample represents one of the biggest challenges facing anyone attempting to document uplift of surfaces in inland regions where markers referenced to sea level can not be readily defined. For example, at an average modern elevation of 5000 m, the Tibetan Plateau is the highest region on earth and has a major impact on global climate, sediment fluxes, and ocean chemistry. Despite its significance as a huge orographic feature, the timing and magnitude of uplift of Tibet are still highly controversial (Molnar et al., 1993; Murphy et al., 1997) with estimates for attainment of nearly its present altitude ranging from Cretaceous to late Pleistocene. Similar controversy surrounds the timing of uplift or collapse of western North America.

How does one determine how high some surface was in the past? One means to assess surface uplift is to study the growth of mountain ranges that impact local climatic conditions. The rise of moist air masses as storms approach the flanks of mountains causes orographic precipitation to be focused on the windward side of the range. To the lee of the range, a rain shadow often develops. If you could detect the development of a rain shadow, you might infer that a mountain range had grown to windward. For example, the Miocene aridification of the western part of the Basin and Range has been attributed to the rise of the Sierra Nevada in California (Axelrod, 1957) and its interception of moisture from Pacific storms that used to penetrate farther into the continental interior (Smith et al., 1992). While this may be correct, it is difficult to place reliable limits on how high the range would have to be in order to produce the observed effect, nor can subsidence of the Basin and Range, as opposed to uplift of the Sierra Nevada, be ruled out as a cause of the observed change. In addition, this approach ignores the impacts of global climate change that occur irrespective of the growth of a given range.

Because atmospheric temperatures generally cool with increasing altitude (commonly assumed to be ~6.5°C/km = moist adiabatic lapse rate), as a region rises tectonically and the surface temperature cools, temperature-sensitive plant species and the animals dependent upon them should migrate off the rising surface and move toward lower sites in order to remain in the same temperature range. Another approach to quantifying surface uplift, therefore, begins with correlations between specific assemblages of modern plants and the ambient mean annual temperature. These analyses rely on the observation that the shape or physiognomy of leaves is dependent on climatic conditions (Wolfe, 1993). A smooth or serrated leaf margin, the presence or absence of a drip tip (an elongate, pointed tip that sheds moisture more readily), leaf size, shape of the base, and spacing of the teeth can all be statistically related to the mean annual temperature at which the plant is growing. For example, there is a well-documented positive correlation between the percentage of entire-margined (nonserrated) species in any assemblage and the mean annual temperature (Wolfe, 1971). Having established these correlations, paleoassemblages of flora are examined and assigned a mean annual temperature (T_{int}) based on their closest modern analog. Subsequently, these temperatures are compared with those reconstructed for assemblages of similar age that existed at sea level (T_{si}). Based on these estimates and an assumed terrestrial lapse rate (*TLR*), a paleoaltitude (z) can be calculated:

$$z = \frac{T_{si} - T_{int}}{TLR} \tag{7.11}$$

Although fairly straightforward, this approach suffers from at least four limitations. First, because many species have a fairly wide temperature tolerance, their presence as fossils may be only a loose indicator of former temperatures. Second, relatively few fossils are preserved in continental strata. In marine studies, the problem resulting from the wide temperature tolerance of any individual species is overcome by examining many co-existing species to determine a limited temperature range for that assemblage. In terrestrial settings, unfortunately, a paucity of fossil remains often precludes estimates with a narrow temperature range. Third, by equating a change in mean annual temperature with a change in altitude of a surface, one ignores the effect of global climate change. The onset of the late Cenozoic ice ages has lowered mean global temperatures, such

that a faunal grouping that might have been well adapted at 3000 m in the past is now confined to much lower altitudes. This could happen irrespective of surface uplift or subsidence. Without independent evidence of the amount of climate change, inferences of altitudinal changes based on temperature-sensitive assemblages alone are highly suspect. Fourth, correlation of fossil assemblages with modern analogs assumes little or no evolution of these plants in response to environmetal change (Wolfe et al., 1998). Finally, the technique also assumes that a terrestrial lapse rate can be reliably assigned to a time often tens of millions of years ago.

Floristic approaches to estimating paleoaltitudes have recently been improved with two key steps. First, application of multivariate analysis to the physiognomy of leaves has led to a quantitative calibration of modern meteorological environments with physiognomy (Wolfe, 1990). Second, rather than assuming a lapse rate, the moist static energy of an air mass is used to calculate paleoaltitude (Wolfe et al., 1998). Moist static energy (h) is a thermodynamic parameter representing the total energy content of a parcel of air, excluding a negligible amount of kinetic energy. It comprises two components: enthalpy (which consists of both latent heat and thermal energy) and potential energy (due to altitude) :

$$h = c_p T + L_v q + gZ = H + gZ \qquad (7.12)$$

where c_p is the specific heat capacity of moist air, T is temperature, L_v is the latent heat of vaporization, q is specific humidity, g is acceleration due to gravity, and Z is height. H is enthalpy and equals $c_p T + L_v q$. Moist static energy is presumed to be conservative, which means that the balance between potential energy, latent heat, and thermal energy may change over time, but their sum remains constant as an air mass moves along a trajectory from a coastal site inland. Multivariate analysis shows that enthalpy is second only to mean annual temperature in terms of its correlation with leaf characteristics. If it is assumed that air masses move zonally (within restricted latitudinal bands) and that the preserved flora are truly isochronous at sites being compared, then changes in enthalpy between these sites in the same latitudinal band can be used to calculate changes in potential energy and, therefore, altitude. Due to likely departures from truly zonal circulation and to uncertainties in the enthalpy calculation, recent paleoaltitude calculations have uncertainties estimated to be 750–900 m (Wolfe et al., 1998). Clearly this approach is unsuitable for determining small variations of altitude at a given site. Although the uncertainty on an individual estimate is large, studies of multiple related sites allow reduction of the overall uncertainty. The validity of the assumptions (isochronous sites, zonal transport) that underpin parts of this methodology are difficult to evaluate in the past, such that the actual uncertainty may depart significantly from the formal uncertainity.

For many years, there has been a lively controversy about the paleoaltitude of western North America. Many researchers concluded that it had risen to its present high elevation during late Cenozoic times. Application of multivariate analyses on leaves (Gregory, 1994; Gregory and Chase, 1992) and enthalpy calculations (Wolfe et al., 1998) now suggest that many of these areas have been high since early Cenozoic times, and that some areas, such as the Basin and Range, are considerably lower now than they were 15 million years ago. Clearly, this changes significantly the way one thinks about the history of western North America!

As storms precipitate on the flanks of mountains, the isotopic composition of their rainfall changes. At higher altitudes, the $^{18}O/^{16}O$ ratio is lighter than at lower altitudes. Surface waters, as well as plants, animals, and minerals that are in equilibrium with the surface waters, reflect the isotopic composition of the water in which they grow, and therefore can preserve a record of the variations in isotopic signature (Fig. 7.21). The presence of these isotopic changes suggests some ways in which the growth of mountain ranges could be documented. For example, the isotopic composition of flora or fauna should differ with altitude and on opposite sides of a range with strong orographic precipitation. Thus, if you were to compare the composition on opposing sides of the range from sites that pre-date and post-date growth of the range, the isotopic difference between the sites should increase significantly as the range rises and increases the fractionation (Fig. 7.21). Because the temperature at the time of precipitation also affects isotopic fractionation, climate change can still affect the isotopic composition of rainfall and needs to be considered. Nonetheless, recent isotopic studies from the South Island of New Zealand clearly demonstrate a strongly increased fractionation from west to east as the Southern Alps rose into the path of storms driven by the prevailing westerly winds during the past 5 Myr (Chamberlain et al., 1996). If many sites representing many time intervals could be sampled, these could place some robust timing constraints on the topographic growth of the range.

FIGURE 7.21. Isotopic fractionation of precipitation and the effects of topography

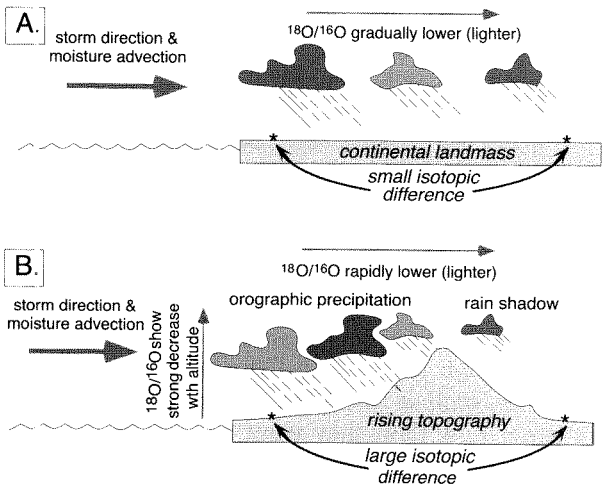

A. In the absence of a mountain range, the oxygen isotopic ratio gradually decreases inland with greater distance from the moisture source. B. In the presence of topography, isotopic fractionation is strongly altitudinally dependent due to orographic precipitation. The increased fractionation also causes a stronger gradient in isotopic ratios across the mountain at the same altitude. Stars mark sites that would display weak (A) and strong (B) contrasts in isotopic ratios before and after the mountain range grew, respectively.

Summary

The balance between erosion and rock uplift lies at the core of tectonic geomorphology. Most landforms in actively deforming areas result from this interplay. New geochronologic tools have greatly enhanced our ability to date surfaces, landforms, and events with increasing precision and accuracy. Underpinning any rate calculations, this new temporal control permits both an assessment of conceptual models, such as that of a topographic steady state, and a calibration of rates of erosion, rock and surface uplift, deposition, and deformation: those factors that modulate the evolution of landscapes.

A key realization of recent studies is that mechanical erosion can proceed at rates as high as 5–10 mm/year. Although the possibility must be assessed in each situation, it is no longer necessary to attribute high rates of cooling (>100°C/My) or rapid decompression (>1 kilobar/My) primarily to tectonic denudation via normal faulting. In some mountain belts, erosion by glaciers, rivers, or landslides has now been measured at rates rapid enough to accommodate nearly all of the documented rates of unloading.

The increasingly widespread availability of digitized topography is permitting rapid characterization of landscapes and facilitates easy calculation of both key topographic variables, such as relief and slope, and geophysical variables, such as mean surface elevation or eroded volumes of rock. Although some of these variables may be statistically tied to erosion, by themselves, they tell us little about the mechanisms of erosion. Key frontiers related to erosion and rock uplift in tectonic geomorphic studies include the documentation and quantification of erosion processes, discovery of new ways to define key variables, such as paleoaltitude or geothermal gradients, and a fuller exploration of the interplay between deformation and erosion in contrasting climatic and tectonic regimes.

CHAPTER 8

Holocene Deformation and Landscape Responses

The modern land surface and Holocene strata typically contain the information used to decipher the paleoseismic record. As seen in Chapter 6, most of this information is derived from narrow zones centered on faults or immediately adjacent to them, because these are the sites where an unambiguous record of deformation can be obtained. The surface deformation attributable to past seismic events, however, typically extends considerably beyond the fault itself. Even when deformation is rather tightly limited to the fault zone, the geomorphic response to the deformation can propagate away from the fault zone to affect other parts of the landscape. Such geomorphic responses to deformation at Holocene time scales form the subject of this chapter.

Despite recognition that many elements of the geomorphic system in alluvial settings are linked to each other, each element does not have a similar response time or sensitivity to changes imposed on it (Whipple and Tucker, 1999). Reconsider, for example, a drainage basin (Fig. 1.3) and the hierarchy of sensitivity of its landscape elements to imposed changes. In order to change the catchment area, the interfluves have to be shifted laterally, but in order to shift the interfluves, the hillslopes that define where the interfluves are located have to migrate in space. Changes in the shape of hillslopes and removal of material from them are typically most sensitive to slope angle, with higher angles leading to less slope stability and more rapid material transport. Changes in the slope angle itself are related to changes in the altitudinal differences between the interfluves and the river channels. If the river channel is lowered due to erosion, the hillslope angle is steepened, rates of creep should increase, and the hillslope may become unstable and prone to landsliding. Thus, the erosion or aggradation of river channels will strongly influence the hillslope responses. In a drainage basin, a hierarchy of sensitivity to most tectonically imposed changes would look like this: (least sensitive) catchment area to interfluves to hillslopes to channels (most sensitive).

Another way to envision the sensitivity of a landscape is to consider the impact on it that a relatively small tectonically induced change might have. For example, if folding causes a region to be tilted 1°, what difference would this make to various elements in the drainage-basin hierarchy? The catchment area and interfluves would be insensitive to such changes at short time scales. If hillslopes were poised at maximum stable slope angles, then some of them could be destabilized by such tilting, but under most circumstances, they, too, would be unaffected. Rivers, on the other hand, typically have equilibrium slopes of considerably less than 1°. An increase of slope of this magnitude would greatly increase the stream power ($\Omega \propto$ discharge • slope), and a river would respond very quickly to this increased power by starting to erode its bed. In a sense, landscape elements like catchment areas and interfluves can be characterized as having considerable geomorphic *inertia*, such that they tend to change slowly, whereas the dynamic nature of rivers and their rapid responses to changing external controls indicate that they have little inertia. In terms of examining the impact of tectonism on Holocene landscapes, it is those elements that have little geomorphic inertia that provide the clearest responses.

It is useful to keep in mind the magnitude of typical deformation rates. Most vertical deformation occurs at rates of a fraction of a millimeter per year. Uplift at 1 mm/yr yields 10 m of uplift in 10 ky and 1 km of uplift in 1 My.

Very rapid and sustained bedrock uplift rates are seen in ranges like the Himalaya (Burbank et al., 1996; Winslow et al., 1994; Zeitler, 1985) and the Southern Alps of New Zealand (Tippett and Kamp, 1993), where rates as high as 10 mm/yr have been documented. Such rates would produce 100 m of vertical displacement in 10 ky. Rates of horizontal displacement on strike-slip faults can be much higher (>40 mm/yr), and might be expected to perturb geomorphic systems even more. Indeed, they cause significant lateral displacements of features at Holocene time scales (Sieh and Jahns, 1984). Because strike-slip faults may induce little differential vertical movement, however, the stability of hillslopes and the profiles of streams along strike-slip faults are typically less affected than in settings dominated by dip-slip faulting.

Given the hierarchy of sensitivity to change within terrestrial geomorphic systems, the magnitude of deformation during Holocene tectonism, and relative impacts of vertical versus horizontal displacements, an examination of Holocene landscape responses to deformation in terrestrial settings focuses naturally on fluvial systems. Although fluvial channels occupy only a tiny fraction of most landscapes, their behavior is a key control on adjacent slopes. We will, therefore, examine some theoretical, experimental, and natural responses of rivers to deformation at the scale of a few meters to tens of meters over periods of decades to thousands of years.

Base Level

John Wesley Powell (1875) introduced the concept of *base level*: the lower limit of the landscape below which rivers cannot erode. In most cases, the ultimate base level is sea level, although in closed tectonic depressions, such as Death Valley or the Dead Sea, it can be lower. The *local base level* refers to the lowest topographic point in a particular area. This could, for example, be a lake which, for the duration of its existence, represents the lowest level to which rivers and hillsides can erode. The *base level of erosion* is a concept that involves all reaches of a fluvial system. It is the "equilibrium (graded) longitudinal profile below which a stream can not degrade and at which neither net erosion nor deposition occurs" (Bull, 1991). When a river is at the base level of erosion, its equilibrium longitudinal profile can be regarded as an infinite succession of adjacent base levels that will be unchanging, until the controlling variables on the system change (Gilbert, 1879). As the river adjusts to imposed changes over time, it may re-establish equilibrium profiles at several positions within the landscape.

Knickpoints

When a reach of a stream is steepened with respect to the adjoining reaches, it defines a topographic *knickpoint* (Fig. 8.1). Such a steepened reach could develop in the absence of tectonism (or eustatic change) simply due to a difference in the erodability of the bedrock: more resistant rocks will tend to underlie steeper reaches of a stream. Tectonically generated knickpoints can be formed through differential folding or faulting of a reach of a river. Normal faulting in which the downthrown (hangingwall) block is in the downstream direction causes a step (knickpoint) to develop in the longitudinal profile of the river. Similarly, thrust faulting that differentially uplifts an upstream reach with respect to a downstream reach will create a knickpoint. In either case, the base level of erosion for the upstream segment of the river has been lowered across the fault. Because the river is no longer in equilibrium, it will begin to adjust its longitudinal profile. Across the steepened knickpoint, stream power will increase due to the increased slope, and erosion of the stream bed will be enhanced. The effect of this erosion is to cause the knickpoint to migrate or propagate upstream.

The mechanism of knickpoint formation and rates of upstream migration in natural settings have not been well documented, especially in relation to faulting events. In an alluviated river valley in New Zealand, local base-level lowering of 4 m (due to artificial lowering of a lake) caused a 2-m-high knickpoint to propagate upstream more than 1 km in less than three months (Mosley, 1984). Rates of knickpoint propagation in bedrock-floored rivers are generally poorly known, but recent studies of knickpoint migration in channels carved into Hawaiian basalts suggest long-term upstream-propagation rates of more than 2 mm/yr (Seidl et al., 1994), whereas rates of vertical incision into Himalayan bedrock of more than 10 mm/yr suggest that knickpoints there may migrate at rates as rapid as 1 m/yr (Burbank et al., 1996). Each of these studies has used cosmogenic nuclide exposure dating of bedrock exposed along channels to determine how rapidly incision and translation have occurred in the past. Without such dating, it becomes difficult to document knickpoint migration in most geomorphic settings. Moreover, in natural settings, it is typically impossible to know the original shape of the knickpoint or how that shape has been modified as it propagated. Is the original

FIGURE 8.1. Development of fluvial knickpoints

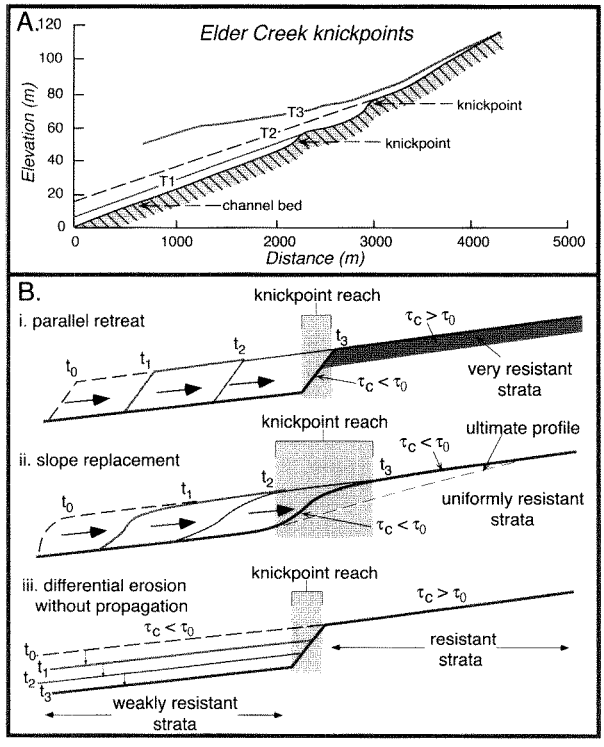

A. Longitudinal river profile of Elder Creek, California, showing two knickpoints. The knickpoints are carved in bedrock. T_1 and T_2 represent strath (bedrock) terraces that appear graded to the crest of individual knickpoints. Modified after Seidl and Dietrich (1992). B. Models for knickpoint migration or formation. τ_c = threshold stress to initiate erosion of bed. τ_0 = actual bed shear stress. i) Parallel retreat of the knickpoint through time with the initial shape being maintained. A resistant rock unit caps the units that are being incised. ii) Knickpoint propagation in uniformly resistant rocks with slope replacement during migration. iii) Knickpoint formation due to differential erosion of strata with contrasting resistance to erosion. No propagation is required here. Modified after Gardner (1983) and Seidl and Dietrich (1992).

shape simply translated through the landscape or is it smoothed and flattened during translation (Fig. 8.1B)? Under circumstances where natural settings reveal little about the geomorphic processes of interest, sometime useful insights on these processes can be obtained through small-scale experiments and modelling which attempt to reproduce key aspects of the natural setting.

Experimental Responses to Base-Level Lowering

In order to mimic base-level lowering, a series of stream-table experiments were conducted in which the level of the outlet of a pre-existing channel network was artificially lowered in order to create a knickpoint and describe its effect on sediment fluxes (Parker, 1977). Following base-level lowering, a knickpoint propagated up the main stem and, as the junction with each of the tributaries was encountered, a new knickpoint would be formed at the mouth of the tributary and would begin to migrate up it. The rate of knickpoint migration was found to be proportional to the discharge (or upstream drainage area), such that as the headwaters were approached, the rate of migration slowed (Fig. 8.2A).

Further stream-table experiments have examined progressive changes in the shape of a knickpoint as a function of the cohesion of the artificial-bedrock and the bed shear stress exerted by the channelized flow (Gardner, 1983). A comparison of the threshold shear stress (τ_c) needed to initiate erosion with the actual bed shear stress (τ_0) serves to predict how and where erosion will occur (Fig. 8.1B). Above the lip of a knickpoint, the channel was observed to become steeper, narrower, and deeper, such that the bed shear stress rapidly increased to a maximum at the lip and promoted rapid erosion at this point. In uniformly resistant bed materials, the originally steep knickpoint evolved through slope replacement into a reach of nearly uniform slope without a clear knickpoint (Fig. 8.2B). On the basis of his experiments, Gardner (1983) concluded that, in homogeneous bedrock, knickpoint retreat would occur only if the rock were pervasively jointed. Alternatively, he observed that knickpoint retreat could occur in layered rocks of variable resistance when a highly resistant layer overlay less coherent rocks. In this situation, undercutting of the lip and its collapse would cause the knickpoint to migrate upstream with little modification of its shape. Even in the stream-table experiments in which slope replacement caused the knickpoint to be transformed into a uniform slope, this transformation took many days during which a clear knickpoint migrated upstream through the channel network.

As the knickpoint migrates through a reach, it is easy to envision that the base of the channel is lowered by erosion and that the new, lowered channel may be graded to its downstream continuation. These stream-table experiments showed, however, that this geometry is only the first stage in a complex response of the fluvial

FIGURE 8.2. Data from stream-table experiments investigating the effects of base-level lowering

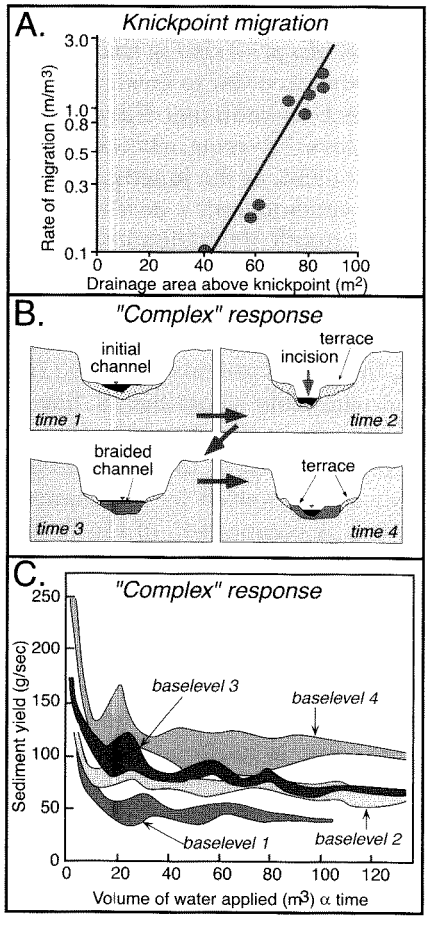

A. Rate of knickpoint migration in stream-table experiments as a function of drainage area (or discharge) contributing to a site. B. Diagrammatic cross sections of channel responding to a knickpoint migrating past it. The alternating intervals of incision and deposition are sometimes termed "complex response." i) Prior to knickpoint passing, small alluvial terraces flank the channel. ii) Immediately after knickpoint passing, the channel has incised through the alluvium and the underlying bedrock. Lateral migration causes it to widen its valley. iii) Increased sediment load from upstream causes the bed to aggrade. iv) Decreased sediment load causes incision of the bed. C. Sediment yield resulting from multiple events of base-level lowering on a stream-table channel network. Note the high variance in yield, the secondary peak that occurs after the initial rapid drop in yield, and the gradual damping of the oscillations in sediment fluxes. Modified after Schumm et al. (1987).

system that is modulated by sediment fluxes. Imagine what happens to the river bottom at a particular point. Prior to the migration of the knickpoint, it "feels" no difference in its base level of erosion and maintains its position. As the knickpoint migrates through, the reach is steepened, stream power increases, more sediment is eroded than is deposited, and the bed is lowered until it is approximately graded to the adjacent downstream reach (although it may not have attained the base level of erosion at this time). As the knickpoint migrates farther upstream, the sediment flux to that downstream site increases due to the enhanced erosion upstream. Without a corresponding increase in discharge or slope, the increase in sediment load causes deposition within the previously scoured channel, so the base of the channel rises. Ultimately, as the knickpoint nears the headwaters, sediment production decreases, and the stream incises into its bed once again (Fig. 8.2B). The multiple events of incision and aggradation described here represent a complex response to simple base-level lowering. The fact that similar responses may be recorded by Holocene fluvial strata suggests that considerable caution may be needed when interpreting phases of aggradation and degradation.

In another stream-table experiment, multiple events of base-level lowering were imposed on the fluvial system, and the sediment yield was measured as the stream network adjusted to the changes. Following each base-level lowering, there was a dramatic increase in sediment yield which subsequently decayed exponentially. This decay was not smooth, however, but was characterized by secondary peaks and troughs (Fig. 8.2C) and by high variance. These curves also indicate a greater amount of total sediment yield for each successive event of base-level lowering. This overall increase may result from the increasing height above base level and the increasing potential energy of the sediments with time (Schumm et al., 1987). The secondary peaks in sediment yield appear to result from sporadic collapses of valley walls that suddenly shunt extra sediment into the channel.

Numerical Experiments

The apparent conflict between Gardner's (1983) observation that knickpoints degenerate into uniform slopes during stream-table experiments using homogeneous material and the field observation that at least some knickpoints in homogeneous bedrock appear to be rather long-lived suggests that other approaches, including

FIGURE 8.3. Simulations of knickpoint evolution

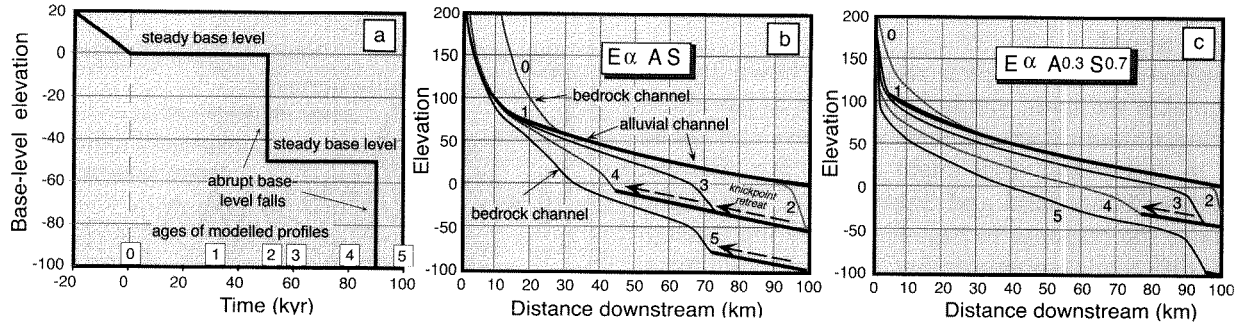

A. Schematic representation of temporal changes in base level. Instantaneous drops punctuate intervals of stable base level. Numbers in boxes refer to the temporal position of the modeled profiles in subsequent frames.
B. Profile evolution when erosion is proportional to stream power. Note the generally consistent height and shape of the knickpoint indicate migration due to "parallel retreat." Heavy lines indicate alluvial reaches of the profile.
C. Profile evolution when erosion is proportional to bed shear stress. Diminishing height and slope of the knickpoint indicate migration due to "slope replacement." This model implies that knickpoints would be unlikely to persist for long periods (>40 kyr). Modified after Howard et al. (1994).

numerical models, may be useful in investigating knickpoint migration. In one such model (Howard et al., 1994), erosion, E, is represented as a function of water discharge, Q, sediment discharge, Q_s, and slope, S:

$$E = K \bullet Q^a \bullet Q_s^b \bullet S^c \qquad (8.1)$$

where K is a constant related to bedrock erodability. Because both Q and Q_s often change systematically with drainage area, drainage area, A, is used as a proxy for discharge. Thus, this equation can be simplified to

$$E = K \bullet A^m \bullet S^n \qquad (8.2)$$

Based on this general erosion equation, Howard et al. (1994) propose two erosional models. One model is based on indirect evidence that in some channels, the erosion rates are proportional to stream power ($S \bullet Q$), such that both m and n are approximately equal to 1 (Seidl and Dietrich, 1992). The second model assumes that erosion rates are proportional to bed shear stress, so that m equals 0.3 and n equals 0.7 (the theoretically expected values for erosion in bedrock). At the start of both models, streams are assumed to be cut in bedrock with a concave profile that is in equilibrium with a slow and constant rate of base-level lowering, such that all parts of the profile are eroding at equal rates. To have equal erosion along the river's length, there is a consistent trade-off between slope and discharge, such that downstream increases in discharge compensate for downstream decreases in slope. Although the stream is cut in bedrock, if the erosion produces gradients that drop below a critical value, there will be alluvial deposition on the stream bed.

As the model begins, long periods of stable base level are punctuated by pulses of base-level lowering (Fig. 8.3A). In both model runs, the knickpoints migrate upstream and alluvial and bedrock terraces are left behind. Former alluvial sections above the knickpoint are largely unaffected until the knickpoint passes that point. When erosion is proportional to stream power (Fig. 8.3B), both the gradient and height of the knickpoint remain quite constant as they migrate upstream. When erosion rates are proportional to bed shear stress (m, $n < 1$), the knickpoints are rounded (Fig. 8.3C) and diminish in both height and gradient as they migrate. Whereas the first model indicates knickpoint migration through parallel retreat, the second is more consistent with slope replacement (Fig. 8.1B). In either model, if the stable gradient of the alluvial reaches is significantly steepened, for example, due to a large increase in mean grain size, then the height, gradient, and persistence of modeled knickpoints diminish during migration (Howard et al., 1994). The utility of these models is that

they illustrate 1) conditions under which knickpoints could be expected to migrate, 2) how knickpoint shapes could change through time, and 3) how multiple events of base-level lowering might be represented in the geomorphic record.

Inspired by the complex response shown by the stream-table sediment yields in response to base-level lowering, numerical experiments were developed in an effort to understand what might control the observed variability (Slingerland and Snow, 1988). The model simulates the response to base-level lowering through partial differential equations that describe nonuniform, unsteady flow and sediment transport in an alluvial channel about 200 km long with tributaries every 20 km. The sediment discharge from the tributaries is a complex function of the changes in bed elevation at the junction (knickpoints) with the trunk stream. With an assumed fixed water discharge (10 m^3/sec) and a fixed basal sediment discharge from the tributaries, the system was tested for the effects of lags in the response of tributaries to base-level changes. Slingerland and Snow (1988) recognized that sediment yields from tributaries do not solely result from erosion within the channel itself: as channels deepen, adjacent hillslopes collapse and gullies discharge sediment into the tributary. Although not modeled as a geomorphic process, these additional sediment sources were represented by a multiplier which increased the sediment yield from each tributary.

The results in the absence of tributaries show a simple exponential decay in sediment yield in which sediment discharge is proportional to the amount of base-level lowering. Time lags alone in tributary responses are insufficient to produce the desired discharge fluctuations, but a lag of 300 years combined with a tributary multiplier of 3 for sediment production results in sediment yields and erosion and aggradation of the main channel (Fig. 8.4) that mimic the changes documented in the experimental runs of Parker (1977). One should ask whether these time lags and sediment multipliers have any meaning for actual river systems. To the extent that "out-of-channel" processes, such as hillslope collapse and emptying of side gullies, dominate the sediment budget in the tributaries, but are not explicitly included as part of the process model, it is not unreasonable to include them. (Recall that actual channels occupy only a small fraction of the landscape.) Also it is clear that hillslope responses will not be instantaneous, so that it is worthwhile to explore numerically possible time lags and the significance these hillslope sediment sources must have in order to produce fluctuations such as those seen in the stream-table experiment (Parker, 1977).

FIGURE 8.4. Numerical model of depth of erosion along a trunk river caused by base-level lowering, knickpoint migration, and complex response

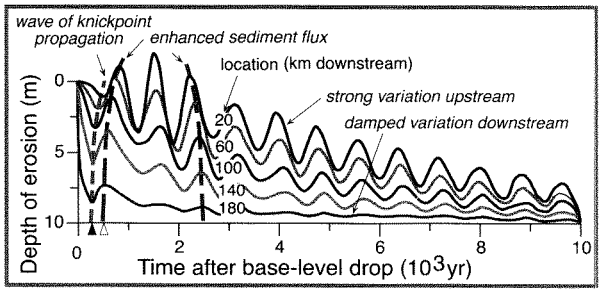

Each curve represents the predicted erosion and deposition at a different distance downstream. By comparing the peaks or valleys at different distances, it is possible to see how waves of erosion and deposition are predicted to migrate upstream and downstream. The damped, oscillatory pattern of erosion and deposition is obtained by specifying a time delay in the response of tributaries to the passage of a knickpoint and by augmenting the tributary channel erosion to account for hillslope contributions. The calculated variability mimics the sediment discharge variations caused by base-level lowering on stream-table channel networks (Fig. 8.2C). Modified after Slingerland and Snow (1988).

Planform Changes: Geometry and Position

Many modern rivers display contrasting channel patterns, including meandering, braided, anastomosing, and straight channels, along their courses, and some of these rivers are known to cross areas of ongoing deformation. Wouldn't it be useful to be able to examine the channel pattern of a river in order to determine the nature of active deformation along its length? To succeed in this, we would need to know how changing channel patterns of the rivers correlate with differences in deformation rates. Moreover, we would need to know how to distinguish between changes in patterns that result from nontectonic versus tectonic causes.

Numerous previous studies of channel patterns indicate (Fig. 8.5) that they respond to several competing controls,

FIGURE 8.5. Classification of fluvial channels

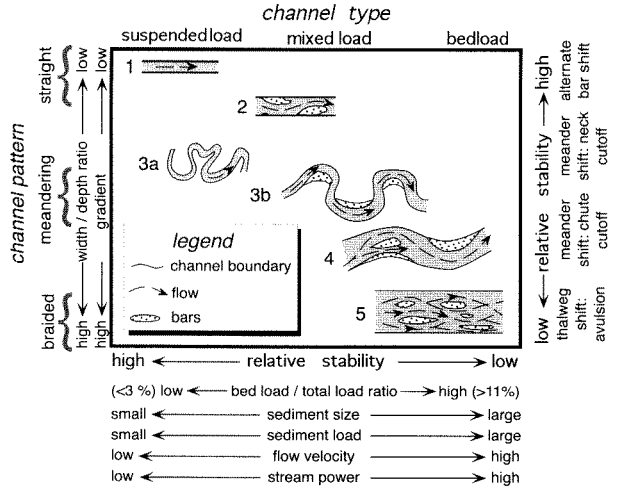

Channel patterns and the persistence of channel shapes are conceptualized as a function of nature of the sediment load, velocity, and stream power. Modified after Schumm (1986).

FIGURE 8.6. Channel pattern as a function of specific stream power during bankfull discharge versus mean grain size of the river bed

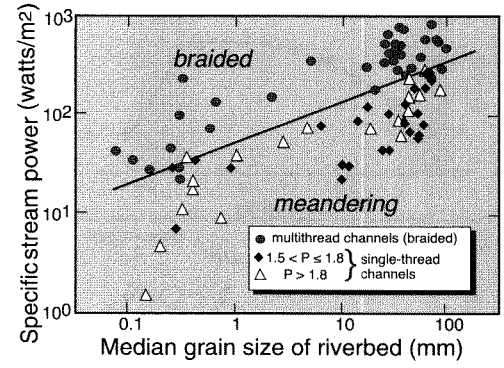

Based on data from >200 rivers. Specific stream power, watts/m^2, calculated from river slope and channel cross section at bankfull stage. Sinuosity (P) is the ratio of the length of the thalweg to the valley length. High sinuosity (P >1.5), single-thread (meandering) rivers define a separate field from that of braided rivers. This plot predicts that, for a given grain size, the channel pattern is a function of specific stream power and that changes in water depth or slope can cause the river to cross the threshold defining the different channel patterns. Modified after van den Berg (1995).

including sediment size and load, flow velocity, and stream power (Schumm, 1986). In general, braided rivers are favored by high sediment fluxes, weak bank material, and high variability in water discharge, whereas meandering rivers are typified by lower sediment loads, more cohesive bank material, lower flow velocity, less variable discharge, and lower stream power. It is common for braided rivers to change downstream into meandering rivers as slope and mean grain size diminish. Each of the variables affecting channel patterns can clearly be independent of tectonic activity. Recent studies (van den Berg, 1995) suggest that, based on a comparison of specific stream power during bankfull discharge ($\omega_{bankfull}$ = watts/m^2) with the mean grain size of the river bed (Fig. 8.6), it is possible to predict whether river channel patterns will be high sinuosity (meandering) or low sinuosity (braided). This relationship suggests that tilting due to tectonic processes could certainly affect whether a river was braided or meandering.

Stream-table Experiments

Stream-table experiments designed to investigate possible responses of channel patterns to changing slopes show predictable transitions in channel forms (Fig. 8.7). As slope increases while discharge and sediment supply are held constant, initially straight channels become more sinuous. Sinuosity continues to increase until a threshold slope is attained, after which any additional steepening of slopes leads to a braided river pattern. Further experiments indicate that, for different discharges, the transition to braided occurs at different stream power, but at approximately the same slope (~0.012–0.013) for each discharge (Edgar, 1973). It is important to note, however, that the grain size is also held constant in these experiments. For each of these stream-table examples, river width increased and depth decreased with increasing slope. Although the reasons that rivers meander are not completely understood, it is clear that meandering rivers, through localized bank erosion and sediment transport, tend to dissipate energy in equal amounts along equal lengths of channel and to minimize the total energy expended along the river course. When a channel is steepened, stream power initially increases, such that a stream formerly in equilibrium will be pushed into a nonequilibrium condition. By increasing

FIGURE 8.7. Effect of slope on river sinuosity in stream-table experiments

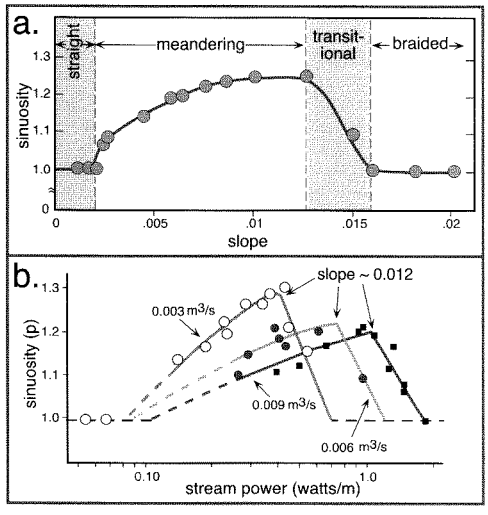

A. Channel sinuosity on a stream table as a function of slope. Modified after Schumm and Khan (1972).
B. Sinuosity as a function of stream power for 3 different discharges. In each, sinuosity begins to decrease at slopes exceeding ~0.012. Modified after Edgar (1973).

sinuosity, the channel is lengthened, the slope along the thalweg decreases and counteracts the increase in the valley gradient. As a consequence, the rate of work done per unit length of channel is lessened.

In a different stream-table experiment, a kink fold was created across an established channel midway along its length (Ouchi, 1985). The fold directly deformed only the middle third of the stream table, and fold growth was mimicked by incrementally increasing the height of the fold crest. Such growth caused an increase in the valley slope on the downstream side of the fold axis, whereas it diminished the slope on the upstream flank of the fold. When folding was superimposed on a pre-existing meandering river pattern, the primary response to the uplift was an increase in the thalweg sinuosity in the downstream part of the uplift, where the slope was steepened (Fig. 8.8A). The elevation of the thalweg itself increased in the uplifted area, but the increased sinuosity compensated for the steeper slope of the "valley" bottom. Thus a convexity developed in the valley slope profile, while little significant aggradation or degradation occurred at the fold crest or on its downstream limb. Upstream of the uplift, the point bar was flooded and the

FIGURE 8.8. Effect of uplift on meandering and braided patterns during stream-table experiments

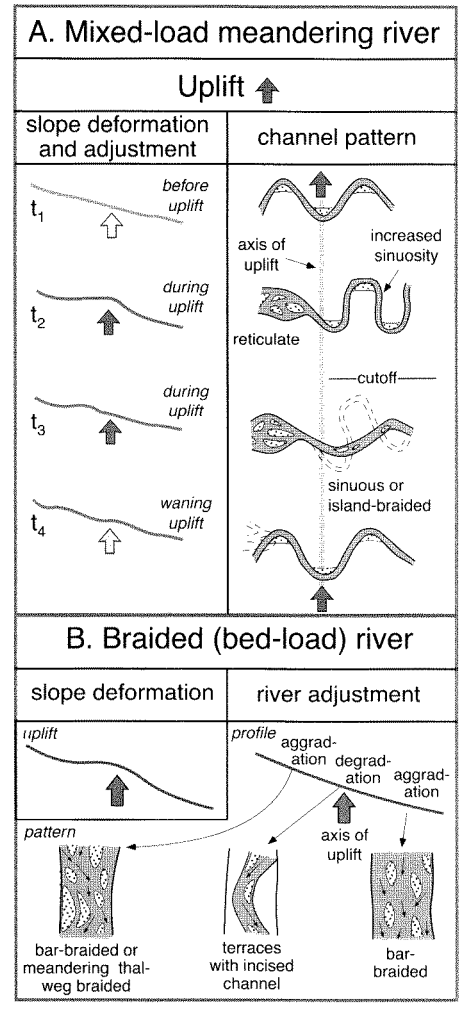

A. Schematic response of a mixed-load meandering river to the growth of an anticline. Right panel shows the change in valley profile with time as uplift is initiated and then wanes. Initial growth causes increased sinuosity on the downstream fold limb and increased deposition on the upstream limb. When the slope threshold is crossed, a braided channel develops, incision occurs across the fold crest, and the locus of erosion migrates upstream. As uplift wanes, meandering pattern is re-established. B. Schematic response of a braided river channel to folding. Changing gradients and elevations promote erosion across the fold crest, increased sediment fluxes downstream, and aggradation on both flanks of the fold. Modified after Ouchi (1985).

thalweg became indistinct due to ponding. Deposition occurred along the shallowing gradient, and there was a tendency to establish multiple stable channels (an anastomosing pattern: Smith and Smith, 1980). With continued uplift, a cutoff formed downstream of the axis of uplift, and the channel steepened, straightened, and assumed an "island-braided" pattern. Folding experiments with a braided river caused erosion across the fold crest where a deepened, single-thread channel bounded by river "terraces" was created (Fig. 8.8B). Downstream of the fold axis, the steepened slope and increased sediment flux (due to erosion of the fold crest) augmented the pre-existing braiding. Upstream, however, the decrease in slope and sediment flux generated alternate bars with a tendency toward a more sinuous, single thalweg.

Given the simple observation that sinuosity tends to increase with increased slope (up to a threshold), it might be expected that active deformation could be revealed by map patterns of meandering rivers showing localized changes in sinuosity along the river course or indicating a temporal change in sinuosity along a given reach. Similarly, along generally braided rivers, zones of incised, single channels bounded by terraces would be likely candidates for zones of active uplift.

Numerical Experiments

Using a numerical model similar to that used to investigate river responses to base-level lowering, Snow and Slingerland (1990) modeled the effect of a domal uplift of deposition and erosion. Although conceptually similar to the experimental stream-table set-up of Ouchi (1985), a sinusoidal fold, rather than a kink fold, was modeled. The model specified a straight channel with a fixed cross section flowing across noncohesive bed material. Maximum rates of uplift were 5 mm/yr, and the folding affected 100 km of stream course (Fig. 8.9). Results of the modelling show major erosion across the axis of uplift and centered on it. Considerable upstream deposition occurs due to growth of the fold and "ponding," whereas more limited downstream deposition results from the enhanced sediment flux and the need to maintain continuity with the uplifted river course. Through time, the zone of erosion widens, and the point of maximum increase of elevation migrates upstream well beyond the axis of the uplift. Deposition rates are the same magnitude as erosion rates during the first few hundred years, then deposition stabilizes, whereas erosion keeps pace with uplift. With time, deposition upstream of the axis of uplift causes the profile to become increasingly

FIGURE 8.9. Modelled response to anticlinal uplift of a stream flowing across a noncohesive bed

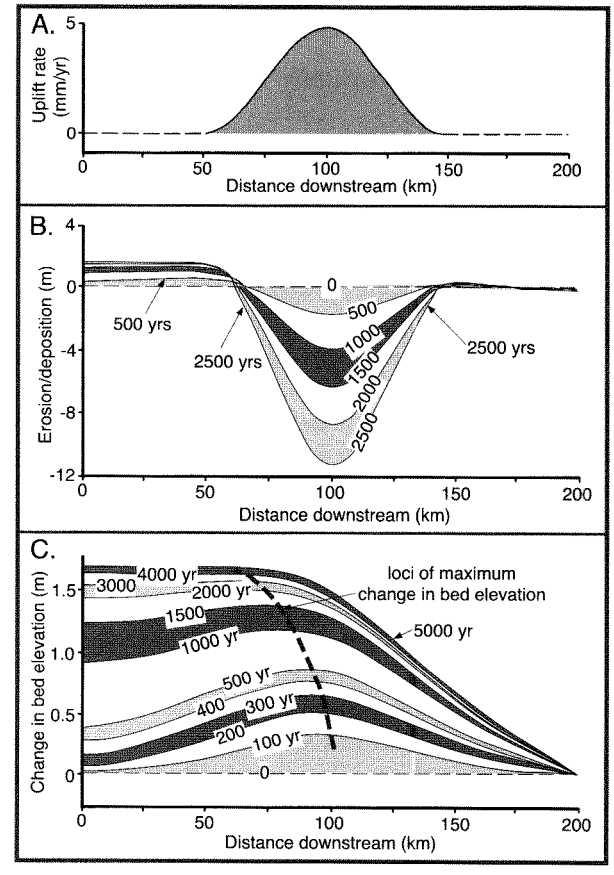

A. Pattern of uplift, reaching a maximum of 5 mm/yr. B. Erosional and depositional responses to uplift. Note that the erosion generally mimics the uplift pattern, but that deposition occurs upstream of the anticline. C. Change in bed elevation. Note that the point of maximum change migrates upstream through time and that the system approaches a steady state (dynamic equilibrium) in 3–5 kyr. Modified after Snow and Slingerland (1990).

asymmetrical and convex. Perhaps most important, despite ongoing uplift, the profile approaches a steady state by approximately 5 kyr that could be viewed as representing a dynamic equilibrium in which each increment of uplift is matched by equivalent erosion.

It is instructive to note that, after 5 kyr and 25 m of "rock" uplift, the elevation of the channel has only increased ~1.5 m, indicating the 95 percent of the

uplifted material has been eroded away (Fig. 8.9). Given the noncohesive character of the material beneath the channel, this is perhaps not surprising. If the model were run with more resistant bedrock, a much greater change in elevation could be expected.

Examples of Tectonically Perturbed Fluvial Systems

Based on the previous descriptions, one can envision several different patterns and orientations of deformation that could affect fluvial patterns. Tilting and uplift or subsidence due to folding perpendicular to a river course will modify valley gradients. Tilting along an axis that is parallel to a river course could deflect or displace a river system. Discrete offsets related to faults will affect the local base level, as well as causing tilting.

Several examples illustrate these different tectonic scenarios. Simple monoclinal folding along the Post-Vicksburg flexure in southeast Texas appears to have caused a considerably steepened valley gradient along the San Antonio River (Fig. 8.10A). Through this steepened reach, the sinuosity doubles (Ouchi, 1985), whereas the gradient of the channel itself only increases by about 10 percent (Fig. 8.10B). One weakness with the analysis of the San Antonio River is that the timing and rate of deformation are poorly known.

Recent studies in the Los Angeles basin have examined folds developing above blind thrusts (Bullard and Lettis, 1993). Although dating indicates that both Quaternary and Holocene rates of vertical deformation are rather low (~0.1–0.3 mm/yr), streams appear to display increased channel slopes, maximum incision, and increased sinuosity across the crest of these growing folds (Fig. 8.11). The crests themselves are also delineated by displaced alluvial surfaces into which the modern stream has incised.

Sometimes evidence for contrasting tectonic regimes can be inferred through comparisons of adjacent drainages that display different channel patterns. A satellite image of northern Pakistan (Fig. 8.12) shows the Indus and Kabul Rivers merging and flowing through a water gap in the Attock Range. At the point of their merger near where they enter the water gap, both rivers are responding to the same local base level. The Indus is flowing on or near bedrock through the Attock Range, and other studies suggest the range is experiencing active bedrock uplift (Burbank and Tahirkheli, 1985). Consequently, for both the Indus and Kabul Rivers, base level is probably slowly rising. Despite this common base level, the planform river patterns upstream from the water gap contrast strongly with each other: the Indus displays a strongly braided channel pattern, while the Kabul shows a nearly straight channel at a comparable distance upstream. It appears the Indus is actively aggrading in response to the rising local base level, whereas the Kabul is incising its bed. Why does this contrast exist? The likely cause can also be inferred from the satellite image. Linear trends to the south of the Kabul River delineate active transpressional faults (Fig. 8.12). The zone of uplift appears to extend across the Kabul River toward the northeast. Throughout this uplifting reach, the Kabul River is incising. Just upstream of this

FIGURE 8.10. Fluvial response to localized uplift

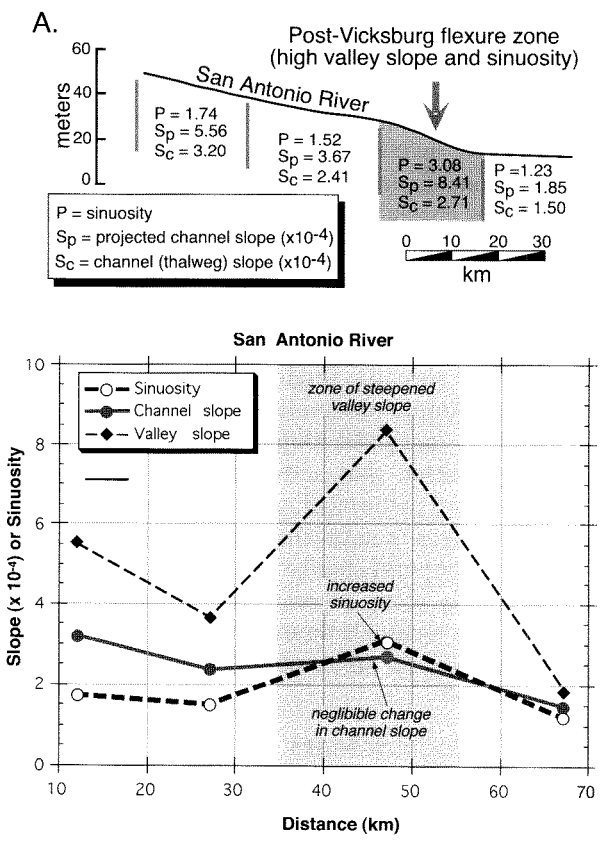

A. Longitudinal profile of the San Antonio River and associated changes in valley slope (S_p), river slope (S_c), and sinuosity (P). Modified after Ouchi (1985). B. Plot of valley gradient, channel slope, and sinuosity along the San Antonio River. Through the reach where the valley slope more than doubles, the sinuosity also doubles, whereas the channel slope is almost unchanged.

FIGURE 8.11. Map of growing anticlines associated with south-vergent, blind thrusts in the Los Angeles basin

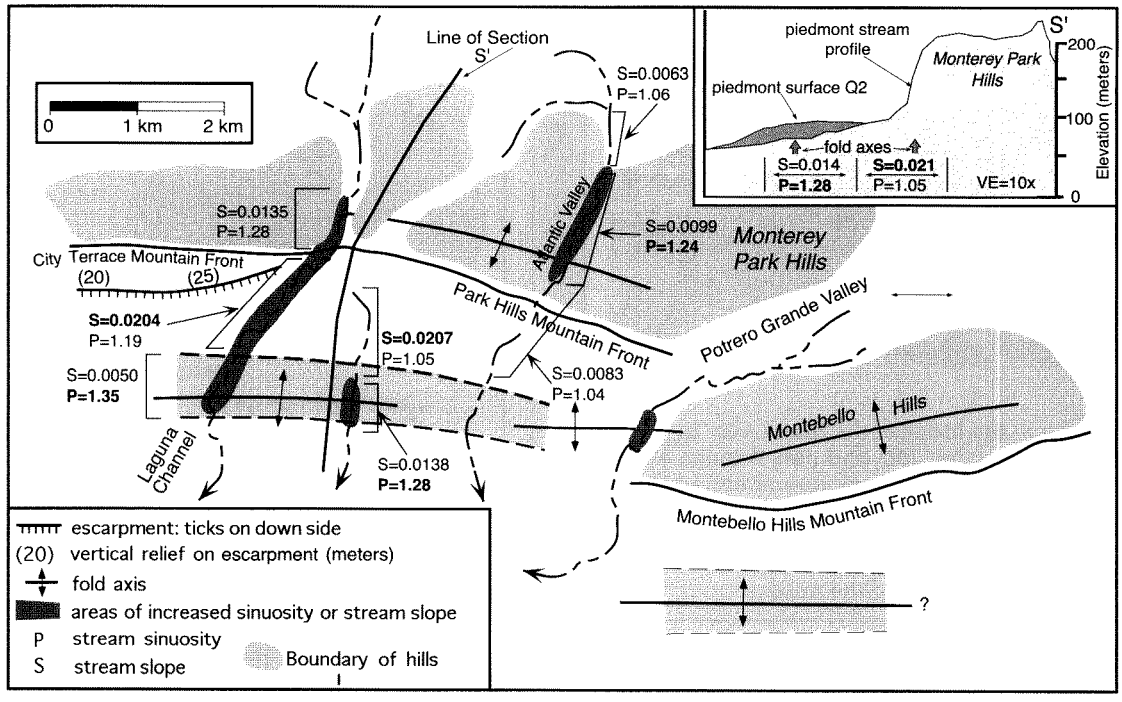

Incised channels, higher stream slopes, and increased sinuosity are associated with slowly growing folds (0.1–0.3 mm/yr) to the south of the main deformed zone. Each of the "hills" is bounded on its south margin by a blind or emergent thrust fault. Note the contrasts in slopes and sinuosity along each valley. Bold-face numbers depict the higher sinuosity or stream slope in adjacent zones. In most cases, as the sinuosity increases, the slope is decreasing. Inset shows a cross section through the older and younger fold. Where folding uplifts the young piedmont surface (*Q*2), sinuosity is enhanced. Modified after Bullard and Lettis (1993).

zone, however, the river displays meanders and swampy regions indicative of low gradients. This suggests that the Kabul system is ponded upstream of the uplift, across which it is incising as rapidly as possible via a straight course and narrow channel with the steepest possible slope and highest resultant stream power.

Most of the examples discussed thus far result from deformation in which the trend of the fault or fold axis is approximately perpendicular to the river. What happens when the tilting axis is more parallel to the river? At least two different scenarios can be envisioned. In the case of coseismic deformation, instantaneous tilting occurs across the affected region, such that part of the former floodplain may experience considerable differential subsidence with respect to another part. The magnitude of displacement can be large (several meters), and the tilting may cause an immediate avulsion of rivers into new low points in the landscape. Alternatively, tilting may occur incrementally through largely aseismic deformation or in small coseismic steps, in which case rivers would respond over longer time scales.

An example of fluvial responses to apparently incremental tilting is found in northern California, where a resurgent dome within Long Valley caldera has inflated and deflated periodically. Between 1979 and 1983, the crest of the dome rose about 40 cm (Fig. 8.13A), and it is still rising (Castle et al., 1984). The Owens River flows along the margin of the dome, and through much of its course, the river is nearly parallel to the elliptical contours of the recent domal deformation (Fig. 8.13A). This most recent uplift has not caused any dramatic shift in the present-day river, but as the river flows around the

FIGURE 8.12. Indus and Kabul Rivers channel patterns

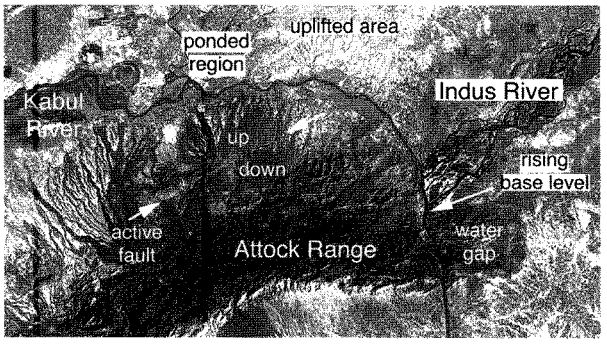

Satellite image of the Indus and Kabul Rivers in northern Pakistan as they join and pass through a water gap in the Attock Range. Note common base level at the water gap through the Attock Range, contrasting planform river patterns, zone of inferred deformation along the Kabul River and ponded (high sinuosity pattern) upstream of the uplift.

flank of the dome, it displays two, parallel meander belts (Fig. 8.13B) separated by 200–300 m (Reid, 1992). Although both belts show similar meander wavelengths and amplitudes, the inner belt (closer to the dome) now contains an underfit stream and is both older and approximately 60 cm higher in elevation than the outer belt (Fig. 8.13C). This configuration has been interpreted to result from systematic, outward avulsion of the Owens River in response to outward tilting of the volcanic dome (Reid, 1992). The most recent avulsion event occurred between 1856 and 1879. Because doming progressively lowers the outer part of the floodplain with respect to the inner part, the river will tend to avulse into this lower, outer region during flooding events. The inner belt is not fully abandoned by the Owens River, but it retains only a fraction of its previous discharge. Consequently it appears to be underfit (Fig. 8.13C). If the region between the belts is considered to have been nearly horizontal prior to deformation, then the present slope between the two channel belts can be projected to the center of the dome to estimate the cumulative recent uplift of the dome.

It is instructive to think about the likely differences in river patterns that would result from slow versus abrupt tilting. If slow tilting occurs, the river channel

FIGURE 8.13. Fluvial response to tilting along the Owens River

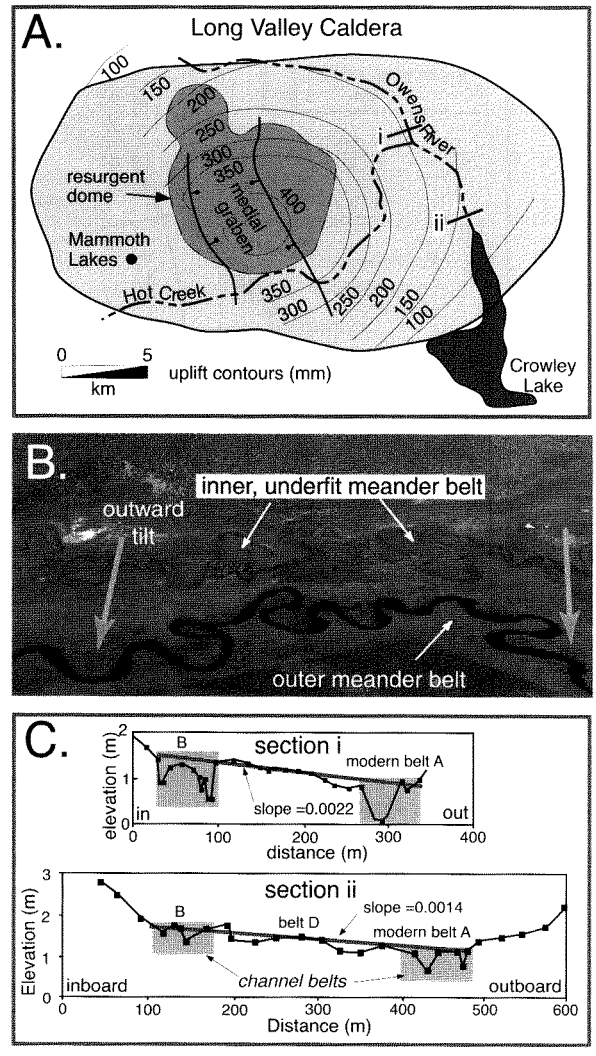

A. Map of recent deformation (1979–1983) of the resurgent dome of Long Valley caldera and the course of the Owens River. Locations of cross sections (i-ii). B. Photograph showing parallel meander belts of the Owens River, but with an underfit stream in the inner belt which is closer to center of the uplifting resurgent dome. Between the two belts is a short section of recently abandoned channel with an underfit stream. C. Topographic cross sections showing the mean slope between the inner and outer meander belts. Projections of these slopes toward the dome's center suggest the cumulative magnitude of recent uplift (15–35 m). Modified after Reid (1992).

will preferentially shift towards the outer, lower part of its meander belt. One way to test whether this has occurred is to measure the position of the active channel with respect to the entire width of the meander belt. By compiling the relative channel position on many transects across the meander belt, the mean position of the channel with respect to the midline of the meander belt can be determined (Reid, 1992). A significant displacement from the statistical center can be interpreted to indicate ongoing tilting that is forcing continued river migration.

At a more regional scale, comparing the position of a channel with respect to the midline of a drainage basin (the axis of symmetry along the basin center) can be used to infer tilting (Cox, 1994). A consistent bias of the position of the active channel with respect to the midline can indicate tilting in the direction of bias. The relative position of the meander belt can be quantified as:

$$T = dO/dL \qquad (8.3)$$

where dO equals the distance of offset of the mean river course or meander belt from the midline and dL equals the distance to the midline from the drainage divide defining the basin margin. When T equals 0, the river is located near the mid-line of the basin, whereas as T approaches 1, the river is shifted increasingly close to the margin of the basin (Cox, 1994). These ratios can be determined from topographic maps and can be easily used to provide a quick overview of potential zones and directions of tilting within a drainage basin.

In the process of shifting, a meandering river will abandon oxbows and meander bends, which then remain as visible scars on the landscape. Under conditions of steady tilt, but without major avulsions that completely relocate the meander belt, one might expect to see a suite of meander scars all facing in the same direction and indicating the generally unidirectional migration of the river across its floodplain toward a low point (Alexander et al., 1994) (Fig. 8.14). If tilting was abrupt and caused a major avulsion and relocation of the meander belt, a different channel pattern would be expected (Figs. 8.14C and 8.15). In the area that has been abandoned, meander scars should face in both directions, as is typical of a modern meandering river, rather than facing one direction and indicating steady migration. Measurements of the relative position of the old channel with respect to the width of the meander belt could indicate whether the channel position was symmetrical within the meander belt and untilted prior to avulsion, whether it had begun to migrate in the direction of tilt prior to avulsion, or whether it had been off center in the opposite direction prior to avulsion, which would suggest that the direction of tilt was suddenly reversed (Reid, 1992). In the Owens River setting, this last condition would be

FIGURE 8.14. Models for responses of meandering rivers to tilting across the floodplain

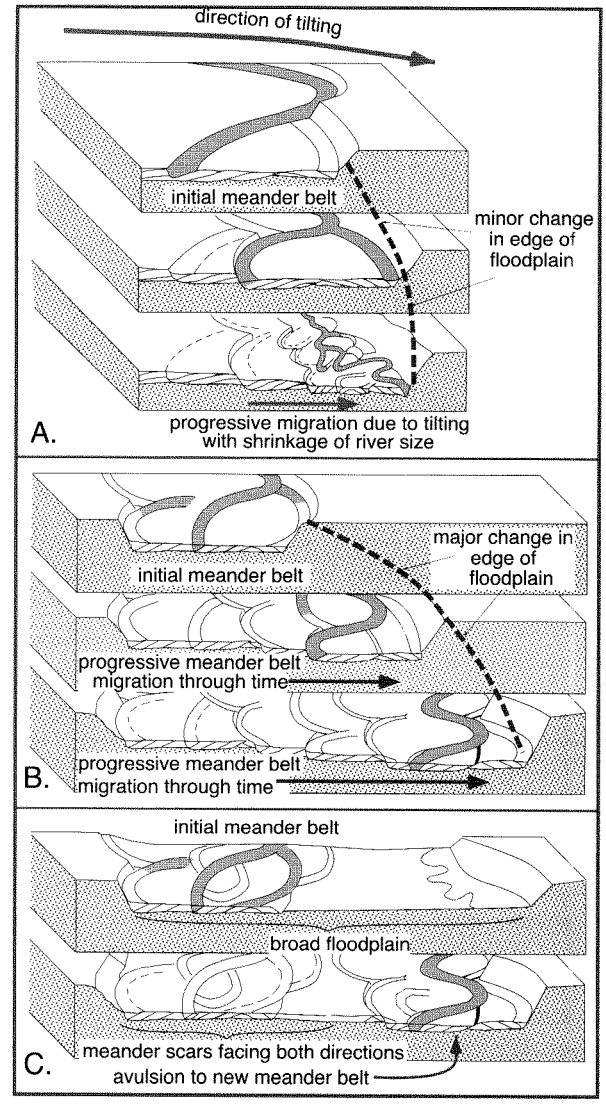

A. Steady tilting with shrinkage of river size.
B. Steady tilting and migration. C. Abrupt tilting and avulsion across a floodplain. Modified after Alexander et al. (1994).

FIGURE 8.15. Pattern of meander scars of the Madison River near the 1959 Hebgen Lake rupture

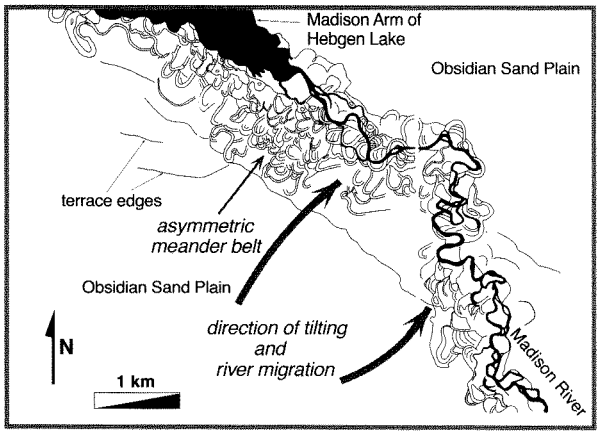

Normal faulting during the Hebgen Lake earthquake caused large, down-to-the-northeast displacement and tilting (see Fig. 4.24). Note the position of the river channel on the northern and eastern margin of its meander belt. The series of meander scars facing toward the present river and the scale of those abandoned meanders suggest that the river maintained its size, but migrated laterally in response to tilting. Modified after Alexander et al. (1994).

FIGURE 8.16. Schematic representation of the profile and associated channel patterns of the Indus River in western Pakistan

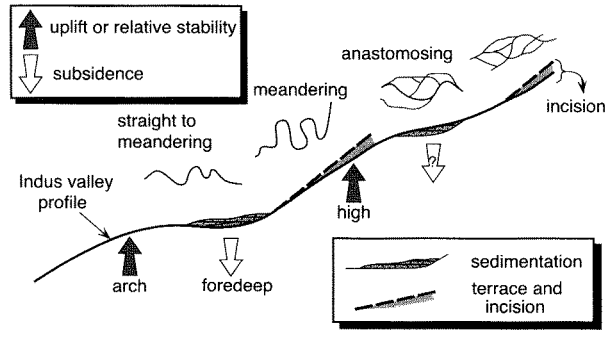

Relationships are depicted between planform river patterns, zones of uplift and subsidence, and regions of erosion and deposition along the Indus River in Pakistan. See text for discussion. Modified after Jorgensen et al. (1993).

analogous to having the dome deflate prior to inflation, whereas with a folded structure, it could be analogous to deformation during a seismic cycle in which the interseismic and coseismic displacements are roughly equal in magnitude, but in opposing directions.

Recent studies of the Indus River in western Pakistan (Jorgensen et al., 1993) indicate clear correlations of the large-scale river planform patterns with ongoing deformation (Fig. 8.16). In steeper upstream reaches, the Indus is strongly braided. Upstream of active uplifts, depositional basins prevail, and the Indus is either anastomosing due to the rising local base level associated with the uplift immediately downstream or the river is fairly straight, although unstable, as it takes the steepest possible course across a gentle reach. Across the active uplifts, there are terraces preserved above the present river channel. These terraces indicate incision has occurred across the crest of the deformation. On the steepened, downstream slope of the uplifts, the Indus becomes meandering again and displays its highest sinuosity (Jorgensen et al., 1993), presumably in response to the increased slope and to the decrease in sediment load (Ouchi, 1985) due to deposition in the subsiding region upstream of the uplift (Fig. 8.16).

Based on an understanding of the ways in which planform patterns may respond to tectonic deformation along a river's course, rapid reconnaissance of domains of tectonic activity can be attempted using maps, aerial photographs, or satellite images. Simple observations of downstream changes in planform patterns, correlation of planform changes with topographic and bedrock forms through which the river passes, and quantification of the channel position with respect to valley margins all serve to delineate potential deformation regimes.

In a satellite image of the foreland fold-belt to the west of the Pamir Range (Fig. 8.17), a repetitive pattern is clear. Upstream of channel constrictions, broad meander belts are present and are often associated with braided channels farther upstream. This braided-to-meandering transition in the middle of large basins suggests that fluvial gradients progressively increase upstream of the basin constriction. Several meander belts are consistently positioned to one side of the basin midline and suggest broad tilting in the direction of offset. The channel constrictions at the basin exits correspond with abrupt transitions from meandering to straight river courses. Several such straight channel reaches correspond with folds visible on the image.

FIGURE 8.17. Satellite image of the western Pamir foreland along the Afghan-Tadzhikistan border

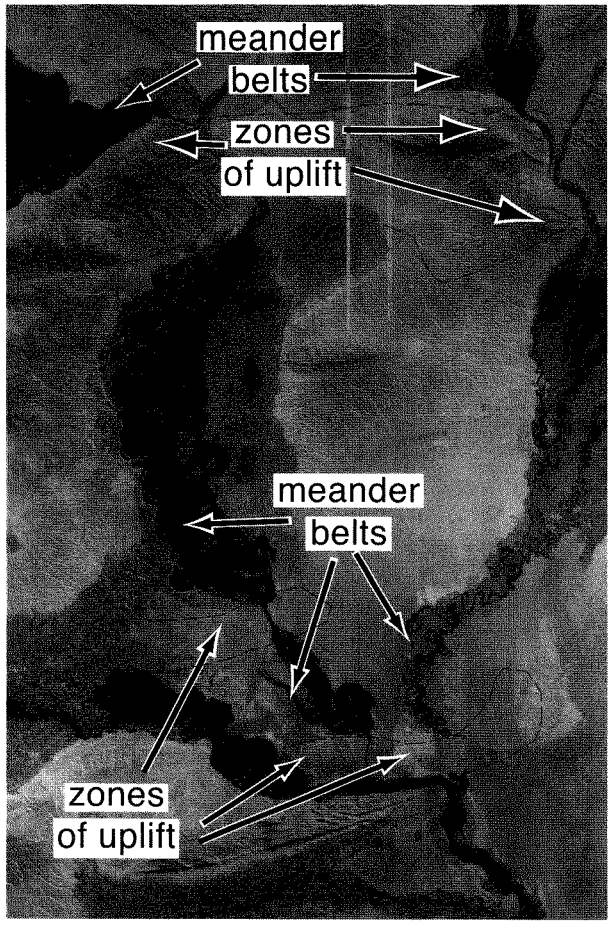

Changes in planform river patterns are intimately associated with tectonic controls exerted by folding, tilting, and possibly faulting. Note the association of straight river stretches either with water gaps across growing folds or with zones where tilting has driven the river against the valley margin. Off-center meander belts suggest gentle tilting across basins. Strike valleys and diversion of rivers around the noses of folds indicate strong structural controls on river position.

Rivers are diverted toward or around the end of some of the growing folds, whereas water gaps have developed across others. Between growing folds or active thrusts, strike valleys with little apparent perturbation of the river courses are present. It is remarkable how much tectonic information can be inferred from planform river patterns such as these. Such insights can be enhanced when fluvial pattern interpretation is combined with structural interpretations of stratal patterns and local drainage patterns indicative of growing folds and faults that are also evident on the image (Fig. 8.17).

Summary

Tilting of the landscape can happen either seismically or coseismically. Many studies assume that nearly all geodetically determined strain is accommodated through faulting (Dolan et al., 1995). Where true, this behavior would impose abrupt changes in base level and tilt on to landscapes. In contrast, recent geophysical studies of Greece compared the rates of plate motion derived from high-precision geodesy with the deformation rates derived from historic records of seismicity (Jackson et al., 1994). A mismatch between geodetic and seismic strain rates in parts of this region suggests that coseismic deformation accounts for less than 50 percent of the shortening. This major deficit implies that considerable deformation in these areas must occur through aseismic folding and faulting or via other mechanisms for accommodating strain, such as pressure solution and granular dislocations.

River planform patterns may provide insight on the distribution and nature of deformation on both historic and prehistoric time scales. Because rivers are very sensitive to changes in gradient, they respond very rapidly to tectonically imposed changes. Whereas tilting of fluvial terraces of a few degrees can usually be revealed only through careful surveying, changes in river patterns along a river's course can be observed instantly from maps, aerial photographs, and satellite images. Because rivers respond to numerous controls (water and sediment discharge, slope, roughness, sediment caliber), observed planform changes often can not be uniquely attributed to a tectonic cause. Nonetheless, the changes in fluvial planform patterns serve to pinpoint areas where deformation may be occurring. Moreover, the type of the planform change, such as from meandering to straight or from lower to higher sinuosity, suggests what the nature of the deformation may be: increasing slope, lateral tilting, and so on.

It is clear that geomorphic systems other than rivers will also initiate responses to tectonic deformation at Holocene time scales. As fluvial knickpoints migrate past the toes of hillslopes, steepened hillslope gradients will initiate changes in the flux of material off the hillside into

the channels and may also influence the rates, efficiency, or nature of the dominant hillslope processes that modify the landscape. At Holocene time scales, however, most such responses may be difficult to discern in the landscape. The scales and rates of tectonic deformation, base-level lowering, and tilting are sufficiently small that hillslopes may not be pushed over a threshold that would provoke a dramatic or readily discernible response. It is only as one examines longer time scales (>10 kyr) that such landscape responses become clear. In the following chapter, deformation and landscape responses at intermediate time scales (10 kyr to 300 kyr) are examined.

CHAPTER 9

Deformation and Geomorphology at Intermediate Time Scales

Studies of tectonic geomorphology at intermediate time scales provide opportunities to gather a different suite of insights on both tectonic deformation and on landscape responses than can be obtained from investigations covering the time scale of the Holocene. By "intermediate" time scales, we refer to intervals extending from the Holocene-Pleistocene boundary (10 ka) to about 300 to 400 ka. Over such time scales, the landscape becomes a summation of both episodic and continuous tectonic and geomorphic processes. Whereas many active faults will have experienced only a few earthquakes during the Holocene, these faults may experience dozens to hundreds of earthquakes over 300,000 years. These repetitive ruptures smooth the variations in displacements that frequently occur between any two successive earthquakes, such as might be seen during the Holocene, and they cumulatively allow better, more confident definition of long-term mean rates of deformation.

Knowledge of such longer-term rates is invaluable when trying either to understand the implications of a shorter-term record, or to assess its validity. For example, geodetic measurements collected over a few years are now being used by a growing number of researchers to characterize rates of regional deformation. But, are the rates measured at decadal scales typical of tectonic rates over 100,000 years or more? Only knowledge of rates at these longer time scales can answer that question. Similarly, the persistence of deformation rates and calculated recurrence intervals based on trenching studies of Holocene faulting can only be assessed using a longer-term record. Thus, by considering intermediate time scales, more representative averages can be obtained for deformation rates.

At time scales of more than 10 kyr, erosion becomes an increasingly important factor in modifying the landscape. Pristine tectonic forms become degraded over these longer intervals. There is sufficient time for interactions between discrete deformation events and ongoing surface processes to shape the landscape into characteristic forms, such that river patterns, dissected limbs of folds, and modified fault scarps can be viewed as recording these interactions. At time scales extending well beyond the Holocene, interpretation of the stratigraphic record becomes increasingly important as an approach to reconstructing past deformation. Such reconstructions, however, can be ambiguous due to the multiple influences (tectonics, climate, sea level, sediment supply) on the stratigraphic record and the fact that preserved strata may be physically disconnected from the site of tectonism, such that correlations between the sedimentary record and the causal tectonic events become more tenuous. As longer and longer time scales are considered, the stratigraphic record often becomes the primary key to understanding past tectonism. At time scales less than 400 kyr, however, there is still sufficient preservation of some tectonically produced geomorphic features, to allow them to be utilized in many reconstructions.

On the one hand, these "ongoing" surface processes, driven as they often are by individual storms or suites of storms, vary significantly through time. One must average the varying weather conditions over decades and even centuries to define a region's climate. In this sense, the longer time scales provide a better average of the stochastic (random) nature of the atmospheric delivery system that drives surface processes. But on the other hand, the climate at intermediate time scales of 300–400 kyr has

undergone several major glacial-interglacial cycles, such that a strong, complex, and highly variable climatic signal has influenced the surface processes that help to shape the landscape. We must therefore expect that 1) ultimate base level has fluctuated strongly as eustatic sea level has varied; 2) climatically modulated changes in water and sediment fluxes have occurred; 3) fluvial systems have probably crossed the threshold of critical power many times; 4) variables related to hillslope stability, such as moisture content and vegetation, will have strongly fluctuated through time; and 5) hillslope diffusivities that were calculated for interglacial, Holocene hillslopes and scarps may fail to represent the longer-term diffusivities. All of these will complicate the interpretation of the landscape.

Although this fact clearly increases the challenge of such interpretation, it can also at times provide additional evidence in the landscape that allows better determination of the tectonic forcing. Geomorphic markers, such as marine terraces, which form in response to climatic variability will provide multiple reference surfaces with which to define the geometry of deformation. If the ages of these markers can be determined, then intermediate-term rates of deformation can be calculated. At these time scales, it is sometimes also possible to distinguish between the climatic and the tectonic imprint on the landscape. Consider the growth of a simple fault-bend fold. At the scale of individual seismic events, its growth is highly episodic, such that instantaneous spurts of growth are followed by extended quiescent intervals. Over the span of numerous faulting events, however, the fold will be seen to grow continuously. In contrast, climatically controlled processes will typically be relatively steady at the scale of a single or a few seismic events, whereas they become highly variable at those intermediate time scales over which tectonic processes may appear steady. Such contrasts between the time scales of episodicity and steadiness in tectonic versus climatic processes provide an excellent opportunity to try to separate their relative influence on both evolving landforms and sedimentary successions related to those landforms. Given a desire to understand how tectonically influenced landscapes evolve through time or to reconstruct depositional or erosional responses that are likely to be preserved in the stratigraphic record, this more time-averaged landscape offers an important geological perspective.

In this chapter, two different aspects of tectonic geomorphology at intermediate time scales will be examined. First, techniques for calibration of rates of deformation are illustrated by focusing on the use of various types of geomorphic markers. Second, some landscape responses are described, using examples of growing folds and tilted mountain ranges.

Calibrating Rates of Deformation

Marine Terraces

Several approaches can be employed to define the vertical deformation pattern along a coastline using either abrasion platforms or coral terraces. A rising coastal landmass is like a strip chart that records and uplifts the geologic record of each successive high sea-level stand. As in all rate studies, one needs knowledge of the initial elevation and final elevation of a marker, and the time it took to traverse that vertical distance. The key here is that the landmass is rising steadily (although perhaps in discrete jumps) while the sea level is varying widely over glacial—interglacial cycles that have periods on the order of tens of thousands to one hundred thousand years. The abrasional or constructional platform that is created at time zero is a level surface with a uniform elevation. Subsequent emergence of a platform implies that the rock mass has moved upward relative to sea level, and submergence implies the opposite. In order to know which has moved, the sea or the land, other information must be brought to bear on the problem. On the other hand, any warping of this surface can be used directly and unambiguously to document relative movement of one part of the coastal landmass with respect to another. Depending on what is already known about the landscape, one can either use the terraces to deduce a sea-level curve, or use the terraces to deduce the rate of uplift of the landmass. In any case, in order to document rates of deformation, one must be able to date the platforms.

The determination of the absolute ages for former sea levels has been something of an industry for a large number of researchers for several decades. Unfortunately, most of the sea-level highstands that we would like to date are older (>40 ka) than can be dated using ^{14}C approaches. As described in Chapter 3, uranium series (U/Th) dates on aragonitic material have provided ages for surfaces several hundred thousand years old.

In the ideal case, we have a reliable global (eustatic) sea-level curve (sea level relative to present versus time) and a flight of dated terraces. The age and the present elevation of each terrace (relative sea level) with respect to the position of the correlative eustatic sea level at the time of terrace formation can be used to define amounts

and rates of uplift through time. But, what if the terraces are undated, or only one of them has an approximate date—can they still be used to define the uplift rate? In this situation, one typically assumes a steady uplift rate (or assigns one, if a single terrace is dated), and then determines graphically (or numerically, on the computer) how well the observed heights of terraces correlate with the predicted position of terraces based on the eustatic sea-level curve and the constant apparent sea-level change (Fig. 9.1A).

In this graphical matching technique, there should be a terrace at an appropriate height above sea level for each of the high sea-level peaks defined in the eustatic curve. If the elevation of each sea-level high stand matches with that of a preserved terrace, then the assumption of constant uplift appears warranted. If the match is poor, then a different uplift rate can be tried. If the match is still unsatisfactory, the rate of uplift might be varied through time in order to obtain a satisfactory match (Fig. 9.1B). If one permits the uplift rate to vary without constraint, however, a perfect, but probably meaningless, match can always be obtained. It is therefore simplest and often most convincing to assume a constant uplift rate. If rates are varied through time to obtain a match, then a geologically convincing rationale for the proposed changes should be offered for this variation. One observation that could support an assumed acceleration in the rate of uplift would be the presence of older, higher terraces that are more closely vertically spaced than younger, lower terraces (Fig. 9.1B). Given the nature of the sea-level curve in which the frequency of high sea-level stands appears lower prior to 125 ka, such a distribution argues for an increase in uplift rates.

If flights of marine terraces can be correlated with the sea-level curve at numerous sites along a coastline, or even if they can only be laterally correlated from one site to the next, these data can be used to define patterns of differential vertical uplift. Abrupt offsets in terrace heights with increasingly larger separations for successively older terraces on the upthrown side will indicate the presence of persistently active faults (Fig. 9.2A and B), whereas steady convergence or divergence between individual terraces of a given age will exemplify broad warping of an area (Fig. 9.3).

The deformed patterns of uplifted Pleistocene terraces are an obvious and readily observed consequence of variable bedrock uplift rates in coastal regions. Moreover, comparisons of the shapes of deformed terraces of different ages allow one to assess spatial and temporal variability in rock uplift rates. Commonly, the

FIGURE 9.1. Use of real sea-level curve and assumed or known uplift rate to predict the elevation of marine terraces

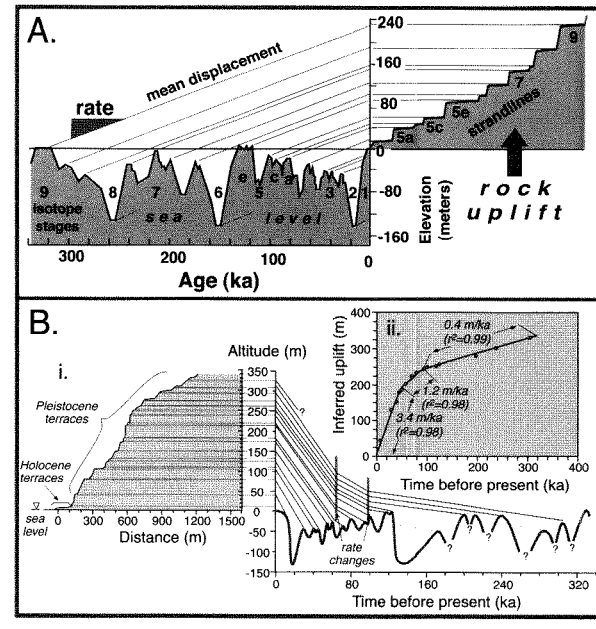

A. Graphical correlation of sea-level variations with coastal terrace record. Note that not all highstands older than 70 ky are represented in the terrace record. Modified after Lajoie (1986). B. i. Example of terrace correlation in northern California based on the assumption of an episodically accelerating rate of uplift. The coastal area has been strongly affected by the passage of the Mendocino triple junction and accelerated uplift is not unreasonable. Note that, irrespective of the smaller number of documented highstands prior to 125 ka in the sea-level record, the close spacing of the older, higher terraces suggests that uplift was slower at the time they formed. ii. In order to correlate each of the observed terraces with a high sea-level stand, the rate of bedrock uplift is inferred to have tripled at ~100 ka and then to have tripled again at ~60 ka. Modified after Merritts and Bull (1989).

faults that are responsible for uplift of the terraces are either blind faults or break the earth's surface below sea level. In such circumstances, these warped terraces take on added significance, because they may permit testing of hypotheses about the behavior of unexposed faults or folds which are thought to be responsible for their uplift. For example, comparisons of coseismic coastal uplift patterns with patterns of warped terraces can be

FIGURE 9.2. Dated and deformed marine terrace sequences in New Zealand

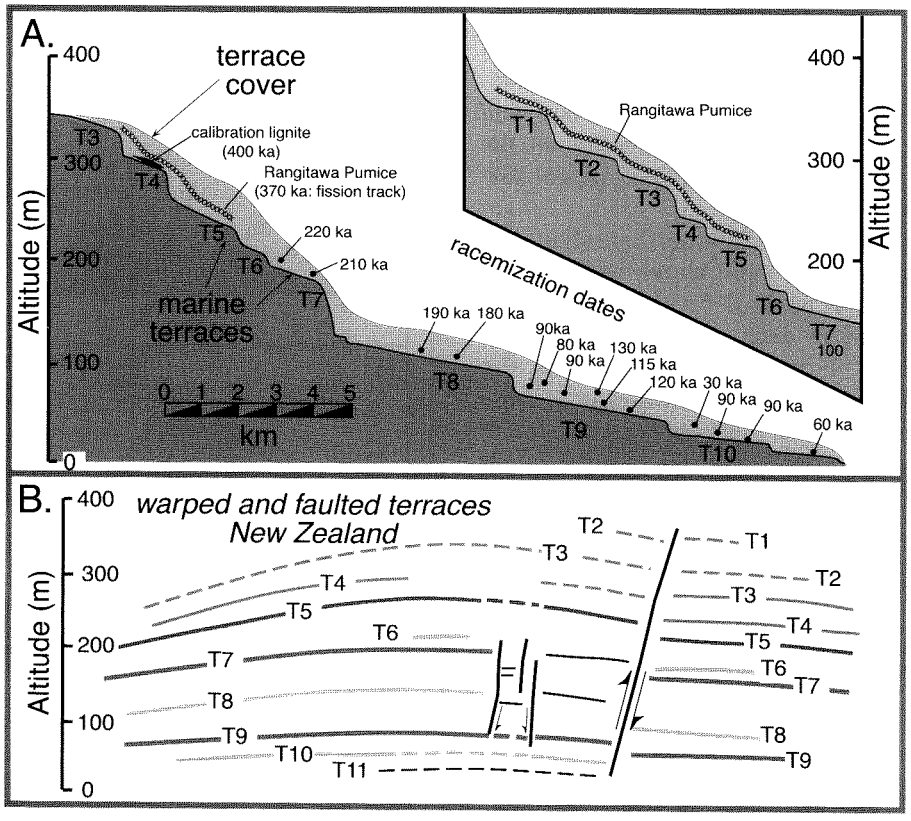

A. Terrace chronology developed using fission-track dating on pumice and amino-acid racemization dating on organic material overlying the terraces. These dates span more than 300 ky and provide minimum ages for each terrace. Correlation among sections is based on pumice, soils stratigraphy, and geomorphic position. B. Same terraces offset across faults. Tracing and correct identification of terraces is key to discovering the correct offset across faults. The progressively greater offsets of older terraces indicate the fault has been periodically active throughout the period of uplift. Note the difference from a faulted trench stratigraphy (see Fig. 6.2a) in which the strata at lower elevations record more displacement than those higher in the trench walls. Modified after Pillans (1983).

used to assess whether a long succession of characteristic earthquakes on one or two local faults could have generated the observed terrace pattern. Such a situation was previously described (see Fig. 4.8) on the California coast in the vicinity of Santa Cruz, where uplifted and broadly warped marine terraces are well preserved. Alternatively, the geometry of warped terraces on the flanks of a growing anticline can be used to deduce the orientation and typical slip direction along the buried fault(s) responsible for terrace uplift (Ward and Valensise, 1994). The terraces are like bathtub rings around the growing fold: each one originally formed on a horizontal surface (see Box 9.1). But now, in their deformed positions, their geometry can be inverted to estimate the depth, dip, and slip on underlying faults.

Most marine abrasion platforms vary from 100–500 m wide. The depth to wave base and the requirement that there be a seaward slope on the platform to permit the removal of debris from the shoreface appears to control the maximum width. In some areas, however, platforms greater than or equal to 1 km wide are preserved. Except in areas of unusual geological conditions where very weak and readily dissolvable rocks permit a wide platform to develop, these unusually wide terraces

Box 9.1. Marine Terraces on Growing Folds

In addition to the effects of differential warping or fault offsets on terrace patterns, one can wonder how a changing sea level would interact with a three-dimensional deforming shape, such as a growing fold that is increasing in amplitude through time. Some simple models of a growing anticline (Ward and Valensise, 1994) predict patterns of strandlines that are not intuitively obvious. In the model (see figure), a fold grows above a buried thrust fault in such a manner that the crest of the fold is uplifted at a steady rate through time. Every 100 kyr a new terrace is cut into the margins of the fold during a highstand, referred to here as a reference sea level. Thus, one might expect that, given a uniformly growing fold and terrace-cutting episodes regularly spaced in time, the terraces would show a uniform spatial distribution. This is not borne out in the model, however, because the emergent part of the fold becomes broader through time. Although uplift is steady at any point along the fold, it decreases from the crest of the fold toward its flanks. Therefore, younger terraces that are formed on the ever-widening fold as it emerges above sea level are spaced more closely than older terraces formed when the emergent fold was narrower. Whereas the changing vertical spacing of the terraces such as those depicted here would often be interpreted as indicating a steady deceleration in the rate of uplift, the variable spacing is in fact a simple consequence of the shape of the steadily growing fold. This model would predict a uniform vertical spacing of terraces only in situations where the coastal region is experiencing a block-like uplift. Thus, in analyzing any coastal terrace sequence, the cause of the oceanward slope of the land surface should be considered. Is it a result of folding such that interior regions have been uplifted more rapidly than the coastal area, or is it a geomorphic surface created in the absence of differential tilting? Given the model predictions described here, the distinction between a tectonically created slope and a geomorphic slope is fundamental to making a reliable interpretation of a terrace succession.

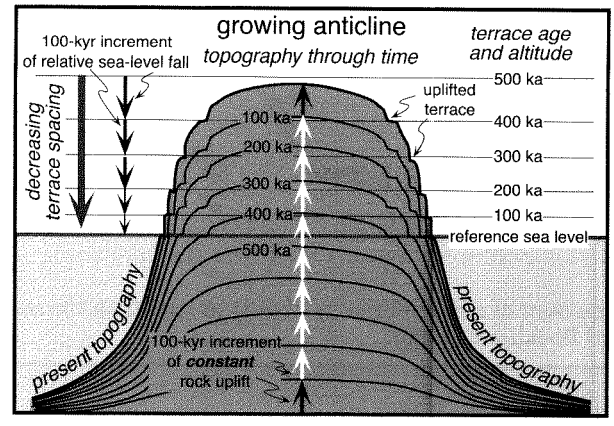

FIGURE 9.3. Broad warping of coral terraces in Huon Peninsula, New Guinea

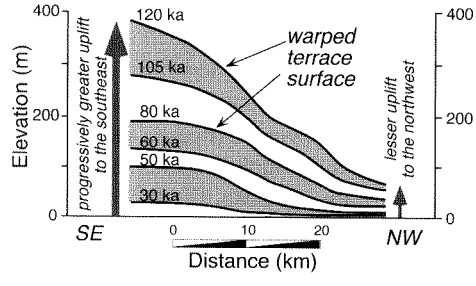

Correlation of terraces along a rapidly deforming coast. Note the locus of enhanced flexure along a given terrace generally coincides with flexures in overlying and underlying terraces. This suggests a consistent pattern of deformation has persisted for the past 125 ky. Modified after Lajoie (1986).

probably result from successive re-occupations of a marine terrace level. If the amount of bedrock uplift between two highstands is just slightly less in magnitude, but in the same direction as the vertical difference in sea level between the two highstands, then a previously formed terrace can be re-occupied by a slightly higher sea level and laterally extended (Fig. 9.4). Broad abrasion platforms along the Cascadia margin in Oregon have been attributed to this origin (Kelsey and Bockheim, 1993). When terraces widened by multiple occupations can be recognized and dated, they provide useful constraints on rates of vertical deformation.

It is important here to note that there exists a "terrace survival problem" analogous to the glacial moraine survival problem (see box 2.3 in Geomorphic Markers: Chapter 2). A sequence of elevations corresponding to a terrace flight at one location along a coastline might be different from another nearby sequence in that one or more terraces might be missing (Anderson et al., 1999). This results from the facts that 1) platform width is dependent on very local variables such as lithology,

FIGURE 9.4. Schematic model for the re-occupation of a terrace and creation of an unusually wide abrasion platform

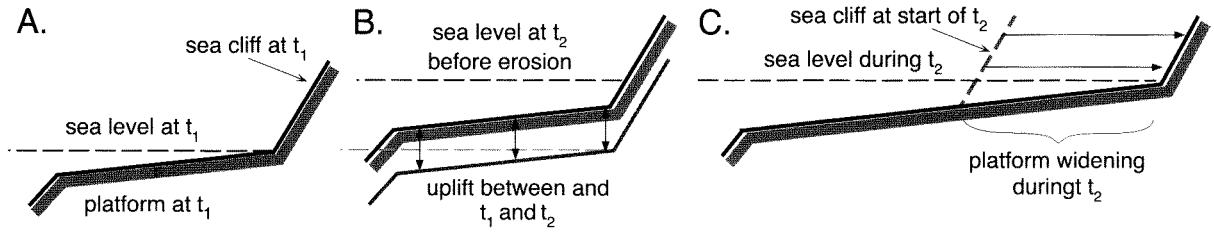

If amount of sea-level rise is slightly greater than the rock uplift, wide terraces can be created. Modified after Kelsey and Bockheim (1993).

structure, and orientation of the coastline relative to the dominant wave energy; and 2) a younger terrace platform grows in width at the expense of older platforms, whose outer edges are progressively nibbled away by the cliff at the back of the younger terrace. Hence, younger terraces can locally eliminate older ones. In addition, this geomorphic reality raises a cautionary flag against using platform width as a correlation tool.

Until recently, only emergent platforms were used in defining uplift patterns. This has changed with the advent of geophysical means of obtaining detailed bathymetry on the seafloor, and with new drilling methods that allow collection of geological materials from the sea floor. A recent example of the use of sub-sea-level platforms utilizes corals dredged from about 2 km deep on a submerged platform in the Huon Gulf of the Solomon Sea (Galewsky et al., 1996). These ancient platforms were first visualized using sidescan sonar and detailed bathymetry, on which the anomalously flat surfaces and occasional spikes (interpreted to be coral pinnacles) were identified as potential targets for dredging. The samples were dated using uranium series at approximately 340 ka, revealing a long term subsidence rate of about 6 mm/yr, one of the first documentations of such sustained rates. The tectonics of the region are complex, but to first order it appears that one can interpret the subsidence of these geomorphic markers as being due to the flexure associated with growth of the Finisterre Range to the east, itself a reflection of the suturing of an island arc terrane onto the margin of the Australian plate. The warping of these ancient platforms can potentially be used to define the flexural rigidity of the plate.

Fluvial Terraces

When a river that is flanked by flights of fluvial terraces is also oriented at a high angle to a strike-slip fault, the terraces displaced by the fault can provide an excellent record of progressive offsets. If some or all of the terraces can also be dated, then the rates of fault displacement over the duration of the dated sequence can be derived. In regions where climatically controlled terraces are widespread, it may not be necessary to date the terraces directly adjacent to the fault, because sequences of soils, loess, or volcanic ashes which overlie the terrace treads may permit correlation with other, better dated terraces in the same region.

The assessment of offset fluvial terraces requires several steps. First, the correlation of terrace treads and risers across the fault must be determined. Because of changes in the river course through time, the height of risers between terraces along strike-slip faults is generally a better guide to correlation than is the width of the terrace tread, which is sensitive to the shape of the former channel. If, however, there is significant vertical (dip-slip) displacement along the fault, then riser height will vary as well. In any case, the most reliable correlation will usually result from consideration of the entire suite of treads and risers and any relative or absolute dating of their surfaces. Second, the offset of formerly continuous risers is measured across the fault for each terrace level. In addition, any other linear features, such as channels or gullies, located on the terrace treads and trending across the fault are also measured (Fig. 9.5). Finally, to the extent permitted by available dates, a history of cumulative offset and rates of offset through

FIGURE 9.5. Displaced fluvial terraces along the Wellington fault, New Zealand

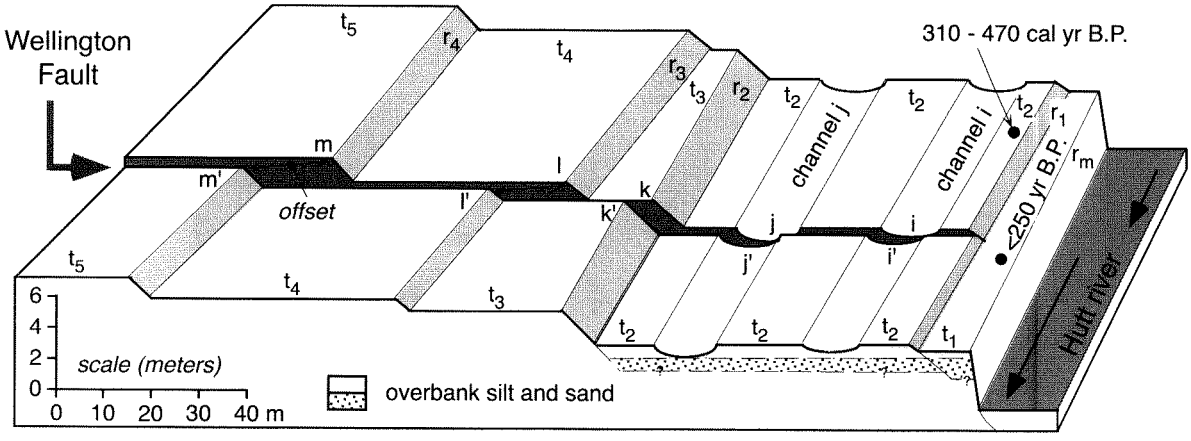

The lowest terrace, dated at <250 yr, is not displaced by this strike-slip fault, whereas the next highest terrace (t_2) and the channels cut across its surface show a displacement of ~4 m attributable to the last major earthquake. Note that any fault displacement of the riser (r_1) between t_2 and t_1 was beveled off during creation of t_1. The amount of offset of the risers increases systematically with each older terrace. Important controls on terrace width are exerted by the geometry of the river channel prior to abandonment (note the triangular shape of t_3). The vertical throw across the fault is small (~10%) compared to the horizontal displacement. Modified after Van Dissen et al. (1992).

time is developed. In general, the displacements of a tread and the riser leading to the next higher tread should be considered together, such that the age of abandonment of the terrace provides a limiting age on the offset measured along its inner edge. Offsets of the riser above the active fluvial surface (the floodplain) which predate terrace abandonment will tend to be beveled off by the active river.

Although a similar methodology could be applied to marine terraces that have been cut by strike-slip faults, fluvial terraces have a considerable advantage in terms of reconstructing the record of the past 10–50 kyr because fluvial terraces of this age are commonly present. This reflects both the glacial—interglacial swings in climate that fluvial systems have experienced in this time frame, as well as the attendant variations in sediment and water discharges in most systems. In contrast, because sea level has been lower than it is at present for most of this interval, marine terraces less than about 80 ka commonly are not subaerially exposed. Offsets on them are therefore buried beneath the sea surface.

Where rivers cross active folds or dip-slip faults, fluvial terraces can also record progressive displacement. Where faults rupture the surface, it is expected that the age and height of the terrace will generally correlate with the magnitude of displacement (Fig. 9.6). Flights of fluvial terraces can overcome some of the limitations imposed on paleoseismological studies by the fact that trench walls in alluvium are often unstable, so that deep exposures in trenches are uncommon. Trenches in any of the terrace risers may reveal paleoseismological data on the last few ruptures displaying perhaps a few meters of displacement in each rupture. In contrast, the entire vertical suite of terraces will serve to define the long-term displacement history, such that several tens to hundreds of meters of displacement can be recorded by the higher terraces. As with any study seeking to define rates, key constraints are provided by dating of the formation and abandonment of each terrace.

Across actively deforming zones in which multiple faults are closely spaced, a single terrace may be displaced by several faults. Even without knowledge of the terrace age, the variable displacement of the marker surface by each fault will indicate the way in which deformation has been partitioned among the active structures, and relative rates of displacement can be defined. Because flexural slip faults exploit weak interbeds as slip surfaces, the limbs of tightening synclines sometimes display fairly closely spaced faults (Fig. 9.7). Studies along the Ventura River in southern California

FIGURE 9.6. Photograph of thrust-faulted fluvial terraces in the Tien Shan, Kyrgyz Republic

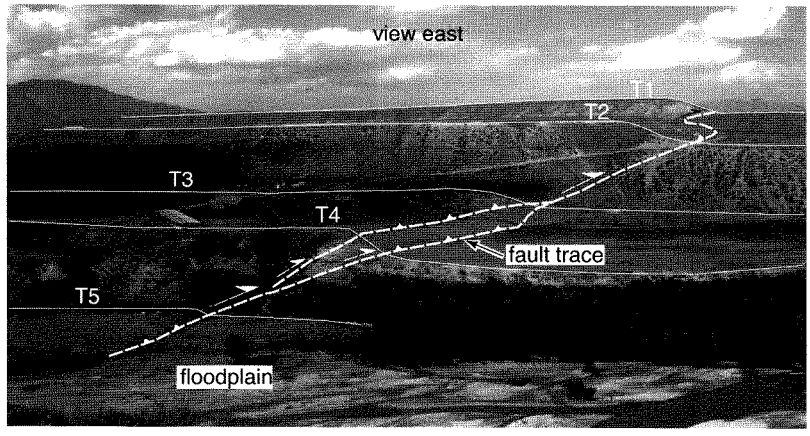

Offsets of the terrace treads and strata discontinuities visible along the terrace risers reveal the trace of the fault. Note the greater displacement of successively older terrace surfaces and the erosional modification of the thrust-fault scarp on each terrace.

of terraces offset across flexural slip faults in the Canada Larga syncline (Rockwell et al., 1984) provide well-calibrated examples of both progressive terrace displacement and differential partitioning of displacement among several faults (Fig. 9.7D).

In the case of growing folds, warped fluvial terraces can provide unique insights into the two-dimensional geometry of the fold and its rate of growth. Antecedent streams that maintain their courses across growing folds will often produce strath terraces which may or may not be mantled with a veneer of alluvial debris. The terraces develop during intervals when lateral abrasion dominates over vertical incision. In cases in which terraces have extensive, down-valley continuity and in which the deformed treads within a rising structure appear to grade into undeformed treads beyond the structure, it is likely that climatic fluctuations controlled the periods of major terrace formation. Alternatively, the growth of the structure itself was tectonically pulsed, such that terraces formed during intervals of reduced deformation rates. Most published work (Medwedeff, 1992; Shaw and Suppe, 1994; Suppe, 1992; Vergés et al., 1996) in which rates of fold growth are well calibrated is inconsistent with this pulsed deformation model.

A clear example of warping of terraces across a simple fold is seen in the southern Tien Shan in China (Molnar et al., 1994) and illustrates one methodological approach for analyzing a growing structure (Fig. 9.8). The modern floodplain and terrace remnants across the structure were surveyed using a total station. Discontinuous preservation of terraces sometimes makes correlation uncertain. The terraces, however, have a sufficient vertical separation that there is rarely much confusion about which level of terrace is being measured. Even more than 200 m above the modern river, some terrace remnants can be traced for several kilometers along the fold. Cosmogenic exposure ages on boulders collected from the lower terrace and in similar structural and geomorphic settings nearby suggest that this terrace was abandoned approximately 15 ky ago at a time of major global climate change. Although none of the other terraces are dated, they have been tentatively correlated with the culminations of major glacial intervals during the Pleistocene (Fig. 9.8). Finally, the gradient of the local river is subtracted from the terrace heights so that the spatial distribution of deformation can be more readily visualized. The results of this analysis (Molnar et al., 1994) suggest crestal uplift of a symmetrical anticline at a rate of about 1 mm/yr (Fig. 9.8B). An alternative correlation of the upper discontinuous terrace remnants would suggest that the anticline was asymmetrical (Fig. 9.8C) and perhaps grew a little less steadily. This latter interpretation would be consistent with the vergence of the underlying thrust fault (it dips to the south), with the steep forelimb and

FIGURE 9.7. Terraces displaced across flexural slip faults

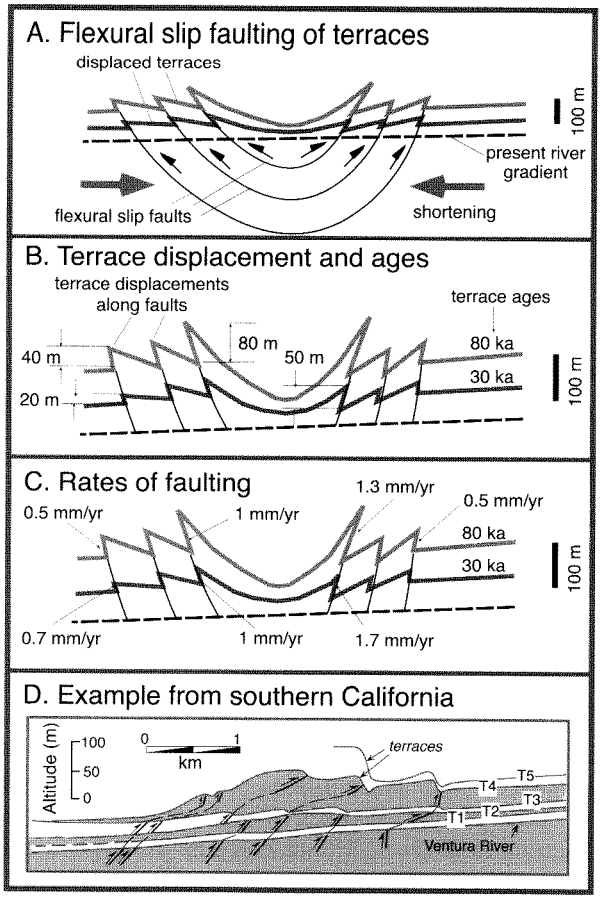

A. Geometry of terrace displacement defines greatest displacement near the core of the fold. B. Terrace ages and displacements of terraces across different faults. Note that offsets are not symmetrical across the synclinal axis and that younger terraces display lesser offsets compared to the older terraces. C. Rates of fault displacement based on offset of dated terraces. Note that rates are not necessarily constant along the same fault through time. D. Displacement of terraces by flexural slip faults along the Ventura River, California. Ages assigned to the terraces are 92 ka (T5), 54 ka (T4), 38 ka (T3), 30 ka (T2), and 17 ka (T1). Modified after Rockwell et al. (1984).

gentle backlimb dips of the youngest terrace, and with the observed asymmetric shape of fault-propagation and trishear folds (see Figure 4.33) (Allmendinger, 1998; Bloch et al., 1993; Medwedeff, 1989).

It is worth stressing that a crucial component in the analysis of both marine and fluvial terraces is the correlations that are drawn between physically isolated terrace remnants (see Fig. 2.16). Often erosion makes it impossible to trace terrace surfaces confidently, even along smoothly folded structures. Whenever faults are encountered, the correlation of terraces on opposite sides of the fault becomes even more difficult. Because any interpretation is entirely dependent on the correlation, characterization of the terrace surface and its subsurface stratigraphy is often a major element in any such study (Merritts et al., 1994). Soil development, loess stratigraphy, tephra layers, and relative and absolute dating techniques can all be used to distinguish between and correlate among terraces.

Landscape Responses at Intermediate Time Scales

We distinguish here between landscape features that permit a direct calibration of deformation rates, such as terraces, and features that represent part of the landscape response to deformation. Calibration features comprise primarily displaced geomorphic markers whose initial shape is relatively well known. The initial geometries of most other elements in the landscape, ranging from stream channels to hillslopes, are less easily traced backward in time, because these geometries represent an integrated response to ongoing deformation, base-level variation, and climate change. These features therefore only indirectly calibrate rates of deformation.

Stream Gradients

River networks represent a hierarchical organization of tributary streams (lower order) routing flow into trunk streams (higher order). In graded rivers, stream power (proportional to the slope-discharge product) remains fairly constant along the river course: as discharge increases downstream, gradients decrease (Hack, 1973). In general, first-order streams will have steeper gradients than the second-order streams to which they contribute, and second-order streams will be steeper than third-order streams.

Now consider a suite of coastal streams flowing across similar rock types and experiencing comparable climatic conditions. How would such streams respond to contrasting bedrock uplift rates? Which segments of these streams would be most sensitive to differences in

FIGURE 9.8. Deformation of fluvial terraces crossing an anticline, Tien Shan, China

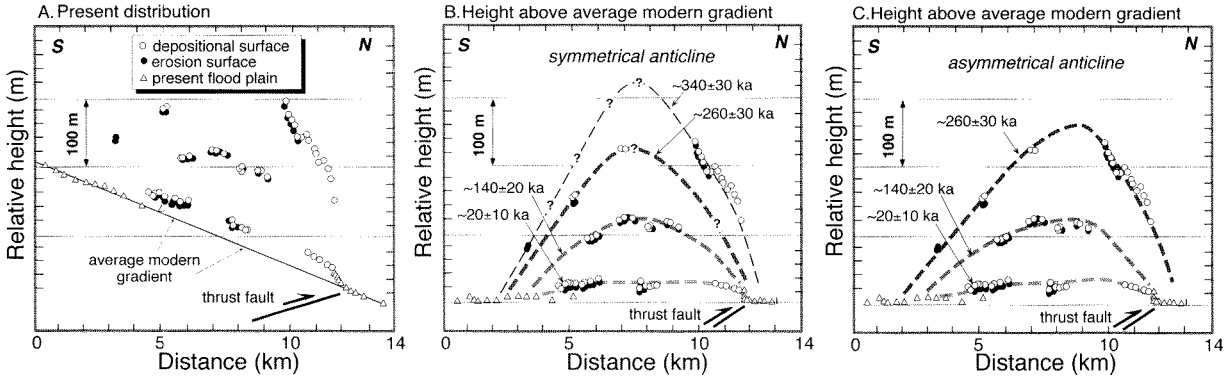

Note the north-vergent thrust fault underlying the fold. A. Surveyed position of terrace remnants and modern river gradient. Both the strath (erosion surface) and the depositional surface of older terraces are shown where surveyed. B. Correlation of terraces across anticline after removal of the modern stream gradient. Ages are assigned based on proposed correlation to isotope stages 2, 6, 8, and 10 (refer to Figure 2.3). Modified after Molnar et al. (1994). C. Alternative correlation of terraces yielding an asymmetric fold geometry.

bedrock uplift rates? In general, changing uplift rates appear to perturb the gradients of the lowest-order streams most strongly (Fig. 9.9). Recent studies in northern California have defined coastal uplift rates that vary from less than 0.5 m/ky to greater than 3 m/ky near the Mendocino triple junction (Merritts and Bull, 1989). Whereas there is a weak correlation between the slope of the trunk (third-order) streams (Fig. 9.9) with uplift rate (Merritts and Vincent, 1989), there is a much stronger correlation of the uplift rate with the slope of the first-order streams ($r = .73$, i.e., ~50% of the variance in first-order stream slopes can be explained by the variation in uplift rates). Uplift rates are also strongly correlated with maximum drainage basin relief ($r = 0.68$), but are not correlated with drainage density. Given that changes in first-order stream gradients and drainage-basin relief in the study of Merritts and Vincent (1989) generally mimic the pattern of differential uplift, systematic gradient variations in other areas might be used to identify potential variations in regional uplift patterns.

Close examination of the stream gradient versus uplift curve shows good correlations for the low-order streams, except in the northernmost area, where streams experiencing intermediate uplift rates have gradients similar to lower-uplift rate streams farther south (Fig. 9.9). This apparent anomaly can be interpreted in the context of the high uplift rates which follow in the wake of the northward sweep of the Mendocino triple junction up the Californian coast. The northern streams have only recently experienced an increase to an intermediate uplift rate (Fig. 9.9), whereas the southern streams have recently experienced strongly decreasing uplift rates. In each case, the streams retain a "memory" of their previous uplift regime, because the slope of the channel reflects cumulative uplift (formally, they see the integral of the uplift rate through time).

Given that changes in first-order stream gradients and drainage-basin relief in the Merritts and Vincent study (1989) generally mimic the pattern of differential uplift, systematic gradient variations in other areas might be used to identify potential variations in regional uplift patterns. This is being tested in the more subtle uplift welt spatially associated with the New Madrid earthquakes of 1811–1812 (Merritts and Hesterberg, 1994).

As a consequence of variable response times, there are time-space differences at any given point between the passage of the Mendocino triple junction and the occurrence of the highest uplift rates, steepest first-order channels, and maximum relief at that point. Assuming a constant migration rate of the triple junction (~6 cm/yr), these features lag passage of the triple junction by 160 kyr, 290 kyr, and 370 kyr, respectively (Merritts and Vincent, 1989). Because both stream gradient and basin relief are dependent on the amount of cumulative bedrock uplift,

FIGURE 9.9. Comparison of bedrock uplift rates with channel gradients of first- through third-order streams in coastal northern California

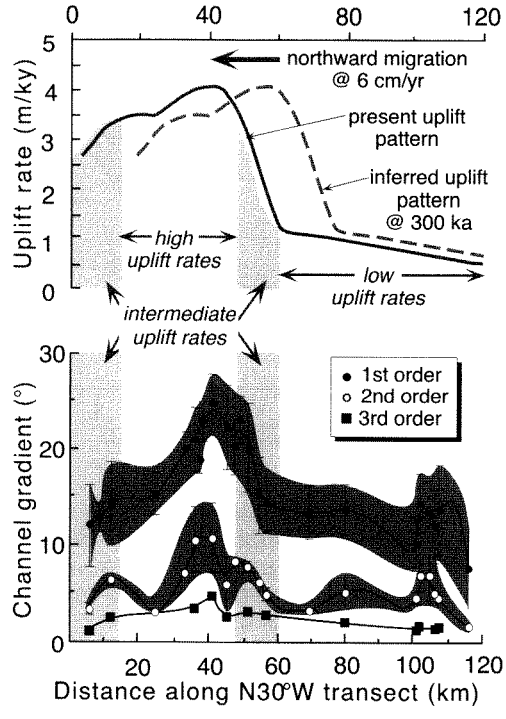

Pattern of uplift as determined from correlation of marine terraces: Figure 9.1B. Northward passage of the Mendocino triple junction at 6 cm/yr is assumed to cause a migration of the pattern of uplift through time, such that a site along the transect initially experiences rapidly accelerating uplift rates followed by slowly decaying uplift rates (upper panel). Gradients of first-order streams (lower panel) are strongly correlated with zones of rapid uplift, whereas second-order streams are less strongly correlated. Because both the cumulative bedrock uplift and the present uplift rates affect modern stream gradients, the zone of steepest stream gradients lies to the south of the peak of the uplift-rate curve. Modified after Merritts and Vincent (1989).

it is expected that they would not correlate with the zone of presently highest uplift rates. The observation that maximum basin relief lags behind attainment of the steepest first-order stream gradients implies that second- and/or third-order streams must continue to steepen as total relief accumulates (compare the gradients of second- and first-order streams adjacent to the southern margin of the high-uplift zone in Figure 9.9). Although bedrock uplift continues farther to the south of the zone of highest relief, the data here suggest that the rate of surface lowering begins to exceed the rate of bedrock uplift, so that relief and stream gradients are reduced in the southern areas.

The results from the Mendocino area (Merritts and Vincent, 1989) suggest that higher-order streams are less affected by tectonism. When streams are rejuvenated by uplift, knickpoints propagate upstream, channels are incised, valleys become narrower, and some stream gradients increase (Whipple and Tucker, 1999). Larger streams may be able to maintain their longitudinal profiles by downcutting sufficiently rapidly to keep pace with the base-level lowering. In contrast, smaller streams are unable to incise an amount equal to the base-level lowering and, through time, accumulate the effects of net base-level fall (Fig. 9.10).

Another approach for identification of areas of active deformation is also based on departures of stream gradients from expected longitudinal profiles (Merritts and Hesterberg, 1994). In areas where active folding is occurring, rivers flowing down the forelimbs of folds will be steepened, whereas rivers flowing "up" the backlimb will have their gradient lessened with respect to unfolded regions. The methodology begins by segmenting a drainage network into its component tributaries (Fig. 9.11A) and measuring 1) the length and 2) the elevation of the upper and lower point along each segment. The elevation range of each segment (y-axis) can then be plotted against the sum of the lengths of the upstream segments and the length of the segment itself (x-axis) (Fig. 9.11B). The lower elevation of each feeder or tributary segment matches the upper elevation of each segment into which it flows. Subsequently, using the x-axis position dictated by the length of the upstream segments, each segment is compared with an idealized logarithmic longitudinal profile (Fig. 9.11C). Significant departures from the ideal profile serve to identify segments that could be interpreted to indicate steepening or shallowing over time due to tilting. When coherent areas are located in which all or most of the streams flowing in a given direction show the same tendency toward steepening or flattening, regional patterns of warping can be defined (Merritts and Hesterberg, 1994). One must, however, exercise considerable caution in the application of such a technique, as it rests on the assumption of an "ideal" profile, and all effects of the variations in lithology or grain size of the material involved in the fluvial system must be assumed to be small compared to the tectonically induced changes in slope.

FIGURE 9.10. Proposed adjustments of stream gradients to bedrock uplift

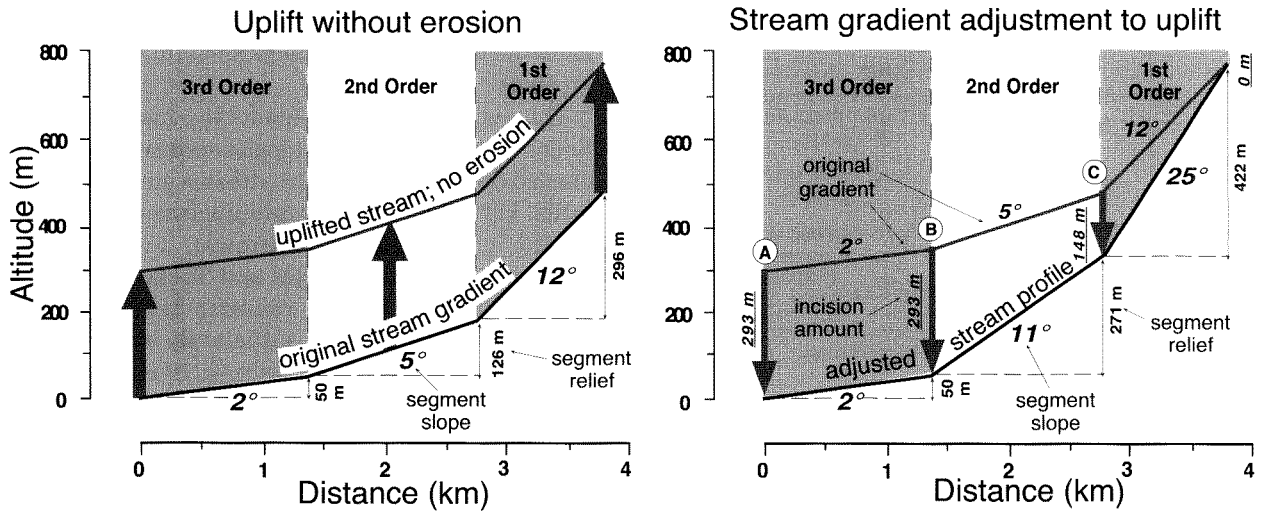

Left-hand panel indicates the typical distribution of channel slopes within a slowly uplifting region (~0.4 m/kyr) along the California coast south of the Mendocino triple junction. The gradient and the amount of relief increases with each lower-order stream segment. Incision during uplift (right-hand panel) causes gradient adjustments in first- and second-order streams. A, B, and C denote the mouths of the third-, second-, and first-order streams, respectively. Amounts of incision at the ends of each segment boundary are underlined. The total rock uplift is about 290 m. The net result of bedrock uplift is an increase in catchment relief in first-order stream gradients and smaller changes in second-order streams. Third-order streams appear to have incised at rates nearly equal to the bedrock uplift rates. Modified after Merritts and Vincent (1989).

Stream-Gradient Indices

Rivers that are not tectonically perturbed typically develop a smoothly changing, concave longitudinal profile. Departures of the river gradient from this ideal smooth shape may reflect variations in the lithology of the river bed, or variations in rock uplift rate of the river bed. Rivers that are tectonically disturbed are predicted to approach a graded profile rather rapidly (Snow and Slingerland, 1987) once such disturbance ceases. Thus, perturbations in river profiles, especially when not correlated to lithologic contrasts, may be interpreted as responses to ongoing tectonism.

One way to quantify perturbations in the longitudinal profile relies on defining changes in the stream-gradient index along the river's course. Hack (1973) showed that in "adjusted" rivers, such as those found in the Appalachians, stream power was nearly constant along the river course. Whereas discharge is impossible to determine without field-based measurements, many studies have shown that there are predictable relationships between discharge, catchment area, and stream length (Leopold and Maddock, 1953). It is straightforward to measure distance from drainage divides (which can then serve as a proxy for discharge) and to calculate approximate slopes of river surfaces on a map. Hack (1973) defined a *stream-gradient index* which is the product of the slope of a reach times the distance from the headwater divide, and which thus serves as a general indicator of available stream power (given that downstream distance is a reasonable proxy for discharge). In a homogeneous catchment, the stream-gradient index of a graded stream will remain approximately constant along its length. Variations in the stream-gradient index along a river typically reflect changes that are attributable to either lithologic controls (for example, more resistant rocks causing steeper gradients) or tectonic controls (zones of differential uplift or subsidence).

For a "graded" stream, a semi-logarithmic plot of the longitudinal profile will yield a nearly straight line, where if H equals altitude, and L equals horizontal

FIGURE 9.11. Gradient analysis of tilted stream segments

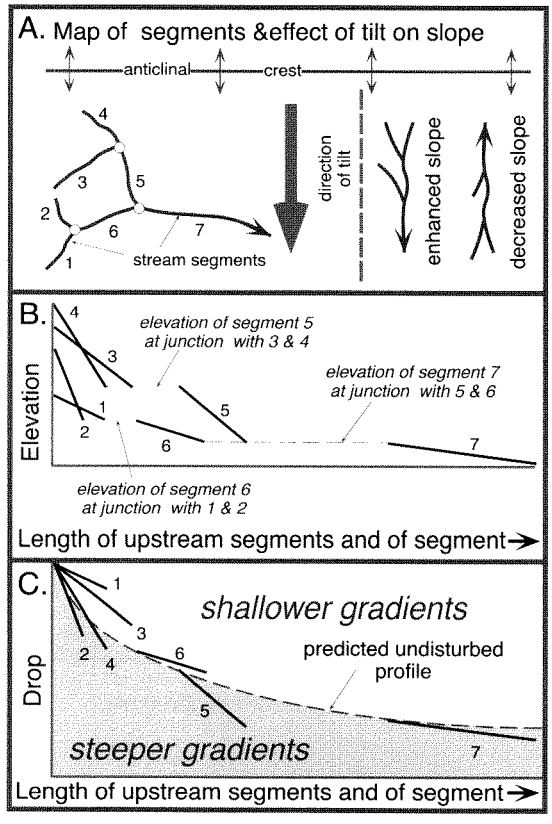

A. Stream network is divided into segments based on positions of stream junctions. The model assumes that, if tilting is occurring, streams flowing in the direction of tilting will have increased gradients, whereas those flowing in the opposite direction will have flattened gradients. B. Depiction of stream gradients. Each stream segment is plotted according to its length and to the elevation of the upper and lower ends of the segment. The upstream end of the segment is determined by the length of segments that are upstream of it and tributary to it. Thus, segments 1 and 2 flow into segment 6, segments 3 and 4 flow into segment 5, and segments 5 and 6 flow into segment 7. Segments 1 to 4 all represent first-order tributaries that have no upstream segments: their upper ends plot on the left-hand margin. The sum of the lengths of segments 1 and 2 determines the horizontal position of the upstream end of segment 6 into which they flow. C. Departure from ideal gradient. When compared to the idealized gradient, steeper segments suggest tilting in the downstream direction. Compare the relative sense of tilting with the hypothesized fold orientation in the top panel. Modified after Merritts and Hesterberg (1994).

length from the drainage divide,

$$H = C - k\ ln(L) \tag{9.1}$$

where C is a constant, and k is the slope of the line (Hack, 1973). The derivative of this equation with respect to L yields the actual stream slope, S:

$$S = dH / dL = d(k\ ln(L))/dL = k / L \tag{9.2}$$

The slope of the semi-logarithmic plot of the river profile is equal to $S \bullet L$. The gradient index, k, or slope of the ideal profile can be specified by:

$$k = (H_i - H_j) / (ln\ L_j - ln\ L_i) \tag{9.3}$$

where i and j refer to two points along the river. The gradient index can be used to characterize either an entire river or any reach of it. The stream-gradient index, SL, of a short reach can usually be approximated by

$$SL = (\Delta H/\Delta L) \bullet L \tag{9.4}$$

where L is measured from the drainage divide to the midpoint of the reach, and the slope of the short reach $(\Delta H/\Delta L)$ is considered constant.

Because river profiles are not necessarily logarithmic in form, one assumption that underpins the definition and interpretation of stream-gradient indices is commonly violated. The use of stream-gradient indices in tectonic geomorphology, however, commonly involves comparisons among different subsets of drainages or identification of anomalies along a single drainage. By using contrasts and anomalies, rather than absolute values, studies of SL values provide useful landscape data in at least three modes: as a reconnaissance tool, as a means to compare landscape responses in regions with different rock-uplift regimes, and as a means to identify anomalous zones of potentially heightened tectonic activity within a catchment.

As a reconnaissance tool, stream-gradient indices are determined along numerous drainages throughout a region of interest. Following some smoothing of the individual SL values, areas of similar stream-gradient indices can be delineated. This approach can identify areas where there are unusually high SL values and thus regions where high levels of tectonic activity might be expected (Fig. 9.12). This map-based approach could be a very useful tool in developing countries to the extent that either accurate topographic maps or high resolution digital elevation data sets are available.

FIGURE 9.12. Stream-gradient indices (SL) in the San Gabriel Mountains, southern California

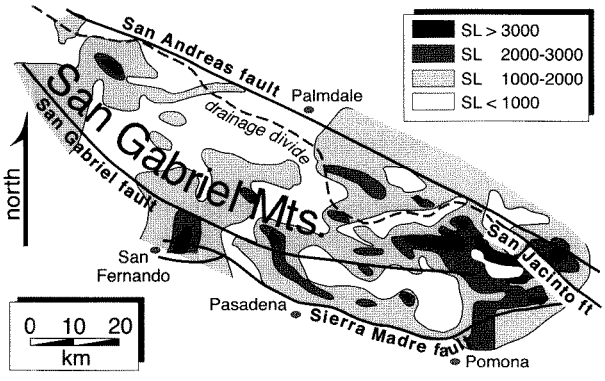

Map of contoured indices identifies areas of known active uplift in the eastern and southern parts of the range, as well as anomalously high rates along the northern San Fernando valley, where the 1971 and 1994 earthquakes occurred. Such a map can point out areas where more detailed studies on active deformation could be warranted. Modified after Keller (1986).

FIGURE 9.13. Stream-gradient indices, topographic profiles, and rock-uplift rates for rivers in northern California

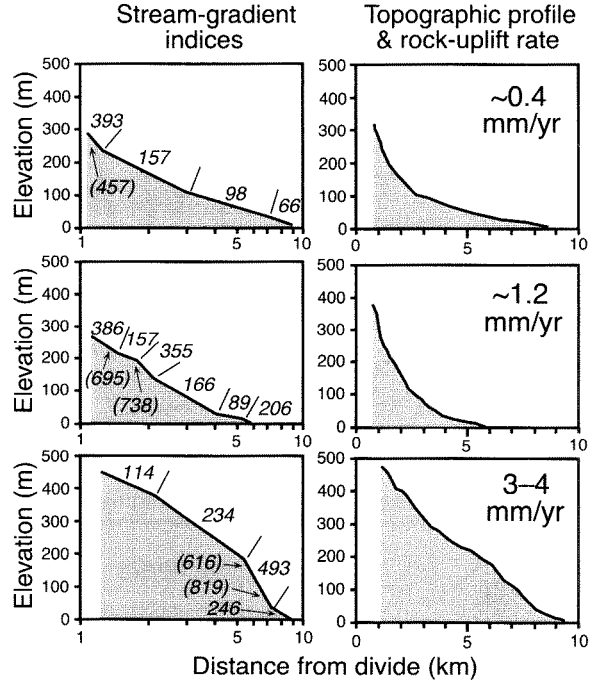

Note that the zone of rapid rock uplift has a steeper gradient, higher relief, and higher gradient indices. Modified after Merritts and Vincent (1989)

Regions such as that surrounding the Mendocino triple junction where rock-uplift rates are already known (Merritts and Vincent, 1989), are good candidates for defining landscape responses using gradient indices. For low (~0.4 m/kyr), intermediate (~1.2 m/kyr), and high (~3-4 m/kyr) uplift-rate areas, one observes the following (Fig. 9.13):

- A low uplift-rate stream has high gradients in its upper part and gradually decreases toward the ocean. The high gradient could be interpreted as a migrated knickpoint resulting from a time when this drainage was in the zone of rapid uplift during earlier passage of the Mendocino triple junction.
- An intermediate-rate uplift stream has high values at mouth, and highly variable SL values in upper reaches.
- A high uplift-rate stream has high values throughout, with highest values in the middle and lower reaches, and a convex semi-log profile.

In many regions of the world, all of these would be considered high uplift-rate streams, given that all are greater than or equal to 0.4 m/kyr. Nonetheless, this analysis suggests that in a regional framework, the relative magnitude of the SL and the positions of knickpoints in the stream may correlate with uplift rate.

As a tool to identify zones of potential tectonic activity, departures of the locally determined stream-gradient index from the gradient index (k) for an entire river are a reasonable way to search for anomalies. Clear departures from the mean, particularly where rivers are considerably steeper than predicted, suggest zones of active deformation. Such an approach may be particularly useful for rapid reconnaissance of poorly known areas. For example, using 1:1,000,000 and 1:250,000 maps predominantly with 1000-foot contour intervals, Seeber and Gornitz (1983) analyzed 26 major Himalayan rivers. They distinguished between local gradient indices (SL) that, when compared to the gradient index (k) for the entire river profile, were significantly steeper (SL/k = 2) and much steeper (SL/k = 10) than the ideal profile (Fig. 9.14). Whereas it might have been expected that the steepest gradients would be associated with the Main Boundary thrust (bounding the southern margin of the

FIGURE 9.14. Longitudinal profiles and gradient index ratios for Himalayan rivers

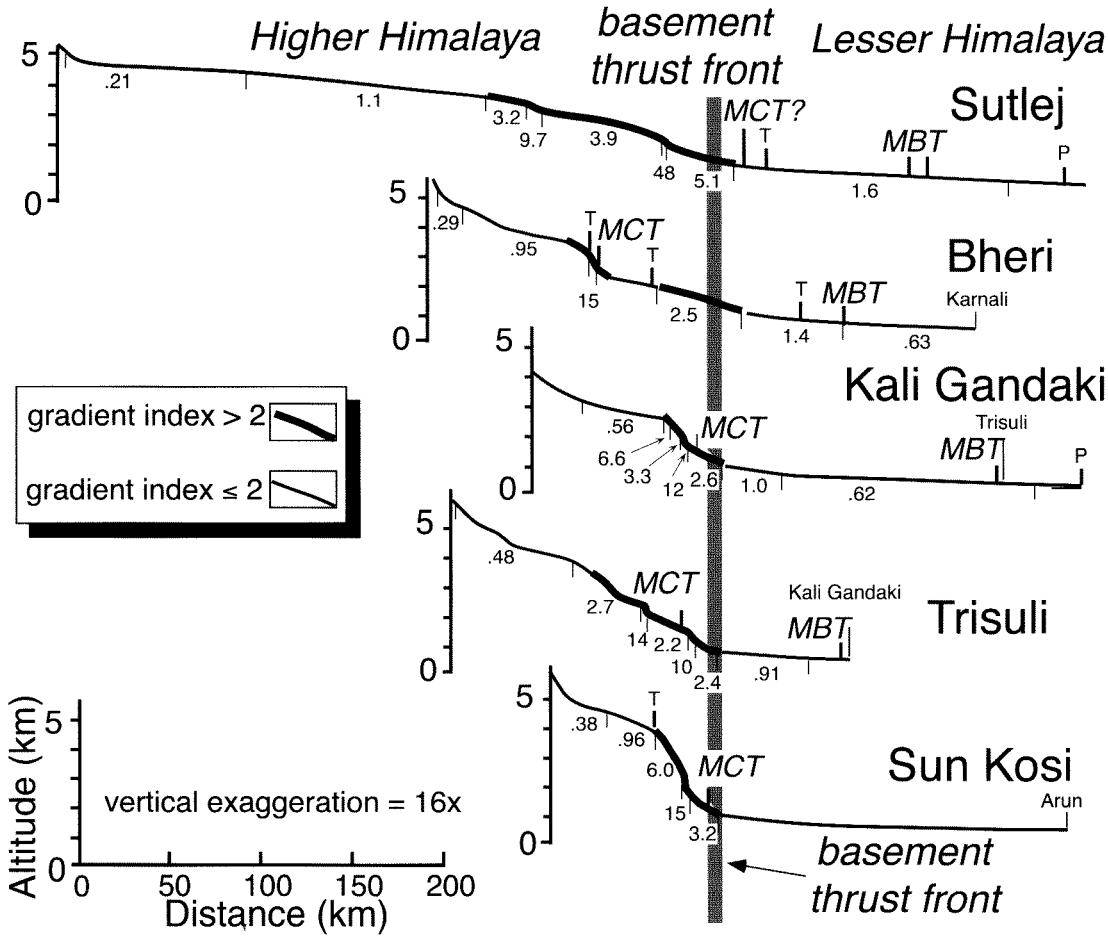

Thicker segments of the profile indicate reaches where the local gradient index (SL) is more than twice the index (k) for the entire profile: SL / k = 2. The steepest gradients are not associated with the Main Boundary thrust or active deformation to the south. Rather they occur near the Main Central thrust and appear to result from upward ramping of the overthrusting Himalayas above a deep-seated basement thrust. Modified after Seeber and Gornitz (1983).

Lesser Himalaya and an active Quaternary thrust) or with deformation within the foreland still farther to the south, Seeber and Gornitz's analysis indicates that the greatest anomalies in stream gradients correspond with the surface trace of the Main Central thrust (MCT). Previously, many researchers thought that this structure had been dead for 5–10 Myr. Seeber and Gornitz's (1983) study suggested instead that a mega-scale fault-bend fold has developed above a ramp in the underthrust basement beneath the trace of the MCT (see Figure 5.4A). This folding has been interpreted to cause regional uplift, reactivation of several faults, including the MCT, and either steepening of river gradients or maintenance of already steep gradients.

Changes in stream gradients occur in response to variably resistant bedrock within a catchment, such that, even in tectonically quiescent areas, steeper gradients are common across more resistant rocks. Potential lithologic controls, therefore, need to be examined prior to assigning a tectonic cause to steep gradients. In the Himalayas, for example, it was suggested that the change to lower gradients coincides with a major lithologic

change to lower grade metamorphic rocks and is not tectonically controlled. Seeber and Gornitz (1983) argue that 1) similarly steep gradients are not seen where the rivers cross high-grade klippe within the Lesser Himalaya, 2) high gradients in some areas are associated with terrestrial clastic strata which are not particularly resistant to erosion, 3) gradient changes in other areas occur within zones of relatively homogeneous rock showing negligible contrasts in erodability, and 4) the steepest gradients occur in areas with very young fission-track ages, indicating rapid denudation. Thus, this study supported a new model for the ongoing growth of the interior as well as the margins of the Himalaya, and it suggested zones where expressions of surface deformation might be expected to occur. A decade after this proposal by Seeber and Gornitz, new radiometric dates along the MCT indicated that the fault has been active at least as recently as about 2 Ma (Harrison et al., 1997; Macfarlane, 1993).

Stream Responses to Regional Tilting

Rivers that flow directly down a newly created slope are *consequent* rivers. Thus, along the surfaces of uplifting folds, tilting fault blocks, or newly emplaced ignimbrite sheets, consequent rivers are commonly present. The effects of changes in the direction of tilt on pre-existing drainage networks are generally predictable. For example, rivers that flow in the direction of tilting will often have steepened gradients, whereas ones flowing in the opposite direction will have shallower gradients. Rivers flowing along the axis of a basin that is being tilted will tend to be shunted toward the downdip edge of the basin (Cox, 1994).

Consider the situation of rivers that flow across a surface in which the overall slope is changing due to ongoing tilting. In general the tilting will cause rivers to be deflected from their original courses toward the steepest gradient. If, however, the rivers are entrenched and can not readily establish new courses, there will be a mismatch between the trends of the rivers on a surface and the regional tilt of the surface itself. For example, the approximately 770-ka eruption of the Long Valley caldera on the east side of the Sierra Nevada, California, created an ignimbrite sheet which sloped southeastward into the northern end of the Owens valley (Bailey et al., 1976). Prior to 125 ka, consequent streams were etched on to that surface (Fig. 9.15) with a mean azimuth of 121–125° (Pinter and Keller, 1995). Subsequently, north-south-trending normal faulting diverted reaches of many streams parallel to the fault scarps. The overall surface itself now slopes at about 3° toward 113°. The mismatch of channel direction versus the regional tilt suggests that this tilting has occurred since the streams became entrenched on the surface.

FIGURE 9.15. Tilting of consequent streams of the surface of the Bishop Tuff ignimbrite sheet

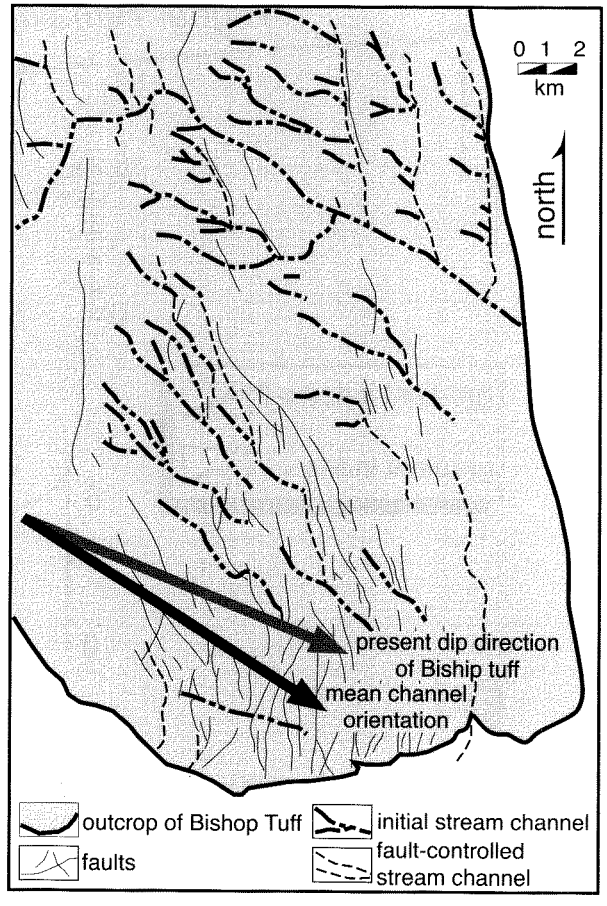

Stream segments are incised in the surface of the tuff and display a mean azimuth of 121–125° where they have not been re-oriented by N-S-trending normal faults. The present regional slope of this surface has an azimuth of ~113° and a dip of ~3°. The mismatch of the average channel direction and the surface slope suggests eastward tilting of the surface following entrenchment of the rivers. Modified after Pinter and Keller (1995).

Even where highly irregular mountainous topography exists, it might be anticipated that regional tilting would steepen the courses of some rivers and decrease the slopes of others. The differential uplift associated

FIGURE 9.16. Tilting of stream channels

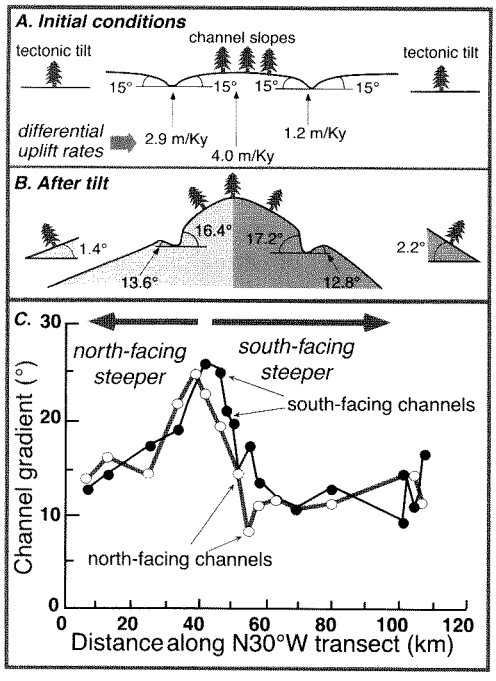

A. Cartoon of channels with uniform slopes of 15° that are then subjected to (B) differential tilting causing a 2.2° southward tilt south of the uplift axis and a 1.4° northward tilt north of the axis. Tilting is predicted to steepen streams flowing in the direction of tilt, while it decreases the slopes of anti-dip streams. C. Data on first-order channel gradients of streams in northern California. Change from streams with steeper north-facing channels to south-facing ones coincides with the axis of maximum uplift (A). Note that the tilting effects on gradients are less significant than the effects of different rock-uplift rates (A). Modified after Merritts and Vincent (1989).

with the Mendocino triple junction causes regional tilting at distances of tens of kilometers away from the axis of uplift (Merritts and Vincent, 1989). Given the duration and rate of differential uplift, tilts of 1–3° should occur along slopes oriented approximately perpendicular to the axis of uplift. Tilts of this magnitude would be expected to produce differences of 2–6° between dip and anti-dip slopes (Fig. 9.16). Analysis of stream channels trending perpendicular (±40°) to the Mendocino uplift axis (Merritts and Vincent, 1989) reveals slope differences which are consistent with the predicted effects of tilting (Fig. 9.16C) and suggests that regional stream-gradient analyses could be useful in defining tilt directions.

Alluvial Fans

Some alluvial fans are segmented and comprise slope segments that are relatively linear and that are characterized by abrupt transitions in slopes (Bull, 1964). This segmentation results from up- and down-fan shifts in the locus of deposition through time and the consequent overlap, onlap, or downlap of younger sediments on to earlier deposited fan strata. Shifting of the depocenter on a fan can result from tectonic and climatic changes. For example, in the face of steady tectonic rates, an increase in water discharge without an accompanying increase in sediment flux will tend to cause entrenchment of the upper fan and down-fan shifting of the depocenter. Because it is common for climate change to drive changes in the sediment and water fluxes, it would be expected that the depocenter would shift repeatedly up- and down-fan in response to these variations. Oftentimes alluvial fans develop along a mountain-piedmont junction which is itself localized by a normal fault. If the rate of uplift of the mountains or subsidence of the basin accelerates along the fault, subsequent deposition will tend to be focused near the fan apex and can create a relatively steep fanhead with an abrupt down-fan transition to a lower gradient surface. In a stratigraphic context, the accelerated relative uplift creates more "accommodation space" near the fanhead which subsequently traps sediments as they emerge from hinterland streams. In contrast, slowing of the rate of relative uplift will decrease the rate at which accommodation space is created near the fanhead, such that streams will tend to entrench the fanhead, sediments will bypass the upper fan, and deposition will occur on the lower reaches of the fan.

If the various segmented fan surfaces can be dated, temporal limits can be placed on the timing of shifts in deposition. Often, it is difficult to ascertain whether the segmentation results from climatic or tectonic causes. One strategy to resolve these ambiguities is to examine a suite of fans bordering a basin. Whereas all of them are likely to have experienced similar climatic variations in the past, their tectonic histories will probably vary considerably. If the pattern and timing of segmentation is similar from fan to fan, the cause of the segmentation is likely to result from a coherent forcing function, like climate change. Increased variability among the fans, but localized coherence where adjacent fans experience

a similar tectonic history would implicate tectonic variations as important controls on fan segmentation.

In the absence of tilting, alluvial fans that debouch on to a low-relief basin floor can generally be described as symmetrical half-cones with slopes that gradually steepen toward the fan apex. The symmetry results from the autocyclic switching of the positions of the main distributary channels on the fan. Over time, this switching serves to distribute sediment uniformly across the fan surface. Under such conditions, topographic contours on the surface will define concentric semicircles on the fan surface. If this fan surface is subsequently tilted (for example, by normal faulting along the basin margin), the topographic contours will become semi-ellipses with their long axes oriented parallel to the direction of tilt (Pinter and Keller, 1995). As an expected consequence of tilting the axis of a cone, therefore, the fan becomes elongated in the direction of tilting, whereas its dimensions parallel to the tilt axis may remain unchanged (Fig. 9.17).

FIGURE 9.17. Elliptical contours on a tilted cone

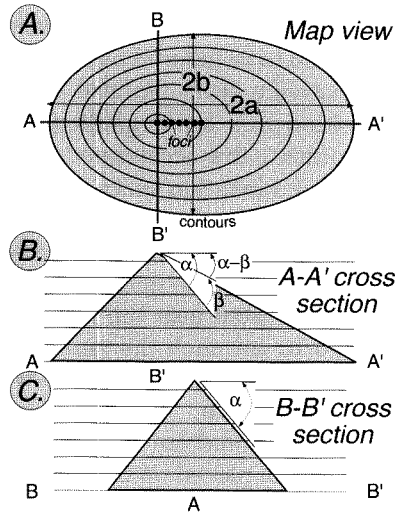

A. AA' defines the major axis of the ellipse, and BB' defines the axis of tilt. Their intersection defines the common focus for each of the ellipses, whereas the dots represents the foci for the other ellipses. B. Cross section along the major axis of the tilted cone (A-A'). The amount β of tilting of the conical axis either increases or decreases the original depositional slope α. C. Cross section along BB' of the tilted cone. The original depositional slope α is unmodified by the tilting. Modified after Pinter and Keller (1995).

Is there a means to quantify the amount of tilting? Geometrical analysis shows that for a cone with an original depositional slope of α whose axis has been tilted by an amount β;

$$\beta = \arccos\left(\left((b/a)^2 \sin^2\alpha + \cos^2\alpha\right)^{0.5}\right) \qquad (9.5)$$

where *2a* and *2b* are the lengths of the major and minor axes of the ellipse (Pinter and Keller, 1995). Thus, if *b/a* and original depositional angle can be defined, then the amount of tilt, β, can be calculated. These dimensions and the amount of tilting can be estimated from analysis of topographic contours on alluvial fans. Initially, a best-fitting ellipse is overlain on that portion of each contour that lies on the fan surface (Fig. 9.18). For a perfect semi-cone with a uniform tilt, the long axes of all of these ellipses will be co-linear, and all of the ellipses will be concentric. In practice, the best-fitting ellipses are not completely co-linear, and their shapes are not concentric. Nonetheless, by measuring the major and minor axes on several ellipses and by measuring the slope α from the contour map, an estimate of the tilt β can be obtained. This methodology assumes that the surface of the fan has not experienced significant deposition since tilting began, because active deposition will continually "anneal" the fan and restore a concentric, untilted conical geometry. Given the variations in sediment fluxes that are associated with many climatic changes,

FIGURE 9.18. Topographic contours and best-fitting ellipses on the Black Canyon fan, Owens valley, California

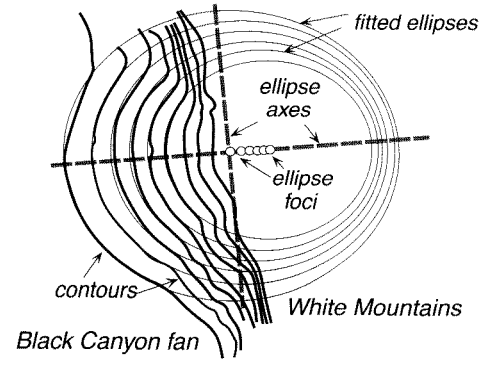

The ratio of the major to minor axes suggests ~4° of tilting has occurred. Modified after Pinter and Keller (1995).

this contour-fitting methodology is primarily applicable to intervals postdating the last major aggradational episode. In many areas, this will restrict its utility to either late glacial or postglacial times (<20 ka). This in turn requires that rates of tilt be relatively rapid in order to produce a discernable effect over this brief interval.

Growing Folds

As described previously, as faults accumulate displacement, they generally increase the size and length of their rupture surface. The plunging noses of hangingwall anticlines and footwall synclines that develop in conjunction with either emergent or blind thrusts would, therefore, be expected to propagate laterally as the tip of the underlying fault migrated with each successive rupture event. Simultaneously, especially in the early stages of development, these growing folds progressively increase in amplitude and breadth with each successive earthquake. As their flanks rise above local base level, they are attacked by erosional surface processes, and their pristine surfaces begin to be modified. Meanwhile, as their noses propagate laterally, the uplift influences the gradients and geometries of nearby fluvial systems. Thus, two rather different responses to growing folds are potentially recorded in the geomorphological record: in one, the shape of the fold is modified by surface processes; in the other, the actual growth of the fold modifies the surface processes (Keller et al., 1999). The degree of surface modification may be an indication of the age of various parts of a fold and the local rate of deformation, whereas river patterns with respect to the fold may reveal their interactions over time. Analysis of these interactions can provide insights on a history of fold growth that are otherwise unattainable (Burbank et al., 1999: Burbank et al., 1996; Keller et al., 1998). Several key data sets can contribute to such a history, including: topographic data on the fold crests, limbs, and nose; dates on geomorphic surfaces and features along the fold; detailed analysis of the underlying structural geometry; and variations of structure along the length of the fold.

Consider first the ways in which a fluvial system that was previously flowing across a relatively low-relief landscape may interact with a growing fold or a suite of growing folds. For any individual fold, as it emerges above the adjacent land, it defines a new drainage divide along its crest and catchments along its flanks: it subdivides formerly continuous drainage systems, and the new catchment configuration is closely tied to the fold geometry. Asymmetrical folds with steep forelimbs will have short, steep catchments on their forelimbs and elongate, gentler catchments on their backlimbs. This asymmetry is readily visible in map patterns of river courses (Talling et al., 1997).

Streams that had formerly flowed across the site of the growing fold either 1) are diverted parallel to the fold axis and around the nose of the fold, 2) become entrenched as antecedent streams which incise through the uplifting fold, or 3) bevel off the top of the emerging fold so that it has little or no topographic expression (Fig. 9.19). In order to maintain its course through a water gap across a rising fold, an antecedent stream must maintain a basinward-dipping gradient across the fold. The stream, therefore, requires sufficient stream

FIGURE 9.19. Satellite image of a fault-related fold in the NW Himalaya

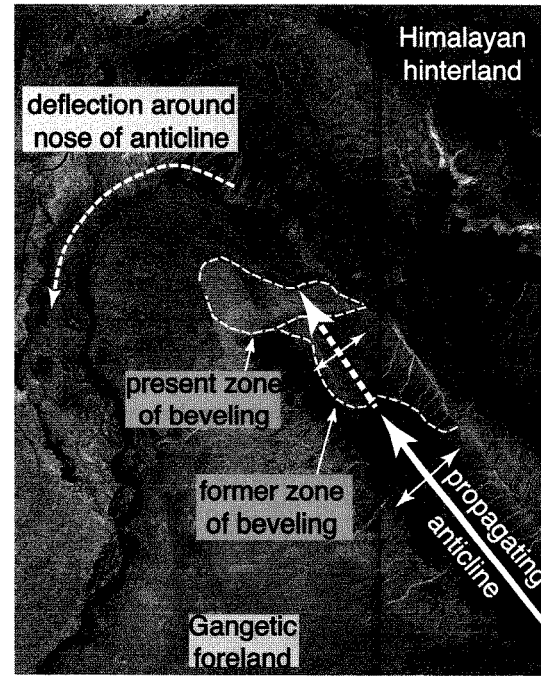

As the fold has propagated to the NW, a major river has been diverted around its plunging nose. As the river impinged on the upstream (proximal) limb of the anticline, it beveled across much of the backlimb and crest of the growing fold and created a low-relief surface which has now been elevated. This pattern is analogous to the current situation in which a broad floodplain has been etched by the modern river across the NE flank of the fold.

power to erode enough of the uplifting structure to sustain that downhill gradient. If the stream power is insufficient, the stream will be defeated, and the former water gap will become a wind gap. The defeated stream on the upstream flank of the fold is likely to flow parallel to the fold until it intersects the next river that traverses the trend of the fold. If the discharge of an antecedent river does not change significantly, then the simple widening of the fold as it grows can lead to defeat of the stream by either of two mechanisms (Burbank et al., 1996). If the elevations of the entrance and exit of the stream from the fold are approximately fixed, then widening of the fold causes the stream gradient across the fold to decrease, and stream power will therefore also decrease. Alternatively, uplift of an anticline commonly forces aggradation to occur upstream of a water gap (Figs. 8.9 and 8.17). Although such aggradation raises the entrance elevation of the stream as it enters the fold and can therefore increase the gradient and stream power across the fold itself, aggradation within the upstream piggyback basin raises the elevation of the stream bed with respect to the adjacent plain and will promote avulsion and diversion of the stream on to lower parts of the plain (Fig. 9.20). By these means, formerly antecedent streams are commonly defeated by growing folds. When analyzing the map pattern of stream valleys associated with growing folds, the expectation should be that a series of wind gaps along the fold crest will record the progressive defeat of older, antecedent streams and that, where a stream is still antecedent, the fold has not broadened and uplifted sufficiently to defeat the stream. As successive antecedent streams are defeated, the remaining streams will capture the discharge of the defeated streams and will augment their stream power as they cross the anticlinal crest. Thus, the most likely location for an antecedent stream is near the propagating nose of a fold (Burbank et al., 1996; Jackson et al., 1996).

FIGURE 9.20. Interactions of an antecedent stream with a growing fold

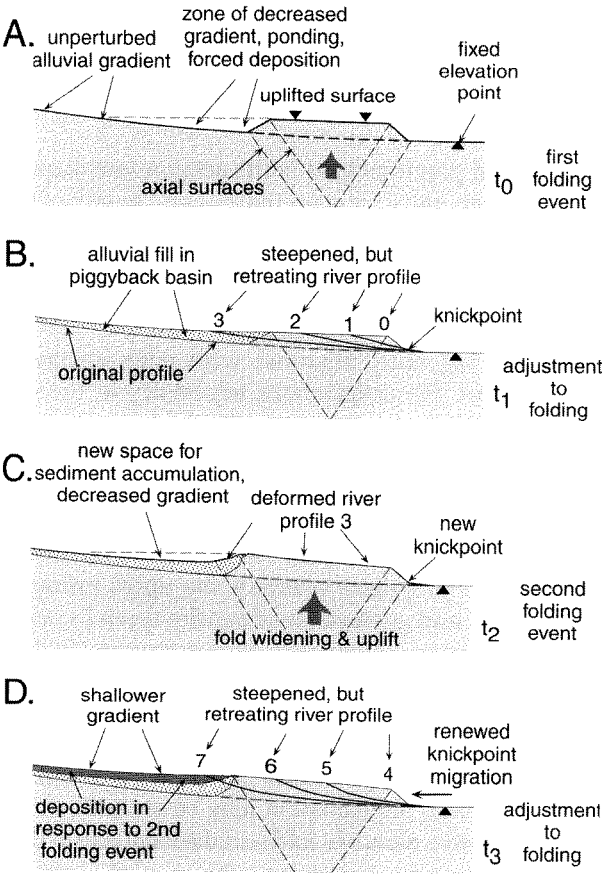

Fold uplift creates accommodation space in the piggyback basin. Deposition in the piggyback basin allows the stream gradient to steepen across the fold, but also raises the river above the surrounding plain. This deposition promotes avulsion, often away from the former water gap. Modified from Burbank et al. (1996).

In order to determine rates of deformation and geomorphological modification of growing folds, dates are needed to define when the fold propagated into a given position and how rapidly it grew vertically and laterally. One such dated structure is the Wheeler Ridge anticline near the southern end of the San Joaquin valley of California (Fig. 4.35). The anticline is strongly asymmetric with a relatively steep (~45°) forelimb and much gentler (17°) backlimb (Medwedeff, 1992). The fault geometry underlying the anticline has been interpreted as a wedge thrust (Fig. 9.21) in which a wedge of allochthonous strata is bounded below by a north-vergent detachment and above by a passive roof thrust. The Wheeler Ridge anticline plunges to the east and dies in the actively aggrading alluvial plain. About 600 m of structural uplift occurs across the easternmost 3 km of the anticline (Medwedeff, 1992). In the vicinity of the wind gap, structural uplift has been nearly 300 m greater than near the water gap (Fig. 9.22). The topographic relief of the fold is considerably less than the amount of structural uplift, because synfolding aggradation has raised the surface of the surrounding depositional basin.

FIGURE 9.21. Block diagram of structure of Wheeler Ridge showing wedge thrust geometry and lateral variation in displacement. Modified after Medwedeff (1992)

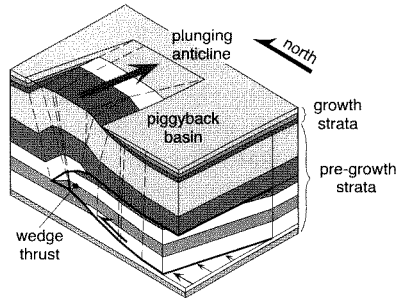

FIGURE 9.22. Schematic cross section along the plunging axis of Wheeler Ridge anticline, showing ages, relief, and propagation rates

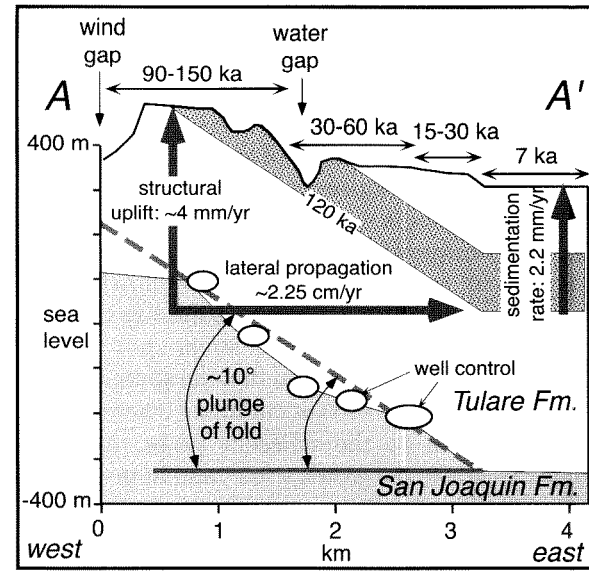

Note the importance of ages in defining the rates of uplift, propagation, and sedimentation. Modified after Medwedeff (1992).

Given a wedge thrust underlying the fold, the synclinal axial surface above the forelimb is active (which is to say that it migrates forward with respect to the strata above the thrust tip), and syntectonic and older beds roll up from the basin through the synclinal axial surface and on to the forelimb. This kinematic geometry provides a basis for dating various parts of the fold, because the formerly actively aggrading surfaces adjacent to the fold are uplifted and incorporated into the fold. Following uplift, they accumulate few new sediments. If the timing of the end of active alluvial deposition or the age of the soil that developed on the uplifted surface can be determined at several points along the fold, these ages will constrain the initiation of fold growth at those points. Based on soil stratigraphy and both radiocarbon and uranium-series dates at Wheeler Ridge (Fig. 9.22), the youngest uplifted area at the emergent eastern end of the anticline is dated at about 7 ka, whereas the alluvial surfaces just east of the wind gap are estimated to date from 90–150 ka (Keller et al., 1998; Medwedeff, 1992; Zepeda et al., 1990). When combined with the structural and stratigraphic data, the ages indicate that, during the past 100 ky, sediment accumulated in the adjacent basin at a rate of about 2 mm/yr, and the crest of the fold uplifted at a rate of about 3–4 mm/yr, while the nose of the fold propagated eastward at a rate of about 23 mm/yr (Fig. 9.22).

If one were to assume that there was a significant earthquake on the underlying fault once every 400 years, these rates imply that, with each rupture, the fold crest would be uplifted approximately 1–2 m, and the fault would extend its eastern tip about 10 m.

The drainage pattern and topography in the vicinity of Wheeler Ridge reveal the basic history of fold growth and river responses (Figs. 4.35 and 9.22). The topographic relief rising from the wind gap to the adjacent ridges is about 300 m, which indicates that an antecedent river had successfully incised across the fold during much of its growth. The floor of the wind gap rests 100 m above the expected unperturbed fluvial gradient across the fold and indicates that this amount of uplift has occurred since the antecedent river was defeated and diverted to the east. A highly asymmetric catchment funnels runoff to the present water gap (Fig. 4.35). This asymmetry suggests the direction of fold propagation and river diversion. The catchment above the water gap is considerably larger than that which would have contributed to the wind gap region, such that the discharge and potential stream power (dependent on the slope) would also be greater. Given the approximately 200 m of relief bounding the water gap (Fig. 4.35 and 9.22), it has persisted for a considerable interval of fold growth.

In the context of the reconstructed history of fold growth, the geomorphic responses to folding and the modification of the fold by surface processes can also be examined in more detail than is commonly possible. The apparently systematic eastward propagation of the Wheeler Ridge anticline permits the ergodic hypothesis to be invoked, whereby space is substituted for time. Visual inspection of Wheeler Ridge (Fig. 4.35A) clearly shows significant changes in the character of the land surface along the length of the fold. Initially as the nose of the fold propagates eastward, a planar region of the alluvial surface is uplifted and gently folded. At this point, the geomorphic surface should precisely mimic the structural geometry of folding. Following uplift, however, surface processes begin to modify the surface in several ways. Where the local stream power is sufficient, gullies begin to be etched into the surface (Dietrich et al., 1992). Alluvial cones accumulate where these gullies debouch on to the adjacent plain. Antecedent streams incise into the growing fold, and in the particular situation at Wheeler Ridge, are commonly localized by transverse tear faults. As gullies deepen, the pristine, but uplifted, alluvial surface becomes more dissected, and landsliding begins to occur on the sides of the larger gullies. As the fold grows and the steep forelimb lengthens, creep and shallow landsliding become increasingly important, and gullies extend their heads toward the crest of the fold. If fold widening and vertical uplift are sufficiently rapid, antecedent streams are defeated and diverted, leaving behind wind gaps.

Inspection of the fold indicates that modification of the geomorphic surface can be analyzed from at least two perspectives: changes along the length of the anticline, and contrasts between the forelimb and the backlimb. The western parts of the anticline are older, have greater topographic relief, and commonly are steeper than the younger, eastern parts of the structure. In any transverse cross section of the fold, the forelimb is consistently steeper than the backlimb. All slope-dependent processes would, therefore, be expected to attack the forelimb more vigorously than the backlimb. Similarly, catchment areas, discharge, and relief increase toward the west. The net result is that the fold becomes increasingly dissected toward the west and that the forelimb is more dissected than the backlimb along any cross section of the fold. Qualitative predictions of changes along the fold (Table 9.1) suggest how various surface processes will be influenced by the growing relief and both lengthening and steepening of the fold limbs.

Analysis of a 30-m digital elevation model (DEM) of Wheeler Ridge permits further quantification of several aspects of the geomorphology. In such a DEM, there is one elevation value in each 30 m by 30 m pixel (picture element). Here, slopes were calculated using the best-fitting plane to a 5 pixel × 5 pixel window (Brozovic et al., 1995), and local relief was calculated within the same windows (Fig. 9.23). The distributions of slopes and relief for selected areas of the fold show that slope, relief, and dissection (Fig. 9.23) are consistently higher on the forelimb than on the backlimb. These data support the hypothesis that the enhancement of slope-dependent processes promotes greater dissection of the fold limbs (Table 9.1).

TABLE 9.1. Effects of slope steepening and lengthening on geomorphology and surface processes

Feature/process	Effect of steepening and slope lengthening	Reason behind effect
Head of 1st-order streams	Channels begin higher upslope	Channel initiation is function of (slope•area)
Ruggedness (mean relief *drainage density)	Increases with steepening and lengthening	More 1st-order channels lower on slope and deeper channels to match relative base-level
Creep and landslides	Increases with steepening and lengthening	Shear stress is a function of slope: $\sigma = \rho g h \sin \alpha$
Exported material	Increases with steepening and lengthening	Flux proportional to dy/dx
Balance of uplift versus incision	Uplift tends to outpace incision for antecedent streams	Width of structure increases with time; discharge stays constant, but river slope and mean stream power decrease

FIGURE 9.23. Wheeler Ridge geomorphology

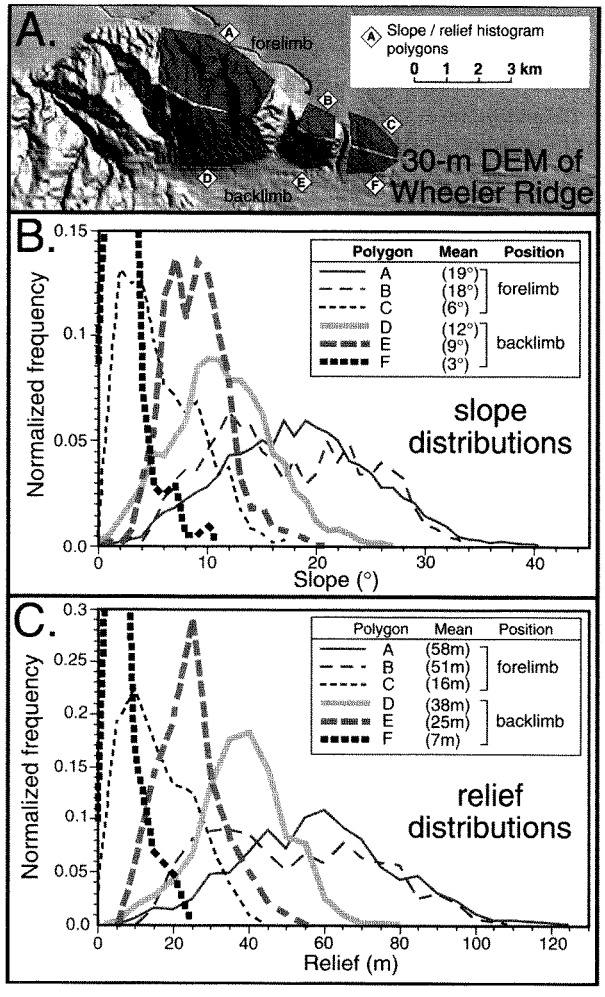

A. Polygonal areas represent calculation areas on either flank of the Wheeler Ridge anticline. The amount of rock uplift and magnitude of dissection increase toward the west. B. Slope distributions for polygons shown above. Slopes are calculated in a 120 × 120-m window. Note progressive changes from old (A) to young (C) and the persistent difference between the forelimb (A-C) and backlimb (D-F). C. Relief distributions for the same polygons. Modified after Brozovic et al. (1995).

FIGURE 9.24. Map of slope angles along Wheeler Ridge anticline

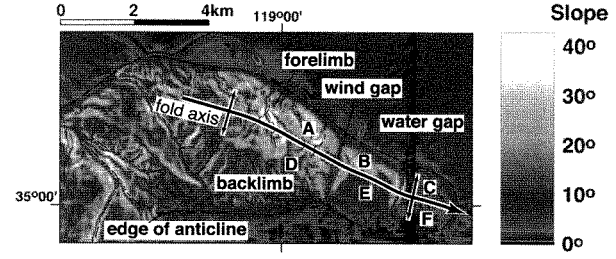

Letters A–F refer to same polygons as in previous figure. Note that the drainages on the forelimb extend beyond the fold crest in the older, more dissected part of the fold (A). Modified after Brozovic et al. (1995).

As described earlier, digital topography can also be used to calculate volumes of eroded material along the anticline (see Figure 7.6). As might be expected at Wheeler Ridge, these calculations indicate that the most extensive erosion has occurred in the older, more strongly uplifted segments of the fold, whereas very little erosion has occurred near the eastern nose of the fold. The magnitude of erosion (eroded volume/source-area size) is always higher on the forelimb rather than the backlimb (Fig. 9.25A); this supports the concept of erosion rates being slope dependent. The rates are also higher on the older parts of the fold, where there is greater relief and has been more time for dissection (Fig. 9.23). A plot of the rates of dissection versus the mean slope (Fig. 9.25B) shows predictable increases in rates for increasingly steep slopes, but also suggests the possible existence of a threshold slope angle of about 17–18°, above which erosion rates are much faster. However, because calculation of the mean slope angle includes pixels of gully bottoms and headwalls, as well as pristine tilted slopes, such an interpretation is likely to be incorrect. Rather than there existing some geomorphologically meaningful threshold at 18°, it is more likely that the longer slopes, greater relief, and more areally extensive gully headwalls in the older part of the fold have promoted more rapid erosion there.

This analysis of Wheeler Ridge highlights some of the ways in which ages on uplifted surfaces, recognition of structural geometries and of geomorphic patterns, and quantification using digital topography can be used to develop a fuller understanding of the rates of fold growth and dissection over thousands of years. If combined with field measurements of geomorphic processes and with paleoseismic analysis, it may be possible to

FIGURE 9.25. Quantified erosion on Wheeler Ridge anticline

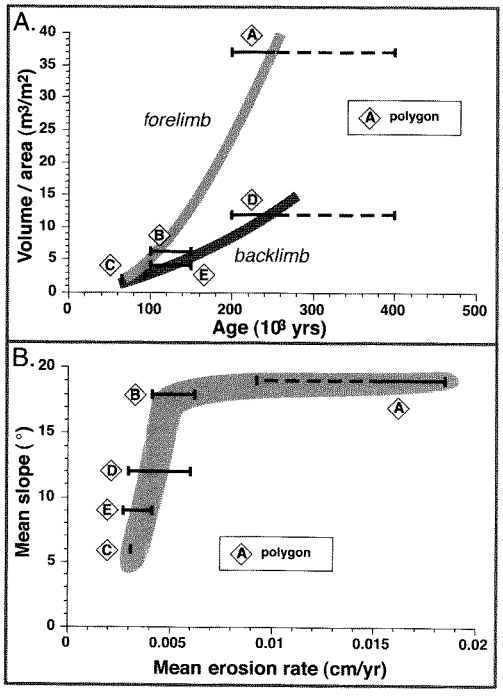

A. Eroded volume per unit area is plotted against the age of the dissected surface. Note persistently higher rates on the forelimb for each age grouping. Poygons are the same as those shown in Figure 9.23. B. Mean erosion rate versus mean slope angle in each polygon. Modified after Brozovic et al. (1995).

develop more realistic models of fold development and modification which span from decades to many thousands of years.

Summary

Tectonic deformation and interactions with surface processes over intervals of hundreds of thousands of years produce the landscapes that we see today in many tectonically active areas. At vertical uplift rates of about 1 mm/yr and horizontal displacement rates of about 1 cm/yr, hundreds of meters of uplift and several kilometers of lateral displacement occur over these "intermediate" time spans. In combination with climatic and lithologic variations, such movements exert a fundamental control on landscape development.

Given the slope dependence of many surface processes and the sensitivity of fluvial systems to small variations in surface gradients, geomorphic responses to specific tectonic perturbations are often predictable. At intermediate time scales, powerful insights are obtainable when the growth of structures can be quantified. Not only does this reveal mean rates of deformation and structural propagation, but it provides a reliable context for interpreting geomorphic responses to deformation and testing predictions concerning those responses.

Numerous difficulties can thwart successful landscape analysis at intermediate time scales. Determination of tectonic rates typically depends on dating of displaced geomorphic surfaces. In many geomorphic settings, dating of surfaces that exceed the range of radiocarbon dating (>40 kyr) is difficult or impossible. Soil chronologies, uranium-series dates, cosmogenic exposure ages, or thermoluminescence ages can sometimes bridge the gap between radiocarbon and argon-argon dating. Because each of these dating approaches may lack accuracy, it is important, whenever possible, to use several techniques in conjunction with each other or to find settings in which redundant ages can be determined for the same surface or in which multiple rate calculations can be made from a succession of offset markers.

In tectonically active coastal settings, ages of terraces are often inferred through correlation with a dated sea-level curve. Numerous uncertainties still exist in this curve with respect to both the magnitude of past sea-level variations and the actual timing of those changes. The interval prior to the last interglaciation (>130 ka) is particularly poorly documented. To the extent that the reliability of the sea-level curve can be improved, the accuracy of deformation rates in coastal domains will improve.

The timing of geomorphic responses to climate variations in terrestrial settings is even less well understood than those along the coast. Development of some geomorphic markers, such as fluvial terraces, have both direct and indirect climate controls. For example, even if climatic conditions are conducive to terrace building, if insufficient sediment is available for transport within the upstream drainage, aggradation will not occur. Geomorphic markers provide an important basis for gauging deformational and denudational processes within many landscapes. Therefore, understanding of the character and rates of response of markers to

climatic changes, as well as the temporal lags in those responses and the potential impact of autocyclic processes, is of paramount importance in reconstructing tectonic and geomorphic histories at intermediate time scales.

Individual folds commonly grow over an interval of a few hundred thousand years in tectonically active settings. During this period, stream patterns and preserved surfaces often provide unambiguous information on the amount and geometry of deformation. If fold growth were to persist at rates of 1 mm/yr for a million years, 1 km of displacement would occur. In most cases, structural relief of this magnitude would cause erosion to obliterate all but the most persistent geomorphic markers, such that the details of fold evolution would be difficult to reconstruct from geomorphology alone. It is at these longer time scales, however, that mountain ranges develop and orogens evolve. In the succeeding chapter, we examine landscapes that represent an integration of geomorphic and tectonic processes at time scales of a million years or more.

CHAPTER 10

Tectonic Geomorphology at Late Cenozoic Time Scales

Tectonic landscapes that evolve over hundreds of thousands to millions of years result from the long-term interplay between the constructional and erosional processes. Mean rates of activity along faults and the resultant bedrock uplift or subsidence will define the shape of an unmodified tectonic landform, whereas the summation of all active erosional and depositional processes will determine how that pristine form is modified. At such long time scales, nearly all geomorphic thresholds can potentially be crossed, such that uncommon, large-scale geomorphic events can play an important (and possibly the most important) role in shaping the landscape. For example, deep-seated landslides in which entire mountain sides collapse may represent the dominant shape-modifying process in some settings. The rarity of such events may dictate that short- and intermediate-term landscapes may not be in dynamic equilibrium. As a consequence, the processes active at these shorter time scales might help trigger rare events. For instance, it may take very long times for gradual incision of a stream to force adjacent hillslopes to cross the rock-strength threshold, generating very rare and catastrophic adjustments of the landscape.

Over these prolonged intervals of tectonic activity, the record of detailed interactions of short-term deformation and surface processes is often obscured due to their incremental impact on the present-day landscape. In the analysis of long-term deformation, the appropriate suite of questions to pose and the approaches to solve them differ from those applied to processes and landforms at shorter time scales. In general, a larger spatial framework (hundreds to thousands of km^2) is appropriate for addressing the products of long-term deformation. Bedrock cooling histories, stratigraphic data from bounding basins, the topographic character of entire ranges, and the geographic character of large river catchments can each provide important clues to the interpretation of the tectonic-geomorphic history. We will see, for example, that newly developed digital data sets, such as DEMs, allow rapid statistical characterization of landscapes at these scales.

Some important questions that are relevant to regions of prolonged deformation include: Are there regional topographic characteristics that permit one to delineate sustained differences in mean rates of deformation? Is there evidence to suggest that the short- and intermediate-term tectonic-geomorphic interactions at smaller scales (which we can understand with less ambiguity) provide useful models for the longer term evolution of the area? Are there patterns, order, predictability, or scaling relationships in the landscape that provide a basis for understanding the sequential development of the region; or are there useful, simple "rules," either empirical or physically based, that can be extracted from the landscape and that explain or predict the long-term behavior of an area? For example, rules concerning cooling and densification of newly produced oceanic crust reliably predict the subsidence patterns adjacent to mid-ocean ridges (Parsons and Sclater, 1977). Are there similar rules that predict under what conditions a steady-state topography will prevail in a mountain range or when a previously active fault will be abandoned and a new one initiated?

In the continental settings on which we have focused in this book, there are three primary tectonic settings: extensional, contractional, and strike-slip regimes. In this chapter, we will examine long-term landscape development in each of these regimes, and will briefly

describe the impact on the tectonic geomorphology exerted by other tectonic phenomena, such as hot-spot tracks or oblique collision, on the topography and geomorphology of nearby regions.

Regions of Extension

It is commonly seen that ruptures on active normal faults can be characterized as a series of linear fault segments separated by transfer zones with more complex geometries (Figs. 4.11 and 4.13). The linear trends result from the fact that most normal faults intersect the surface at high angles (~60°), such that the trace of the fault is only slightly deflected by surface topography. In many cases, normal faults also approximately define a boundary between an erosional domain in the uplifted footwall and a depositional, nearly horizontal domain above the downthrown hangingwall. As seen earlier, there is a predictable pattern of co- and interseismic vertical motions (Figs. 4.24 and 4.25), with the greatest magnitude of footwall uplift and hangingwall subsidence proximal to the fault. Enhanced hangingwall subsidence near the fault tends to guide depositional systems toward the fault, and subsequently, these tend to fill the space available to accommodate sediment to the extent that the sediment supply permits. Despite such deposition, coseismic footwall uplift commonly results in positive topography that bounds the depositional basin along the fault. One would, therefore, expect that recurrent normal faulting would produce a relatively linear mountain front delineating the footwall-hangingwall boundary. This would be most common if the bounding fault carries bedrock to the surface in the footwall block.

Facets and Drainage Spacing

The topographic evolution of that mountain front depends strongly on the relative rates of faulting, erosion, and deposition (Ellis et al., 1999). Rivers flowing across the fault from the footwall uplift will tend to dissect and embay the mountain front, whereas active faulting will tend to restore its linear character (Fig. 10.1). The spacing of facets along range fronts reflects the evolution of drainage basins within the footwall block. Given a simple block uplift with two sloping sides bounded by faults, each flank will be characterized by regularly spaced, similarly sized and shaped basins, sometimes called "wine glass" or "goblet" valleys due to their wide upper basins tapering to narrow throats as they pass across the active range front. The actual spacing of the basins depends on how elongate or circular they are. The more circular the basins are, the less efficiently they fill space and the broader will be the triangular facets (Fig. 10.2) (Mayer, 1986). More elongate basins, on the other hand, will produce smaller, more closely spaced facets. Spacing can be measured as the ratio between the mean length of the basins (i.e., the mean distance from the main drainage divide to the mountain front) to the mean spacing of the mouths of the basins along the range front (Wallace, 1978). For tectonically active, extensional fault blocks, length-to-spacing ratios are typically

FIGURE 10.1. Large-scale geomorphology of rapidly deforming and slowly deforming normal faulted mountain ranges

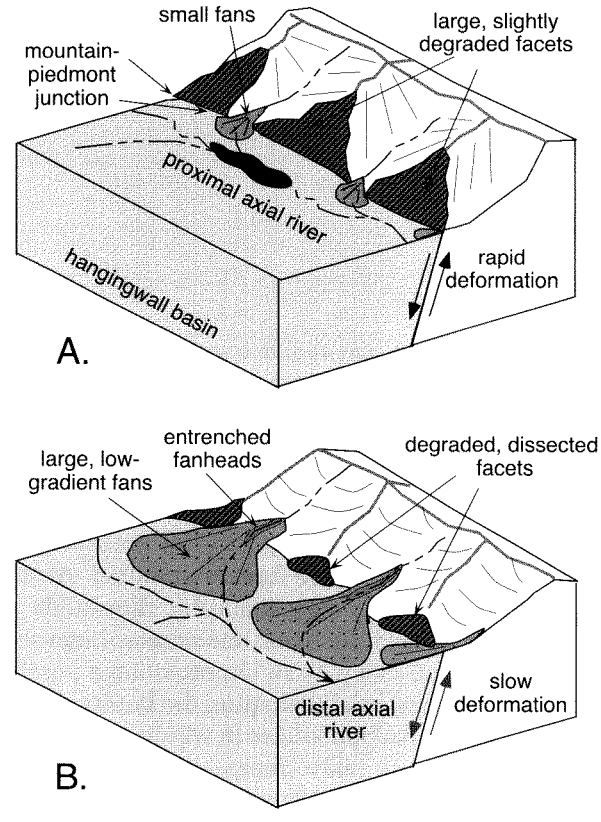

A. Rapid hangingwall subsidence and footwall uplift create a linear range front, large facets, small piedmont fans, and proximal axial river.
B. Slower deformation leads to large, low-gradient fans, small facets, entrenched fan heads, and distal axial rivers.

FIGURE 10.2. Facet spacing and shape in relationship to basin geometries within the footwall. Modified after Mayer (1986)

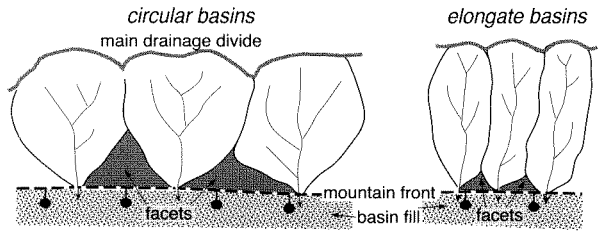

FIGURE 10.3. Major drainages on fault-block mountains in the Basin and Range

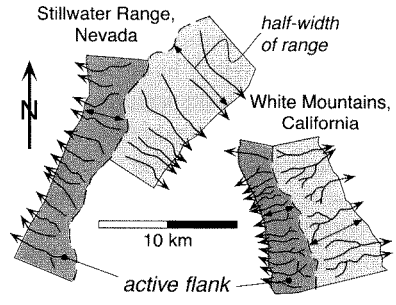

Note that the average spacing of the outlets scales with the average length of the drainages, such that more closely spaced outlets are found with shorter tributary basins. Modified after Talling (1998).

between 1.8 and 4 (Wallace, 1978) with a mean of about 2.5 (Talling et al., 1997). In "well behaved" ranges, when opposing flanks are compared, differences in the distance to the main divide are clearly reflected in differences in the spacing of the major rivers draining each side, such that shorter drainages are associated with more closely spaced rivers (Fig. 10.3). In terms of trying to decipher the tectonic regime from the drainage patterns, the key attribute of these patterns is that shorter and steeper drainages are commonly found on the more tectonically active flank of the range. In more complex geological uplifts and in older mountains, where drainages have had more time to integrate or cannibalize other nearby drainages, basin shapes are more irregular and river-outlet spacing can be wider, yielding spacing ratios as low as 1.2 (Wallace, 1978).

Traditionally, triangular facets (Fig. 10.1) were interpreted as variably degraded remnants of the fault-generated footwall scarp (Wallace, 1978). Having "relaxed" to the angle of repose, this degraded scarp defines the height of a facet, whereas the spacing of drainages incised into the footwall defines the facet width (Wallace, 1978). Recent models of surface processes interacting with a footwall uplift extend these earlier interpretations and suggest that, rather than being remnant landforms, facets with quite uniform slopes can be active geomorphic features resulting from landsliding in landscapes that are limited by rock strength (Ellis et al., 1999). Approximately uniform facet slopes reflect the stable angle of repose in homogeneous bedrock, whereas facet width is dictated by the spacing of the drainages incising into the footwall. The nature and slope of the bounding scarp and facets depend greatly on the rate of uplift and on the material being cut. For example, scarps formed in alluvium rapidly degrade to slopes of ~30° and then gradually wear back to much shallower slopes. Scarps in fractured bedrock degrade to and then can maintain a considerably steeper slope for long intervals (thousands of years) (Fig. 10.4). The shaping of valleys within the footwall is related both to downcutting by streams and rates of valley-wall retreat due to landsliding, incision by tributary streams, and slower hillslope processes such as creep (Mayer, 1986).

Geomorphology and Depositional Geometries

It is useful to try to conceptualize the geomorphic character of a mountain front that has experienced persistent rock uplift. Mountains in the footwall block may rise more than 1000 m above the adjacent basins. Rapid footwall uplift tends to result in a linear mountain front characterized by high relief and deeply incised streams. Within the footwall uplift, these V-shaped valleys have steep gradients and small to nonexistent floodplains. Within the hangingwall basin, the length and gradient of transverse streams or fans, and the relative distance from the depocenter to the mountain front in comparison to the width of the basin, provide indicators of the balance between tectonically driven subsidence and sediment supply. Lower transverse river gradients, longer fan lengths, and increasingly distal depocenters should indicate lower rates of active deformation and subsidence along the basin-bounding fault, whereas short, relatively steep alluvial fans, the presence of clear fault scarps, and proximal depocenters typify regimes of more

FIGURE 10.4. Observed changes in stable slope angles through time

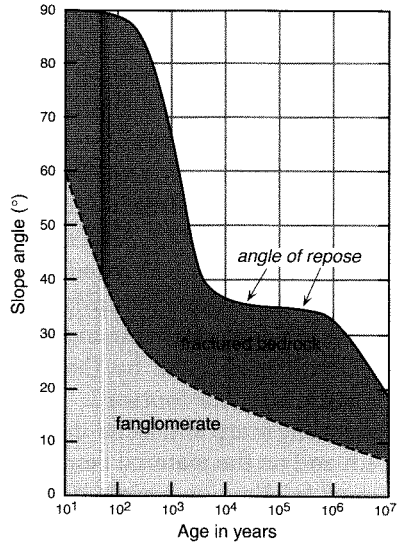

Faulted and uplifted sedimentary strata will degrade to slope angles of <30° in less than 1000 years, whereas fractured bedrock can maintain high initial slope angles and will only gradually degrade to an angle of repose that can be maintained for 10^6 years. Modified after Wallace (1978).

rapid faulting (Fig. 10.1). In humid settings, short transverse streams sourced in the footwall can be tributary to axially flowing master rivers that are located near the mountain front. In drier climates, closed-basin lakes could be located at the toes of the short tributary fans.

Whereas the slopes on short, range-front fans may approach 15° near their apices, in general, when more than 0.5 km from the fault, fans typically have slopes of 1–3° (Wallace, 1978). If it is observed that the mean slope of a group of fans or a bajada is ≥3–4° over distances of ≥2 km, such slopes suggest that this portion of the fan is underlain by tilted bedrock and that faulting has propagated out into the basin (Wallace, 1978).

Quantitative Assessment of Range-Front Faulting

In order to deduce the current state of activity on a normal fault, several different attributes of the mountain front and of the associated depositional and erosional systems can be examined. The amount of incision at the apex of fans aligned along the mountain front-piedmont junction is determined by 1) the balance between the rock uplift rate in the footwall, 2) rates of fluvial erosion in the footwall, and 3) variations in sediment supply. If active uplift is elevating the stream within the mountains more rapidly than it is incising, there will be active deposition on the apex of the fan (Bull and McFadden, 1977). To the extent that incision outpaces footwall uplift, the fan head will tend to become entrenched. The degree of entrenchment and the age of the dissected remnants of the former fan apex provide a general indicator of the amount and timing of the change from active to less active footwall uplift. It must also be realized, however, that sediment fluxes can vary rapidly as the climate changes. Changes in sediment and water discharge can lead to fan-head incision or aggradation that is independent of any tectonic variations. Therefore, entrenchment that persists through several climate cycles is more likely to be a response to tectonic forcing than will entrenchment occurring solely within one cycle.

Several numerical measures of the mountain front and its related fluvial system have been used to classify the state of long-term tectonic activity. Because an active front is generally straight, whereas an inactive one becomes increasingly embayed, the *sinuosity* of the mountain front is a useful indicator of the level of long-term tectonic activity (Bull and McFadden, 1977). *Sinuosity*, S, is determined by dividing the length of the mountain-piedmont junction, L_{mp}, by the length of the associated range, L_r (Fig. 10.5):

$$S = (L_{mp}) / (L_r) \qquad (10.1)$$

A sinuosity of close to 1 is usually interpreted to characterize an actively deforming range, whereas as the sinuosity increases to 2 or more, it indicates an embayed range front with relatively little active faulting. These data can be readily derived from topographic maps, although some subjectivity is involved when designating the mountain-piedmont junction. This technique may also be relatively insensitive to reactivation of old faults. Furthermore, if renewed faulting has been insufficient to restore a linear range front, even a presently active mountain front will appear embayed on a topographic map.

If rates of tectonic activity decrease or stop, then surface processes will dominate further evolution of the landscape. Lateral planation by transverse rivers will widen their valleys within the mountains, and gradual back-wearing will decrease their gradients. As valley widening extends into the footwall uplift, lateral and

FIGURE 10.5. Sinuosity of faulted mountain fronts

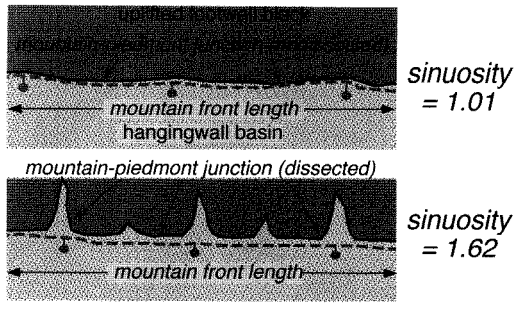

Top: active normal faulting with linear mountain-piedmont junction leading to low sinuosity. Bottom: embayment of mountain front along less active fault creates higher sinuosity.

FIGURE 10.6. Measurements of valley shapes in footwall blocks

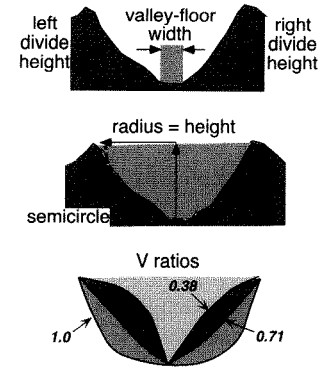

Top: Valley-floor width-to-height ratio. Middle: Parameters for calculating a "V ratio." Bottom: Examples of V ratios for several valley shapes.

frontal slopes of triangular facets will be further reduced, and the mountain front will become increasingly embayed. Within the depositional basin, decreasing subsidence will decrease the space available for deposition, leading to progradation of the transverse fans, fan-head entrenchment, and basinward displacement of axial rivers or lacustrine depocenters (Fig. 10.1).

In order to evaluate mountain-front sinuosity along an extensive range front, it is often useful to develop criteria for subdividing the range front into segments. Such criteria could include: major changes in lithological resistance, major changes in the orientation of the range front or steps in the bounding faults, cross-cutting river valleys that are large in proportion to the range, and significant changes in the geomorphic character of the range (Wells et al., 1988).

Topographic cross-sections parallel to the mountain front, but within the footwall block, can be examined to determine the *ratio of valley width to the height, R*, of the adjacent drainage divides (Fig. 10.6) in order to evaluate the effect of tectonism on valley geometries (Bull and McFadden, 1977). Small width-to-height ratios suggest prolonged incision and uplift, whereas high ratios indicate that degradational processes, such as valley widening and ridge-crest lowering, have dominated the recent landscape. Because it takes time for base-level effects to propagate upstream into the footwall block, measurements are usually made close to the range front: for example, 1 km upvalley. The width of the valley floor, *wdf*, is divided by the mean relief represented by the height of the right and left drainage divides, e_{ddr}, e_{ddl}, above the valley bottom, e_{vb}.

$$R = wdf / [[(e_{ddr} - e_{vb}) + (e_{ddl} - e_{vb})] / 2] \qquad (10.2)$$

Another way to evaluate the cross-valley profiles is to determine the ratio of the area of the actual valley cross section (in other words, that region that has been eroded away) to the area of a semicircle with a radius equal to the height of the adjacent drainage divide (Mayer, 1986) (Fig. 10.6). Valley ratios (V ratios) near or greater than 1.0 signify U-shaped valleys; valleys with V ratios greater than 1 are usually broad and shallow, whereas valleys with cross sectional area of less than 0.5 are usually steeply incised (Fig. 10.6). Interpretation of the valley-floor width-to-height ratios can be complicated by variations in both stream size and lithologic resistance. Weaker lithologies and larger rivers will lead to broader valley floors than will more resistant rocks and smaller rivers in the same uplift regime. Consequently, due to the complexity imposed by geologic conditions, "quantitative" measures, such as sinuosity or V ratios, should be regarded as qualitative guides to the status of tectonic activity over multiple climate cycles.

Drainage Basins in Extensional Ranges

As opposed to individual fault scarps, which may be strongly modified over short time intervals, drainage basins have considerable persistence as geomorphic landscape elements. As a consequence, drainage basins

provide insights on the long-term evolution of the landscape. Basin geometries develop in response to the nature and distribution of uplift and subsidence, the spatial arrangement of faults, the relative resistance of different rock types, and climatically influenced hydrologic parameters. Because of the nearly linear character of many normal faults and quite readily predicted pattern of subsidence and uplift associated with them (King and Ellis, 1990; King et al., 1988), it is reasonable to develop a conceptual scheme for drainage basins in extensional terrains based on modern examples and theories.

Because many extensional faults bound half-grabens, an asymmetric footwall uplift is commonly produced as a response to recurrent faulting. The resultant back-tilted blocks usually have long, relatively gentle basins on the "back" side of the block and steep short drainages on the side abutting the fault scarp. Thus one criterion to distinguish the relative activity of range-bounding normal faults is to examine the size and steepness of basins on either flank of a range: the flank facing the more active fault will tend to have smaller, shorter, and steeper drainage basins (Fig. 10.7, Fig. 10.8) (Leeder and Jackson, 1993). In some fault-bounded grabens, there is a master fault delineating one boundary of the graben and one or more antithetic faults cutting the hangingwall and defining the opposite boundary. In this circumstance, the relative size and steepness of the opposing drainage basins developed on the footwall uplifts of each fault can sometimes indicate which is the more active fault (Leeder and Jackson, 1993). Similarly, if there is an axial river flowing through the basin, it will tend to be displaced from the center of the basin toward the more active fault, where subsidence is generally the greatest.

Fault terminations and fault offsets or step-overs along range fronts, where displacement is transferred from one major fault strand to another, often have distinctive relationships with drainage basins. If we accept that, as faults accumulate more displacement, they lengthen (Cowie and Scholz, 1992), it would be expected that rivers would tend to be displaced away from the zone of maximum uplift and toward or around the growing tip. As fault tips propagate toward or past each other, deflected rivers will tend to be localized into the space between the tips, which may eventually be considered a "transfer" zone. The reason these catchments become large is that, as the fault propagates, the catchment incrementally expands toward and beyond the fault tip. Often, rather large drainage basins oriented obliquely, rather than

FIGURE 10.8. Extensional mountain ranges in the Basin and Range, Nevada

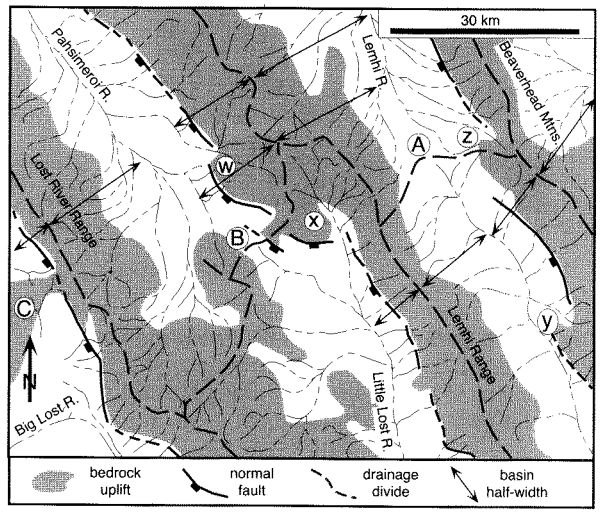

Note the asymmetry of transverse basins with short basin half-widths associated with active extensional faults. Axial drainages flowing to the NW or SE are separated by basement ridges at A, B, and C. Oblique drainages that develop near fault terminations or step-overs occur at W, X, Y, and Z. Modified after Leeder and Jackson (1993).

FIGURE 10.7 Asymmetric drainage basins responding to differences in the activity of range-bounding faults in the Aegean Sea

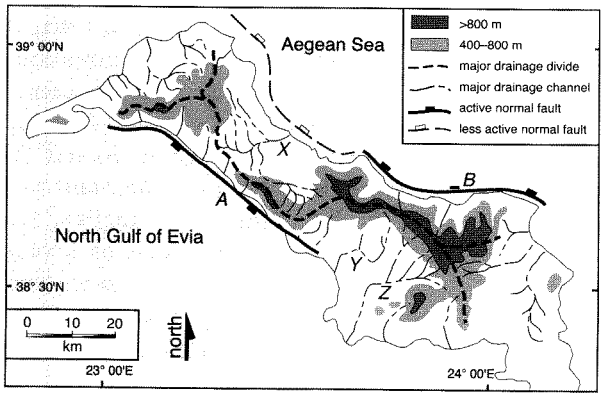

Active normal faults at A and B show a clear spatial association with short, steep footwall drainages. Large rivers (X, Y, Z) flow down the backslopes of these blocks. Modified after Leeder and Jackson (1993).

orthogonally, to the range front develop near fault terminations or transfer zones (Fig. 10.8, Fig. 10.9). As faults grow and their tips overlap, one fault may predominate over the other and accommodate some of the displacement which was previously taken up on the other fault (Fig. 10.10). Evidence that a propagating fault is accumulating displacement at the expense of another fault (Fig. 10.10) may be derived from a combination of:

1. The diminution of topographic relief along the footwall of the propagating fault. Despite active faulting along the propagating fault, the amount of footwall uplift and topographic relief is minimal along these young faults;
2. Changes in the size of alluvial fans and their proximity to the range front. As faulting steps forward into the hangingwall, the proximal part of the former hangingwall becomes part of the footwall of the new fault. Footwall uplift drives incision (fanhead entrenchment) of the old fans and displaces their apices away from the topographic range front; and
3. Changes in drainage basin size and orientation in the newly formed footwall. Large, oblique catchments that marked the termination of the older fault may be incorporated into the footwall of the new fault, where most of the catchments are small and orthogonal to the fault (Fig. 10.9, Fig. 10.10).

In the Basin and Range, comparison of the overlapping Pearce and Tobin faults in Pleasant Valley, Nevada (Fig. 10.10) shows that the size of the fans, the amount of topographic relief, and the size of the footwall catchments all decrease toward the tip of the propagating young fault and toward the zone of overlap, whereas the amount of entrenchment and the distance of the active fan-head from the fault trace increase in the same direction.

Displacement Gradients and Fault Linkage

Theoretical calculations indicate that hangingwall subsidence and footwall uplift should be maximized where fault displacement is the greatest (King and Ellis, 1990). For faults that propagate symmetrically from an initial central rupture, this implies that maximum subsidence and fault displacement should occur near the mid-point of the fault trace. At the same time, we know that as multiple faults propagate along a given trend, either they can link up to form a continuous displacement surface or their tips can propagate past each other. This raises the issue of how one determines whether a given normal fault resulted from a linking up of several faults or from the growth of a single rupture.

FIGURE 10.9. Summary of drainage geometries in extensional basins

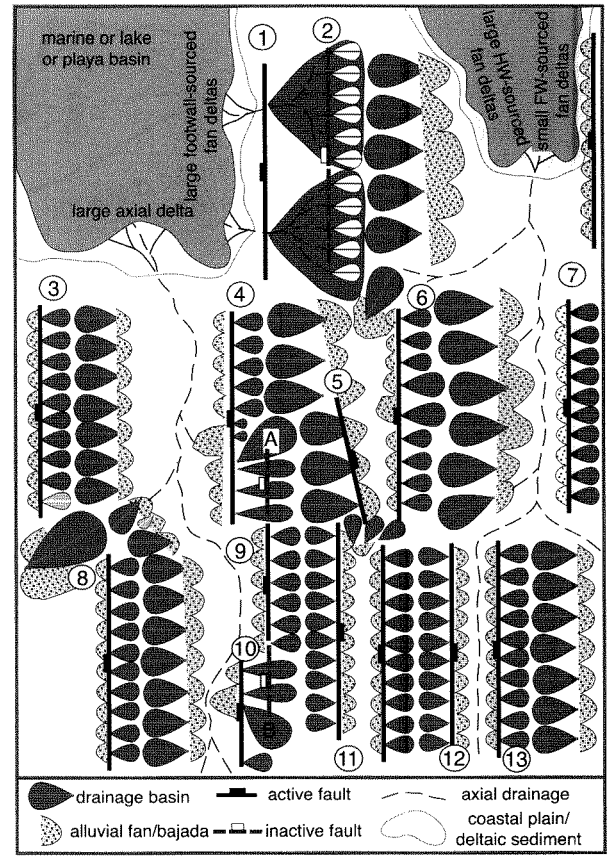

Active normal faults (3, 8, 13) have short, steep drainages adjacent to the fault and longer, gentler drainages on the back-tilted flank, which are commonly hangingwall basins. Large catchments oriented oblique to the range front occur near fault terminations and step-overs, such as between faults 3 and 8 or 2 and 6. Large oblique drainages (A and B) mark the terminations of fault 9, which have become inactive due to the propagation of faults 4 and 10. Abandonment of fault 2 as fault 1 becomes active causes large catchments to form in the sediments of the footwall to fault 1. Axial rivers tend to be deflected toward the more active basin margin. Closed basins develop near faults 5 and 11. Modified after Leeder and Jackson (1993).

One starting point is to delineate competing models for the fault evolution, footwall topography, and basin subsidence (Fig. 10.11). In the case of a single fault that

FIGURE 10.10. Large-scale geomorphology where young fault tip propagates past an older normal fault

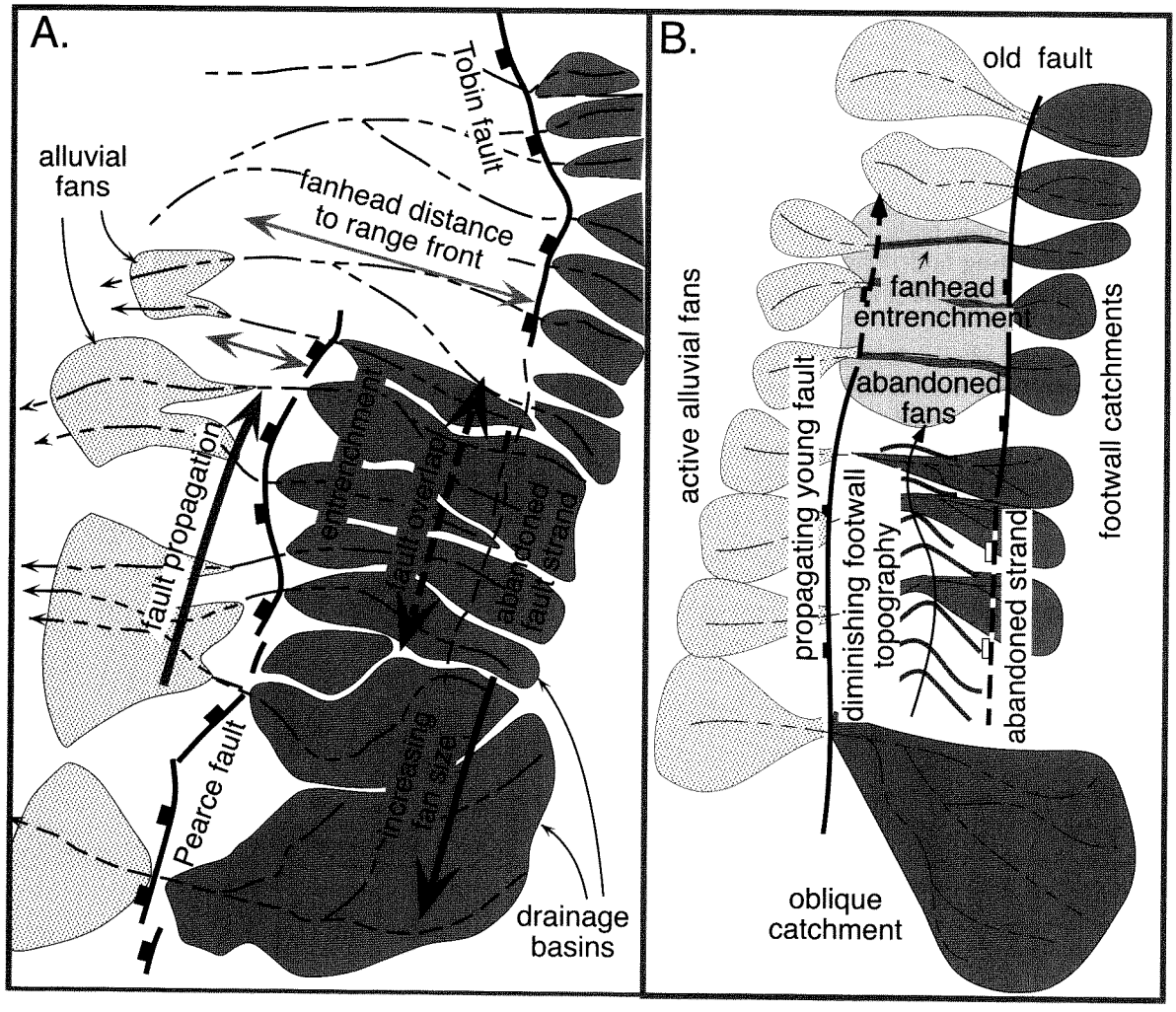

A. Interpretation of the overlap zone of active normal faults in Pleasant Valley, Nevada, where the Pearce fault is propagating northward past the tip of the Tobin fault. B. Cartoon of major geomorphic features in such zones of overlap. Note diminishing footwall topography toward the propagating fault tip, incorporation into the young footwall of oblique catchment marking the end of the old fault, and entrenchment of the fans that sat in the hangingwall of the older fault and are in the footwall of the new fault. Modified after Leeder and Jackson (1993).

simply increases its length and displacement through time, the "bow-and-arrow" rule should apply, such that a systematic decrease in displacement occurs toward the fault tips (Fig. 10.11A-i). In the case where a fault consists of segments that have linked together, the footwall topography should show displacement "deficits" near the segment boundaries, such that there are topographic saddles and basement highs at the segment boundaries (Fig. 10.11A-ii). This would be consistent with the contention (Schwartz and Coppersmith, 1984) that the segments rupture with characteristic earthquakes, such that strain should accumulate in a predictable fashion with more strain in mid-segment and less at the segment boundaries. In the case where segmented faults link together and then compensate for the displacement deficits at the segment boundaries, the geometry could be

FIGURE 10.11. Development of segmented and unsegmented normal faults

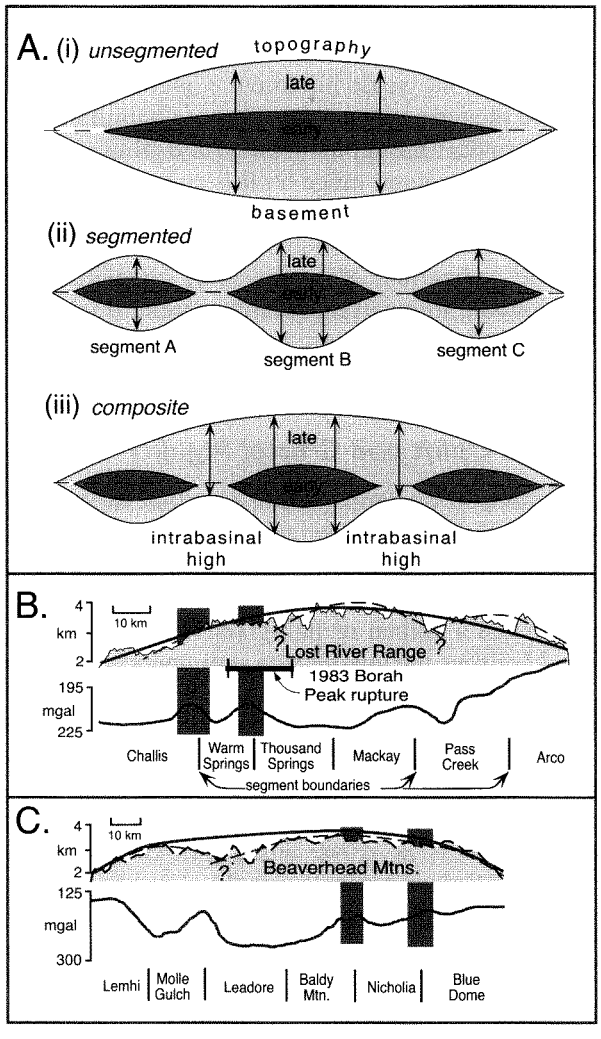

A. Models for displacement showing topography of the crest of the uplifted footwall and of the downthrown hangingwall. Darker shaded areas show early displacement on fault(s). i) Unsegmented fault with monotonic decrease in displacement toward the tips of the fault. ii) Segmented fault with more displacement in the center of each segment than at the tips. Older faults have joined, but there is a persistent displacement deficit at the segment boundaries. Both the footwall topography and basement ridges reflect the fault segmentation. iii) Following linkage of segmented early faults, displacement deficits at the boundaries are erased in the footwall topography. Intrabasinal high-standing basement ridges are sites where deformation is distributed among several smaller normal faults. B. Footwall topography of the Lost River Range, Nevada, and gravity anomalies of the bounding hangingwall basin. Generally smooth footwall topography could be interpreted to consist of three segments (dashed lines), but these do not consistently correspond with known fault segments. Gravity highs are associated with high-standing bedrock ridges that partition the hangingwall basin. Several mapped segment boundaries correspond with basement ridges. The darkly shaded zones indicate where gravity highs correspond with zones of complex faulting of basement ridges. Overall, this range appears consistent with model A-iii (above). The extent of the 1983 Borah Peak rupture is indicated. C. Footwall topography and gravity anomalies of the Beaverhead Range, Nevada. The Molle Gulch-Leadore segment boundary is associated with a gravity high, complexly faulted basement ridge, and a topographic saddle. The Beaverhead Range appears to show aspects of models A-ii and A-iii (above). Modified after Anders and Schleische (1994).

indistinguishable from that of a single growing fault (Fig. 10.11A-i). Alternatively, the footwall topography could show smooth displacement gradients, whereas intrabasinal high points could mark the former segment boundaries (Fig. 10.11A-iii) (Anders and Schlische, 1994).

Next, the character of the landscape in question should be examined. Does the range display a smooth topographic profile or do saddles separate major crests? Does the bounding fault display a clear segmentation with discrete regions where faults step-over, overlap, or break into numerous smaller faults? Do regional gravity anomalies show a gravity low above a hangingwall basin that extends the full length of the range and is systematically deeper toward its center, or do the gravity anomalies indicate the presence of intrabasinal basement ridges? If there are intrabasinal ridges, do they correlate spatially with segment boundaries or topographic saddles in the footwall?

Using digital elevation data, it may be possible to test whether segment boundaries are associated with slip deficits (Simpson and Anders, 1992). For example, consider some range fronts that have been interpreted as being bounded by segmented normal faults and in which there is some visual correspondence between the segment boundaries and topographic lows in the footwall. If topography is controlled by segment boundaries and

characteristic offsets on each segment, then the topography should slope downwards from the mid-points to the end-points in each segment. If, on the other hand, the entire range can be treated as being controlled by a single fault, then for half of each segment, the topography should increase toward the end-point, rather than decrease.

The topography and structure of the Lost River Range in the Basin and Range illustrates some ways to choose among these different models for fault growth. Although mapping along the range front (Anders and Schlische, 1994) suggests that the bounding fault is segmented, the footwall topography does not reveal significant slip deficits associated with the segment boundaries (Fig. 10.11B). Gravity anomalies indicate the presence of intrabasinal basement ridges at some, but not all, of the segment boundaries. At several sites, mapping reveals multiple, sometimes anastomosed, faults associated with these basement highs and segment boundaries (dark shaded bands, Fig. 10.11B). These observations suggest that several smaller faults did indeed link together in the past. But, since then, there has been accelerated displacement near the segment boundaries which has smoothed any deficits in the footwall topography (Anders and Schlische, 1994). For at least some segment boundary zones, the basement ridges do not represent displacement deficits, but rather are sites of more distributed deformation (Fig. 10.11B) accommodated by multiple normal faults. Although the summed displacement across all the faults on the basement ridge is about the same as that on either side of it, the smaller displacement on each individual fault cutting the basement maintains the bedrock near the surface and accounts for the intrabasinal gravity highs.

Another example comes from the Beaverhead Mountains (Fig. 10.11C), where many characteristics mimic those seen in the Lost River Range (Anders and Schlische, 1994). At some segment boundaries, such as the Nicholia-Blue Dome boundary, there is no slip deficit in the topography, and mapping across the basement high at this segment boundary shows that six smaller faults have together accommodated as much displacement as the single bounding fault does in the middle of the segment (Anders and Schlische, 1994). This is consistent with model A-iii (Fig. 10.11). In contrast, the Molle Gulch-Leadore segment boundary is associated with an apparent slip deficit as indicated by a topographic saddle, such that the linkage between segments appears to have happened more recently. This is consistent with a model in which segment boundaries represent zones of persistent slip deficits (Fig. 10.11 A-ii).

Do all normal faults that link together tend toward a state in which displacement gradients change smoothly from end to end along the entire composite fault, eventually eliminating deficits associated with former segment boundaries? This seems to be clearly true for some ranges, but we do not know whether slip deficits observed at some present-day segment boundaries will persist through time or be smoothed and eliminated. The position of any given range on this spectrum from segmented to unsegmented can be evaluated by comparing model predictions for these end members (Fig. 10.12) to surface and subsurface data on fault geometries and displacement, footwall topography, stratal thicknesses, and stratal tilt in the hangingwall basins.

Footwall Uplift and Crustal Rigidity

If a region is in isostatic equilibrium prior to extension, rupturing of the crust through normal faulting, erosion of uplifting footwall blocks, and deposition on subsiding hangingwall blocks redistributes the load on the crust. When a graben or half-graben is formed due to normal faulting, the low-density sediments that fill it act as a negative load (in comparison to the original crust) on the Earth's surface. Owing to the long length scale associated with the flexural rigidity of the lithosphere, the isostatic response to this negative load is more regional than the load itself and induces uplift of the flanks of the graben (Masek et al., 1994; Small and Anderson, 1995; Weissel and Karner, 1989). Due to the elastic nature of the upper crust, the greatest uplift is expected to be adjacent to the graben, where the negative load is imposed, and the magnitude of uplift should diminish away from the graben margin. The horizontal distance or wavelength over which the deflection decreases depends on the effective flexural rigidity of the crust and the depth of compensation. If the depth of compensation is shallow, for example, in the lower crust, the wavelength will be narrower and the vertical deflection greater than if the compensation occurs in the mantle (Fig. 10.13). The wavelength of compensation can also be interpreted in terms of the effective elastic thickness of the upper crust. In comparison to the response of a less rigid crust to a given load, a more rigid crust yields a smaller vertical displacement at the graben margin, while the wavelength of the affected area is greater. Thus, the width and magnitude of the flexure of the footwall provide an indication of the depth of compensation and the effective elastic strength of the crust.

FIGURE 10.12. Summary of displacement and basin characteristics for normal faults that link together during their development

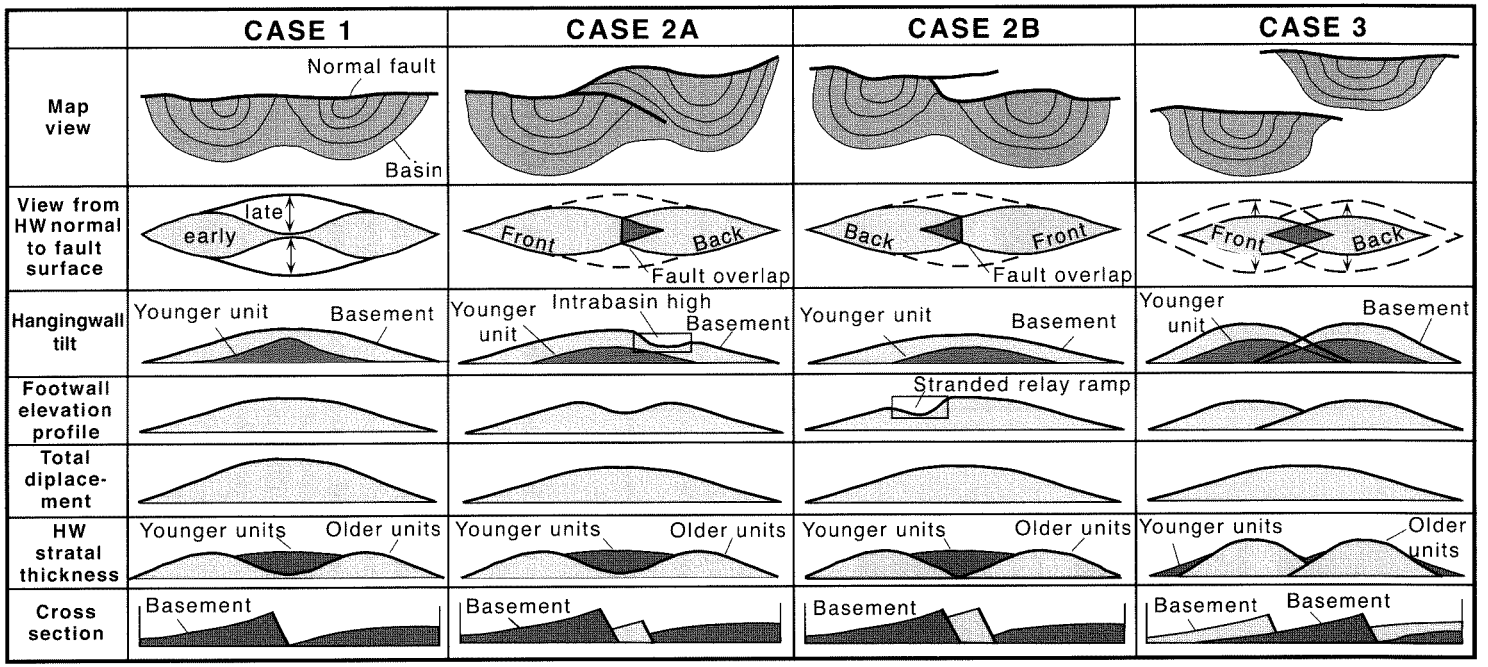

Four scenarios are depicted. In the map view, the shaded area represents the hangingwall basin with contours on the sediment thickness. In the view from the hangingwall, the dashed line (cases 2 and 3) represents the predicted geometry following more displacement. Note that all cases have the same total displacement and displacement gradient, but that differences in stratal tilting, and footwall topography distinguish among them. Case 1: faults link along a plane. Case 2A: rearward fault intersects front, basinward fault. Case 2B: front, basinward fault intersects rear fault. Case 3: overlapping, but nonintersecting faults. Modified after Anders and Schlische (1994).

FIGURE 10.13. Models for compensation and topography in extensional regimes

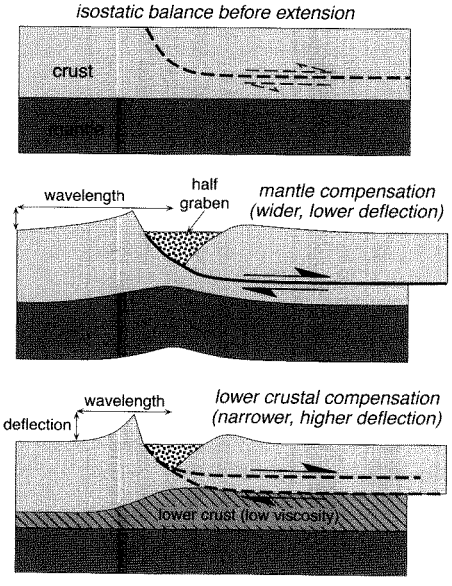

The "negative" load of a half-graben fill induces regionally compensated footwall uplift. For the same amount of extension, compensation in the mantle yields a broader, but lower footwall uplift (middle panel) than does lower-crustal compensation (lower panel). Modified after Masek et al. (1994).

FIGURE 10.14. Comparison of mean topography across a rift-flank uplift with predicted flexure for three different crustal rigidities

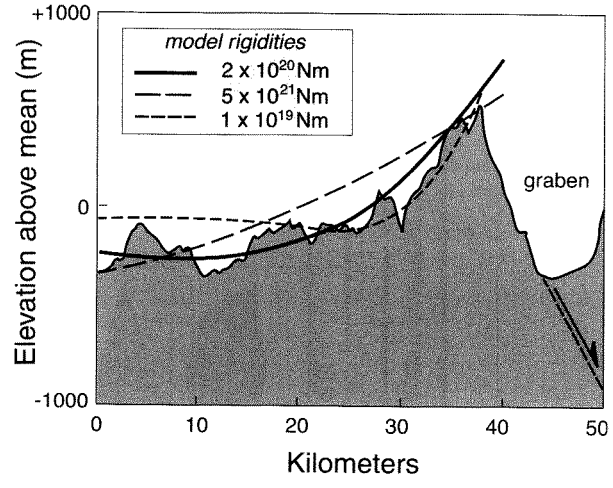

Only the general trend of the topography, not the small-scale wiggles, should be compared to the curves. The mismatches between the curves and the actual topographic trends provide an estimate of the precision attainable with this approach. Modified after Masek et al. (1994).

This conceptual framework suggests that, barring extensive erosion, the topography of the footwall could reveal key insights on the nature of the crust. Indeed, recent topographic studies on the Tibetan Plateau (Masek et al., 1994) help to resolve a controversy concerning the presence or absence of a low-viscosity lower crust under the plateau. Based on a 3-arcsecond (~90-m grid) DEM, topographic data were averaged along swaths 12 km wide that were oriented perpendicular to the strike of the Tibetan grabens. The resultant profiles (Masek et al., 1994) provide clear evidence that the wavelength of the footwall uplifts are short (30–40 km) and are associated with grabens that are narrow compared to many continental rifts (Fig. 10.14). By comparing the mean topography with the crustal flexure expected for various elastic thicknesses (Fig. 10.14), it is possible to show that, despite actual Tibetan crustal thicknesses up to about 70 km, the effective elastic thickness is only between 2–6 km, equivalent to a rigidity of approximately 5×10^{20} Nm (Masek et al., 1994). These data suggest the presence of a ductile, low viscosity lower crust beneath Tibet.

Regions of Contraction

The Himalaya, Tibetan Plateau, Caucasus, Alps, Zagros, Taiwan, and many of the major, non-volcanic mountain ranges of the world have developed over spans of millions of years in response to compressional stresses exerted between converging plates. Contrasting landscape and tectonic characteristics emerge in this setting at differing spatial and temporal scales. In the previous chapter, we described the growth of a single fold, such as Wheeler Ridge, California, over a span of 10–200 Kyr. Here we consider what happens to such folds over longer time spans and how multiple growing folds and faults may interact in the landscape. Because convergence between two plates can be sustained for millions of years, rock uplift in contractional mountain belts can persist for similarly long time spans. But the height of mountains can't grow vertically forever. Thus, we examine here how a balance between rock uplift and erosion is attained in such

circumstances and how we may recognize whether or not this balance has been achieved.

Individual and Multiple Folds

Consider the growth of folds under these basic assumptions: both blind thrusts and ones that cut the surface drive surface folding; faults propagate laterally as they accumulate strain; and erosive forces attack hangingwalls when they are uplifted above local base level. What governs similarities or differences in the geomorphic evolution of individual folds? Certainly, the geometry of the causative fault is important. For example, the hangingwall of a fault-bend fold will never be uplifted more than the height of the footwall ramp, whereas uplift in a displacement-gradient fold can greatly exceed the ramp height (see Figure 4.33). Variations in the stratigraphy and erosional resistance of the hangingwall also affect its evolution. During the development of the fold-and-thrust belts that are commonly found associated with collisional mountain ranges, thrust faults propagate beneath and into the foreland basins bounding the range. When the hangingwall consists only of the sediments that have previously filled the foreland, their relatively uniform and often low resistance to erosion will yield a more uniform and predictable pattern of dissection than when resistant bedrock is also uplifted in the hangingwall. When both foreland-basin strata and bedrock are uplifted and exposed to erosion, the large contrasts in erodability between the sediments and the bedrock promote a distinct erosional and topographic pattern. During initial stages of uplift (which could amount to 1–5 km, depending on the stratal thicknesses in the foreland), relatively rapid dissection and stripping can occur of the weakly cemented sediments. Thus, the fold might develop limited surface topography with only a few hundred meters of relief, representing a small fraction of the total rock uplift (Fig. 10.15). As resistant bedrock is elevated above base level, rates of surface erosion can drop dramatically and a much higher fraction of the rock uplift may begin to be reflected in surface uplift. In semi-arid to arid landscapes, these bedrock ridges may be almost undissected despite several km of uplift. Such is the case in the Tien Shan of Kyrgyzstan (Burbank et al., 1999), where folded and faulted bedrock ridges have been lifted more than 2 km above local base level (Fig. 10.16). Prior to uplift, the bedrock was overlain by about 5 km of Cenozoic sediment. Now, these sediments have been stripped from nearly all fold flanks rising more than 300 to 500 m above local base level. These exhumed bedrock ridges display generally bow-shaped topographic profiles, suggestive of more recent and lesser displacement near the fold tips, whereas along the central part of the forelimbs of many of the larger folds, faults have cut the surface (Fig. 10.16).

Not only do the Tien Shan provide excellent examples of bedrock-cored folds that grew over the past 1 My, but they also illustrate how displacement may be transferred between multiple structures. Imagine a convergence between two semi-rigid blocks with growing folds accommodating the shortening between them. In zones of overlap of the fold tips, one would expect a trade-off in the amount of shortening: as the shortening that one fold accommodated decreased toward its tip, the shortening in the overlapping fold should increase (Fig. 10.17). Based on analysis of an approximately 90-m DEM, topographic profiles oriented perpendicular to the fold axes and across the overlapping tips of two folds illustrate this accommodation of shortening between the two folds (Burbank et al., 1999). Simple topographic profiles can serve to illustrate such shortening only when the topographic surface approximately coincides with a structural marker. In the Tien Shan, the exhumed unconformity that cuts across the bedrock and that underlies the weak Cenozoic strata serves this purpose.

Drainage Development

If several folds are growing simultaneously and their noses are propagating toward or past each other, complex river patterns and topography can sometimes reveal their history of lateral propagation and vertical growth. Envision the propagation of a young fold adjacent and parallel to an older fold. Similar to normal faulted terrains, steep and short drainages develop on the forelimbs of such folds prior to any interference between them. In the direction of fold propagation, the crest of the younger fold is likely to decline in height, and the width of the fold commonly narrows (Fig. 10.18). Streams that formerly flowed unimpeded from the older fold into the basin will be diverted parallel to the young fold and will leave wind gaps along the crest of the young fold as they are sequentially defeated. The diverted drainage systems are typically asymmetrical because the defeated rivers are commonly diverted toward the nose of the fold, that is, in the direction of fold propagation. Growth of an asymmetric upstream catchment that encompasses the diverted streams continues until the discharge and stream power through a water gap closer to the fold's nose is sufficient to balance the uplift rate. Excellent examples are displayed in

FIGURE 10.15. Structural and geomorphic development of a fold in which bedrock underlies sediments in the hangingwall

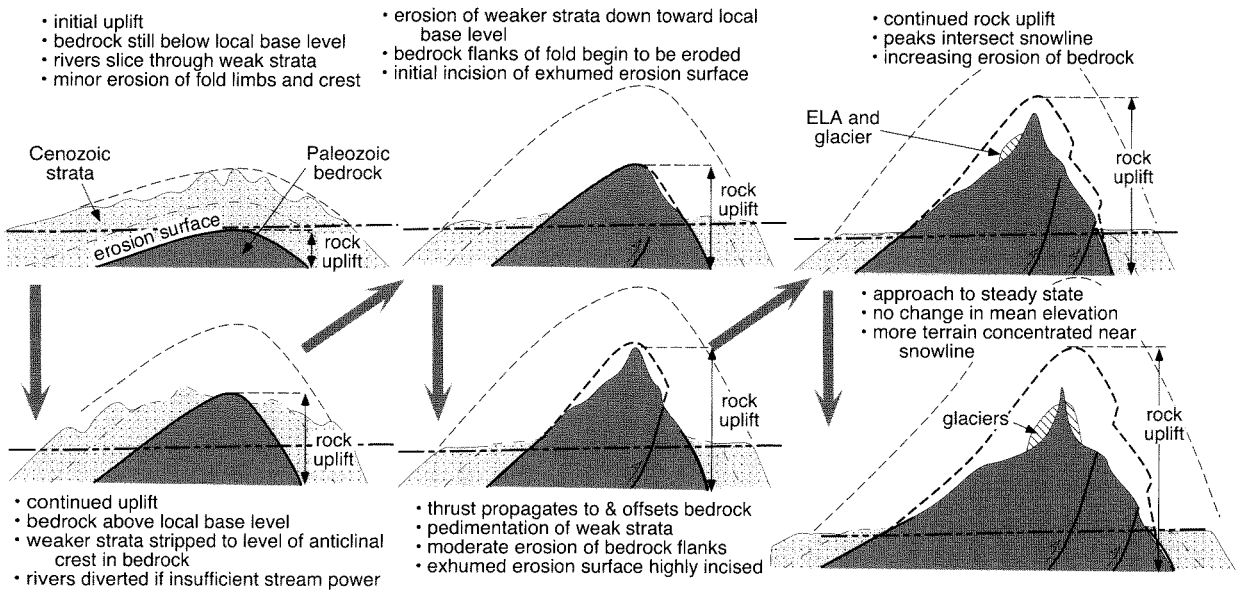

Strong contrasts in erodability favor rapid removal of the overlying, weakly cemented strata, whereas the well-lithified basement rocks resist erosion. The unconformity between these strata provides a reliable marker with which to track the deformation. With sufficient rock uplift and steepening of slopes, the bedrock also begins to be significantly modified by erosion. Modified after Burbank et al. (1999).

FIGURE 10.16. Longitudinal topographic profiles along the bedrock folds showing bow-shaped displacement gradients in the southern Naryn basin, Tien Shan, Kyrgyzstan

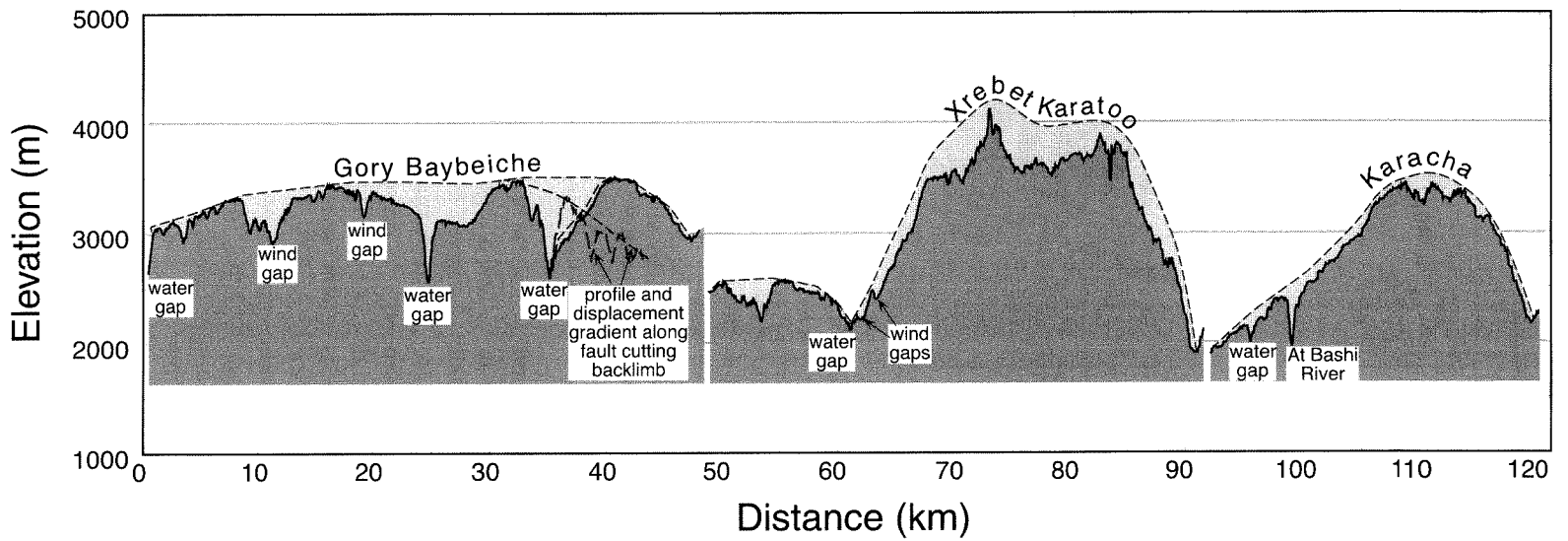

Total uplift of the bedrock with respect to adjacent basins is about 7 km, and their relief above the surface of the basins is about 2 km. Especially near the termini of the folds, the unconformity surface capping the Paleozoic bedrock has been little modified by erosion. Consequently, the topography mimics the displacement. Prominent water gaps, such as that occupied by the At Bashi River in the Karacha fold, occur near the tips of some structures. Note the wind gaps preserved along several of the folds. The elongate, box-like profile of the Gory Baybeiche structure is interpreted to result from along-strike linkage of several folds. Water gaps through the Gory Baybeiche fold are interpreted to correspond with zones where folds propagating toward each other subsequently linked up. Modified after Burbank et al. (1999).

FIGURE 10.17. Transfer of displacement among two *en echelon* folds

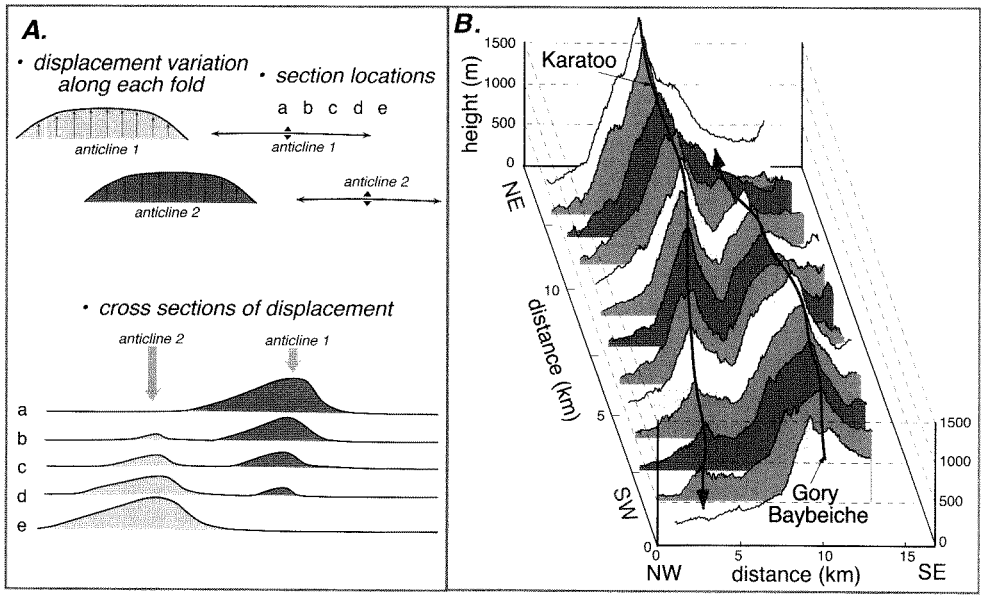

A. Models of displacement transfer between overlapping folds. As displacement decreases toward the nose of one fold, it increases in the adjacent fold. Shortening recorded by bed-length changes in each fold shows displacement compensation which smoothes the integrated displacement variation between the two folds. B. Topographic profiles across the oppositely plunging and overlapping termini of the Gory Baybeiche and Xrebet Karatoo folds, Tien Shan, Kyrgyzstan. The lines of the topographic profiles are oriented approximately perpendicular to the fold axes. Except low on the flanks where Cenozoic strata remain, the topographic surface of both folds is defined primarily by the only slightly dissected regional unconformity that represents the upper limit of the bedrock, such that a similar structural level is being measured in each fold. Note the similarity of the topographic profiles to that predicted when deformation is transferred between two oppositely growing structures (A): as one dies, the other grows, and the total shortening remains fairly constant along strike, despite more than 2 km of structural relief.

central Otago, New Zealand (Jackson et al., 1996) of wind gaps along plunging fold crests, asymmetric drainages in piggyback basins, diverted drainages, and persistent water gaps that developed in response to growth of a suite of thrust-related folds (Fig. 10.18). The asymmetry of the underlying folds, the relative timing of fold growth, and the propagation directions of the multiple folds are readily interpretable from these folds. What remains unclear in central Otago are the absolute timing and rates of fold growth, but given reasonable assumptions about recurrence intervals, these folds are likely to encompass more than 0.5 Myr of growth (Jackson et al., 1996). When the drainages develop in folded ranges with weakly lithified sediments draping over bedrock, there is another interesting uncertainty. Did the drainage patterns that are found today develop due to interactions of rivers with the resistant bedrock once it became exposed, or with the mantle of overlying sediments (Oberlander, 1985; Tucker and Slingerland, 1996)? Often, the answer to this must be gleaned from the stratigraphic record where changes in provenance and river systems can be documented.

In response to prolonged convergence, suites of folds and faults interact to form entire mountain belts. The drainages that develop on these ranges might be expected to differ in their geometric properties in response to contrasts in climate, lithology, rock-uplift rate, and/or erosion rates in different settings. In fact, such variation is remarkably limited among many ranges. Instead, studies of the spacing (S) of major drainages and comparisons to the half-width (W) of the ranges on which they developed demonstrate a strikingly consistent relationship, with a spacing ratio (W/S) of about 2 (Fig. 10.19). This consistency suggests that some of the early-formed irregularities in river courses developed in response to

FIGURE 10.18. Stream patterns in interfering bedrock folds

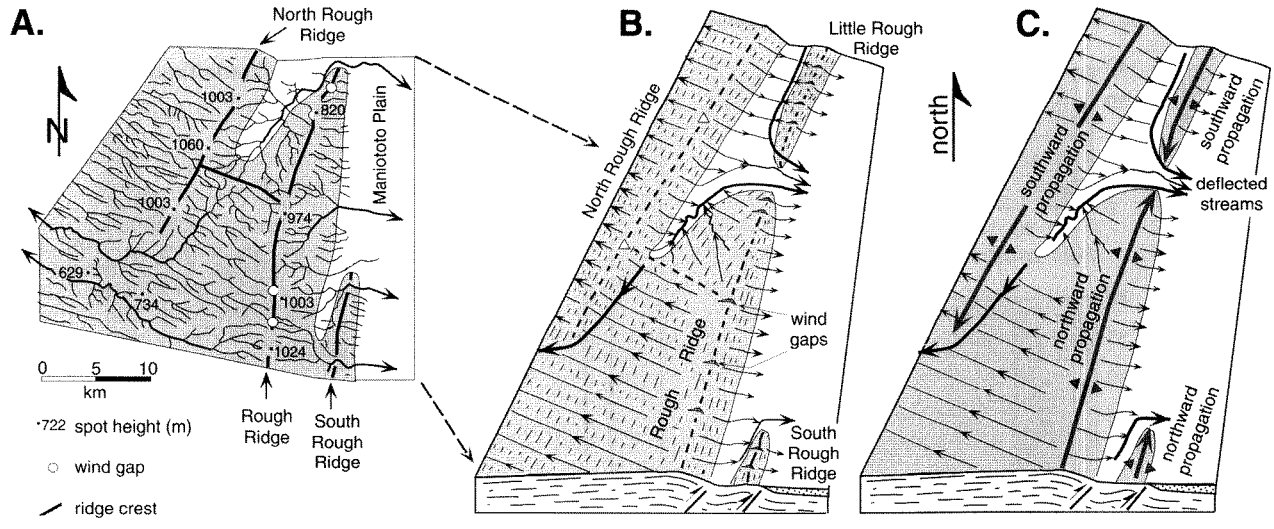

A. Drainage network, fold crests, plunging fold noses, water gaps, wind gaps and their elevations in the vicinity of Rough Ridge, central Otago, New Zealand. Note that the elevation of the wind gaps decreases as the fold nose is approached and that within the piggyback basins, highly asymmetrical drainages extend upstream of the water gaps. B. Cartoon of the drainage patterns in the vicinity of Rough Ridge. Note the clear diversion of drainages around the nose of each growing fold. C. Interpretation of the history of growth of the four anticlines and drainage development along their flanks. Modified after Jackson et al. (1996).

individual growing folds or faults are smoothed during the drainage expansion and competition among drainages that occurs as mountains grow (Talling et al., 1997). This consistent ratio has another intriguing implication: as a range widens, there must be capture of some laterally adjacent drainages to maintain the drainage spacing. This process of lateral capture is hard to document in many modern mountains, but in the Himalaya, growing structures along the leading edge of the Lesser Himalaya appear to have caused strong drainage diversion and likely capture, such that the spacing ratio is as low as 1.2 (Hovius, 1996).

Morphometric Assessment of Range-Front Deformation

Although initially conceived as indicators of tectonic activity on normal faults in arid settings, the parameters of sinuosity and valley height to width have also been successfully applied to some thrust-faulted ranges, such as those found in the tropical forests of Costa Rica. At least two complications can affect such applications. First, dense vegetation can obscure the topography, making it difficult to define the width of the valley floor. Second, because thrust faults often intersect the Earth's surface at relatively shallow angles (10–45°), their traces are more commonly deflected by topography than are the traces of normal faults. As a consequence, even a freshly ruptured thrust may display a sinuous trace. Despite these caveats, the topographic signature of thrusting was sufficiently clear in Costa Rica to permit assessment of the relative activity of different segments of the forearc (Wells et al., 1988) landward of the Middle America trench, where the Cocos plate is subducting northeastward at about 9–10 cm/yr. Thrusts typically are manifested in the topography by abrupt increases in slope in the hangingwall (Fig. 10.20). Such changes are discernible despite the vegetation. Many of the trench-parallel thrusts are apparently active, as shown by low sinuosity mountain fronts (mean value of ~1.3 for ~200 mountain-front segments). Stream concavity was assessed using the hypsometric integral, such that higher integrals are associated with greater convexity. Valley width-to-height ratios are usually lowest just upstream of thrusts,

FIGURE 10.19. Half-width (W) of major mountain ranges plotted against the average spacing (S) of outlets for major drainages in those ranges

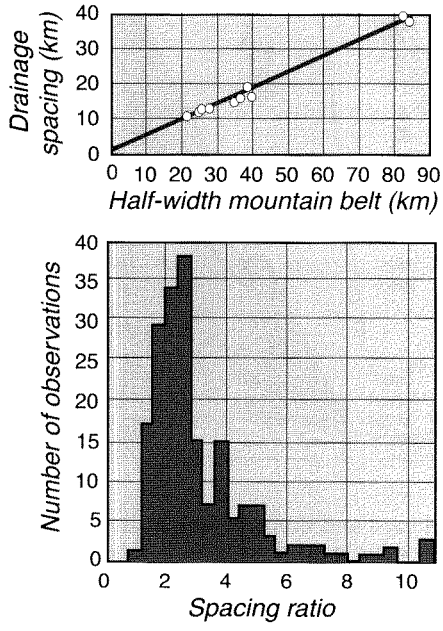

A regression of these data yields: S = 0.46W – 0.80. As another means of representing this data, the spacing ratio (W/S) is commonly about 2. Modified after Hovius (1996).

FIGURE 10.20. Topographic parameters of thrust-bounded ranges in Costa Rica

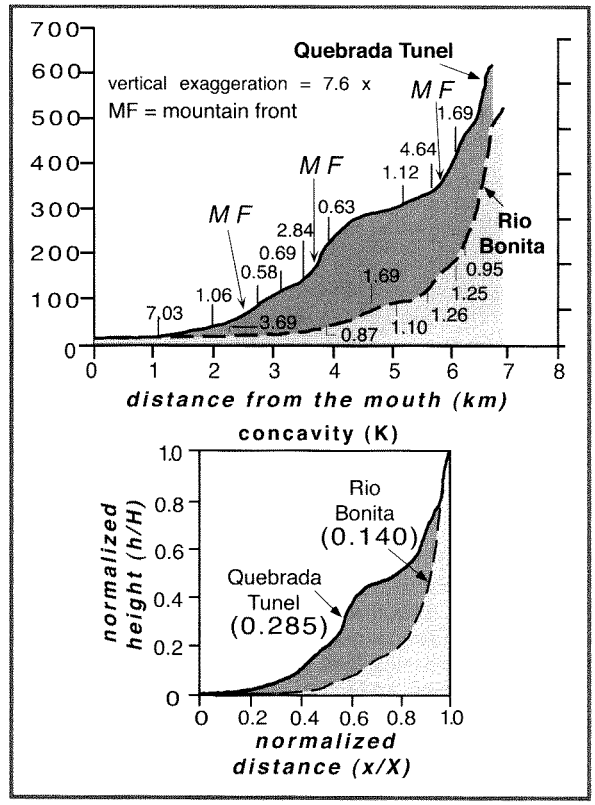

Top: Topographic profiles and valley width-to-height ratios along two rivers. Increases in topographic slope occur above active thrusts which coincide with mountain fronts (MF). Stream valleys become narrower and valley width-to-height ratios decrease just upstream of active thrusts. Bottom: Higher hypsometric integrals are associated with more active mountain fronts. By this criterion, Quebrada Tunel is considerably more active than Rio Bonita. Modified after Wells et al. (1988).

and stream profiles are often convex upward in these same reaches (Fig. 10.20). The general pattern of width-to-height (V_f) ratios along several transverse streams is: an overall increase in V_f ratios downstream as streams widen their courses and the relief on the adjacent ridges decreases, V_f ratios of less than 1.0 at or just upstream from the intersection with a fault (and associated with narrow canyons), and larger V_f ratios directly downstream of faults (Wells et al., 1988). The general lesson to be gleaned from these studies is that, even in a tropical rain forest, the topographic signature in thrust belts can sometimes be discerned and quantified in a meaningful way.

Steady-State and Pre–Steady-State Mountains

Mountain systems like the Himalaya-Tibetan Plateau system attest to the fact that prolonged convergence can build very large regions of high topography. But the mountains can not grow forever. At some point, rates of erosion or tectonic extension ought to balance the rates of rock uplift, so that the range comes into a topographic steady state. Prior to that time, the mean surface elevation can increase through time, reflecting rates of rock uplift that outpace erosion rates, whereas in post–steady-state conditions, erosion outstrips rock uplift (see Fig. 1.4). Even in steady-state conditions, rock uplift will not be

FIGURE 10.21 Steady-state in convergent ranges in which rock uplift and erosion are balanced at a point

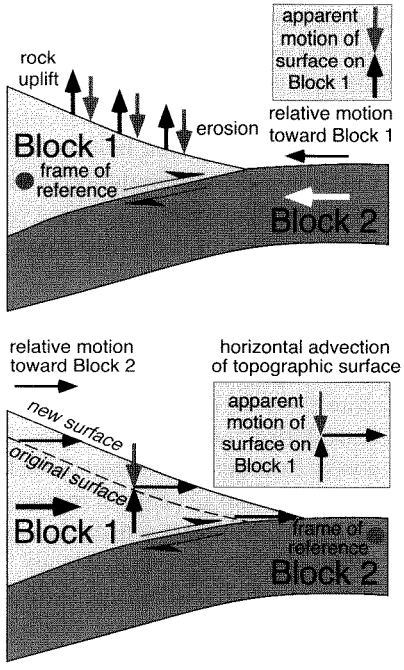

Depending on the frame of reference, the elevation of the surface may or may not change. Top: Block 1 is treated as a stationary frame of reference, such that the topography on it is in steady state, with rock uplift and erosion in balance. Bottom: Block 2 is the stationary frame of reference. Although rock uplift and erosion are balanced in block 1, the surface of block one appears to rise as a function of the horizontal advection of material in block 1 with respect to block 2.

balanced by erosion at every point in the landscape at all time scales. On average, however, under steady-state conditions, this balance should exist at time scales exceeding several hundred thousand years. In most convergent ranges, rock is also being advected horizontally, so that the change in height of the surface depends on the sum of the rock uplift, erosion, and horizontal advection (Fig. 10.21).

How does one identify a pre–steady-state mountain range in a convergent orogen? There are few, if any, infallible rules, but some guidelines typically apply. Early in the development of structures ranging from folds to ranges, the facts that rocks have finite cohesion and high angles of internal friction, and that most geomorphic processes require topographic gradients, dictate that topography must build before erosional processes can increase to the point of matching rock uplift rates. In some ranges, there are sufficient measurements of rates of rock uplift and erosion to provide a reasonable comparison. Obvious mismatches suggest the absence of a steady state. Chronologic and stratigraphic controls may indicate rates of rock and surface uplift that are clearly unbalanced. For example, in Papua New Guinea, lower Quaternary marine strata deposited at ocean depths of more than 1–2 km are now found at elevations of more than 2 km (Abbott et al., 1997)! Moreover, many of these strata are readily erodable, and yet are still preserved on mountain tops. Clearly, rock uplift has dominated this setting in the past. This mantle of weak strata is now being torn apart by massive landslides that are stripping large portions of mountainsides down to the level of more resistant rocks (Hovius, 1998). In comparison to past rates, these landslides have driven an increase in denudation, but it is unclear whether these are sufficiently rapid to balance the present rock uplift rates.

Erosion surfaces formed at low altitudes, but now preserved at high altitudes are indicative of a pre–steady-state range. For example, the extensive, exhumed bedrock planation surface now preserved at 4000 m in the crests of folds and thrusted ranges of the Tien Shan (Fig. 10.15, Fig. 10.16) indicates that a steady state has not yet been attained. The simple presence of a high-elevation plateau does not guarantee that a range is not in a steady state, because such a surface may have formed at high altitude. Some plateaus, such as the Tibetan Plateau, are in fact interpreted as representing a dynamic steady state (Molnar et al., 1993), like a pressure regulator that produces the most efficient energy expenditure. Work is required to lift rocks vertically within a plateau. At a certain elevation, it becomes more energy efficient for the plateau to grow outward, rather than upward, in response to continued convergence. The rather uniform height (5 km) and generally smooth topography of the Tibetan Plateau (Fielding et al., 1994) supports this interpretation.

Although conceptually simple, documenting steady-state topography is also challenging. With the application of some of the previously described techniques for documenting rock uplift and erosion rates, it may be possible to compare these rates. The available data are often relevant to different time scales. For example, GPS may define decadal to annual deformation, whereas apatite fission-track dates can be interpreted in terms of mean denudation rates over millions of years. When measuring

with a short time-scale method, one has to be concerned about whether the rates represent well the long-term averages. If they are acquired during an interseismic or interglacial period, they may be highly biased. If they are measured at a point, one must worry about whether the geomorphic history at that point has sufficiently averaged the process rates. If it can be shown that convergence has been rapid and that mountain building has been sustained for tens of millions of years, then it may be almost inevitable that the range is in a steady state, because rocks have a finite strength and can only be piled so high. In some settings, such as the Southern Alps of New Zealand (Hovius et al., 1996) and the NW Himalaya (Burbank et al., 1996), documentation of generally balanced erosion and sustained rock uplift rates of 5–10 mm/yr argue for a steady state. On the other hand, in Taiwan, the Central Range appears to vary from pre-steady state in the south, where mountain building is just beginning, to steady-state topography in the north where deformation has been prolonged (Stark and Hovius, 1998).

Consider also a mountain range where lateral variations in rock uplift rates have been documented, via geodetic or geochronologic means. If the landscape were in dynamic steady state or equilibrium, then a river flowing across these regions of varying uplift rates should change its character along its route. Steeper and narrower river courses should coincide with regions of more rapid rock uplift. In large, actively deforming ranges, a self-adjusting river might be considered as a dynamic geomorphic marker that records spatial variations in rock uplift.

In the context of the attainment of a steady-state landscape, it is illuminating to consider two different ranges that have resulted from the Indo-Asian collision: the Indian-Nepalese Himalaya and the Kyrgyz Tien Shan. Recent geodetic studies (Abdrakhmatov et al., 1996; Bilham et al., 1997) indicate that each of these ranges is shortening at about 20–25 mm/yr and are, in fact, presently absorbing most of the Indo-Asian convergence. It seems likely that this condition has persisted for at least several million years. Yet, unlike the Himalaya, the extensive planation surfaces preserved through much of the Kyrgyz Tien Shan clearly indicate that the Tien Shan are not in a topographic steady state. The reason for the contrast appears to lie in the duration and localized rate of shortening. Whereas shortening and crustal thickening in the Himalaya probably began before 45 Ma, shortening the Tien Shan has been estimated as either beginning about 10 Ma (Abdrakhmatov et al., 1996; Molnar et al., 1993) or perhaps as early as 20–25 Ma (Yin et al., 1998). In either case, it seems likely that less than about 200 km of shortening has occurred across the Tien Shan, whereas perhaps five times that much has occurred across the Himalaya. Another clue that a range is likely to be in a pre-steady state can come from thermochronology. For example, many apatite fission-track ages in bedrock of both the Chinese (Sobel and Dumitru, 1997) and Kyrgyz Tien Shan are pre-Cenozoic. This means that these samples cooled below 110°C before 65 Ma and that less than 4 km of denudation is likely to have occurred since then. These rates are more than ten-fold slower than those typical of the likely steady-state conditions in the Nepal Himalaya.

In areas where steady state appears to prevail and there are defined spatial variations in rock uplift, at least two end-member topographic signatures can be envisioned to define the relationship between slopes, rock uplift, and denudation rates (Fig. 10.22). In the first, slopes would vary in some proportion to rock uplift rate, under the assumption that the flux of material from hillslopes can be summarized as a diffusive process that is strongly related to slope angle (Penck, 1953). Alternatively, if most of the hillslope sediment flux is delivered by landslides, then most slopes would lie close to the threshold angle for failure (Fig. 10.22) and would be similar among areas with differing rock uplift rates. In both cases, the rate of river incision would balance the rock-uplift rate.

To assess whether a landscape more closely mimics one end-member or the other, it is necessary to document the spatial variation in rock uplift, denudation, and slope angles. A good case study emerges from the NW Himalaya in the vicinity of Nanga Parbat, where some of the greatest relief on Earth is found: from the Indus River to the summit of Nanga Parbat, there is over 7 km of relief across a distance of about 20 km. Geochronologic studies in the vicinity of Nanga Parbat (Zeitler, 1985) document greater than tenfold differences in bedrock cooling rates and inferred long-term denudation rates. These rates appear to vary systematically across the region (Fig. 10.23). As described previously (Fig. 7.11), short-term bedrock incision rates by rivers show a similar spatial pattern of denudation (Burbank et al., 1996). Based on an approximately 90-m DEM, average slopes can be defined (300 m-by-300 m moving windows were used here) and then can be compared between areas of very rapid versus slower denudation. Histograms of the slope distributions (Fig. 10.24A) show a remarkable similarity among almost all these mountainous regions (Burbank et al., 1996). The mean slope angle for each of

FIGURE 10.22. Different ways to attain a topographic steady state

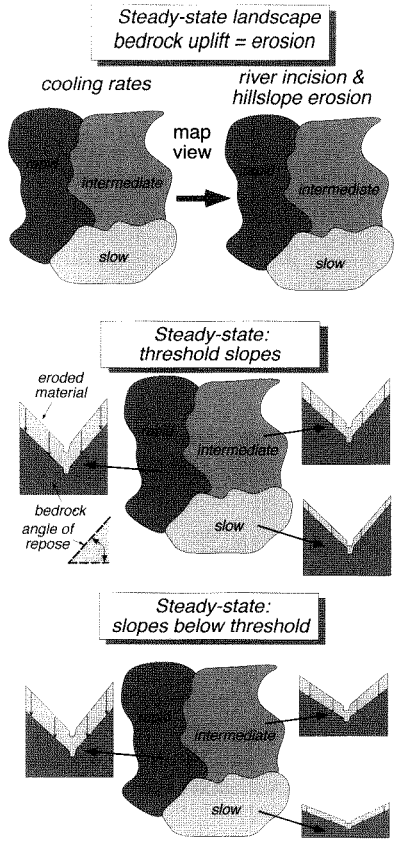

Top panel: If variations in cooling rates or rock uplift correlate spatially with variations in denudation or incision, a steady-state topography can be inferred. Middle panel: If slopes everywhere are at threshold angles for stability, then there will be no spatial variability in mean slope angles (assuming uniform rock strength), and denudation will be solely a function of the rate of river incision (local base-level lowering). Lower panel: If slopes are proportional to the denudation rate, then spatial variations in slope would correlate with variations in rock uplift.

these areas is 32° plus or minus 2°: an angle similar to the angle of repose in dry non-cohesive materials. In the context of the fractured bedrock and the very large hillslope lengths that characterize this region, these slopes can be interpreted as threshold slopes in which the slope angle is generally independent of denudation rate (Fig. 10.22).

FIGURE 10.23. Schematic map of the NW Himalaya in the vicinity of Nanga Parbat (NP) and the Indus River, northern Pakistan

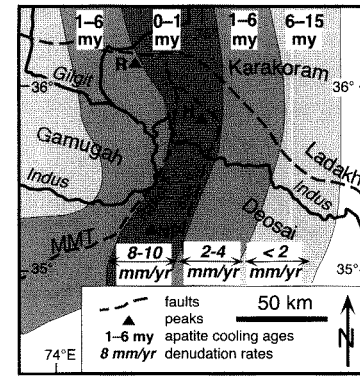

Other peaks over 7500 m in the area include Haramosh (H) and Rakaposhi (R). Based on numerous apatite fission-track ages (Zeitler, 1985), dated cooling zones are defined. The N-S zone centered on Nanga Parbat and Haramosh cooled below approximately 110°C within the last 1 Myr. Spatial variability in long-term cooling rates is approximately matched by spatially variable incision rates (given in mm/yr) derived from dating of strath terraces (see Fig. 7.11). Each varies by about tenfold. MMT: Main Mantle Thrust. Modified after Burbank et al. (1996).

Once spatial variations in long-term rates of denudation have been documented across an area, a new suite of questions can be posed in these contractional settings. To what extent can variations in both mean and maximum topography be explained as an isostatic response to erosion? Does mean topography correlate with mean rock uplift and denudation rates? Are regional variations in topography largely independent of climate and the specific surface processes that control erosion?

Returning again to the NW Himalaya, we can address some of these questions. By exploiting the regional DEM, regional topographic characteristics and trends can be documented (Brozovic et al., 1997). For example, while the Nanga Parbat region contains the highest topography (>8000 m), its mean elevation is only about 3800 m (Fig. 10.25). The mean elevation of the nearby Deosai Plateau is nearly 4300 m, whereas the terrain between them, which could be envisioned as the dissected margin of the plateau, averages about 4100 m. If it were assumed that a plateau of about 4300 m altitude previously covered this entire region, then the observed topography today

FIGURE 10.24. Slope distributions from subregions (see B) in the NW Himalaya

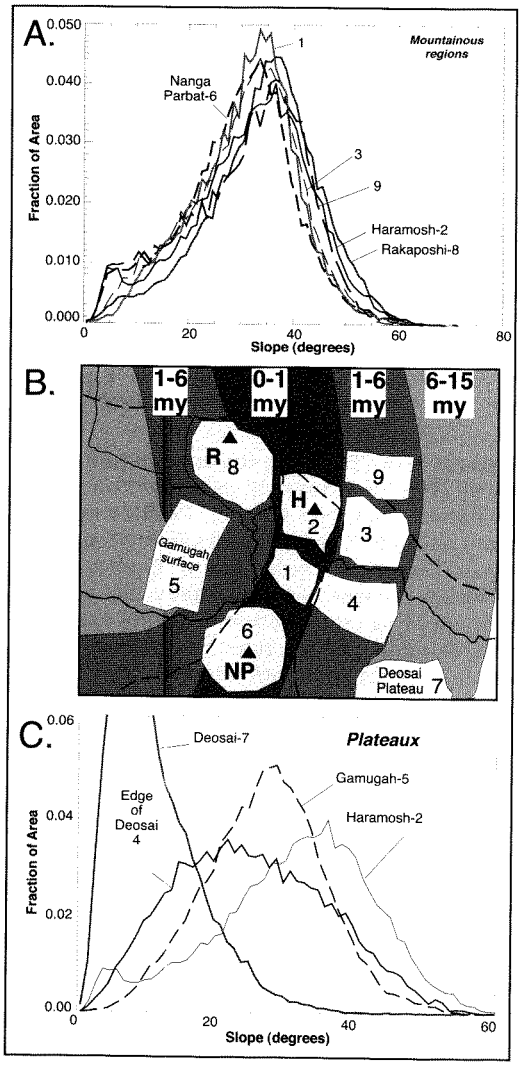

A. Slopes are calculated as best-fit planes to a 4 × 4 matrix in this 3-arcsecond (about 90-m) DEM. Note that even though these subregions span areas with ten-fold contrasts in denudation rates, there are few significant differences among them. B. Areal boundaries used for slope distributions. These are designed to sample regions with different denudation and uplift rates. C. Slope distributions from plateaus, with the distribution from Haramosh (area 2) for comparison. The Deosai Plateau is largely undissected, whereas its marginal area and the Gamugah region are both significantly dissected. Modified after Burbank et al. (1996).

FIGURE 10.25. Mean elevations and mean snowlines in the NW Himalaya

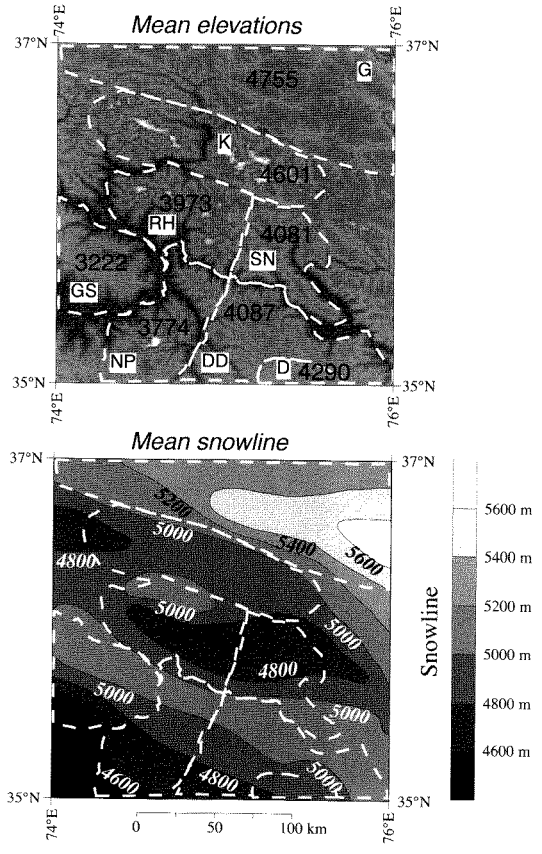

Top: Mean elevation (in meters) of subregions in the NW Himalaya. Note that mean elevations increase toward the northwest. D: Deosai Plateau; DD: dissected Deosai; NP: Nanga Parbat; RH: Rakaposhi-Haramosh; SN: Skardu north; K: Karakoram; G: Ghujerab. Bottom: Elevation of modern snowline in the same region as shown above. Note that snowlines rise toward the northwest and generally lie ~700-1000 m above the mean elevations. The topographic and snowline gradients lie at nearly right angles to the tectonic gradients in this region (Fig. 10.22). Modified after Brozovic et al. (1997).

from Nanga Parbat to the Deosai could be interpreted simply as an isostatic response to the dissection of the plateau. On the plateau itself, isolated peaks rise to about 5 km. As the dissection increases away from the center of the plateau, peak heights increase to about 6 km, but the mean elevation decreases by 200 m. Finally, around Nanga Parbat, the highest peaks are about 8 km,

FIGURE 10.26. Schematic diagram of erosionally driven isostatic uplift of peaks

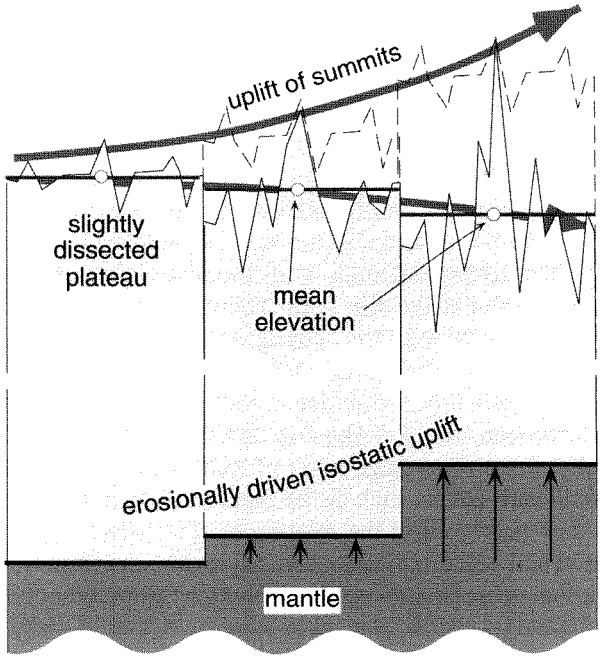

Mean elevations of the topography decrease to the right, but the heights of the summits (undissected remnants in the landscape) increase in this direction. Note that for each increment of lowering of the mean elevation, rock uplift is about 6 times greater than the amount of surface lowering, and in this scheme, uplift of some peaks is also about 6 times greater.

FIGURE 10.27. Generalized relationships in landscape where tectonics and topography are decoupled, and climate and topography are coupled

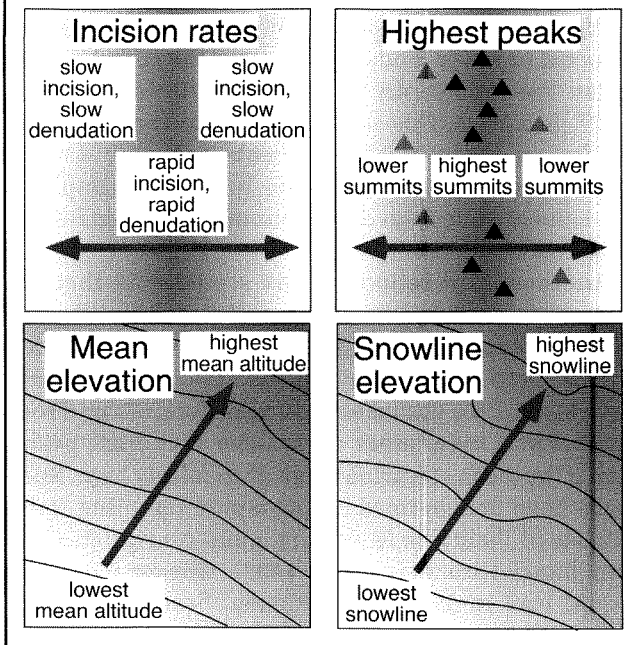

Top panels: Highest incision and denudation rates correspond with the zone of the highest peaks. In this cartoon, the tectonic gradient is oriented east-west. Bottom panels: The gradient of mean elevation trends at a high angle to the tectonic/erosion gradients, but is parallel to the snowline gradient.

but the mean elevation is 500 m below the plateau. Recall that if we ignore flexural rigidity, about five-sixths of the mass removed by erosion should be compensated by isostatic uplift, so that 100 m of erosion lowers the mean surface by only about 17 m. Thus, to lower the mean elevation around Nanga Parbat by 500 m requires approximately 3 km of erosion. If some parts of the hypothesized plateau remained uneroded, they could now rest near 8 km in height, as is observed today at Nanga Parbat. Thus, this part of the topography could be explained simply by an isostatic response to variable erosion (Fig. 10.26).

It is clear from observing the mean elevations in the NW Himalaya (Fig. 10.25) and comparing these with the cooling/denudation data for this area (Fig. 10.23) that zones of rapid rock uplift do not correspond with zones of high mean elevation, although these rapidly uplifting zones do contain many of the highest summits. At the regional scale, a north-northeastward rising gradient in the mean topography is apparent, with an approximately 1 km rise across 200 km (Fig. 10.25).

The fact that the regional topographic trend is nearly orthogonal to the tectonic zonation in the NW Himalaya forces one to conclude that the topography is quite independent of variations in tectonic forcing at this scale (Fig. 10.27), but it also raises the question of what controls the mean topography. No definitive answer is available at present, but we note that regional snowlines also rise toward the north-northeast (Fig. 10.25). At present, the snowlines sit about 700–1000 m above the height of the mean topography (Brozovic et al., 1997), while during the last glaciation, the snowline and the mean

topography would have nearly coincided. This spatial coincidence suggests that glacial erosion may have exerted significant control on the topography. In particular, intense erosion is expected to occur near the snowline where the ice flux on glaciers is greatest (Anderson and MacGregor, 1998). Such erosion could be expected to lower landscapes toward the snowline and flatten the topography in this zone (Brozovic et al., 1997). If correct, this scenario leads to the surprising conclusion that climatic gradients can play a more important role in controlling steady-state topography at the regional scale than do variations in tectonic forcing (Brozovic et al., 1997).

Another implication of this scenario is that the glaciers on areas experiencing rapid rock uplift must erode more rapidly than glaciers at the same elevation in less tectonically active areas. Two factors could serve to enhance glacial erosion in regions of rapid rock uplift. First, these areas often have very high peaks, even if the mean elevation is not particularly high. Such peaks have been termed "topographic lightning rods" because of their role in causing more precipitation on their flanks (Brozovic et al., 1997). Greater ice fluxes should lead to more rapid erosion. Second, although one's eyes are attracted to the high summits at 8 km height, only a small fraction (2–4%) of the topography lies above 6 km in these areas. Most of the land surface is concentrated near the snowline. As a result, if rock uplift drives surface uplift, more of the land surface is pushed into the accumulation zone for the glaciers. This, too, will enhance the ice flux and hence glacial erosion (Brozovic et al., 1997). This is an interesting example of a negative feedback in which an increase in mean elevation creates the conditions that should lead to a lowering of the mean elevation through enhanced erosion.

Regions of Strike-Slip Deformation

In a purely strike-slip regime, crustal blocks should slide laterally past each other with few topographic effects. The vertical deformation that can occur near the termination of a seismic rupture zone along a strike-slip fault tends to be smoothed by subsequent ruptures. The observation that, despite several hundred kilometers of accumulated offset, parts of the San Andreas fault zone are bounded by nearly horizontal plains clearly signals that little topographic expression needs to accompany strike-slip faulting. On the other hand, many of the geomorphic features that develop during successions of a few earthquakes can become amplified into major topographic features. The same advection of topography parallel to a fault that creates shutter ridges (see Figure 4.18) can also translate whole mountain ranges along a strike-slip fault. The classic offset streams that are displaced a few meters in individual seismic cycles can become rivers that are offset laterally by tens to hundreds of kilometers over long time intervals of sustained erosion.

Most strike-slip zones also have some degree of extension or compression across them. In fact, depending on fault orientation and curvature, it is common to switch between transpressional and transtensional regimes along a major strike-slip fault. There are several key differences between the topographic, tectonic, and geomorphic attributes of extensional and contractional regimes and those associated with transpression and transtension along strike-slip faults. Some strike-slip faults move at average rates of more than 2–4 cm/yr. Single fault zones, such as the San Andreas, may accommodate nearly all of the relative motion between plates for several millions of years and may accumulate hundreds of kilometers of displacement. Although thrust and normal faults can be displaced at rapid rates, the accumulated displacement on a single fault and sustained mean rates are typically far lower than those of major strike-slip faults. Another prominent contrast is that, in strike-slip regimes, the deformation is largely localized along an elongate zone straddling the fault trend. Zones of significant mountain building due to transpression are often limited to restraining bends or transpressional step-overs in the fault trend (see Figure 4.17). A good example of this geometry occurs along the San Andreas fault near the Santa Cruz Mountains in northern California (Anderson, 1994). A restraining bend in the San Andreas can be conceptualized as a persistent regional scale asperity that localizes deformation adjacent to it. Earthquakes, some of them on the master strike-slip fault itself, and others on ancillary structures that fail in oblique events (such as the 1989 Loma Prieta earthquake), drive rock uplift in the region of the bend. The topography so created is then subsequently rafted passively along the fault, out of the region of the bend and its uplift, and therefore decays with distance from the bend.

A second and larger example of transpressional deformation occurs in the vicinity of the "Big Bend" in the San Andreas fault system in southern California. As it slices between the Los Angeles basin and the Mojave block, the NW-SE-oriented trace of the dextral-slipping San Andreas deviates to a more E-W trend and defines

a broad restraining bend (Fig. 10.28). Compressional stresses through this bend have resulted in growth of an entire fold-and-thrust belt that extends southward into the Los Angeles basin and in the rise of the San Gabriel Mountains which boast peaks of more than 3000 m. Relative motion of the Pacific plate past the North American plate is about 5 cm/yr, much of which is localized along the San Andreas fault (see discussion of southern California in Chapter 5). The rate of north-south shortening in the vicinity of the Big Bend is about 1 cm/yr (Feigl et al., 1993) or 10 km/Myr (see Figure 5.12). The San Gabriel Mountains are bounded on their southern margin by active south-vergent thrust faults. Note the sinuous trace of some of these thrusts: despite their present activity, they delineate a sinuous mountain front due to the relatively low angle of thrusting (Fig. 10.28). Given typical ramp angles, the mean Holocene shortening rates of about 3 mm/yr (~30% of the regional N-S shortening) on these thrusts yield rock uplift rates in the hangingwall of about 1 mm/yr or 1 km/Myr.

Long-term rock uplift and denudation of this approximate magnitude can also be interpreted from the young (~3–5 Ma) apatite fission-track dates in the hangingwall (Blythe et al., 1996). In fact, an extensive campaign of fission-track and [U-Th]/He dating in the San Gabriel Mountains has delineated regionally varying cooling patterns that apparently reflect contrasting deformational and erosional regimes (Fig. 10.28). The youngest apatite ages, greatest relief, highest peaks, and steepest slopes are found in the eastern San Gabriel Mountains, where rock uplift appears to have been most prolonged and rapid. This region could be in a steady state with balanced erosion and rock uplift. In northwestern areas, partially dissected low-relief topographic surfaces at heights of about 2 km and apatite FT ages of more than 40 Ma suggest a pre–steady-state condition in which erosion lags behind the uplift. Thus, within this single, modest-sized, transpressional mountain range, we find evidence for both steady-state and pre–steady-state topography.

In transtensional regimes, normal faults develop at dilational jogs or step-overs in strike-slip fault systems. The resulting pull-apart basins (or rhombochasms) can undergo rapid subsidence. Mountains formed by footwall uplift along the normal faults, as well as rivers flowing into the strike-slip fault zone, deliver sediments that can accumulate at high rates in these basins. Often, however, during times of active strike-slip motion, the rates of subsidence exceed the sediment-supply rate, so that extensive closed depressions are formed. The Dead Sea and the basin bounding provide a clear example of the geomorphic and stratigraphic consequences of sustained subsidence in a dilational zone along a transform or strike-slip fault.

Hotspots Under Continents

Seamount chains are clear geomorphic expressions of the interaction of hotspots with oceanic plates. Many of the characteristics of seamount chains, such as the depth of the base of the seamount, volume of erupted magma, degree of dissection, and loading of the adjacent crust, are predictable based on fairly simple models of mantle plumes impinging on oceanic crust that is moving with respect to the seamount. Although there are many fewer known occurrences of hotspots interacting with continental crust, where they are available, they create landscapes with multi-million-year histories and distinctive geomorphic characteristics. As also seen with plunging, propagating folds, the lateral migration of hotspots permits a time-for-space (ergodic) substitution that highlights the evolution of landscape.

If one looks at the topography of the western United States, one of the most striking features is the low topographic trough of the NE-SW-trending Snake River Plain as it transects the generally N-S-oriented ranges of the Basin and Range. This trough is interpreted to result from passage of the Yellowstone hotspot. The history of volcanic eruptions along the Snake River Plain shows a systematic decrease in age toward the NE that is used to define the history of the hotspot track (Pierce and Morgan, 1992; Smith et al., 1994). Around 15 Ma, the volcanism associated with the hotspot plume was located about 700 km SW of Yellowstone. Tracking of eruptive centers through space and time suggests that the plate initially moved WSW at about 7 cm/yr and slowed to about 3 cm/yr at approximately 10 Ma as its direction shifted to more directly SW (Pierce and Morgan, 1992). Today, the Snake River Plain represents a clear topographic signature of the passage of the hotspot during the past 12 Myr.

With respect to the hotspot, one might want to know: 1) what are the topographic characteristics of its past and present position; 2) how and why do these vary; 3) how does the topography relate to active deformation; and 4) what other geomorphic indicators of deformational responses to the hotspot exist?

The topography of the hotspot track can be defined in terms of two end-members. The largest geoidal anomaly in the United States is a 1000-km-wide bulge centered

FIGURE 10.28. Transpressional deformation in the Big Bend, California

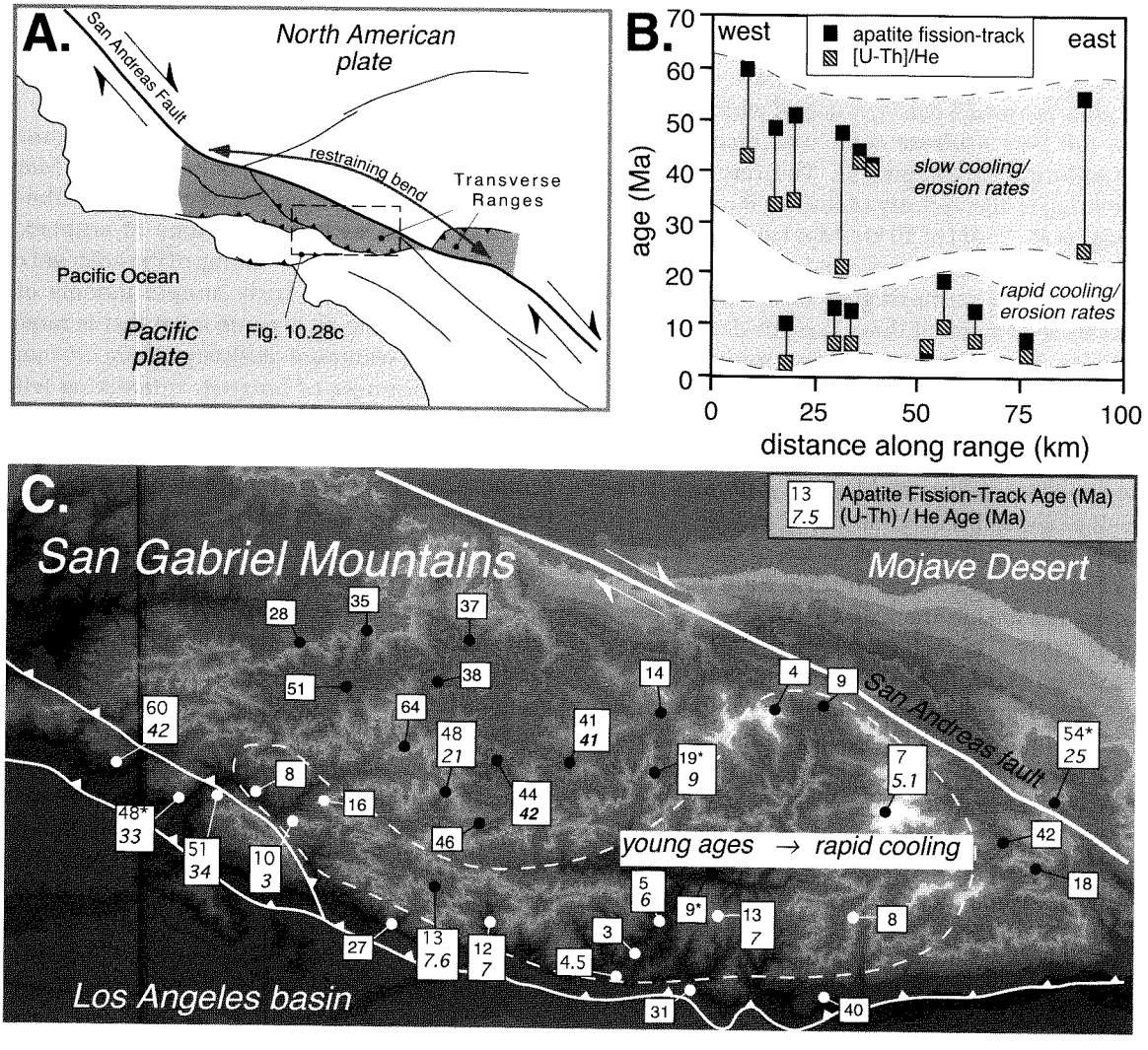

A. Major faults, restraining bend along the San Andreas, and location of the Transverse Ranges in southern California. B. Paired fission-track and U-Th-[U-Th]/He dates on apatites projected on to a east-west section along the San Gabriel Mountains. Note the consistency of the paired dates and the large offset among data from the rapidly versus the slowly cooling and eroding areas. C. Cooling ages, structure, and topography of the San Gabriel Mountains. Modified after Blythe et al. (2000).

over the Yellowstone hotspot (Smith et al., 1993). The magnitude of the geoidal anomaly is comparable to that associated with other hotspots, and is attributable to thermal doming and dynamic uplift associated with the head of the mantle plume. Following passage of the hotspot, subsidence due to cooling is expected. However, because denser magmas have been emplaced in the upper crust as a result of hotspot volcanism, the topography along the hotspot track is lowered with respect to the pre-hotspot topography (Fig. 10.29). Thus, the low-relief trough of the Snake River Plain represents an isostatic and thermal response to passage of the hotspot.

FIGURE 10.29. Topography and gravity-anomaly profiles oriented perpendicular to the trend of the Snake River Plain

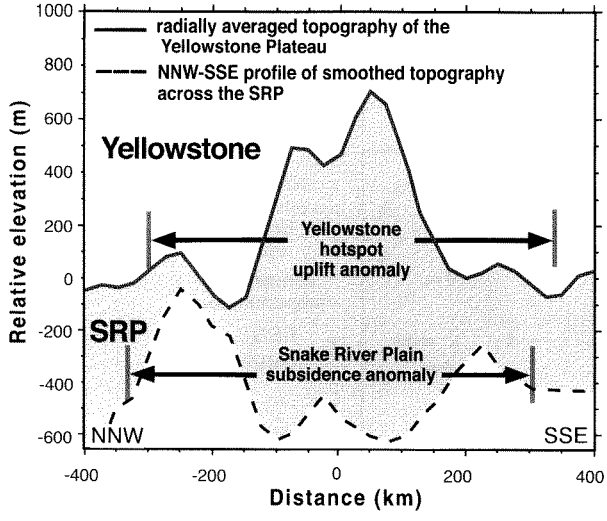

The low topography in the Snake River trough is an isostatic response to the emplacement of dense magmas in the upper crust, whereas the high topography of the Yellowstone uplift is a result from thermal doming. Modified after Smith and Braille (1994).

Along its length, there is a systematic altitudinal decrease of 1.5–2 km of the Snake River Plain toward the SW (Fig. 10.30). The surface topographic decay fits the expression: $z = 3.07 - 0.52 \cdot (t)^{0.5}$ (where t is the age of silicic volcanism in Myr) (Smith et al., 1993). This square-root-of-time dependence is the usual one for thermally controlled topography related to oceanic hotspots and midocean ridges (Sclater and Francheteau, 1970).

The topographic response to the hotspot has been likened to a parabolically shaped bow-wave centered on the plume. Thus, as the hotspot moves relative to the continent, a point in its path would be expected to experience accelerating uplift toward a peak elevation, followed by subsidence. The amount of subsidence would be variable, depending on the position relative to the center of the hotspot trace and whether or not mafic intrusions had "densified" the underlying upper crust. Although some of the crustal accommodation of the passing bow-wave is via simple doming or deflation, many normal faults are either created or reactivated in its wake. The broad array of faults apparently responding to the hotspot passage can be categorized (Pierce and Morgan, 1992) based on the timing of activity (Holocene, Pleistocene, or Tertiary), whether or not the faults are reactivated older faults, the lateral extent of the fault, the amount of relief of the fault escarpment, and the presence or absence of facets.

The resulting categories define a spatial zonation with respect to the hotspot. In the outer zone, where hotspot-induced uplift is just beginning, there are "lesser and reactivated Holocene faults" characterized by low relief (<200 m), small or absent escarpments, and rejuvenated facets. Inside of this zone is located the region of major active uplift. Here there are "major Holocene" faults, that is to say, faults that have ruptured within the past 15 ky. (The reason for choosing 15 ky is that the major outwash plains in the northern Rockies date from that time, and they provide a convenient horizon for gauging offsets without having to date each one.) These faults are associated with high, steep facets and greater than 700 m of relief. They represent the most tectonically active zone. A third zone encompasses both "major late Pleistocene" and "lesser late Pleistocene" faults. The major faults have relief of more than 500 m and moderate facets, whereas the lesser faults have low relief (<200 m) and low or absent facets. The major faults are interpreted as having experienced major activity in the Late Pleistocene, but have been waning during the Holocene. This is the zone that can be conceived of as lying inside the crest of the bow-wave, which is now beginning to relax after passage of the topographic bulge. On the south side of the Snake River Plain, there is a fourth zone that encompasses both major and lesser Tertiary faults. Whereas the major Tertiary faults are associated with large relief (>500 m), they have muted escarpments that suggest considerable degradation since their last major offsets. As defined by Pierce and Morgan (1992), these zones form generally parabolic regions centered on the hotspot track. Although they are based on geomorphic and chronologic criteria for past fault motions, they also accord quite well with the distribution of seismicity (Fig. 10.31). Most of the major quakes in the Intermountain Seismic Zone fall within zones 2 and 3, the regions with active major Holocene and late Pleistocene faults.

The tilting associated with the hotspot bulge also creates topographic and geomorphic asymmetries (Pierce and Morgan, 1992). Along rivers flowing eastward from Yellowstone toward the Bighorn Basin, fluvial terraces converge downstream in a fashion consistent with differential uplift of upstream reaches and regional tilting to the east (Fig. 10.32). Whereas such convergence could

FIGURE 10.30. Model of changes in topography and subsidence along the track of the Yellowstone hotspot

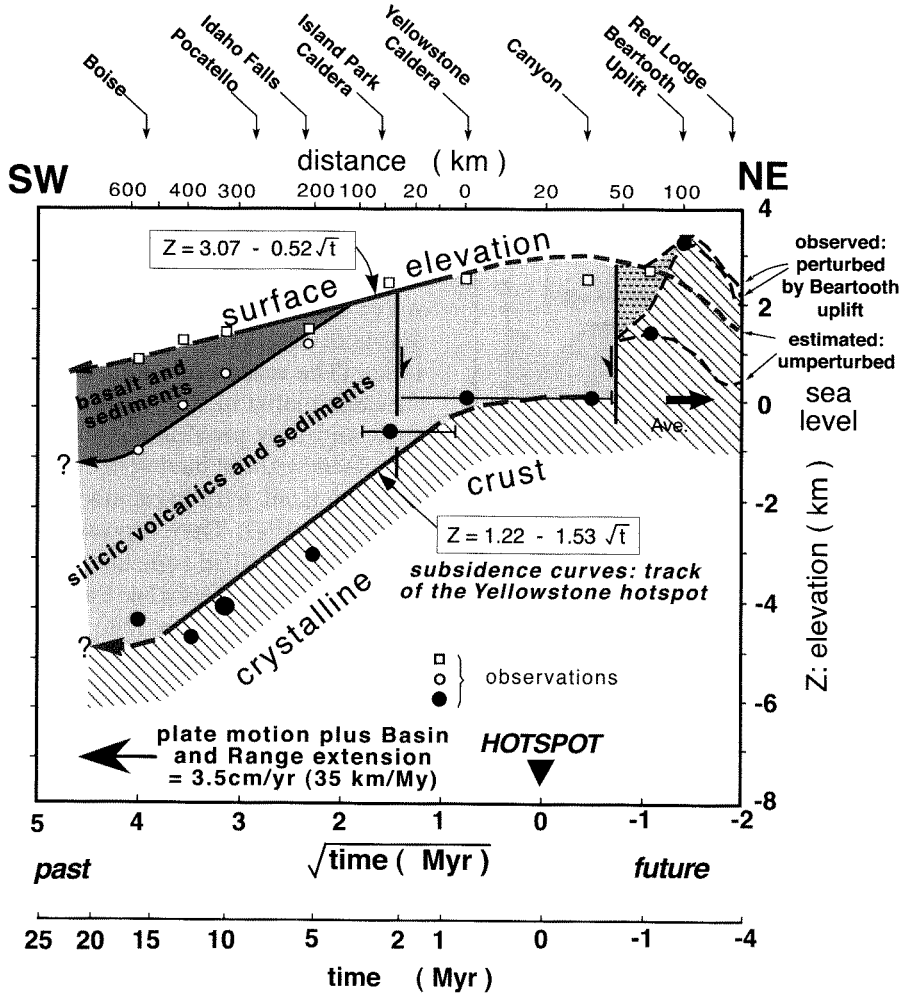

Note the predictable lowering of the surface and the top of the crystalline crust in the wake of the hotspot due to cooling of mafic magmas. Modified after Smith and Braille (1994).

result from nontectonic causes, rivers flowing in the opposite direction (westward) have built terraces that diverge, rather than converge, downstream. The divergence of terraces toward the west, irrespective of whether the river is flowing east or west, implicates regional tilting toward the east as a likely cause of the divergence.

These studies of the Yellowstone hotspot illustrate the way in which data at different time and length scales can be integrated to enhance understanding of the way landscapes evolve over long intervals of time. Whereas broad topographic gradients define the region of influence of the hotspot at scales of hundreds of kilometers, the relief on mountain fronts, the activity on faults, and geometry of river terraces are observed at much shorter length scales (1–20 km) and commonly represent landscape responses at time scales of less than 300 ky. Such observations provide the data that permit us to elaborate upon regional topographic generalizations and to define the rich detail of the seismic, geomorphic, and topographic zonations associated with the hotspot.

FIGURE 10.31. Distribution of seismicity and faulting in the vicinity of the Yellowstone hotspot

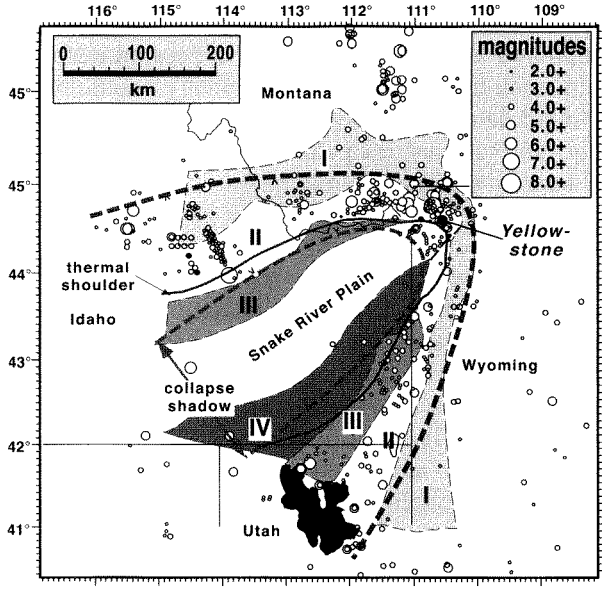

Note the parabolic pattern with respect to the apparent direction and tip of hotspot motion. The zonations (I to IV) represent regions with similar faulting and topographic character. The outermost (I) is the youngest and represents the initiation of deformation, region II is the most active; and region III represents a waning of seismic activity and faulting. Modified after Smith and Braille (1994).

FIGURE 10.32 Fluvial terraces on the margins of the Bighorn Basin

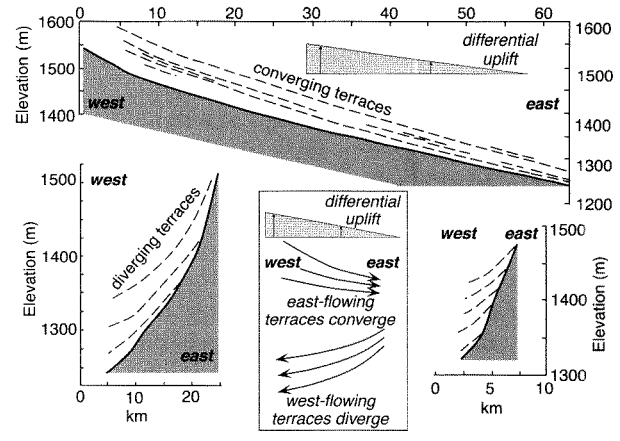

Eastward-flowing terraces converge in the downstream directions, whereas westward-flowing terraces diverge downstream. Modified after Pierce and Morgan (1992).

Summary

Interpretations of landscapes that have evolved over millions of years provide a significant challenge to tectonic geomorphology due to the likely superimposition of numerous climatic, tectonic, and geomorphic events over that time period. Any pristine feature, such as a fault scarp, in such a landscape relates only to the most recent phases of its evolution. Such features, however, can provide a useful template and should provoke these questions: If the processes that created this feature were repeated innumerable times, would it generate this large-scale landscape? If not, why not? Because plate motions tend to be rather steady over millions of years, the ultimate driving forces and input of energy into a deforming region may remain approximately steady through time. On one hand, this could lead to predictable patterns of deformation that simply become structurally amplified through time and are only obscured through erosional modification. On the other hand, as rocks deform and rotate, initial geometries may be overprinted by later ones, and simple correlation of structures with the plate motions may become increasingly obscured. When interpreting terrains with prolonged and complex histories, the challenge becomes one of discerning the signature of earlier tectonic events in the now-degraded geomorphological record, and of utilizing structural, stratigraphic, and chronologic data to reconstruct successions of past deformational and erosional episodes.

In recent years, several new tools or data sets have assisted studies of long-term tectonic landscapes. New dating techniques permit far broader and more reliable dating of events and processes within landscapes than was previously possible. Digital topography allows rapid characterization of the land surface. We have seen that the regional overviews that can be readily attained with DEMs provide a key basis for comparing different areas and for quantifying some of their geomorphically and geophysically important characteristics.

Although the crust is heterogeneous and can deform in some unexpected ways, we find that there are some predictable patterns of deformation and landscape evolution. The sinuosity of mountain fronts has been shown to be a good indicator of fault activity. Drainage systems not only

help delineate present-day structural geometries, but their persistence as geomorphic entities means that they also record aspects of earlier history. Thus, the lateral propagation of mountain ranges can be recorded by the rivers that drain them. Similarly, the erosional modification of the morphology of faulted range fronts provides insight into the degree of activity of a given mountain front.

We have seen that the concept of a dynamic equilibrium or long-term steady state in which rock uplift is balanced by erosion within a deforming landscape is easy to articulate, but difficult to test. It is likely rare that such equilibrium exists at human time scales. The problems lie in part in the mismatch between the time and length scales over which the available geological tools operate. When one compares the periodicities of climate change (thousands of years), the effect that climate exerts on rates of erosion, and the shifting loci of deformation within an orogen, it seems apparent that the only useful definition for a steady state is one which spans sufficient time (>100 ky) to average among the fluctuating forcing functions of landscape evolution.

In addition to these temporal challenges, there are challenges related to the spatial distribution of data. For a given mountain range, direct and unambiguous geomorphic or structural measures of rock uplift and of erosion rates are typically available from only a few, if any, sites, and it is difficult to know whether these represent well the rates in the remainder of the mountain range. The interpretation of raw data also often relies on a model of how the system has worked through time. For example, interpretation of radiometrically determined cooling rates in terms of erosional histories commonly relies on assumptions about the thermal field through which the rock cooled, which itself is dictated by the spatial and temporal distribution of erosion rates. And again, such interpretations are typically based on a few scattered dates. New ways to integrate data from across ranges and to assess the patterns of long-term rock-uplift and erosion are needed.

Numerical modeling is another approach to understanding how landscapes may evolve. Considerable progress has been made in recent decades in quantifying the ways in which fluvial, hillslope, and glacial processes relate to erosion, sediment transport, water flux, slope gradients, and rock strength. These data underpin new generations of numerical models of surface processes. Similarly, improved geodetic, seismic, and structural data aid in constraining new numerical models for the geophysical processes involved in building mountains: plastic deformation in collisional orogens, crustal deformation through the seismic cycle on individual faults, fault propagation and linkage, and broad-scale isostatic compensation associated with evolving topographic loads. In the following chapter, the fundamentals of modeling landscape evolution are described, and examples of the integration of surface and tectonic processes in landscape evolution are examined at a range of spatial and temporal scales.

CHAPTER 11

Numerical Modeling of Landscape Evolution

We have demonstrated throughout this book that the processes involved in generating landscapes, both those geophysical processes that generate rock uplift and those surface processes that attack and rearrange the rock, are complex in both time and space. The processes interact with one another to generate interesting and complicated feedbacks in the system. Within the last two decades, earth scientists have turned to the use of numerical models as a means of exploring the richness of these linkages. As computers have increased in both speed and memory size, these models have become more capable of treating the real-world complexity by discretizing space and time into smaller and smaller bites. These models have allowed scientists to understand in a quantitative sense the linkages among the processes. They have provided a set of visual images of how a mountain range or hillslope or channel ought to evolve under a prescribed set of rules. They have forced us to document process rates in the landscape that must be embedded in the models, and to face difficult questions such as just how did a particular landscape begin? Finally, and perhaps most importantly, by embedding our knowledge of surface and tectonic processes in a logical (rigid, unforgiving) framework, these models allow us to explore where our understanding of these processes is flawed or weak, toward which new research efforts should be focused.

In this chapter we explore the elements of such models, and provide examples from models that are designed to operate at different time and length scales. Some, for instance, are designed to illustrate or mimic the evolution of individual fault scarps, while others are aimed at mountain range or even orogen scales. Each will therefore require a different set of assumptions that make the problem tractable, given the computer resources at the time the model was generated. In all cases, the goals of such modeling exercises are to enhance our abilities to derive insights into the operation of the many processes that conspire to generate tectonic landscapes.

We have seen throughout the book that a landscape owes its shape to the combination of tectonic and climatic forces. Rock is moved with respect to the geoid, either upward or downward, by tectonic processes, some of which result in smooth displacement (creep), others in discrete displacement (seismic). This displacement of rock changes the local elevation of the earth's surface. This affects geomorphic rates to the extent that geomorphic processes are altitude dependent, directly in some instances (e.g., the dominant process switches to glacial erosion for elevations above the snowline), and indirectly in others (e.g., as streams seek a base level, most often sea level, that is independent of the local rock mass). In addition, gradients in the vertical deformation from place to place result in tilting of the earth's surface. As geomorphic processes are largely driven by gravity, and the component of gravity operating parallel to the surface is dictated by the slope of the surface, process rates will be affected by displacement gradients. Of course, as we have already discussed, there are direct connections between geomorphic and tectonic processes in particular instances, including, for example, seismically induced mass wasting. Because tectonic and geomorphic processes are so tightly coupled, and their results so tightly intertwined in the landscape, one must often resort to numerical modeling of landscapes in order to extract the tectonic signal. In fact, if the tectonic signal

is known, such tectonically active landscapes can be "inverted" for the geomorphic process rates.

We will discuss in this chapter a wide variety of models of landscape evolution that have been developed largely within the last couple decades. These will serve to illustrate the couplings within the landscape system, demonstrating how tectonic and geomorphic systems conspire to generate particular landforms, and how documentation of the shapes of these landforms can be used to infer tectonic process rates. We hope to impress upon the reader that the generation of numerical landscape evolution models and the collection of relevant field data are intimately coupled intellectual exercises.

Approaches

The approach one takes to the incorporation of both tectonic and geomorphic processes in a landscape evolution model depends on the questions being asked of the landscape. Is the goal one of deducing the paleoseismic record? Or of deducing long-term changes in slip rates on a fault? Is the exercise a generic one, in which a class of landforms is being addressed, or is it site-specific, in which the attributes of a particular site are being used as a means of assessing the "fit" of a particular model.

We will focus on numerical models that rely on solving equations on a grid of points. Although these are more common in the computer age, it is well worth noting that these are still representations of differential equations for the physics (and sometimes chemistry) involved. In certain restricted but important cases, these equations can be solved analytically (with paper, pencil, and brain), which allows very rapid assessment of the dependence of the model solution on one or another process or process rate. These analytic solutions also form important tests of numerical codes. Unfortunately, the real world is complex in that 1) several processes are acting simultaneously, 2) some of these processes are nonlinear, 3) the tectonic and climatic forcing of the system is non-uniform in both space and time, and 4) the geometric boundaries of the features are complex. In general, these complexities preclude analytical solutions to the problems, and require that we turn to numerical models.

Numerical models come in several flavors: finite difference, finite element, and boundary element. Finite difference models operate on a discretized space, and solve for the change in some property of each cell in the space (e.g., its elevation) by approximating the differential equation at finite (as opposed to infinitesimal) temporal steps. For example, the differential equation

$$\frac{\partial z}{\partial t} = aA\frac{\partial z}{\partial x}$$

could be written

$$\Delta z_i = aA\frac{z_i - z_{i-1}}{dx}dt$$

where dx is the node spacing in the x direction, dt is the time step, and i is the index of the node. The change in the elevation of node I is calculated, and then the new elevation is obtained by summing the old elevations with the changes in elevation.

Boundary element (BE) and finite element (FE) methods differ in essence by the characterization of the boundaries and of the region of interest (see Crouch, 1983). Mathematically, this translates into FE solutions that are exact at the nodes but approximate elsewhere, and for BE methods that are approximate at nodes but exact elsewhere. Each method has its pros and cons. BE methods are relatively simple and are able to handle multiple discontinuities (each properly influencing the other). FE methods cannot handle discontinuities (although faults can be simulated by so-called slippery nodes or "shear zones") but they are more amenable to more complex rheological and thermal states. (One might argue, however, that once a problem gets that complicated,the numerical technique loses it pedagogic value, and the number of model parameters becomes large enough that it rapidly becomes very specialized.)

The choice of model scale in a numerical code, how much that model can resolve in both time and space, depends on the goals of the modeling exercise. One must decide whether the feature being studied is simple enough to allow characterization and hence modeling in only one dimension (i.e., $z(x)$), where z, the elevation, is the dependent variable being assessed on a one-dimensional grid of points in x, or whether the model requires two dimensions (i.e., $z(x,y)$). We note as an aside that although the landscape being explored in these two-dimensional models is in fact a three-dimensional object, the model is still strictly speaking two-dimensional (some call it two-dimensional planform), as the vertical dimension is a dependent variable. The choice of modeling strategy is not simple. To understand the choices, one must have in mind a target feature and know to what degree this feature is describable in one or two dimensions. Is the scarp being assessed essentially a linear

feature whose profile is everywhere the same? Is the tectonic deformation profile symmetrical in some way (radially or cylindrically)? Modeling strategies generally consist of setting up the problem, embedding in the code the differential equations for the various processes to be modeled (all of which will have free parameters such as the diffusivity or the rate of regolith generation or the fault slip rate), and finally sweeping through a set of model runs to explore the dependence of the final results on 1) initial conditions, 2) boundary conditions, and 3) various model parameters that set the relative importance of one or another process. The complexity and computational requirements increase manifold as one moves to higher dimensions. This therefore limits the degree to which a particular parameter can be explored, because this exploration requires many model runs.

For example, we can clearly discriminate between models whose goal it is to explore the degradation of a single fault scarp, from those in which an entire mountain range is to be addressed. The length scales for the former might be 1–100 m, while those of the latter might be 10–100 km. Obviously, the details of the single fault being addressed can be treated in the smaller fault model, while decisions must be made about how to treat the reality of numerous faults and their geometrical complexity when modeling at the mountain-range scale. Given the computational limitations, this might require that the fault scarp model be capable of resolving meters, while the mountain range will be resolved at 100 m. Although this seems at first a simple scaling problem, it becomes clear quickly that the lower resolution of the mountain-range model limits the detail with which certain processes can be treated, and requires that other processes either be ignored altogether, or more likely be parameterized in some manner in the model. This scaling issue forms a large part of the art of modeling, and of the challenge faced by the modelling community.

The Building Blocks

We first illustrate the components of a landscape evolution model, all of which must be linked in the final model. Please note that this is by no means an exhaustive catalogue of such model components! Numerical models discretize space and time into small increments, dx and dy for two-dimensional, dx alone for one-dimensional, for space, and dt for time. The numerical landscape (in either finite element or finite difference cases) lives within this discretized space as a set of nodes whose attributes include the elevation of the point, the thickness of the crust at that point, the amount of soil or regolith or channel sediment at that point, and so on. One must prescribe rules that allow these attributes to change in a physically reasonable way. In general, these rules simply represent physical processes, the rate at which they operate being dependent on other attributes of the point of concern, such as the distance from a fault, which might dictate the local tectonic uplift rate, the local slope, the local rainfall, and so on. These rules are generally mathematical representations of differential equations, the solutions to which require both initial and boundary conditions. The differential equations represent abstracts of the physics of the problem, including the conservation of mass and of momentum, equations for the response of crustal materials to stress fields, rate of weathering of bedrock, and so on. We have also seen in previous chapters the importance of being able to define how a landscape begins (as a sea cliff with a known geometry; a river with a given profile). In the model world this translates into the need to specify *initial conditions*. In addition, we have to worry about the edges of the model, that is, its *boundary conditions*. The numerical model ends abruptly, but the real space it is meant to represent is connected to the rest of the world through exchange of materials and forces. Models therefore differ not only in how the processes are mimicked, but in how these boundary and initial conditions are set up. If faults are present within the model space, forming internal boundaries to blocks within the volume, boundary conditions must be applied on each of the faults.

The Rules

It is inevitable that any model is a simplification or idealization of the real world. The "rules" discussed here are the rules used within the model, and are not necessarily the rules by which the real world operates. The art of modelling lies in choosing a set of model rules that are appropriate for the given problem, that capture the essence of the problem. These model rules must evolve as our knowledge of the physical processes evolves. It is here that the links must be forged tightly with both the tectonics and the geomorphic communities.

Tectonic

The sophistication of tectonic models varies widely. The most commonly employed model for tectonic deformation associated with discrete faults is based upon the expected elastic deformation associated with a dislocation

FIGURE 11.1. Definition sketch for the elements of a dipping fault that must be prescribed in models of landscape evolution with specific faults

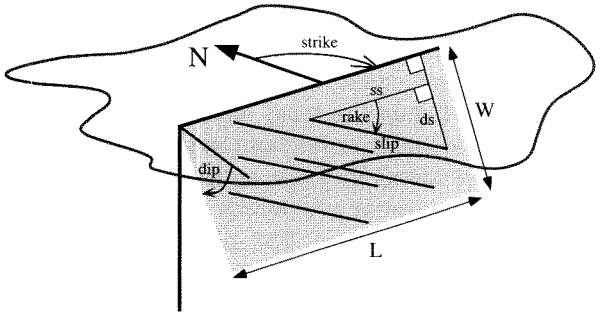

The spatial orientation of the fault is dictated by the strike and dip of the fault, and the size of the fault is dictated by the length (L, horizontal) and height (also sometimes called width (W, downdip) of the fault. The slip on the fault may be prescribed by either specifying the dip-slip (ds) and strike-slip (ss) components, or the total slip and the rake of the slip event. Parallel lines scribed on the fault surface are meant to indicate slickenlines associated with slip on the fault.

within the material across which no shear stresses are transmitted. In all such models the fault plane or planes must be defined (Fig. 11.1). The full location requires one point on the fault, the fault strike and dip, and the vertical and horizontal extent of the plane. The slip on the fault must also be either determined or specified. In boundary element models, the slip on any dislocation within the volume can be calculated in several ways. The boundary conditions on the faults within the space can be either displacements (same as specifying the slip on the faults), or stresses (stress drop can be specified; zero shear stress can be specified). These latter modes can be driven by specifying remote stresses on the volume, or by specifying the strain within the volume. For example, a right lateral shear strain within the volume can be imposed by dictating that the east edge of the block has moved to the south relative to the west edge of the block. If the slip is instead specified, it can be defined in two equivalent ways (Fig. 11.1). One may specify the fault rake and the magnitude of the total slip, or one may specify the dip-slip and the strike-slip components of displacement. In general, the slip on the fault is assumed to be either uniform or variable from point to point on the fault plane.

Given these specifications of the fault, and of the boundary conditions on the faults and on the edges of the volume, one then calculates the expected material displacements (and, if desired, the strains and stresses) at any other point within the material. As most measurements of displacement are made on the surface of the earth, it is usually the deformation field (horizontal and vertical) at the surface of the earth that is solved for and reported by the code. Given that elastic problems are linear, one may superpose the solutions for any number of discrete dislocations (faults) within the material. For example, fault bends and step-overs are dealt with by breaking the fault into several discrete segments, each with its own deformation pattern. One may also calculate the displacement field associated with a complex pattern of slip on a single planar fault by breaking up the fault into a series of smaller planes. The simplest pattern of slip is of course uniform. More complex patterns can be constructed that either vary smoothly, for example in an elliptical pattern (Crider and Pollard, 1996; Willemse et al., 1996), or more irregularly. Examples of the deformation field associated with a single fault, driven by an imposed displacement of the edges of the volume, are shown in Figure 11.2 for both normal and reverse faults, and for both faults that do and that do not cut the surface.

Models differ in how they deal with the material at depths greater than those expected to behave in an elastic manner. The simplest assume that the entire earth behaves as an elastic half-space, but more recent work employs a region at moderate depths that relaxes viscously (e.g., King et al., 1988).

One of the more widely available boundary element codes (3DDEF: Gomberg (1993) and Gomberg and Ellis (1994)) is now being used to assess the cross-talk between faults in complicated real-world settings. Given the ability to calculate the changes in the state of stress within the material imposed by the slip on one fault, one may calculate how one rupture loads up other nearby faults, placing them either closer to or further from failure, as we have discussed elsewhere in this book (e.g., Stein and Ekstrom (1992), Simpson et al. (1994), Simpson and Reasenberg (1994), Li et al. (1998), Harris and Day (1993), and Harris et al. (1995)).

Those models that operate at the orogen scale cannot possibly take into account all the discontinuities in the crustal material. The strategy here is instead to capture the large-scale forcing within the lithospheric mass as it responds to lithospheric scale tectonic forcing, for example, continental collision rates. One strategy is kinematic: a

FIGURE 11.2. 3DDEF models of three cases: A. normal fault, B. reverse fault, and C. blind reverse fault

A. Normal fault, pure shear, dip 60°, cuts surface

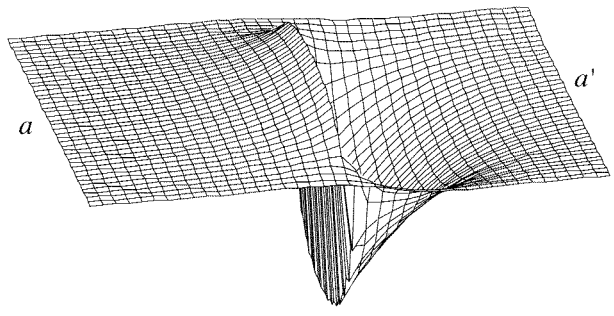

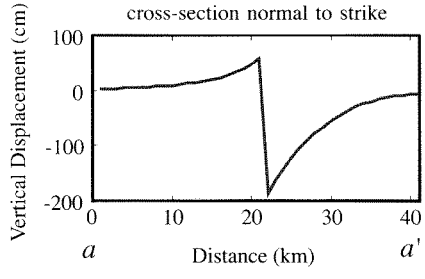

B. Reverse fault, pure shear, dip 60°, cuts surface

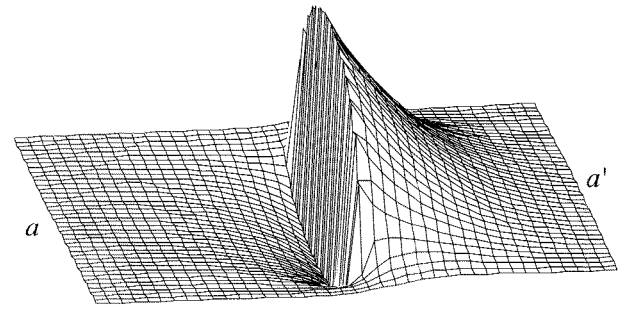

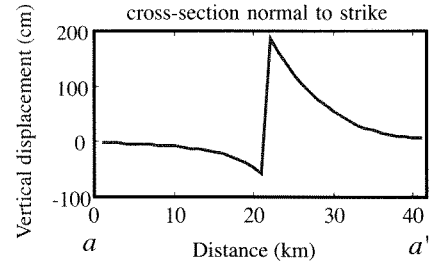

C. Blind thrust fault, pure shear, 60° dip

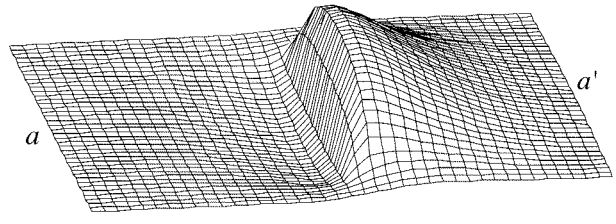

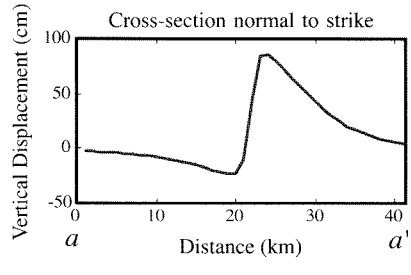

Dislocations have the same scales and orientations (60° dip, same strike) in each model, although the top of the dipping plane is buried in the blind fault case, C. Each is driven by far-field pure shear stresses rather than a prescribed slip on the fault. At the base of each mesh plot is a cross section of the vertical displacement field. Note the similarity of the normal and reverse cases, the principal difference being in the asymmetry: in the normal fault case the maximum displacement is downward, on the hangingwall block, while in the reverse case, it is upward, again on the hangingwall block. Note that the vertical exaggeration is more than one hundredfold.

vertical and/or horizontal deformation pattern is simply assumed. Other models that more properly capture the dynamics, although still in their infancy, will ultimately be more useful in the exploration of the nature of the feedbacks in these systems. The dynamic models differ in the assumptions made about the rheology of the lithosphere at long time and length scales. For example, in some models the rheology is assumed to be captured by a nonlinear flow law in which the flow parameter corresponding to the effective viscosity of the material is temperature dependent, and the shear strain rate goes as a power of the local shear stress. This sort of model requires that the thermal evolution of the lithosphere be properly modeled as well. While such models are therefore quite complex, they embody important feedbacks between the tectonic forcing and the geomorphic response.

Flexure

Over long time scales, deep earth materials behave as a fluid. All fluids flow in response to pressure gradients, moving from sites of high pressure to sites of low pressure. As the pressure at depth depends on the density and height of the column of rock above it, the tectonic and geomorphic modification of the topography represents a rearrangement of surface loads, which can force flow of the deep earth materials. This flow in turn modifies the surface topography on long wavelengths and on time scales of many thousands of years, and operates in such a fashion as to reduce the pressure gradients at depth. This process is one of *isostatic adjustment*, the static case being one of *isostatic equilibrium* (*iso-static* meaning equal pressure). That the near-surface rock is too strong to deform ductily over these same time scales requires that it respond instead as a broad, flexing elastic plate. The wavelength of the response of the surface to this motion at depth, called the *flexural wavelength*, is dictated by the average rigidity of the near-surface materials. The flexural response (Fig. 11.3) is calculated as if it were the bending of a beam of uniform thickness. This thickness is fictitious in that one could not drill to this depth and find either a material or a chemical discontinuity; rather, this represents the thickness of a beam that reflects the mean strength of the near-surface rock. The complexity of the flexural component of the models depends on the symmetry of the problem. For simple one-dimensional cases, one may easily turn to analytic solutions reviewed in Turcotte and Schubert (1982). For two dimensionally distributed loads, one must turn to the solutions for a point load or disk load (see, for example, Lambeck, 1988). Although these too are analytic solutions, the flexural response to complex loads, those that vary spatially in such a way that they cannot be described as a simple symmetrical pattern, is calculated by turning to a numerical code that sums the vertical displacement associated with each of many point, disk, or line loads. We show a simple case employing the superposition of many line loads meant to represent one or two mountain crests in Figure 11.3. Finally, one must know something about

FIGURE 11.3. Flexural response to a distributed set of line loads

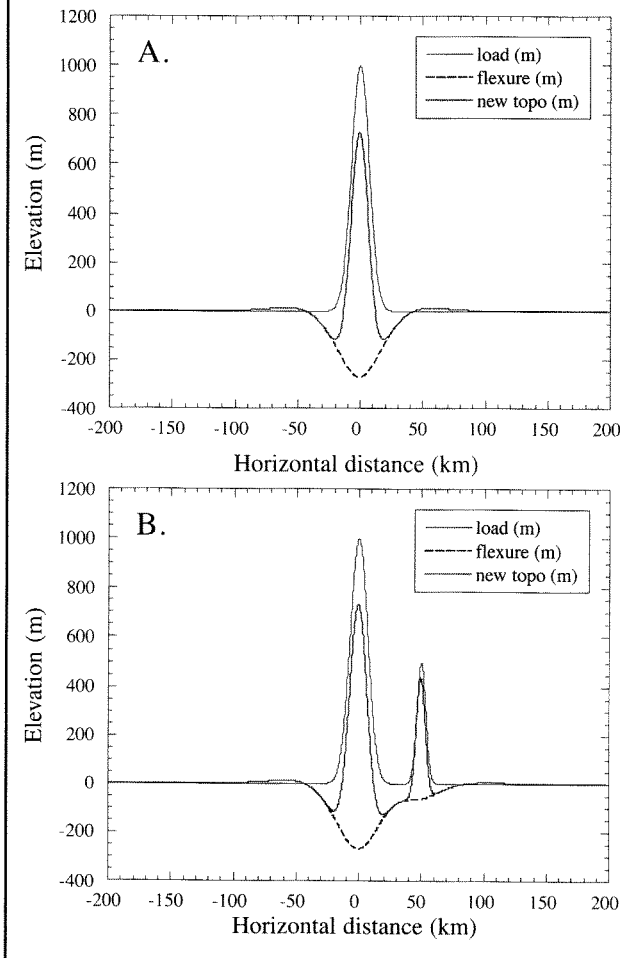

Load is solid thin line; flexural response to the load is thick black line; final topography (the sum of the load and the flexure) is the grayed line. Load shape in A is a single linear mountain range with a gaussian cross section 1 km tall. Load in B has in addition a second crest centered at 50 km to the right of the first, with 500 m amplitude. Effective elastic thickness of 10 km is used in both cases.

FIGURE 11.4. Estimated distribution of effective elastic thicknesses across North America, derived from analysis of gravity and topographic data. Modified from Bechtel et al. (1990)

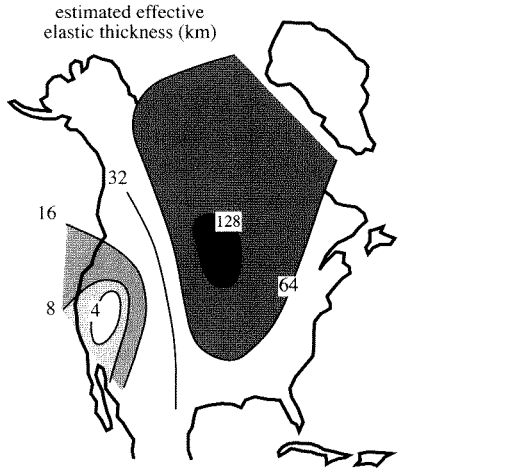

the expected flexural rigidity in a particular landscape. In Figure 11.4 we show a map of the broad scale features of the effective thickness in North America, estimated from analysis of the gravity and topographic fields. Note the strong rigid lithosphere of the shield, and the distinctive lower effective thicknesses in the western US.

Surface Processes

To first order, landscapes subjected simply to geomorphic processes tend to degrade through time, high places losing material, low places gaining. The specific processes and their rates vary from climate to climate, and from one lithology to the next. This general behavior can be captured mathematically with the diffusion equation, in which changes in the elevation of a point depend entirely on the local curvature. In other words, in one dimension

$$\frac{\partial z}{\partial t} = \kappa \frac{\partial^2 z}{\partial x^2} \qquad (11.1)$$

where x is horizontal distance and z is elevation, and κ is a landscape diffusion coefficient. The simplicity of the diffusion equation is appealing, although we will point out its drawbacks. In particular, simple diffusion-based models of surface processes generally ignore the need to produce regolith before it can be transported (a problem only if the feature involves bedrock to begin with), and they cannot account for channels in a landscape. In addition, if we wish to explore the dependence of the surface processes on climatic factors such as precipitation or temperature, which change in both space and time, we need to prescribe geomorphic rules that explicitly acknowledge these dependencies. This field is fast-evolving as both field instrumentation and dating methods allow documentation of these spatial and temporal variations in process rates.

Surface processes can be broken down loosely into those that produce mobile material, or *regolith*, from intact bedrock, usually by the processes of *weathering*, and those that move such material about on the landscape. At any point at which the rate at which the mobile material is stripped away from a point outpaces the rate of generation of mobile material, the landscape will be bare bedrock. We call such landscapes or points on the landscape *weathering limited*; the pace of weathering limits the pace of landscape change. In such instances, one cannot simply operate on the numerical landscape with a transport rule—which might lead to diffusive behavior—but must as well embed in the model a rule, or mathematical representation, for the generation of regolith (see the next section; Anderson and Humphrey, 1990).

In such circumstances, one therefore needs a rule for what sets the rate at which regolith is produced. Once produced from bedrock, particles are moved down slopes first on hillslopes and then in channels. One must therefore determine where the channels lie within a landscape, how effective they are in transporting sediment, and, if bare bedrock is exposed in the channel, how fast the bedrock is being eroded.

Regolith Generation

Our understanding of the long-term controls on the conversion of bedrock to regolith is incomplete. To first order, we would expect that the wetter the climate is the faster will be the weathering of rock. Gilbert (1877) hypothesized that within any particular landscape, and he was then considering arid landscapes of the Henry Mountains in Utah, the regolith production rates should be a strong function of the regolith thickness as well. Bare bedrock can effectively shed water, thereby protecting itself from chemical attack, whereas even a thin regolith cover should allow significant chemical attack of the underlying rock. Beyond a given thickness, however, the bedrock lies at such a great depth beneath the surface that wetting events may not penetrate, and the conversion rate might be expected to diminish. A mathematical statement

of this conceptual picture has been incorporated in a number of numerical landscape evolution models within the last couple of decades. While appealing, this conceptual picture has been difficult to document in the real world, because the weathering rates are far too low to measure on human time scales. Hope has emerged, however, with the aid of cosmogenic radionuclides in constraining the constants in at least a few geologic and climatic settings (see, for example, Pavich and Hack, 1985, Pavich, 1986, and McKean et al., 1993, who use garden variety ^{10}Be, and Small et al., 1999, who use in situ produced ^{10}Be and ^{26} Al).

Hillslopes

Material is moved down slopes by a number of processes, the type of which and the rates of which are dictated by the local climate and slope materials. All hillslope processes are dictated to some degree by the local slope angle. The simplest model rule is therefore something like:

$$Q = -k\frac{\partial z}{\partial x} \tag{11.2}$$

where $\partial z/\partial x$ is the local gradient of the topography, or the slope, in the x-direction. The constant k reflects the long-term efficiency of sediment motion, which might be expected to be a function of the climate. Several workers have modified this rule in order to mimic regolith landslides by enhancing the transport nonlinearly as a threshold slope angle is approached.

This type of rule is not capable of treating such potentially important processes as bedrock-involved landsliding. Unfortunately, in some landscapes this process is the dominant means of pulling rock from the adjoining hillslopes toward the bounding channels. Algorithms that attempt to capture this process come in several flavors. The simplest is one in which there is assumed to be a bedrock slope threshold above which a slope cannot be maintained; any material found above an envelope that v's upward from the channel is therefore shaved off and delivered instantly to the channel. Another approach essentially modifies the hillslope efficiency, k, rapidly increasing as an angle of repose is approached from lower angles (Anderson and Humphrey, 1990; Howard, 1994; Howard et al., 1997). Yet other approaches explicitly employ failure thresholds that entail both local slope and height, and an assumed rock mass strength (Densmore et al., 1998; Schmidt and Montgomery, 1995; Schmidt and Montgomery, 1996). In these latter cases, the failed masses must then be distributed in the landscape in a realistic manner, capturing the material properties of the masses subsequent to failure.

Channel Initiation

Most models of landscape evolution embed some rule for where in the landscape the channels lie. As shown convincingly in map and field analysis by Montgomery and Dietrich (1988; 1989; 1992), channels occur wherever a stream-power threshold has been exceeded. This is usually captured in the numerical models by embedding a threshold product of the local slope, S, with the local drainage area, A. Nodes at which this product is greater than some constant are considered channels, while all others remain hillslopes. The sensitivity of the landscape character to the choice of the channel initiation threshold is explored in detail through numerical models by Whipple and Tucker (1999).

Bedrock Incision

Our knowledge of the complex process by which rivers etch into bedrock is only recently been addressed by field and modeling studies. The physical processes include abrasion by particles entrained in the flow, plucking of blocks from the bed, and cavitation (Hancock et al., 1998). Most model rules that purport to capture the essence of this suite of processes use a stream-power argument (Howard and Kerby, 1983; Rosenbloom and Anderson, 1994; Seidl and Dietrich, 1992). This is often abstracted further to a rule in which the rate of erosion is dependent upon the local channel slope, S, and the drainage area at that point, A (i.e., the slope-area product):

$$\frac{\partial z_c}{\partial t} = dSA \tag{11.3}$$

where d is a coefficient of erosion. This equation is undoubtedly only a crude approximation of bedrock channel behavior. For instance, the coefficient d collapses any number of sins including the resistance of the rock, the effective discharge of the river, the runoff efficiency, and so on, into a single model parameter (e.g., Hancock et al., 1998).

Alluvial Transport

Many transport rules have been used in geomorphic models. We can only touch upon a couple of classes here. Most model rules embed the empirical result that sediment transport increases with the boundary shear stress of the flow, or the discharge of the water, above some

entrainment threshold. The simplest such statement is the DuBoys equation, relating sediment flux per unit width of flow, Q_s, to the local boundary shear stress, τ_b:

$$Q_s = b(\tau_b - \tau_c) \tag{11.4}$$

where τ_c is the shear stress necessary to entrain the sediment. As the shear stress ($\tau_b = \rho g H S$) requires a knowledge of the flow depth, H, most model strategies rewrite this rule in terms of the water discharge, Q, which is a quantity that is more directly tied to the climatic forcing of the system. This results in a yet simpler statement that

$$Q_s = cQ \tag{11.5}$$

Examples

Given the stated set of rules, a wide array of models can be generated that differ in their initial and boundary conditions, and in the tectonic pattern. We start with simple fault scarp models, and move to larger features.

Scarp Degradation Modelling

In many instances, none of the absolute dating methods discussed in Chapter 3 can be applied to a particular landform, be it a fault scarp, a lake shoreline or a marine terrace. The reason is most often a lack of datable material. In these circumstances, researchers have turned to theoretical models of how a scarp should evolve in the face of the surface processes active on it. The idea is simple: because in most cases scarp shape evolves monotonically from sharp-edged toward smoother forms, a knowledge of the initial shape of the scarp, and documentation of the detailed shape of the scarp, through surveying in the field, may be used to estimate the age of the feature.

Theory

Most models are based on the diffusion equation, starting with the extensive work of Culling in the 1960s (Culling, 1960; Culling, 1963; Culling, 1965). A useful introduction can also be found in Carson and Kirkby (1972). In direct analogy with the well understood thermal problem (Carslaw, 1986), the relevant equations derive from two statements: 1) mass is conserved, and 2) the flux of mass is proportional to the local topographic slope (Fig. 11.5). The first statement may be

FIGURE 11.5. Schematic illustration of the components of a hillslope evolution model that might be used to assess scarp evolution

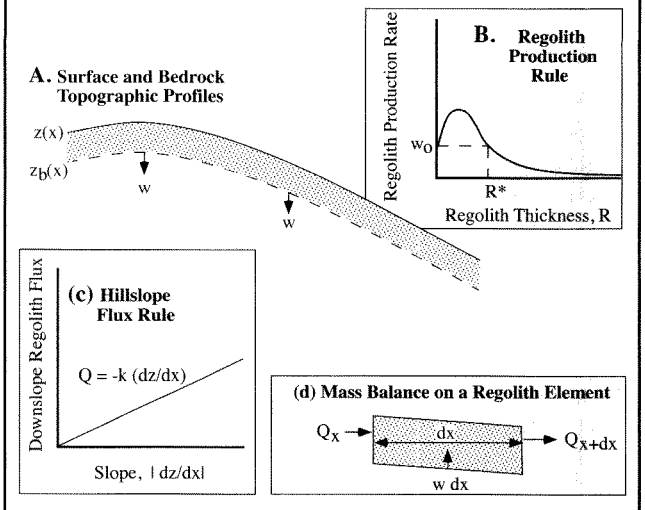

A. Topographic, $z(x)$, and bedrock, $z_b(x)$, profiles, with in general a nonuniform regolith thickness, $R(x)$. B. Regolith production rule, here taken to be dependent only on the local regolith thickness. C. Hillslope regolith specific discharge rule, one in which the discharge is linearly proportional to the local slope of the landscape.

written, for the one-dimensional case:

$$\frac{\partial z}{\partial t} = -\frac{1}{\rho_b}\frac{\partial Q_x}{\partial x} \tag{11.6}$$

where Q_x is the flux of mass in the x direction, through whatever processes are operating, ρ_b is the bulk density of the material being moved, and z is the elevation of the surface. The surface will decline in elevation (erosion) if the gradient in mass flux is positive (more mass leaves the element than arrives), and will increase in elevation (deposition) if the gradient in flux is negative (more mass arrives than leaves). This is a very general and broadly applicable statement; it holds for hillslopes, riverbeds, and seafloors alike. What changes from one system to the next is the surface process, and how that process is related to such measurable quantities in the landscape as local slope, the distance from a ridge crest, or distance downstream, and so on. What is needed to close the system is a process rule that describes what

controls the hillslope fluxes, Q_x. In the simplest case on a single hillsope, of which a scarp is an example, the flux of mass is taken to be simply proportional to the local slope. Stated mathematically,

$$Q_x = -k\frac{\partial z}{\partial x} \tag{11.7}$$

where k is a proportionality constant reflecting the efficiency of the process. Note that the negative sign reflects the fact that mass is being moved in the downslope direction. The local slope in two dimensions is $\frac{\partial z}{\partial x}$, while in three dimensions, it is, ∇z or

$$\frac{\partial z}{\partial x} + \frac{\partial z}{\partial y}.$$

This is a subset of a large suite of possible models for the flux of mass on a hillslope, in which in general there is a dependence on x, possibly to some power, and in which slope may come in to some power (e.g., Carson and Kirkby, 1972).

In general, then, the rule may be stated:

$$Q_x = -kx^m\left(\frac{\partial z}{\partial x}\right)^n \tag{11.8}$$

Under conditions in which the transport efficiency, k, is uniform with x, and the flux is dictated linearly by the local slope (i.e., $m = 1$, $n = 0$) the combination of the mass flux and mass conservation equations results in the diffusion equation:

$$\frac{\partial z}{\partial t} = \kappa\frac{\partial^2 z}{\partial x^2} \tag{11.9}$$

The rate of change of the elevation of the surface depends solely on the local curvature of the surface. Here the diffusion coefficient, called by some the landscape diffusivity, κ, reflects both the bulk density of the material being transported and the efficiency of the transport process: $\kappa = k/\rho_b$. Diffusivity always has units of L^2/T. Note that this is easily extended to both x and y directions, although we will focus on simple landforms described by a single profile, $z(x)$.

Solution of the diffusion equation, a second-order differential equation, requires specification of initial conditions. In addition, estimation of the age of a feature requires knowledge of the diffusion constant. In analogy with the problem of thermal evolution within a slab with an initial step in temperature, scarp evolution may be represented as an error function (Fig. 11.6). One of the features of this solution is that the slope at the midpoint of the scarp, which is often the steepest slope on the feature, decays as the square root of time, making the measurement of this slope in the field a useful target for constraining the scarp age (Hanks et al., 1984). The simplicity of this approach is indeed appealing, although one must be very aware of the geomorphic and seismic setting to apply this technique properly for the dating of scarp-like features.

FIGURE 11.6. The evolution of a scarp profile

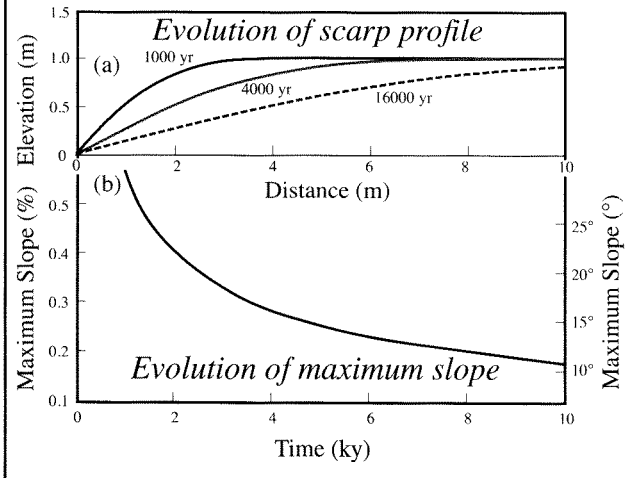

A. The top half of a scarp profile at several times after initiation of a 2 m vertical step in the surface, and B. the evolution of the maximum slope through the same time interval. Note that the maximum slope declines rapidly at first, and more gently later, reflecting the square root of time dependence of diffusive processes. Modified after Hanks (1984).

Applications

Early application to tectonically active landscapes included the treatment of wave cut scarps in the Lake Bonneville basin, Utah, whose age had been determined independently (by ^{14}C), and which were cut by recent faulting or warped by isostatic deformation. Knowledge of the present profiles, an estimate of the initial profile shape by appeal to modern wavecut features, and knowledge of the age, led to constraints on the diffusivity κ, of 5–100 m^2/ky. Using these estimates of diffusivity, ages of scarps of unknown age in arid landscapes nearby were subsequently estimated (Buchnam and Anderson, 1979; Colman and Watson, 1983; Mayer, 1986; Nash, 1984; Nash, 1988; Wallace, 1978).

FIGURE 11.7 Terrace degradation in Tibet

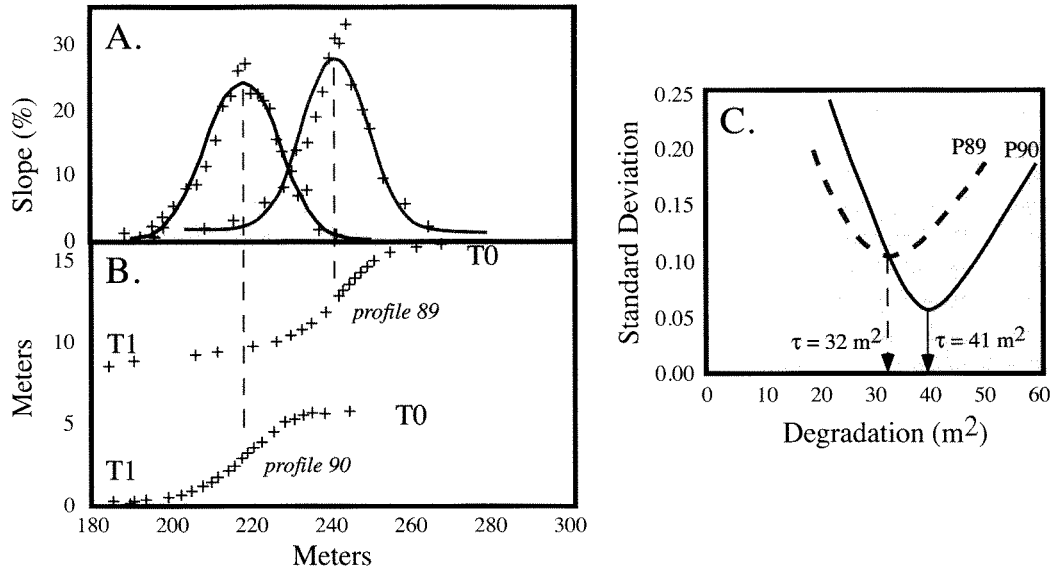

Derived from work on faulted terrace risers in Tibet, A. slope distributions from B. profiles 89 and 90 between terrace surfaces T1 and T0. Vertical dashed lines connect midpoints in the scarps with their respective slope distributions. C. Misfits of models for various choices of the breadth of the gaussian function describing the slope distributions. Resulting degradation reflects the product of the diffusivity (m^2/yr) and the scarp age (yr). The two profiles shown yield degradations of 41 and 32 m^2. Modified after Avouac (1993).

Using another feature of the solutions to the diffusion equation, Avouac et al. (1993) have surveyed numerous profiles across scarps separating terrace risers in arid Tibet to deduce the ages of the terraces. They then plot the pattern of the derivative of the topography (i.e., the slopes; Fig. 11.7). This pattern should be a broadening gaussian through time if diffusion controlled the evolution of the terrace riser (Avouac, 1993). Avouac uses the best fits to the breadth of this distribution to constrain what they call the scarp degradation (in m^2), which is the product of the diffusivity and time since the scarp step was generated. If the diffusivity is uniform from scarp to scarp, then the scarp degradation should be a good surrogate for scarp age.

Complexities

Geomorphologists have recognized several pitfalls of modeling scarp evolution with the simple diffusion equation. In the development outlined in the previous section, and in the applications cited, several assumptions were made, among them: 1) the proper initial condition is that left by whatever erosional or tectonic process caused the topographic step in the first place, 2) the diffusion coefficient is spatially uniform along the profile, which allowed pulling the k out of the derivative when the two equations were combined, 3) the diffusion coefficient is not dependent upon the aspect (facing direction) of the slope, (i.e., would be the same from profile to profile within the same landscape), 4) the simple linear relation of flux to local slope is valid (i.e., it is not nonlinearly related, and not related to other factors such as distance from the top of the slope), and 5) weathering of the material to be transported may be ignored. We summarize subsequent work addressing some of these complexities in the following paragraphs.

Initial Conditions

It was early recognized, in dealing with fault (and other) scarps in arid regions, that another process not well described by diffusion was operating in the early stages of scarp decay. Rapid failure of the scarp by slumping and talus formation leads to angle of repose slopes

within a matter of decades to centuries—times much shorter than the presumed ages of the scarps (Pierce and Colman, 1986). This angle of repose slope is therefore likely the more appropriate initial condition for diffusion-based modelling of the scarp. Estimates of scarp age are made knowing that there is a slight lag associated with the development of the angle of repose slope. Alternatively, one may postulate process rule that mimics the generation of the angle of repose slope, and start the calculation from the initial oversteepened step. Examples of this treatment include that in Anderson and Humphrey (1990) and in Howard et al. (1994) and Howard et al. (1997), where the downslope flux departs from a linear relation with slope angle, increasing rapidly as the slope steepens toward the angle of repose.

Nonuniform Diffusivity

Working on the late glacial fluvial terrace scarps in central Idaho, Pierce and Colman (1986) were able to assess the dependence of the diffusion coefficient on the orientation of the slope (slope aspect). They document a several-fold difference between north- and south-facing slopes, which they attribute largely to the dependence of vegetation density on solar radiation. They also note a dependence on height of the scarp, tall scarps having higher effective diffusion coefficients, which they attribute to the operation of slopewash process that are dependent on slope length—in other words, the equation describing flux is no longer simply dependent on slope, but is dependent on position on the slope, x.

Weathering-Limited Situations

In landforms that are not entirely composed of loose, transportable materials, one must take into account the transformation of the cohesive material (or bedrock) into material capable of being transported by the available surface processes. This was recognized early by Gilbert (1909), in his classic word picture of how convex hilltops operate. Mote recently, Anderson and Humphrey (1990) have modeled the evolution of scarps and moraines in the face of weathering and linear diffusion. Here one must pose a second rule in the problem, representing this transformation to transportable material; call it the weathering rate, W. Anderson and Humphrey followed the proposal of Ahnert (1970), who was following Gilbert's (1877) word picture, in which the rate of transformation depends solely on the thickness of the regolith (defined as the layer of transportable material). Although other rules could be entertained, they use a simple exponential, in which the maximum rate of regolith production was achieved on bare bedrock (no regolith) and decayed exponentially with increasing regolith thickness:

$$\frac{\partial z_b}{\partial t} = -W = -R_0 \exp(-R/R*) \qquad (11.10)$$

where z_b is the local elevation of the regolith-bedrock interface, R is the regolith thickness, R_0 is the rate of bare bedrock weathering, and R^* is a regolith thickness at which the rate of regolith production is 1/e of that on bare bedrock. The rule set must now include the rate of lowering of the bedrock interface, and the rate of change of the regolith due to surface processes, which is controlled by the diffusion equation (see Fig. 11.5). The relevant diffusion equation is now

$$\frac{\partial R}{\partial t} = \kappa \frac{\partial^2 z}{\partial x^2} \qquad (11.11)$$

and the surface elevation at any point in time is $z = z_b + R$. With these modifications, Anderson and Humphrey (1990) show that the symmetry one expects from pure diffusion in the absence of weathering is broken (Fig. 11.8). It takes longer for a crest to round than for the base of the slope to round. Especially at early times, the sharp curvature at the hillcrest (or scarp crest) results in rapid removal of the existing regolith; thereafter, the rate at which this portion of the slope declines is dictated by the weathering rate on bare bedrock; it is weathering limited. All the while, the material transported downslope forms the smoothed colluvial apron at the base of the slope.

Given that this could potentially explain the asymmetry of the marine terrace risers studied by Hanks (1984), Rosenbloom and Anderson (1994) incorporated such a rule set into their models of hillslope evolution, and demonstrated that considerably better fits to the profiles could be attained when both weathering and diffusive surface processes were treated explicitly (Fig. 11.9). It was not necessary to appeal to surface processes that resulted in nonlinear diffusion.

In an application to glacial moraines, which have been used in eastern California to constrain both the ages of the glaciations and the faulting rates on the Sierran frontal fault (Bursik and Gillespie, 1993), Hallet and Putkonen (1994) have shown that the interpretation of cosmogenic radionuclide (CRN) results from boulders on moraine surfaces is not straight-forward. They argue that use of a numerical model of the moraine evolution, which employs a slightly modified form of the diffusion

FIGURE 11.8. Illustration of the effects of weathering-limited case on the evolution of scarp profiles

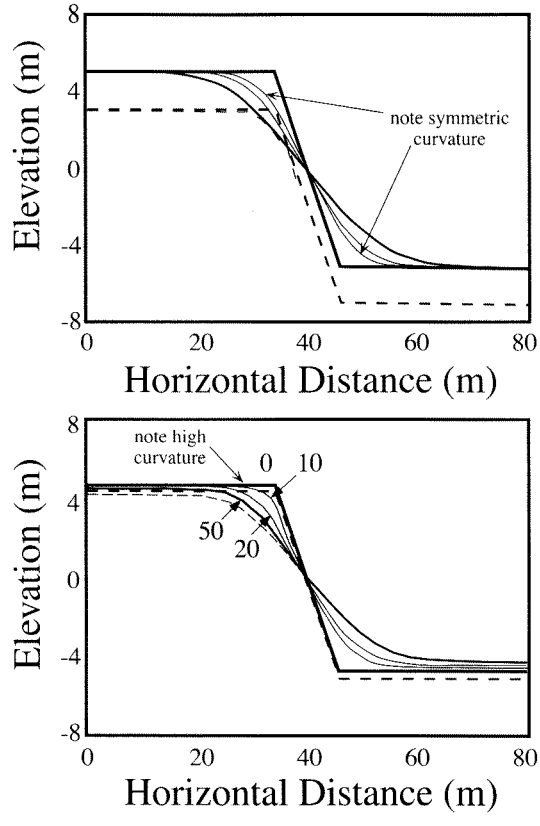

Bedrock interface is shown as dashed lines, early (bold) and at termination of the simulation (50 ka), and surface topography is shown at 0 (bold), 10, 20, and 50 ka. A. Pure diffusion case is allowed by dictating that the initial bedrock interface be very deep. It is etched into only late in the simulation. B. Shallow initial bedrock interface (0.2 m) restricts rate of rounding of the scarp crest, while surface processes still effectively smear the growing colluvial wedge. This breaks the symmetry of the pure diffusion case, the top of the scarp being consistently higher curvature than the base. Modified after Anderson and Humphrey (1990).

FIGURE 11.9. Evolution of marine terrace profiles, north of Santa Cruz, California

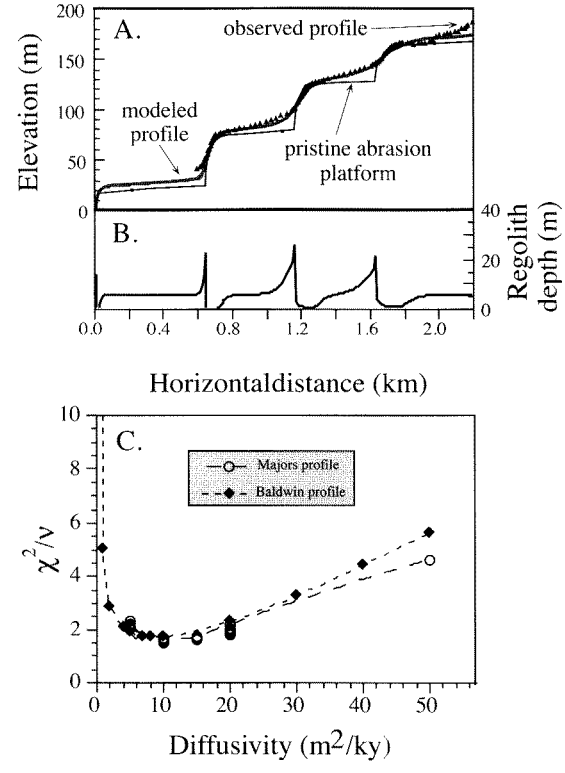

Modeled terrace surface profiles are shown along with the surveyed data. A. Wavecut platforms are shown as inserted into the model at the distances required by the locations of the paleo-cliffs and the times prescribed by the assumed ages of the sea's abandonment of the inner edges. The intervening wedge of material is a combination of original marine terrace deposits (here assumed to be uniformly 6 m thick upon retreat of the sea), and colluvium derived from the decay of the sea cliff backing any particular terrace. B. The regolith depth as a function of position. Note the spike associated with the base of the cliff and the taper that grows through time. Regolith is absent on the bedrock-dominated edge of the first cliff but has a finite but low depth on the upper edges of older cliffs. The terrace surfaces of old or narrow platforms will dip significantly more toward the sea than will younger and broader surfaces, suggesting that caution is warranted in interpreting dips of these surfaces as tilt of the original platforms. C. Sensitivity analyses of the parameters controlling the shapes of the model hillslope profiles. Tests used the reduced χ^2 statistic relating model calculations to survey data. For both surveyed profiles the minimum χ^2 corresponds to $\kappa = 10$ m^2 kyr^{-1}. Adapted from Rosenbloom and Anderson (1994).

equation described previously, can fit the moraine topographic profiles. By tracking in addition the buildup of cosmogenic radionuclides in boulders that are slowly exhumed from within the moraine during its shape evolution, they show that 1) on old moraines the boulders commonly used to date them should yield only a

minimum age for the moraine, and 2) the mean CRN age of boulders sampled from a moraine surface can in fact decrease with the true age of the moraine. This example highlights the need to take into account the dynamic nature of the geomorphic surfaces on which CRN techniques are currently being employed, requiring the marriage of cosmogenic and numerical landscape evolution modelling techniques.

Conclusions from Modelling at the Hillslope Scale

Proper use of this sort of modelling to estimate ages of scarps and similar topographic features requires:

1. Knowledge of initial conditions
2. Awareness of taluslike processes that violate the linear diffusion process rule in the early stages of topographic evolution
3. Treatment of out-of-plane processes that might remove material from the cross section, thereby violating the one-dimensional conservation of mass equation
4. Explicit treatment of the generation of transportable particles if cohesive materials or bedrock are involved in the original scarp
5. Awarenes of possible dependence of the diffusion coefficient on slope aspect, through a dependence on process efficiency and possibly process type with orientation
6. Estimation of the diffusion coefficient by appeal to nearby or climatically relevant estimates from other well-dated sites in similar materials.

Given these complexities, it is perhaps best not to rely on a single slope within the scarp (e.g., midpoint slope) to infer age, but rather to construct a forward numerical model of the entire scarp that explicitly addresses the issues outlined previously. Modeled scarp profiles can then be assessed against field-collected profile data using goodness of fit estimates for a range of possible models, in which the full range of possible weathering rates and diffusion coefficients may be explored.

Mountain Range-Scale Models

At the mountain range scale, numerical models have evolved significantly over the last decade. Early attempts involved one-dimensional models of the evolution of simple one-fault bounded ranges. These included a uniform-slip dislocation model of a single planar fault, diffusion of resulting topography, and flexural compensation for the rearrangement of rock mass. In a pair of prescient papers (King et al., 1988; Stein et al., 1988), these authors both developed the fundamental principles behind such linked models, and applied them to specific settings in the American West. The faults were allowed to be both normal and thrust. Importantly, they found that the flexural rigidity of the crust played importantly into setting the width of the zone over which the sediments eroded from the rising mountain mass were spread (Fig. 11.10). For example, they argue for a very low rigidity in the basin and range province (e.g., effective elastic thicknesses of only a few km) in order to match the very narrow depositional basins near the active faults. The simplicity of the models, being one-dimensional with only three major components, allowed efficient exploration of the roles of each of the processes in the problem. Note, however, that the entirety of the geomorphic suite of processes is boiled down into a single diffusion coefficient. No channels exist. No weathering exists. None of the complex feedbacks between these processes are allowed. Nonetheless, much was accomplished by this suite of models. Was it necessary to incorporate these other processes? Was it worth the effort of moving to two dimensions, as is necessary if attempting to distinguish channels and hillslopes? At the same time, models along these lines were also being constructed of thrust faulted settings, with more attention being paid to the stratigraphic package generated in the bounding basin (e.g., Flemings and Jordan, 1989; 1990). Again, no attention was paid to the details of the processes generating the debris, nor of the delivery mechanisms of that debris to the basin edge. The focus was on the details of the stratigraphic package, and how these reflected either episodes of rapid motion along the fault, or of climate variations.

The first numerical model to both move to a two-dimensional planform, and to incorporate channels as critical elements in the evolving landscape was that of Koons (1989), who focused on the Southern Alps of New Zealand. Koons incorporated a simple geometrically reasonable and geologically defensible rock uplift pattern; inserted a set of streams that lived in specific places within this uplift pattern, that did not move, and that draped smoothly and logarithmically from a channel head near the uplift maximum to the base level of the sea; and dictated that the surface processes that operated upon the interfluves between these stream channels could be approximated by diffusion that was allowed to be spatially variable. In particular, wishing to mimic the strong

FIGURE 11.10. Mountain range models

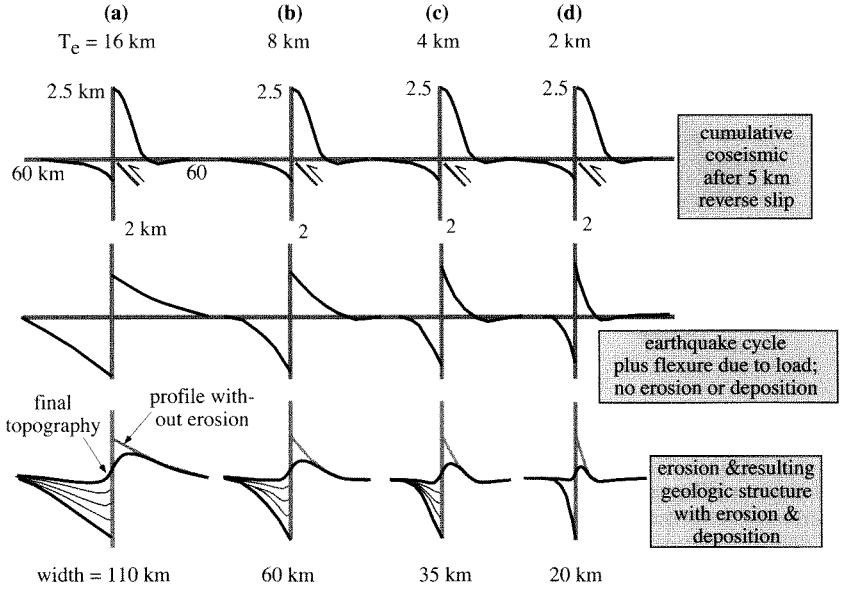

Matrix of mountain range scale model results in which the effective elastic thickness (T_e) is varied (columns a-d). In the top line, the pattern of vertical displacements associated with a prescribed total slip of 5 km on the thrust fault is shown (scales on left-most plot, in km). All patterns are the same and show 2.5 km of maximum rock uplift on the hanging wall block, 2 km of maximum subsidence on the footwall block. The pattern is then allowed to flex in response to relaxation at depth; the resulting sum of dislocation plus flexural compensation for the altered topographic load is shown in the second line of plots. The difference in the plots reflects the assumed effective elastic thickness, declining from 16 km to 2 km from left to right. The width scale of the resulting mountain range–basin pair declines dramatically from 100 to 20 km. The last line of plots reflects a crude redistribution of mass by erosion of the mountain crest and deposition in the adjacent basin. The scale and the asymmetry of the geologic structure vary significantly with the flexural rigidity. Modified after King et al. (1988).

orographic forcing caused by the fact that the Southern Alps are embedded in the westerlies, he tied the diffusivity to the rainfall rate. As shown in Figure 11.11, the essence of the ridge topography is simulated well using this simple set of model rules. The ridgeline is highest near the coast on an interfluve that is wider than the others in the simulation. This reflects the fact that the steady state relief depends on the square of the interfluve width (Koons, 1989). The simplicity of this model, which is as simple as a two-dimensional planform model can get, allows rapid exploration of the various controls on the topography. This Koons does very effectively, varying the spatial pattern of the uplift pattern, and of the rainfall pattern (hence diffusivity).

One of the drawbacks to this model are that the channels are not interactive. Their profiles are dictated, rather than reflecting the real dynamics of the channel system. Nonetheless, just as much was learned from the Stein, King and Rundle models in one dimension, much is learned from the Koons two-dimensional approach. It took the modelling community one strong step toward realizing the relative importance of one or another process, and in particular alerted the geomorphic community to the importance of bedrock channel incision.

In the 1990s, several attempts were made to incorporate more interactive channels and hillslopes into the mountain range evolution models. This required integration of rules for the sediment transport down channels, and for the incision of bedrock by channels. Anderson (1994) addressed the problem of topographic evolution in a region of 30 × 100 km near a restraining bend in a major strike-slip fault (the San Andreas). The rock-uplift pattern was simply dictated at the outset, as a two-dimensional gaussian rock-uplift pattern whose scale

FIGURE 11.11. First planview landscape evolution model showing importance of channels, nonuniform precipitation, and uplift pattern in setting the long term landscape geometry

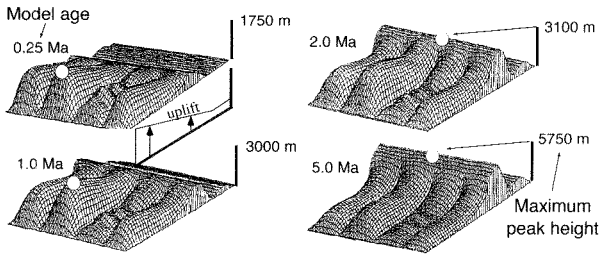

For each model age step, the position of the highest topography is shown by the open circle. Channels are dictated to have a particular shape draping between the mountain crest and the sea. The complex ridge pattern reflects the essence of that observed in the Southern Alps of New Zealand. Modified after Koons (1989).

was set by the requirement for conservation of crustal volume arriving at the bend; crust was then translated through this pattern, any parcel of crust experiencing a time-varying history of uplift dictated by what portion of the uplift pattern it intersected. The coarse 1 km resolution of the model required significant abstraction of the hillslope scale processes. Even small-scale channels with drainage areas of less than 1 km^2 were subsumed in the numerical pixels. The remaining major channels were inserted in the calculation space, were tied to the bedrock as it slid horizontally relative to the fixed fault bend, and were allowed to evolve as bedrock channels with their drainage area playing a proxy for local stream power. No attempt was made to incorporate orographic effects; rainfall was taken to be uniform. Arguing that landslides were the dominant delivery mechanism for debris to the channels, Anderson (1994) simply set the hillslope angles in the landscape and allowed the hillslopes to come down at the rate dictated by the incision rate of the local channel. Flexure was taken into account in two dimensions, allowing both the topographic envelope and the crustal response to erosional unloading to be followed through time.

More recently, Densmore and others (1998) have incorporated more realistic landsliding rules in their model, dubbed ZSCAPE (Fig. 11.12). The tectonic component of this model is based on the Gomberg and Ellis (1993) and Gomberg (1993) 3DDEF boundary element code for tracking the displacement field to be expected from a set of prescribed dislocations in an elastic medium. The setting addressed by Densmore et al. (1988) and by Ellis et al. (1999) is the Basin Range province of western North America. High-angle normal faults are prescribed. The surface processes for which model components exist in the code include regolith production, diffusion of regolith, landsliding, fluvial sediment transport, and fluvial bedrock incision. The code is flexible enough to deal with spatially nonuniform precipitation. The 100 m pixels resolve considerably more detail. Initial conditions of a flat or of a slightly tilted topography were explored. Many of the salient characteristics of such mountain ranges are captured well in the model, including triangular facets at the mountain front, and benches in spur ridges. Exploration of the relative importance of various surface processes demonstrated that bedrock-involved landsliding was likely the dominant process in this setting.

Orogen-Scale Models

In a series of models that extended the early work and ideas of Koons (1989) on the Southern Alps, Beaumont and coworkers (e.g., Beaumont et al. (1992); Willett et al. (1993) and Beaumont et al. (1996)) have added interactive channels, and have added explicit treatment of both the geometry and the rheology of the crust in sometimes quite complicated collisional settings. The crust is allowed to deform by two mechanisms: shallow crust behaves as a cohesionless frictional-plastic (coulomb) material with a specified yield strength. At depth the deformation mechanism alters to one of thermally activated power-law creep. The switch-over (loosely speaking, the brittle-ductile transition) between these two mechanisms is determined dynamically within the model, and depends on the thermal and mineralogical structure. In the surface processes components of these models, the code is simplified considerably by treating both hillslope and channel processes in any particular node (see Kooi and Beaumont, 1994; 1996).

In an important contribution, Kooi and Beaumont (1996) have explored more generic mountain range evolution (Fig. 11.13). They illustrate that the older conceptual models of many early geomorphologists as diverse as King, Gilbert and Davis, each of whom developed their conceptual models with particular real-world landscapes in mind, can be illustrated by such a generic model by paying attention to one or another phase of the

FIGURE 11.12. Results from the numerical model ZSCAPE

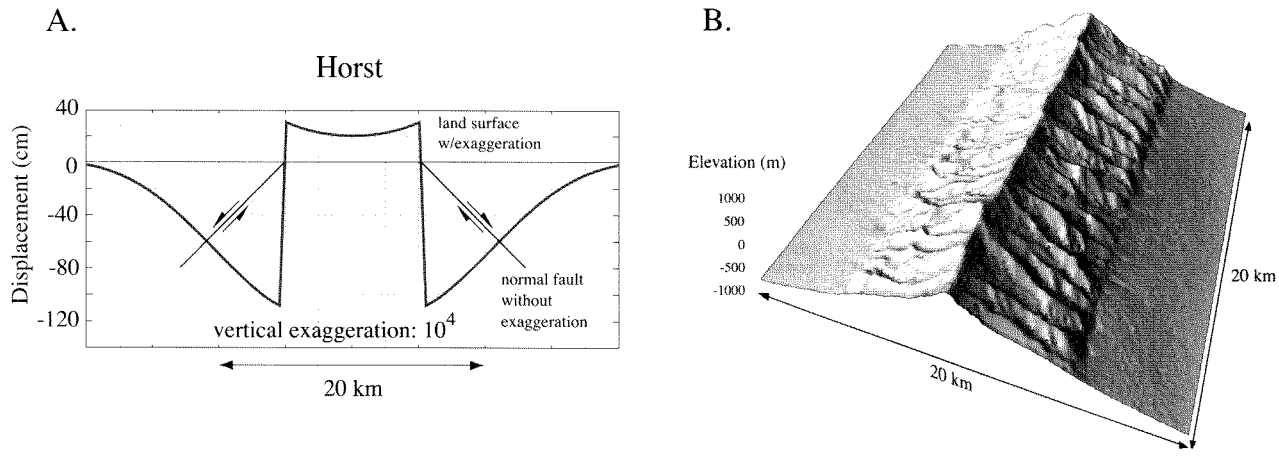

Both an explicit fault geometry and a suite of surface processes including bedrock landsliding are employed in this finite difference model (Densmore et al., 1998; Ellis et al., 1999). Resolution of the model = 100 m. A. Cross section of the tectonic forcing of the system with two opposing normal faults driving both vertical and horizontal deformation fields. Dislocations dip 60°. B. Resulting topography after 1 million years. Precipitation pattern is uniform. Channels are self-formed, and incise at rates driven by local stream power. Landsliding dominates the hillslope evolution. Triangular facets form on both faulted mountain fronts. Adapted from Densmore et al. (1998).

development, or by setting the tectonic and surface process rates differently.

Considerable attention has been devoted recently to the two-sided orogen (Koons, 1990; Willett et al., 1993; Willett, 1999). Much of this work followed on the notion that there could be a strong coupling between the surface processes that actively rearrange the load on the crust with the deformation field at depth. This is exciting in that it allows the geomorphology and those who study it into the tectonic game. This is illustrated in the work of Willett (1999), who has constructed a model of collisional orogens with examples from Taiwan and the Himalayas in mind. These are cross-sectional models, normal to the orogenic collision, in which the rheology of the crustal materials involved in the collision are assessed explicitly (Fig. 11.14). The surface process component of this model is simple, as it must be one dimension. Reflecting the assumption that the dominant surface process is bedrock fluvial incision, and that the hillslopes will essentially come along for the ride, Willett uses a steam-power-based incision rule. The spatial distribution of power goes as the precipitation falling upstream of the node being assessed. Orographic forcing of the precipitation is allowed. Importantly, these models illustrate the strong coupling of the spatial pattern of erosion rates with the deep crustal strain rate field. This class of models quantifies the conceptual ideas of Koons that show the potential influence of the atmospheric conditions (primarily the wind direction) on the asymmetry of the strain field in collisional settings (Fig. 11.14). That this degree of coupling can be simulated in realistic models has acted as a catalyst for a wide range of earth scientists to collect the sort of field information (topography, meteorology, exhumation patterns) that will act both as tests of the present models, and as constraints on further models at the mountain range scale. For example, recent work in New Guinea reveals that this coupling has been operating to localize the strain in the collisional orogen in Iryan Jaya (e.g., Weiland and Cloos, 1996).

Present Limits and the Next Generation of Models

Although progress has been tremendous in the last decade, the present generation of models fall short on several counts. These include lack of proper treatment of a few key processes that become important in certain circumstances, a lack of agreement on how such models

FIGURE 11.13. Landscape model incorporating a triangular uplift pattern and a self-forming channel pattern, showing several snapshots of the landscape as it grows and then decays in relief

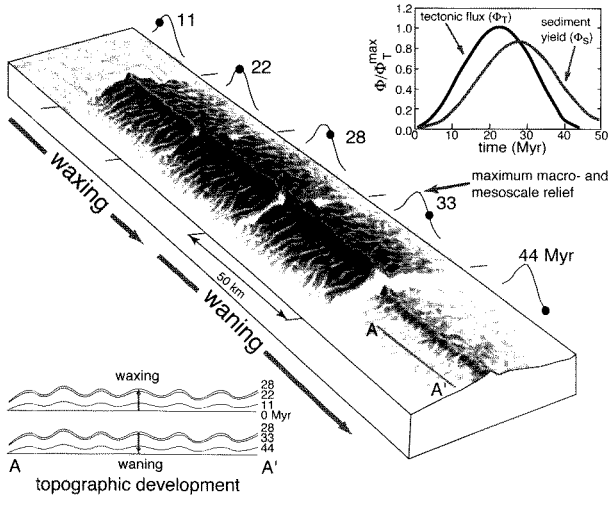

The total sediment flux leaving the model landscape lags the history of the rate at which mass is being added by tectonic forcing, as shown in the inset. Modified after Kooi and Beaumont (1996).

FIGURE 11.14. Cross-sectional model of crust and topography in a collisional orogen

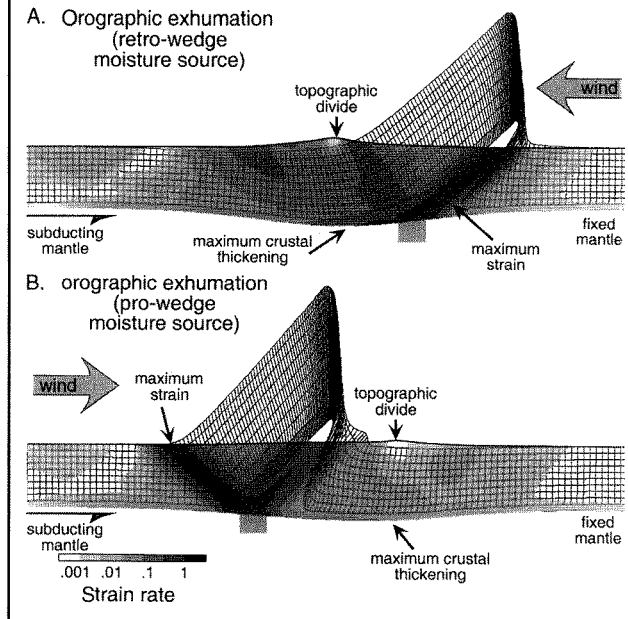

The two panels display contrasting topographies and exhumation patterns associated with wind direction from two different directions, one (A) in the same direction as the subducting slab, the other (B) opposing it. The initial mesh, attached to material particles, was rectilinear, and has been deformed significantly. Substrate detachment point is given by the grey rectangular block. Crust deforms according to a temperature-dependent viscous constitutive law below the Coulomb yield stress. The final topography is shown as the solid bold line in each model. The portion of the rock mass within the "Lagrangian tracking mesh" above this line has been exhumed and has been lost to erosion. Modified after Willett (1999).

ought to be calibrated or tested, and the perennial problem of the mismatch of the scales of time and space at which the real-world processes act and those at which the models can efficiently operate.

Processes that are not fully incorporated include mass movements and glacial erosion. The bedrock landslide algorithms we have discussed have only crude means of dispersing the masses involved in the failures. Recent work in volcanic terrain (Iverson et al., 1998) has shown the far reach of debris flows and lahars. The treatment of such events requires careful routing of the debris mixtures down their channels, and a proper rule set for determining the conditions that promote the ultimate deposition of this mass flow.

Glacial erosion becomes an important process when some portion of the landscape rises through the snowline, meaning that more snow accumulates in the winter than melts in the summer. Ice, too, is routed down channels. A glacier's ability to slide, through the process of regelation, allows temperate glaciers (those whose beds are at the pressure melting point) to be very effective erosional agents (Hallet et al., 1996). Erosion rates commonly range from 0.1 mm/yr to many mm/yr over that portion of the landscape mantled by temperate ice. Landscape evolution models attempting to incorporate glacial erosion as a process therefore need to be able to mimic the meteorological conditions that dictate the mass balance of glaciers, the physics that controls the movement of the ice down-channel, and in particular the sliding component of that motion, and must have rule set that connects the erosion pattern to the pattern of sliding. Only recently have such models begun to be developed (see, for example, Harbor et al. (1988), Harbor (1992), and Oerlemans (1984)).

As we have discussed, the initial conditions imposed on a model run can play an important role in setting the final look of the landscape. This reflects the fact that the most difficult feature of a landscape to change is the planview shape of the drainage pattern; streams most efficiently cut downward, and unless strongly forced, do not wander significantly once established in a bedrock channel. Unfortunately, it is most difficult to establish with confidence through geological evidence what the channel pattern might have been at the inception of a mountain-building episode. Although this remains a challenge, the process of stream capture, and the distortion of channel patterns through crustal deformation of the rock mass in which they are embedded need to be addressed in future models. These processes may have played extremely important roles in the evolution of portions of the Himalayas.

In general, these numerical landscape evolution models must begin to incorporate additional constraints from a variety of geological, geomorphic, and geochronological data sets. That is to say, they ought to be constructed in such a way as to predict the patterns of not only the topographic field, and of exhumation patterns, but of other geophysical fields such as heat flow and gravity. Even more relevant than the predicted exhumation pattern, these models can and should be capable of predicting patterns of fission track ages and track length distributions. This will require, for instance, incorporation of thermal components of the code so that the thermal trajectory of any parcel of crust can be followed throughout a simulation. The testing of generic models is even more difficult. Because they will not mimic a particular topography, we are left with only statistical tests. For example, we might ask whether the resulting topography has the same distribution of surface area with elevation (the hypsometry), or distribution of slopes as a real range. This information is now readily available from DEMs of varying resolution (e.g., Brozovic et al., 1997).

Summary

We have tried to expose the reader to a variety of modelling techniques and results, covering a range of scales from scarps to mountain ranges. Both the tectonic forcing of the system, and the suite of geomorphic processes acting to modify the tectonically generated landscape must somehow be incorporated in the model. One must choose a modelling strategy that suits the problem. This includes decisions about the dimensionality of the space to be modeled, and the style of model (analytical or numerical; finite difference or finite element or boundary element). One must comb the literature and collect new field information against which the model will be tested.

It is well worth reiterating that the purpose of modelling in this field is most often the development of insight into the complexity of the various processes interacting to produce a tectonic landscape. We always make simplifications in these efforts. The art lies in the decisions about what degree of detail must be preserved in the model in order to remain faithful enough to the real world to answer the specific questions being asked of it. No model of a scarp will treat every sand grain in the scarp. No model of a mountain range will treat every little bend in the faults bounding it. Finally, the development of models of landscape evolution must go hand in hand with the generation of data sets that are capable of constraining these models. The excitement at present lies in the interplay between these efforts, as new models force the generation of new data, and new data forces the incorporation of new elements in the models.

References Cited

Abbott, L.D., Silver, E.A., Anderson, R.S., Smith, R., Ingle, J.C., Kling, S.A., Haig, D., Small, E., Galewsky, J., and Sliter, W., 1997, Measurement of tectonic surface uplift rate in a young collisional mountain belt: Nature, v. 385, p. 501–507.

Abdrakhmatov, K.Y., Aldazhanov, S.A., Hager, B.H., Hamburger, M.W., Herring, T.A., Kalabaev, K.B., Makarov, V.I., Molnar, P., Panasyuk, S.V., Prilepin, M.T., Reilinger, R.E., Sadybakasov, I.S., Souter, B.J., Trapeznikov, Y.A., Tsurkov, V.Y., and Zubovich, A.V., 1996, Relatively recent construction of the Tien Shan inferred from GPS measurements of present-day crustal deformation rates: Nature, v. 384, p. 450–453.

Adams, K.D., Wesnousky, S.G., and Bills, B.G., 1999, Isostatic rebound, active faulting, and potential geomorphic effects in the Lake Lahontan basin, Nevada and California: Geological Society of America Bulletin, v. 111, p. 1739–1756.

Ahnert, F., 1970, Functional relationships between denudation, relief, and uplift in large mid-latitude basins: American Journal of Science, v. 268, p. 243–263.

Aitken, M.J., 1985, Thermoluminescence dating: London, Academic Press, 280 p.

Aitken, M.J., 1998, An introduction to optical dating: the dating of Quaternary sediments by the use of photon-stimulated luminescence: Oxford, Oxford University Press, 267 p.

Aki, K., 1984, Asperities, barriers, characteristic earthquakes and strong motion prediction: Journal of Geophysical Research, v. 89, p. 5867–5872.

Alexander, J., Bridge, J.S., Leeder, M.R., Collier, R.E.L., and Gawthorpe, R.L., 1994, Holocene meander-belt evolution in an active extensional basin, southwestern Montana: Journal of Sedimentary Research, v. B64, p. 542–559.

Allen, C.R., 1986, Seismological and paleoseismological techniques of research in active tectonics, Active Tectonics: Washington, D.C., National Academy Press, p. 148–154.

Allen, P.A., 1997, Earth surface processes: Oxford, Blackwell Science, 404 p.

Allmendinger, R.W., 1998, Inverse and forward numerical modeling of trishear fault-propagation folds: Tectonics, v. 17, p. 640–656.

Anders, M.H., and Schlische, R.W., 1994, Overlapping faults, intrabasin highs, and the growth of normal faults: Journal of Geology, v. 102, p. 165–180.

Anderson, D.W., and Rymer, M.J., 1983, Tectonics and sedimentation along faults of the San Andreas system: Los Angeles, Pacific Section, Society of Economic Paleontologists and Mineralogists, 110 p.

Anderson, E.M., 1951, The dynamics of faulting and dyke formation, with applications to Britain: Edinburgh, Oliver and Boyd, 206 p.

Anderson, P.M., Barnosky, C.W., Bartlein, P.J., Behling, P.J., Brubaker, L., Cushing, E.J., Dodson, J., Dworetsky, B., Guetter, P.J., Harrison, S.P., Huntley, B.J.C., Roberts, N., Ruddiman, W.F., Salinger, M.J., Spaulding, W.G., Street-Perrott, F.A., Thompson, R.S., Wang, P.K., Webb, T., III, Winkler, M.G., and Wright, H.E., Jr., 1988, Climatic changes of the last 18,000 years: observations and model simulations: Science, v. 241, p. 1043–1052.

Anderson, R.S., 1994, Evolution of the Santa Cruz Mountains, California, through tectonic growth and geomorphic decay: Journal of Geophysical Research, v. 99, p. 20,161–20,179.

Anderson, R.S., and Humphrey, N.F., 1990, Interaction of weathering and transport processes in the evolution of arid landscapes, *in* Cross, T.A., ed., Quantitative Dynamic Stratigraphy: Englewood Cliffs, NJ, Prentice-Hall, p. 349–361.

Anderson, R.S., and MacGregor, K.C., 1998, The role of glacial erosion in mountain range evolution: EOS (Transactions of the American Geophysical Union), v. 79, p. 337.

Anderson, R.S., and Menking, K.M., 1994, The Santa Cruz marine terraces: evidence for two coseismic uplift mechanisms: Geological Society of America Bulletin, v. 106, p. 649–664.

Anderson, R.S., Densmore, A.L., and Ellis, M.A., 1999, The generation and degradation of marine terraces: Basin Research, v. 11, p. 7–20.

Anderson, R.S., Repka, J.L., and Dick, G.S., 1996, Explicit treatment of inheritance in dating depositional surfaces using in situ ^{10}Be and ^{26}Al: Geology, v. 24, p. 47–51.

Anderson, S.P., and Anderson, R.S., 1990, Debris-flow benches; dune-contact deposits record paleo-sand dune positions in North Panamint Valley, Inyo County, California: Geology, v. 18, p. 524–527.

Atwater, B.F., 1992, Geologic evidence for earthquakes during the past 200 years along the Copalis River, southern coastal Washington: Journal of Geophysical Research, v. 97, p. 1901–1919.

Atwater, B.F., and Yamaguchi, D.K., 1991, Sudden, probably coseismic submergence of Holocene trees and grass in coastal Washington State: Geology, v. 19, p. 706–709.

Atwater, B.F., Nelson, A.R., Clague, J.J., Carver, G.A., Yamaguchi, D.K., Bobrowsky, P.T., Bourgeois, J., Darienzo, M.E., Grant, W.C., Hemphill-Haley, E., Kelsey, H.M., Jacoby, G.C., Nishenko, S.P., Palmer, S.P., Peterson, C.D., and Reinhart, M.A., 1995, Summary of coastal geologic evidence for past great earthquakes at the Cascadia subduction zone: Earthquake Spectra, v. 11, p. 1–18.

Atwater, B.F., Stuiver, M., and Yamaguchi, D.K., 1991, Radiocarbon test of earthquake magnitude at the Cascadia subduction zone: Nature, v. 353, p. 156–158.

Avouac, J.-P., 1993, Analysis of scarp profiles: evaluation of errors in morphologic dating: Journal of Geophysical Research, v. 98, p. 6745–6754.

Avouac, J.-P., and Peltzer, G., 1993, Active tectonics in southern Xinjiang, China: analysis of terrace riser and normal fault scarp degradation along the Hotan-Qira fault system: Journal of Geophysical Research, v. 98, p. 21,773–21,807.

Avouac, J.-P., Tapponnier, P., Bai, M., You, H., and Wang, G., 1993, Active thrusting and folding along the northern Tien Shan and late Cenozoic rotation of the Tarim relative to Dzungaria and Kazakhstan: Journal of Geophysical Research, v. 98, p. 6755–6804.

Axelrod, D.I., 1957, Late Tertiary floras and the Sierra Nevada uplift: Geological Society of America Bulletin, v. 68, p. 19–46.

Bada, J.L., 1972, The dating of fossil bones using the racemization of isoleucine: Earth and Planetary Science Letters, v. 15, p. 223–231.

Bada, J.L., Luyendyk, B.P., and Maynard, J.B., 1970, Marine sediments; dating by the racemization of amino acids: Science, v. 170, p. 730–732.

Bailey, R.A., Dalrymple, G.B., and Lanphere, M.A., 1976, Volcanism, structure, and geochronology of Long Valley caldera, Mono Country, California: Journal of Geophysical Research, v. 81, p. 725–744.

Baker, D.M., Lillie, R.J., Yeats, R.S., Johnson, G.D., Yousuf, M., and Zamin, A.S.H., 1988, Development of the Himalayan thrust zone: Salt Range, Pakistan: Geology, v. 16, p. 3–7.

Bakun, W.H., and McEvilly, T.V., 1984, Recurrence models and Parkfield, California, earthquakes: Journal of Geophysical Research, v. 89, p. 3051–3058.

Bard, E., Arnold, M., Hamelin, B., Tisnerat-Laborde, N., and Cabioch, G., 1998, Radiocarbon calibration by means of mass spectrometric $^{230}Th/^{234}U$ and ^{14}C ages of corals; an updated database including samples from Barbados, Mururoa and Tahiti: Radiocarbon, v. 40, p. 1085–1092.

Bard, E., Hamelin, B., Fairbanks, R.G., and Zindler, A., 1990, Calibration of the ^{14}C timescale over the past 30,000 years using mass spectrometer U-Th ages from Barbados corals: Nature, v. 345, p. 405.

Beanland, S., and Clark, M.M., 1994, The Owens Valley fault zone, eastern California, and surface faulting associated with the 1872 earthquake: U. S. Geological Survey Bulletin, v. B 1982, p. 29.

Beaumont, C., Ellis, S., Hamilton, J., and Fullsack, P., 1996, Mechanical model for subduction-collision tectonics of Alpine-type compressional orogens: Geology, v. 24, p. 675–678.

Beaumont, C., Fullsack, P., and Hamilton, J., 1992, Erosional control of active compressional orogens, *in* McClay, K.R., ed., Thrust Tectonics: London, Chapman and Hall, p. 1–18.

Bechtel, T.D., Forsyth, D.W., Sharpton, V.L., and Grieve, R.A.F., 1990, Variations in effective elastic thickness of the North American lithosphere: Nature, v. 343, p. 636–638.

Benedict, J.B., 1967, Recent glacial history of an alpine area in the Colorado Front Range, U.S.A.; Part 1, Establishing a lichen-growth curve: Journal of Glaciology, v. 6, p. 817–832.

Benson, L.V., Currey, D.R., Dorn, R.I., Lajoie, K.R., Oviatt, C.G., Robinson, S.W., Smith, G.I., and Stine, S., 1990, Chronology of expansion and contraction of four Great Basin lakes during the past 35,000 years: Palaeogeography, Palaeoclimatology, Palaeoecology, v. 78, p. 241–286.

Berger, G.W., 1988, Dating Quaternary events by luminescence, *in* Easterbrook, D.J., ed., Dating Quaternary sediments: Boulder, Geological Society of America Special Paper 227, p. 13–50.

Beroza, G.C., and Jordan, T.H., 1990, Searching for slow and silent earthquakes using free oscillations: Journal of Geophysical Research, v. 95, p. 2485–2510.

Beschel, R.E., 1961, Dating rock surfaces by lichen growth and its application to glaciology and physiography (lichenometry): Geology of the Arctic, v. 2, p. 1044–1062.

Biddle, K.T., and Christie-Blick, N., 1985, Strike-slip deformation, basin formation, and sedimentation, *in* Biddle, K.T., and Christie-Blick, N., eds., Strike-slip deformation, basin formation, and sedimentation: Society of Economic Paleontologists and Mineralogists Special Publication 37, p. 375–385.

Bierman, P., and Gillespie, A., 1991, Range fires; a significant factor in exposure-age determination and geomorphic surface evolution: Geology, v. 19, p. 641–644.

Bierman, P.R., 1994, Using *in situ* produced cosmogenic isotopes to estimate rates of landscape evolution; a review from the geomorphic perspective: Journal of Geophysical Research, v. 99, p. 13,885–13,896.

Bierman, P.R., and Gillespie, A.R., 1991, Accuracy of rock-varnish chemical analyses; implications for cation-ratio dating: Geology, v. 19, p. 196–199.

Bilham, R., Larson, K., Freymuller, J., and Project Idylhim members, 1997, GPS measurements of present-day convergence across the Nepal Himalaya: Nature, v. 386, p. 61–64.

Birkeland, P.W., 1990, Soil-geomorphic research; a selective overview: Geomorphology, v. 3, p. 207–224.

Bloch, R.B., von Huene, R., Hart, P.E., and Wentworth, C.M., 1993, Style and magnitude of tectonic shortening normal to the San Andreas fault across the Pyramid Hills and Kettleman Hills South Dome, California: Geological Society of America Bulletin, v. 105, p. 464–478.

Bloom, A.L., Broecker, W.S., Chappell, J.M., Matthews, R.K., and Mesolella, K.J., 1974, Quaternary sea level fluctuations on a tectonic coast: New $^{230}Th/^{234}U$dates from the Huon Peninsula, New Guinea: Quaternary Research, v. 4, p. 185–205.

Blum, J.D., Gazis, C.A., Jacobson, A.D., and Chamberlain, C.P., 1998, Carbonate versus silicate weathering in the Raikhot watershed within the High Himalayan Crystalline Series: Geology, v. 26, p. 411–414.

Blythe, A.E., Burbank, D.W., Farley, K., and Fielding, E.J., 2000, Structural and topographic evolution of the central Transverse Ranges, California, from apatite fission-track, (U-Th)/He and DEM analyses: Basin Research, v. 12, p. 97–114.

Blythe, A.E., Fielding, E.J., and Burbank, D.W., 1996, Morphology as a function of bedrock uplift and climate: a case study of the Transverse Ranges, Southern California, from apatite fission-track and DEM analyses: Eos (American Geophysical Union Transactions), v. 77, p. 644.

Bock, Y., Agnew, D.C., Fang, P., Genrich, J.F., Hager, B.H., Herring, T.A., Hudnut, K.W., King, R.W., Larsen, S., Minster, J.B., Stark, K., Wdowinski, S., and Wyatt, F.K., 1993, Detection of crustal deformation from the Landers earthquake using continuous geodetic measurements: Nature, v. 361, p. 337–340.

Braun, J., and Sambridge, M., 1997, Modelling landscape evolution on geological time scales: a new method based on irregular spatial discretization: Basin Research, v. 9, p. 27–52.

Brown, E.T., Stallard, R.F., Larsen, M.C., Raisbeck, G.M., and Yiou, F., 1995, Denudation rates determined from the accumulation of in situ-produced ^{10}Be in the Luquillo experimental forest, Puerto Rico: Earth and Planetary Science Letters, v. 129, p. 193–202.

Brozovic, N., Burbank, D.W., and Meigs, A.J., 1997, Climatic limits on landscape development in the northwestern Himalaya: Science, v. 276, p. 571–574.

Brozovic, N., Burbank, D.W., Fielding, E., and Meigs, A.J., 1995, The spatial and temporal topographic evolution of Wheeler Ridge California: New insights from digital elevation data: Geological Society of America Abstracts with Programs, v. 27, p. 396.

Brune, J.N., 1996, Precariously balanced rocks and ground-motion maps for southern California: Bulletin of the Seismological Society of America, v. 86, p. 43–54.

Bucknam, R.C., and Anderson, R.E., 1979, Estimation of fault-scarp ages from a scarp-height-slope-angle relationship: Geology, v. 7, p. 11–14.

Bull, W.B., 1964, Geomorphology of segmented alluvial fans in western Fresno County, California: U.S. Geological Survey Professional Paper 352-E, p. 89–129.

Bull, W.B., 1991, Geomorphic responses to climatic change: London, Oxford University Press, 326 p.

Bull, W.B., 1996, Dating San Andreas fault earthquakes with lichenometry: Geology, v. 24, p. 111–114.

Bull, W.B., and Brandon, M.T., 1998, Lichen dating of earthquake-generated regional rockfall events, Southern Alps, New Zealand: Geological Society of America Bulletin, v. 110, p. 60–84.

Bull, W.B., and Cooper, A.F., 1986, Uplifted marine terraces along the Alpine fault, New Zealand: Science, v. 234, p. 1225–1228.

Bull, W.B., and McFadden, L.D., 1977, Tectonic geomorphology north and south of the Garlock Fault, California, *in* Doehring, D.O., ed., Geomorphology in arid regions: Binghamton, N.Y., State University of New York at Binghamton, p. 115–138.

Bull, W.B., King, J., Kong, F., Moutoux, T., and Phillips, W.M., 1994, Lichen dating of coseismic landslide hazards in alpine mountains: Geomorphology, v. 10, p. 253–264.

Bullard, T.F., and Lettis, W.R., 1993, Quaternary fold deformation associated with blind thrusting, Los Angeles basin, California: Journal of Geophysical Research, v. 98, p. 8349–8369.

Burbank, D.W., 1992, Causes of recent Himalayan uplift deduced from deposited patterns in the Ganges basin: Nature, v. 357, p. 680–682.

Burbank, D.W., and Beck, R.A., 1989, Early Pliocene uplift of the Salt Range: temporal constraints on thrust wedge development, northwest Himalaya, Pakistan, *in* Malinconico, L.L., and Lillie, R.J., ed., Tectonics and Geophysics of the Western Himalaya, Geological Society of America Special Paper 232, p. 113–128.

Burbank, D.W., and Beck, R.A., 1991, Rapid, long-term rates of denudation: Geology, v. 19, p. 1169–1172.

Burbank, D.W., and Raynolds, R.G.H., 1984, Sequential late Cenozoic structural disruption of the northern Himalayan foredeep: Nature, v. 311, p. 114–118.

Burbank, D.W., and Raynolds, R.G.H., 1988, Stratigraphic keys to the timing of thrusting in terrestrial foreland basins: Applications to the Northwestern Himalaya, *in* Kleinspehn, K.L., and Paola, C., ed., New Perspectives in Basin Analysis: New York, Springer-Verlag, p. 331–351.

Burbank, D.W., and Tahirkheli, R.A.K., 1985, Magnetostratigraphy, fission-track dating, and stratigraphic evolution of the Peshawar intermontane basin, northern Pakistan: Geological Society of America Bulletin, v. 96, p. 530–552.

Burbank, D.W., and Vergés, J., 1994, Reconstruction of topography and related depositional systems during active thrusting: Journal of Geophysical Research, v. 99, p. 20,281–20,297.

Burbank, D.W., Leland, J., Fielding, E., Anderson, R.S., Brozovic, N., Reid, M.R., and Duncan, C., 1996, Bedrock incision, rock uplift, and threshold hillslopes in the northwestern Himalaya: Nature, v. 379, p. 505–510.

Burbank, D.W., Meigs, A., and Brozovic, N., 1996, Interactions of growing folds and coeval depositional systems: Basin Research, v. 8, p. 199–223.

Burbank, D.W., McLean, J.K., Bullen, M., Abdrakhmatov, K.Y., and Miller, M.G., 1999, Partitioning of intermontane basins by thrust-related folding, Tien Shan, Kyrgyzstan: Basin Research, v. 11, p. 75–92.

Burchfiel, B.D., Zhileng, C., Hodges, K.V., Yuping, L., Royden, L.H., Changrong, D., and Jiene, X., 1992, The South Tibetan detachment system, Himalayan orogen: Extension contemporaneous with and parallel to shortening in a collisional mountain belt, 41 p.

Burg, J.P., and Chen, G.M., 1984, Tectonics and structural zonation of southern Tibet: Nature, v. 311, p. 219–223.

Bursik, M.I., and Gillespie, A.R., 1993, Late Pleistocene glaciation of Mono Basin, California: Quaternary Research, v. 39, p. 24–35.

Carslaw, H.S., and J.C.J., 1986, Conduction of heat in solids: New York, Oxford University Press, 510 p.

Carson, M.A., and Kirkby, M.J., 1972, Hillslope form and process: London, Cambridge University Press, 475 p.

Carter, W.E., Robertson, D.S., and Mackay, J.R., 1985, Geodetic radio interferometric surveying: Applications and result: Journal of Geophysical Research, v. 90, p. 4577–4588.

Cartwright, J.A., Trudgill, B.D., and Mansfield, C.S., 1995, Fault growth by segment linkage: an explanation for scatter in maximum displacement and trace length data from the Canyonlands grabens of SE Utah: Journal of Structural Geology, v. 17, p. 1319–1326.

Carver, G.A., Jayko, A.S., Valentine, D.W., and Li, W.H., 1994, Coastal uplift associated with the 1992 Cape Mendocino earthquake, Northern California: Geology, v. 22, p. 195–198.

Castle, R.O., Estrem, J.E., and Savage, J.C., 1984, Uplift across the Long Valley caldera, California: Journal of Geophysical Research, v. 89, p. 11,507–11,516.

Cerling, T.E., and Craig, H., 1994, Geomorphology and in-situ cosmogenic isotopes: Annual Review of Earth and Planetary Sciences, v. 22, p. 273–317.

Chadwick, O.A., Hall, R.D., and Phillips, F.M., 1997, Chronology of Pleistocene glacial advances in the Central Rocky Mountains: Geological Society of America Bulletin, v. 109, p. 1443–1452.

Chamberlain, C.P., Poage, M.A., Reynolds, R.C., and Craw, D., 1996, The topographic evolution of the Southern Alps, New Zealand, from the isotopic analysis of clay minerals: Geological Society of America Abstracts with Programs, v. 28, p. 249.

Chappell, J., 1974, Geology of coral terraces, Huon Peninsula, New Guinea: A study of Quaternary tectonic movements and sea-level changes: Geological Society of America Bulletin, v. 85, p. 553–570.

Chappell, J., Omura, A., Esat, T., McCulloch, M., Pandolfi, J., Ota, Y., and Pillans, B., 1996, Reconciliation of late Quaternary sea levels derived from coral terraces at Huon Peninsula with deep sea oxygen isotope records: Earth and Planetary Science Letters, v. 141, p. 227–236.

Chediya, O.K., 1986, Morphostructure and neo-tectonics of the Tien Shan: Frunze, Academia Nauk Kyrgyz CCP, 313 p.

Chorley, R.J., Schumm, S.A., and Sugden, D.E., 1984, Geomorphology: London, Methuen, 605 p.

Christie-Blick, N., and Biddle, K.T., 1985, Deformation and basin formation along strike-slip faults, *in* Biddle, K.T., and Christie-Blick, N., eds., Strike-slip deformation, basin formation, and sedimentation, Society of Economic Paleontologists and Mineralogists, Spec. Pub. 37, p. 1–34.

Church, M., and Slaymaker, O., 1989, Disequilibrium of Holocene sediment yield in glaciated British Columbia: Nature, v. 337, p. 452–454.

Clark, D.H., Bierman, P.R., and Larsen, P., 1995, Improving in situ cosmogenic chronometers: Quaternary Research, v. 44, p. 367–377.

Coates, R.J., Frey, H., Bosworth, J., and Mead, C.D., 1985, Space age geodesy: The NASA crustal dynamics project: IEEE Transactions on Geoscience and Remote Sensing, v. GE-23, p. 358–368.

Cohen, S., Holdahl, S., Caprette, D., Hilla, S., Safford, R., and Schultz, D., 1995, Uplift of the Kenai Peninsula, since the 1964 Prince William Sound earthquake: Journal of Geophysical Research, v. 100, p. 2031–2038.

Colman, S.M., 1986, Levels of time information in weathering measurements, with examples from weathering rinds on volcanic clasts in the Western United States, *in* Colman, S.M., and Dethier, D.P., eds., Rates of chemical weathering of rocks and minerals: Orlando, Academic Press, p. 379–393.

Colman, S.M., and Dethier, D.P., 1986, Rates of chemical weathering of rocks and minerals: Orlando, Academic Press, 603 p.

Colman, S.M., and Pierce, K.L., 1992, Varied records of early Wisconsinan alpine glaciation in the Western United States derived from weathering-rind thickness, *in* Clark, P.U., and Lea, P.D., eds., The last interglacial-glacial transition in North America, Geological Society of America Special Paper 270, p. 269–278.

Colman, S.M., and Watson, K., 1983, Ages estimated from a diffusion equation model for scarp degradation: Science, v. 221, p. 263–265.

Cotton, C.A., 1926, Geomorphology of New Zealand, Part I. Systematic: Wellington, New Zealand Board of Science and Art, 462 p.

Cowie, P.A., and Scholz, C.H., 1992, Displacement-length scaling relationship for faults: data synthesis and discussion: Journal of Structural Geology, v. 14, p. 1149–1156.

Cox, A., Doell, R.R., and Dalrymple, G.B., 1963, Geomagnetic polarity epochs and Pleistocene geochronometry: Nature, v. 198, p. 1049–1051.

Cox, A., Doell, R.R., and Dalrymple, G.B., 1964, Reversals of the earth's magnetic field: Science, v. 144, p. 1537–1543.

Cox, R.T., 1994, Analysis of drainage-basin symmetry as a rapid technique to identify areas of possible Quaternary tilt-block tectonics: an example from the Mississippi embayment: Geological Society of America Bulletin, v. 104, p. 571–581.

Craw, D., Koons, P.O., Winslow, D., Chamberlain, C.P., and Zeitler, P., 1994, Boiling fluids in a region of rapid uplift, Nanga Parbat massif, Pakistan: Earth and Planetary Science Letters, v. 128, p. 169–182.

Creer, K.M., 1962, The dispersion of the geomagnetic field due to secular variation and its determination for remote times from paleomagnetic data: Journal of Geophysical Research, v. 67, p. 3461–3476.

Creer, K.M., 1967, Application of rock magnetism to investigations of the secular variation during geological time, magnetism and the cosmos: Univ. Newcastle upon Tyne, NATO Advanced Study Inst. Planetary and Stellar Magnetism, p. 45–59.

Crider, J.G., and Pollard, D.D., 1996, Breached normal-fault relays and the generation of fault patterns; results from 3D numerical models and field observation: Geological Society of America, 28th annual meeting, Abstracts with Programs, v. 28, p. 242.

Crone, A.J., and Machette, M.N., 1984, Surface faulting accompanying the Borah Peak earthquake, central Idaho: Geology, v. 12, p. 664–667.

Crook, R., Jr., 1986, Relative dating of Quaternary deposits based on P-wave velocities in weathered granitic clasts: Quaternary Research, v. 25, p. 281–292.

Crook, R., Jr., and Gillespie, A.R., 1986, Weathering rates in granitic boulders measured by P-wave speeds, *in* Colman, S.M., and Dethier, D.P., eds., Rates of chemical weathering of rocks and minerals: Orlando, Academic Press, p. 395–417.

Crouch, S.L., and Starfield, A.M., 1983, Boundary element methods in solid mechanics: with applications in rock mechanics and geological engineering: London, Allen & Unwin.

Culling, W.E.H., 1960, Analytical theory of erosion: Journal of Geology, v. 68, p. 336–344.

Culling, W.E.H., 1963, Soil creep and the development of hillside slopes: Journal of Geology, v. 71, p. 127–161.

Culling, W.E.H., 1965, Theory of erosion on soil-covered slopes: Journal of Geology, v. 73, p. 230–254.

Culmann, C., 1875, Die Graphische Statik: Zurich, Meyer and Zeller.

Davis, W.M., 1899, The geographical cycle: Geographical Journal, v. 14, p. 481–504.

Dawers, N.H., and Anders, M.H., 1995, Displacement-length scaling and fault linkage: Journal of Structural Geology, v. 17, p. 607–614.

Dawers, N.H., Anders, M.H., and Scholz, C.H., 1993, Growth of normal faults: Displacement-length scaling: Geology, v. 21, p. 1107–1110.

Deng, Q., Zhang, P., and Chen, S., 1986, Structure and deformation character of strike-slip fault zones: Pure and Applied Geophysics, v. 124, p. 203–223.

Densmore, A.L., Ellis, M.A., and Anderson, R.S., 1998, Landsliding and the evolution of normal-fault-bounded mountains: Journal of Geophysical Research, v. 103, p. 15,203–15,219.

Denton, G.H., and Karlen, W., 1973, Lichenometry: its application to Holocene moraine studies in southern Alaska and Swedish Lapland: Arctic and Alpine Research, v. 5, p. 347–372.

Dietrich, W.E., Wilson, C.J., Montgomery, D.R., McKean, J., and Bauer, R., 1992, Erosion thresholds and land surface morphology: Geology, v. 20, p. 675–679.

Dixon, T.H., 1991, An introduction to the global positioning systems and some geological applications: Reviews of Geophysics, v. 29, p. 249–276.

Dolan, J.F., Sieh, K., Rockwell, T.K., Yeats, R.S., Shaw, J., Suppe, J., Huftile, G.J., and Gath, E.M., 1995, Prospects for larger or more frequent earthquakes in the Los Angeles metropolitan region: Science, v. 267, p. 199–205.

Douglas, B.C., 1991, Global sea level rise: Journal of Geophysical Research, v. 96, p. 6981–6992.

Dowdeswell, J.A., Unwin, B., Nuttall, A.M., and Wingham, D.J., 1999, Velocity structure, flow instability and mass flux on a large Arctic ice cap from satellite radar interferometry: Earth and Planetary Science Letters, v. 167, p. 131–140.

Duller, G.A.T., 1996, Recent developments in luminescence dating of Quaternary sediments: Progress in Physical Geography, v. 20, p. 127–145.

Edgar, D.E., 1973, Geomorphic and hydraulic properties of laboratory rivers [M.Sc. thesis], Colorado State University, Fort Collins, 156 p.

Edmond, J.M., 1992, Himalayan tectonics, weathering processes, and the strontium isotope record in marine limestones: Science, v. 258, p. 1594–1597.

Edwards, R.L., Beck, J.W., Burr, G.S., Donahue, D.J., Chappell, J.M., Bloom, A.L., Druffel, E.R.M., and Taylor, F.W., 1993, A large drop in atmospheric $^{14}C/^{12}C$ and reduced melting in the Younger Dryas, documented with ^{230}Th ages of corals: Science, v. 260, p. 962–968.

Edwards, R.L., Taylor, F.W., and Wasserburg, G.J., 1988, Dating earthquakes with high-precision thorium-230 ages of very young corals: Earth and Planetary Science Letters, v. 90, p. 379–381.

Ellis, M.A., Densmore, A.L., and Anderson, R.S., 1999, Evolution of mountainous topography in the Basin and Range Province: Basin Research, v. 11, p. 21–42.

England, P., and Molnar, P., 1990, Surface uplift, uplift of rocks, and exhumation of rocks: Geology, v. 18, p. 1173–1177.

Erslev, E.A., 1991, Trishear fault-propagation folding: Geology, v. 19, p. 617–620.

Fairbanks, R.G., 1989, A 17,000-year glaci-eustatic sea-level record: influence of glacial melting rates on the Younger

Dryas event and deep-ocean circulation: Nature, v. 342, p. 637–642.

Feigl, K.L., Agnew, D.C., Bock, Y., Dong, D., Donnellan, A., Hager, B.H., Herring, T.A., Jackson, D.D., Jordan, T.H., King, R.W., Larsen, S., Larson, K.M., Murray, M.H., Shen, Z., and Webb, F.H., 1993, Space geodetic measurement of crustal deformation in central and southern California, 1984–1992: Journal of Geophysical Research, v. 98, p. 21,677-21,712.

Fielding, E.J., Isacks, B.L., Barazangi, M., and Duncan, C., 1994, How flat is Tibet?: Geology, v. 22, p. 163–167.

Fitch, T.J., and Scholz, C.H., 1971, Mechanism of underthrusting in southwest Japan: a model of convergent plate interactions: Journal of Geophysical Research, v. 76, p. 7260–7292.

Fitzgerald, P.G., Sorkhabi, R.B., Redfield, T.F., and Stump, E., 1995, Uplift and denudation of the central Alaska Range: a case study in the use of apatite fission track thermochronology to determine absolute uplift parameters: Journal of Geophysical Research, v. 100, p. 20,175–20,191.

Flemings, P.B., and Jordan, T.E., 1989, A synthetic stratigraphic model of foreland basin development: Journal of Geophysical Research, v. 94, p. 3851–3866.

Flemings, P.B., and Jordan, T.E., 1990, Stratigraphic modeling of foreland basins: interpreting thrust deformation and lithospheric rheology: Geology, v. 18, p. 430–434.

Fort, M., 1987, Sporadic morphogenesis in a continental subduction setting: an example from the Annapurna Range, Nepal Himalaya: Zeitschrift für Geomorphologie, v. 63, p. 9–36.

Fritts, H.C., 1976, Tree rings and climate: Academic Press, 567 p.

Fruneau, B., Achache, J., and Delacourt, C., 1996, Observation and modelling of the Saint-Etienne-de-Tinee landslide using SAR interferometry: Tectonophysics, v. 265, p. 181–190.

Galewsky, J., Silver, E.A., Gallup, C.D., Edwards, R.L., and Potts, D.C., 1996, Foredeep tectonics and carbonate platform dynamics in the Huon Gulf, Papua New Guinea: Geology, v. 24, p. 819–822.

Galindo-Zaldivar, J., Jabaloy, A., Serrano, I., Morales, J., and González-Lodeiro, F., 1999, Recent and present-day stresses in the Granada Basin (Betic Cordilleras): Example of a late Miocene-present-day extensional basin in a convergent plate boundary: Tectonics, p. 686-702.

Galy, A., France-Lanord, C., Hutrez, J.E., and Lucazeau, F., 1996, Mass transfer during Himalayan erosion during the monsoon: mineralogical and geochemical constraints: EOS (Transactions of the American Geophysical Union), v. 77, p. 236.

Gardner, T.W., 1983, Experimental study of knickpoint migration and longitudinal profile evolution in cohesive homogeneous material: Geological Society of America Bulletin, v. 94, p. 664–672.

Gardner, T.W., Jorgensen, D.W., Shuman, C., and Lemieux, C.R., 1987, Geomorphic and tectonic process rates: effects of measured time interval: Geology, v. 15, p. 259–261.

Gaudemer, Y., Tapponier, P., and Turcotte, D., 1989, River offsets across active strike-slip faults: Annales Tectonicae, v. 3, p. 55–76.

Gawthorpe, R.L., and Hurst, J.M., 1993, Transfer zones in extensional basins: their structural style and influence on drainage development and stratigraphy: Journal of the Geological Society of London, v. 150, p. 1137–1152.

Ghose, S., Mellors, R.J., Hamburger, M.W., Pavlis, T.L., Korjenkov, A.M., Omuraliev, M., and Mamyrov, E., 1996, The M_s = 7.3 1992 Suusamyr, Kyrgyzstan, earthquake in the Tien Shan; 2, Aftershock focal mechanisms and surface deformation: Bulletin of the Seismological Society of America, v. 87, p. 23–38.

Gibbons, A.B., Megeath, J.D., and Pierce, K.L., 1984, Probability of moraine survival in a succession of glacial advances: Geology, v. 12, p. 327–330.

Gilbert, G.K., 1877, Report on the geology of the Henry Mountains [Utah]: Publication of the Powell Survey, 160 p.

Gilbert, G.K., 1879, Geology of the Henry Mountains (Utah): Washington, D.C., United States Government Printing Office, 170 p.

Gilbert, G.K., 1890, Lake Bonneville: United States Geological Survey Monograph 1, 438 p.

Gilbert, G.K., 1909, The convexity of hilltops: Journal of Geology, p. 344–350.

Gillespie, A., and Molnar, P., 1995, Asynchronous maximum advances of mountain and continental glaciers: Reviews of Geophysics, v. 33, p. 311–364.

Gillespie, A.R., 1982, Quaternary glaciation and tectonism in the southeastern Sierra Nevada, Inyo County, California, California Institute of Technology, Pasadena, CA, United States, 738 p.

Gomberg, J., and Ellis, M., 1994, Topography and Tectonics of the Central New Madrid Seismic Zone-Results of Numerical Experiments Using a Three-Dimensional Boundary Element Program: Journal of Geophysical Research, v. 99, p. 20,299–20,310.

Gomberg, J.S., 1993, Tectonic deformation in the New Madrid seismic zone; inferences from map view and cross-sectional boundary element models: Journal of Geophysical Research, v. 98, p. 6639–6664.

Gomberg, J.S., and Ellis, M., 1993, 3D-DEF; a user's manual (a three-dimensional, boundary element modeling program): USGS Open File Report OF 93-0547, p. 15.

Granger, D.E., Kirchner, J.W., and Finkel, R., 1996, Spatially averaged long-term erosion rates measured from in situ-produced cosmogenic nuclides in alluvial sediment: Journal of Geology, v. 104, p. 249–257.

Grapes, R., and Wellman, H., 1988, The Wairarapa fault, Victoria University of Wellington, p. 54.

Grapes, R.H., and Wellman, H.W., 1993, Field guide to the Wharekauhau Thrust (Palliser Bay) and Wairarapa Fault (Pigeon Bush): New Zealand Geological Society Miscellaneous Publication, v. 79B, p. 27–44.

Gregory, K., 1994, Palaeoclimate and palaeoelevation of the 35 Ma Florrisant flora, Front Range, Colorado: Palaeoclimates, v. 1, p. 23–57.

Gregory, K.M., and Chase, C.G., 1992, Tectonic significance of paleobotanically estimated climate and altitude of the late Eocene erosion surface, Colorado: Geology, v. 20, p. 581–585.

Grootes, P.M., 1983, Radioactive isotopes in the Holocene, *in* Wright, H.E., ed., Volume 2 of Late Quaternary Environments of the United States: Minneapolis, University of Minnesota, p. 86–105.

Gupta, S., Cowie, P.A., Dawars, N.H., and Underhill, J.R., 1998, A mechanism to explain rift-basin subsidence and stratigraphic patterns through fault-array evolution: Geology, v. 26, p. 595–598.

Hack, J.T., 1973, Stream-profile analysis and stream-gradient indices: United States Geological Survey Journal of Research, v. 1, p. 421–429.

Hack, J.T., 1975, Dynamic equilibrium and landscape evolution, *in* Melhorn, W.N., and Flemal, R.C., eds., Theories of Landform Evolution: Boston, Allen and Unwin, p. 87–102.

Hallet, B., Walder, J.S., and Stubbs, C.W., 1991, Weathering by segregation ice growth in microcracks at sustained subzero temperatures: Verification from an experimental study using acoustic emissions: Permafrost and Periglacial Processes, v. 2, p. 283–300.

Hallet, B., and Putkonen, J., 1994, Surface dating of dynamic landforms: Young boulders on aging moraines: Science, v. 265, p. 937–940.

Hallet, B., Hunter, L., and Bogen, J., 1996, Rates of erosion and sediment evacuation by glaciers: a review of field data and their implications: Global and Planetary Change, v. 12, p. 213–235.

Hancock, G.S., Anderson, R.S., Whipple, K.X., and Wohl, E.E., 1998, Beyond power; bedrock river incision process and form: Rivers over rock; fluvial processes in bedrock channels, Geophysical Monograph, v. 107, p. 35–60.

Hanks, T.C., Bucknam, R.C., LaJoie, K.R., and Wallace, R.E., 1984, Modification of wave-cut and faulting controlled landforms: Journal of Geophysical Research, v. 89, p. 5771–5790.

Harbor, J.M., 1992, Numerical modeling of the development of U-shaped valleys by glacial erosion: Geological Society of America Bulletin, v. 104, p. 1364–1375.

Harbor, J.M., Hallet, B., and Raymond, C.F., 1988, A numerical model of landform development by glacial erosion: Nature, v. 333, p. 347–349.

Harden, J.W., 1982, A quantitative index of soil development from field descriptions; examples from a chronosequence in central California: Geoderma, v. 28, p. 1–28.

Hardy, S., and Ford, M., 1997, Numerical modeling of trishear fault propagation folding: Tectonics, v. 16, p. 841–854.

Hardy, S., and Poblet, J., 1994, Geometric and numerical model of progressive limb rotation in detachment folds: Geology, v. 22, p. 371–374.

Harp, E.L., and Jibson, R.W., 1996, Landslides triggered by the 1994 Northridge, California, earthquake: Bulletin of the Seismological Society of America, v. 86, p. S319–S332.

Harris, R.A., and Day, S.M., 1993, Dynamics of fault interaction; parallel strike-slip faults: Journal of Geophysical Research, v. 98, p. 4461–4472.

Harris, R.A., Simpson, R.W., and Reasenberg, P.A., 1995, Influence of static stress changes on earthquake locations in southern California: Nature, v. 375, p. 221–224.

Harrison, T.M., Copeland, P., Kidd, W.S.F., and Yin, A., 1992, Raising Tibet: Science, v. 255, p. 1663–1670.

Harrison, T.M., Ryerson, F.J., Le Fort, P., Yin, A., Lovera, O.M., and Catlos, E.J., 1997, A late Miocene-Pliocene origin for the central Himalayan inverted metamorphism: Earth and Planetary Science Letters, v. 146, p. E1–E7.

Hearty, P.J., and Miller, G.H., 1987, Global trends in isoleucine epimerization. Data from the circum-Atlantic, the Mediterranean, and the South Pacific: Geological Society of America Abstracts with Program, v. 19, p. 698.

Heimsath, A.M., Dietrich, W.E., Nishiizumi, K., and Finkel, R.C., 1997, The soil production function and landscape equilibrium: Nature, v. 388, p. 358–361.

Heki, K., Miyazaki, S., and Tsuji, H., 1997, Silent fault slip following an interplate thrust earthquake at the Japan Trench: Nature, v. 386, p. 595–598.

Heller, P.L., Angevine, C.L., Winslow, N.S., and Paola, C., 1988, Two-phase stratigraphic model of foreland basin development: Geology, v. 16, p. 501–504.

Hemphill-Haley, E., 1995, Diatom evidence for earthquake-induced subsidence and tsunami 300 yr ago in southern coastal Washington: Geological Society of America Bulletin, v. 107, p. 367–378.

Herring, T.A., and others, 1986, Geodesy by radio interferometry: Evidence for contemporary plate motion: Journal of Geophysical Research, v. 91, p. 8341–8347.

Hickman, S.H., Healy, J.H., and Zoback, M.D., 1985, In situ stress, natural fracture distribution, and borehole elongation in the Auburn geotherm well, Auburn, New York: Journal of Geophysical Research, v. 90, p. 5497–5512.

Hodges, K., Bowring, S., Davidek, K., Hawkins, D., and Krol, M., 1998, Evidence for rapid displacement on Himalayan normal faults and the importance of tectonic denudation in the evolution of mountain ranges: Geology, v. 26, p. 483–486.

Hovius, N., 1996, Regular spacing of drainage outlets from linear mountain belts: Basin Research, v. 8, p. 29–44.

Hovius, N., 1998, Landslide-driven drainage network evolution in a pre-steady-state mountain belt: Finisterre Mountains, Papua New Guinea: Geology, v. 26, p. 1071–1074.

Hovius, N., Stark, C.P., and Allen, P.A., 1997, Sediment flux from a mountain belt derived by landslide mapping: Geology, v. 25, p. 231–234.

Howard, A.D., 1994, A detachment-limited model of drainage basin evolution: Water Resources Research, v. 30, p. 2261–2285.

Howard, A.D., and Kerby, G., 1983, Channel changes in badlands: Geological Society of America Bulletin, v. 94, p. 739–752.

Howard, A.D., Dietrich, W.E., and Seidl, M.A., 1994, Modeling fluvial erosion on regional to continental scales: Journal of Geophysical Research, v. 99, p. 13,971–13,986.

Howard, A.D., Summerfield, M.A., and Burt, T.P., 1997, Badland morphology and evolution; interpretation using a simulation model: Geomorphic processes/landscape evolution, Earth Surface Processes and Landforms, v. 22, p. 211–227.

Huber, N.K., 1981, The amount and timing of Late Cenozoic uplift and tilt of the central Sierra Nevada, California—evidence from the upper San Joaquin river basin: United States Geological Survey Professional Paper, 1191, 28 p.

Hummon, C., Schneider, C.L., Yeats, R.S., Dolan, J.F., Sieh, K.E., and Huftile, G.J., 1994, Wilshire fault: earthquakes in Hollywood?: Geology, v. 22, p. 291–294.

Humphrey, N.F., and Heller, P.L., 1995, Natural oscillations in coupled geomorphic systems: An alternative origin for cyclic sedimentation: Geology, v. 23, p. 499–502.

Hyndman, R.D., and Wang, K., 1995, The rupture zone of Cascadia great earthquakes from current deformation and the thermal regime: Journal of Geophysical Research, v. 100, p. 22,133–22,154.

Innes, J.L., 1984, Lichenometric dating of moraine ridges in Northern Norway; some problems of application: Geografiska Annaler. Series A: Physical Geography, v. 66, p. 341–352.

Innes, J.L., 1985, Lichenometry: Progress in Physical Geography, v. 9, p. 187–254.

Iverson, R.M., Schilling, S.P., and Vallance, J.W., 1998, Objective delineation of lahar-inundation hazard zones: Geological Society of America Bulletin, v. 110, p. 972–984.

Iwata, S., 1987, Mode and rate of uplift of the central Nepal Himalaya: Zeitschrift für Geomorphologie, v. Suppl. Bd. 63, p. 37–49.

Jackson, J., Haines, J., and Holt, W., 1994, A comparison of satellite laser ranging and seismicity data in the Aegean region: Geophysical Research Letters, v. 21, p. 2849–2852.

Jackson, J., Norris, R., and Youngson, J., 1996, The structural evolution of active fault and fold systems in central Otago, New Zealand: evidence revealed by drainage patterns: Journal of Structural Geology, v. 18, p. 217–234.

Jackson, M., and Bilham, R., 1994a, Constraints on Himalayan deformation inferred from vertical velocity fields in Nepal and Tibet: Journal of Geophysical Research, v. 99, p. 13,897-13,912.

Jackson, M.E., and Bilham, R., 1994b, 1992–1992 GPS measurements across the Nepal Himalaya: Geophysical Research Letters, v. 21, p. 1169–1172.

Jackson, M., Barrientos, S., Bilham, R., Kyestha, D., and Shrestha, B., 1992, Uplift in the Nepal Himalaya revealed by spirit leveling: Geophysical Research Letters, v. 19, p. 1539–1542.

Jacoby, G.C., Jr., Sheppard, P.R., and Sieh, K.E., 1988, Irregular recurrence of large earthquakes along the San Andreas fault: evidence from trees: Science, v. 241.

Johnson, C., Harbury, N., and Hurford, A.J., 1997, The role of extension in the Miocene denudation of the Nevado-Filábride Complex, Betic Cordillera (SE Spain): Tectonics, v. 16, p. 189–204.

Jorgensen, D.W., Harvey, M.D., Schumm, S.A., and Flam, L., 1993, Morphology and dynamics of the Indus River: Implications for the Mohen Jo Daro site, *in* Shroder, J.F., Jr., ed., Himalaya to the Sea: Geology, Geomorphology, and the Quaternary: London, Routledge, p. 288–326.

Kanamori, H., and Kikuchi, M., 1993, The 1992 Nicaragua earthquake; a slow earthquake associated with subducted sediments: Seismological Society of America, 88th annual meeting, v. 64, p. 13–14.

Kaufman, D.S., and Miller, G.H., 1992, Overview of amino acid geochronology: Comparative Biochemistry and Physiology, v. 102B, p. 199–204.

Kaufman, D.S., Miller, G.H., and Andrews, J.T., 1992, Amino acid composition as a taxonomic tool for molluscan fossils; an example from Pliocene-Pleistocene Arctic marine deposits: Geochimica et Cosmochimica Acta, v. 56, p. 2445–2453.

Keller, E.A., 1986, Investigation of active tectonics: use of surficial earth processes, Active Tectonics: Washington, D.C., National Academy Press, p. 136–147.

Keller, E.A., Bonkowski, M.S., Korsch, R.J., and Shlemon, R.J., 1982, Tectonic geomorphology of the San Andreas fault zone in the southern Indio Hills, Coachella Valley, California: Geological Society of America Bulletin, v. 93, p. 46–56.

Keller, E.A., Gurrola, L., and Tierney, T.E., 1999, Geomorphic criteria to determine direction of lateral propagation of reverse faulting and folding: Geology, v. 27, p. 515–518.

Keller, E.A., Zepeda, R.L., Rockwell, T.K., Ku, T.L., and Dinklage, W.S., 1998, Active tectonics at Wheeler Ridge, southern San Joaquin Valley, California: Geological Society of America Bulletin, v. 110, p. 298–310.

Kelsey, H.M., and Bockheim, J.G., 1994, Coastal landscape evolution as a function of eustasy and surface uplift rate, southern Cascadia margin, USA: Geological Society of America Bulletin, v. 106, p. 840–854.

King, G., and Ellis, M., 1990, The origin of large local uplift in extensional regions: Nature, v. 348, p. 689–693.

King, G., and Stein, R., 1983, Surface folding, river terrace deformation rate and earthquake repeat time in a reverse faulting environment: the Coalinga, California earthquake

of May, 1983: California Division of Mines and Geology Special Publication, v. 66, p. 261–274.

King, G.C.P., Stein, R.S., and Rundle, J.B., 1988, The growth of geological structure by repeated earthquakes 1. Conceptual framework: Journal of Geophysical Research, v. 93, p. 13,307-13,318.

Kooi, H., and Beaumont, C., 1994, Escarpment evolution on high-elevation rifted margins: insights derived from a surface processes model that combines diffusion, advection, and reaction: Journal of Geophysical Research, v. 99, p. 12,191-12,209.

Kooi, H., and Beaumont, C., 1996, Large-scale geomorphology: classical concepts reconciled and integrated with contemporary ideas via a surface processes model: Journal of Geophysical Research, v. 101, p. 3361–3386.

Koons, P.O., 1989, The topographic evolution of collisional mountain belts: A numerical look at the Southern Alps, New Zealand: American Journal of Science, v. 289, p. 1041–1069.

Koons, P.O., 1990, The two-sided orogen: collision and erosion from the sand box to the Southern Alps: Geology, v. 18, p. 679–682.

Ku, T.-L., 1976, The uranium-series methods of age determination: Annual Review of Earth and Planetary Sciences, v. 4, p. 347–379.

Lajoie, K.R., 1986, Coastal tectonics, Active Tectonics: Washington, D.C., National Academy Press, p. 95–124.

Lal, D., 1988, *In situ* produced cosmogenic isotopes in terrestrial rocks and some applications to geochronology: Annual Reviews of Earth and Planetary Sciences, v. 16, p. 355–388.

Lal, D., 1991, Cosmic ray labeling of erosion surfaces: *in situ* nuclide production rates and erosion: Earth and Planetary Science Letters, v. 104, p. 424–439.

Lambeck, K., 1988, Geophysical geodesy, the slow deformations of the Earth: Oxford, Clarendon.

Larsen, S., and Reilinger, R., 1992, Global positioning system measurements of deformations associated with the 1987 Superstition Hills earthquake: evidence for conjugate faulting: Journal of Geophysical Research, v. 97, p. 4885–4902.

Lavé, J., 1997, Tectonique et érosion: L'apport de la dynamique fluviale à l'étude sismotectonique de l'Himalaya du Népal central [Ph. D. thesis]: Paris, Université de Paris VII.

Leeder, M.R., and Jackson, J.A., 1993, The interaction between normal faulting and drainage in active extensional basins, with examples from the western United States and central Greece: Basin Research, v. 5, p. 79–102.

Leeder, M.R., Harris, T., and Kirkby, M.J., 1998, Sediment supply and climate change; implications for basin stratigraphy: Basin Research, v. 10, p. 7–18.

Leeder, M.R., Ord, D.M., and Collier, R., 1988, Development of alluvial fans and fan deltas in neotectonic extensional settings: implications for the interpretation of basin-fills, *in* Nemec, W., and Steel, R.J., eds., Fan Deltas, Sedimentology and Tectonics Settings, Blackie and Son, p. 173–185.

Leopold, L.B., and Maddock, T., 1953, Hydraulic geometry of streams and some physiographic implications: U. S. Geological Survey Professional Paper 252, 57 p.

Li, Y., Schweig, E.S., Tuttle, M.P., and Ellis, M.A., 1998, Evidence for large prehistoric earthquakes in the northern New Madrid seismic zone, central United States: Seismological Research Letters, v. 69, p. 270–276.

Libby, W.F., 1955, Radiocarbon dating: Chicago, University of Chicago Press, 175 p.

Lindvall, S.C., Rockwell, T.K., and Hudnut, K.W., 1989, Evidence for prehistoric earthquakes on the Superstition Hills fault from offset geomorphic features: Bulletin of the Seismological Society of America, v. 79, p. 342–361.

Lisowski, M., Savage, J.C., and Prescott, W.H., 1991, The velocity field along the San Andreas fault in central and southern California: Journal of Geophysical Research, v. 96, p. 8,369-8,389.

Little, T.A., Grapes, R. and Berger, G.W., 1998, Late Quaternary strike slip on the eastern part of the Awatere Fault, South Island, New Zealand: Geological Society of America Bulletin, v. 110, p. 127–148.

Locke, W.W., III, Andrews, J.T., and Webber, P.J., 1979, A manual for lichenometry: British Geomorphological Research Group Bulletin, v. 26, 47 p.

Lund, S.P., 1996, A comparison of Holocene paleomagnetic secular variation records from North America: Journal of Geophysical Research, v. 101, p. 8007–8024.

Luyendyk, B.P., 1991, A model for Neogene crustal rotations, transtension, and transpression in southern California: Geological Society of America Bulletin, v. 103, p. 1528–1536.

Macfarlane, A.M., 1993, Chronology of tectonic events in the crystalline core of the Himalaya, Langtang National Park, central Nepal: Tectonics, v. 12, p. 1004–1025.

Machette, M.N., Personius, S.F., and Nelson, A.R., 1992a, Paleoseismicity of the Wasatch Fault zone: a summary of recent investigation, interpretations, and conclusions, *in* Gori, P.L., ed., Assessment of regional earthquake hazards and risk along the Wasatch Front, Utah: United States Geological Survey Professional Paper 1500, p. A1–A30.

Machette, M.N., Personius, S.F., and Nelson, A.R., 1992b, The Wasatch Fault zone, U.S.A.: Annales Tectonicae, v. 6, p. 5–39.

Mancktelow, N.S., and Grasemann, B., 1997, Time-dependent effects of heat advection and topography on cooling histories during erosion: Tectonophysics, v. 270, p. 167–195.

Marshall, J.S., and Anderson, R.S., 1995, Quaternary uplift and seismic cycle deformation, Peninsula de Nicoya, Costa Rica: Geological Society of America Bulletin, v. 107, p. 463–473.

Masek, J.G., Isacks, B.L., Fielding, E.J., and Browaeys, J., 1994, Rift-flank uplift in Tibet: evidence for crustal asthenosphere: Tectonics, v. 13, p. 659–667.

Masek, J.G., Isacks, B.L., Gubbels, T.L., and Fielding, E.J., 1994, Erosion and tectonics at the margins of continental plateaus: Journal Geophysical Research, v. B99, p. 12,941–13,956.

Massonnet, D., Feigl, K., Rossi, M., and Adragna, F., 1994, Radar interferometric mapping of deformation in the year after the Landers earthquake: Nature, v. 369, p. 227–230.

Massonnet, D., Rossi, M., Carmona, C., Adragna, F., Peltzer, G., Feigl, K., and Rabaute, T., 1993, The displacement of the Landers earthquake mapped by radar interferometry: Nature, v. 364, p. 138–142.

Mayer, L., 1986, Tectonic geomorphology of escarpments and mountain fronts, Active Tectonics: Washington, D.C., National Academy Press, p. 125–135.

McFadden, L.D., Tinsley, J.C., and Bull, W.B., 1982, Late Quaternary pedogenesis and alluvial chronologies of the Los Angeles basin and San Gabriel Mountain areas, southern California, *in* Tinsley, J.C., Matti, J.C., and McFadden, L.D., eds., Late Quaternary pedogenesis and alluvial chronologies of the Los Angeles basin and San Gabriel Mountain areas, southern California, and Holocene faulting and alluvial stratigraphy within the Cucamonga fault zone; Field Trip 12, Cordilleran Section of the Geological Society of America, p. 1–13.

McGill, S.F., 1994, Variability of surficial slip in the 1992 Landers earthquake: implications for studies of prehistoric ruptures, Proceedings of the workshop on paleoseismology, Volume 94-568: Menlo Park, U.S. Geological Survey Open-File Report.

McGill, S.F., and Sieh, K., 1991, Surficial offsets on the central and eastern Garlock fault associated with prehistoric earthquakes: Journal of Geophysical Research, v. 96, p. 21,597-21,621.

McKean, J.A., Dietrich, W.E., Finkel, R.C., Southon, J.R., and Caffee, M.W., 1993, Quantification of soil production and downslope creep rates from cosmogenic ^{10}Be accumulations on a hillslope profile: Geology, v. 21, p. 343–346.

Medwedeff, D.A., 1989, Growth fault-bend folding at southeast Lost Hills, San Joaquin Valley, California: American Association of Petroleum Geologists Bulletin, v. 73, p. 54–67.

Medwedeff, D.A., 1992, Geometry and kinematics of an active, laterally propagating wedge thrust, Wheeler Ridge, California, *in* Mitra, S., and Fisher, G.W., eds., Structural geology of fold and thrust belts: Baltimore, Johns Hopkins University Press, p. 3–28.

Meghraoui, M., Jaegy, R., Lammali, K., and Albarede, F., 1988, Late Holocene earthquake sequences on the El Asnam (Algeria) thrust fault: Earth and Planetary Science Letters, v. 90, p. 187–203.

Meghraoui, M., Philip, H., Albarede, F., and Cisternas, A., 1988, Trench investigations through the trace of the 1980 El Asnam thrust fault: evidence for paleoseismicity: Bulletin of the Seismological Society of America, v. 78, p. 979–999.

Merritts, D., and Bull, W.B., 1989, Interpreting Quaternary uplift rates at the Mendocino triple junction, northern California, from uplifted marine terraces: Geology, v. 17, p. 1020–1024.

Merritts, D., and Hesterberg, T., 1994, Stream networks and long-term surface uplift in the New Madrid seismic zone: Science, v. 265, p. 1081–1084.

Merritts, D., and Vincent, K.R., 1989, Geomorphic response of coastal streams to low, intermediate and high rates of uplift, Mendocino triple junction region, northern California: Geological Society of America Bulletin, v. 101, p. 1373–1388.

Merritts, D.J., Vincent, K.R., and Wohl, E.E., 1994, Long river profiles, tectonism, and eustasy: A guide to interpreting fluvial terraces: Journal of Geophysical Research, v. 99, p. 14,031-14,050.

Meynadier, L., Valet, J.-P., Weeks, R., Shackleton, N.J., and Hagee, V.L., 1992, Relative geomagnetic intensity of the field during the last 140 ka: Earth and Planetary Science Letters, v. 114, p. 39–57.

Miller, G.H., and Brigham-Grette, J., 1989, Amino acid geochronology; resolution and precision in carbonate fossils: Quaternary International, v. 1, p. 111–128.

Milliman, J.D., and Meade, R.H., 1983, World-wide delivery of river sediment to the oceans: Journal of Geology, v. 91, p. 1–21.

Milliman, J.D., and Syvitski, J.P.M., 1992, Geomorphic/tectonic control of sediment discharge to the ocean: The importance of small mountainous rivers: Journal of Geology, v. 100, p. 525–544.

Minster, J.B., and Jordan, T.H., 1987, Vector constraints on western U.S. deformation from space geodesy, neotectonics, and plate motions: Journal of Geophysical Research, v. 92, p. 4798–4804.

Minster, J.B., Jordan, T.H., Hager, B.H., Agnew, D.C., and Royden, L.H., 1990, Implications of precise positioning, *in* Rundle, J.B., ed., Geodesy in the year 2000: Washington, D.C., National Academy Press, p. 23–45.

Mohr, J.J., Reeh, N., and Madsen, S.N., 1998, Three-dimensional glacial flow and surface elevation measured with radar interferometry: Nature, v. 391, p. 273–276.

Molnar, P., and England, P., 1990, Late Cenozoic uplift of mountain ranges and global climatic change: chicken or egg?: Nature, v. 346, p. 29–34.

Molnar, P., and Gipson, J.M., 1994, Very long baseline interferometry and active rotations of crustal blocks in the western Transverse Ranges, California: Geological Society of America Bulletin, v. 106, p. 595–606.

Molnar, P., Brown, E.T., Burchfiel, B.C., Deng, Q., Feng, X., Li, J., Raisbeck, G.M., Shi, J., Wu, Z., Yiou, F., and You, H., 1994, Quaternary climate change and the formation of river terraces across growing anticlines on the north flank of the Tien Shan, China: Journal of Geology, v. 102, p. 583–602.

Molnar, P., England, P., and Martinod, J., 1993, Mantle dynamics, uplift of the Tibetan Plateau, and the Indian monsoon: Reviews of Geophysics, v. 31, p. 357–396.

Montgomery, D.R., and Dietrich, W.E., 1988, Where do channels begin?: Nature, v. 336, p. 232–234.

Montgomery, D.R., and Dietrich, W.E., 1989, Source areas, drainage density, and channel initiation: Water Resources Research, v. 25, p. 1907–1918.

Montgomery, D.R., and Dietrich, W.E., 1992, Channel initiation and the problem of landscape scale: Science, v. 255, p. 826–830.

Morley, C.K., 1989, Extension, detachments, and sedimentation in continental rifts (with particular reference to east Africa): Tectonics, v. 8, p. 1175–1192.

Morris, J.D., 1991, Applications of ^{10}Be to problems in the earth sciences: Annual Review of Earth and Planetary Sciences, v. 19, p. 313–350.

Mosley, M.P., 1984, Response of the Ohau River and delta to lake level lowering: Earth Surface Processes and Landforms, v. 9, p. 181–187.

Muhs, D.R., 1992, The last interglacial-glacial transition in North America; evidence from uranium-series dating of coastal deposits: Geological Society of America Special Paper 270, p. 31–51.

Muhs, D.R., and Szabo, B.J., 1994, New uranium-series ages of the Waimanalo Limestone, Oahu, Hawaii; implications for sea level during the last interglacial period: Marine Geology, v. 118, p. 315–326.

Muhs, D.R., Kennedy, G.L., and Rockwell, T.K., 1994, Uranium-series ages of marine terrace corals from the Pacific coast of North America and implications for last-interglacial sea level history: Quaternary Research, v. 42, p. 72–87.

Mulder, T.J., and Burbank, D.W., 1993, Changes in patterns of fluvial deposition resulting from initial uplift of the Salt Range, northwest Himalayan Foreland, Pakistan, *in* Marzo, M., and Puigdefabregas, C., eds., Alluvial Sedimentation, Volume I.A.S. Special Publication 17: Oxford, Blackwell Scientific, p. 521–539.

Murphy, M.A., An, Y., Harrison, T.M., Dürr, S.B., Chen, Z., Ryerson, F.J., Kidd, W.S.F., Wang, X., and Zhou, X., 1997, Did the Indo-Asian collision alone create the Tibetan plateau?: Geology, v. 25, p. 719–722.

Nash, D.B., 1984, Morphologic dating of fluvial terrace scarps and fault scarps near West Yellowstone, Montana: Geological Society of America Bulletin, v. 95, p. 1413–1424.

Nash, D.B., 1998, Influence of scarp height on the accuracy of morphologic dating: Geological Society of America Abstracts with Programs, v. 30, p. 329.

Nishiizumi, K., Winterer, E.L., Kohl, C.P., Klein, J., Middleton, R., Lal, D., and Arnold, J.R., 1989, Cosmic ray production rates of ^{10}Be and ^{26}Al in quartz from glacially polished rocks: Journal of Geophysical Research, v. 94, p. 17,907-17,915.

Noller, J.S., Sowers, J.M., and Lettis, W.R., 2000, Quaternary geochronology: methods and applications, AGU Reference Shelf 4: Washington, American Geophysical Union, 582 p.

Oberlander, T.M., 1985, Origin of drainage transverse to structures in orogens, *in* Morisawa, M., and Hack, J.T., eds., Tectonic geomorphology: Proceedings, 15th Annual Binghamton Geomorphology Symposium: Boston, Allen and Unwin, p. 155–182.

Oerlemans, J., 1984, Numerical experiments on large-scale glacial erosion: Zeitschrift für Gletscherkunde und Glazialgeologie, v. 20, p. 107–126.

Ohmori, H., 1992, Morphological characteristics of the scar created by large-scale rapid mass movement: Japanese Geomorphological Union Transactions, v. 13, p. 185–202.

Olsson, I.U., 1968, Modern aspects of radiocarbon dating: Earth-Science Reviews, v. 4, p. 203–218.

Ota, Y., Brown, L.J., Berryman, K.R., Fujimori, T., and Miyauchi, T., 1995, Vertical tectonic movement in northeastern Marlborough: stratigraphic, radiocarbon, and paleoecological data from Holocene estuaries: New Zealand Journal of Geology and Geophysics, v. 38, p. 269–282.

Ota, Y., Chappell, J., Kelley, R., Yonekura, N., Matsumoto, E., Nishimura, T., and Head, J., 1993, Holocene coral reef terraces and coseismic uplift of Huon Peninsula, Papua New Guinea: Quaternary Research, v. 40, p. 177–188.

Ouchi, S., 1985, Response of alluvial rivers to slow active tectonic movement: Geological Society of America Bulletin, v. 96, p. 504–515.

Paola, C., Heller, P.L., and Angevine, C.L., 1992, Large-scale dynamics of grain-size variation in alluvial basins, 1: Theory: Basin Research, v. 4, p. 73–90.

Parker, R.A., 1977, Experimental study of basin evolution and its hydrologic implications [Ph.D. thesis], Colorado State University, Fort Collins.

Parsons, B., and Sclater, J.G., 1977, An analysis of the variation of ocean floor bathymetry with age: Journal of Geophysical Research, v. 82, p. 803–827.

Pavich, M., 1986, Processes and rates of saprolite production and erosion on a foliated granitic rock of the Virginia Piedmont, *in* Colman, S. and Dethier, D., eds., Rates of chemical weathering of rocks and minerals: Orlando, Academic Press, p. 552–590.

Pavich, M.J., and Hack, J.T., 1985, Appalachian Piedmont morphogenesis; weathering, erosion, and Cenozoic uplift: Tectonic geomorphology, Binghamton Symposia in Geomorphology: International Series, v. 15, p. 299–319.

Pavich, M.J., Brown, L., Klein, J., and Middleton, R., 1984, ^{10}Be accumulation in a soil chronosequence: Earth and Planetary Science Letters, v. 68, p. 198–204.

Penck, A., and Brückner, E., 1909, Die Alpen im Eiszeitalter: Leipzig, Tauchnitz, 1199 p.

Penck, W., 1953, Morphological analysis of landforms: New York, St. Martin's Press, 429 p.

Philip, H., and Meghraoui, M., 1983, Structural analysis and interpretation of the surface deformations of the El Asnam earthquake of October 10, 1980: Tectonics, v. 2, p. 17–49.

Phillips, F.M., Leavy, B.D., Jannik, N.O., Elmore, D., and Kubik, P.W., 1986, The accumulation of cosmogenic chlorine-36 in rocks; a method for surface exposure dating: Science, v. 231, p. 41–43.

Phillips, F.M., Zreda, M.G., Gosse, J.C., Klein, J., Evenson, E.B., Hall, R.D., Chadwick, O.A., and Sharma, P., 1997, Cosmogenic ^{36}Cl and ^{10}Be ages of Quaternary glacial and fluvial deposits of the Wind River Range, Wyoming: Geological Society of America Bulletin, v. 109, p. 1453–1463.

Pierce, K.L., and Colman, S.M., 1986, Effect of height and orientation (microclimate) on geomorphic degradation rates and processes, late-glacial terrace scarps in central Idaho: Geological Society of America Bulletin, v. 97, p. 869–885.

Pierce, K.L., and Morgan, L.A., 1992, The track of the Yellowstone hot spot: Volcanism, faulting, and uplift, *in* Link, P.K., Kuntz, M.A., and Platt, L.B., eds., Regional geology of eastern Idaho and western Wyoming, Geological Society of America Memoir 179, p. 1–53.

Pierce, K.L., Obradovich, J.D., and Friedman, I., 1976, Obsidian hydration dating and correlation of Bull Lake and Pinedale glaciations near West Yellowstone, Montana: Geological Society of America Bulletin, v. 87, p. 703–710.

Pillans, B., 1983, Upper Quaternary terrace chronology and deformation, South Taranaki, New Zealand: Geology, v. 11, p. 292–297.

Pinet, P., and Souriau, M., 1988, Continental erosion and large-scale relief: Tectonics, v. 7, p. 563–582.

Pinter, N., and Keller, E.A., 1995, Late-Quaternary deformation in northern Owens Valley, California: Geomorphic analysis of tectonic tilt: Geologische Rundschau, v. 84, p. 200–212.

Plafker, G., 1972, Alaskan earthquake of 1964 and Chilean earthquake of 1960: implications for arc tectonics: Journal of Geophysical Research, v. 77, p. 901–924.

Plafker, G., and Ward, S.N., 1992, Backarc thrust faulting and tectonic uplift along the Caribbean sea coast during the April 22, 1991 Costa Rica earthquake: Tectonics, v. 11, p. 709–718.

Platt, J.P., 1986, Dynamics of orogenic wedges and the uplift of high-pressure metamorphic rocks: Geological Society of America Bulletin, v. 97, p. 1037–1053.

Plumb, R.A., and Hickman, S.H., 1985, Stress-induced borehole elongation: a comparison between the four-arm dipmeter and the borehole televiewer in the Auburn geothermal well: Journal of Geophysical Research, v. 90, p. 5513–5521.

Poblet, J., Muñoz, J.A., Travé, A., and Serra-Kiel, J., 1998, Quantifying the kinematics of detachment folds using three-dimensional geometry: Application to the Mediano anticline (Pyrenees, Spain): Geological Society of America Bulletin, v. 110, p. 111–125.

Pollard, D.D., and Segall, P., 1987, Theoretical displacements and stresses near fractures in rock; with applications to faults, joints, veins, dikes, and solution surfaces, *in* Atkinson, B.K., ed., Fracture mechanics of rock: London, Academic Press, p. 277–349.

Pollitz, F.F., Bürgmann, R., and Romanowicz, B., 1998, Viscosity of oceanic asthenosphere inferred from remote triggering of earthquakes: Science, v. 280, p. 1245–1249.

Porter, S.C., 1975, Glaciation limit in New Zealand's Southern Alps: Arctic and Alpine Research, v. 7, p. 33–37.

Porter, S.C., 1981a, Lichenometric studies in the Cascade Range of Washington; establishment of Rhizocarpon geographicum growth curves at Mount Rainier: Arctic and Alpine Research, v. 13, p. 11–23.

Porter, S.C., 1981b, Glaciological evidence of Holocene climatic change, *in* Wigley, T.M.L., Ingram, M.J., and Farmer, G. (eds): Climate and history; Studies in past climates and their impact on man; Cambridge University Press, Cambridge, p. 82–110.

Porter, S.C., 1989, Late Holocene fluctuations of the fiord glacier system in Icy Bay, Alaska, U.S.A: Arctic and Alpine Research, v. 21, p. 364–379.

Porter, S.C., 1989, Some geological implication of average Quaternary glacial conditions: Quaternary Research, v. 32, p. 245–261.

Porter, S.C., and Orombelli, G., 1981, Alpine rockfall hazards: American Scientist, v. 69, p. 67–75.

Powell, J.W., 1875, Exploration of the Colorado River of the west (1869–72): Washington, D.C., Smithsonian Institute.

Quade, J., Roe, L., DeCelles, P.G., and Ojha, T.P., 1997, The late Neogene 87-Sr/86-Sr record of lowland Himalayan rivers: Science, v. 276, p. 1828–1831.

Raymo, M.E., and Ruddiman, W.F., 1992, Tectonic forcing of late Cenozoic climate change: Nature, v. 359, p. 117–122.

Raymo, M.E., Ruddiman, W.F., and Froelich, P.N., 1988, Influence of late Cenozoic mountain building on ocean geochemical cycles: Geology, v. 16, p. 649–653.

Raynolds, R.G.H., and Johnson, G.D., 1985, Rates of Neogene depositional and deformational processes, north-west Himalayan foredeep margin, Pakistan, *in* Snelling, N.J., ed., The Chronology of the Geologic Record, The Geological Society of London Memoir 10, p. 297–311.

Reid, H.F., 1910, The mechanism of an earthquake, The California earthquake of April 18, 1906, Report of the earthquake investigation commision, 2: Washington, D.C., Carnegie Institution, p. 1–192.

Reid, J.B., Jr., 1992, The Owens River as a tiltmeter for Long Valley caldera, California: Journal of Geology, v. 100, p. 353–363.

Repka, J.L., Anderson, R.S., and Finkel, R.C., 1997, Cosmogenic dating of fluvial terraces, Fremont River, Utah: Earth and Planetary Science Letters, v. 152, p. 59–73.

Richter, C.F., 1935, An instrumental earthquake-magnitude scale: Bulletin of the Seismological Society of America, v. 25, p. 1–32.

Richter, F.M., Rowley, D.B., and DePaolo, D.J., 1992, Sr isotope evolution of seawater: the role of tectonics: Earth and Planetary Science Letters, v. 109, p. 11–23.

Ritter, J.B., Miller, J.R., Enzel, Y., Howes, S.D., Nadon, G., Grubb, M.D., Hoover, K.A., Olsen, T., Seneau, S.L., Sack, D., Summa, C.L., Taylor, I., Touysinhthiphonexay, K.C.N., Yodis, E.G., Schneider, N.P., Ritter, D.F., and Wells, S.G., 1993, Quaternary evolution of the Cedar Creek alluvial fan, Montana: Geomorphology, v. 8, p. 287–304.

Rockwell, T.K., Keller, E.A., Clark, M.N., and Johnson, D.L., 1984, Chronology and rates of faulting of Ventura River terraces, California: Geological Society of America Bulletin, v. 95, p. 1466–1474.

Rogers, A.E.E., and others, 1983, Very-long baseline radio interferometry: The Mark-III system for geodesy, astrometry and aperture synthesis: Science, v. 219, p. 51–54.

Rosenbloom, N.A., and Anderson, R.S., 1994, Hillslope and channel evolution in a marine terraced landscape, Santa Cruz, California: Journal of Geophysical Research, v. 99, p. 14,013-14,029.

Rubin, C.M., 1996, Systematic underestimation of earthquake magnitudes from large intercontinental reverse faults: historical ruptures break across segment boundaries: Geology, v. 24, p. 989–992.

Rubin, C.M., Lindvall, S.C., and Rockwell, T.K., 1998, Evidence for large earthquakes in metropolitan Los Angeles: Science, v. 281, p. 398–402.

Ryan, J.W., and Ma, C., 1998, NASA-GSFC's geodetic VLBI Program; a twenty-year retrospective: Geodesy and global change: Physics and Chemistry of the Earth, v. 23, p. 1041–1052.

Sadybakasov, I., 1990, Neotectonics of High Asia (in Russian): Moscow, Nauka, 176 p.

Sarna-Wojcicki, A.M., Lajoie, K.R., Meyer, C.E., Adam, D.P., and Rieck, H.J., 1991, Tephrochronology correlation of upper Neogene sediments along the Pacific margin, conterminous United States, *in* Morrison, R.B., ed., Quaternary nonglacial geology; conterminous U.S., v. K-2, p. 117–140

Satake, K., Shimazaki, K., Tsuji, Y., and Ueda, K., 1996, Time and size of a giant earthquake in Cascadia inferred from Japanese tsunami records of January 1700: Nature, v. 379, p. 246–249.

Savage, J.C., and Thatcher, W., 1992, Interseismic deformation at the Nankai Trough, Japan, subduction zone: Journal of Geophysical Research, v. 97, p. 11,117-11,135.

Schlische, R.W., Young, S.S., Ackermann, R.V., and Gupta, A., 1996, Geometry and scaling relations of a population of very small rift-related normal faults: Geology, v. 24, p. 683–686.

Schmidt, K.M., and Montgomery, D.R., 1995, Limits to relief: Science, v. 270, p. 617–620.

Schmidt, K.M., and Montgomery, D.R., 1996, Rock mass strength assessment for bedrock landsliding: Environmental & Engineering Geoscience, v. 2, p. 325–338.

Scholz, C.H., 1990, The mechanics of earthquakes and faulting: Cambridge, Cambridge University Press, 439 p.

Scholz, C.H., 1998, A further note on earthquake size distributions: Bulletin of the Seismological Society of America, v. 88, p. 1325–1326.

Schumm, S.A., 1986, Alluvial river response to active tectonics, Active Tectonics: Washington, D.C., National Academy Press, p. 80–94.

Schumm, S.A., and Khan, H.R., 1972, Experimental study of channel patterns: Nature, v. 233, p. 407–409.

Schumm, S.A., Mosley, M.P., and Weaver, W.E., 1987, Experimental fluvial geomorphology: New York, John Wiley and Sons, 413 p.

Schwartz, D.P., and Coppersmith, K.J., 1984, Fault behavior and characteristic earthquakes: examples from the Wasatch and San Andreas fault zones: Journal of Geophysical Research, v. 89, p. 5681–5698.

Sclater, J.G., and Francheteau, J., 1970, The implications of terrestrial heat flow observations on current tectonic and geochemical models of the crust and upper mantle of the Earth: The Geophysical Journal of the Royal Astronomical Society, v. 20, p. 509–542.

Scott, K.M., and Williams, R.P., 1978, Erosion and sediment yields in the Transverse Ranges, Southern California: U. S. Geological Survey Professional Paper 1030.

Seeber, L., and Gornitz, V., 1983, River profiles along the Himalayan arc as indicators of active tectonics: Tectonophysics, v. 92, p. 335–367.

Seidl, M.A., and Dietrich, W.E., 1992, The problem of channel erosion into bedrock: Catena Supplement, v. 23, p. 101–124.

Seidl, M.A., Dietrich, W.E., and Kirchner, J.W., 1994, Longitudinal profile development into bedrock: an analysis of Hawaiian channels: Journal of Geology, v. 102, p. 457–474.

Shackleton, N.J., and Opdyke, N.D., 1973, Oxygen isotope and paleomagnetic stratigraphy of equatorial Pacific core V28–238: Oxygen isotope temperatures and ice volumes on a 10^5 and 10^6 year scale: Quaternary Research, v. 3, p. 39–55.

Shaw, J.H., and Suppe, J., 1994, Active faulting and growth folding in the eastern Santa Barbara Channel, California: Geological Society of America Bulletin, v. 106, p. 607–626.

Sheppard, P.R., and White, L.O., 1995, Tree-ring responses to the 1978 earthquake at Stephens Pass, northeastern California: Geology, v. 23, p. 109–112.

Shi, B., Anooshehpoor, A., Zeng, Y., and Brune, J.N., 1996, Rocking and overturning of precariously balanced rocks by earthquakes: Bulletin of the Seismological Society of America, v. 86, p. 1364–1371.

Shimaki, K., and Nakata, T., 1980, Time-predictable recurrence model for large earthquakes: Geophysical Research Letters, v. 7, p. 279–282.

Sieh, K., 1978, Prehistoric large earthquakes produced by slip on the San Andreas fault at Pallett Creek, California: Journal of Geophysical Research, v. 83, p. 3907–3939.

Sieh, K., Stuiver, M., and Brillinger, D., 1989, A more precise chronology of earthquakes produced by the San Andreas fault in Southern California: Journal of Geophysical Research, v. 94, p. 603–623.

Sieh, K.E., 1984, Lateral offsets and revised dates of large earthquakes at Pallett Creek, southern California: Journal of Geophysical Research, v. 89, p. 7641–7670.

Sieh, K.E., and Jahns, R.H., 1984, Holocene activity of the San Andreas fault at Wallace Creek, California: Geological Society of America Bulletin, v. 95, p. 883–896.

Simpson, D.W., and Anders, M.H., 1992, Tectonics and topography of the western United States-an application of digital mapping: GSA Today, v. 2, p. 117–121.

Simpson, R.W., and Reasenberg, P.A., 1994, Earthquake-induced static-stress changes on Central California faults: USGS Professional Paper 1550-F, p. F55–F89.

Simpson, R.W., Harris, R.A., and Reasenberg, P.A., 1994, Stress changes caused by the 1994 Northridge earthquake: Seismological Research Letters, v. 65, p. 240.

Slingerland, R., and Snow, R.S., 1988, Stability analysis of a rejuvenated fluvial system: Zeitschift für Geomorphologie, v. Supple.-Bd. 67, p. 93–102.

Small, E.E., and Anderson, R.A., 1998, Pleistocene relief production in Laramide mountain ranges, western United States: Geology, v. 26, p. 123–136.

Small, E.E., and Anderson, R.S., 1995, Geomorphically driven Late Cenozoic rock uplift in the Sierra Nevada, California: Science, v. 270, p. 277–280.

Small, E.E., Anderson, R.S., Hancock, G.S., and Finkel, R.C., 1999, Estimates of regolith production from ^{10}Be and ^{26}Al: Evidence for steady state alpine hillslopes: Geomorphology, v. 27, p. 131–150.

Small, E.E., Anderson, R.S., Repka, J.L., and Finkel, R., 1997, Erosion rates of alpine bedrock summit surfaces deduced from *in situ* ^{10}Be and ^{26}Al: Earth and Planetary Science Letters, v. 150, p. 413–425.

Smith, D.G., and Smith, N.D., 1980, Sedimentation in anastomosed river systems, examples from alluvial valleys near Banff, Alberta: Journal of Sedimentary Petrology, v. 50, p. 157–164.

Smith, G.I., and Street-Perrott, F.A., 1983, Pluvial lakes of the western United States, *in* Porter, S.C., ed., Late Quaternary environments of the United States: the Late Pleistocene: Minneapolis, Univ. of Minnesota Press, p. 190–212.

Smith, G.I., Friedman, I., Gleason, J.D., and Warden, A., 1992, Stable isotope composition of waters in southeastern California; 2, Groundwaters and their relation to modern precipitation: Journal of Geophysical Research, v. 97, p. 5813–5823.

Smith, R.B., and Braile, L.W., 1994, The Yellowstone hotspot: Internal structure of volcanoes and geophysical precursors of eruptions: Journal of Volcanology and Geothermal Research, v. 61, p. 121–187.

Smith, R.B., and Braile, L.W., 1993, Topographical signature, space-time evolution, and physical properties of the Yellowstone-Snake River plain volcanic system; the Yellowstone hotspot: Geology of Wyoming Memoir 5, p. 694–754.

Snow, R.S., and Slingerland, R.L., 1987, Mathematical modelling of graded river profiles: Journal of Geology, v. 95, p. 15–33.

Snow, R.S., and Slingerland, R.L., 1990, Stream profile adjustment to crustal warping: nonlinear results from a simple model: Journal of Geology, v. 98, p. 699–708.

Sobel, E.R., and Dumitru, T., 1997, Thrusting and exhumation around the margins of the western Tarim basin during the India-Asia collision: Journal of Geophysical Research, v. 102, p. 5043–5064.

Souter, B.J., and Hager, B.H., 1997, Fault propagation fold growth during the 1994 Northridge, California, earthquake: Journal of Geophysical Research, v. 102, p. 11,931-11,942.

Stark, C.P., and Hovius, N., 1998, Evolution of a mountain belt toward steady state: analysis of the Central Range, Taiwan: EOS (Transactions of the American Geophysical Union), v. 79, p. 357.

Stein, R.S., 1981, Discrimination of tectonic displacement from slope-dependent errors in geodetic leveling from southern California, 1953–1979, *in* Simpson, D.W., and Richards, P.G., eds., Earthquake prediction: an international review, Maurice Ewing series 4: Washington, D.C., American Geophysical Union, p. 441–456.

Stein, R.S., and Ekstrom, G., 1992, Seismicity and geometry of a 110-km-long blind thrust fault 2. Synthesis of the 1982–1985 California earthquake sequence: Journal of Geophysical Research, v. 97, p. 4865–4883.

Stein, R.S., King, G.C.P., and Rundle, J.B., 1988, The growth of geological structure by repeated earthquakes 2. Field examples of continental dip-slip faults: Journal of Geophysical Research, v. 93, p. 13,319-13,331.

Stevens, G., 1974, Rugged landscape: the geology of central New Zealand: Wellington, Reed Ltd., 286 p.

Stuiver, M., 1970, Tree ring, varve and carbon-14 chronologies: Nature, v. 228, p. 454–455.

Stuiver, M., and Reimer, P.J., 1993, Extended ^{14}C data base and revised CALIB 3.0 ^{14}C age calibration program: Radiocarbon, v. 35, p. 215–230.

Stüwe, K., White, L., and Brown, R., 1994, The influence of eroding topography on steady-state isotherms: application to fission track analysis: Earth and Planetary Science Letters, v. 124, p. 63–74.

Summerfield, M.A., 1991, Global geomorphology. An introduction to the study of landforms: Essex, England, Longman Scientific Technical, 537 p.

Summerfield, M.A., and Hulton, N.J., 1994, Natural controls of fluvial denudation rates in major world drainage basins: Journal of Geophysical Research, v. 99, p. 13,871-13,883.

Suppe, J., 1983, Geometry and kinematics of fault bend folding: American Journal of Science, v. 283, p. 648–721.

Suppe, J., and Medwedeff, D.A., 1990, Geometry and kinematics of fault-propagation folding: Eclogae Geologicae Helvetiae, v. 83.

Suppe, J., Sabat, F., Muñoz, J.A., Poblet, J., Roca, E., and Vergés, J., 1997, Bed-by-bed fold growth by kink-band migration: Sant Llorenc de Morunys, Eastern Pyrenees: Journal of Structural Geology, v. 19, p. 443–461.

Suppe, J.S., Chou, G.T., and Hook, S.C., 1992, Rates of folding and faulting determined from growth strata, *in* McClay, K.R., ed., Thrust tectonics: London, Chapman and Hall, p. 105–122.

Sylvester, A.G., 1986, Near-field tectonic geodesy, Active Tectonics: Washington, D.C., National Academy Press, p. 164–180.

Sylvester, A.G., 1988, Strike-slip faults: Geological Society of America Bulletin, v. 100, p. 1666–1703.

Talling, P.J., Stewart, M.D., Stark, C.P., Gupta, S., and Vincent, S.J., 1997, Regular spacing of drainage outlets from linear fault-blocks: Basin Research, v. 9, p. 275–302.

Thatcher, W., 1986a, Geodetic measurement of active-tectonic processes, Active Tectonics: Washington, D.C., National Academy Press, p. 155–163.

Thatcher, W., 1986b, Cyclic deformation related to great earthquakes at plate boundaries: Royal Society of New Zealand Bulletin, v. 24, p. 245–272.

Thorson, R.M., 1989, Glacio-isostatic response of the Puget Sound area, Washington: Geological Society of America Bulletin, v. 101, p. 1163–1174.

Tippett, J.M., and Kamp, P.J.J., 1993, Fission track analysis of the Late Cenozoic vertical kinematics of continental Pacific crust, South Island, New Zealand: Journal of Geophysical Research, v. 98, p. 16,119-16,148.

Tippett, J.M., and Kamp, P.J.J., 1995, Quantitative relationships between uplift and relief parameters for the Southern Alps, New Zealand, as determined by fission track analysis: Earth Surface Processes and Landforms, v. 20, p. 153–175.

Tucker, G.E., and Slingerland, R., 1996, Predicting sediment flux from fold and thrust belts: Basin Research, v. 8, p. 329–349.

Turcotte, D.L., and Schubert, G., 1982, Geodynamics applications of continuum physics to geological problems: New York, John Wiley and Sons, 450 p.

Van Arsdale, R.B., Stahle, D.W., Cleaveland, M.K., and Guccione, M.J., 1998, Earthquake signals in tree-ring data from the New Madrid seismic zone and implications for paleoseismicity: Geology, v. 26, p. 515–518.

Van den Berg, J.H., 1995, Prediction of alluvial channel pattern of perennial rivers: Geomorphology, v. 12, p. 259–279.

Van Dissen, R.J., Berryman, K.R., Pettinga, J.R., and Hill, N.L., 1992, Paleoseismicity of the Wellington—Hutt valley segment of the Wellington fault, North Island, New Zealand: New Zealand Journal of Geology and Geophysics, v. 35, p. 165–176.

Vergés, J., Burbank, D.W., and Meigs, A., 1996, Unfolding: an inverse approach to fold kinematics: Geology, v. 24, p. 175–178.

Vincent, K.R., Bull, W.B., and Chadwick, O.A., 1994, Construction of a soil chronosequence using the thickness of pedogenic carbonate coatings: Journal of Geological Education, v. 42, p. 316–324.

Walcott, R.I., 1975, Recent and late Quaternary changes in water level: EOS, v. 56, p. 62–72.

Walder, J., and Hallet, B., 1985, A theoretical model of the fracture of rock during freezing: Geological Society of America Bulletin, v. 96, p. 336-346.

Wallace, R.E., 1978, Geometry and rates of change of fault-generated range fronts, north-central Nevada: Journal of Research of the United States Geological Survey, v. 6, p. 637–650.

Ward, S.N., 1990, Pacific-North America plate motions: new results from very long baseline interferometry: Journal of Geophysical Research, v. 95, p. 21,965-21,981.

Ward, S.N., and Valensise, G., 1994, The Palos Verdes terraces, California: bathtub rings from a buried reverse fault: Journal of Geophysical Research, v. 99, p. 4485–4494.

Watterson, J., 1986, Fault dimension, displacements, and growth: Pure and Applied Geophysics, v. 124, p. 365–373.

Wehmiller, J.F., Belknap, D.F., Boutin, B.S., Mirecki, J.E., Rahaim, S.D., and York, L.L., 1988, A review of the aminostratigraphy of Quaternary mollusks from United States Atlantic Coastal Plain sites, *in* Easterbrook, D.J., ed., Dating Quaternary sediments: Boulder, Geological Society of America Special Paper 227, p. 69–110.

Weiland, R.J., and Cloos, M., 1996, Pliocene-Pleistocene asymmetric unroofing of the Irian fold belt, Irian Jaya, Indonesia: Apatite fission-track thermochronology.: Geological Society of America Bulletin, v. 108, p. 1438–1449.

Weissel, J.K., and Karner, G.D., 1989, Flexural uplift of rift flanks due to mechanical unloading of the lithosphere during extension: Journal of Geophysical Research, v. 94, p. 13,919-13,950.

Weldon, R.J., 1986, Late Cenozoic geology of Cajon Pass; implications for tectonics and sedimentation along the San Andreas fault [Ph.D. thesis], California Institute of Technology, Pasadena.

Wells, S.G., Bullard, T.F., Menges, C.M., Drake, P., P.A., K., Kelson, K.I., Ritter, J.B., and Wesling, J.R., 1988, Regional variations in tectonic geomorphology along a segmented convergent plate boundary, Pacific coast of Costa Rica: Geomorphology, v. 1, p. 239–265.

Wesson, R.L., Helley, E.J., Lajoie, K.R., and Wentworth, C.M., 1975, Faults and future earthquakes, *in* Borchardt, R.D., ed., Studies for seismic zonation of the San Francisco Bay region, U.S. Geological Survey Professional Paper 941A, p. 5–30.

Westgate, J.A., and Gorton, M.P., 1981, Correlation techniques in tephra studies, *in* Self, S., and Sparks, R.S.J., eds., Tephra Studies: North American Treaty Organization Advanced Studies Institute Series C: Dordecht, Reidel Publishing, p. 73–94.

Whipple, K.E., Kirby, E., and Brocklehurst, S.H., 1999, Geomorphic limits to climate-induced increases in topographic relief: Nature, v. 401, p. 39–43.

Whipple, K.X., and Dunne, T., 1992, Debris-flow fans in Owens Valley, California: Geological Society of America Bulletin, v. 104, p. 887–900.

Whipple, K.X., and Tucker, G.E., 1999, Dynamics of the stream-power river incision model: Implications for height limits of mountain ranges, landscape response timescales, and research needs: Journal of Geophysical Research, v. 104, p. 17,661–17,674.

Wickham, J., 1995, Fault displacement-gradient folds and the structure at Lost Hills, California (U.S.A.): Journal of Structural Geology, v. 17, p. 1293–1302.

Willemse, E.J.M., Pollard, D.D., and Aydin, A., 1996, Three-dimensional analyses of slip distributions on normal fault arrays with consequences for fault scaling: Journal of Structural Geology, v. 18, p. 295–309.

Willett, S., Beaumont, C., and Fullsack, P., 1993, Mechanical model for the tectonics of doubly vergent compressional orogens: Geology, v. 21, p. 371–374.

Willett, S.D., 1999, Orogeny and orography: the effects of erosion on the structure of mountain belts: Journal of Geophysical Research, v. 104, p. 28,957-28,982.

Winslow, D.M., Zeitler, P.K., Chamberlain, C.P., and Hollister, L.S., 1994, Direct evidence for a steep geotherm under conditions of rapid denudation, Western Himalaya, Pakistan: Geology, v. 22, p. 1075–1078.

Wintle, A.G., 1993, Luminescence dating of aeolian sands: an overview, *in* Pye, K., ed., The dynamics and environmental context of aeolian sedimentary systems: London, Geological Society of London Special Publication 72, p. 49–58.

Wolfe, J.A., 1971, Tertiary climatic fluctuations and methods of analysis of Tertiary floras: Palaeogeography, Palaeoclimatology, Palaeoecology, v. 9, p. 27–57.

Wolfe, J.A., 1990, Paleobotantical evidence for a major temperature increase following the Cretaceous/Tertiary boundary: Nature, v. 343, p. 153–156.

Wolfe, J.A., 1993, A method of obtaining climatic parameters from leaf assemblages, U. S. Geological Survey Bulletin, p. 71 (5 sheets).

Wolfe, J.A., Forest, C.E., and Molnar, P., 1998, Paleobotanical evidence of Eocene and Oligocene paleoaltitudes in midlatitude western North America: Geological Society of America Bulletin, v. 110, p. 664–678.

Wolfe, S.A., Huntley, D.J., and Ollerhead, J., 1995, Recent and late Holocene sand dune activity in southwestern Saskatchewan: Current Research, Geological Survey of Canada, v. 1995-B, p. 131–140.

Working Group on California Earthquake Probabilities, 1995, Seismic hazards in Southern California: probable earthquakes, 1994 to 2024: Bulletin of the Seismological Society of America, v. 85, p. 379–439.

Wyss, M., and Brune, J.N., 1967, The Alaska earthquake of 28 March 1964; a complex multiple rupture: Bulletin of the Seismological Society of America, v. 57, p. 1017–1023.

Yamaguchi, D.K., and Hoblitt, R.P., 1995, Tree-ring dating of pre-1980 volcanic flowage deposits at Mount St. Helens, Washington: Geological Society of America Bulletin, v. 107, p. 1077–1093.

Yamaguchi, D.K., Atwater, B.F., Bunker, D.E., Benson, B.E., and Reid, M.S., 1997, Tree-ring dating the 1700 Cascadia earthquake: Nature, v. 389, p. 922–923.

Yamanaka, H., and Iwata, S., 1982, River terraces along the middle Kali Gandaki and Marsyandi Khola, central Nepal: Journal of Nepal Geological Society, v. 2, p. 95–112.

Yin, A., Nie, S., Craig, P., Harrison, T.M., Ryerson, F.J., Qian, X., and Yang, G., 1998, Late Cenozoic tectonic evolution of the southern Chinese Tian Shan: Tectonics, v. 17, p. 1–17.

Zachariasen, J.A., 1998, Paleoseismology and paleogeodesy of the Sumatran subduction zone; a study of vertical deformation using coral microatolls [Ph.D. thesis], California Institute of Technology, Pasadena.

Zeitler, P.K., 1985, Cooling history of the NW Himalaya, Pakistan: Tectonics, v. 4, p. 127–151.

Zepeda, R.L., Keller, E.A., and Rockwell, T.K., 1990, Soil chronology and active tectonics at Wheeler Ridge, southern San Joaquin Valley, California, Soils and Landscape Evolution, 21st annual Binghamton Geomorphology Symposium, Program and Abstracts: Binghamton, State University of New York at Binghamton, p. 41.

INDEX

A

Absolute dating methods, 38–52, 39*t*
  amino acid racemization, 44–45, 45*f*
  cosmogenic radionuclide dating, 47–52
  dendrochronology, 39–40, 40*f*
  luminescence, 45–47, 46*f*
  radiocarbon, 40–42, 41*f*, 42*f*
  uranium/thorium, 42–44, 43*f*
Absolute erosion rates, 141, 141*f*
Absolute vertical ocean surface changes, 18
Accelerator mass spectrometric (AMS) dating, 41, 42
Acropora palmata dating, 42
Additive paleodose dating, 46, 47*f*
Aegean Sea, 206*f*
Age, known, 13, 31. *See also* Dating
Aggradational phases, 114–115
Aggradational river terraces, 22–24, 25*f*
Air mass moist static energy, 157
Alaskan earthquake (1964), 72–73, 73*f*, 90
Alignment arrays, 86–88, 102
Alluvial fans, 26–27, 31
  contours of tilted, 192*f*
  deformation, 191–193, 192*f*
  faulted, 27*f*
Alluvial transport models, 238–239
Amino acid racemization, 44–45, 45*f*
Anastomosing rivers, 164. *See also* Braided streams
Annealing zones. *See* Partial annealing zones (PAZ)
Antithetic faults, 69, 70*f*
Antithetic interbasinal ridges, 69, 70*f*
Antithetic interference zones, 69, 70*f*
Apparent sea-level, 18, 19*f*
Aseismic creep, 85, 87–88
Asperities, 58, 58*f*, 59, 82
Atomic clocks, 38–39
Autocyclic processes, geomorphic markers and, 13
Awatere Fault, New Zealand, 115*f*
Axial surfaces, 78, 80

B

Balanophyllia elegans dating, 42
Barbados corals, 44*f*
Barriers, 58, 58*f*
Base levels, 160
  experimental lowering, 161–162, 162*f*
  intermediate time scales and, 176
  numerical models of lowering, 163–164, 163*f*, 164*f*
Basin and Range, Nevada
  drainages, 203*f*
  extensional ranges, 206*f*
  fault growth models, 209*f*, 210
  normal fault overlap zone, 207, 208*f*
  numerical modeling, 246, 247*f*
Basins. *See* Drainage basins
Beach ridges, 20, 20*f*, 120, 120*f*
Beaverhead Mountains, 209*f*, 210
Bedrock
  cosmogenic radionuclide dating, 48, 50
  erosion rates and, 133
  growing folds and, 213, 214*f*, 214, 215*f*
  incision models, 238
  incision rates, 142–143
  terraces, 23–24
Bedrock uplift, 132, 132*f*
  rate, 131
  total, 153
Bed shear stress, 161, 163–164, 163*f*
Beheaded streams, 29, 29*f*, 68*f*, 69, 69*f*
Bending-moment faults, 76–77, 77*f*
Bishop Tuff, Calif., 60, 61*f*, 65*f*, 190*f*
Bleach paleodose dating, partial, 46, 47*f*
Blind faults, 77, 80*f*
Blind thrust faults, 82, 168, 169*f*, 235*f*
Body forces, 53
Borah Peak earthquake (1983), 64*f*, 70, 72*f*
Borehole breakouts, 55, 55*f*
Boundary conditions, 233
Boundary element (BE) models, 232, 234
Braided streams
  sinuosity, 165–166, 165*f*
  transitions to meandering, 172–173, 173*f*
  uplift effects, 166–167, 166*f*

C

Cajon Creek, Calif., 25–26, 26*f*
Calaveras fault, trilateration arrays of, 88, 89*f*, 90
Canada Larga syncline, Calif., 181–182
Carbon 14 dating, 40–42, 41*f*, 42*f*
Carbonate coatings, dating and, 36–37
Cascadia subduction zone, Wash.-Oreg., 121–123, 121*f*, 178–179
Catchment size, fluvial erosion rates and, 135
Channel initiation modeling, 238, 249
Channels. *See* Rivers
Characteristic earthquakes, 8, 58–60, 59*f*, 82
  fault displacement variations and, 61–62
  versus random earthquakes, 10*f*
Chemical weathering, 133
Clast seismic velocity dating method, 33–34, 34*f*
Climate change, 2–3, 3*f*, 156–157, 176, 229
Coalfield faults, 61, 61*f*
Coalinga earthquake, Calif. (1983), 92, 92*f*
Collisional orogen cross-sectional model, 247, 248*f*
Colluvial wedges, 109*f*, 110, 111–112
Common mode signals, 93
Compaction, 131–132, 132*f*
Conjugate fault planes, 54
Conjugate Reidel shears, 66, 66*f*
Conjugate shears, bending-moment and, 74, 75*f*
Consequent rivers, 190–191, 190*f*
Contraction zones, 212–224
  drainage development, 213–217, 216, 217*f*

Note: *b* refers to boxes, *f* refers to figures, and *t* refers to tables.

Contraction zones (*continued*)
individual and multiple folds, 213, 214*f*, 215*f*
quantitative assessments, 216–217, 218*f*
steady-state and pre–steady-state mountains, 217–223
Cooling rates, minerals, 147–149, 147*f*
calculated age pattern, 148*f*
Coral reefs, 15–17, 16*f*. *See also* Marine terraces
dating, 42, 44*f*, 118
growth during seismic cycles, 119, 120*f*
Coseismic deformation/displacement, 71, 73, 73*f*, 96
Coseismic interval, 56, 57*f*
Cosmogenic radionuclides (CRNs)
background, 48, 49*b*
bedrock incision rates calculation, 143
dating, 47–52, 51*f*
erosion rate and, 145–146, 146*f*
interpretation, 51–52
knickpoint propagation dating, 160–161
numerical modeling and, 238, 243–244
regolith production rates using, 142, 142*f*
Costa Rica, thrust-bounded ranges, 216–217, 218*f*
Crustal Dynamics Project, 97
Crustal rigidity, footwall uplift and, 210–212, 212*f*

D

Dams, fluvial erosion rates and, 135, 137
Dating, 2, 33–52, 229
absolute, 38–52
alluvial fan tilting and, 192–193
apatite fission-track, 219, 220, 221*f*
of offset features, 117–118
paleoaltitude estimates and, 158
relative, 33–38
Davis (William Morris) theories, 5, 5*f*, 7, 7*f*
Dead Sea and basin, 224
Debris basins, 137
Debris flows, 27–28
Deformation
rates, 159–160
spatial patterns, 59–60
styles, 86
Degradational river terraces, 22, 23, 25*f*
Deltas, 21–22
DEM. *See* Digital topographic models
Dendrochronology, 39–40, 40*f*
of coral, 119
Denudation, 132, 132*f*
tectonic, 149–151
Denudation rates, 131–151
basin scale, cosmogenic radionuclide techniques for, 145–146
bedrock incision, 142–143
conceptual framework, 133–134
definitions, 131–133
estimating approaches, 134, 134*f*
isotopic interpretations, 140–141, 141*f*
by landslides, 143–145, 145*f*
local *versus* regional, 132–133
radiometric ages and, 146–149
regolith production rates, 141–142
sedimentary fluxes in rivers, 134–137
stream power and, 163–164, 163*f*
structural/stratigraphic controls and, 137–139
topographically constrained, 139–140
Deposition, 131–132, 132*f*
Depositional basins, 135, 202
Depositional geometries, 203–204
Depositional surfaces, dating, 50–51
Detachment fold, 79–80, 79*f*
Deviatoric stresses, 54–55. *See also* Strains
Differential equations, 232
Diffusion equations, 237, 239–241
nonuniform, 242
Digital topographic models, 158, 229. *See also* Numerical modeling
databases, 2
of footwall uplift and crustal rigidity, 210–212
of individual and multiple folds, 213
mean surface elevation calculations and, 153
of segment boundaries and slip deficits, 209–210
of Wheeler Ridge fold, Calif., 195–196
Dip domains, 78, 80
Dip-slip faults, 64
colluvial wedges and, 109*f*, 111–112
fluvial terrace deformation and, 180, 181, 182*f*
"salami slicing," 109
trenching practicalities for, 129
Displaced geomorphologic features, 114–121
along strike-slip fault, 116, 116*f*
marine settings, 118–121
terrestrial settings, 114–118
Displacement-gradient folds, 78–79, 79*f*, 213
Displacement magnitude histograms, 116, 116*f*
Displacement patterns, 86, 87*f*
Displacement-predictable uplift, 119
Displacement variations, faults, 60–62, 61*f*
Drainage basins, 6–7, 6*f*, 159, 229. *See also* Rivers
in contraction regions, 213–217, 216, 217*f*, 218*f*
in extensional ranges, 205–208, 206*f*, 207*f*, 208*f*
numerical modeling, 249
spacing, 202–203, 203*f*
spacing *versus* range half-width, 214, 218*f*
subsidence models, 207–210
Dynamic equilibrium, 9–11, 10*f*
Dynamic (numerical) models, 236

E

Earthquakes, 56–58, 59, 59*f*. *See also* Characteristic earthquakes; Faults; *specific earthquakes*
alternative models, 57–58
asperities, 58, 58*f*
barrier regions, 58, 58*f*
classical model, 56, 56*f*
ground acceleration during, 127*b*
incision/deposition and, 115
prediction, 8–9, 82, 119
slip-predictable model, 57–58, 57*f*
subduction-zone, 121–123, 121*f*
time-predictable model, 57, 57*f*, 119
East African rift system, 70, 71*f*
El Asnam earthquake (Algeria 1980)
complex fault geometries, 76–77, 77*f*
deformation styles and inferred stress patterns, 76*f*
hangingwall folding, 74
stratigraphic response to, 123, 124*f*
thrust front and crestal grabens, 75*f*
thrust front and oblique grabens, 75*f*
Elastic limit, 54
Elastic strain, 56, 73, 94, 121*f*
Electronic distance meter (EDM), 86*f*, 88, 114
En echelon fractures, 66, 66*f*, 68
Energetics, 4–5
Ephemeral features, 14
Equilibrium topography theory, 5*f*, 6
Erosion, 2, 27*f*, 229
base level of, 160
geomorphic markers and, 14
glaciers *versus* fluvial, 8
intermediate time scales and, 175

isostatic response to, 222, 222*f*
knickpoints, 160–164
magnitude, 197
over fault terminations, 110
rates, 131–151
river terrace, 22, 23
terrace surface analysis and, 183
uplift and, 156*f*
Erosional remnants, 28
Erosion rates, 131–151
bedrock incision, 142–143
conceptual framework, 133–134
definitions, 131–133
estimating approaches, 134, 134*f*
isotopic interpretations, 140–141, 141*f*
by landslides, 143–145, 145*f*
local *versus* regional, 132–133
radiometric ages and, 146–149
regolith production rates, 141–142
sedimentary fluxes in rivers, 134–137
slope dependence of, 197, 198*f*
stream power and, 163–164, 163*f*
structural/stratigraphic controls and, 137–139
topographically constrained, 139–140
Eustatic sea-level changes, 18, 93
Extensional ranges, 202–212
depositional geometries, 203–204
displacement gradients and fault linkage, 207–210
drainage basins, 205–208, 206*f*, 207*f*
facets and drainage spacing, 202–203, 203*f*
footwall uplift and crustal rigidity, 210–212
quantitative assessments, 204–205

F

Facets, drainage spacing and, 202–203, 203*f*
Fans. *See* Alluvial fans
Far-field geodetic measurements, 86, 96–101
global positioning systems (GPS), 85, 86*f*, 97–100
radar interferometry, 100–101
very long baseline interferometry (VLBI), 85, 86*f*, 96–97, 99*f*, 101
Fault-angle depressions, 69
Fault-bend folds, 78, 79*f*, 213
Fault-block mountains, drainages on, 203*f*
Fault-propagation fold, 78, 79*f*
Faults, 2, 54–55. *See also* Dip-slip faults; Normal faults; Strike-slip faults; Thrust faults
antithetic, 69, 70*f*
bending-moment, 76–77, 77*f*
blind, 77, 80*f*
flexural-slip, 76–77, 77*f*, 181–182, 183*f*
geomorphic expression of, 64–77
multiple, displacement compensation among, 63, 64*f*
numerical models of, 234*f*
overlapping, 207–208, 208*f*
overturned thrust, 77, 77*f*
radial propagation growth of, 60–62, 62*f*
range-front, 63–64
segment linkage, 62–63, 62*f*, 207–210, 211*f*
synthetic, 69, 70*f*, 71*f*
tear, 194–195
transfer, 69, 70*f*, 71*f*
Fault terminations, 110
Finisterre Range, Papua New Guinea, 154
Finite difference models, 232
Finite element (FE) models, 232
Fissure filling, 110, 110*f*
Flats, 78
Flexural-slip faults, 76–77, 77*f*
river terrace displacement, 181–182, 183*f*
Flexural wavelength, 236
Flexure (numerical) modeling, 236–237, 236*f*, 237*f*
Flow velocity, 165*f*
Fluvial channels. *See Rivers*
Fluvial terraces. *See River* terraces
Folds, 77–82. *See also* Growing folds
fluvial terrace deformation and, 181, 182*f*
lateral foldgrowth, 80–82
models of, 78–80, 79*f*
stream gradient changes and, 185, 187*f*
strike-slip faults and, 66
Footwalls, 54, 70*f*
normal fault, 69
thrust fault subsidence, 71, 73*f*
topographic models, 207–210
uplift, crustal rigidity and, 210–212, 212*f*
Foraminifera, 17
Fossil remains, 156
Freeze-thaw cycles, 5
Fringing reefs, 119, 120*f*
Frost cracking, 133

G

Garlock Fault, Calif.
displaced markers plot, 116*f*
displacement histogram, 116*f*
Geodesy, 85–103
far-field techniques, 86, 96–101
near-field techniques, 86–96
techniques, 86*f*
Geomorphic cycle theory, 5, 5*f*
Geomorphic erosion. *See* Erosion
Geomorphic markers, 1–2, 13–32
common problems with, 31
linear, 29–31
planar, 14–28
Glacial erosion modeling, 248
Glaciation
basin erosion rates, 135, 135*f*
isotopic record of, 17–20, 17*b*, 18*f*
mountain uplift and, 8
Global climate change, 156–157
Global positioning systems (GPS), 2, 86*f*, 97–100, 101–102
data collection duration and, 99–100
geodetic measurements and, 85
horizontal crustal strain in *S.* Calif. using, 99*f*
Landers earthquake, Calif. (1992), 100*f*
permanent, 98, 99
Goblet valleys, 202
Grabens, 69, 70*f*, 74, 75*f*, 76
fault-bounded, 206–207
Gravitational potential energy, 4
Great Lakes water-level records, 96
Greece, deformation studies, 173
Growing folds, 193–198, 199. *See also* Wheeler Ridge fold, Calif.
antecedent stream interactions with, 194, 194*f*
displacement transfer among, 214, 216*f*, 217*f*
drainage development, 214, 216
fluvial terraces on, 182
individual and multiple, 213, 214*f*, 214, 215*f*
marine terraces on, 179*f*
surface processes effects of, 196*t*
Growth strata, 78–79

H

Hack (John) theories, 5*f*, 6, 7, 7*f*
Hangingwalls, 54
erosion, 137–138, 138*f*
folding, 74, 213, 214*f*, 214
normal fault, 69, 70*f*
thrust fault uplift, 71
thrust fault variable flexure, 72–73, 73*f*
Hebgen Lake, Mont., earthquake (1959), 70–71, 72*f*, 172*f*
Hillslopes. *See also* Scarp degradation modeling; Slope angles

Hillslopes (*continued*)
diffusivities of, 176
numerical modeling, 238, 239*f*
stability of, 176
Himalayan foreland, Nepal
erosion rates in, 140–141
precise leveling measures of, 90–92, 91*f*
as steady state region, 219–220
Himalayan uplift. *See also* Tibetan Plateau
controls on, 222–223, 223*f*
digital elevation modeling of, 221–222, 222*f*
fault-related fold, 193*f*
stream-gradient indices and, 188–190, 189*f*
thrusting and normal faulting in, 151
Histograms, displacement, 116, 116*f*
Holocene deformation, landscape responses, 3, 159–174, 226–227
base-level lowering models, 162–164, 163*f*, 164*f*
base levels, 160
base-level uplift, 168–169, 170*f*
domal uplift models, 167–168, 167*f*
incremental river tilting, 169–170, 170*f*
knickpoints, 160–164
localized uplift, 168, 168*f*, 169*f*
river pattern changes, 164–173
slow *versus* abrupt tilting and, 170–172
stream-table experiments, 165–167
tectonically-perturbed rivers, 168–173
Horizontal movements measurements, 88, 97
Horsts, 69, 70*f*
Hotspots under continents, 224–228, 227*f*. *See also* Yellowstone hot spot categories, 226–227
Snake River Plain, 225–226
Huon Gulf seafloor marine terraces, 180
Huon Peninsula, New Guinea, 17–18, 19*f*, 179*f*
Hydrofracturing, 55–56

I

Indus River, Pakistan, 168, 170*f*, 172, 172*f*
bedrock incision along, 143, 144*f*
steady state development in, 220–221
Inertia, geomorphic, 159
Initial conditions, 233, 241–242
Interbasin transfer zones, 70*f*
Intermediate time scales deformation, 175–199
alluvial fans, 191–193
calibration techniques, 176–183
fluvial terraces deformation calibration, 180–183
growing folds, 193–198
landscape responses, 183–198
marine terraces, 176–180
stream-gradient indices, 186–190
stream gradients, 183–185, 185*f*
stream responses to regional tilting, 190–191, 191*f*
International Radio Interferometric Surveying (IRIS), 97
Interseismic deformation/displacement, 73, 74*f*, 85, 90
Interseismic interval, 56, 57, 57*f*
Island-braided stream pattern. *See* Braided streams
Isostatic adjustment, 70, 236
erosion and, 8, 9*f*
Isostatic equilibrium, 236
Isotopic record
erosion rates interpretations, 140–141
of glaciation, 17–20, 17*b*, 18*f*
paleoaltitude estimates and, 157, 158*f*

J

Japan, southwest coast
interseismic/coseismic deformation of, 95*f*, 96
oceanographic correction from, 93–94, 93*f*
relative sea-level change, coastal deformation, 94*f*
time-predictable uplift pattern, 119, 119*f*

K

Kabul River, Pakistan, 168–169, 170*f*
Kali Gandaki River, Nepal, 152, 153*f*
Kern County, Calif. earthquake (1952), 71, 73*f*, 74
Kinetic energy, 4
Kink bends, 78, 80
Knickpoints, 160–164
base-level lowering experiments, 161–162, 162*f*
development of, 161*f*
numerical experiments, 162–164, 163*f*, 164*f*

L

Lacustrine shorelines, 20–21, 21*f*
Lake Bonneville, Utah, 20, 21*f*, 51*f*, 240
Landers earthquake, Calif. (1992)
offset mapping discoveries after, 117–118, 117*f*
permanent GPS array and, 100, 100*f*
SAR interferogram, 101, 102*f*
Landscape development models, 5–8, 5*f*
Landslides, 2, 27–28, 143–145, 145*f*
numerical models of, 246
Lava flows, 27–28, 152–153
Leaf physiognomy, paleoaltitude estimates and, 156, 157
Lesser and reactivated Holocene faults, 226
Lesser late Pleistocene faults, 227
Lesser Tertiary faults, 227
Leveling-line surveys, 92, 102
Lichenometric dating, 37–38, 37*f*
rockfalls, 126–128, 126*f*, 128*f*
Linear geomorphic markers, 29–31
Linear valleys, 68–69, 68*f*
Lithostatic state of stress, 54
Lithostatic stress, 54
Local base level, 160
Lomo Prieta, Calif., earthquake, 60, 60*f*, 127*b*
Long Valley caldera, Calif., 169–170, 170*f*, 190
Los Angeles basin, Calif., 82, 137, 168, 169*f*
Los Gatos River, Calif., 92, 93*f*
Lost River Valley, Idaho, 36*f*. *See also* Borah Peak earthquake (1983)
Luminescence dating, 45–47, 46*f*

M

Major Holocene faults, 226–227
Major late Pleistocene faults, 227
Major Tertiary faults, 227
Man-made geomorphic markers, 30–31
Marine plants/animals zonations, 20
Marine terraces, 14–20, 176–180
abrupt offsets *versus* broad warping, 177–178
beach ridges, 20
corals and coralline algae, 15–17
cosmogenic radionuclide dating, 50–51
dating, 42, 44*f*
fission-crack dating, 178*f*
graphical matching technique, 177–179, 177*f*
on growing folds, 178–179, 179*f*
oxygen isotopic composition of sea water, 17–20
re-occupations, 178–179, 180*f*
seafloor, 180
survival problem, 179–180
uplift rates, 151
warped, 60, 60*f*, 177–178, 179*f*

Mark-III VLBI system, 96–97
Mattole River, Calif., 32*f*
McCall, Idaho, weathering rinds, 35*f*
Mean annual temperature, 156
Meandering streams
  sinuosity, 165, 165*f*
  slow *versus* abrupt tilting of, 170–172, 171*f*
  uplift effect, 166–167, 166*f*
Meander scars, 171, 172*f*
Mean elevation, 153
Mean surface uplift, 151, 153
Mechanical weathering, 133, 158
Mendocino triple junction, Calif., 184–185, 185*f*, 188, 188*f*, 190–191
Moine-thrust earthquakes, 60–61, 61*f*
Moment magnitudes, 106–107, 117
Monterey Bay, Calif., 88, 89*f*
Moraines, 29–30, 30*b*
  numerical modeling, 242–244
Mt. Lassen, Calif, weathering rinds, 35*f*
Mountain-range scale (numerical) models, 244–246
  interactive channels and hillslopes, 245–246
  landsliding rules, 246
  mountain range evolution, 246–247, 248*f*
  one-dimensional, 244, 245*f*
  two-dimensional, 244–245, 246*f*
Muir, John, 125

N

Nanga Parbat, Pakistan, 220–221, 221*f*
Nankai Trough earthquakes (1994, 1946), 93–94, 94*f*, 95*f*
NASA Crustal Dynamics Project, 97
Near-field geodetic measurements, 86–96
  alignment arrays, 86–88
  deformation styles, 86
  precise leveling, 90–92
  tide gauges, 92–96
  trilateration arrays, 88, 89*f*, 90
Nepal, Himalayan foreland. *See* Himalayan foreland, Nepal
New Madrid earthquakes (1811–1812), 184
Normal faults, 67, 67*f*, 69–71, 70*f*
  alluvial fans and, 192–193, 192*f*
  earthquake prediction and, 82
  linkage, 211*f*
  model of, 235*f*
  overlap zone, 208*f*
  quantitative assessments, 204–205
  rapid *versus* slow deformation after, 202–203, 202*f*
North America
  elastic thicknesses across, 237, 237*f*
  western, paleoaltitude estimates of, 157
Numerical modeling, 4, 9, 229, 231–249
  approaches, 232–233
  base-level lowering, 162–164, 163*f*, 164*f*
  building blocks, 233
  domal uplift, 167–168, 167*f*
  flexure, 236–237, 236*f*, 237*f*
  limitations and prospects, 247–249
  mountain-range scale, 244–246
  orogen-scale, 246–247
  rules, 233–239
  scarp degradation, 239–244
  surface processes, 237–239
  tectonic, 233–236, 234*f*

O

Observation (OB), 86*f*
Obsidian hydration, dating and, 35–36, 36*f*
Oceanographic corrections, tide-gauge data, 93
Offset fan, 69*f*
Offset features, 114–115
Offset streams. *See* Beheaded streams
Optically stimulated luminescence (OSL), 45–47, 46*f*
Otago, New Zealand, 214, 217*f*
Out-of-syncline thrusts, 76–77, 77*f*
Overturned thrust fault, 77, 77*f*
Owens River, Calif., 169–170, 170*f*, 171–172, 192*f*
Oxygen isotopes, as glaciation markers, 17–20, 17*b*

P

Paired river terraces, 25*f*
Paleoaltitude, 154*f*, 156–157
Paleodepth, 154*f*
Paleodose, luminescence dating, 45–46
Paleoelevations, 153–154
Paleoseismicity, 59, 116
Paleoseismology, 8–9, 105–129
  buried thrust faults, 128–129
  characteristic earthquake data, 59
  dip-slip faults, 129
  displaced geomorphologic features, 114–121
  indirect observations, 121–128
  moment magnitudes, 106–107
  river terrace riser trenches data, 181
  seismic moment, 106–107
  trenching, 107–114
Palimpsest landscapes, 114
Pamir Range, Afghan-Tazhikistan border, 172–173, 173*f*
Papua New Guinea, coseismic uplift in, 118–119, 118*f*, 119*f*, 218
Partial annealing zones (PAZ), 149, 150*f*
Partial bleach paleodose dating, 46, 47*f*
Pediments, erosional, 28
Penck (Walther) theories, 5–6, 5*f*, 7, 7*f*
Peneplains, erosional, 28
Perched boulders, 127*b*
Periodic earthquake model, 56, 57*f*
Piercing point, 13
Planar geomorphic markers, 14–28
  alluvial fans, 26–27
  deltas, 21–22
  erosional surfaces, 28
  lacustrine shorelines, 20–21
  lava flows, debris flow, and landslides, 27–28
  marine terraces, beaches, shorelines, 14–20
  river terraces, 22–26
Plants, paleoaltitude estimates and, 156
Pleistocene faults, 227
Ponding effects, 167, 169
Precise leveling, 90–92
Preservation potential over time, 13
Pre–steady-state mountains, 217–223
  controls on, 222–223
  development, 220, 220*f*, 221*f*
  indicators, 214*f*, 215*f*, 217–220
  isostatic response to erosion, 222, 222*f*
Process-response model, 7, 7*f*
Pull-apart basins, 67, 67*f*
Pulsed deformation model, 182

Q

Quaternary Geochronology (Noller), 33
Quaternary sea level, 17, 17*b*

R

Radar interferometry, 2, 100–101
Radial propagation fault growth, 62*f*
Radiocarbon dating, 40–42, 41*f*, 42*f*
  of Cascadian earthquakes, 122–123
  of desert varnish around boulder pedestals, 127*b*
  limitations, 176
  of river terraces, 143
  of trench strata, 107, 112

Radiometric ages, erosion rates and, 146–149
Radiometric dating systems, 147, 147*f*
Ramps, 78
Range-front faults segmentation, 63–64
Real sea-level, 18–19, 19*f*
Recurrence intervals, earthquake, 8, 117
Regenerative paleodose dating, 46, 47*f*
Regional sequences, geomorphic markers in, 31
Regolith, 141–142, 237–238
Reidel shears, 66
Relative dating methods, 33–38, 34*t*
  clast seismic velocity dating, 33–34, 34*f*
  lichenometry, 37–38, 37*f*, 38*f*
  obsidian hydration, 35–36, 36*f*
  soil development, 36–37, 36*f*
  weathering, 34–35, 35*f*
Relative erosion rates, 141, 141*f*
Relative motion measurement, 96–97
Relative sea-level, 18, 19*f*, 176–177
Relative uplift, 151
Relay ramps, 69, 70*f*, 71*f*
Releasing bends, 67, 67*f*
Releasing step-overs, 68
Reservoirs, fluvial erosion rates and, 135, 137
Response time, geomorphic system, 14
Restraining bends, 67, 67*f*
Restraining step-overs, 68
Reverse fault model, 235*f*
Rhizocarpon lichen, dating and, 37, 38*f*
Richter magnitude scale, 106–107
Ridge crests, 29
Rivers. *See also* Braided streams; Drainage basins; Meandering streams; Straight-channel rivers; Stream-gradient indices; Stream patterns; Stream power
  across growing folds, 193
  base-level uplift, 168–169, 170*f*
  channel initiation modeling, 238, 249
  classification, 165*f*
  critical power thresholds, 176
  equilibrium slopes of, 159
  erosion rates, 135*f*
  gradients, bedrock uplift and, 183–185, 185*f*, 186*f*, 187*f*
  growing folds and, 214, 216, 216*f*
  incision, climate variability and, 114–115
  incremental tilting, 169–170, 170*f*
  knickpoints, 160–164
  as linear geomorphic markers, 29
  localized uplift, 168, 168*f*, 169*f*
  pattern changes, 164–173
  reconstructed profiles of, 152–153
  regional tilting and, 190–191, 191*f*
  sedimentary fluxes in, 134–137, 136*t*
  slow *versus* abrupt tilting and, 170–172
  stream-gradient indices, 186–190
  stream-table experiments, 165–167
  strike-slip faults and, 68–69
  tectonically-perturbed examples, 168–173
  tectonic loading/erosional unloading and, 155
  valley ratio measurements, 205, 205*f*
River terraces, 22–26, 25*f*, 26*f*, 31
  assessment, 180–181, 181*f*
  bedrock incision rates, 142–143
  climate controls on, 199
  common problems with, 31, 32*f*
  cosmogenic radionuclide dating, 50–51
  deformation, 180–183
  diachronous, 22–26
  flexural-slip fault displacement, 183*f*
  folding experiments and, 167
  as geomorphic markers, 13
  hot spots under continents and, 227–228, 228*f*
  warped, 182–183, 182*f*
Rockfalls, 125–128
Rock uplift, 2, 151. *See also* Bedrock uplift; Uplift rates

S

Sag ponds, 68*f*, 69
Salt Range thrust, Pakistan, 137–138, 138*f*
San Andreas fault, Calif.
  geodetic measurements, 85
  GPS measurements, 98–99, 99*f*
  paleoseismology data, 113–114, 113*f*
  Parkfield asperity, 59
  Salton Trough features, 69*f*
  stream-gradient indices, 188*f*
  terrace formation, 25–26, 26*f*
  transpressional deformation, 224, 226*f*
  trilateration arrays, 88, 89*f*, 90
  VLBI, 97
  Wrightwood tree ring chronology, 125, 125*f*
San Antonio River, Tex., 168, 168*f*
San Gabriel Mountains, Calif., 188*f*, 224, 226*f*
Santa Cruz, Calif., 178, 224
SAR (synthetic aperture radar), 100–101
  interferogram, 101, 102*f*
Satellite laser ranging (SLR), 86*f*
Scarp degradation modeling, 239–244
  applications, 240–241
  complexities, 241–244
  initial conditions, 241–242
  nonuniform diffusivity, 242
  profile evolution, 240*f*
  theory, 239–240
  weathering-limited situations, 242–244
Seafloor marine terraces, 180
Sea level. *See also* Tide gauges
  displaced features and, 118
  local, 92–93
  Quaternary, isotropic record of, 17, 17*b*
  variations, 19*f*
Sedimentary fluxes in rivers, 134–137, 136*t*
Sediment size/load, 165*f*
Segment boundaries, 66*f*, 209–210, 211*f*
Seismic moment, 106–107, 116–117
Seismic shaking index, 127–128, 128*f*
Seismometers, 106
Sensitivity (amplitude of response), 14
Shadow zones, 63
Shutter ridges, 68*f*, 69, 69*f*, 223
Sierra Nevada, Calif., 38*f*, 156
Sinuosity
  mountain front assessments, 204–205, 205*f*, 228
  river, 165–166, 166*f*
Sinusoidal folds, 167–168, 167*f*
Slip deficits, 56*f*, 63, 65*f*, 209–210
Slip direction indicators, 110
Slip-predictable earthquake model, 57–58, 57*f*
Slip rates, 117
Slope angles, 197, 197*f*, 203–204, 204*f*. *See also* Hillslope stream patterns and changes in, 165–166, 166*f*
"Slow" earthquakes, 57
Snake River Plain hotspot, 226, 227*f*
Soils, dating, 36–37, 36*f*, 42–43
Solar energy, 4–5
Southern Alps, New Zealand, 144–145, 145*f*, 244–245
South Island, New Zealand, 128*f*, 157
South Tibetan Detachment Fault, 151
Specific stream power, 22
Spirit leveling, 92

Steady-state topography, 10–11, 10*f*, 217–223, 219*f*
development of, 220, 220*f*, 221*f*
documentation of, 219
isostatic response to erosion, 222, 222*f*
pre–steady state indicators, 214*f*, 215*f*, 217–220
thermochronology, 220
Step-overs, 67, 67*f*, 224
Straight-channel rivers, 164, 167–168, 167*f*, 172
Strains, 54–55
unrecoverable, 57
Strath terraces, 23–24, 25*f*
Stratigraphic record, 107–108, 109, 121–123. *See also* Trenching
dip-slip faults, 129
intermediate time scales and, 175
uplift evidence, 151–152, 152*f*
Stream-gradient indices, 186, 188*f*. *See also* Rivers
for landscape response definition, 187, 188
for potential tectonic activity zones identification, 187, 188–190
as reconnaissance tool, 187
Stream patterns. *See also* Rivers
across folds, 81, 193–198
changing slopes and, 165–166, 166*f*
interfering bedrock folds and, 217*f*
kink fold and, 166–167
Stream power, 22, 23*b*, 24*f*, 165*f*. *See also* Rivers
erosion rates and, 163, 163*f*
stream-gradient indices and, 186–190
uplifting folds and, 193–194
Stress, 53–54
fault orientations and, 54*f*
present-day directions, 55–56
Strike-slip faults, 54*f*, 55, 64–65, 66–69
deformation models for, 87*f*
displacement distances along, 116, 116*f*
earthquake model for, 56*f*
earthquake prediction and, 82
multiple splays, 112*f*
overview of, 68*f*
"salami slicing," 109
surface strands of, 112
trenches on, 108*f*, 112*f*
trilateration arrays and, 88
Strike-slip zones, 223–224
Structure contour maps, 114
Subduction-zone earthquakes, 121–123, 121*f*
Surface forces, 53
Surface processes (numerical) modeling, 7, 7*f*, 237–239
Surface uplift, 2, 131, 132, 151
rates, 153–156
Surface-wave magnitudes, 106
Surveying
geodetic measurements and, 86
GPS and, 98
precise leveling, 90
trilateration arrays, 88
Swedish Lapland lichen growth, 37*f*
Synthetic aperture radar (SAR), 100–101
interferogram, 101, 102*f*
Synthetic faults, 69, 70*f*, 71*f*

T

Tear faults, 194–195
Tectonic denudation, 132, 132*f*, 149–151
Tectonic (numerical) models, 233–236, 234*f*
Tectonic processes, 2
Tectonic uplift, 153–156, 156*f*
Temperature, mean annual, 156
Terrestrial settings, 114–118, 156
Tertiary faults, 227
Theodolites, 88, 114
Thermochronology, 220
Thermoluminescence (TL), 45–47, 46*f*, 112
Thorium dating, 42–44, 43*f*
Threshold of critical (river) power, 22, 24*f*
Threshold shear stress, 161
Thrust-fault ranges, 216–217
displacement transfer, 216*f*
drainage development, 214, 216, 217*f*
individual and multiple folds, 213, 214*f*, 214, 215*f*
Thrust faults, 54–55, 54*f*, 71–76
blind, folds and, 80–81, 80*f*
buried, 128–129
earthquake prediction and, 82
earthquakes, 60–61, 61*f*, 123
fluvial terrace treads offsets, 182–183, 182*f*
ramps, flats and folding, 78
strain models, 74*f*
strike-slip faults and, 66, 67, 67*f*
Tibetan Plateau, 156, 212, 212*f*, 219
scarp degradation modeling, 241, 241*f*
South Tibetan Detachment Fault, 151
Tide gauges, 92–94, 95*f*, 96, 102
oceanographic correction, 93*f*
relative sea-level change and, 94*f*
Tien Shan, Kyrgyztan, 27*f*, 28*f*, 218–220
bedrock fold growth, 214*f*, 214, 215*f*
displacement transfer between overlapping folds, 214, 216*f*
river terraces, 182–183, 182*f*, 184*f*
Time-predictable earthquake model, 57, 57*f*, 119
Time scales, 2–4, 3*f*
Topography, 114, 115*f*, 133
erosion rates and, 139–140, 139*f*
Tractions, 53
Transfer faults, 69, 70*f*, 71*f*
Transfer zones, 206–207
Transverse Ranges, Calif., 88, 89*f*, 97, 226*f*
Tree rings, 122, 123–125, 125*f*. *See also* Dendrochronology
Trenching, 107–114
colluvial wedges, 109*f*, 110, 111–112
dating techniques in, 112–113
fissure filling, 110, 110*f*
objectives, 107
orientation, 107–108
stratigraphic/structural relationships in, 109–110, 109*f*
on strike-slip fault, 108*f*
strike-slip fault with multiple splays, 112*f*
Trilateration arrays, 88, 89*f*, 90, 102
Trishear folds, 79*f*, 80
Trishear geometry, 79*f*
Tsunami deposits, 122, 123
Turakirae Head, New Zealand, 20*f*, 120–121, 120*f*

U

Unconformity surfaces, 28
Undeformed geometry, 13
Uniform-slip earthquakes, 59, 59*f*
Unit stream power, 22
Uplift rates, 151–157, 159–160
constant long-term, 119
marine terraces, 151
paleoaltitude estimates, 156–157
river profiles, 152–153
stratigraphic constraints, 151–152
tectonic and surface, 153–156
Uranium dating, 42–44, 43*f*, 176

V

Valley ratio measurements, 205, 205*f*
Variable-slip earthquakes, 59, 59*f*
Velocity, fault zone/block rigidities and, 87*f*
Ventura River, Calif., 181–182, 183*f*
Vertical movements, geodesic measurements of, 90, 92, 93, 102
with GPS, 97
tide-gauge data and, 96

Very long baseline interferometry (VLBI), 85, 86*f*, 96–97, 99*f*, 101
Volcanoes, continental, 224–228
  Snake River Plain, 225–226, 227*f*
V ratio. *See* Valley ratio measurements

W

Wairarapa fault, North Island, New Zealand, 29, 29*f*, 120, 120*f*
Wasatch Range, Utah, 63, 65*f*, 66*f*, 111*f*, 112
Water gaps, 81
Wave-cut benches, 20–21, 31
Wave-like tectonic forcing theory, 5–6, 5*f*
Weathering, 35*f*, 237
  limits, 237, 242–244
Weathering rinds, 34–35, 35*f*
Wedge thrusts, 194–195, 195*f*
Wellington fault, New Zealand, 181*f*
Wheeler Ridge fold, Calif., 81*f*, 195–196, 197, 197*f*, 198*f*
  eroded material calculation, 139*f*
  wedge thrust under, 194, 195*f*
Wind gaps, 81, 214, 217*f*
Wind River Range, Wyo., 140, 142
Wine glass valleys, 202
Working Group on California Earthquake Probabilities, 127*b*

Y

Yellowstone hot spot, 225–228, 228*f*
  fluvial terraces of, 227–228, 228*f*
  seismicity and faulting distribution, 227*f*
  topographic changes and subsidence along, 227*f*
Yield strength, 54

Z

ZSCAPE (numerical modeling tool), 246, 247*f*